

00731

UNITED STATES AIR FORCE
SUMMER RESEARCH PROGRAM -- 1992
SUMMER RESEARCH EXTENSION PROGRAM
FINAL REPORTS

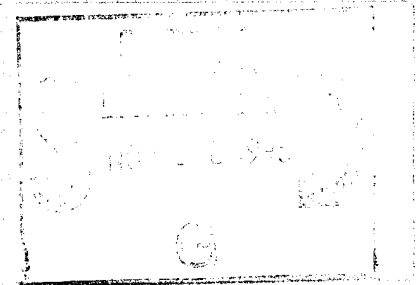
VOLUME 2

PHILLIPS LABORATORY

RESEARCH & DEVELOPMENT LABORATORIES

5800 UPLANDER WAY
CULVER CITY, CA 90230-6608

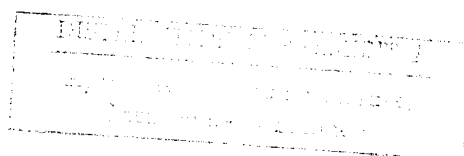
SUBMITTED TO:
LT. COL. CLAUDE CAVENDER
PROGRAM MANAGER



AIR FORCE OFFICE OF SCIENTIFIC RESEARCH

BOLLING AIR FORCE BASE
WASHINGTON, D.C.

MAY 1993



REPORT DOCUMENTATION PAGE

Form Approved
OMB No. 0704-0188

Public reporting burden for this collection of information is estimated to average 1 hour per response, including the time for reviewing instructions, searching existing data sources, gathering and maintaining the data needed, and completing and reviewing the collection of information. Send comments regarding this burden estimate or any other aspect of this collection of information, including suggestions for reducing this burden, to Washington Headquarters Services, Directorate for Information Operations and Reports, 1215 Jefferson Davis Highway, Suite 1204, Arlington, VA 22202-4302, and to the Office of Management and Budget, Paperwork Reduction Project (0704-0188), Washington, DC 20503.

1. AGENCY USE ONLY (Leave blank)

2. REPORT DATE
28 Dec 92

3. REPORT TYPE AND DATES COVERED

Annual 1 Sep 91 - 31 Aug 92

4. TITLE AND SUBTITLE

1992 Summer Faculty Research Program (SFRP)

Volume: 2 (SREP)

5. FUNDING NUMBERS

F49620-90-C-0076

6. AUTHOR(S)

Mr Gary Moore

7. PERFORMING ORGANIZATION NAME(S) AND ADDRESS(ES)

Research & Development Laboratoeis (RDL)
5800 Uplander Way
Culver City CA 90230-66008. PERFORMING ORGANIZATION
REPORT NUMBER

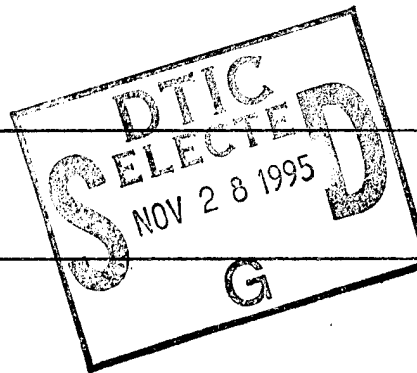
AFOSR-TR-95

9. SPONSORING/MONITORING AGENCY NAME(S) AND ADDRESS(ES)

AFOSR/NI
110 Duncan Ave., Suite B115
Bldg 410
Bolling AFB DC 20332-0001
Lt Col Claude Cavender

0736

11. SUPPLEMENTARY NOTES



12a. DISTRIBUTION/AVAILABILITY STATEMENT

UNLIMITED

12b. DISTRIBUTION CODE

13. ABSTRACT (Maximum 200 words)

The purpose of this program is to develop the basis for continuing research of interest to the Air Force at the institution of the faculty member; to stimulate continuing relations among faculty members and professional peers in the Air Force to enhance the research interests and capabilities of scientific and engineering educators; and to provide follow-on funding for research of particular promise that was started at an Air Force laboratory under the Summer Faculty Research Program.

During the summer of 1992 185 university faculty conducted research at Air Force laboratories for a period of 10 weeks. Each participant provided a report of their research, and these reports are consolidated into this annual report.

19951127 016

14. SUBJECT TERMS

15. NUMBER OF PAGES

16. PRICE OF COPY

17. SECURITY CLASSIFICATION
OF REPORT

UNCLASSIFIED

18. SECURITY CLASSIFICATION
OF THIS PAGE

UNCLASSIFIED

19. SECURITY CLASSIFICATION
OF ABSTRACT

UNCLASSIFIED

UL

20. DATE OF REPORT

UNITED STATES AIR FORCE
SUMMER RESEARCH PROGRAM -- 1992
SUMMER RESEARCH EXTENSION PROGRAM FINAL REPORTS

VOLUME 2

PHILLIPS LABORATORY

RESEARCH & DEVELOPMENT LABORATORIES

5800 Uplander Way
Culver City, CA 90230-6608

Program Director, RDL
Gary Moore

Program Manager, AFOSR
Lt. Col. Claude Cavender

Program Manager, RDL
Scott Licoscas

Program Administrator, RDL
Gwendolyn Smith

Submitted to:

AIR FORCE OFFICE OF SCIENTIFIC RESEARCH

Bolling Air Force Base

Washington, D.C.

May 1993

DTIC QUALITY INSPECTED 5

PREFACE

This volume is part of a five-volume set that summarizes the research of participants in the 1992 AFOSR Summer Research Extension Program (SREP). The current volume, Volume 2 of 5, presents the final reports of SREP participants at Phillips Laboratory.

Reports presented in this volume are arranged alphabetically by author and are numbered consecutively -- e.g., 1-1, 1-2, 1-3; 2-1, 2-2, 2-3, with each series of reports preceded by a 22-page management summary. Reports in the five-volume set are organized as follows:

VOLUME

TITLE

- | | |
|----|--|
| 1A | Armstrong Laboratory (part one) |
| 1B | Armstrong Laboratory (part two) |
| 2 | Phillips Laboratory |
| 3 | Rome Laboratory |
| 4A | Wright Laboratory (part one) |
| 4B | Wright Laboratory (part two) |
| 5 | Air Force Civil Engineering Laboratory, Arnold Engineering Development Center,
Frank J. Seiler Research Laboratory, Wilford Hall Medical Center |

Accession For	
NTIS	CRA&I <input checked="" type="checkbox"/>
DTIC	TAB <input type="checkbox"/>
Unannounced <input type="checkbox"/>	
Justification _____	
By _____	
Distribution / _____	
Availability Codes	
Dist	Avail and/or Special
A-1	

1992 SUMMER RESEARCH EXTENSION PROGRAM FINAL REPORTS

1992 Summer Research Extension Program Management Report INTRODUCTION - 1

Phillips Laboratory

<u>Report Number</u>	<u>Report Title</u>	<u>Author</u>
1	Heterodyne Laser Speckle Imaging through Atmosphere	Richard Anderson
2	Numerical Studies of Inversion Problems Arising in Lidar Measurements	Frank P. Battles
3	Rates and Scaling Rules for Vibrational Relaxation of OH(n) in Collisions with Atmospheric Constituents	Ronald J. Bieniek
4	Dispersion Effects in Fiberoptic Interferometry	Douglas A. Christensen
5	Vibration Suppression of the ASTREX Structure During Slewing Maneuvers	Ephraim Garcia
6	The Development and Use of Digital Geographic Information within the Advanced Research Initiative for Simulation and Tactical Aids (ARISTA)	William L. Hamilton
7	Modeling of Liquid Jet Atomization Processes	Stephen D. Heister
8	Scanning Tunneling Microscopy (STM) and Atomic Force Microscopy (AFM) and Synchrotron Radiation Work for the Development of a New Detector	R. W. Hoffman
9	Model Reduction and Control of ASTREX	Ashok Iyer
10	Theoretical Study Concerning Instabilities Excited in the Ionosphere by the Obliquely Transmitting Powerful Radio Waves	S. P. Kuo
11	Studies of Broad-Band Optical Absorbers for Solar-Powered Rocket Systems	Peter W. Langhoff
12	Radiative Energy Transfer in Wave Optics	Arvind S. Marathay
13	Improvised Passive Damping in Composite Tubes Used in Large Space Structures	Christopher A. Rotz
14	Chemical and Structural Effects Caused by Hypervelocity Impacts to Polysulfone Graphite Reinforced Composite and Its Resin	Jon H. Shively
15	End Point Trajectory Control of Elastic Multi-Body System	Sahjendra N. Singh
16	Nuclear and Plasma Physics with Antiprotons	Gerald A. Smith
17	Spectroscopic Parameters of Oxygen for Atmospheric Modeling	R. H. Tipping
18	Experimental Investigation of Homogeneous and Heterogeneous Nucleation/Condensation Processes and Products in Coil	Philip D. Whitefield

1992 SUMMER RESEARCH EXTENSION PROGRAM (SREP) MANAGEMENT REPORT

1.0 BACKGROUND

Under the provisions of Air Force Office of Scientific Research (AFOSR) contract F49620-90-C-0076, September 1990, Research & Development Laboratories (RDL), an 8(a) contractor in Culver City, CA, manages AFOSR's Summer Research Program. This report is issued in partial fulfillment of that contract (CLIN 0003AC).

The name of this program was changed during this year's period of performance. For that reason, participants' cover sheets are captioned "Research Initiation Program" (RIP), while the covers of the comprehensive volumes are titled "Summer Research Extension Program" (SREP). The program's sponsor, the Air Force Office of Scientific Research (AFOSR), changed the name to differentiate this program from another which also bore its original name.

Apart from this name change, however, the program remained as it has been since its initiation as the Mini-Grant Program in 1983. The SREP is one of four programs AFOSR manages under the Summer Research Program. The Summer Faculty Research Program (SFRP) and the Graduate Student Research Program (GSRP) place college-level research associates in Air Force research laboratories around the United States for 8 to 12 weeks of research with Air Force scientists. The High School Apprenticeship Program (HSAP) is the fourth element of the Summer Research Program, allowing promising mathematics and science students to spend two months of their summer vacations at Air Force laboratories within commuting distance from their homes.

SFRP associates and exceptional GSRP associates are encouraged, at the end of their summer tours, to write proposals to extend their summer research during the following calendar year at their home institutions. AFOSR provides funds adequate to pay for 75 SREP subcontracts. In addition, AFOSR has traditionally provided further funding, when available, to pay for additional SREP proposals, including those submitted by associates from Historically Black Colleges and Universities (HBCUs) and Minority Institutions (MIs). Finally, laboratories may transfer internal funds to AFOSR to fund additional SREPs. Ultimately the laboratories inform RDL of their SREP choices, RDL gets AFOSR approval, and RDL forwards a subcontract to the institution where the SREP associate is employed. The subcontract (see Attachment 1 for a sample) cites the SREP associate as the principal investigator and requires submission of a report at the end of the subcontract period.

Institutions are encouraged to share costs of the SREP research, and many do so. The most common cost-sharing arrangement is reduction in the overhead, fringes, or administrative charges institutions would normally add on to the principal investigator's or research associate's labor. Some institutions also provide other support (e.g., computer run time, administrative assistance, facilities and equipment or research assistants) at reduced or no cost.

When RDL receives the signed subcontract, we fund the effort initially by providing 90% of the subcontract amount to the institution (normally \$18,000 for a \$20,000 SREP). When we receive the end-of-research report, we evaluate it administratively and send a copy to the laboratory for a technical evaluation. When the laboratory notifies us the SREP report is acceptable, we release the remaining funds to the institution.

2.0 THE 1992 SREP PROGRAM

SELECTION DATA: In the summer of 1991, 170 faculty members (SFRP associates) and 142 graduate students (GSRP associates) participated in the summer program. Of those, 147 SFRPs and 10 GSRPs submitted SREP proposals; 88 SFRP SREPs and 7 GSRP SREPs were selected for funding (total: 95).

	Summer 1991 Participants	Submitted SREP Proposals	SREPs Funded
SFRP	170	147	88
GSRP	142	10	7

The funding was provided as follows:

Contractual slots funded by AFOSR	75
Laboratory-funded	13
Additional funding from AFOSR	<u>7</u>
Total	95

Seven HBCU/MI associates from the 1991 summer program submitted SREP proposals; five were selected (one was lab-funded; four were funded by additional AFOSR funds).

By laboratory, the applications submitted and selected show in the following table:

	Applied	Selected
Air Force Civil Engineering Laboratory	6	4
Armstrong Laboratory	34	20
Arnold Engineering Development Center	12	2
Frank J. Seiler Research Laboratory	5	3
Phillips Laboratory	30	18
Rome Laboratory	16	11
Wilford Hall Medical Center	1	1
Wright Laboratory	53	36
TOTAL	157	95

Note: Phillips Laboratory funded 2 SREPs; Wright Laboratory funded 11; and AFOSR funded 7 beyond its contractual 75.

ADMINISTRATIVE EVALUATION: The administrative quality of the SREP associates' final reports was satisfactory. Most complied with the formatting and other instructions RDL provided to them. In the final days of December 1992 and in the first two months of 1993, several associates called and requested no-cost extensions of up to six months. After consultation with our AFOSR Contracting Officer's Representative, RDL approved the requests but asked that all such associates provide an interim report to be included in this volume. That caused an AFOSR-approved delay beyond the 1 April 1993 submission of this report. The subcontracts were funded by \$1,893,616 of Air Force money. Institutions' cost sharing amounted to \$948,686.

TECHNICAL EVALUATION: The form we used to gather data for technical evaluation and the technical evaluations of the SREP reports are provided as Attachment 2. This summary evaluation is shown by SREP number. The average rating range was from 3.1 to 5.0. The overall average for those evaluated was 4.6 out of 5.00. The three rating factors with the highest average scores were:

- o The USAF should continue to pursue the research in this RIP report.
- o The money spent on this RIP report was well worth it.
- o I'll be eager to be a focal point for summer and RIP associates in the future.

Thus it is clear that the laboratories place a high value on AFOSR's Summer Research Program: SFRP, GSRP, and SREP.

3.0 SUBCONTRACTS SUMMARY

Table 1 lists contractually required information on each SREP subcontract. The individual reports are published in volumes as follows:

<u>Laboratory</u>	<u>Volume</u>
Air Force Civil Engineering Laboratory	5
Armstrong Laboratory	1
Arnold Engineering Development Center	5
Frank J. Seiler Research Laboratory	5
Phillips Laboratory	2
Rome Laboratory	3
Wilford Hall Medical Center	5
Wright Laboratory	4

TABLE 1: SUBCONTRACTS SUMMARY

Researcher's name	Highest Subcontract Degree	Number	Duration
Institution	Department		
Location	Amount		Sharing
Abbott, Ben A Vanderbilt University Nashville, TN 37235	MS	135	01/01/92-12/31/92 Dept of Electrical Engineering 19966.00 0.00
Acharya, Raj State University of New York, Buffalo Buffalo, NY 14260	PhD	151	01/01/92-12/31/92 Dept of Electrical & Comp Engrg 20000.00 0.00
Adams, Christopher M Oklahoma State University Stillwater, OK 74078	PhD	68	01/01/92-12/31/92 Dept of Chemistry 20000.00 0.00
Anderson, Richard A University of Missouri, Rolla Rolla, MO 65401	PhD	50	01/01/92-12/31/92 Dept of Physics 20000.00 5000.00
Arora, Vijay K Wilkes University Wilkes-Barre, PA 18766	PhD	3	10/01/91-09/30/92 Dept of Electrical & Comp Engrg 19996.00 36208.00
Ball, William P Duke University Durham, NC 27706	PhD	71	01/01/92-12/31/92 Dept of Civil & Environmental Eng 20000.00 26747.00
Battles, Frank P Massachusetts Maritime Academy Buzzard's Bay, MA 025321803	PhD	152	01/01/92-12/31/92 Dept of Basic Sciences 20000.00 22000.00
Bieniek, Ronald J University of Missouri, Rolla Rolla, MO 65401	PhD	147	01/01/92-12/31/92 Dept of Physics 19945.00 4000.00
Blystone, Robert V Trinity University San Antonio, TX 78212	PhD	127	01/01/92-12/31/92 Dept of Biology 20000.00 14783.00
Cha, Soyoung S University of Illinois, Chicago Chicago, IL 60680	PhD	011	01/01/92-12/31/92 Dept of Mechanical Engineering 20000.00 3842.00
Chandra, D. V. Satish Kansas State University Manhattan, KS 66506	PhD	89	01/18/92-10/17/92 Dept of Electrical Engineering 20000.00 11170.00
Chenette, Eugene R University of Florida Gainesville, FL 32611	PhD	106	01/01/92-12/31/92 Dept of Electrical Engineering 20000.00 0.00
Christensen, Douglas A University of Utah Salt Lake City, UT 84112	PhD	83	01/01/92-12/31/92 Dept of Electrical Engineering 19999.00 5000.00

Chubb, Gerald P Ohio State University Columbus, OH 43235	PhD 26 Dept of Aviation 20000.00	01/01/92-12/31/92 7600.00
Courter, Robert W Louisiana State University Baton Rouge, LA 70803	PhD 8 Dept of Mechanical Engineering 20000.00	10/01/91-09/30/92 445.00
Dey, Pradip P Hampton University Hampton, VA 23668	PhD 120 Computer Science Department 19921.00	01/01/92-12/31/92 0.00
Draut, Arthur W Embry Riddle Aeronautical University Prescott, AZ 86301	PhD 133 Computer Science Dept 19431.00	01/06/92-05/08/92 0.00
Dreisbach, Joseph University of Scranton Scranton, PA 185104626	PhD 108 Dept of Chemistry 20000.00	12/01/91-12/01/92 4000.00
Dror, Itiel Harvard University Cambridge, MA 02138	BS 76 Dept of Psychology 20000.00	01/01/92-12/31/92 0.00
Drost-Hansen, W. University of Miami Coral Gables, FL 33124	PhD 124 Dept of Chemistry 20000.00	12/01/91-12/01/92 12000.00
Dunleavy, Lawrence P University of South Florida Tampa, FL 33620	PhD 41 Dept of Electrical Engineering 20000.00	01/01/92-12/31/92 6463.00
Evans, Joseph B University of Kansas Lawrence, KS 66045	PhD 96 Dept of Electrical & Comp Engrg 20000.00	01/01/92-12/31/92 0.00
Flowers, George T Auburn University Auburn, AL 368495341	PhD 73 Dept of Mechanical Engineering 19986.00	01/01/92-12/30/92 12121.00
Gantenbein, Rex E University of Wyoming Laramie, WY 82071	PhD 22 Dept of Computer Science 20000.00	01/01/91-12/31/92 26643.00
Garcia, Ephrarim Vanderbilt University Nashville, TN 37235	PhD 32 Dept of Mechanical Engineering 20000.00	12/01/91-11/30/92 9659.00
German, Fred J Auburn University Auburn University, AL 36830	PhD 49 Dept of Electrical Engineering 20000.00	01/01/92-12/31/92 0.00
Gould, Richard D North Carolina State University Raleigh, NC 276957910	PhD 87 Dept of Mech and Aerospace Engrg 20000.00	01/01/92-12/31/92 14424.00
Gove, Randy L University of Alabama, Huntsville Huntsville, AL 35899	MS 122 Dept of Physics 20000.00	01/01/92-12/31/92 3469.00
Grabowski, Marek University of Colorado, Colorado Springs Colorado Springs, CO 809337150	PhD 92 Dept of Physics 19700.00	01/01/92-12/31/92 0.00

Gunaratne, Manjriker University of South Florida Tampa, FL 33620	PhD 90 Dept of Civil Engrg & Mechanics 19994.00	01/01/92-12/31/92 10062.00
Hall, Ernest L University of Cincinnati Cincinnati, OH 452210072	PhD 134 Dept of Robotics Research 19975.00	01/01/92-12/31/92 0.00
Hamilton, William L Salem State College Salem, MA 01970	PhD 47 Dept of Geography 20000.00	01/01/92-12/31/92 32000.00
Hamilton, Kirk L Xavier University of Louisiana New Orleans, LA 70125	PhD 57 Dept of Biology 20000.00	01/01/92-12/31/92 16100.00
Harris, Harold H University of Missouri, St. Louis St. Louis, MO 63121	PhD 94 Dept of Chemistry 19300.00	01/01/92-12/31/92 8600.00
Hartung, George H University of Hawaii Honolulu, HI 96822	PhD 46 Dept of Physiology 20000.00	01/01/92-12/31/92 7530.00
Hatfield, Steven L University of Kentucky Lexington, KY 40506	BS 23 Dept of Materials Science & Engrg 20000.00	01/01/92-12/31/92 28625.00
Hedman, Paul O'Dell Brigham Young University Provo, UT 84602	PhD 17 Dept of Chemical Engineering 19999.00	01/01/92-12/31/92 6928.00
Heister, Stephen D Purdue University West Lafayette, IN 47907	PhD 5 School of Aero & Astronautics 20000.00	01/01/92-12/31/92 4419.00
Hess, David J University of Texas, Austin Austin, TX 78713	BA 149 Dept of Psychology 19914.00	01/01/92-12/31/92 8784.00
Hoffman, R. W Case Western Reserve University Cleveland, OH 44106	PhD 99 Dept of Physics 19770.00	01/01/92-12/31/92 0.00
Huerta, Manuel A University of Miami Coral Gables, FL 33124	PhD 62 Dept of Physics 20000.00	01/01/92-12/31/92 1207.00
Hui, David University of New Orleans New Orleans, LA 70148	PhD 116 Dept of Mechanical Engineering 20000.00	01/01/92-12/31/92 0.00
Iyer, Ashok University of Nevada, Las Vegas Las Vegas, NV 89154	PhD 74 Dept of Electrical & Comp Engrg 20000.00	01/01/92-12/31/92 18549.00
Khonsari, Michael M University of Pittsburgh Pittsburgh, PA 15260	PhD 53 Dept of Mechanical Engineering 20000.00	01/01/92-12/31/92 32958.00
Kibert, Charles J University of Florida Gainesville, FL 32611	PhD 2 Dept of Fire Testing & Research 20000.00	01/01/92-12/31/92 6928.00

Klarup, Douglas G University of Montana Missoula, MT 59812	PhD 84 Dept of Chemistry 20000.00	01/01/92-12/31/92 0.00
Koblasz, Arthur J Georgia Institute of Technology Atlanta, GA 30332	PhD 145 Dept of Civil Engineering 19956.00	01/01/92-09/30/92 0.00
Kornreich, Philipp Syracuse University Syracuse, NY 13244	PhD 35 Dept of Electrical & Comp Engrg 20000.00	10/01/91-09/30/92 0.00
Kuo, Spencer P Polytechnic University Farmingdale, NY 11735	PhD 59 Dept of Electrical Engineering 20000.00	01/01/92-12/31/92 9916.00
Langhoff, Peter W Indiana University Bloomington, IN 47402	PhD 115 Dept of Chemistry 20000.00	01/01/92-12/31/92 35407.00
Lee, Byung-Lip Pennsylvania State University University Park, PA 16802	PhD 93 Dept of Engrg Science & Mechanics 20000.00	01/01/92-12/31/92 8173.00
Leigh, Wallace B Alfred University Alfred, NY 14802	PhD 118 Dept of Electrical Engineering 19767.00	01/01/92-12/31/92 18770.00
Liddy, Elizabeth Syracuse University Syracuse, NY 132444100	PhD 104 Dept of Information Studies 20000.00	01/01/92-12/31/92 0.00
Liu, Cheng University of North Carolina, Charlotte Charlotte, NC 28270	PhD 6 Dept of Engineering Technology 20000.00	11/01/99-12/31/92 0.00
Main, Robert G California State University, Chico Chico, CA 959290504	PhD 28 Dept of Communication Design 20000.00	01/01/92-06/30/92 7672.00
Mains, Gilbert J Oklahoma State University Stillwater, OK 74078	PhD 52 Dept of Chemistry 19071.00	01/01/92-12/31/92 8746.00
Marathay, Arvind S University of Arizona Tucson, AZ 85721	PhD 51 Dept of Optical Sciences 20000.00	01/01/92-12/31/92 0.00
Martin, Charlesworth R Norfolk State University Norfolk, VA 23504	PhD 125 Dept of Physics & Engineering 20000.00	01/01/92-12/31/92 0.00
Mayes, Jessica L University of Kentucky Lexington, KY 405034203	BS 16 Dept of Material Science & Engrng 20000.00	01/01/92-12/31/92 28625.00
Mulligan, Benjamin E University of Georgia Athens, GA 30602	PhD 54 Dept of Psychology 19895.00	01/01/92-12/31/92 13677.00
Munday, Edgar G University of North Carolina, Charlotte Charlotte, NC 28223	PhD 38 Dept of Mechanical Engineering 20000.00	10/01/91-10/30/92 11638.00

Nurre, Joseph H Ohio University Athens, OH 45701	PhD 56 Dept of Electrical & Comp Engrg 19842.00	01/01/92-12/31/92 15135.00
Orkwis, Paul D University of Cincinnati Cincinnati, OH 452210070	PhD 14 Dept of Engineering Mechanics 19966.00	10/01/91-10/30/92 23017.00
Patra, Amit L University of Puerto Rico Mayaguez, PR 00681	PhD 69 Dept of General Engineering 20000.00	01/01/92-12/31/92 2750.00
Peters II, Richard A Vanderbilt University Nashville, TN 37235	PhD 160 Dept of Electrical Engineering 20000.00	01/01/92-12/31/92 0.00
Pollack, Steven K University of Cincinnati Cincinnati, OH 452200012	PhD 31 Dept of Materials Sci & Engrg 20000.00	01/01/92-12/31/92 14877.00
Prescott, Glenn E University of Kansas Lawrence, KS 66045	PhD 72 Dept of Electrical Engineering 20000.00	01/01/92-12/31/92 8000.00
Price, James L University of Iowa Iowa City, IA 52242	PhD 48 Dept of Sociology 20000.00	01/01/92-12/30/92 8600.00
Qazi, Salahuddin SUNY, Utica Utica, NY 13504	PhD 129 Dept of Electrical Engineering 20000.00	01/01/92-12/31/92 25000.00
Rappaport, Carey M Northeastern University Boston, MA 02115	PhD 58 Dept of Electrical & Comp Engrng 19999.00	01/01/92-06/30/92 0.00
Rawson, Jenny L North Dakota State University Fargo, ND 58105	PhD 144 Dept of Electrical Engineering 19997.00	01/01/92-12/31/92 19826.00
Riccio, Gary E University of Illinois, Urbana Urbana, IL 61821	PhD 80 Dept of Human Perception 20000.00	01/01/92-12/31/92 0.00
Rotz, Christopher A Brigham Young University Provo, UT 84602	PhD 136 Dept of Manufacturing Engineering 20000.00	12/01/91-12/31/92 11814.00
Schwartz, Martin University of North Texas Denton, TX 762035068	PhD 55 Dept of Chemistry 20000.00	01/01/92-12/31/92 18918.00
Senseman, David M University of Texas, San Antonio San Antonio, TX 78285	PhD 77 Dept of Information 20000.00	12/01/91-11/30/92 19935.00
Sensiper, Martin University of Central Florida Orlando, FL 32816	BS 15 Dept of Electrical Engineering 20000.00	11/01/91-05/31/92 0.00
Shamma, Jeff S University of Texas, Austin Austin, TX 78713	PhD 70 Dept of Electrical Engineering 20000.00	01/01/92-12/31/92 0.00

Shively, Jon H California State University, Northridge Northridge, CA 91330	PhD 140 Dept of CIAM 20000.00	01/01/92-12/31/92 14553.00
Singh, Sahjendra N University of Nevada, Las Vegas Las Vegas, NV 89014	PhD 79 Dept of Electrical Engineering 20000.00	01/01/92-12/31/92 20595.00
Smith, Gerald A Pennsylvania State University University Park, PA 16802	PhD 63 Dept of Physics 20000.00	07/01/92-07/01/93 0.00
Stephens, Benjamin R Clemson University Clemson, SC 29634	PhD 114 Dept of Psycology 19988.00	01/01/92-12/31/92 4250.00
Sudkamp, Thomas Wright State University Dayton, OH 45435	PhD 97 Dept of Computer Science 20000.00	01/01/92-08/31/92 18739.00
Sydor, Michael University of Minnesota, Duluth Duluth, MN 55804	PhD 11 Dept of Physics 20000.00	01/01/92-12/31/92 0.00
Tankin, Richard S Northwestern University Evanston, IL 60208	PhD 44 Dept of Mechanical Engineering 20000.00	01/01/92-12/31/92 29103.00
Taylor, Michael D University of Central Florida Orlando, FL 32816	PhD 141 Dept of Mathematics 20000.00	05/01/92-07/31/92 1587.00
Teegarden, Kenneth J University of Rochester Rochester, NY 14627	PhD 98 Dept of Optics 20250.00	01/01/92-12/31/92 60600.00
Tew, Jeffrey D Virginia Polytech Instit and State Univ Blacksburg, VA 24061	PhD 137 Dept of Industrial Engineering 17008.00	03/01/92-09/30/92 4564.00
Tipping, Richard H University of Alabama Tuscaloosa, AL 35487	PhD 81 Dept of Physics & Astronomy 20000.00	01/01/92-05/31/92 15000.00
Tripathi, Ram C University of Texas, San Antonio San Antonio, TX 78249	PhD 105 Dept of Mathematics 20000.00	01/01/92-12/31/92 2274.00
Wells, Fred V Idaho State University Pocatello, ID 83209	PhD 155 Dept of Chemistry 20000.00	01/01/92-12/31/92 8000.00
Whitefield, Phillip D University of Missouri, Rolla Rolla, MO 65401	PhD 25 Dept of Chemistry 19991.00	01/01/92-12/31/92 25448.00
Wolfenstine, Jeffrey B University California, Irvine Irvine, CA 92717	PhD 18 Dept of Mechanical Engineering 20000.00	01/01/92-12/31/92 11485.00
Wolper, James S Idaho State University Pocatello, ID 83209	PhD 138 Dept of Mathematics 20000.00	01/15/92-09/30/92 4828.00

Zavodney, Lawrence D
Ohio State University
Columbus, OH 43210

PhD 148 01/01/92-12/31/92
Dept of Engineering Mechanics
20000.00 0.00

Zimmerman, Wayne J
Texas Women University
Denton, TX 76204

PhD 111 01/01/92-12/31/92
Dept of Mathematics
19990.00 8900.00

ATTACHMENT 1:
SAMPLE SREP SUBCONTRACT

**AIR FORCE OFFICE OF SCIENTIFIC RESEARCH
1993 SUMMER RESEARCH EXTENSION PROGRAM SUBCONTRACT 93-36**

BETWEEN

**Research & Development Laboratories
5800 Uplander Way
Culver City, CA 90230-6608**

AND

**University of Delaware
Sponsored Programs Admin.
Newark, DE 19716**

**REFERENCE: Summer Research Extension Program Proposal 93-36
Start Date: 01/01/93 End Date: 12/31/93
Proposal amount: \$20000.00**

- (1) PRINCIPAL INVESTIGATOR: Dr. Ian W. Hall
Materials Science
University of Delaware
Newark, DE 19716**
- (2) UNITED STATES AFOSR CONTRACT NUMBER: F49620-90-C-09076**
- (3) CATALOG OF FEDERAL DOMESTIC ASSISTANCE NUMBER (CFDA): 12.800
PROJECT TITLE: AIR FORCE DEFENSE RESEARCH SOURCES PROGRAM**
- (4) ATTACHMENTS 1 AND 2: SREP REPORT INSTRUCTIONS**

***** SIGN SREP SUBCONTRACT AND RETURN TO RDL *****

1. BACKGROUND: Research & Development Laboratories (RDL) is under contract (F49620-90-C-0076) to the United States Air Force to administer the Summer Research Programs (SRP), sponsored by the Air Force Office of Scientific Research (AFOSR), Bolling Air Force Base, D.C. Under the SRP, a selected number of college faculty members and graduate students spend part of the summer conducting research in Air Force laboratories. After completion of the summer tour participants may submit, through their home institutions, proposals for follow-on research. The follow-on research is known as the Research Initiation Program (RIP). Approximately 75 RIP proposals annually will be selected by the Air Force for funding of up to \$20,000; shared funding by the academic institution is encouraged. RIP efforts selected for funding are administered by RDL through subcontracts with the institutions. This subcontract represents such an agreement between RDL and the institution designated in Section 5 below.
2. RDL PAYMENTS: RDL will provide the following payments to RIP institutions:
 - 90 percent of the negotiated RIP dollar amount at the start of the RIP Research period.
 - the remainder of the funds within 30 days after receipt at RDL of the acceptable written final report for the RIP research.
3. INSTITUTION'S RESPONSIBILITIES: As a subcontractor to RDL, the institution designated on the title page will:
 - a. Assure that the research performed and the resources utilized adhere to those defined in the RIP proposal.
 - b. Provide the level and amounts of institutional support specified in the RIP proposal.
 - c. Notify RDL as soon as possible, but not later than 30 days, of any changes in 3a or 3b above, or any change to the assignment or amount of participation of the Principal Investigator designated on the title page.
 - d. Assure that the research is completed and the final report is delivered to RDL not later than twelve months from the effective date of this subcontract. The effective date of the subcontract is one week after the date that the institution's contracting representative signs this subcontract, but no later than January 15, 1992.
 - e. Assure that the final report is submitted in the format shown in Attachment 1.

- f. Agree that any release of information relating to this subcontract (news releases, articles, manuscripts, brochures, advertisements, still and motion pictures, speeches, trade association meetings, symposia, etc.) will include a statement that the project or effort depicted was or is sponsored by: Air Force Office of Scientific Research, Bolling AFB, D.C.
 - g. Notify RDL of inventions or patents claimed as the result of this research in a format specified in Attachment 1.
 - h. RDL is required by the prime contract to flow down patent rights and technical data requirements in this subcontract. Attachment 2 to this subcontract contains a list of contract clauses incorporated by reference in the prime contract.
4. All notices to RDL shall be addressed to:
- RDL Summer Research Program Office
5800 Uplander Way
Culver City, CA 90230-6608
5. By their signatures below, the parties agree to the provisions of this subcontract.

Abe S. Sopher
RDL Contracts Manager

Date

Signature of Institution Contracting Official

Typed/Printed Name

Title

Institution

Date/Phone

Attachment 1
Final Report Format

1. All RIP Principal Investigators will submit a final report of the research conducted.
2. One copy of the report is due to RDL no later than twelve months after the effective date of the RIP subcontract. At the same time, submit one copy to the Air Force laboratory focal point.
3. The title page should contain the title of the research, the Principal Investigator and or other co-investigators, the month and year of issue, the university with department and address, and acknowledgement of sponsorship by AFOSR (see clause 3f of this subcontract).
4. For text, use a font that is 12 characters per inch (elite) and as close to letter quality as possible. Start with the title in all caps one and one-half inches from the top of the first page; if the title requires two or more lines, single space it. Double space below the title, and then center and type the researcher's title and name. Then space twice and begin the double-spaced text.

Use a one-and-one-half-inch left margin and a one-inch right margin for the body of the text. Center page numbers at the foot of each page, one inch from the bottom. Each page should have a one-inch margin at the top. The format should be that of a standard research paper: it should begin with a one-paragraph abstract (on its own page) summarizing your work and should be followed by an introduction, a discussion of the problem, a results section, and a conclusion. Since multiple copies of your report may be required, assure that all pages can be readily copied to a black-and-white 8 1/2" by 11" page. (No colors, such as blue or green, that don't photocopy well, and no foldouts, please.)

5. The report must be accompanied by a separate statement on whether or not any inventions or patents have resulted from this research. If yes, use a DD Form 882 (supplied by RDL on request) to indicate the patent filing date, serial number, title, and a copy of the patent application, and patent number and issue date for any subject invention in any country in which the subcontractor has applied for patents.

Attachment 2
Contract Clauses

This contract incorporates by reference the following clauses of the Federal Acquisition Regulations (FAR), with the same force and effect as if they were given in full text. Upon request, the Contracting Officer or RDL will make their full text available (FAR 52.252-2).

<u>FAR CLAUSES</u>	<u>TITLE AND DATE</u>
52.202-1	DEFINITIONS (APR 1984)
52.203-1	OFFICIALS NOT TO BENEFIT (APR 1984)
52.203-3	GRATUITIES (APR 1984)
52.203-5	COVENANT AGAINST CONTINGENT FEES (APR 1984)
52.304-6	RESTRICTIONS ON SUBCONTRACTOR SALES TO THE GOVERNMENT (JUL 1985)
52.203-7	ANTI-KICKBACK PROCEDURES (OCT 1988)
52.203-12	LIMITATION ON PAYMENTS TO INFLUENCE CERTAIN FEDERAL TRANSACTIONS (JAN 1990)
52.204-2	SECURITY REQUIREMENTS (APR 1984)
52.209-6	PROTECTING THE GOVERNMENT'S INTEREST WHEN SUBCONTRACTING WITH CONTRACTORS DEBARRED, SUSPENDED, OR PROPOSED FOR DEBARMENT (MAY 1989)
52.212-8	DEFENSE PRIORITY AND ALLOCATION REQUIREMENTS (MAY 1986)
52.215-1	EXAMINATION OF RECORDS BY COMPTROLLER GENERAL (APR 1984)
52.215-2	AUDIT - NEGOTIATION (DEC 1989)
52.222-26	EQUAL OPPORTUNITY (APR 1984)
52.222-28	EQUAL OPPORTUNITY PREAWARD CLEARANCE OF SUBCONTRACTS (APR 1984)
52.222-35	AFFIRMATIVE ACTION FOR SPECIAL DISABLED AND VIETNAM ERA VETERANS (APR 1984)
52.222-36	AFFIRMATIVE ACTION FOR HANDICAPPED WORKERS (APR 1984)

52.222-37	EMPLOYMENT REPORTS ON SPECIAL DISABLED VETERANS AND VETERANS OF THE VIETNAM ERA (JAN 1988)
52.223-2	CLEAN AIR AND WATER (APR 1984)
52.232-6	DRUG-FREE WORKPLACE (MAR 1989)
52.224-1	PRIVACY ACT NOTIFICATION (APR 1984)
52.224-2	PRIVACY ACT (APR 1984)
52.225-13	RESTRICTIONS ON CONTRACTING WITH SANCTIONED PERSONS (MAY 1989)
52.227-1	AUTHORIZATION AND CONSENT (APR 1984)
52.227-2	NOTICE AND ASSISTANCE REGARDING PATENT AND COPYRIGHT INFRINGEMENT (APR 1984)
52.227-10	FILING OF PATENT APPLICATIONS - CLASSIFIED SUBJECT MATTER (APR 1984)
52.227-11	PATENT RIGHTS - RETENTION BY THE CONTRACTOR (SHORT FORM) (JUN 1989)
52.228-6	INSURANCE - IMMUNITY FROM TORT LIABILITY (APR 1984)
52.228-7	INSURANCE - LIABILITY TO THIRD PERSONS (APR 1984)
52.230-5	DISCLOSURE AND CONSISTENCY OF COST ACCOUNTING PRACTICES (SEP 1987)
52.232-23	ASSIGNMENT OF CLAIMS (JAN 1986)
52.237-3	CONTINUITY OF SERVICES (APR 1984)
52.246-25	LIMITATION OF LIABILITY - SERVICES (APR 1984)
52.249-6	TERMINATION (COST-REIMBURSEMENT) (MAY 1986)
52.249-14	EXCUSABLE DELAYS (APR 1984)
52.251-1	GOVERNMENT SUPPLY SOURCES (APR 1984)

<u>DoD FAR CLAUSES</u>	<u>TITLE AND DATE</u>
252.203-7001	SPECIAL PROHIBITION ON EMPLOYMENT (MAR 1989)
252.203-7002	STATUTORY COMPENSATION PROHIBITIONS AND REPORTING REQUIREMENTS RELATING TO CERTAIN FORMER DEPARTMENT OF DEFENSE (DoD) EMPLOYEES (APR 1988)
252.223-7500	DRUG-FREE WORK FORCE (SEP 1988)
252.225-7001	BUY AMERICAN ACT AND BALANCE OF PAYMENTS PROGRAM (APR 1985)
252.225-7023	RESTRICTION ON ACQUISITION OF FOREIGN MACHINE TOOLS (JAN 1989)
252.227-7013	RIGHTS IN TECHNICAL DATA AND COMPUTER SOFTWARE (OCT 1988)
252.227-7018	RESTRICTIVE MARKINGS ON TECHNICAL DATA (OCT 1988)
252.227-7029	IDENTIFICATION OF TECHNICAL DATA (APR 1988)
252.227-7034	PATENTS - SUBCONTRACTS (APR 1984)
252.227-7037	VALIDATION OF RESTRICTIVE MARKINGS ON TECHNICAL DATA (APR 1988)
252.231-7000	SUPPLEMENTAL COST PRINCIPLES (APR 1984)
252.231-7001	PENALTIES FOR UNALLOWABLE COSTS (APR 1988)
252.231-7003	CERTIFICATION OF INDIRECT COSTS (APR 1986)
252.251-7000	ORDERING FROM GOVERNMENT SUPPLY SOURCES (APR 1984)
252.271-7001	RECOVERY OF NONRECURRING COSTS ON COMMERCIAL SALES OF DEFENSE PRODUCTS AND TECHNOLOGY AND OF ROYALTY FEES FOR USE OF DoD TECHNICAL DATA (FEB 1989)

7 November 1991

AFOSR/PKO
Bldg. 410, Room C-124
Bolling AFB, DC 20332-6448

Attn: Ms. Kathleen Wetherell

Dear Ms. Wetherell:

Enclosed for your approval is the model subcontract for the Research Initiation Program under the Summer Research Programs (Contract F9620-90-C-0076). The blanks will be filled by merging information from our dBase IV database.

Sincerely,

Abe S. Sopher
Contracts Manager

cc: AFOSR/NI (Lt. Col. Cavendar)

ATTACHMENT 2:
SAMPLE TECHNICAL EVALUATION FORM AND TECHNICAL
EVALUATION SUMMARY

1992 RESEARCH INITIATION PROGRAM TECHNICAL EVALUATION

RIP NO: 92-2

RIP ASSOCIATE: Dr. Charles Kibert

Provided are several evaluation statements followed by ratings of (1) through (5). A rating of (1) is the lowest and (5) is the highest. Circle the rating level number you best feel rates the statement. Document additional comments on the back of this evaluation form.

Mail or fax the completed form to:

RDL

Attn: 1992 RIP TECH EVALS

5800 Uplander Way

Culver City, CA 90230-6608

(Fax: 310 216-5940)

- | | |
|--|-----------|
| 1. This RIP report has a high level of technical merit | 1 2 3 4 5 |
| 2. The RIP program is important to accomplishing the lab's mission | 1 2 3 4 5 |
| 3. This RIP report accomplished what the associate's proposal promised | 1 2 3 4 5 |
| 4. This RIP report addresses area(s) important to the USAF | 1 2 3 4 5 |
| 5. The USAF should continue to pursue the research in this RIP report | 1 2 3 4 5 |
| 6. The USAF should maintain research relationships with this RIP associate | 1 2 3 4 5 |
| 7. The money spent on this RIP effort was well worth it | 1 2 3 4 5 |
| 8. This RIP report is well organized and well written | 1 2 3 4 5 |
| 9. I'll be eager to be a focal point for summer and RIP associates in the future | 1 2 3 4 5 |
| 10. The one-year period for complete RIP research is about right | 1 2 3 4 5 |

****USE THE BACK OF THIS FORM FOR ADDITIONAL COMMENTS****

LAB FOCAL POINT'S NAME (PRINT): _____

OFFICE SYMBOL: _____

PHONE: _____

TECHNICAL EVALUATION SUMMARY

Technical Evaluation Questionnaire Rating Factors

Subcontract no.	1	2	3	4	5	6	7	8	9	10	Average
135	5	4	5	4	4	4	4	4	5	5	4.4
50	4	4	5	4	4	4	4	3	5	5	4.2
3	4	3	3	3	3	3	3	3	3	4	3.2
71	4	4	4	4	3	5	5	4	5	5	4.3
152	3	4	3	4	4	3	4	3	4	5	3.7
147	5	5	5	5	5	5	5	5	5	4	4.9
011	4	4	5	4	5	5	5	4	5	4	4.5
106	5	5	4	5	5	5	5	5	5	5	4.9
83	5	4	5	5	5	5	5	5	5	4	4.8
26	5	4	4	5	5	5	5	5	4	4	4.6
8	5	3	4	4	5	5	5	3	5	5	4.4
120	1	5	2	4	5	3	2	1	4	4	3.1
133	3	2	4	5	5	4	3	4	3	5	3.8
108	5	4	4	5	5	5	5	5	5	5	4.8
76	5	5	5	5	5	5	5	5	5	3	4.8
122	5	5	5	5	5	4	5	5	5	5	4.9
92	4	5	5	5	5	5	5	5	5	5	4.9
47	5	5	5	5	5	4	4	5	5	5	4.8
57	4	4	4	5	5	4	4	4	4	2	4.0
17	5	5	5	5	5	5	5	5	5	5	5.0
5	5	3	4	4	4	5	5	5	4	3	4.2
62	5	4	5	4	4	5	5	5	5	5	4.7
74	4	3	4	4	4	4	5	4	4	5	4.1
53	4	3	4	4	3	4	3	5	3	4	3.7
84	5	4	4	5	5	5	5	5	5	4	4.7
145	4	4	5	4	5	5	5	5	5	4	4.6
35	5	5	5	5	5	5	5	5	5	5	5.0

Technical Evaluation Questionnaire Rating Factors

Subcontract no.	1	2	3	4	5	6	7	8	9	10	Average
59	5	4	5	5	5	5	5	5	5	5	4.9
115	5	5	5	5	5	5	5	5	5	5	5.0
118	4	5	5	5	5	5	5	4	5	4	4.7
104	5	3	4	3	5	4	5	5	4	5	4.3
6	3	5	5	5	3	5	5	4	5	3	4.3
28	5	4	5	5	5	4	5	4	4	4	4.5
51	5	5	4	5	5	5	5	5	5	4	4.8
16	5	5	5	5	5	4	5	5	5	5	4.9
54	5	4	5	4	5	4	5	5	5	5	4.7
56	3	3	5	4	5	3	4	5	5	5	4.2
69	4	5	4	5	5	4	5	5	5	5	4.7
72	5	5	5	5	5	5	5	5	5	5	5.0
129	5	5	5	5	5	5	5	5	5	5	5.0
58	3	4	5	4	3	4	5	4	4	4	4.0
144	5	5	5	5	5	5	5	5	5	5	5.0
80	5	5	5	5	5	5	5	5	4	4	4.8
136	5	4	5	5	5	5	5	5	5	4	4.8
55	5	5	5	5	5	5	5	5	5	4	4.9
77	5	4	3	4	3	4	4	4	5	4	4.0
15	5	4	5	5	5	5	5	4	5	5	4.8
70	5	4	4	5	5	5	5	5	5	4	4.7
140	5	5	5	5	5	5	5	5	5	5	5.0
79	4	3	5	4	5	4	5	5	4	5	4.4
63	5	5	5	5	5	5	5	5	5	5	5.0
97	5	4	4	5	5	5	5	5	5	5	4.8
11	5	4	4	4	4	5	4	4	5	3	4.2
44	5	5	5	5	5	5	5	5	5	5	5.0
141	5	4	5	4	4	5	5	5	5	4	4.6
98	5	5	5	5	5	5	5	5	5	5	5.0

Technical Evaluation Questionnaire Rating Factors

Subcontract no.	1	2	3	4	5	6	7	8	9	10	Average
81	4	4	3	4	4	4	4	5	5	4	4.1
105	5	5	5	5	5	5	5	5	5	5	5.0
25	4	4	4	5	5	5	4	5	4	2	4.2
18	5	3	5	5	5	3	5	5	5	4	4.5
138	5	4	5	5	5	5	5	3	5	3	4.5
111	5	5	5	5	5	5	5	5	5	5	5.0
Avg by factor:	4.5	4.2	4.5	4.6	4.7	4.6	4.7	4.6	4.7	4.4	4.6

HETERODYNE LASER SPECKLE IMAGING THROUGH ATMOSPHERE

Richard Anderson
Professor
Department of Physics

University of Missouri-Rolla
Rolla, MO 65401

Final Report for:
Research Initiation Program
Phillips Laboratory

Sponsored by:
Air Force Office of Scientific Research
Bolling Air Force Base, Washington, D.C.

December 1992

HETERODYNE LASER SPECKLE IMAGING THROUGH ATMOSPHERE

Richard Anderson, Professor

Department of Physics

Steve E. Watkins, Assistant Professor

Rathnakar Gopisetty

Electrical Engineering Department

University of Missouri-Rolla

Abstract

Coherent heterodyne imaging can provide information on atmospheric targets such as satellites. A heterodyne imaging system can be successfully used for finding the parameters such as target image and velocity by recording the field scattered by the diffuse target when illuminated with coherent light. The heterodyne systems can record both phase and intensity of the scattered field. Non-heterodyne systems detect only the light intensity and therefore loses some target information. For instance, photographic plate recording is useful only to find the velocity under noiseless conditions¹. To extract the incoherent target image from the recorded field, the data of a large number of frames is spatial Fourier transformed and averaged assuming the target motion is negligible between the frames. If there is a small shift in the target position between the frames, the multiple imaging can produce a set of fringes from which the components of perpendicular velocity of the target are determined. Large target shifts between the frames will result in change in the target perspective from one frame to another. Within certain limits of the target movements, these frames remain correlated and a cross-correlation of images of different frames can produce the target velocity.

HETERODYNE LASER SPECKLE IMAGING THROUGH ATMOSPHERE

Dr. Richard Anderson, Dr. Steve E. Watkins, Rathnakar Gopisetty

INTRODUCTION

In the case of coherent speckle imaging of atmospheric targets, the target parameters of interest are incoherent target image and target motion. The target speckle pattern which encode this information can be detected by using a heterodyne system that can record the magnitude and phase of the scattered field from the target. The target speckle is produced by taking a spatial Fourier transform of this field. A high signal to noise ratio is obtained by mixing the weak target field with a strong Local Oscillator(LO) field³.

Speckle is a random intensity distribution produced when coherent light is either scattered by a rough surface or propagated through a medium with random refractive indices. The statistical properties of this speckle depend both on the coherence of the incident light and the properties of the rough surface being illuminated⁵. The light rays falling on the random surface will be scattered in different directions and the speckle pattern produced is due to the complex addition of many elementary contributions of the light rays. In a sense the speckle patterns code the information about the object yielding a high degree of redundancy. Because of this, a speckle pattern may be used as a random carrier of the information. In the following sections some of these properties of the speckle are used to characterize object motion when illuminated by a collimated laser beam.

A study of speckle properties show that multiple imaging of the speckle patterns can determine the parameters of the target motion⁵. The target image is also obtained by averaging a number of speckle patterns at different time intervals. This procedure leads to the removal of speckle noise in the images. Further the perpendicular motion in the target between the frames is found by analyzing the shift in the field in the target plane. A considerable movement of the target between the frames can also change the perspective of the speckles produced in the consecutive frames. But within certain limits these speckles remain correlated when the correlation coefficient between the these speckles is greater than $1/e$. In such cases the cross-

correlation between the frames can provide the target velocity. The theoretical study of the cross-correlation to be used both in target and detector planes is carried out using scalar field theory.

THE HETERODYNE IMAGING SYSTEM

In the case of the heterodyne imaging system, the scattered field is heterodyned or mixed with the local oscillator field which is about 10 times that of the reflected field. The illuminating beam and the Local Oscillator beam are produced from the same source by using a beam splitter as shown in Fig.1.

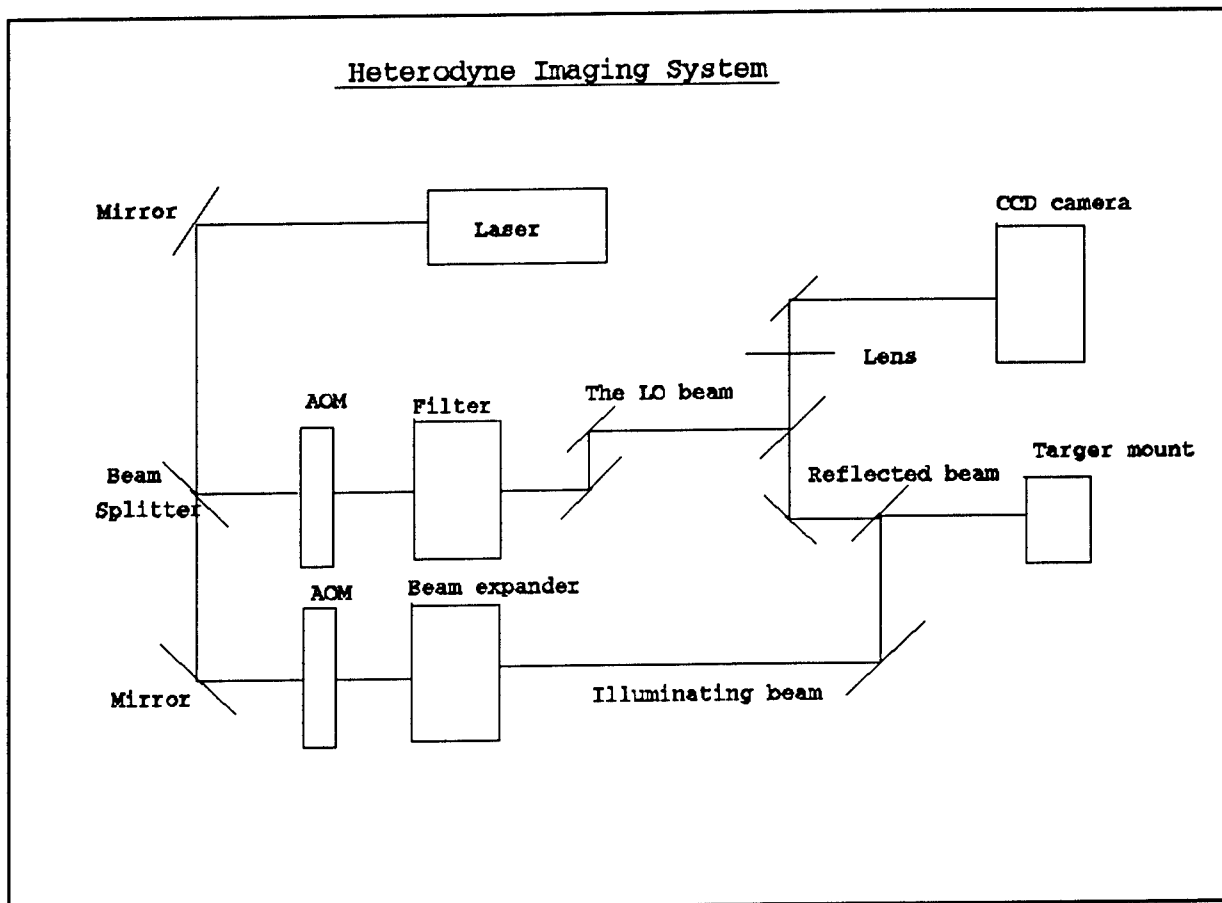


Figure 1

The acousto-optic modulator shifts the frequency of the beam when passed through it so

that both the beams have different frequencies. The reflected field from the target is mixed with the LO field by means of a beam splitter so aligned that both the fields propagate in the same direction. Before mixing the reflected field and the LO field are polarized in the same sense by using two polarizers (not shown in Fig. 1). The heterodyning results in four different terms, the LO intensity, the target intensity and two interference intensity terms which lie at the intermediate frequency. This frequency is the difference between the LO frequency and reflected field frequency. The LO field is real and constant while the reflected field from the target is a complex function. The heterodyned field is scanned by the CCD array placed the focal length of the lens.

The target parameters can be found by using multiple imaging technique in which the target intensities are recorded and superimposed on a photographic plate¹. But the presence of atmospheric noise distort the signal and the technique cannot be useful in such conditions. The main advantages of the heterodyne system are that it is used to retrieve very weak signals present in the target field. It improves the signal-to-noise ratio to a large extent. It is also used to find the phase between the real and the imaginary components in the target field. This phase can be useful in finding the target information. The field measured in the detector plane will be directly proportional to the complex field scattered by the target. Since it gives the complex field, instead of intensity, as in photographic plate recording¹, the phase components can be extracted by separating the real and imaginary parts of the field.

The target plane corresponds to the plane of motion of the target. The target is considered to move in the direction normal to the illuminating beam. At each position the target is scanned by a CCD array placed at the focal length of a lens. The scan rate of CCD is high such that the

motion of target within each frame is negligible and the target is virtually at the same position. Hence a same speckle perspective is realized in each frame.

DETERMINATION OF TARGET IMAGE

The imaging system contains two planes, the target plane and the detector plane. The position vector in the target plane is u which can be represented by the coordinates (u_x, u_y) and let r be the position vector in the detector plane. A optical signal of field E_i is incident on a rough target such that

$$E_i = E_o \exp(j\omega_o t) \quad (1)$$

The scattered field from the target surface depends upon the reflection coefficient of the target surface. This reflection coefficient depends upon the wavelength and the positional vector and is given by⁴

$$\overline{\rho}(u) = \rho(u) \exp(j\phi(u)) \quad (2)$$

where E and ϕ depends upon the incident and scattered angles at that particular position vector.

We have

$$\overline{\rho}(u) = \frac{\text{Scattered field}}{\text{Incident field}} \quad (3)$$

This implies, the emergent field from the target is

$$E_s(u,t) = \bar{\rho}(u)E_o \exp(jw_o t) \quad (4)$$

$$= \rho(u)E_o \exp[j\phi(u)] \exp(jw_o t) \quad (5)$$

The factor $\rho(u)E_o$ represents the amplitude of the emergent waves and is proportional to the square root of the intensity.

$$\bar{\rho}(u)E_o = K\sqrt{I(u)} \text{ where } K \text{ is a constant} \quad (6)$$

Before the heterodyning process, the Local Oscillator beam is spatially filtered and there is a phase difference between the signal incident on the target and the LO signal. This phase difference is neglected in the following treatment. The emergent signal from the target is mixed with this local oscillator beam. The LO signal field is given by

$$E_{LO}(u,t) = E_{LO} \text{cyl}(u) e^{j(w_{LO}t)} \quad (7)$$

where $\text{cyl}(u)$ is a cylinder function due to the spatial filter.

These two fields are mixed by a beam splitter and passed through a lens where they are detected by a CCD detector array placed at the focal length. Hence in the detector plane, the fields due to the target and LO are given by the Fourier transform of $E_s(u,t)$ and $E_{LO}(u,t)$ respectively. The position vector of each point in this plane is given by r . Therefore the field in the detector plane due to the target signal can be given by

$$E_{DS}(r,t) = K \sqrt{H\left(\frac{r}{\lambda f}\right)} \frac{e^{jkf}}{2\pi jf} e^{jw_o t} \quad (8)$$

In the above equation, the phase term is ignored as it cannot be used in calculations. Due to the

Fourier transform, the position vector u will be replaced with the transfer function given by

$$\text{Optical Transfer Function} = \frac{r}{\lambda f} \quad (9)$$

where f is the focal length of the lens between the two planes. Also the field due to the LO in the detector plane is given by²

$$E_{DLO}(r,t) = E_{LO} \exp[j(\omega_{LO}t)] F[\text{cyl}(u)] \quad (10)$$

The Fourier transform of the cylinder function $F[\text{cyl}(u)]$ will produce a sombero function⁴

$$\text{Somb}\left(\frac{r}{\lambda f}\right) \frac{\exp(jkf)}{j\lambda f} \quad (11)$$

When the pinhole of the spatial filter is very small, the sombero function is nearly unity.

Therefore we have

$$E_{LO}(r,t) = \frac{\pi E_{LO}}{j\lambda f} \exp(jkf) \exp[j(\omega_{LO}t)] \quad (12)$$

The total mixed field detected at any point on the detector is the sum of these two fields. These two fields are also polarized in the same order.

$$E_T(r,t) = E_{DS}(r,t) + E_{DLO}(r,t) \quad (13)$$

This resulting signal is at the intermediate frequency which is the difference between the signal and the LO frequencies. The heterodyne signal intensity in the detector plane will be proportional to the square of the sum of these two signal fields and is given by

$$s(r,t) \propto (E_{DS} + E_{DLO})^* (E_{DS} + E_{DLO}) \quad (14)$$

This will produce

$$s(r,t) = C_1 |E_{DS}|^2 + C_2 |E_{DLO}|^2 + C_3 [E_{DS} E_{DLO}^* \exp(jw_{IF}t) + E_{DLO} E_{DS}^* \exp(-jw_{IF}t)] \quad (15)$$

Where C_1 , C_2 and C_3 are constants. The contribution of the first two terms which are small signal intensities, is negligible. Therefore the heterodyne signal at the intermediate frequencies is given by

$$s(r,t) = E_{DS} E_{DLO}^* \exp(jw_{IF}t) + E_{DLO} E_{DS}^* \exp(-jw_{IF}t) \quad (16)$$

This signal is the sum of the two sidebands at the positive and negative intermediate frequencies, w_{IF} and $-w_{IF}$ respectively. From this equation, the magnitude of the signal at the positive intermediate frequency is

$$m(r, w_{IF}) = K \sqrt{I_{LO}} S(r) \text{ where } S(r) = \sqrt{H\left(\frac{r}{\lambda f}\right) \otimes \exp[j\phi\left(\frac{r}{\lambda f}\right)]} \quad (17)$$

A spatial inverse Fourier transform of this signal represents the field in the target plane (u plane) at the positive intermediate frequency and can be given as

$$M(u, w_{IF}) = K \sqrt{I_{LO}} \sqrt{I(u)} \exp(j\psi(u)) \quad (18)$$

where $\psi(u)$ is the Fourier transform of $\phi(r/\lambda f)$.

A complex conjugate of the above equation will represent the signal at the negative intermediate frequency.

$$M(u, -w_{IF}) = M^*(u, w_{IF}) = K \sqrt{I_{LO}} \sqrt{I(u)} \exp[-j\psi(u)] \quad (19)$$

The image of the target can be successfully extracted by taking a product of terms due to the signals at $+w_{IF}$ and $-w_{IF}$ intermediate frequencies in the target plane. This will also represent the power density spectrum of the signal detected in the detector plane².

$$I(u) = M(u, w_{IF}) M^*(u, w_{IF}) \quad (20)$$

In order to remove the speckle noise, N such images from N different frames are taken and averaged. Within each frame, the motion is considered to be very small and the target is virtually at rest.

$$I_{avg}(u) = \frac{1}{N} \sum_{i=0}^{i=N} M(u, w_{IF}) M^*(u, w_{IF}) \quad (21)$$

This will give an improved heterodyne image of the target with a high reduction in the speckle.

INTENSITY FOR FINITE TARGET DISPLACEMENTS

As described above, a spatial Fourier transform of the field obtained in the detector plane yields the signal $M(u, w_{IF})$ at the positive intermediate frequency w_{IF} in the target plane and is given by

$$M(u, w_{IF}) = K \sqrt{I_{LO}} \sqrt{I(u)} \exp[j\psi(u)] \quad (22)$$

A complex conjugate of this term will give the field in the target plane at the negative intermediate frequency $-w_{IF}$. From this the intensity in the target plane is given by averaging the power spectral density over a large number of frames which is

$$I(u) = \frac{1}{N} \lim_{N \rightarrow \infty} \sum_{k=1}^{k=N} M(u, w_{IF}) M^*(u, w_{IF}) \quad (23)$$

In all of these derivations, the target motion is very small and assumed negligible between the recordings of two different frames and the target is assumed to be nearly at the same position.

In practice, if the scan rate of the CCD detector is low compared to the target motion, there will be some amount of displacement in the target position whose effect cannot be ignored.

Due to this motion, the original speckle pattern will be shifted with a new speckle representation occurring at the initial position. This shifted speckle pattern can have a different appearance in which case the target perspective is considered to be changed.

Let the target is moving with a constant speed and let there are equal time periods between the scans of two consecutive frames. But within a frame, the target motion can be considered to be small enough that the target is virtually at the same position. The positive modulus of the field in the target plane produced due to the point u in the first frame is

$$M(u, w_{IF}) = K\sqrt{I_{LO}}\sqrt{I(u)}\exp[j\psi(u)] \quad (24)$$

In the detector plane, the $+w_{IF}$ sideband of the signal is given by taking the spatial Fourier transform as in Eqn. 17.

$$m(r) = K\sqrt{I_{LO}}S(r) \quad (25)$$

where

$$S(r) = F[\sqrt{I(u)}\exp(j\psi(u))] \quad (26)$$

where F represents the Fourier transform of the term. In the second frame, let the target move a distance d from the initial position. Since the imaging and recording angles don't change, $\psi(u)$ depends only on the point under consideration which is now $(u+d)$. Therefore, theoretically in the target plane, the modulus of the field after the target motion will become

$$M(u+d) = K\sqrt{I_{LO}}\sqrt{I(u+d)}\exp[j\psi(u+d)] \quad (27)$$

This shift can be expressed as a convolution of the original field with a delta function as¹

$$M(u+d, w_{IF}) = K\sqrt{I_{LO}} [\sqrt{I(u)}\exp[j\psi(u)]] \otimes \delta(u+d) \quad (28)$$

The motion is assumed to be only in one direction, say u_x . A spatial Fourier transform of this field will give the field in the detector plane after the shift. The convolution with the delta function will result in multiplication with the exponential term in the detector plane.

$$m_d(r, w_{IF}) = K\sqrt{I_{LO}} S(r) \exp[-jkd] \text{ where } k = \frac{r}{\lambda f} \quad (29)$$

where $m_d(r)$ represents the field at any point r after the target has shifted a distance d and f represents the focal length. Thus due to the shift in the target position, the original field will be modulated by an exponential term and therefore it cannot be used for the averaging purpose to remove the speckle noise.

One method to overcome this problem is that at each position $(u+nd)$ where n is any integer, in the target plane, the field obtained in the detector plane $m_{nd}(r, w_{IF})$ must be inverse Fourier transformed to find the field in the target plane $M(u+nd)$. This field should be convoluted with an appropriate delta function $\delta(u-nd)$ to remove the shift in the target plane. For a shift d in the target plane, the field obtained is

$$M(u+d, w_{IF}) = K\sqrt{I_{LO}} \sqrt{I(u+d)} \exp[j\psi(u+d)] \quad (30)$$

This is convoluted with $\delta(u-d)$ and we have

$$M'(u+d, w_{IF}) = K\sqrt{I_{LO}} \sqrt{I(u+d)} \exp[j\psi(u+d)] \otimes \delta(u-d) \quad (31)$$

Taking a spatial Fourier transform of this function will result

$$m_d(r) = K\sqrt{I_{LO}}S(r)\exp[jkd]\exp[-jkd] \quad (32)$$

$$= K\sqrt{I_{LO}}S(r) \quad (33)$$

which is equivalent to the original target field before the shift and this factor can be used for the averaging purpose to extract the target image removing the speckle.

Therefore if $M(u+d)$, $M(u+2d)$... $M(u+nd)$ are the positive modulii of the fields in the target plane taken in the frames 1, 2, ..N respectively with a displacement d of the target between the consecutive frames, then a method for averaging these N samples in order to remove the speckle noise is

$$M_{total}(u) = M(u) + M(u+d) \otimes \delta(u-d) + M(u+2d) \otimes \delta(u-2d) + \dots + M(u+nd) \otimes \delta(u-nd) \quad (34)$$

In practice the velocity of the target is not known and it is one of the factors to be determined. Without the information about the velocity, d cannot be estimated for averaging purpose. For the field in each frame, the power spectral density in the target plane can be given by

$$P(u,u) = M(u)M^*(u) = KI_{LO}I(u) \quad (35)$$

This is proportional to the target image. The noise free target image can be successfully obtained by averaging N such frames. A Fourier transform of this function will give the intensity in the detector plane. This function also represent the autocorrelation of the signal in the detector plane.

$$C(r,r)=KI_{LO}H\left(\frac{r}{\lambda f}\right) \quad (36)$$

The target has experienced a displacement d between the frames and therefore the power spectral density becomes

$$P(u+d,u+d)=KI_{LO}I(u+d) \quad (38)$$

Then, in the detector plane, the intensity factor will be given by taking a Fourier transform of this function.

$$C_d(r,r)=KI_{LO}H\left(\frac{r}{\lambda f}\right)e^{-jLd} \quad \text{where } L=r/\lambda f \quad (39)$$

If N such samples are summed in the target plane, we have

$$I_N(u)=KI_{LO}[I(u)+I(u+d)+I(u+2d)+\dots+I(u+Nd)] \quad (40)$$

Therefore in the detector plane we get a Fourier transform of this function

$$H_N(r)=KI_{LO}H\left(\frac{r}{\lambda f}\right)[1+e^{jLd}+e^{j2Ld}+\dots+e^{jNLd}] \quad (41)$$

Summing up the geometrical series, we have

$$H_N(r)=KI_{LO}H\left(\frac{r}{\lambda f}\right)\left[\frac{\sin\frac{(N+1)Ld}{2}}{\sin\left(\frac{Ld}{2}\right)}\right] \quad (42)$$

This equation will give a set of fringes at the positive and the negative intermediate frequencies. The distance between the consecutive fringe peaks will be proportional to the distance d . Thus d can be found and since the time period between the frames is known, the velocity $v=d/T$,

which T is the time period between the consecutive frames can be found.

VELOCITY ESTIMATION USING CROSS-CORRELATION

In the earlier cases we have dealt with the shift in the target field in the target plane in which the resulting target field after the shift can be expressed by the same function as before the shift. This is valid for small target shifts in which the noise introduced is relatively the same for the fields before and after the shifts. If $M_1(u)$ is the target field at positive intermediate frequency in the target plane, and if the target shifts by a small distance d , then the resulting field is expressed as $M_1(u+d)$. But if d is large enough, then a different field realization takes place in the target plane and it cannot be represented as a function of M_1 . Let this field be expressed by a different function $M_2(u+d)$. A cross-correlation between these two functions will produce the amount of similarity between these two functions and is expressed as

$$R_{M_1 M_2}(d) = \int \int M_1(u) M_2(u+d) du \quad (43)$$

Unlike the auto-correlation function which always has a peak value at the origin, the cross-correlation function has a peak value shifted from the center. This shift of the peak value corresponds to the shift in the target field between the two functions. Since the time period between the two field recordings is known, the knowledge of the shift in the peak value can directly lead to the determination of the velocity of the object.

One of the important requirements is to determine whether the field obtained after the target motion can be correlated with the initial field and obtain the information about the target. A powerful tool for expressing the amount of correlation between the two is to estimate the

correlation coefficient function given by⁸

$$\rho_{M_1 M_2}(r) = \frac{R_{M_1 M_2}(d) - \mu_{M_1} \mu_{M_2}}{\sqrt{[R_{M_1 M_1}(0) - \mu_{M_1}^2][R_{M_2 M_2}(0) - \mu_{M_2}^2]}} \quad (44)$$

$$\text{where } R_{M_1 M_1}, R_{M_2 M_2} \text{ are the autocorrelation functions} \quad (45)$$

$$\mu_{M_1}, \mu_{M_2} \text{ are mean values.} \quad (46)$$

The correlation coefficient function varies between 0 and 1 depending upon amount of correlation between the two fields. If the correlation coefficient is zero, then the two fields are totally uncorrelated and they are independent with respect to one another. On the other hand if correlation coefficient is unity, the two fields can be represented by the same function and are totally similar. In most cases, a correlation coefficient greater than 1/e is considered to be required to correlate the two fields and find the information from them. If this function is less than 1/e, then it is regarded that no information is obtained by correlating the two fields.

As can be seen from the equations, the process of finding the cross-correlation and the correlation in the target plane involves complex integrations. In order to simplify the representations, the correlation estimation can be also performed in the detector plane where the complex integrations can be eliminated. The cross-spectral density due to the two fields can be estimated by complex multiplication of the two fields obtained in the detector plane. The fields obtained in the detector plane are the spatial Fourier transforms of the fields in the target plane. The cross-spectral density is also equal to the Fourier transform of the cross-correlation obtained in the target field. Let $m_1(r)$ represent the field which is Fourier transform of $M_1(u)$ and $m_2(r)$ is the Fourier transform of the $M_2(u)$. Therefore the cross-spectral density can be given by⁸.

$$S_{M_1M_2}(r) = F[R_{M_1M_2}(d)] \quad (47)$$

$$= m_1(r)m_2^*(r) \quad (48)$$

where r represents the spatial units in the detector plane. These two are directly proportional to the signals obtained in the detector plane. Unlike the power spectral density, the cross-spectral density is the complex function. In order to find the information about correlation, the quantity must be expressed in terms of real and imaginary parts. This can be expressed as

$$S_{M_1M_2}(r) = C_{M_1M_2}(r) - jQ_{M_1M_2}(r) \quad (49)$$

The real part called the coincident spectral density or cospectrum can be expressed in terms of cross-correlation as

$$C_{M_1M_2}(r) = \int_{-\infty}^{+\infty} R_{M_1M_2}(m) \cos 2\pi r m \, dm \quad (50)$$

The imaginary part in terms of cross-correlation can be expressed as

$$Q_{M_1M_2}(r) = \int_{-\infty}^{+\infty} R_{M_1M_2}(m) \sin 2\pi r m \, dm \quad (51)$$

In terms of magnitude and phase the cross-spectral density can be expressed as

$$S_{M_1M_2}(r) = |S_{M_1M_2}(r)| \exp[-j\theta_{M_1M_2}(r)] \quad (52)$$

where

$$|S_{M_1M_2}(r)| = \sqrt{C_{M_1M_2}^2(r) + Q_{M_1M_2}^2(r)} \quad (53)$$

$$\theta_{M_1M_2}(r) = \tan^{-1} \left[\frac{Q_{M_1M_2}(r)}{C_{M_1M_2}(r)} \right] \quad (54)$$

Unlike the power spectrum which is an even function with a peak at the origin, the cross-spectral density has the peak shifted from the origin. This shift in the peak value is directly proportional to the target shift from the initial position of the target. By using the optical transfer function between the two planes, the corresponding shift in the target plane can be estimated. The transfer function in this case is given by

$$u = \frac{r}{\lambda f}$$

where f is the focal length of the lens used in between the target and the detector planes.

Since the time period between the recordings of the two target fields is known, the perpendicular velocity of the target can be estimated. The direction of the velocity can be found by the sign of the phase i.e., the sign of the quad spectrum. The positive phase angle means $M_2(u)$ follows $M_1(u)$ and thus there is a positive spatial shift in the target field. This means the target has moved in the positive u direction. The negative sign of quad function means the target is moving in the negative u direction.

For estimating the amount of correlation in the detector plane, the coherence function can be calculated. This function is equivalent to the correlation coefficient function in the target plane and is written as

$$\gamma_{M_1 M_2}^2(r) = \frac{|S_{M_1 M_2}(r)|^2}{S_{M_1 M_1}(r) S_{M_2 M_2}(r)} \quad (55)$$

where $S_{M_1 M_1}(r)$, $S_{M_2 M_2}(r)$ represent power spectral densities

This function varies between 0 and 1. The coherence function of unity represents the ideal case or the totally correlated case and coherence function of zero represents the complete uncorrelated case of the fields. An important property of this coherence function is that it doesn't vary due to the linear transformations of the two fields in which the resulting fields can be represented by the same function. If $M_1(u)$ is shifted to $M_1'(u) = M_1(u+d)$ and $M_2(u)$ is shifted to $M_2'(u) = M_2(u+d)$, then the resulting coherence function between the shifted fields is equal to the initial one. i.e,

$$\gamma_{M_1 M_2}^2 = \gamma_{M_1' M_2'}^2 \quad (56)$$

These theoretical analysis can be better interpreted if the cross-correlation and the cross-spectrum of the speckle images obtained by the experiment are performed.

Conclusions

Heterodyne imaging can be used to find the field in the target plane by a direct spatial transform of the field in the detector plane. It can detect both the magnitude and phase of the field scattered by the target. The overall signal-to-noise ratio in the detected field will be highly reduced. The incoherent target image is found by averaging a large number of frames assuming the target motion be negligibly small between the frames. This type of temporal filtering will lead to the reduction in the speckle noise. Fringe patterns can be formed by taking multiple recordings in the detector plane and superimposing them. In this case the target has moved a

finite distance between the frames which cannot be neglected. These fringes can provide detection of perpendicular target velocity.

If the motion between the frames is large, a different speckle is realized in each frame. The cross-correlation of two different speckle images can be done to estimate the velocity of the target, if the speckles are correlated. These speckles remain correlated till the correlation coefficient is greater than $1/e$. Theoretical analysis show that the cross-spectral density found in the detector plane provide a similar interpretation as the cross-correlation in the target plane.

References:

1. E.Archbold and A.E.Ennos, "Displacement measurement from Double exposure laser photographs", *Optica Acta*, Vol.19, No.4, 253 (1972).
2. Sturat.R.D., "Introduction to Fourier Analysis", *Brans and Noble Inc, NY, 1966*.
3. David L. Fried, "Optical Heterodyne Detection of Atmospherically Distorted Signal Wave Front", *Proceedings of IEEE*, Vol.55, No.1, (1967).
4. Richard Anderson, "Coherent Laser Radar and Array Imaging", *Summer Research Program, Phillips Laboratory, 1991*.
5. J.W.Goodman, "Statistical properties of Laser speckle pattern", *Speckle and Related Phenomena*, J.C.Dainty ed., *Springer-Verlag, Berlin, (1975)*.
6. J.W.Goodman, "Introduction to Fourier Optics", *McGraw-Hill Book Company, NY, 1968*
7. J.H.Shapiro, B.A.Capron, and R.C.Harney, "Imaging and target detection with a heterodyne-reception optical radar", *Appl.Optics*, Vol.20, 3292 (1981).
8. Julius S.Bendant, Allan G.Piersol, "Engineering applications of Correlation and Spectral analysis", *Wiley Interscience Publication, NY, 1980*.
9. J.C.Leader, "Speckle effects on coherent laser radar detection efficiency", *Optical Engineering*, Vol.25, No.5, 644 (1986)
10. J.H.Shapiro, Kin Wai Leong, "Phase and Amplitude uncertainties in multimode heterodyning", *Optics Communications*, Vol.58, No.2, pp.73-79 (1985)
11. M.Francon, "Laser Speckle and Applications in Optics", *Academic Press, NY, 1979*

NUMERICAL STUDIES OF INVERSION PROBLEMS
ARISING IN LIDAR MEASUREMENTS

Frank P. Battles
Professor
Department of Basic Sciences

Massachusetts Maritime Academy
PO Box D
Buzzards Bay, MA 02532-1803

Final Report for:
Research Initiation Program
Geophysics Directorate of Phillips Laboratory

Sponsored by:
Air Force Office of Scientific Research
Bolling Air Force Base, Washington, D.C.

and

Massachusetts Maritime Academy

December 1992

Numerical Studies of Inversion Problems
Arising in Lidar Measurements

Frank P. Battles
Professor
Department of Basic Sciences
Massachusetts Maritime Academy

Abstract

The refractive index structure parameter, C_n^2 , is a typical parameter which cannot be measured directly, but can possibly be inferred by ground based lidar measurements of some related parameter. The measured parameter is typically related to C_n^2 via a weighted integral. To a first approximation, the integral equation can be replaced by a lower triangular system of linear equations which can then be inverted either iteratively or by matrix inversion. We have looked at the nature of such solutions for different weighting functions taking into account the possible ill-conditioning of the system and have looked at the response of solutions to the inherent randomness of both the measured parameter and C_n^2 . We find that even very small errors (of the order of $\frac{1}{2}\%$) have severe effects on the inversion process. On the other hand, the crossed path technique due to the sharp peaking of the associated weighting functions looks very promising as a ground based lidar measurement method for measuring C_n^2 .

NUMERICAL STUDIES OF INVERSION PROBLEMS ARISING IN LIDAR MEASUREMENTS

Frank P. Battles

INTRODUCTION

We begin by summarizing a general formulation of the lidar approach to C_n^2 due to Beland and Krause-Polstroff¹, the primary reference of this report which will here after be referred to as BK. Suppose that g is some optical effect measured by a lidar system using a gated return from an altitude z_i . Then

$$g(z_i) = \int_0^{z_i} C_n^2(h) W(\lambda, z_i, h) dh$$

where the integration is to be carried out along the path of propagation and λ is the optical wavelength. Assuming a weak altitude variation of C_n^2 over a range gate, we replace C_n^2 with $C_n^2(z_j)$, a weighted average of C_n^2 over the altitude bin (z_{j-1}, z_j) . We approximate the above by

$$g(z_i) = \sum_{j=1}^i W_{ij} C_n^2(z_j)$$

or

$$\underline{G} = \underline{W} \underline{C} \tag{*}$$

where the matrix \underline{W} is lower triangular with elements

$$W_{ij} = \int_{z_{j-1}}^{z_j} W(\lambda, z_i, h) dh, \text{ for } j \leq i$$

and

$$W_{ij} = 0, \text{ for } j > i.$$

\underline{G} and \underline{C} are vectors whose elements consist of $g(z_i)$ and $C_n^2(z_i)$ respectively.

We have two methods of inverting equation (*):

$$\underline{C}^{-1} = \underline{W}^{-1} \underline{G}$$

or

$$C_n^2(z_i) = (W_{ii})^{-1} [g(z_i) - \sum_{j=i}^{i-1} W_{ij} C_n^2(z_j)]$$

i.e. by matrix inversion or by iteration.

BK next goes on to look at several specific optical parameters (image dancing in particular) and the associated weighting functions. Qualitative speculation suggests some possible problems with inverting equation (*). This we will look at quantitatively.

The bulk of BK looks at the crossed path technique and this we shall also consider.

GENERAL APPROACH

Throughout we assume a source or sources at $z = 10000$ m. We will first either assume an exponential form for $C_n^2(z_i)$ or used measured values to calculate a value for \underline{G} . We next allow for experimental error by letting each $g(z_i)$ be replaced by $g(z_i) \pm \Delta$ where Δ is a certain percent of either $g(z_i)$ or $g(10)$ times a randomly generated fraction ≤ 1 . Given this slightly altered form for \underline{G} we then re-solve for C_n^2 and compare to the inputted profile.

IMAGE DANCING

Let $g(z_i) = \langle \delta^2(z_i) \rangle$ represent the mean square beam wander. Then it may be shown¹ that

$$W_{ij} = K \frac{3}{8} z_i \{ [1 - (z_{j-1}/z_i)^{8/3} - [1 - (z_j/z_i)]^{8/3} \} \text{ for } j \leq i$$

where K is a constant which depends on the geometry of the lidar system.

In what follows, we take $K = 1$, $z_{max} = 10$ km and let $n =$ the number of subdivisions. In Table 1 is shown the matrix \underline{W} for $n = 10$. By qualitative argument, BK points out that it is to be expected that $W_{ii}/W_{ij} \ll 1$ for $i < j$ which we can see is true for this case.

To investigate numerical stability for this case we assume a C_n^2 profile of the form 2^{10-z} . From this profile we calculate $g(z_i)$ and then invert the system (using both matrix inversion and iteration) to resolve for C_n^2 . In Table 2 is shown the results of such a computation for $n = 10$. In this Figure, CN2in is the assumed profile and CN2out is the calculated profile. The %diff column gives the percent difference, which although not exactly zero, is of the order of 10^{-11} for this case for either inversion method. This column remains essentially zero until n is increased to about 26 where roundoff and truncation errors take over, even with double precision. We therefore conclude that for $n = 10$, these errors are negligible and either matrix inversion or iteration may be used.

We next introduce some randomness into our calculations. We assume the same input profile for C_n^2 , calculate \underline{G} , add to each component of \underline{G} a random percent of $g(i)$ and recalculate C_n^2 . We find that, except for extremely small perturbations, the recomputed C_n^2 bears no resemblance to the inputted profile for $z > 3$ km. Table 3 shows a sample output where we allow each g_i to vary by 0.5%. In this table, $gr(z_i)$ is the randomly generated value of $g(z_i)$; then $gr(z_i)$ is used to recompute C_n^2 . We next looked at the effects of allowing each $g(z_i)$ to vary by a random percentage of $g(10)$ which should more accurately reflect the effects of experimental error. These results are shown in Table 4.

It was also suggested that we use a "real" profile of C_n^2 in that the assumed functional dependence may be too smooth. Shown in Figure 1 is a thermosonde derived profile of C_n^2 for $z > 3$ km. Below this altitude we used a model of the form $C_n^2 = 10^{-14}/z$. Results obtained were no different than before. See Tables 5-6 for typical results. These tables are again for a random component of 0.5% on each $g(z_i)$, with percentage calculated on each $g(z_i)$ in Table 5 and on $g(10)$ in Table 6.

We also looked at letting other parameters such as each W_{ij} and z_i vary randomly. Again even small variations have drastic results on the recomputed C_n^2 profile. It was further suggested that we look at the results of averaging sets of random calculations for C_n^2 out. Again drastic variation is observed.

SCINTILLATION

For a point source at altitude z_i , the variance of log-amplitude (scintillation) observed by a receiver at ground level is given by¹

$$\sigma_{\chi}^2(z_i) = 0.56k^{7/6} \int_0^{z_i} C_n^2(\eta)(\eta/z_i)^{5/6} (z_i - \eta)^{5/6} d\eta$$

where $k = 2\pi/\lambda$.

In this case the weighting function is peaked at the path midpoint. Making the same approximations as in the case of image dancing and assuming that we can approximate the exponent of 5/6 with 1 (this latter approximation has no qualitative effect on what follows) we have

$$W_{ij} = K \{ [z_j^2/2 - z_j^3/(3z_i)] - [z_{j-1}^2/2 - z_{j-1}^3/(3z_i)] \} \text{ for } j \leq i.$$

We again set $K = 1$. Shown in Table 7 is the matrix \mathbf{W} for $z = 10$ km. In Table 8 we show the results of inputting C_n^2 as an exponential function, calculating \mathbf{g} , and inverting to find C_n^2 . There is no problem with the inversion process for $n \leq 25$. The "0"'s in the %diff column are of the order of 10^{-12} . In Tables 9-10 we show the effects of slightly perturbing \mathbf{g} ; in Table 9 $g(z_i) = g(z_i) \pm .5\% g(z_i)$ and in Table 10, $g(z_i) = g(z_i) \pm .5\% g(10)$. Even this slight perturbation has drastic effects on the inversion process although less so than in the case of image dancing. Tables 11-12 show representative effects for an actual C_n^2 profile.

CROSSED PATH TECHNIQUE

Based on the above discussion we conclude that very small errors in the measurements of \underline{G} result in unacceptable results for $C_n^2(z_i)$ for all but very low lying levels. This is due to the fact that a small error in a value of $g(z_i)$ for z_i will effect all of the values of $C_n^2(z_j)$ for $j \leq i$. This in turn is due to the fact that the weighting functions involved in image dancing and scintillation are rather broad in spatial width.

In BK an extensive treatment of the theory of the crossed path technique is given. Here what is measured is the log amplitude covariance $\langle \chi_1 \chi_2 \rangle$ received from two sources by two receivers. See Figure 2 which is reproduced from this reference. For the idealized case of point sources and point receivers it is shown that

$$\langle \chi_1 \chi_2 \rangle = \int dz' C_n^2(z') W(z, z')$$

where

$$W(z, z') = 4\pi^2 k^2 \int K dK \Phi_0(K) J_0(K | \gamma S - (1 - \gamma) S_0 | \sin^2[\gamma(1 - \gamma)zK^2/2k]$$

and Φ_0 is the modified von Karman spectrum, J_0 is the zeroth order Bessel function and $\gamma = z'/z$. This function is sharply peaked for $\gamma = \frac{1}{2}$. In Figure 3 is shown a plot of $W(10000m, z')$ vs z' and $W(9000m, z')$ vs z' for a suitable choice of parameters. We note that each is sharply peaked with negligible overlap and that each has a Gaussian half width of the order of 150 m. For comparison in Figure 4 is shown a plot of $W(10000m, z')$ for the crossed path technique and for the case of scintillation.

Figure 4 shows clearly the advantage of the crossed path technique. Even when corrections are made for finite source/receivers the weighting function remains relatively sharply peaked. This method should allow for ground based measurements of $C_n^2(z_i)$ as averaged over an altitude range of the order of 200 meters as a function of time and avoids the inversion problems discussed here.

ACKNOWLEDGEMENTS

I would like to gratefully acknowledge Robert R. Beland and J. Krause-Polstroff of the Geophysics Directorate of Phillips Laboratory for many helpful conversations regarding this work and Edmund Murphy for serving as my Local Effort Point.

REFERENCE

Lidar Measurements of Optical Turbulence: Theory of the Crossed Path Technique by Robert R. Beland and J. Krause-Polstroff, PL-TR-91-2139, Environmental Research Papers, No. 1089.

FIGURES

CN2 versus ALTITUDE (Thermosonde Profile)

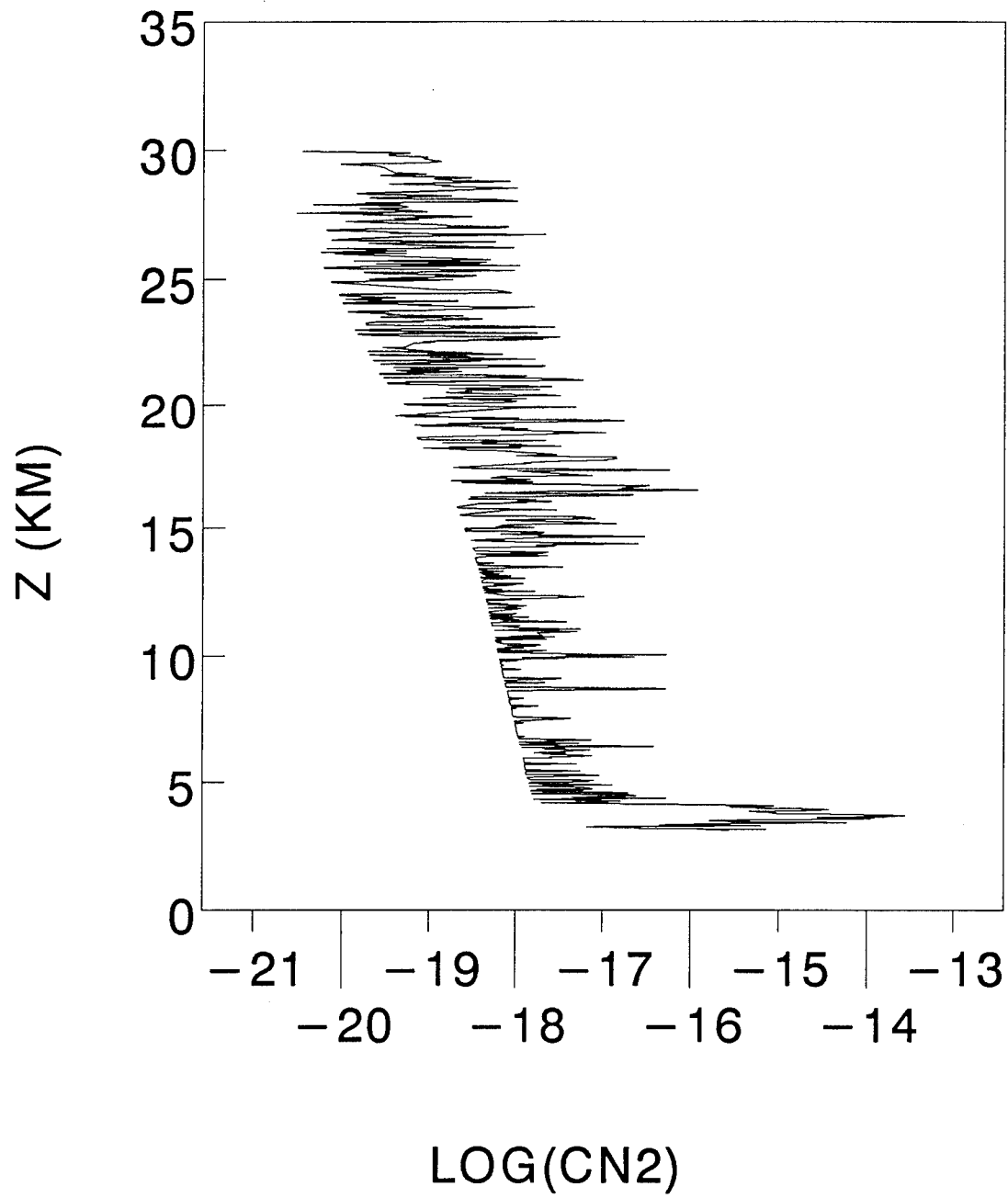


FIGURE 1

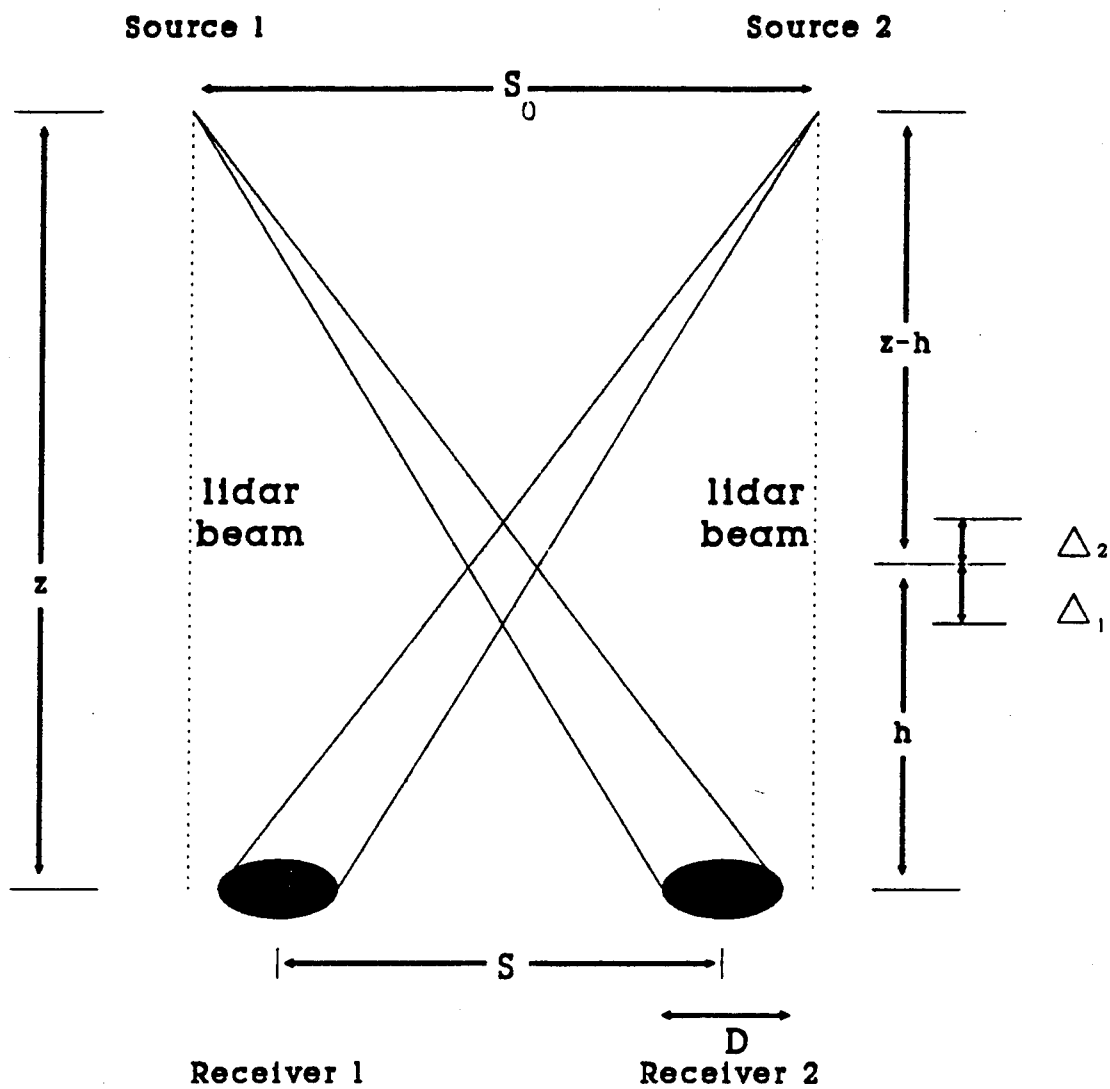


FIGURE 2

$W(z')$ vs z' for $z=9000$ and $z=10000$
Crossed Path Weighting Functions

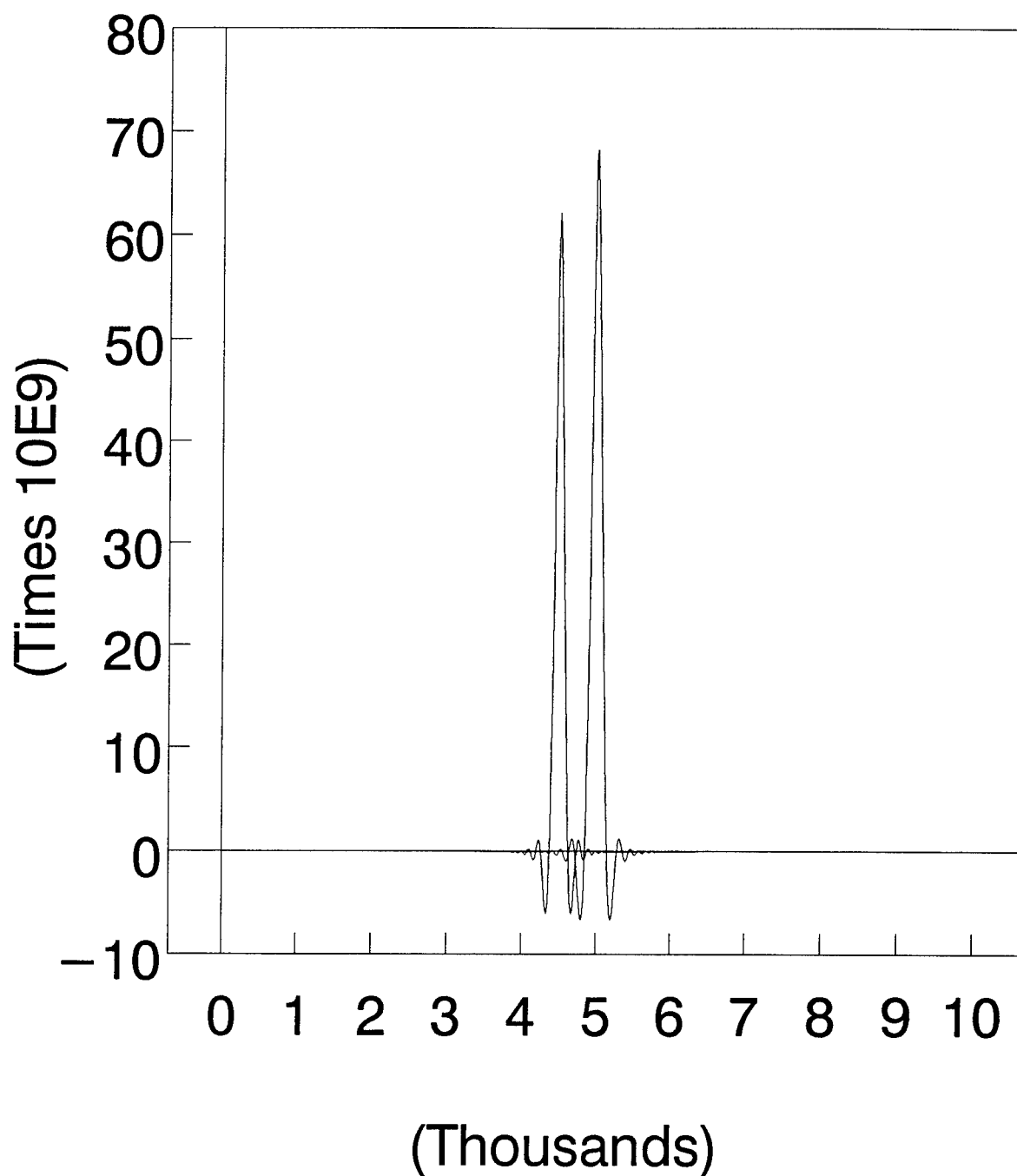


FIGURE 3

$W(z')/W_{\max}$ vs z' for $z=10000$
Crossed Path and Scintillation

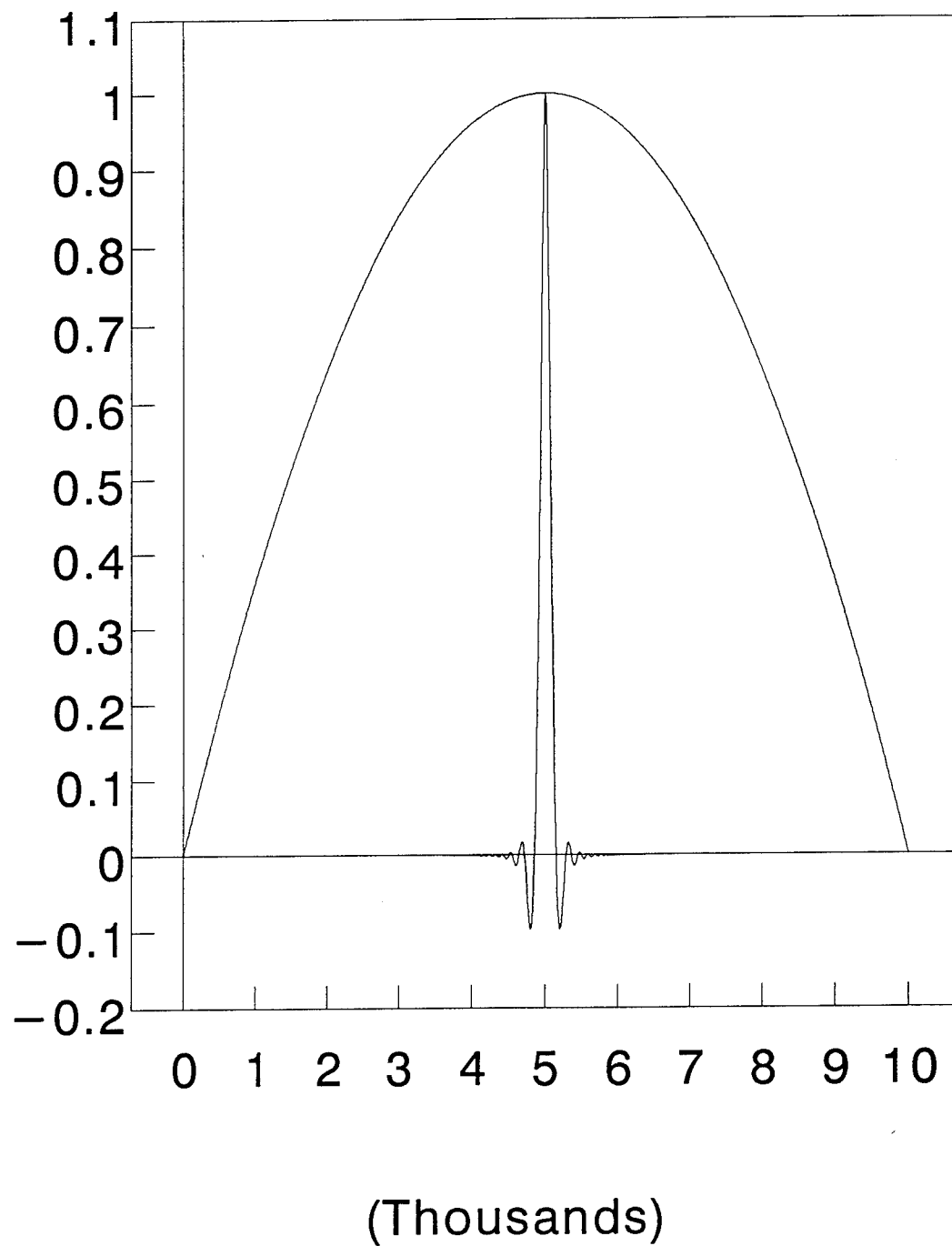


FIGURE 4

TABLES

W(i,j) for image dancing

0.375	0	0	0	0	0	0	0	0	0
0.632	0.118	0	0	0	0	0	0	0	0
0.743	0.321	0.060	0	0	0	0	0	0	0
0.803	0.460	0.199	0.037	0	0	0	0	0	0
0.841	0.554	0.317	0.137	0.026	0	0	0	0	0
0.866	0.621	0.409	0.234	0.101	0.019	0	0	0	0
0.885	0.670	0.480	0.316	0.181	0.078	0.015	0	0	0
0.899	0.708	0.536	0.384	0.253	0.145	0.063	0.012	0	0
0.910	0.739	0.582	0.441	0.316	0.208	0.119	0.052	0.010	0
0.919	0.763	0.620	0.488	0.370	0.265	0.174	0.100	0.043	0.008

TABLE I

Z	CN2in	g	CN2out	% diff
1	512	192	512	0
2	256	354	256	0
3	128	471	128	0
4	64	557	64	0
5	32	623	32	0
6	16	673	16	0
7	8	713	8	0
8	4	746	4	0
9	2	772	2	0
10	1	794	1	0

TABLE 2

Z	CN2in	g	gr	CN2out	%diff
1	512	192.00	191.73	511.29	0.14
2	256	353.76	352.44	248.62	2.88
3	128	470.63	470.06	166.90	-30.39
4	64	557.08	556.07	-64.51	200.79
5	32	622.56	619.90	317.25	-891.42
6	16	673.27	670.63	-625.78	4011
7	8	713.37	712.41	1727.59	-21495
8	4	745.68	744.85	-4554.17	113954
9	2	772.16	770.38	11600.44	-579922
10	1	794.19	790.88	-29659.75	2966075

TABLE 3

Z	CN2in	g	gr	CN2out	%diff
1	512	192.00	191.85	511.61	0.08
2	256	353.76	350.77	232.73	9.09
3	128	470.63	466.89	195.10	-52.42
4	64	557.08	556.45	-15.35	123.99
5	32	622.56	619.00	3.01	90.61
6	16	673.27	671.97	415.57	-2497
7	8	713.37	711.54	-1293.23	16265
8	4	745.68	743.29	3410.92	-85173
9	2	772.16	770.87	-8540.43	427122
10	1	794.19	791.42	21432.34	-2143134

TABLE 4

Z	CN2in	g	gr	CN2out	%diff
1	1.00E-14	37.50	37.45	9.99E-15	0.14
2	5.00E-15	69.09	69.13	5.11E-15	-2.23
3	3.33E-15	92.42	92.25	2.64E-15	20.81
4	6.10E-16	110.22	110.10	2.93E-15	-379.87
5	3.10E-18	123.20	123.46	-4.74E-15	153038
6	3.80E-18	132.72	132.57	7.92E-15	-208421
7	1.00E-18	139.92	139.61	-1.73E-14	1730230
8	1.20E-18	145.52	145.20	4.45E-14	-3704269
9	9.70E-19	150.01	149.79	-1.13E-13	11636805
10	3.70E-18	153.67	153.90	2.92E-13	-7896866

TABLE 5

Z	CN2in	g	gr	CN2out	%diff
1	1.00E-14	37.50	37.42	9.98E-15	0.22
2	5.00E-15	69.09	69.25	5.25E-15	-5.00
3	3.33E-15	92.42	92.48	2.38E-15	28.73
4	6.10E-16	110.22	110.17	2.98E-15	-388.89
5	3.10E-18	123.20	123.37	-4.86E-15	156724
6	3.80E-18	132.72	132.43	8.66E-15	-227715
7	1.00E-18	139.92	140.02	-1.54E-14	1537003
8	1.20E-18	145.52	145.44	3.20E-14	-2668601
9	9.70E-19	150.01	150.36	-7.29E-14	7514219
10	3.70E-18	153.67	153.56	1.72E-13	-4650644

TABLE 6

W(i,j) for scintillation

0.167	0	0	0	0	0	0	0	0	0
0.333	0.333	0	0	0	0	0	0	0	0
0.389	0.722	0.389	0	0	0	0	0	0	0
0.417	0.917	0.917	0.417	0	0	0	0	0	0
0.433	1.033	1.233	1.033	0.433	0	0	0	0	0
0.444	1.111	1.444	1.444	1.111	0.444	0	0	0	0
0.452	1.167	1.595	1.738	1.595	1.167	0.452	0	0	0
0.458	1.208	1.708	1.958	1.958	1.708	1.208	0.458	0	0
0.463	1.241	1.796	2.130	2.241	2.130	1.796	1.241	0.463	0
0.467	1.267	1.867	2.267	2.467	2.467	2.267	1.867	1.267	0.467

TABLE 7

Z	CN2in	g	CN2out	% diff
1	512	85	512	0
2	256	256	256	0
3	128	434	128	0
4	64	592	64	0
5	32	724	32	0
6	16	832	16	0
7	8	919	8	0
8	4	990	4	0
9	2	1047	2	0
10	1	1094	1	0

TABLE 8

Z	CN2in	g	gr	CN2out	%diff
1	512	85.33	85.21	511.24	0.15
2	256	256.00	255.42	255.02	0.38
3	128	433.78	433.01	128.62	-0.49
4	64	592.00	590.24	61.33	4.18
5	32	724.27	722.56	35.77	-11.78
6	16	832.00	830.08	12.15	24.06
7	8	919.05	918.50	14.81	-85.17
8	4	989.50	987.94	-6.65	266.34
9	2	1046.93	1041.91	6.05	-202.26
10	1	1094.20	1090.05	5.01	-400.88

TABLE 9

Z	CN2in	g	gr	CN2out	%diff
1	512	85.33	83.61	501.65	2.02
2	256	256.00	250.66	250.32	2.22
3	128	433.78	429.17	137.04	-7.06
4	64	592.00	590.33	62.96	1.63
5	32	724.27	723.80	31.58	1.30
6	16	832.00	828.05	6.71	58.08
7	8	919.05	916.08	24.00	-200.04
8	4	989.50	985.80	-13.76	444.04
9	2	1046.93	1042.68	18.40	-819.93
10	1	1094.20	1090.14	-12.89	1389.34

TABLE 10

Z	CN2in	g	gr	CN2out	%diff
1	1.00E-14	16.67	16.64	9.98E-15	0.18
2	5.00E-15	50.00	49.88	5.02E-15	-0.36
3	3.33E-15	87.96	87.88	3.32E-15	0.46
4	6.10E-16	120.60	120.65	6.22E-16	-2.00
5	3.10E-18	142.43	142.44	-7.22E-18	332.80
6	3.80E-18	157.01	157.35	1.28E-17	-237.56
7	1.00E-18	167.45	167.66	-7.08E-18	807.70
8	1.20E-18	175.28	174.91	8.54E-18	-611.89
9	9.70E-19	181.39	181.78	-5.79E-18	696.42
10	3.70E-18	186.29	186.13	9.97E-18	-169.53

TABLE 11

Z	CN2in	g	gr	CN2out	%diff
1	1.00E-14	16.67	16.45	9.87E-15	1.29
2	5.00E-15	50.00	49.67	5.13E-15	-2.58
3	3.33E-15	87.96	87.90	3.22E-15	3.32
4	6.10E-16	120.60	120.81	6.99E-16	-14.52
5	3.10E-18	142.43	142.53	-7.18E-17	2417.47
6	3.80E-18	157.01	156.71	6.94E-17	-1725.63
7	1.00E-18	167.45	167.47	-5.77E-17	5867.14
8	1.20E-18	175.28	175.06	5.45E-17	-4444.80
9	9.70E-19	181.39	181.72	-4.81E-17	5058.83
10	3.70E-18	186.29	185.88	4.93E-17	-1231.50

TABLE 12

RATES AND SCALING RULES FOR VIBRATIONAL RELAXATION
OF OH(n) IN COLLISIONS WITH ATMOSPHERIC CONSTITUENTS

Ronald J. Bieniek
Associate Professor
Department of Physics

University of Missouri - Rolla
Rolla, MO 65401-0249

Final Report for:
Research Initiation Program
Phillips Laboratory

Sponsored by:
Air Force Office of Scientific Research
Bolling Air Force Base, Washington, D.C.

and

University of Missouri

December 1992

RATES AND SCALING RULES FOR VIBRATIONAL RELAXATION
OF OH(n) IN COLLISIONS WITH ATMOSPHERIC CONSTITUENTS

Ronald J. Bieniek
Department of Physics
University of Missouri-Rolla

Abstract

The vibrational relaxation rates of OH($X^2\Pi, n$), through collisions with various atmospheric constituents, are needed to understand and model the behavior of certain atmospheric layers, and for the remote analysis of emission from atmospheric disturbances (such as exhaust plumes). The results of theoretical investigations are reported here, in direct support of information needed for the analysis of experimental data for OH relaxation rates obtained in the continuing mission of the LABCEDE group within the Optical Environment Division, Phillips Laboratory. It was discovered that absolute rates from quantum mechanical computations based on an adiabatic distorted-wave infinite-order sudden approximation were very sensitive to the detailed nature of the perturbational interaction. However the relative increase of rates with collisional energy and initial vibrational excitation did not exhibit such sensitivity, and should be more reliable. The quantal results gave much information that was useful for an analytic treatment of the relaxation process, based on exact first-order solutions for an exponential potential. The resulting analytic formula, presented in this report, gives absolute relaxation rates for OH(n) + O₂ collisions that are in excellent agreement with the rates obtained in the LABCEDE experiments. With this success, absolute relaxation rates for OH(n) + Ar collisions could be predicted. The OH(n) + Ar relaxation rates for the n=1-6, are 0.91, 2.4, 4.7, 8.3, 14, and 22 (10^{-13} cm³s⁻¹), for a temperature of 300 K. It was also found that the rate increases more rapidly with temperature, the higher the initial level of vibrational excitation. Finally, progress was made in developing a semi-quantal formalism for the evolution of flux on various collisional channels, which offers an alternate and more simple approach to scattering problems than the usual set of coupled second-order equations. The semi-quantal equations are only first-order in time, and are designed to be path independent - an unusual feature for trajectory-based computations. These equations should make the computation of molecular collision problems more tractable, even in cases where asymptotic states are being pumped by an external radiation field.

RATES AND SCALING RULES FOR VIBRATIONAL RELAXATION
OF OH(n) IN COLLISIONS WITH ATMOSPHERIC CONSTITUENTS

Ronald J. Bieniek

I. Introduction

The general purpose of this project was to investigate induced relaxation of vibrationally excited molecular OH(n) in the ground $X^2\Pi$ electronic state, due to thermal collisions with certain atmospheric constituents. One of the major compelling reasons for this study was to support directly the ongoing experimental program of the LABCEDE group of the Optical Environment Division, Geophysics Directorate of Phillips Laboratory.^{1,2} This group has measured vibrational relaxation of OH(n=1-6) in collision with O₂.³ However, to interpret their data properly, the group required relaxation rates due to background Ar gas, used in the Hot LABCEDE spectrometer to slow down electrons employed in the excitation process. The relaxation rates caused by the Ar bath gas must be known, so that its contribution can be subtracted out in the analysis of the relaxation rates caused by atmospheric constituents of interest to the Division's mission. Earlier classical computations by Thompson on the problem produced numerical values and trends that were at variance to what was observed.^{1,4}

Since only total vibrational relaxation to all final rotational levels is needed, one can adequately describe the atom-diatom interaction by a spherically averaged breathing-sphere potential.^{5,8} This is equivalent to summing over all final rotational states in the infinite-order sudden approximation. This breathing-sphere approximation forms the basis for the study of collisional relaxation of vibrationally excited OH.

II: Quantum Mechanical Computations

Quantum mechanical computations of vibrational relaxation rates for OH(n) in collisions with Ar and O₂ were undertaken using an adiabatic distorted-wave infinite-order sudden (ADWIOS) approximation.⁹ In an earlier study, this method was successfully employed to study the collisional vibrational relaxation of SiO molecules. In these studies, the numerical form of the perturbational interactions is crucial, since it produces the vibrational transitions.

Unfortunately, no full OH-Ar(O₂) potential hypersurface exists. At the time of submission of the proposal, Esposti and Werner had recently published an *ab initio* OH-Ar potential. This is not only useful for studying OH(n) + Ar collisions, but also for OH(n) + O₂ because of the electronic similarities between the systems. Unfortunately, Esposti and Werner only determined the OH-Ar surface for the equilibrium separation $r_e=1.0107$ Å of the OH molecule, i.e., for a rigid-diatom.

To get vibrational relaxation rates, the dependence of the interaction on

the O-H stretch distance r is required. There was high hopes that the Werner group in Bielefeld would compute the dependence on O-H stretch by the time this report was due, or that the Lester group, at the University of Pennsylvania, would produce sufficient semi-empirical data to model the interaction. Unfortunately, neither proved to be the case. Bowman et al. have reported some information on the stretch dependence of the electronically excited Σ states, but the vibrational relaxation in the LABCEDE project occurs from the ground Π electronic state.¹⁰

Two internationally recognized experts in the field, upon being appraised of my dilemma in private communications, both suggested that I could approximate the stretch dependence with that of HCl-Ar; they indicated that J.M. Hutson, at University of Durham, be contacted.^{11,12} He has recently published an HCl-Ar potential hypersurface.¹³ Unfortunately, the iterative semiempirical method Hutson uses does not express the stretch dependence in terms of the molecular coordinate r , but rather expands it in terms of mass-reduced vibrational quantum numbers related to diagonal matrix elements of harmonic oscillators. The net result of this is that the off-diagonal elements ($\Delta n \neq 0$) needed for vibrational relaxation are very difficult to extract in theory. However, there is even a larger practical problem. The dependence of Hutson's potential on $(r-r_e)$ and on $(r-r_e)^2$ are both linear in the reduced quantum number, and to differentiate the two poses insurmountable practical problems and inaccuracies at the moment.^{14,15} Since the linear and quadratic dependence of the potential on the O-H stretch is the main source of vibrational relaxation coupling, the inherent uncertainties of the potential make quantitative conclusions from *ab initio* quantal scattering computations very limited. This also meant no new meaningful conclusions could be drawn about the contribution to direct multi-quanta transitions from T-matrix elements that are off the energy shell.

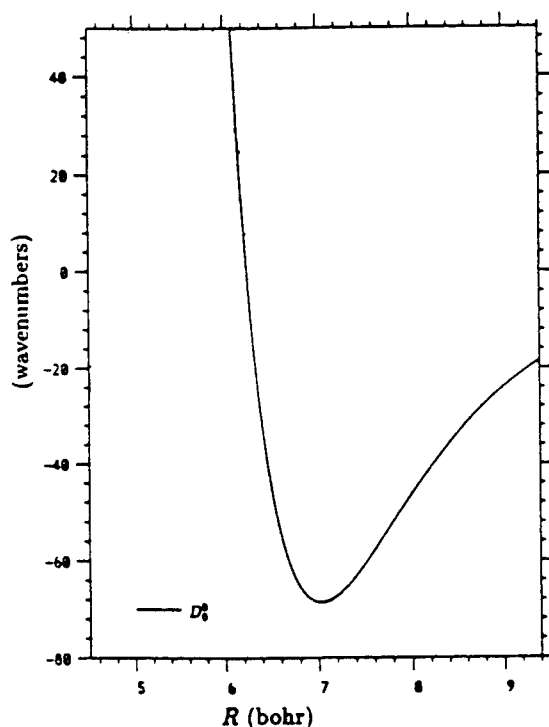
However, certain things could be investigated using a breathing sphere potential produced from the rigid-diatom potential of Eposti and Werner. The breathing sphere model corresponds to the zeroth-order coefficient of the Legendre-expansion of the angular dependence of the complete Eposti-Werner potential interaction.⁹ This spherically averaged interaction (which corresponds to integrating over all orientations of the rigid diatom) will be designated as $V_{EW}(R)$, where R is the collisional coordinate between OH and Ar. The numerical values of $V_{EW}(R)$ utilized in this study were generated from a computer code that Werner kindly sent.¹⁶ The potential is shown in Figure 1. Note that there is an attractive well in the $V_{EW}(R)$ OH-Ar potential, with depth of $D_m = 68.6 \text{ cm}^{-1} = 3.1275576 \cdot 10^{-4}$ hartrees. (The hartree is the unit of energy in atomic units, with 1 hartree = 27.211 eV = $2.19476 \cdot 10^5$, just as the atomic unit of distance is the bohr, with 1 $a_0 = 0.529176 \text{ \AA} = 0.529176 \cdot 10^{-8} \text{ cm}$.) Unfortunately the Eposti-Werner potential is completely unreliable for distances much smaller than

$R_i = 3.308 \text{ \AA} = 6.250 a_0$, the zero crossing point of $V_{EW}(R)$. Thus, the nature of the repulsive core interaction is rather uncertain. To check the sensitivity of the quantal rates to the exact form of the potential, an alternative potential was constructed, using a standard Morse-like analytic fit to $V_{EW}(R)$ was made for distances closer in than the potential minimum at $R_m = 3.71685 \text{ \AA} = 7.02385 a_0$. The second, fitted potential used in the quantal computations is then given by:

$$V_f(R, r|\gamma) = \begin{cases} D_m \cdot [e^{2\zeta(R_m-R)} - 2e^{\zeta(R_m-R)}] & , R \leq R_m \\ V_{EW}(R) & , R > R_m \end{cases} \quad \text{Eq. (1)}$$

where $\zeta = \ln(2)/(R_m - R_i)$. The analytic form in the interval of $[R_i, R_m]$ differs from the Eposti-Werner potential by typically less than 0.1%. Although remarkably the same for $R > R_i$, the differences in these two potentials is sufficient to cause major effects on absolute rates.

Figure 1: Spherically-averaged $\text{OH}(X^2\Pi, n=0) + \text{Ar}(^1S_0)$ potential from the analysis of Eposti and Werner



To get the vibrational relaxation cross sections, the O-H stretch dependence of the potential hypersurface had to be modelled. This was done by multiplying the potential at equilibrium separation r_e , by an exponential

dependence, which has proved useful in relaxation studies with other molecules:^{6,17-19}

$$V(R, r | \gamma) = V(R) \cdot e^{\gamma(r-r_e)} \quad \text{Eq. (2)}$$

where $V(R)$ is either $V_{EW}(R)$ or $V_f(R)$. The value of γ is typically in the range of 0.2 - 2 a_0 for molecular collisions. We will see, Section III, that the effective value of γ for the OH-Ar(O_2) collision system is $\approx 0.39 a_0^{-1}$, well within the expected range. This is the potential that was used for the quantal scattering computations for collisional vibrational relaxation of OH(n).

Quantal computations using the ADWIOS approximation and the potential of Eq. (2) were done at various collisional energies E . Since the LABCEDE experiment was conducted at a temperature of $T = 300$ K, the discussion of results in this report concentrate on a collisional energy of $E_1 = 1.5 \cdot kT = 1.425 \cdot 10^{-3}$ hartrees = 0.03878 eV, which is characteristic of the thermal energy in the LABCEDE experiment at $T = 300$ K, and at $E_2 = 6 \cdot kT = 5.7 \cdot 10^{-3} = 0.1551$ eV, which is representative of the higher collisional energies in the thermal tail. These two energies gave much insight into the dependence of relaxation rates on collisional energy and initial vibrational excitation. Unfortunately, the quantal relaxation cross sections at these collisional energies were changed by over an order of magnitude when the R dependence of the potential was changed from $V_{EW}(R)$ to $V_f(R)$. It is unclear whether or not this sensitivity arose from the very small difference between the potential in the collisional well region, or was due to the projected potentials in the uncertain repulsive region ($R < R_2$). If this is physically the case, it is discouraging because then the potentials would have to be known extremely accurately to obtain *ab initio* relaxation rates. It would be difficult to obtain such accurate potentials by *ab initio* molecular structure calculations, and would also be difficult to extract semi-empirically because bound molecular states do not adequately probe the repulsive core of the interaction.¹⁶ There is the possibility, of course, that the ADWIOS approximation breaks down for some reason in the OH-X system at thermal energies. This possibility is one of the reasons that the preliminary development of an alternative, coupled-equations method was proposed in the grant, which will be discussed in Section IV.

It was discovered, though, that the relative changes in relaxation rates as a function of initial vibrational excitation, when compared to the fundamental $n = 1 \rightarrow 0$ transition, varied little when the R dependence of the potential was switched between $V_{EW}(R)$ and $V_f(R)$. They were also independent of γ . Thus, this ratio seems to have much more computational believability. The ratios for the two collisional energies for OH-Ar and OH- O_2 collisions are shown in Table I, based on the numerical Esposti-Werner potential. One additional result obtained from the quantal computations at the two energies, and useful in the modelling

of the next section, is that the energy dependence of the relaxation rate for the fundamental transtion is given by $v\sigma_{1\rightarrow0}(E_2=0.155 \text{ eV})/v\sigma_{1\rightarrow0}(E_1=0.0388 \text{ eV}) = 1.8$ for $X = \text{Ar}$, and 3.6 for $X = \text{O}_2$.

TABLE I: Increase of relaxation rate with initial level of excitation in $\text{OH}(n) + X$ collisions (quantal results)

$v\sigma_{n \rightarrow n-1}(E)/v\sigma_{1 \rightarrow 0}(E)$ for OH(n)-Ar		$v\sigma_{n \rightarrow n-1}(E)/v\sigma_{1 \rightarrow 0}(E)$ for OH(n)-O ₂		
n	E = 0.0388 eV	E = 0.155 eV	E = 0.0388 eV	E = 0.155 eV
1	1	1	1	1
2	2.1	4.2	3.4	1.5
3	5.4	5.8	4.8	4.9
4	7.1	12	11	7.0
5	14	26	17	15
6	24	29	25	19

It should also be noted that, for a given initial vibrational state n , the ratio undulated about a smoothly increasing mean, as the collisional energy was increased. Such behavior should be expected as the result of the oscillatory nature of the underlying collisional wavefunctions.

III: Simple, Accurate Analytic Formulae for Relaxation Rates

During the Summer Faculty Research project that was the prelude to this study, a simple analytic formula was developed that adequately predicted the relative increase of relaxation rates with initial vibrational excitation, as measured in the LABCEDE experiment on $\text{OH}(n) + \text{O}_2$. This was reviewed in the grant proposal that led to the current research reported here. However, as indicated in the proposal, the dependence of the relaxation rates on collisional energy (and consequently temperature) could not be predicted by the formula. Furthermore, the absolute numerical values of the rates could not be predicted.

It is with great pleasure to announce that these restrictions have been successfully removed in the current project. As before, the beginning point for the analytic formulae is the exact, first-order distorted-wave solution for collisional vibrational relaxation. The basic assumption is that changes in vibrational state through collisions are largely due to the striking of the inner core of the potential interaction, where perturbations are large. If we approximate this repulsive core with an exponential form,

$$V(r,R) = [\gamma(r-r_0) - \alpha R] - \epsilon \quad \text{Eq. (4)}$$

the analytic solution for the T-matrix elements for collisional energy E is:^{17,18}

$$T_{l,nj} = \frac{1}{16} \alpha (k_n k_j)^{-1/2} [(1 - \delta_{nj}) V_{nj}/V_{jj}] (V_{nn}/V_{jj})^{1/2} [(q_j^l)^2 - (q_n^l)^2] \quad \text{Eq. (5a)}$$

where

$$\times \frac{[q_n^l q_j^l \sinh(\pi q_n^l) \sinh(\pi q_j^l)]^{1/2}}{\sinh[\frac{1}{2}\pi(q_j^l + q_n^l)] \sinh[\frac{1}{2}\pi(q_j^l - q_n^l)]} {}_2F_1(1 + \frac{1}{2}i[q_j^l + q_n^l], 1 - \frac{1}{2}i[q_j^l - q_n^l]; 2; 1 - V_{nn}/V_{jj})$$

$$q_n^l = 2\alpha^{-1} \{k_n^2 + 2m\epsilon - \alpha^2/(l+1) [\gamma r_e + \ln(2mA/(k_n^2 + 2m\epsilon))]\}^{-1/2} \quad \text{Eq. (5b)}$$

and μ is the collisional reduced mass, l the collisional angular momentum quantum number, and $V_{ij} = \langle i | e^{r(r-\infty)} | j \rangle$ is a matrix element of the vibrational states.

Fortunately the confluent hypergeometric function ${}_2F_1$ in Eq. (5a) is nearly unity for all reasonable values of its arguments in a collisional problem. If we approximate the vibrational states as harmonic oscillators, the ratios of vibrational matrix elements that appear in Eq. (5) take on a simple form. Furthermore, for most collision problems at thermal energies, the ratio of the hyperbolic sine functions in the T-matrix elements becomes $2 \cdot \exp[-\pi \cdot |\Delta k_n(l)|/\alpha]$, where $\Delta k_n(l)$ is the change in collisional wavenumber for the $n \rightarrow n-1$ transition for angular momentum l . One of the most important steps in the derivation of simple analytic formulae is the accurate evaluation of this change in wavenumber. If we let ω_e and $x_e \omega_e$ be the standard expansion term values for the vibrational energy,²⁰ such that $hc \cdot [\omega_e(n+\frac{1}{2}) - x_e \omega_e(n+\frac{1}{2})^2]$ is the energy of vibrational state n , then the change in energy in the single quantum relaxation is approximately $hc \omega_e(1 - 2 \cdot x_e \cdot n)$, where $x_e = x_e \omega_e / \omega_e$ is the anharmonicity parameter. (For OH, $\omega_e = 3735.21 \text{ cm}^{-1}$, and $x_e \omega_e = 82.81 \text{ cm}^{-1}$, making $x_e = 0.02217$.) The next step must be accurately executed to get the dependence of rates on both n and E . We can make a simplifying, but accurate approximation if the collisional energy is significantly less than the vibrational spacing. If we let $\hbar\omega$ be the energy associated with first-order vibrational term ω_e (i.e., $\hbar\omega = hc\omega_e$), the approximation implies that $kT < \hbar\omega$. The change in wavenumber is then such that:

$$2\pi |\Delta k_n(l)|/\alpha = \beta(\alpha) \cdot [y - a(n) \cdot y^2 + b(n) \cdot y^4 - \frac{1}{2} y^6] \quad \text{Eq. (6a)}$$

where

$$\beta(\alpha) = 2\pi \cdot [2\mu\hbar\omega]^{1/2} \cdot [\hbar\alpha]^{-1} \quad \text{Eq. (6b)}$$

$$a(n) = \frac{1}{2} [1 + x_e \cdot n \cdot (1 + 1.5 \cdot x_e \cdot n)] \quad \text{Eq. (6c)}$$

$$b(n) = 0.125 \cdot [1 + 3 \cdot x_e \cdot n] \quad \text{Eq. (6d)}$$

with

$$y^2 = [E_c + \epsilon - \{(\ell + \frac{1}{2})/R_c\}^2] \cdot [\hbar\omega]^{-1} \quad \text{Eq. (6e)}$$

where $\mu = (m_1 + m_2) \cdot M_p / (m_1 + m_2 + M_p)$ is the collisional reduced mass, with m_1 the mass of O, m_2 the mass of atomic H, and M_p the mass of projectile X (Ar or O₂). R_c is a

collisional coordinate characteristic of the location where the dynamical transition occurs. In this project, it was taken to be the collisional turning point for the initial state at a collisional energy of $1.5 \cdot kT$. For the OH-Ar potential used here, $R_c = 5.65 a_0$.

With the approximation of Eq. (6a), the sum over angular momenta ℓ for the partial waves in the exponential slope model can be accomplished semi-analytically. The sum is converted into an integral over ℓ , and then manipulated until the variable y of Eq. (6e) can be substituted as the variable of integration. The grand result for the thermally averaged rate $R(n,T)$ for single-quantum $n \rightarrow n-1$ relaxation collision at temperature T is:

$$R(n,T) = \int_{0.1}^8 v\sigma(n,z \cdot kT) \cdot \sqrt{z} \cdot e^{-z} dz \quad \text{Eq. (7a)}$$

where

$$A(\alpha, \gamma) = \frac{16\pi^3}{h^2} \cdot \frac{(R_c \cdot \gamma)^2}{\alpha^4} \cdot \frac{\mu}{m} \cdot (h\omega)^{2.5} \cdot \sqrt{2 \cdot \mu} \cdot e^{-\beta(\alpha)} \quad \text{Eq. (7b)}$$

$$P(n, \alpha, E) = \frac{\int_0^{Y(E)} y^2 \cdot \sqrt{1 + (1 + 2 \cdot x_e \cdot n) \cdot y^2} \cdot e^{\beta(\alpha) \cdot (y - a(n) \cdot y^2 + b(n) \cdot y^4 - 0.5 \cdot y^6)} dy}{E \cdot \sqrt{1 + \frac{1 + 2 \cdot x_e \cdot n}{h\omega} \cdot E}} \quad \text{Eq. (7c)}$$

$$Q(\alpha, n) = n \cdot (1 - 2 \cdot x_e \cdot n) \cdot e^{\beta(\alpha) \cdot x_e \cdot n} \cdot [1 + 0.5 \cdot x_e \cdot n \cdot (1 + x_e \cdot n)] \quad \text{Eq. (7d)}$$

and

$$v\sigma(n, E) = A(\alpha, \gamma) \cdot P(n, \alpha, E) \cdot Q(\alpha, n) \quad \text{Eq. (7e)}$$

with $Y(E) = [(E + \epsilon)/h\omega]^{1/2}$.

The rate for a single collisional energy E , $v\sigma(n, \alpha, E)$, nicely factors into three parts. $A(\alpha, \gamma)$ depends only upon basic system parameters, $P(n, \alpha, E)$ accounts for the dependence of rates on collisional energy, while $Q(\alpha, n)$ gives the major dependence on vibrational quantum number n and anharmonicity x_e . In numerical tests, the difference between **absolute** rates computed by Eq. (7) and those produced by the exact, first-order treatment of Eq. (5) is negligible. This was extremely satisfying. The lower limit on the integral for the thermal average is not zero because the $P(n, \alpha, E)$ from the exponential slope model of Eq. (7) does not go to zero at zero collisional energy. However, since the actual low-energy

rates would only make a small contribution to the total thermalized rate, setting the lower to 0.1 instead of zero will introduce little error. The upper limit of 8 includes all the collisional energies that will substantially contribute to the collision, i.e., $E \leq 8kT$.

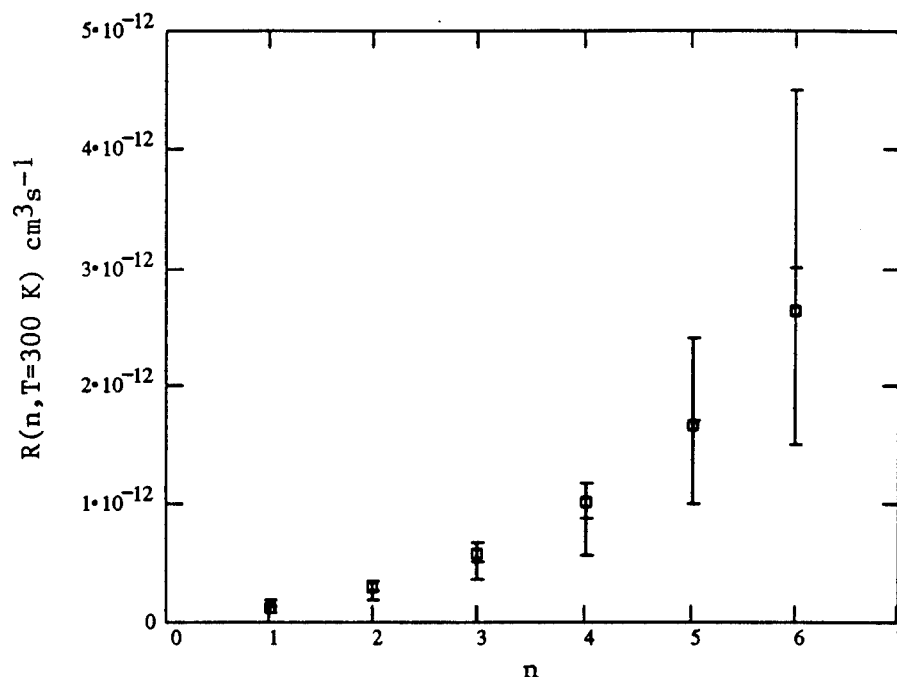
To apply Eq. (7) to the OH-X systems at hand requires setting the various parameters. It was discovered that the increase of rates with vibrational excitation, as indicated in Table I, was largely determined by the exponential slope, α , in the model, although a range of values [10.7,12.2] adequately reproduced the increases. After some iterations, a value of $\alpha = 11.5 \text{ a}_0^{-1}$ seemed optimal for the OH-Ar(O_2) collision system. The value of ϵ has two major effects. It can significantly affect the absolute value of the rate, but more importantly, it affects the change of rate with collisional energy. It should be on the order of the well depth D_m of the collisional potential ($3.2 \cdot 10^{-4}$ hartree for OH-Ar). However, one must be careful about just setting it to the well depth, because we wish to model the effect of the potential on the collision. As noted above, the rate for the fundamental $n = 1 \rightarrow 0$ relaxation transition increases by a factor of 1.8 in the OH-Ar collision, and by a factor of 3.6 for the OH- O_2 case, as the collisional energy increases from $E_1 = 1.5 \cdot kT$ to $E_2 = 6 \cdot kT$ for $T = 300 \text{ K}$. The difference in the two systems was largely due to the slow undulations with energy in the rates. Consequently, it was decided to choose 2.6 as the characteristic factor increase of rates from E_1 to E_2 for OH-X. For $\epsilon = 1.5 \cdot 10^{-3}$ hartree, the factor increase is 4.2; for $\epsilon = 3.0 \cdot 10^{-3}$ hartree, the increase is 1.8. It was found that $\epsilon = 2.2 \cdot 10^{-3}$ hartree achieved the desired factor increase of 2.6. The predicted increase in rates from the analytic exponential model are shown in Table II. The values compare favorably to the quantal values found in Table I, particularly when the undulations in the quantal results will be smoothed in thermal averaging.

TABLE II: Predicted increase of relaxation rate with initial level of excitation in OH(n) + X collisions

n	$v\sigma_{n \rightarrow n-1}(E)/v\sigma_{1 \rightarrow 0}(E)$ for OH(n)-Ar		$v\sigma_{n \rightarrow n-1}(E)/v\sigma_{1 \rightarrow 0}(E)$ for OH(n)- O_2	
	E = 0.0388 eV	E = 0.155 eV	E = 0.0388 eV	E = 0.155 eV
1	1	1	1	1
2	2.6	2.6	2.6	2.5
3	5.2	4.9	5.0	4.8
4	9.1	8.4	8.8	8.2
5	15	14	14	13
6	24	21	23	20

With $\alpha = 11.5 \text{ a}_0^{-1}$ and $\epsilon = 2.2 \cdot 10^{-3}$ hartree set, the value of γ , the exponential vibrational coupling, can be determined by comparison to experimental data. It should be observed that this coupling appears in the dimensionless quantity $R_c \gamma$ of Eq. (7). It is a simple matter to compute the relative thermal rate for vibrational relaxation of $\text{OH}(n=1) + \text{O}_2$, and determine the value of $R_c \gamma$ that would yield the result of $1.3 \cdot 10^{-13} \text{ cm}^3 \text{ s}^{-1}$ obtained in the LABCEDE experiment.³ It was found that $R_c \gamma = 2.20$ produced the most desirable results over the range of vibrational levels. As discussed above, $R_c = 5.65 \text{ a}_0$, the collisional turning point at $E=1.5 \cdot kT$. This makes $\gamma=0.39 \text{ a}_0^{-1}$, well within the range expected of molecular systems. With $R_c \gamma = 2.20$, the absolute relaxation rates of OH-Ar and OH-O_2 can be computed, and the latter compared to experimental results. This comparison is done in Figure 2. As can be readily seen, the thermalized rates predicted by the simple analytic formula for vibrational relaxation of OH in collisions with O_2 at $T = 300 \text{ K}$ easily fall within the error bars of the LABCEDE results.

Figure 2: Comparison of theoretical and experimental results for absolute thermal rates for vibrational relaxation in $\text{OH}(n) + \text{O}_2$ collisions: (\square) Predicted from analytic exponential formula (+ with error bars) Experimental LABCEDE results



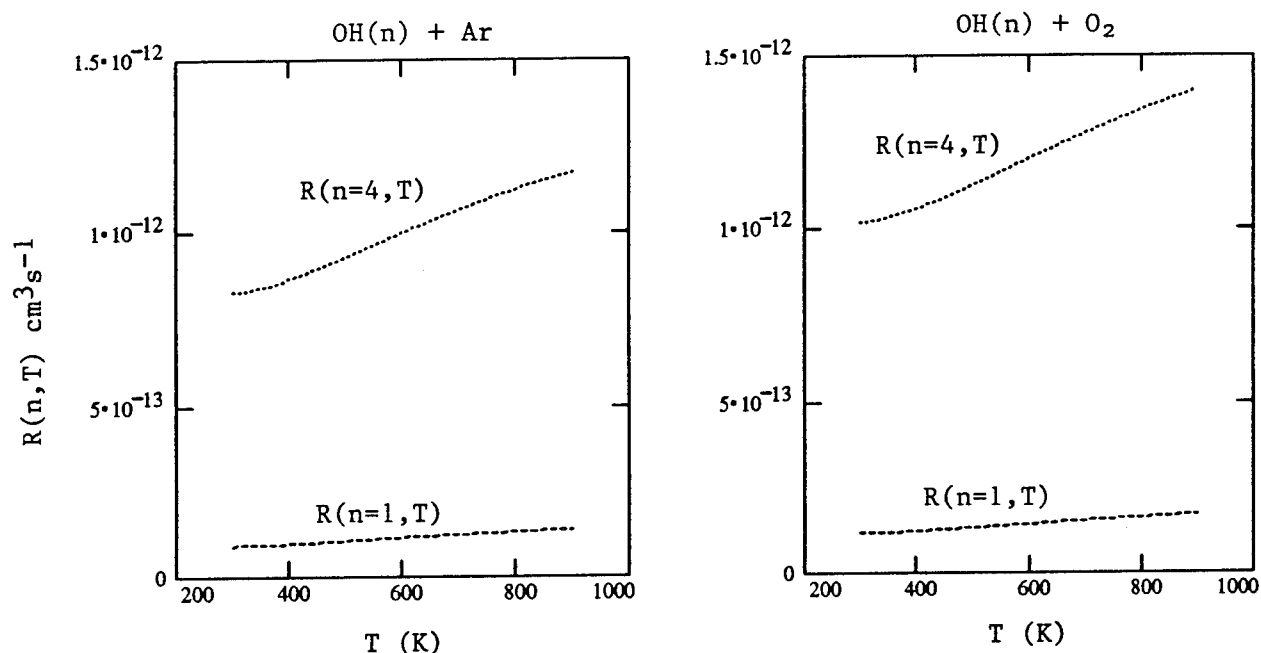
Using the same values of parameters, except for the mass M_p of the colliding partner, thermalized vibrational relaxation rates for $\text{OH}(n)$ in collision with Ar can be predicted. The results are displayed in Table III.

TABLE III: Predicted thermal relaxation rate for OH-Ar collisions at
T = 300 K

n	$R_{\text{OH-Ar}}(n, T)^{\text{analytic}}$ ($10^{-13} \text{ cm}^3 \text{ s}^{-1}$)
1	0.91
2	2.4
3	4.7
4	8.3
5	14
6	22

Table III is one of the primary results of this project, since the numerical values can be used to subtract out the effects of the background Ar gas in the LABCEDE experiment. Figure 3 displays the temperature dependence of rates for two representative levels of excitation ($n=1$ and $n=4$) over a thermal range of possible interest. Note that the higher level of initial excitation is more drastically affected by temperature change. The analytic computations described here can be easily done using inexpensive, commercially available software products, such as Mathcad®. The LABCEDE group in the Optical Environment Division of the Phillips Lab, Hanscom AFB, which is directly impacted by this study, has been sent copies of the relevant computer files.

Figure 3: Temperature dependence of absolute rates for vibrational relaxation in thermal OH(n) + Ar(O₂) collisions



IV. Semi-quantal Dynamical Density Matrix

As mentioned in Section II, there is some possibility that the quantal ADWIOS approximation is overly sensitive to small differences in the potentials V_{EW} and V_I at thermal collision energies. Furthermore, molecular scattering computations are often horrendously difficult because of number of coupled second-order differential equations involved. As outlined in the grant proposal, preliminary investigations were pursued on developing a more simple set of coupled equations that would adequately described vibrational changing collisions. The initial stage of this has been completed. The result is a set of more simple semiquantal first-order coupled equations for the flux along the different channels. It is analogous to a semiclassical density matrix approach, but is numerically independent of the trajectory path chosen - a distinct advantage over most semiclassical treatments. Another advantage of these equations is that that rather complicated optical pumping of the vibrational states can be naturally accomodated by the formalism.

We will begin with the coupled equation for inelastic scattering.²¹ Let $V_{\alpha\alpha}(R)$ be the total electronic-radiation field Hamiltonian, including stimulated emission and absorption, which is a function of internuclear separation R . For the moment, it does not include decay terms. Let U be a convenient portion of $V_{\alpha\alpha}$, with a set of electronic-photon states $\{|\beta(R)\rangle\}$ that adequately span the space. U is diagonal in this basis; i.e. $U_{\alpha\beta}(R) = U_{\alpha\alpha}(R)\delta_{\alpha\beta}$. The remaining part of the electronic-radiation Hamiltonian is given by $V = V_{\alpha\alpha} - U$, which may or may not have residual diagonal elements in the $\{|\beta(R)\rangle\}$ basis.

We now introduce the associated heavy-particle radial eigenfunctions of potential U :

$$[\partial_R^2 - k_\alpha(R)^2] h_\alpha^\pm(R) = 0 \quad (8a)$$

where

$$k_\alpha(R)^2 = E - U_{\alpha\alpha}(R) \quad (8b)$$

where $k_\alpha(R)^2 = E - U_{\alpha\alpha}(R)$, and the \pm indicates outgoing and incoming wave conditions. The total scattering state can be expanded as

$$|\Psi\rangle = \sum_\beta c_\beta^\pm(R) h_\beta^\pm(R) |\beta\rangle \quad (9)$$

with boundary condition of $c^-(0) = c^+(0)$. With this, we can obtain the coupled scattering equations:

$$\partial_R^2 c_\alpha + 2\partial_R \ln(h_\alpha) \partial_R c_\alpha = (2\mu/\hbar^2) \sum_\beta [h_\beta/h_\alpha] V_{\alpha\beta} c_\beta \quad (10)$$

We now make a uniform semi-quantal JWKB approximation for the uncoupled

channel wavefunctions, using a modified amplitude $A_\alpha(R)$ that is valid both near to and far from turning points:²²

$$h_\alpha^\pm(R) = A_\alpha(R) \exp\{\pm i[\phi_\alpha(R) + \frac{1}{4}\pi]\} \quad (11a)$$

where

$$A_\alpha(R) = \pi^{1/2} [\chi_\alpha(R) k_\alpha(R)^{-2}]^{1/4} [Ai(-\chi_\alpha)^2 + Bi(-\chi_\alpha)^2]^{1/2} \quad (11b)$$

$$\chi_\alpha(R) = [3\phi_\alpha(R)/2]^{2/3} \quad (11c)$$

$$\phi_\alpha(R) = \int^R k_\alpha(q) dq \quad (11d)$$

We now make a second assumption, that the expansion coefficients $c_\alpha(R)$ are slowly varying; i.e.,

$$\begin{aligned} \partial_R^2 c_\alpha &< \partial_R \ln(h_\alpha) \partial_R c_\alpha = ik_\alpha + 2A_\alpha^{-1} \partial_R A_\alpha \\ &= ik_\alpha(R) [1 - iz_\alpha(R)] \end{aligned} \quad (12)$$

where $z_\alpha(R) = \frac{1}{4}[T_{\alpha\alpha}(R) k_\alpha(R)]^{-1} dU_\alpha(R)/dR$, and $T_{\alpha\alpha}(R) = (\hbar k_\alpha)^2/(2\mu)$ is the local kinetic energy. If we assume that the $\partial_R^2 c_\alpha$ term is insignificant, then the coupled equations reduce to

$$\partial_R c_\alpha(R) = (i\hbar)^{-1} \sum_\beta Q_{\alpha\beta} V_{\alpha\beta} \exp[i(\phi_\beta - \phi_\alpha)] c_\beta \quad (13a)$$

where

$$Q_{\alpha\beta}(R) = A_\beta(R) \{v_\alpha(R) [1 - iz_\alpha(R)] A_\beta(R)\}^{-1} \quad (13b)$$

The fact that we now have a set of *first-order* equations will prove to be a major simplification, and a source of physical insight.

As an intermediate step to the density-matrix, we define a modified expansion coefficient $a(R)$ that "absorbs" the phase oscillations of the JWKB wavefunction:

$$a_\alpha^\pm(R) = c_\alpha^\pm(R) \exp\{\pm i[\phi_\alpha(R) + \frac{1}{4}\pi]\} \quad (14)$$

The $\{a_\alpha(R)\}$ correspond to the expansion coefficients normally associated with a semiclassical view of the time evolution of the electronic state. To see this and to set up some concepts used later, we introduce the notion of a "reference path" $R_0(t)$. This is the time-dependent position produced by solving the trajectory equation $dR_0 = v_0(R_0) dt$, where $\frac{1}{2}\mu v_0(R)^2 = E - u_0(R)$ and $u_0(R)$ is some convenient potential for which all relevant R is classically accessible at the collisional energy E . One of the actual channel potentials in the physical process under study may be selected for $u_0(R)$, but one may also choose it to be

zero (i.e., a straight-line trajectory).

If the defined $\{a_\alpha\}$ are inserted into the set of first-order Eqs. (13), which are then multiplied by $v_\alpha[R_0(t)]$, we find:

$$i\hbar \partial_t a_\alpha(R_0) = \sum_\beta \hat{v}_{\alpha\beta}(R_0) a_\beta(R_0) - 2\mathfrak{J}_{\alpha\alpha}(R_0) a_\alpha(R_0) \quad (15a)$$

$$i\hbar \partial_t \mathbf{a} = \hat{\mathbf{v}} \mathbf{a} - 2\mathfrak{J} \mathbf{a} \quad (15b)$$

where

$$\mathfrak{J}_{\alpha\beta}(R_0) = T_{\alpha\beta}(R_0) C^\circ_{\alpha\beta}(R_0) \quad (15c)$$

$$\hat{v}_{\alpha\beta}(R_0) = V_{\alpha\beta}(R_0) C^\circ_{\alpha\beta}(R_0) \quad (15d)$$

with

$$C^\circ(R_0) = v_0(R_0) Q(R_0) \quad (15e)$$

In what follows, the subscript on R_0 will be dropped.

The $\{C^\circ_{\alpha\beta}(R)\}$ are crucial "correction" factors that coordinate time on different channels, in the sense that they adjust time steps for equal steps in dR . One would expect this to be inherently related to channel velocities. This can be easily seen in the correction factors when simple JWKB amplitudes are used (valid when $\frac{1}{2}k_\alpha^{-1}dk_\alpha/dR \ll 1$). In this case the amplitudes in $Q_{\alpha\beta}$ are simply given by $A_\alpha(R) = k_\alpha(R)^{-1/2}$, and the correction factors become:

$$C^\circ_{\alpha\beta}(R) = [v_0(R)/v_\alpha(R)]^{1/2} [v_0(R)/v_\beta(R)]^{1/2} \quad (16)$$

As can be seen, the velocities of all channels appear in a symmetrical manner.

To see the connection of Eq. (15) with traditional equations for the semiclassical evolution of asymptotic basis states (whether atomic electronic states or vibrational molecular states), we will consider a two-level system interacting with a laser field, detuned from the atomic resonance line by $\Delta\omega = \omega - \omega_0$. Let $u_1(R)$ and $u_2(R)$ be the quasi-molecular potentials that form during the collision, defined such that $u_\alpha(\infty) = 0$. Asymptotically, $|1\rangle \sim |g, n\rangle$, the ground atomic state and n photons, while $|2\rangle \sim |e, n-1\rangle$, the excited atomic state and $(n-1)$ photons. Then

$$\mathbf{V}_{\text{tot}} = \mathbf{U} + \mathbf{V} = \begin{pmatrix} u_1 & 0 \\ 0 & u_2 \end{pmatrix} + \begin{pmatrix} 0 & -\hbar\Omega \\ -\hbar\Omega & -\hbar\Delta\omega \end{pmatrix} \quad (17)$$

With this choice of separating \mathbf{V}_{tot} , one has for $R_0 \rightarrow \infty$ (which corresponds to $t \rightarrow \pm\infty$), $C^\circ(R \rightarrow \infty) \sim 1$, producing the asymptotic coupled equations:

$$i\hbar\partial_t \mathbf{a} \sim_{t \rightarrow \infty} \begin{pmatrix} 0-2E & \hbar\Omega \\ \hbar\Omega & \hbar\Delta\omega-2E \end{pmatrix} \begin{pmatrix} a_1 \\ a_2 \end{pmatrix}$$

or

(18)

$$i\hbar\partial_t \mathbf{a} \sim (\mathbf{V}-2E\mathbf{1}) \mathbf{a}$$

Since the $2E$ term only produces a global phase factor, these are the usual equation for atomic states coupled by a radiation field.

It is instructive in this case to consider a dressed-state basis, $\{|I\rangle, |II\rangle\}$, which are asymptotically eigenstates of Eq. (12). If we expand a two-level state in this basis, we have

$$|\psi\rangle = f_I(t) |I\rangle + f_{II}(t) |II\rangle \quad (19)$$

The asymptotic behavior of this state must be

$$|\psi\rangle \sim F_I(\pm\infty) \exp(-iE_I t) |I\rangle + F_{II}(\pm\infty) \exp(-iE_{II} t) |II\rangle \quad (20)$$

Eqs. (9) evolves this state. We can see the effect of collisions by preparing the system in ground-like state; i.e., $|\psi(t=-\infty)\rangle = |I\rangle$. If no collisional interactions occur (all interactions are constant), then $|F_I(+\infty)| = \delta_{II}$, implying no transitions occurred.

Initially ($t=-\infty$), and Eqs. (15) and (18) are equivalent. However since the potentials are not constant as the collision proceeds, Eqs. (15) changes with time, and evolution occurs. Note that when the collision is over ($t=+\infty$), Eqs. (15) and (18) are again identical, implying the dynamical evolution due to scattering in the presence of a radiation field reduces to the well-known case of an isolated atom. We would find, though, that an inelastic transition has occurred, i.e., $|F_{II}(+\infty)| \neq 0$. From Eq. (20), we see that the electronic state now oscillates between the two dressed states. By examining Eqs. (10) and (18), we discover that this oscillation comes, in the scattering picture, from asymptotic oscillations in the expansion coefficients $\{c_a\}$. This in turn arises from the diagonal term $V_{22} = -\hbar\Delta\omega$ in the coupling potential. Physically, this represents the fact that two kinetic energies are now present, $E-E_I$ and $E-E_{II}$. Since the channel wavefunctions all have the same asymptotic wavenumbers, the oscillations of $\{c_a\}$ are required to account for the two possible final kinetic energies.

Because the $a_a(R)$ can be associated with expansion coefficients of electronic states, we form a local "dynamical" density matrix $\rho_{\alpha\beta} = a_\alpha a_\beta^*$ from

them:

$$\rho = a a^\dagger \quad (21)$$

If V is Hermitian (implying its diagonal elements are real), one can use Eq. (15) to obtain a set of coupled *first-order* equations for the dynamical density (or channel flux) matrix:

$$i\hbar\partial_t \rho = [(\hat{H} - 2\mathcal{G}), \rho] \quad (22)$$

This is one of the principal results of this project, and will be form the basis, hopefully, of a more practical and tractical method of computing vibrational relaxation rates.

This equation simplifies to the usual one for the dynamical evolution of electronic density matrix during a semiclassical collision, i.e., one in which all the channel velocities are nearly the same at each R . The same equation would describe a semiclassical density matrix for molecular vibrational states. In this semiclassical limit, we can achieve

$$i\hbar\partial_{t_{\alpha\beta}} \rho_{\alpha\beta} = [V_{\text{tot}}(R(t_{\alpha\beta})), \rho]_{\alpha\beta} \quad (23)$$

if we choose a very particular reference path: $dR_0 = \frac{1}{2}(v_\alpha + v_\beta) dt_{\alpha\beta}$. This is the semiclassical equation usually used for the evolution of the density matrix in a collision.²³ But note that there is the difficulty of choosing a different average path for each pair of indices. This highlights the long-standing problem of choosing the "best" classical path in a process involving more than two sates. The full JWKB density-matrix equations do not suffer from this complication.

It is indeed hoped that the implementation of Eq. (22) for studies of state-changing molecular collisions will prove as useful as it seems for studying atomic collisions involving transitions in electronic states coupled by a laser field. One must "merely" change the nature of the basis states. However, there is no intrinsic barrier to do this. The simplification of the problem to a first-order, path-independent computation bodes well for future treatments.

REFERENCES

1. S.J. Lipson, private communication.
2. W.A.M. Blumberg, private communication.
3. J.A. Dodd, S.J. Lipson, and W.A.M. Blumberg, *J. Chem. Phys.* **95**, 5752 (1991).
4. D.L. Thompson, *Chem. Phys. Lett.* **92**, 383 (1982); and *J. Phys. Chem.* **86**, 2538 (1982).
5. R.B. Bernstein (ed.), *Atom-Molecule Collision Theory: A Guide for the Experimentalist* (Plenum, New York, 1979); and references therein.
6. D. Rapp and T. Kassa, *Chem. Rev.* **69**, 61 (1969).
7. R.J. Bueniek, *J. Chem. Phys.* **73**, 851 (1980).
8. R.J. Bueniek and S. Green, *Astrophys. J. Lett.* **265**, L29 (1983); **270**, L101 (1983).
9. A.D. Esposti and H.-J. Werner, *J. Chem. Phys.* **93**, 3351 (1990).
10. J.M. Bowman, B. Gazdy, P. Schafer, and M.C. Heaven, *J. Phys. Chem.* **94**, 2226 (1990).
11. M.I. Lester, private communication.
12. D.C. Clary, private communication.
13. J.M. Hutson, *J. Phys. Chem.* **96**, 4237 (1992).
14. J.M. Hutson, *J. Chem. Phys.* **96**, 6752 (1992).
15. J.M. Hutson, private communication.
16. H.-J. Werner, private communication.
17. F.H. Mies, *J. Chem. Phys.* **40**, 523 (1964).
18. T.F. Ewing and R.W. Conn, *Chem. Phys.* **26**, 201 (1977).
19. T.F. Ewing and R.W. Conn, *Chem. Phys.* **36**, 407 (1979); and references therein.
20. G. Herzberg, *Spectra of Diatomic Molecules* (van Nostrand, New York, 1950).
21. R.A. Broglia, S. Landowne, R.A. Malfliet, V. Rostokin, and Aa. Winther, *Phys. Rep.* **11**, 2309 (1988).
22. R.J. Bueniek, *J. Chem. Phys.* **72**, 1225 (1980); **73**, 4712 (1980).
23. J.B. Delos, W.R. Thorson, and S.K. Knudson, *Phys. Rev. A* **6**, 709 (1972).

DISPERSION EFFECTS IN FIBEROPTIC INTERFEROMETRY

Douglas A. Christensen
Professor
Department of Electrical Engineering

University of Utah
Salt Lake City, Utah 84112

Final Report for:
Research Initiation Program
Phillips Laboratory

Sponsored by:
Air Force Office of Scientific Research
Bolling Air Force Base, Washington D.C.

and

University of Utah

December 1992

DISPERSION EFFECTS IN FIBEROPTIC INTERFEROMETRY

Douglas A. Christensen
Professor
Department of Electrical Engineering
University of Utah

Abstract

Optical fibers offer the promise of flexibility, ease of use, and low cost when utilized to recombine the light in two branches of a long baseline interferometer intended for imaging stellar objects with high resolution, such as geosynchronous satellites, the sun, and stars. The research described in this report was carried out to ascertain the effects of unequal fiber length on the performance of such an interferometer. Unequal path lengths will occur, for example, if optical steering of the interferometer away from the vertical direction is accomplished by inserting a fiberoptic delay line in one arm of the interferometer to compensate for the atmospheric path inequality in the steered direction. Dispersion over this inserted fiber length will lead to a degradation of the fringe visibility for a broadband source. To characterize this effect, we set up a fiberoptic 2x3m Mach-Zehnder interferometer in our laboratory using polarization-maintaining (PM) single-mode fiber which had the capability of utilizing fiber arms of different lengths, sources with different wavelengths (from 488 to 870 nm) and coherence lengths, and which could be phase-locked by a piezoelectric phase modulator. We designed a computer-controlled motorized translation stage to precisely obtain interferograms for a variety of source and fiber parameters. After considerable effort to achieve a low-vibration environment and using specially designed photodetector analog-to-digital (A/D) circuitry, we obtained interferograms for a high coherence length (single longitudinal mode) HeNe laser at 633 nm; two medium coherence length (multi-mode) HeNe lasers at 543 nm and 633 nm; and a low coherence length (variable drive current) visible laser diode at 675 nm. A series of interferograms at 675 nm with the low coherence length source using unequal fiber lengths (up to approximately 9 cm difference) showed that the fringe visibility envelope both decreases in visibility and increases in spatial extent as the fiber lengths become more unequal. These experimental data are consistent with theoretical predictions. In addition, we were successful in phase-locking the interferometer using a quadrature technique under conditions of unequal fiber length.

DISPERSION EFFECTS IN FIBEROPTIC INTERFEROMETRY

Douglas A. Christensen

INTRODUCTION

Long-baseline interferometry is an established technique for obtaining high spatial resolution images of distant objects, such as stars or other stellar features. The technique was first demonstrated with microwaves, then later extended to millimeter waves and optics. Long-baseline interferometers accomplish high resolution by employing two (or more) widely separated receivers and combining the signals from each arm interferometrically, preserving both amplitude and phase information. In the microwave region, recombination is done relatively easily with cables, but recombining the beams in optics is problematic, since the phase information must be preserved over the length of the recombining paths and, due to the short wavelength of light, small path variations can cause large phase changes.

One current way of recombining the optical beams is to use air or vacuum tunnels with complex alignment and temperature control requirements; vacuum tunnels are especially expensive to implement. Optical fibers offers a potentially attractive means of transmitting the light from each subaperture for beam recombination since beam alignment is much more flexible due to the inherent guiding properties of the fibers, and there is no concern for beam divergence [1,2]. Also the fibers are lightweight and relatively low in cost.

One significant consideration when using fiberoptic paths, however, is the dispersion properties of the fiber when compared to a vacuum (or air) path. This dispersion causes an additional phase variation through the fiber as a function of wavelength, and the effect is more pronounced for broadband light. If the two paths of the interferometer contain equal lengths of fiber, their dispersion effects effectively cancel and broadband fringes can be obtained. This was demonstrated in summer 1991 at Phillips Lab with an interferometer containing two 60 m spools of single-mode fiber [3]. However, there are some situations, such as pictured in Fig. 1--showing the viewing angle of the interferometer steered away from the vertical direction by inserting an additional length of fiber--where one path will contain more fiber than the other and the dispersion effects no longer will be balanced.

The goals of this project were to determine the effect of dispersion in a fiberoptic interferometer with unequal fiber lengths under conditions of different source characteristics, and to record the fringe visibility patterns (interferograms) under these conditions. To accomplish these goals, we designed and assembled a prototyping fiberoptic interferometer in

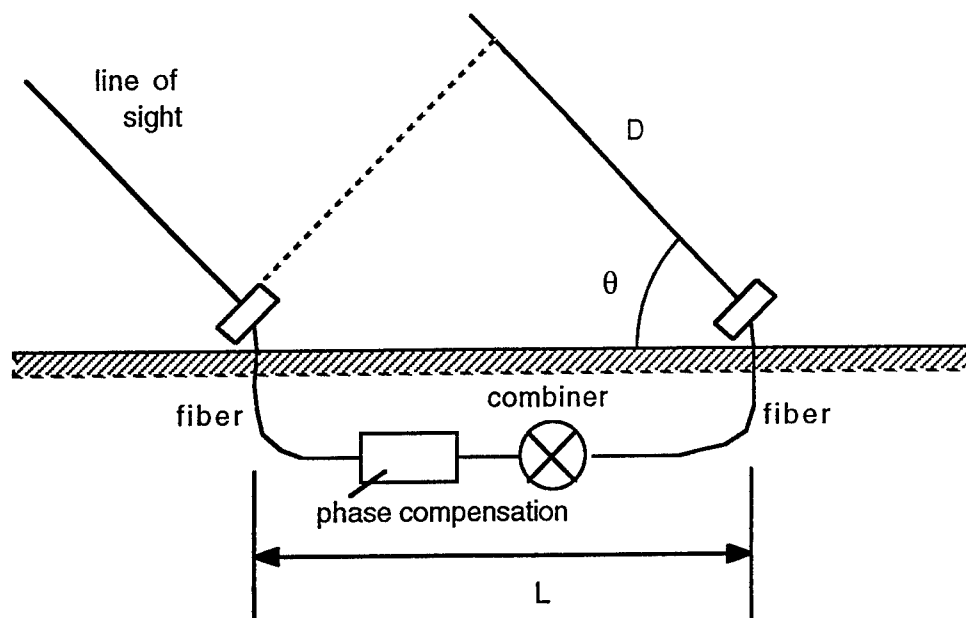


Figure 1. Steering the direction of sight of a long baseline interferometer by inserting a phase compensation element (an additional fiber length) into one path.

our laboratory, which required considerable attention to the reduction of vibrations on the optical bench in order to record stable interferograms. We also designed and built digital-to-analog and analog-to-digital circuitry to allow computer control and acquisition of the interferograms.

We used this setup to obtain fringe contrast data for a variety of sources with varying wavelengths and coherence characteristics. Interferograms were obtained for unequal fiber lengths using a laser diode operating at a condition of very low coherence length. These showed both an envelope lengthening and visibility reduction as a function of path inequality. A theoretical calculation gives results consistent with the experimental data.

In addition, we were able to phase-lock the interferometer under conditions of unequal path length using a quadrature phase-locking technique. These results are explained in detail in the following sections.

OPTICAL PROTOTYPING APPARATUS

Optical Components - As an optical setup for measuring the effects of dispersion and phase locking on a fiber interferometer, we assembled and tested the arrangement shown in Fig. 2. This setup consisted of a Mach-Zehnder interferometer with two fiberoptic arms. One arm of the interferometer contained 2.993 m of Newport F-SPA single-mode (SM) polarization

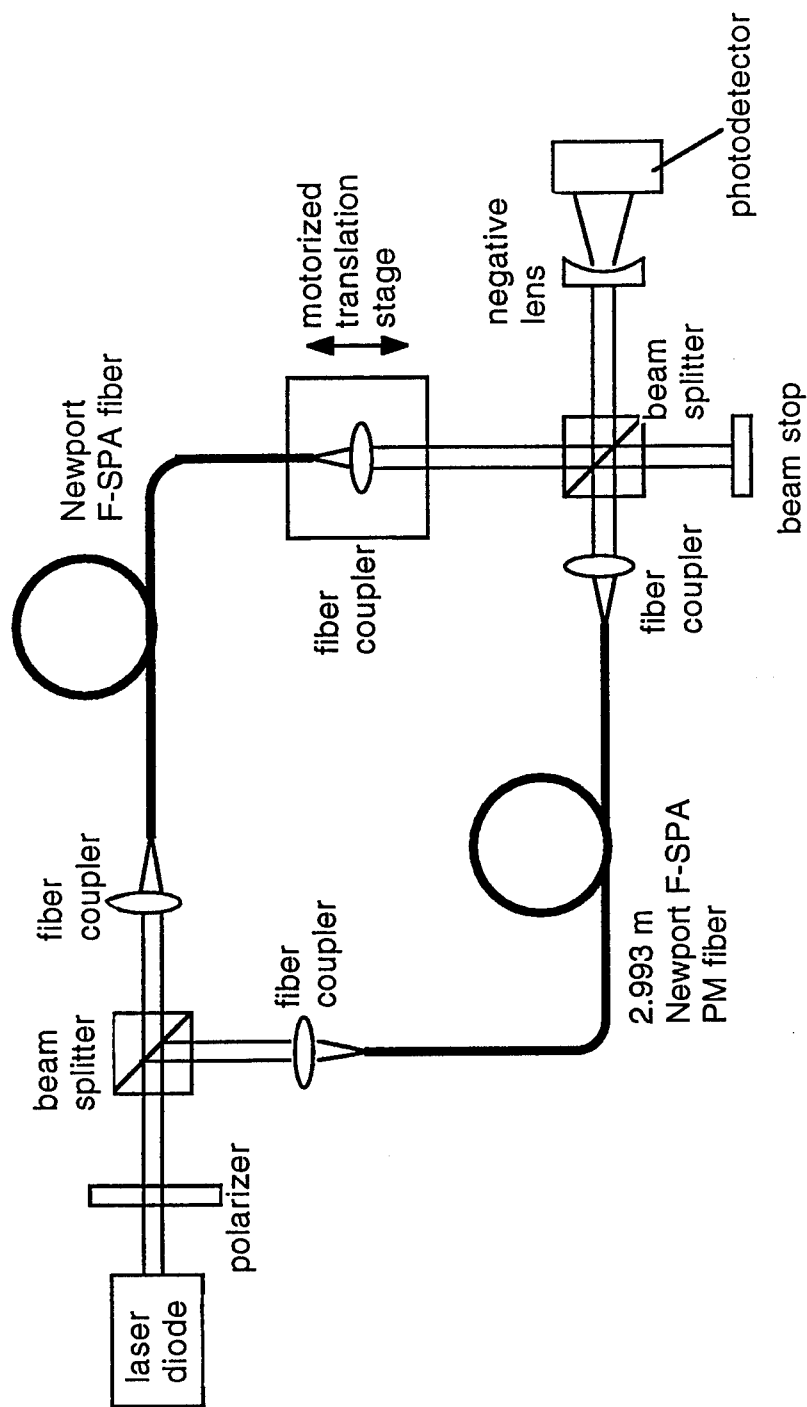


Fig. 2 - Fiberoptic interferometer configuration developed in this research project.

maintaining (PM) fiber. Varying lengths of the same fiber were used in the other arm of the interferometer. The source could be selected from several lasers, both gas and diode lasers, as described later. The optical pathlength difference was adjusted using a micrometer translation stage driven by a DC motor micrometer (Oriel Encoder Mike Drives).

When the interferometer was initially set up and tested, it was found that there were extraneous 125 Hz fringe shifts due to vibrations in the table, most likely coming from vibrations in the floor being coupled through the table legs. To eliminate this problem, tire inner tubes were placed under each leg of the optics table. The tire tubes had 6 inch inner diameters and were filled with air to 10 psi. The tire tubes were surrounded with sections of a 14 inch diameter hollow circular tube made of hard cardboard. Circular sections of 0.75 inch thick plywood were placed on top of the tire tubes to evenly distribute the weight of the table. The tire tubes effectively decoupled the optics table from ground vibrations and virtually eliminated the 125 Hz fringe shifts.

Computer Interface - To allow for accurate position control and data storage for future data processing, the fringe visibility scans (interferograms) were controlled using a Macintosh IIsi computer. A National Instruments Lab-NB A/D board was used to provide the motor drive signal, to read the photodetector voltage and to monitor the travel distance of the motor micrometer. These signals were connected to the computer via the A/D board as shown in the block diagram in Fig. 3. The A/D board has eight analog input channels, two analog output channels, 24 lines of digital I/O, and three 16 bit counter/timer channels.

The fringe intensity was monitored using a silicon *pin* photodiode (Thorlabs). An amplifier circuit was designed and built to convert the current signal from the photodiode to a voltage signal that could be read by the computer. This circuit is shown in Fig. 4. The analog channels on the A/D board have a jumper selectable range of either -5V to +5V or 0 to 10V. To provide maximum sensitivity, the 0 to 10V range was chosen and a second stage with variable gain was added to the photodetector amplifier circuit.

The motor micrometer drive voltage and current specifications are 0-12V DC at 0-100 mA. The motor speed was controlled by the drive voltage and the direction of travel was controlled by the motor drive voltage polarity. The maximum current from the A/D board is 1 mA for the -5V to +5V range. Therefore, a current amplifier circuit was added between the analog output channel and the motor mike, as shown in Fig. 5.

The motor micrometer contains an optical encoder for accurate position control. The optical encoder provides ten 5V pulses per micron travel. The optical encoder signal was connected to the clock input of one of the counter/timer chips on the A/D board. This allows the

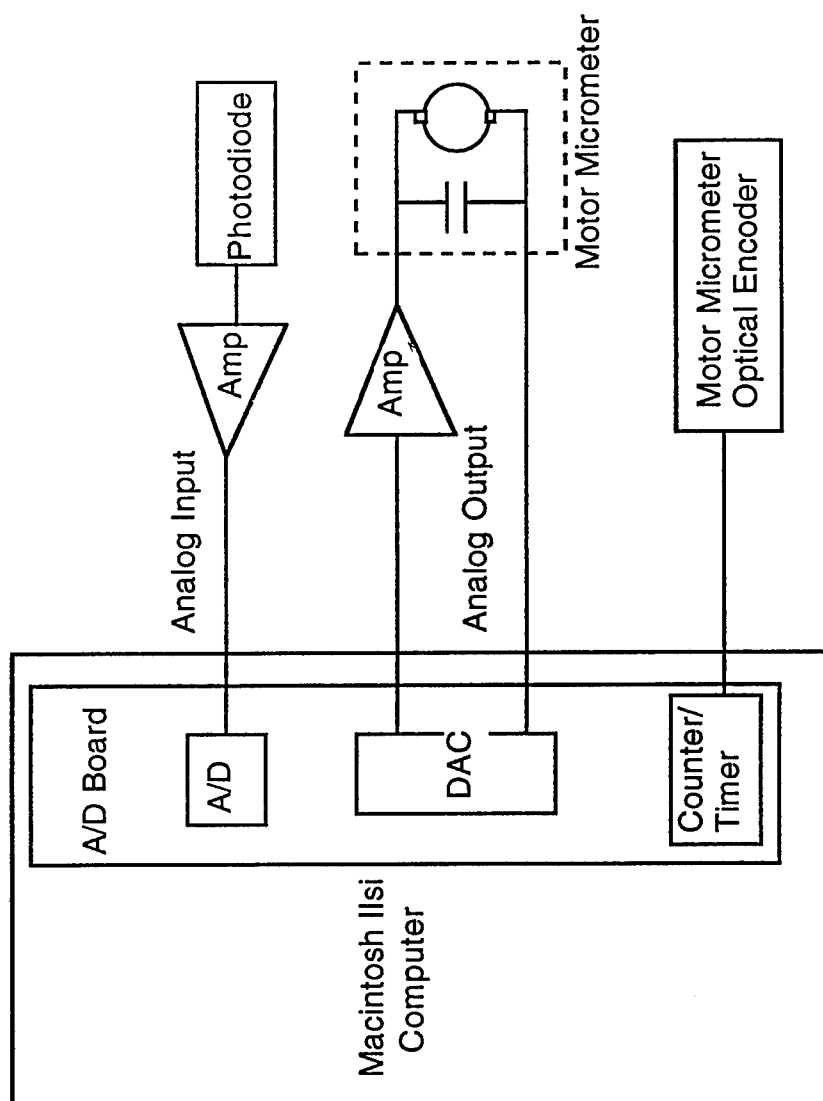


Fig. 3 - Schematic of the electronic components for computer control of the motorized translation stage and for data acquisition of the interferograms.

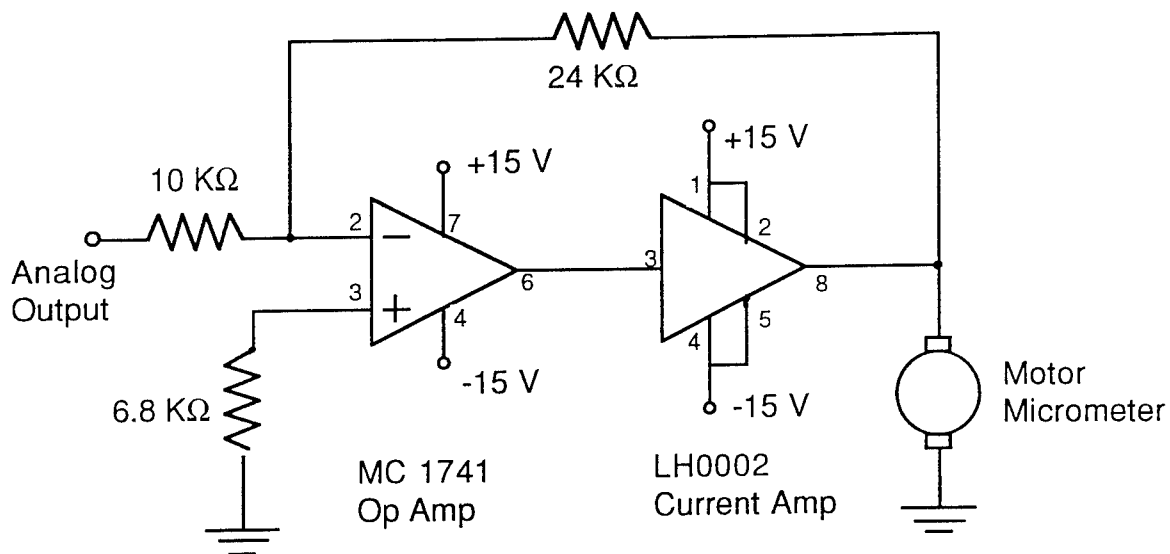


Fig. 4 - Circuit diagram of the photodetector and amplifier.

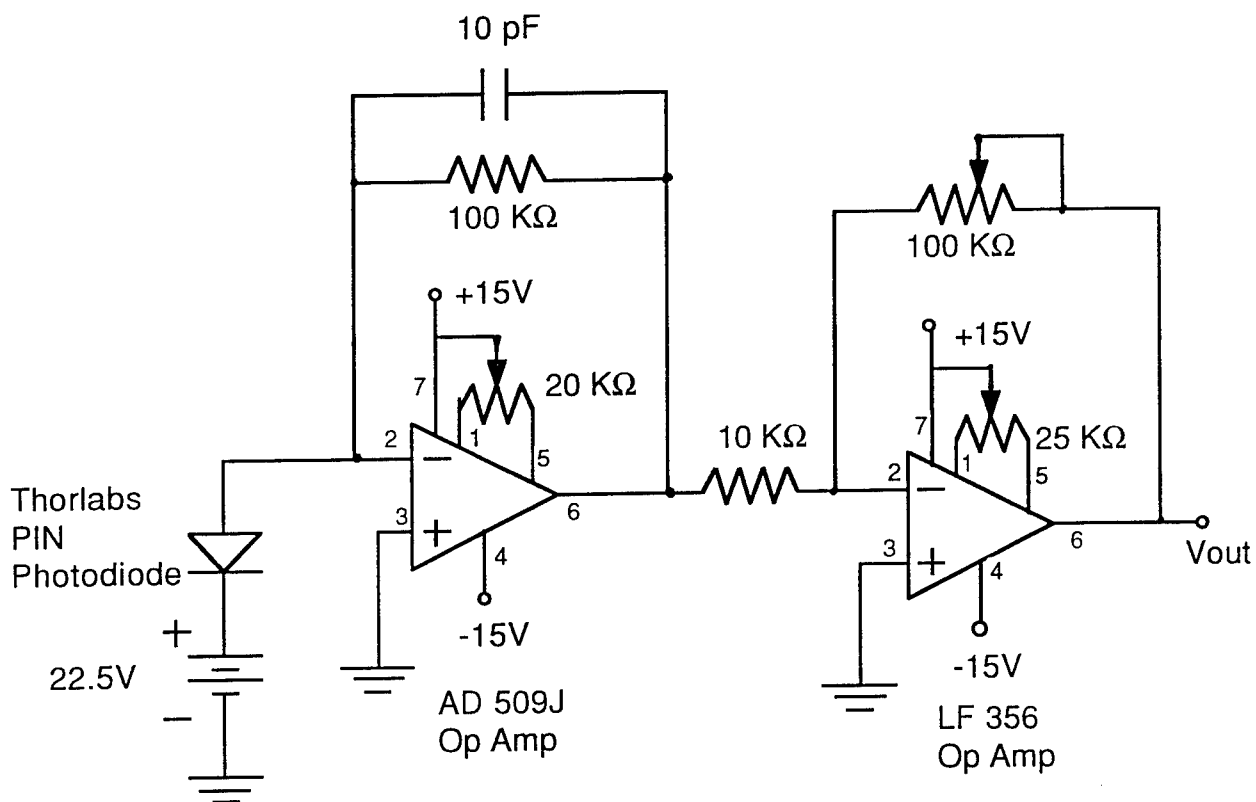


Fig. 5 - Circuit diagram of the motor driver for the computer-controlled translation stage.

optical encoder pulses to be monitored continuously, and pulse counting is not interrupted by software commands to read the photodetector voltage or update the motor drive voltage. The counter/timer chip has the additional advantage that it can be read "on the fly," which means that the pulse counting is not interrupted by commands to read the total count. Thus, the distance that the micrometer table has traveled can be accurately determined with no error due to missed pulses from the motor micrometer's optical encoder.

Software - A software program was written to drive the motor micrometer, read the photodetector voltage, and read the optical encoder to determine the distance the micrometer table had traveled. This software program was written using LabView (National Instruments), which is a graphical programming environment.

INTERFEROGRAMS

Results with Different Sources - Using optical setup described above, we determined the fringe visibilities for both unequal (difference = 8.7 cm) and equal fiber lengths for a variety of sources:

Single-longitudinal mode HeNe laser at a wavelength of 633 nm - As expected, the coherence length of this laser is so long (on the order, in fact, of the overall fiber length), that fringes were obtained easily and no effect of unequal fiber lengths or dispersion was seen. In practice, because of the advantage that its long coherence length produces no extraneous fringe visibility reduction under a wide variety of fiber conditions, this laser was used as the testing laser to determine the cause of the vibrations in the table and to verify the solution of the vibration problem using the inner tubes under each leg.

Multi-longitudinal mode HeNe lasers, wavelengths of 633 nm and 543 nm - The coherence lengths of these lasers are shorter than that of the single-mode laser, and distinct peaks and valleys corresponding to spectral mode spacings were observed in the fringe visibility envelopes for each of these lasers. Differences in their spectral characteristics (i.e., the number of oscillating modes, which could not be directly determined), however, prevented a precise comparison between the two of them regarding the effect of the wavelength shift on the interferogram patterns.

Visible laser diode with variable drive current, wavelength of 675 nm - This source is extremely useful for investigating the effects of spectral purity on fringe visibility due to its variation of spectral width with drive current [4]. When the current to a laser diode is varied, its mode structure changes from a few narrow-linewidth longitudinal modes at high current to broad spontaneous emission at low current below threshold [5]. Correspondingly, its

coherence length varies from several millimeters down to only tens of micrometers. Thus, the laser diode spans the gap between the HeNe lasers and broadband sources, and guides the tuning of the pathlength difference in the interferometer toward the condition of zero difference.

We used this laser diode source at high drive current (60 mA) to initially maximize coupling to the fibers, then reduced the current to much below threshold (30 mA) while adjusting the path length difference. At the low drive current, the spectral width is broad--approximately 14 nm as measured with a Spex 3/4 m Czerny-Turner grating spectrometer [4]. At this broad spectral condition, the laser diode was then used to record the interferograms shown below for equal and unequal fiber lengths.

Effects of Dispersion on Interferograms - Using the broadband laser diode as source, a baseline interferogram was scanned by the computer-controlled stage and recorded in computer memory for initially *equal* fiber lengths (as measured by a ruler to an estimated accuracy of 1.0 mm). This interferogram is shown in Fig. 6. As can be seen in the figure, the recorded fringe visibility is high and well defined, with the envelope of the fringes being symmetrical and relatively vibration-free.

Unequal fiber lengths were then employed by inserting extra fiber sections (or, in the case when the piezoelectric modulator module was used, a new length for the entire fiber arm), and the overall path mismatch compensated by increasing the air path in the other arm. A typical result for a fiber length difference of 8.7 cm is shown in Fig. 7.

Note that for the combination of a broad spectral width source (14 nm, same as for Fig. 6) and unequal fiber lengths, the interferogram envelope is much longer, approximately 120 μm , and the peak fringe visibility at the center of the envelope has been reduced to 38% of that seen in Fig 6. For other fiber length differences, these effects were seen as well, in approximate proportion to the fiber length mismatch. These consequences of dispersion on the fringe visibility are discussed further in the next section.

THEORETICAL ANALYSIS -

Fringe Visibility - For the purposes of theoretical analysis, the spectrum of a laser diode for general drive current can be approximately modeled as the sum of two parts, a lorentzian-shaped curve representing the spontaneous emission background and a smaller periodic portion (modeled as the product of a cosine function with a gaussian envelope) representing the longitudinal modes of stimulated emission:

$$S(\nu) = aL(\nu) + bG(\nu) \cdot \cos(2\pi\nu / \Delta\nu')$$

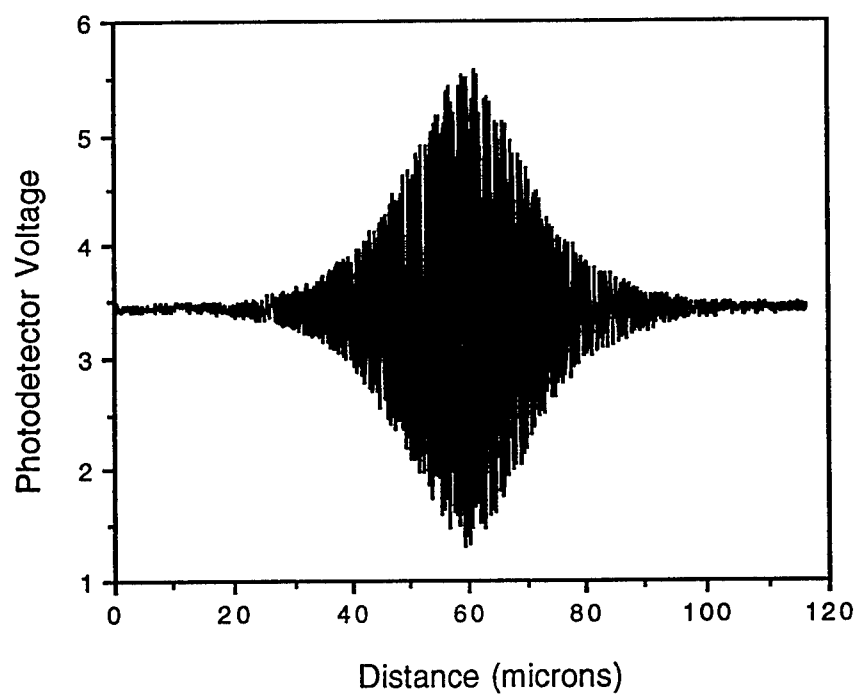


Fig. 6 - Interferogram for equal fiber lengths, with broadband laser diode (30 mA drive current) as the source.

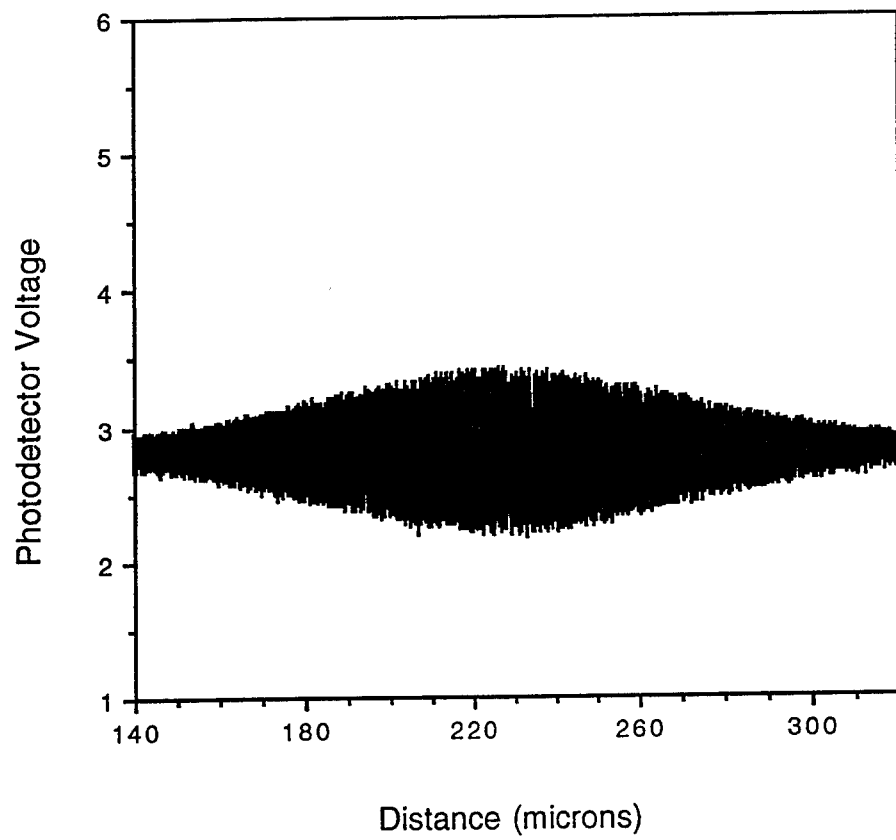


Fig. 7 - Interferogram for unequal fiber lengths (difference = 8.7 cm). Same broadband source as for Fig. 6.

where $S(\nu)$ is the power spectral density, $L(\nu)$ is a lorentzian function with FWHM linewidth of $\Delta\nu_L$, $G(\nu)$ is a gaussian function with FWHM linewidth of $\Delta\nu_G$, and a and b are relative spectral strengths. For the case of the diode operating much below threshold (giving broadband emission as in Figs. 6 and 7), $b = 0$ and only the spontaneous lorentzian component is present.

The fringe visibility $V(x)$ in the interferogram resulting from this source can then be obtained from the following relationships [6]:

$$\begin{aligned} V(x) &= K_1 \gamma(x/c) \\ \gamma(\tau) &= \left| \frac{\int_0^\infty 4S(\nu) e^{-j2\pi\nu\tau} d\nu}{\int_0^\infty 4S(\nu) d\nu} \right| \\ &= K_2 \left| \int_0^\infty S(\nu) e^{-j2\pi\nu\tau} d\nu \right| \equiv K_2 \left| \mathcal{F}^+ \{S(\nu)\} \right| \end{aligned}$$

where $V(x)$ is the fringe visibility, $\gamma(\tau)$ is the modulus of the complex degree of coherence, K_1 and K_2 are constants, and \mathcal{F}^+ represents the Fourier transform for positive frequencies only.

The Fourier transform of the lorentzian part of $S(\nu)$ leads to an exponential term in the fringe visibility, with a FWHM width of:

$$\Delta\tau_L = 0.44 / \Delta\nu_L.$$

Calculation of Spectral Width of Laser Diode at 30 mA Drive Current - From Fig. 6, the width Δx_L of the interferogram envelope is seen to be approximately $\Delta x_L = c\Delta\tau_L = 19 \mu\text{m}$.

Thus $\Delta\lambda = \Delta\nu \lambda^2 / c = 0.44 \lambda^2 / c\Delta\tau_L = 11 \text{ nm}$, which agrees reasonably well with the 14 nm linewidth measured by the spectrometer.

Theory of Dispersion Effects on Fringe Visibility - Let σ_λ be the spectral width of the light into a single-mode fiber of length L . Due to dispersion, the optical length of the fiber will appear longer for the shorter wavelengths of the spectrum than for the longer wavelengths. Let $\Delta L'$ be the effective difference in optical length as seen at the two extreme wavelengths of the spectrum. There will be two contributions to $\Delta L'$, material dispersion and waveguide dispersion.

1. Material Dispersion - Since the index of refraction n varies with wavelength, the optical pathlength through the fiber also varies. This effect gives $\Delta L'_{\text{matl}} = L \sigma_{\lambda} (dn/d\lambda)$. For a silica core fiber at a wavelength near 675 nm, $dn/d\lambda \approx -1.52 \times 10^{-5}/\text{nm}$ [7]. Thus, for $\sigma_{\lambda} = 11$ nm, $\Delta L'_{\text{matl}} = -167 \mu\text{m}$ per meter of fiber.

2. Waveguide Dispersion - The effective propagation constant of the lowest mode varies slightly with wavelength, leading to $\Delta L'_{\text{wg}} = L n_2 \Delta \sigma_{\lambda} [b - d(Vb)/dV] / \lambda$, where n_2 is the clad index, Δ is the normalized index difference between core and clad, b is the normalized propagation constant, and V is the normalized frequency. For the single-mode fiber in this experiment, $V = 2.2$, $b = 0.47$, $d(Vb)/dV = 0.98$, $n_2 = 1.45$, $\Delta = 0.01$, and $\lambda = 675$ nm. Then, again for $\sigma_{\lambda} = 11$ nm, $\Delta L'_{\text{wg}} = -120 \mu\text{m}$ per meter of fiber.

Putting these two factors together, $\Delta L' = \Delta L'_{\text{matl}} + \Delta L'_{\text{wg}} = -287 \mu\text{m}$ per meter of fiber for the parameters of this experiment.

Calculation of Fiber Length Mismatch to Reduce Fringe Visibility by One-Half - The effect of dispersion is to cause a variation of the effective fiber pathlengths over the source spectrum. A key calculation is to determine the length of uncompensated fiber length L for which $\Delta L'$ is equal to the coherence length. It is reasonable to expect that for this fiber mismatch, the fringe visibility will be reduced to approximately one-half its value at the peak of the envelope. For the case shown in Fig. 7, the coherence length of the source (from Fig. 6) is approximately $19 \mu\text{m}$. Then $|L| = 19 / 287 \text{ m} = 0.066 \text{ m} = 6.6 \text{ cm}$. This value is consistent with the results shown in Fig. 7, which indicates a fringe visibility reduction of about 38% for a fiber length mismatch of 8.7 cm.

PHASE-LOCKING THE INTERFEROMETER -

One important consideration when using an interferometer to capture image phase information is controlling the phase introduced by the interferometer itself. Due to temperature and mechanical drifts in the components, there will be phase drifts between the two fiber arms of the interferometer which will confuse the measurement of the object's phase. Therefore, the interferometer itself must be phase-locked such that there is a constant, stabilized phase difference maintained between its two branches. This requires monitoring and controlling the

branch phase difference with a metric system. We investigated the phase-locking of our fiber interferometer under the condition of unequal fiber lengths, using the phase-lock scheme described next.

Phase Locking by Direct Comparison of Intensity Levels - In this technique, the phase of the system is controlled such that the detected fringe intensity I is kept at some given level, say at a level I' . The control signal is then simply proportional to $\Delta I = I - I'$, which changes sign as I is on either side of I' and which is nulled when $I = I'$. In our studies, we locked the intensity I to an internally generated intensity by using the complementary fringe pattern for I' to that which gives I . This scheme is shown in Fig. 8. At the output of the distal beamsplitter of the interferometer there are two fringe patterns, one produced by through transmission of branch A and reflection of branch B by the beamsplitter, the other by transmission of branch B and reflection of branch A. Conservation of energy considerations show that these fringe patterns are complementary, i.e., when one is a maximum the other is a minimum.

The phasor representation of the addition of the complex signals from the two branches for each of the two outputs is shown in Fig. 9, where the beamsplitters have a 50/50 splitting ratio. Let ϕ be the phase angle difference between the two arms, and let $\phi = \pi/2 + \beta$ where β is the deviation of ϕ from 90° . The absolute magnitude of the resultant R for the output path that gives intensity I is given by the law of cosines as

$$|R| = [A^2 + B^2 - 2AB \cos \phi]^{1/2} = [A^2 + B^2 + 2AB \sin \beta]^{1/2}.$$

Thus the intensity I is given by:

$$I = |R|^2 = A^2 + B^2 + 2AB \sin \beta. \quad (1)$$

In a similar fashion, the absolute magnitude of the resultant R' at the other output is

$$|R| = [A^2 + B^2 - 2AB \sin \beta]^{1/2}$$

and the intensity I' is given by:

$$I' = |R|^2 = A^2 + B^2 - 2AB \sin \beta. \quad (2)$$

Therefore the difference between these intensities, which gives the feedback control signal, is, from (1) and (2)

$$\Delta I = I - I' = 4AB \sin \beta. \quad (3)$$

Notice that this signal is a null at the point $\beta = 0$, and it changes its sign in the neighborhood around $\beta = 0$. It therefore meets the requirement for a proper feedback control signal. Also, the locking condition is held near $\beta = 0$ regardless of the relative amplitude of the signals from the two branches (although the strength of the feedback signal, and the

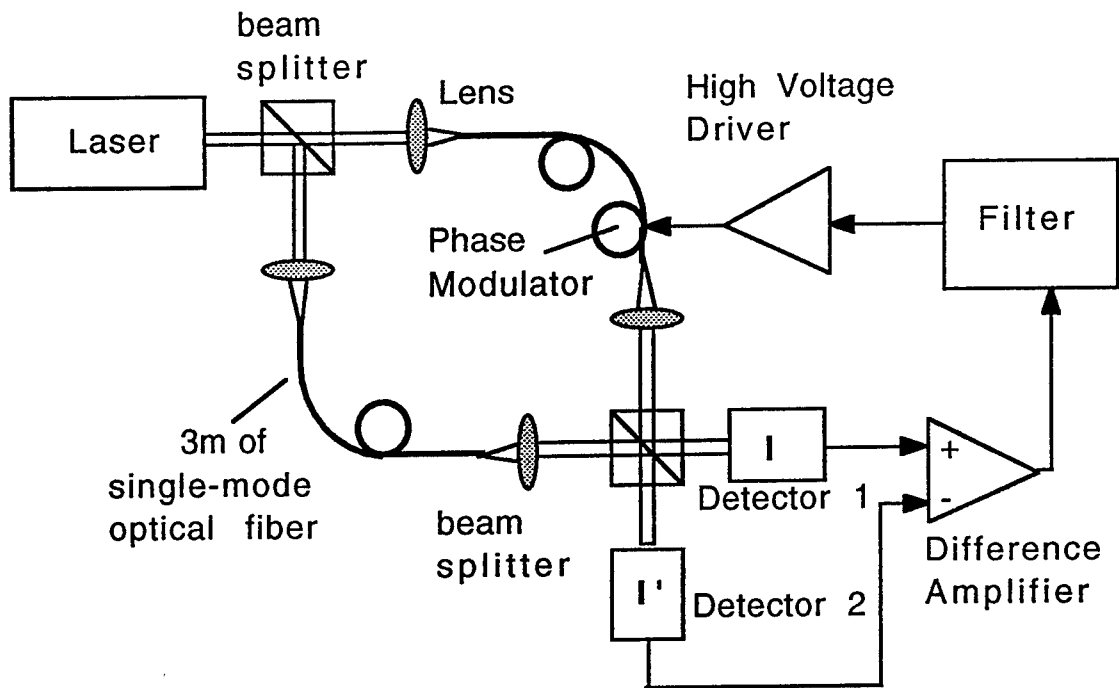


Fig. 8- Phase-locking technique using a comparison between the two detected intensities at the output beamsplitter (internal referencing) to phase lock the interferometer to quadrature.

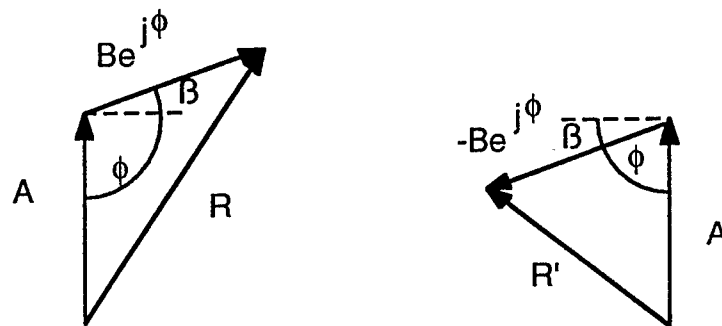


Fig.9 - Phasor representation of the two complementary outputs for the interferometer: Resultant R produces intensity I; Resultant R' produces intensity I'.

corresponding "tightness" of the control, does depend upon the magnitudes of A and B). Thus the locked phase angle is independent of the magnitudes of the signals in the two branches.

Since this scheme locks the system to the condition where $\beta = 0$, and therefore $\phi = 90^\circ$, it is called a "quadrature" phase locking technique.

The modulator used in this experiment was a Canadian Instrumentation and Research device with an oval fiber path, composed of two passive hemi-cylindrical ends with two planar piezoelectric sections in between. The fiber is wrapped seven turns around this path. It is epoxied over about 2/3 of the length of each piezo crystal and also, for keeping it in place, at the hemi-cylindrical ends. The modulator has a printed circuit driver board attached, with an op amp front end for accepting a signal input, and a single transistor high voltage driver connected to the piezo crystals.

As measured in earlier studies [8], the modulator sensitivity is 3.85 rad/V and it has a fringe range of 110.3 fringes for 0-180 volts dc. Its 3 dB frequency (the frequency at which the response or modulation depth is reduced to one-half of its low frequency value) is 2.5 kHz, high enough to be operated in the phase-lock experiments described next.

Phase-Lock Results - With a 8.7 cm fiber path mismatch and using the laser diode as source, the fiber interferometer was phase locked using the technique shown in Fig. 8. The fringe stability with the phase-lock system in operation was considerably better than when the feedback was removed. Without the feedback in operation, the fringes gradually drifted (due to temperature variation in the fibers themselves and in the fiber fixtures). However, with the feedback system turned on, the fringe intensity was very stable over the time scale of the measurements.

CONCLUSIONS -

In this project, we were successful in designing, fabricating, and testing a fiberoptic interferometer for the purposes of evaluating the effects of unequal fiber length on its operation. We found that:

1. Vibrations must be carefully controlled to a higher level than found in our normal lab environment to achieve stable interferograms. We accomplished this by placing home-made pneumatic dampers under each table leg.
2. Our computer-controlled motorized translation stage and A/D signal acquisition circuitry were well suited for rapid and accurate recording of interferograms.
3. We used several different laser sources in obtaining fringe patterns. The single-mode HeNe laser was ideal for initial setup and vibration control. The variable drive-current laser

diode was useful for giving broadband emission at low drive current to test dispersion effects.

4. The broadband (11 nm) interferogram at equal fiber lengths gave good fringe visibility and its width agreed well with theoretical predictions.

5. The broadband (11 nm) interferograms for unequal fiber lengths showed a marked increase in length and a decrease in fringe visibility. For a length mismatch of 8.7 cm, the interferogram was lengthened to 120 μm and fringe visibility reduced to 38%.

6. The experimental results are consistent with a theoretical prediction that fringe visibility will be reduced by dispersion to approximately 50% when the fiber mismatch is 6.6 cm.

7. We successfully phase-locked the fiber interferometer using a quadrature phase-lock technique.

ACKNOWLEDGMENTS - Valuable input was provided to this project by Phillips Lab and Rockwell Power Systems personnel, including Gary Loos, Andrew Klemas, Jim Rotge, and Bob McBroome. Shellee Dyer, a graduate student in the Electrical Engineering Department at the University of Utah, helped with many of the experimental studies and did the computer interfacing.

REFERENCES -

1. P.Connes, C.Froehly and P.Facq, "A fiber-linked version of TRIO," Proc. Colloquium on Kilometric Optical Arrays in Space (Cargese, Corsica, France) ESA SP-226, 49-61 (1985).
2. S.Shaklan and F.Roddier, "Single-mode fiber optics in a long-baseline interferometer," Appl. Opt. 26, 2159-2163 (1987).
3. D.A. Christensen, "Final Report: Fiberoptic Interferometer Studies," AFOSR Summer Faculty Research Program, September 18, 1991.
4. J.Rotge, D.Christensen, A.Klemas, G.Loos, and D.Merriman, "Laser diode coherence length variation with drive current: a tool for dispersion measurements," SPIE Proc. Design Modelling and Control of Laser Beam Optics, 1625 (1992).
5. E.W.Williams and R.Hall, Luminescence and the Light Emitting Diode, Pergamon Press, Oxford (1978).
6. J.W.Goodman, Statistical Optics, John Wiley & Sons, New York (1985).
7. G. Keiser, Optical Fiber Communications, 2nd Edition, McGraw-Hill, New York (1991).
8. D.A. Christensen, "Final Report: Use of Optical Fibers in Long Baseline Interferometric Imaging," AFOSR Summer Faculty Research Program, September 1992.

VIBRATION SUPPRESSION OF THE ASTREX STRUCTURE DURING SLEWING MANEUVERS

Ephraim Garcia
Assistant Professor
Smart Structures Laboratory
Department of Mechanical Engineering

Vanderbilt University
24th Avenue South at Garland Ave.
Nashville, Tennessee 37212

Final Report for:
Research Initiation Program
Air Force Phillips Laboratory

Sponsored by:

Air Force Office of Scientific Research
Bolling Air Force Base, Washington, D.C.

December 1992

VIBRATION SUPPRESSION OF THE ASTREX STRUCTURE DURING SLEWING MANEUVERS

Ephraim Garcia
Assistant Professor
Smart Structures Laboratory
Department of Mechanical Engineering
Vanderbilt University

ABSTRACT

The ASTREX (Advanced Structural Research Experiment) facility located at the Phillips Laboratory, Edwards AFB, is a ground based test facility for the analysis of structural characteristics of a realistic complex structure. The impetus of this paper is to analyze and design control schemes to suppress tip motion of the structure to maintain alignment between the secondary and primary substructures with motivation to enhance line-of-sight (LOS) performance. Various velocity feedback control methods were evaluated based on their ability to control tip deflections of the ASTREX. A reduced order model of the structure was created via the combination the mass and stiffness information obtained through a finite element model and experimentally determined damping ratios obtained through ERA (Eigensystem Realization Algorithm). A modal structural model and actuator model were then integrated into a single form for use in vibration control. Finally, the effects of slewing on the dynamics of the structure, most notably on the ability to maintain LOS, was considered and the control of these motions was investigated with respect to a quadratic regulator scheme, where an optimal feedback technique was employed.

INTRODUCTION

The inherent flexibility of light weight space structures unfortunately makes them easily susceptible to vibrations caused by various external stimuli. Also, because of various mission requirements, these relatively flimsy space frames with multiple flexible appendages may need to be reoriented into a new positions. This may be necessary so that one of these appendages, perhaps an antenna, lens or other optical device can be aimed accurately. The attitude adjustment of this structure, or just that of a single appendage, will induce loads that can cause the structure to vibrate for an unacceptable period of time, making the rapid pointing and repointing virtually impossible. Since the ASTREX is a structural model configured in order to perform tracking studies, the effects of attitude adjustments, i.e. slewing accelerations, on the performance of the structures will need to be investigated. Such a maneuver will induce loads, and hence flexure, on the tripod arms which connect the primary to the secondary. Uncontrolled dynamics caused by these loads will greatly reduce the ability of the structure to maintain signal fidelity. By decreasing the settling time of the structure's response, the structure can be made to retarget more rapidly.

Lim and Horta (1990) investigated the vibration control for the pointing of structures by comparing various techniques such as LVF(local velocity feedback) and the optimal control scheme LQG. They developed an LOS criterion to judge the performance of each technique they analyzed. This criterion was based on the pointing geometry of the NASA Langley Evolutionary model. This criteria is the basis for the LQG penalty functions, and hence, used in the formulation of the control gains. Similarly in this paper, suppression of the relative tip motions is used as a performance indicator. These feedback signals are used in the cost function for the optimal control studies. Meirovitch and Quinn (1987) and Meirovitch and Kwak (1988) developed the equations of motion for a structure with a flexible appendage and the later of these papers suggests a possible use of this study as a line-of-sight stabilization of this appendage. Prior to all these aforementioned authors, Hughes (1972) develops similar equations of motion for use in the study of slewing flexible satellites. The significance of their derivation is the development of the equations of motion of a slewing flexible structure while encompassing in these equations the flexibility of the appendage (i.e. antenna or laser) by inclusion of the inertial cross coupling terms. It is the inertia of the structure which induces loads on the appendage that is incorporated into the model via the flexibility of

the appendage. In this paper study, a first order approximation to these terms will be derived.

One of the key thrusts behind this study is to develop anticipatory flexure in the structure during slewing maneuvers. That is, to send the slewing command signal not only to the slewing actuators, the gas thrusters, but additionally to the actuators on the structure that control flexure, the torque wheel actuators (see Garcia and Inman 1990). In this way, the structure itself can be made active to anticipate the expected slewing loads, and assume a flexural posture that will aid in the vibration suppression.

SYSTEM DYNAMICS

Actuator Dynamics

Figure 1 shows a simplified top view of the test article. In order to accurately determine the performance of the different controller designs, the dynamics of the actuator were modeled and included into the global system model. The actuator used in this model was a torque wheel actuator (TWA). This actuator, mounted the secondary, can be easily modeled as a motor with a circular disk attached, to provide the necessary inertia to counteract tip deflections. The actuator equations can be expressed in state space form given by

$$\begin{bmatrix} \frac{d\omega}{dt} \\ \frac{di}{dt} \end{bmatrix} = \begin{bmatrix} -\frac{B}{J} & \frac{K_t}{J} \\ -\frac{K_b}{L} & -\frac{R}{L} \end{bmatrix} \begin{bmatrix} \omega \\ i \end{bmatrix} + \begin{bmatrix} 0 \\ \frac{1}{L} \end{bmatrix} V_i \quad (1)$$

$$T_m = [0 \quad K_t] \mathbf{x}_a \quad (2)$$

where the output of this system is torque, which is fed back into the structure via the structural input matrix and V_i is the a function of the sensor signal.

Structural Dynamics

The structural model is used in its modal form because this affords us the ability to integrate experimentally found damping information into the model. A few of the frequencies and corresponding damping ratios are given in Table 1. The modal equation of motion with a single input is

$$I \ddot{\mathbf{q}} + \phi^T D \phi \dot{\mathbf{q}} + \phi^T K \phi \mathbf{q} = \phi^T B_f \mathbf{u}_s \quad (3)$$

This can be transformed into a state space representation as follows:

$$\dot{\mathbf{x}}_s = \begin{bmatrix} 0 & I \\ -\Lambda_K & -\Lambda_D \end{bmatrix} \mathbf{x}_s + \begin{bmatrix} 0 \\ \phi^T B_f \end{bmatrix} \mathbf{u}_s \quad (4)$$

where the ϕ is the mass normalized eigenvector matrix and $\mathbf{x}^T = [\mathbf{q} \ \dot{\mathbf{q}}]^T$. The transformation between physical and modal coordinates is therefore $\xi = \phi \mathbf{q}$. The state space model is of the form $\dot{\mathbf{x}} = \mathbf{A} \mathbf{x} + \mathbf{B} \mathbf{u}$, where the addition of multiple inputs (i.e. multiple actuators) simply constitutes adding columns to the \mathbf{B} matrix.

MODE No.	ω Hz	ζ
1	13.2263	.00529
2	13.4066	.00190
3	17.6819	.00880
4	19.2488	.00590
5	19.4623	.00950

Table 1. Table of the first five frequencies and damping ratios.

CONTROLLABILITY AND STABILITY

Typically control laws are based on a reduced order models. When using such a model, the question on how the introduction of a controller based on this model will effect the stability of the overall system when implemented experimentally. The closely spaced modes, in particular the first two flexible tripod modes are spaced such that they display a beating effect which can be seen in the open loop response of the system to a unit impulse in the x and y directions (Fig. 3). It seems that while these modes cannot classified as

repeated, the coupling between these modes is quite evident. It will be shown that the presence of closely spaced frequencies necessitates more than one actuator be employed to effectively control the dynamics.

To further the question of stability, we now ask how our choice of feedback effects the system. Ideally, to ensure a stable system, the sensor and actuator pair is collocated. This collocation will ensure that the gain feedback matrix will be symmetric. While precise collocation is possible with piezoelectric actuators (Dosch, et al 1992), care must be taken in applying electromechanical actuators. For these systems, sensors must be physically collocated, and produce a signal which is analytically collocated. The effect of an unsymmetric feedback matrix can potentially destabilize a system by responding with a control force that is in phase with motion of the system, thus adding energy to the system rather than the effect intended. The LVF is directly effected by the type of feedback as well as how close to a collocated signal we are able to obtain.

Finally, conditions are considered for ensuring and quantifying the controllability of the system with respect to the each individual mode. The degree of controllability, which can be formulated in several ways, is a vehicle by which we can assess how controllable each mode is with respect to each other. From this information, we can infer the number of actuators warranted for a high degree of authority for the ensuing control law.

The first method discussed was proposed by Hughes and Skelton (1980) for a general second order system. Similarly in 1979, these author published a study under the auspice of including rotational and rigid body modes to model flexible spacecraft dynamics. They propose the development of a controllability norm. Consider the following undamped system.

$$M \ddot{\xi} + K \xi = B u \quad (5)$$

The reason for excluding damping effects in the formulation of the controllability condition is that the dissipative energy effects typically serve as another avenue for coupling in the system and will always inherently increase the controllability. The opposite of this is not valid, and therefore neglecting damping is more conservative design approach.

Making use of the special properties of the mass and stiffness matrices, $M=M^T > 0$ and $K=K^T > 0$. We can formulate the modal matrix ϕ and transform the above equation into

$$I \ddot{q} + K q = \bar{B} u \quad (6)$$

where $I = \phi^T M \phi$, $\Lambda_K = \phi^T K \phi$ and $\bar{B} = \phi^T B$, as previously stated. Transforming this into state space, we have the following matrices

$$\underline{x} = \begin{bmatrix} q \\ \dot{q} \end{bmatrix} \quad A = \begin{bmatrix} 0 & I \\ -\Lambda_K & 0 \end{bmatrix} \quad B_1 = \begin{bmatrix} 0 \\ \bar{B} \end{bmatrix} \quad (7)$$

Making use of the typical test for controllability and using the special form of the above matrices, the controllability matrix can be re configured in the following form.

$$C = rk \left[\begin{array}{c|c|c|c|c|c} 0 & \bar{B} & 0 & -\Lambda_K \bar{B} & \dots & (-\Lambda_K^{N-1}) \bar{B} \\ \hline \bar{B} & 0 & -\Lambda_K \bar{B} & 0 & \dots & 0 \end{array} \right] = 2N \quad (8)$$

Noticing the repeatability of this matrix, sufficient criteria for controllability can be redefined as

$$C = rk \left[\bar{B} \quad \Lambda_K \bar{B} \quad \Lambda_K^2 \bar{B} \quad \dots \quad \Lambda_K^{N-1} \bar{B} \right] = N \quad (9)$$

While equations (8) and (9) make use of the modal form of the system. They only answer the question of whether the system is or is not controllable. However it would behoove us to be able to evaluate each mode separately. Thus, if our system was uncontrollable we could deduce from this analysis what mode was the culprit. A second method is to determine the degree of controllability is to evaluate the singular values of the A matrix. The singular values are the positive square roots of the eigenvalues of the matrix $A^T A$ (Golub and Van Loan (1983)). The two methods are compared for our system in Table 2.

Comparison of Singular Values and Modal Participation Factors
balanced system

ω_i	Single Actuators		Dual Actuators	
	σ_i	$\ b_i\ $	σ_i	$\ b_i\ $
13.2263	0.0016442	0.0240739	0.0406313	0.1966608
13.4066	0.0390196	0.0706435	0.0644075	0.3033061
19.2488	0.0000013	0.0017501	0.0000211	0.0115361
19.4623	0.0018089	0.0299140	0.0006387	0.0310526

* All Values Normalized To One

Table 2 Comparison of methods for relative controllability

Continuing with the analysis, we can restructure \bar{B} to take into consideration the multiplicities (i.e. repeated eigenvalues) of the elements of Λ_K , we have

$$B_Q = \begin{bmatrix} 0 \\ \vdots \\ \bar{B}_Q \end{bmatrix} \quad (10)$$

where Q is the number of distinct roots. We are assured some degree of controllability if every row of the \bar{B} is populated, but their again this does not enlighten us with respect to each mode. This leads to the necessary and sufficient condition of $rk(\bar{B}_Q) = N_Q$, which Hughes and Skelton redefined as the controllability norm to test each mode individually.

$$C_Q = (\det b_Q b_Q^T)^{1/2N_Q} \quad (11)$$

For controllability, $C_Q > 0$. This norm provides a relative measure of the controllability of the repeated modes which can be used as a guide to the placement and number of actuators. However, if all the modes of Λ_K are distinct then equation (11) can be simplified to

$$C_n = \|b_n\| > 0, \quad n=1 \dots Q \quad (12)$$

where this is simply the Euclidean norm of the row vectors of \bar{B}_Q , the modal participation factors.

The above method is compared to a singular value decomposition in Table 2. Since technically all the modes are distinct, we use the norm in equation (12). This norm as well as a singular value decomposition is performed for the two pairs of closely spaced modes at 13 and 19 Hz. The tests are performed for single and dual TWA configuration. For the single actuator case, the TWA produces a torque about the X axis and for the dual actuator case there is an additional TWA producing a moment about the Y axis. From Table 2, it is evident that the value of the norm and singular value for a particular mode yield consistent results in that they increase at least by an order of magnitude with addition of a second actuator. Intuitively, this make sense that the degree of controllability is ultimately increased with the number of columns in the **B** matrix.

VIBRATONAL CONTROL

Before the control of tip motion during a slewing maneuver is pursued, the vibration suppression of the secondary to a unit impulse in the X and Y directions is analyzed. For the orientation of the actuators and the position of the angular velocity sensors refer to Fig. 1. To ensure a collocated feedback, it is assumed that the angular velocity is fed back into a collocated TWA.

The first control method analyzed is a local velocity feedback (LVF) designed via classical methods (i.e. gains chosen by root locus method). As stated earlier the form of the feedback is the angular velocity about point O. The feedback is of the form

$$y = \begin{bmatrix} V_y \\ V_x \end{bmatrix} = K \begin{bmatrix} \omega_y \\ \omega_x \end{bmatrix} \quad (13)$$

where **K** is the gain matrix and V_x and V_y are the voltage inputs into the actuators. The LVF control design is one of the least complex control schemes to implement both analytically as well as

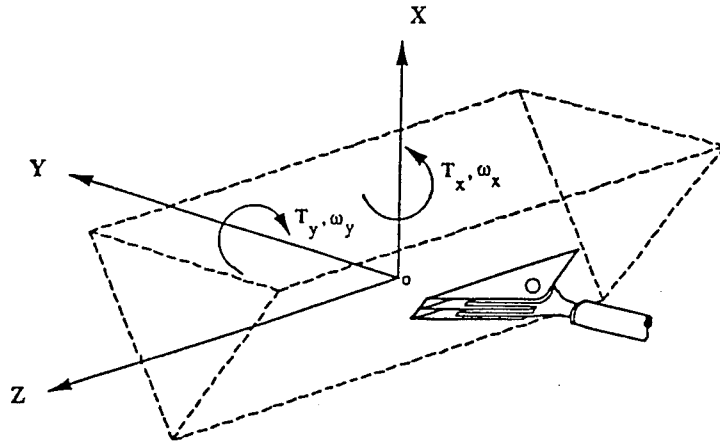


Fig. 1. View of the secondary structure and one of the three tripod legs.
View shows the orientation of the coordinate system.

experimentally. In contrast to the simplicity of the LVF method, the linear quadratic regulator (LQR) is a design method which analytically is relatively easy to employ, but experimentally is not implementable without the use of a state estimator. The advent of high powered computers facilitates the analytical implementation of a method such as LQE, an LQR with a state estimator. This control scenario unlike the LVF method requires full state feedback which for the purpose of simulations is not unreasonable. However, experimentally this requires the estimation of states which leads to large on line computational burdens for a complex structure. Because of the experimental complexity of the LQE method, the LVF method is often more attractive if satisfactory performance levels are achieved. The LQR design method is an optimal control scheme in which acceptance of a gain matrix is based upon the minimization of a cost function. The cost function chosen for the optimal control analyses in this paper is as follows:

$$J = \int_{t_1}^{t_2} (y^T Q y + u^T R u) dt \quad (14)$$

The reason for adapting this form of J , rather than the traditional form, $x^T Q' x$, is that this allows for the direct penalization of the angular rotation and displacement of the secondary. The vector y is the same that is used in equation (13). Thereby allowing the inclusion of the feedback into the cost function. The cost function is transformed into the

traditional form by converting the Q in equation (14) into $Q' = C^TQC$, where C is the output matrix.

The LVF controller substantially reduces the settling time of the response as shown in Fig. 5 to about .5 seconds. The dominant 13 Hz modes were reduced by well over an order of magnitude (Fig. 6). As stated earlier, the simplicity of experimental implementation of the LVF makes it attractive if experimental goals are achievable. To accurately assess the performance of the LVF method it is compared to an LQR analysis. The benefit of an optimal controller is that it will efficiently control the dynamics of the system, while typically not expending any unnecessary power.

Weighting matrices were chosen to closely mimic the time response of the LVF. Fig. 8 shows that like the LVF controller, tip displacements settled in about .5 seconds. Although, the frequency response of the LQR shows a slightly larger reduction in peak frequency (Fig. 9). Since by investigation of the displacement histories both methods were cosmetically performing about the same, it was necessary to see if either method had higher current or speed demands upon the actuators. From Figs. 7 and 10, it is quite evident that the two methods perform similarly. Thus making the complexity of the LQR unnecessary in this case.

OPTIMAL SLEWING CONTROL

Employing a full state feedback scheme, it is proposed to optimize the vibration suppression of the ASTREX during a slewing maneuver about its vertical axis (Fig. 2). This is done by including the inertia terms about the slewing axis as well as the cross coupling flexural terms in the mass matrix. A first order approximation to this system in modal coordinates is:

$$\begin{bmatrix} I_{11} & M_{12}\phi \\ \phi^T M_{21} & I \end{bmatrix} \ddot{q} + \begin{bmatrix} 0 & 0 \\ 0 & \Lambda_D \end{bmatrix} \dot{q} + \begin{bmatrix} 0 & 0 \\ 0 & \Lambda_K \end{bmatrix} q = \begin{bmatrix} 0 & 0 \\ \phi^T B_{fy} & \phi^T B_{fx} \end{bmatrix} u_s \quad (15)$$

where I_{11} is the moment of inertia of the whole structure about the slewing axis, I is the identity matrix, $\phi^T M_{21}$ and $M_{12}\phi$ are the structural cross coupling terms. These cross coupling terms

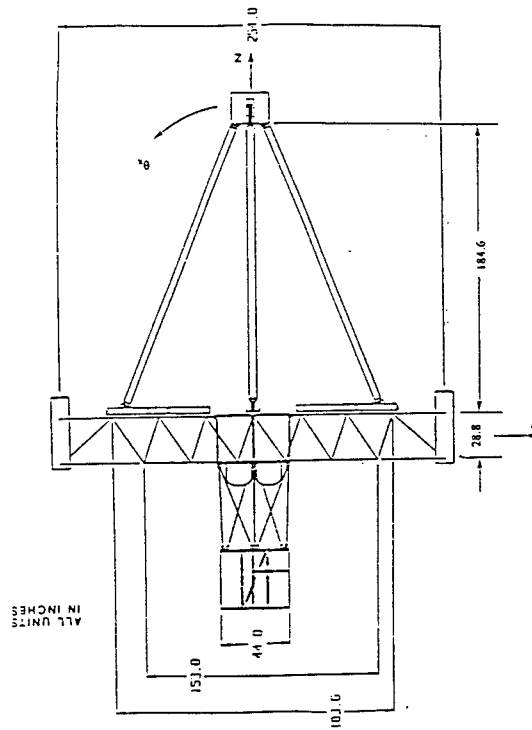


Fig. 2. Schematic of the orientation of the ASTREX about the slewing axis.

constitute the mass of the appendage being slewed, integrated over the length of the appendage. For a more thorough treatment of these equations see references [2,5,9,10]. Using this model combined with actuator dynamics an optimal study is performed for small slewing angles. For this study a slew angle of 1° was chosen. Small rotational angles were chosen because conceivably spacecraft such as the ASTREX will be aiming at targets at great distances. For instance, a space based antenna communicating with and Earth fixed installation. In such cases the change of attitude by a single degree would mean huge changes on Earth. For the same reasons, tip vibrations, generating LOS errors, would be intolerable. Again the optimal output version of the LQR cost function, equation (14), is used, however in this case the output vector y not only contains the input voltages to the actuators but also the angle of rotation of the overall structure about the slewing axis. The control vector u contains the control voltages for the TWA as well as the control torque for the slewing maneuver.

The optimal slewing was simulated in such a manner as to track a new reference angle from the initial orientation in Fig. 2. In this case the new reference was a 1° step function. Weighting matrices were chosen to optimize several criteria. First, to minimize the settling time of the tip oscillations. Secondly, to minimize the overshoot to the new reference position while minimizing maneuvering time. Lastly, to minimize the amount of current required by the torque wheel as well as the angular velocity of the rotating masses. To stay within the operating limits of the physical hardware, i.e. limits of the

gas-thrusters used in slewing, was precisely why an optimal slewing study was performed.

From Fig. 13a it can be seen that the peak time of the system is about .75 seconds while the system only overshoots by 3.5%. The settling of the tip motion is improved in the X direction to about two seconds whereas in the Y direction the amplitude increase, however oscillations damp out much sooner than in the open loop response of Figs. 11a,c. Also, it is seen in Fig. 11b that the peak time increases to about 1.2 seconds for the open loop maneuver. Comparing the rotational speed of the global structure during the open loop slew (Fig. 11d) to the closed loop (Fig. 13b), the rate for the open loop case is much slower, thus explaining the increased peak time. These results give credence to the benefits of slewing an active structure where the actuators act as an inertial assist for the maneuvering structure.

CONCLUDING REMARKS

The contents of this paper are an attempt to control small amplitude vibrations that will undoubtedly be very significant for satellites that must reorient themselves quickly before transmitting a signal in space. Small attitude changes in space will translate into large errors for a far distant target. A small slewing angle was chosen to optimize the tracking of such space structures. Simulations show that vibrations can be suppressed to decrease the settling time of the ASTREX by more than one order of magnitude. Further study will be focussed on the advantages of attitude adjustments with an active structure [2]. This could potentially extend the life of spacecraft by conserving fuel meant for thrusters by allowing the actuators to help in the slewing maneuver where the actuators power source would typically be solar. Also it was shown that it is possible to obtain adequate control with a simplistic type controller such as LVF rather than the sophistication necessary for an LQR type controller. This will also be advantageous for spacecraft with weight limits where the need for extravagant computer equipment used for control would be reduced.

ACKNOWLEDGMENT

The authors wish to acknowledge the contributions of the Drs. Nandu Abaankar, Joel Berg and Alok Das of the Phillips Laboratory's Structures and Control Division at Edwards AFB, California, and an AFOSR Research Initiation Program grant #92-32, administered through the Research and Development Laboratory, Incorporated.

REFERENCES

1. Dosch, J., Inman, D.J., and Garcia, E., "A Self-Sensing Piezoelectric Actuator For Collocated Control," *Journal of Intelligent Material Systems and Structures*, vol. 3, no.1, January, 1992.
2. Garcia, E. and Inman, D.J., "Advantages Of Slewing an Active Structure," *Journal of Intelligent Material Systems and Structures*, Vol. 1, July 1990, pp. 261 - 272
3. Golub, G. H. and Van Loan, C.F., *Matrix Computations*, Baltimore, Maryland, Johns Hopkins University Press.
4. Lim, K.B. and Horta, L.G., "A Line-Of-Sight Performance Criterion for Controller Design of a Proposed Laboratory Model," AIAA-90-1226-CP, pp. 349 - 359
5. Hughes, P.C., "Dynamics of Flexible Space Vehicles with Active Attitude Control," *Celestial Mechanics*, Vol. 9, 1974, pp. 21 - 39
6. Hughes, P.C. and Skelton, R.E., "Controllability and Observability of a Linear Matrix-Second-Order System," *Journal of Applied Mechanics*, Vol. 47, June 1980, pp. 415 - 420
7. Hughes, P.C. and Skelton, R.E., "Controllability and Observability for Flexible Spacecraft," *Journal of Guidance and Control*, Vol. 3, No. 5, Sept.- Oct. 1980, pp. 452 - 459
8. Inman, D.J., *Vibration and Control, Measurement, and Stability*, Prentice Hall, Englewood Cliffs, New Jersey, 1989
9. Meirovitch, L. and Moon, K.K., "Dynamics and Control of Spacecraft with Retargeting Flexible Antennas," *Journal of Guidance, Control and Dynamics* Vol. 13, No. 2, Mar.- Apr. 1990, pp. 241 - 248
10. Meirovitch, L. and Quinn, R.D., "Equations of Motion for Maneuvering Flexible Spacecraft," *Journal of Guidance, Control and Dynamics*, Vol. 10, No. 5, Sept.- Oct. 1987, pp. 453 - 465

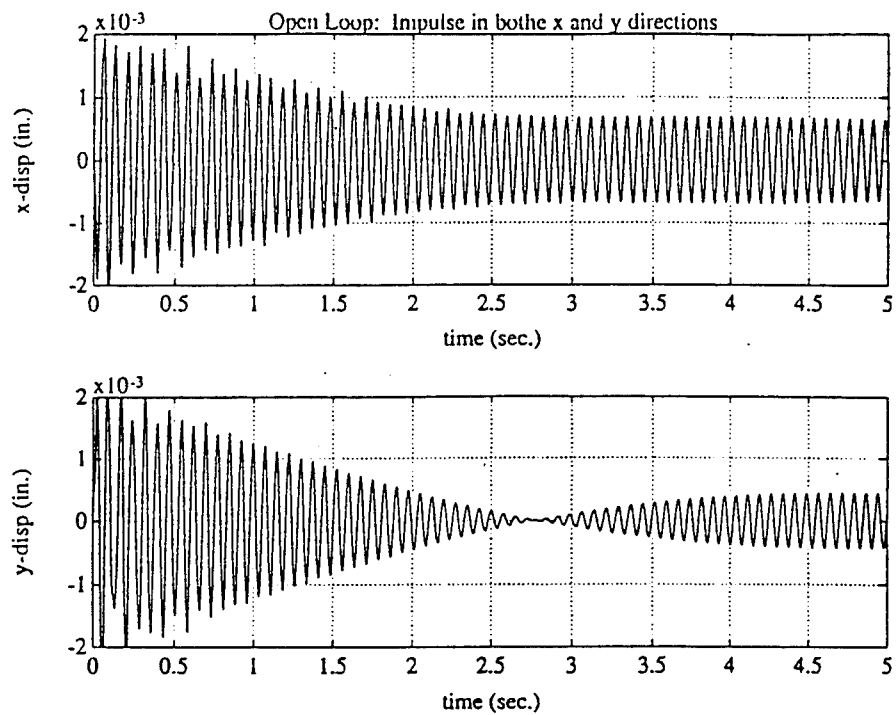


Fig. 3. Open loop time history for an impulse in both x and y directions.

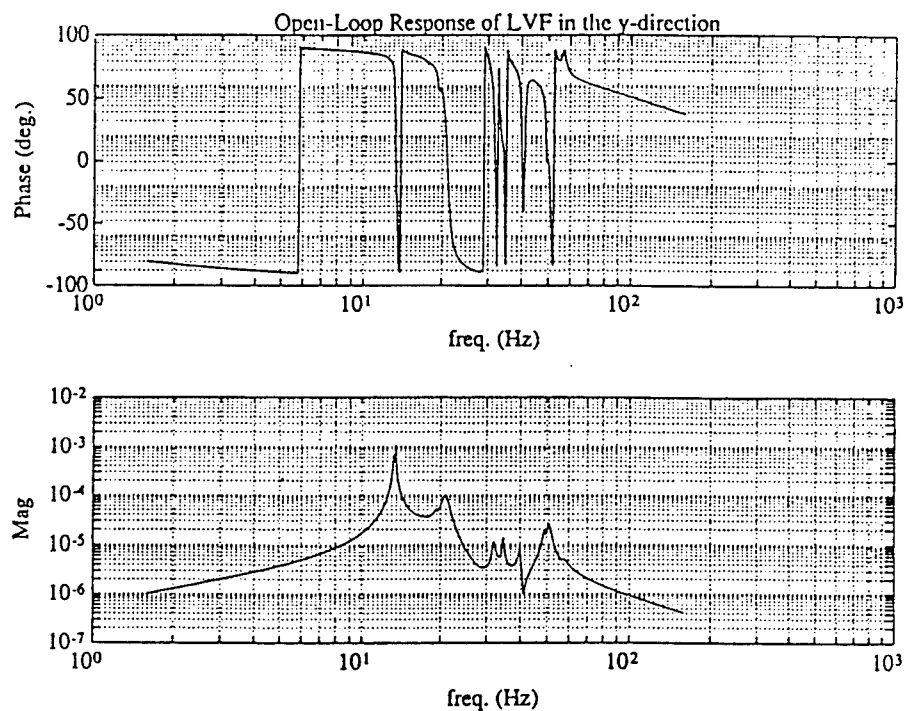


Fig. 4. Open loop frequency response

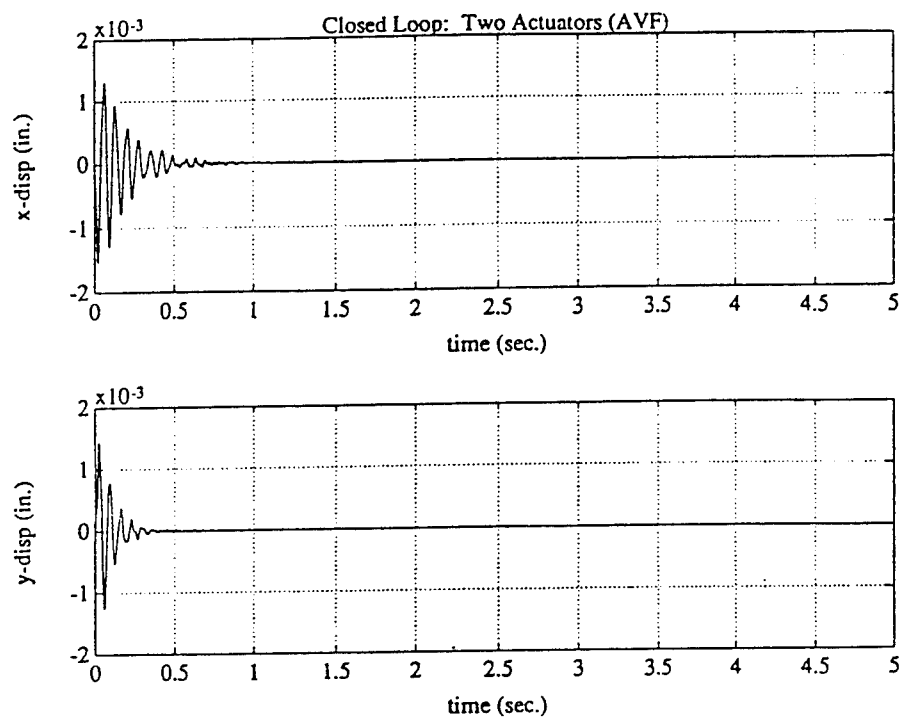


Fig. 5. Closed loop time history for local velocity feedback through the use of classical design methods.

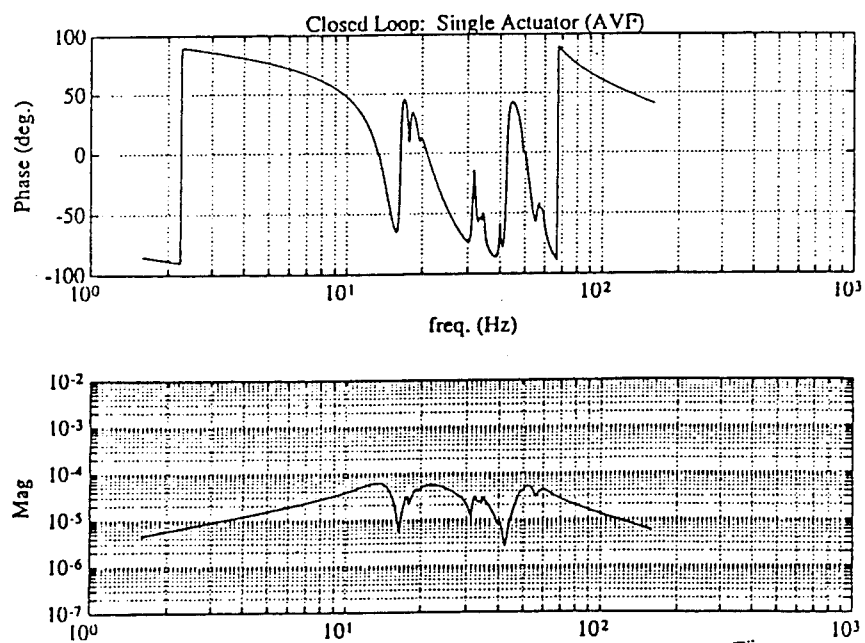


Fig. 6. Closed loop frequency response using classical design methods.

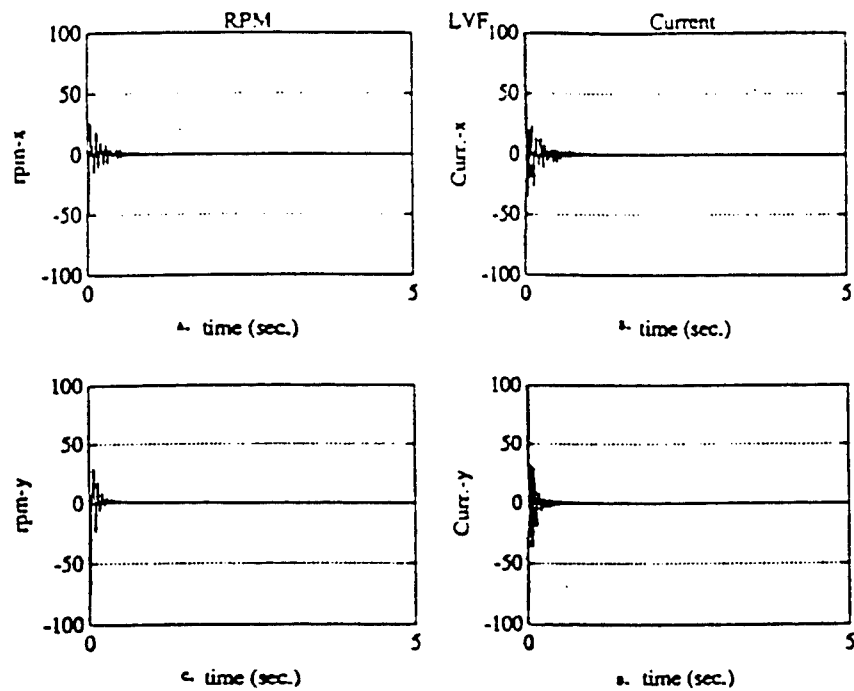


Fig. 7. Closed loop performance using LVF. (a) Ang. Vel. of the TWA the y axis (b) current for the TWA about the y axis (c) Ang. Vel. of the TWA the x axis (d) current for the TWA about the x axis

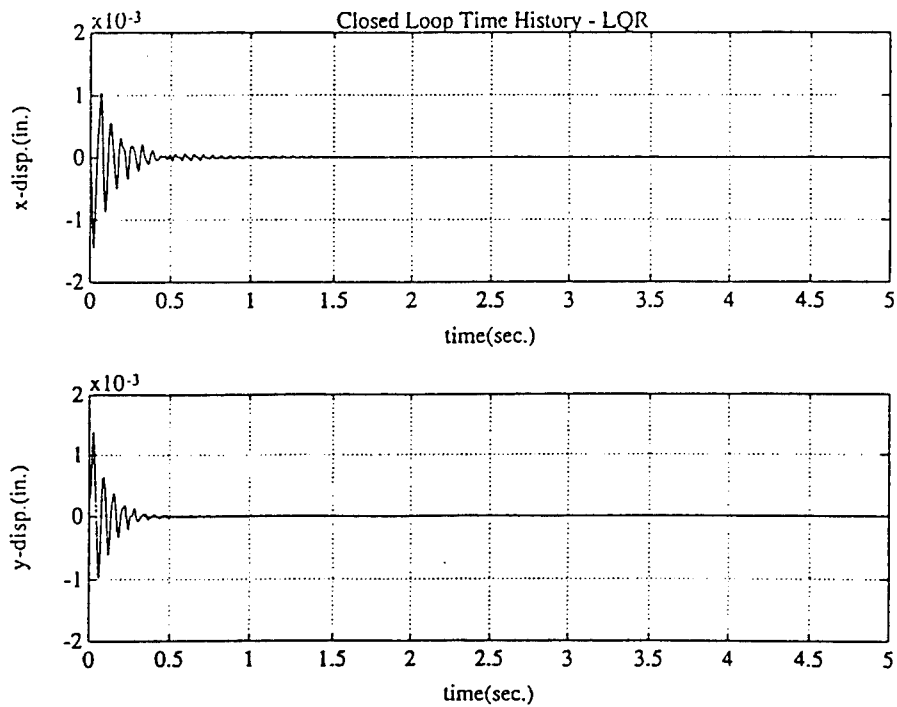


Fig. 8. Closed loop time history for unit impulse in the x and y directions - LQR design.

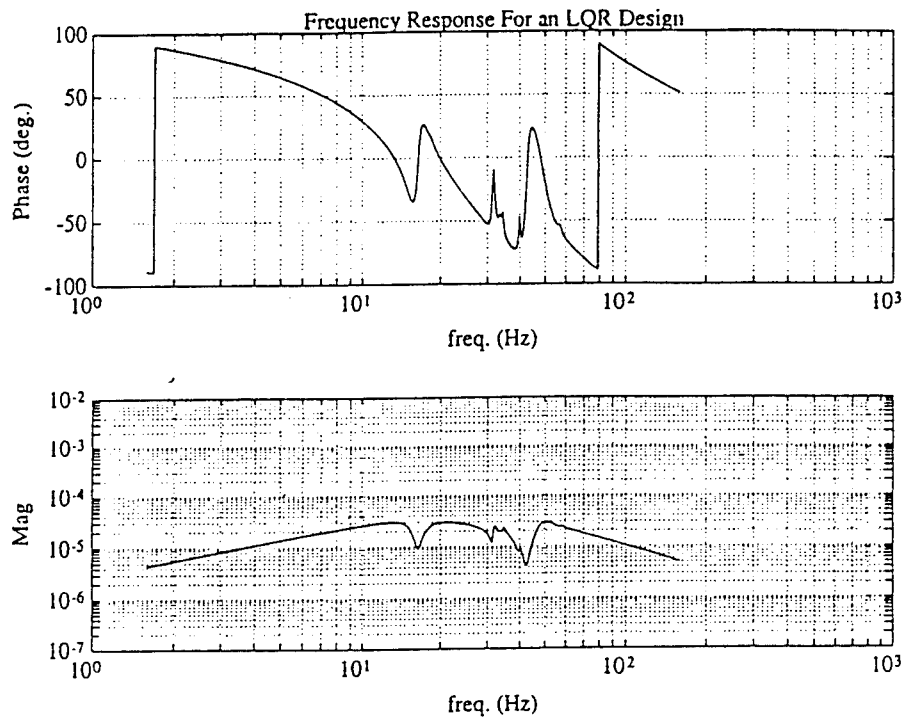


Fig. 9. Closed loop frequency response using LQR design method.

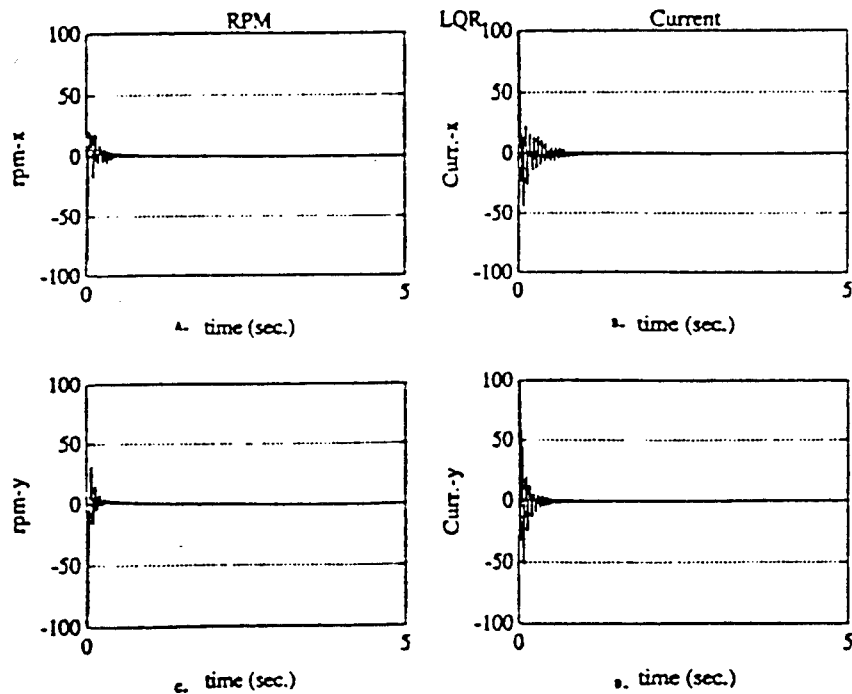


Fig. 10. Closed loop performance using LQR. (a) Ang. Vel. of the TWA the y axis (b) current for the TWA about the y axis (c) Ang. Vel. of the TWA the x axis (d) current for the TWA about the x axis

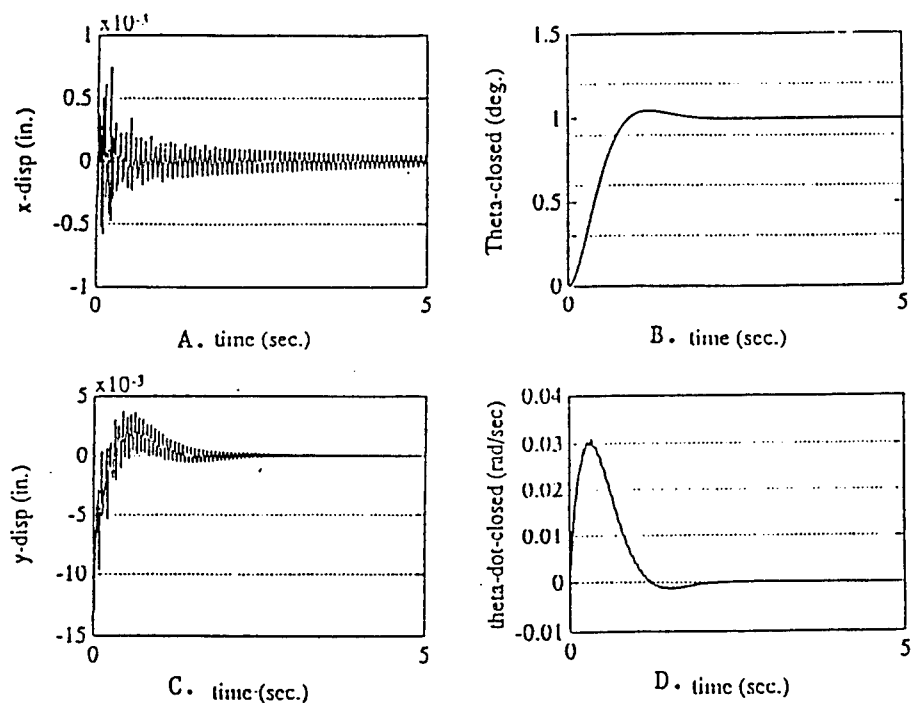


Fig. 11. Open loop slewing simulation. (a) tip displacement in the x direction (b) rotation angle of the global structure (c) tip displacement in the y direction (d) rotational rate of the structure

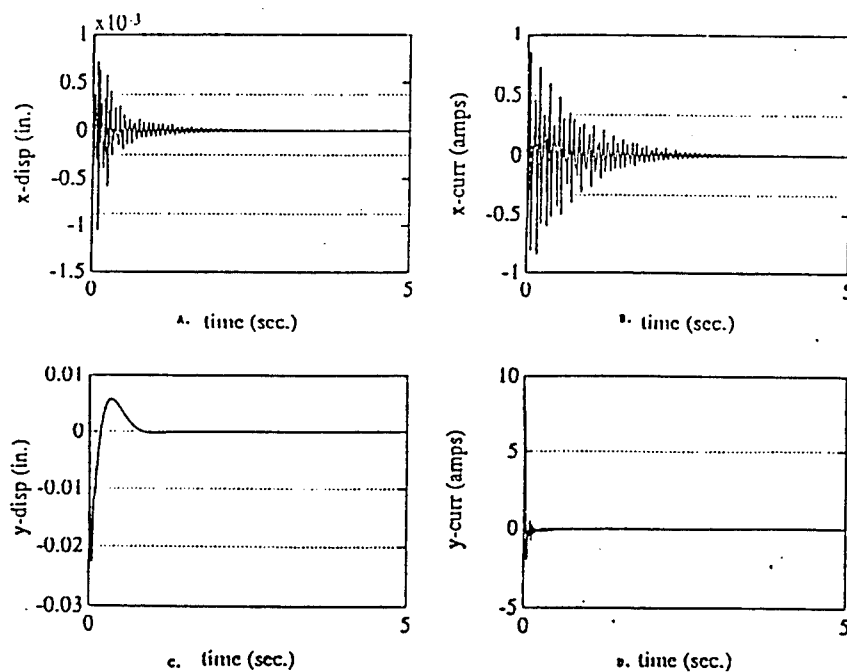


Fig. 12. Closed loop slewing simulation. (a) tip displacement in the x direction (b) current for the TWA in the X (c) tip displacement in the y direction (d) current for the TWA in the Y

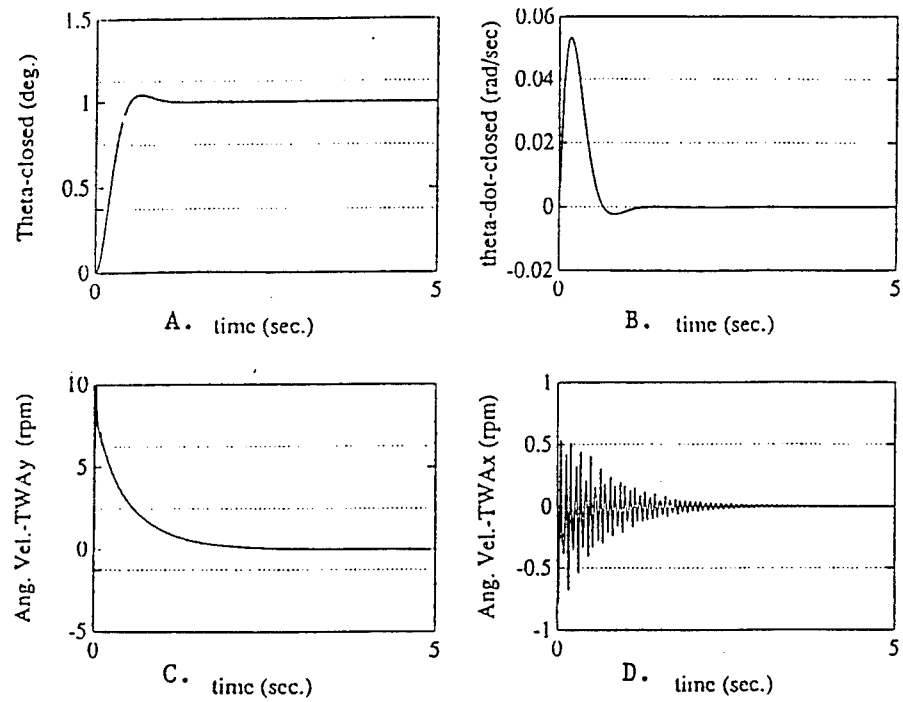


Fig. 13. Closed loop slewing simulation. (a) rotation angle of the global structure (b) rotational rate of the structure (c) Angular vel for the TWA in the about the X (d) Angular vel for the TWA in the about the Y

THE DEVELOPMENT AND USE OF DIGITAL GEOGRAPHIC INFORMATION
WITHIN
THE ADVANCED RESEARCH INITIATIVE FOR SIMULATION AND TACTICAL AIDS
(ARISTA)

William L. Hamilton, Ph.D.
Associate Professor
Department Of Geography

Salem State College
352 Lafayette Street
Salem, Massachusetts

Final Report For:
Research Initiation Program
Phillips Laboratory

Sponsored By:
Air Force Office Of Scientific Research
Hanscom Air Force Base, Bedford, MA

and

Salem State College

December 1992

THE DEVELOPMENT AND USE OF DIGITAL GEOGRAPHIC INFORMATION
WITHIN
THE ADVANCED RESEARCH INITIATIVE FOR SIMULATION AND TACTICAL AIDS
(ARISTA)

William L. Hamilton, Ph.D.
Associate Professor
Department Of Geography
Salem State College

Abstract

Digital geographic information is necessary for the proper performance of several models used in the Advanced Research Initiative for Simulation and Tactical Aids (ARISTA). The major tasks for this research initiative were to investigate the analytic development and uses of digital geographic information for scene simulations and to provide data for physical model implementation within ARISTA. The primary geographic information under investigation were the deployment of Digital Elevation Models (DEM) and the utilization of satellite based remote sensing technologies for the generation of Digital Feature Data (DFD). A detailed analysis of the generic capabilities and formation of DEM's is presented. Additionally, the methods engaged to build a DEM for the Hanscom AFB, Massachusetts and surrounding area are detailed. An analysis of the use of the LANDSAT system to develop DFD is presented including requisite digital image processing procedures and associated recommendations. The architecture of a logical Geographic Information System (GIS) data structure with its concomitant physical implementation employing a relational database system is addressed. The logical design of the GIS allows for both data management and information acquisition by coordinate address. Finally, recommendations for future research activities are detailed.

1. INTRODUCTION

This document represents the final report on research conducted by personnel at the Atmospheric Structure Branch at Phillips Laboratory (PL/GAA) and Salem State College - Salem, MA. Within the original proposal four tasks were developed to aid Electro-Optical Tactical Decision Aids (EOTDA) and particularly the Advanced Research Initiative for Simulation and Tactical Aids (ARISTA) programs. Four tasks were originally set fourth for the one year research project:

- Task 1 - Develop Spatial Databases For Hanscom AFB including Digital Elevation Models (DEM) and Digital Feature Data (DFD).
- Task 2 - Develop GIS Analytic Procedures and Topologic Rectification For Tactical Scene Development
- Task 3 - Develop Data Visualization Procedures
- Task 4 - Integrate Applications Derived From Tasks 1, 2, and 3, into the ARISTA program architecture.

Tasks 1 and 2 were accomplished in the development of the DEM and DFD for the Hanscom AFB and surrounding area and comprise the largest part of the research effort both in time and computation (section 2). Along with the actual development of the data, analysis and recommendations on the deployment of DEMs and DFD have been presented. Task 3 was altered slightly as the Digital Cartographic Application (DCA) Software necessary for this function could not be procured in time to adequately provided analysis support. Instead software developed at the Phillips Labs was used for graphic support and DEM and DFD data were structured appropriately. Recommendations for digital display of geographic information are detailed in section 2.3.1 and 2.3.2. Task 4 was addressed through the development of a logical data structure which was physically implemented by PL/GAA personnel on the Tropospheric Environment Simulation Laboratory (SimLab) UNIX base platform (NEXT station) (Section 3).

2 DEVELOPMENT OF TOPOLOGICALLY RECTIFIED SPATIAL DATABASES WITH ASSOCIATED GIS ANALYTIC PROCEDURE RECOMMENDATIONS.

The purpose of this section is to provide information regarding the development, possible uses, accuracies, validity, reliability and operational recommendations with respect to Digital Elevation Models (DEM). While much of the material is generated from analysis of USGS DEM's, comments their use, accuracy, validity, and reliability can generally be extrapolated to other DEM products. The intended use of the document is to give the PL/GAA scientists the necessary information on DEM development and accuracies so that informed decisions can be made about their application in EOTDA products.

2.1. METHODOLOGY

The methods used to compile the following information were library research, telephone interview, cartometric analysis, and personal experience. The first analysis partition addresses types of DEM's, DEM formation methods, and DEM uses. The second analysis partition addresses the effect of DEM source documentation accuracies on basic cartometric measurements (distance, area, volume, gradient). The third analysis partition reports on the methods use to develop the Hanscom AFB DEM with associated operational recommendations.

2.2. DIGITAL ELEVATIONS MODELS

Digital Elevation Model (DEM) is a generic term given to any contiguous representation of continuous data generally representing relative relief. Another term commonly found in the literature is Digital Terrain Model (DTM). However, the term terrain carries a connotation of land use when in fact the terrain model can be of any continuous variation for any data type (ie; temperature, barometric pressure, etc., etc.,) and the term DEM is more commonly accepted.

Digital Elevation Models play an important part in many GIS analysis procedures as they can provide requisite data for environmental modeling, be manipulated to provide secondary and tertiary data sets, and provide general geographic orientation for other GIS analysis products. Some of the more common uses of DEM are as follows:

- Storage of digital topographic data from national analog databases.
- Three dimensional portrayal of data for planning, landscape design, landscape architecture, and environmental modeling.
- Development of viewshed analysis (cross-country visibility)
- Planning of roads, dams, and other environmental infrastructure features.
- Computing slope, aspect, slope profiles, and surface roughness to assist in terrain analysis, or provide commonly needed parameters to initialize physical environmental models.
- As a background file to the display of other thematic data thereby allowing the user to orient themselves and provide greater map utility and viability.

- By employing model algorithms on non-altitude data the DEM can portray surfaces of travel time, cost, indices, groundwater levels, etc., etc.

Clearly the DEM offers great potential in military GIS analysis and can be used to generate data and populate data bases with a wide array of information given a relatively small amount of source information.

2.2.1 The Digital Elevation Point Model

One of the DEM's offered by the United States Geological Survey (USGS) and Defense Mapping Agency (DMA) is the Digital Elevation Point Model (DEPM) which is comprised of an altitude matrix. Advantages associated with the model are:

- Allows for fast manipulation of data.
- Enables the user to analyze large spatial areas as the data is provided on a topographic quadrangle basis.
- Allows ease of digital integration with existing automated and analytic algorithms common to many computer-assisted cartographic and GIS products.

Disadvantages of the DEPM include:

- Data redundancy in areas of low relative relief
- Inability to adjust the sampling scheme to match topographic complexity.

Population of the grid is normally accomplished by one or a combination of the following methods.

2.2.1.1 Photogrammetric

The most common method to develop the DEPM is to determine elevations from quantitative measurements using a stereo-plotter. The analytical stereo plotter of choice by the is the Gestalt Photo Mapper II (GPM2). When employed correctly the GPM2 obtains parallax measurement at 2,444 points for each 8 x 9mm area on a stereo-photo model (model scale 1:80000). Normally the subsets (the 8 x 9mm areas) are selected (subjectively) to match terrain conditions. While this process works well for open areas with clear ground conditions problems arise in areas where ground elevation cannot be clearly determined (ie. forests, over water) producing the digital

effect of low amplitude random noise within the data set.

2.2.1.2 Profiling Devices

Another method used by Federal agencies to generate DEPM data is to employ a semi-automatic profiling device. In this case the stereoplotter is interfaced to a digital profile recorder which automatically scans the photo and records point elevation data at some predefined interval. For a USGS 30m DEM the scan line is usually accomplished in the y direction of the photograph for 90m profiles with sampling occurring every 30m. These profile samples are then reassembled into the USGS 30m grid specification for DEM distribution. As with most reassembled scan data the points located along the profile line exhibit a larger spatial autocorrelation imparted partly by the motion of the scanner as it is sampling the point along the profile. This stronger spatial autocorrelation results in striping in the DEM as the data is directionally elastic (anisotropic) resulting in significant errors (Brabb, 1987). Studies have estimated that approximately one third of the USGS 30m DEM contain the systematic striping error (Elassal and Caruso, 1983). Suggestions for correcting the banding phenomena are offered in section 2.7.

2.2.1.3 DEM Digital Line Graph Augmentation

A final method of DEM development recently is to develop the altitude matrix from digitized contour lines (Digital Line Graphs [DLG]). This process entails smoothing and editorial correction of the altitude matrix to known planimetric hypsography from DLG products (either photogrammetric or topographic map source). This melding of the DEPM and DLG provides a improved DEM product virtually eliminating the systematic errors found when profiling devices are singularly used. The problems with this method are a) only a limited number of DEM at the 7.5 minute series are available and b) greater emphasis within the Federal agencies has been placed upon the development of DLG products (Private communication with USGS Earth Resource Division).

Obviously the USGS and DMA offer a variety of point model development methodologies to the end user. Unfortunately the modeling methods vary depending upon the spatial domain of the product. For example, DEPM's at the 7.5 minute quadrangle 1:24000 scale are primarily comprised of GPM2 and semi-automatic profiling technologies although some (unspecified by USGS) are also DLG

enhanced. At a smaller scale (1:250000) the DEM's are produced using different modeling methods (both point and line models) which alters their accuracy characteristics. Combining this data either in overlay analysis or in spatial array requires careful attention as to the mixing of various accuracies by the GIS analyst in order to ensure valid results.

2.2.2 Digital Elevation Line Models

The Digital Elevation Line Model (DLG) is not unlike the point model except that the spatial phenomena under investigation exists at a higher spatial dimensional plane, the line. The intended benefits of the using the Digital Elevation Line Model are to:

- produce a higher quality model by eliminating some of the systematic data capture error associated with point models (banding or striping).
- reduce the extended interpolation procedures required to produce a hypsometric curve which matches the topographic series from which the model was derived.

The USGS has begun to develop a Digital Elevation Line Model known as Digital Line Graphs (DLG). The DLG is a topologically structured vector based line file produced from the interpolation of digitized contours (Rinehart and Coleman, 1988). The USGS digitizes from both the photogrammetric process (second generation data) and the topographic map (third generation data) to produce the DLG (private communication with USGS). While the DLG offered by the USGS does provide those benefits mentioned above they also have the following disadvantages associated with them.

- DLG require more mass storage space (approximately four times as much space) as compare point DEM's of the same spatial area.
- More time is required for retrieval of either a stored point or an interpolated point.
- More time is required in producing DEM derivative products such as slope and aspect data.

- DLG, because of their size, need to be redefined back into DEM point models to meet the processing limitations of most commercial GIS software (generally the number of points which can be processed for DEM derivatives).

2.3. USES OF DIGITAL ELEVATION MODELS

There are a variety of analyses that can be derived from DEM's which are beneficial to scene simulations. All analyses detailed in the following sections can be developed from either the DEPM or the DLG employing data structures that are either matrices, irregular point data, or triangulated networks.

2.3.1 Three Dimensional Views (Block Diagram) and Profiles

The most common use of the DEM is to produce a three dimensional perspective commonly referred to as a block diagram. The block diagram is particularly useful to the novice map reader where geomorphology can be used for orientation purposes while thematic data is overlaid to add additional attribute information.

The block diagram can also be used for digital terrain analysis where exaggeration of the vertical axis is commonly employed to develop flood boundary for different levels of hydrologic events or for contaminant flow analysis.

Profile analysis is employed for various forms of terrain analysis or in digital image processing. With respect to DMA DEMs one can determine the terrain profile along a user specified course. This function is of particular use in transport planning when developing personnel and/or heavy equipment routes.

2.3.2 ViewShed (Line Of Sight) Analysis

With proper manipulation the DEM can provide a measure of the intervisibility of points. This information is of particular interest to military planners, communication designers, weapon placement and targeting systems, and other military operations. Most viewshed algorithms function by using site elevations and direction data and executing hidden line removal algorithms employed in the development of block diagrams. The algorithms calculate unobstructed view matrices which can be contoured and portrayed on a map commonly referred to as a viewshed. More sophisticated algorithms have recently been developed to allow the user to place the location and height of known blockades (faults) into the process allowing for more realistic results.

While many studies have focused on positive viewsheds (how wide or long an unobstructed view that can be obtained) other studies have demonstrated the use of the negative viewshed (limited view). Examples for negative viewshed analysis would be include placement of high security facilities and penal compounds.

2.3.3 Determination of Slope, Aspect, Concavity, and Convexity

Many type of physical environmental models require as input measures of geographic topography which can generally be described by slope, aspect, concavity, and convexity. Manipulation of DEM data allows for the precise development of these topographic descriptors over large geographic areas. There is, at times, confusion as to what these various terms represent and it is imperative that the analyst understand their meaning as it relates to product specifications.

Slope is generally divided into two components; gradient and aspect. Gradient can be defined as the rate of altitude for any given distance and is usually given in degrees. Aspect is defined as the compass direction of the gradient and is calculated in degrees and then converted to a compass bearing. Convexity is defined as the change rate of slope and concavity is the numerical opposite of convexity both described in degrees per unit distance. With the exception of gradient, all of these measures are a function of some kernel (usually a square) of the DEM. Generally the user is allowed to specify the size of the kernel which is based upon the density of observation within the DEM.

Obvious uses for gradient and slope maps are within the field of hydrology and meteorology. Concavity and convexity are frequently used in civil engineering and can provide critical information for troop deployment and heavy equipment movement.

2.3.4 Contour Maps

Contour mapping is concerned with the direction and magnitude of continuous data distribution which is more formally known as isarithmic analysis. Within the realm of the cartographic sciences it is generally recognized that no other map form has proven to be as useful and is the most often requested in the scientific community. The two primary forms of the isarithmic map are isometric and isoplethic. Isometric surfaces are defined by any type of data distribution which can exist as a point in either statistical or non-statistical formats (ie. altitude, daily temperature, etc.,etc.). Isoplethic surfaces are defined by any type of continuous data distribution which cannot exist at a point and are

normally in the form of a statistical or mathematical coefficient (ie. trend surface, Fourier surface, residual surface etc., etc.). The primary benefits of developing contour maps are providing a predefined view of a surface and portraying the locations of attribute data with respect to that view. The elements involved with the development of contour maps include location and number of control data, interpolation procedures, selection of class intervals and method of projection. Generally, the contour map can be displayed in two or three dimensional views and represented by line or filled contours (see appendix).

2.4 DEM ACCURACIES

Cartographic accuracy can be defined as the difference, systematic or unsystematic, between mapped information and that which exists in reality. Because all maps are transformations of reality to another vector space inaccuracies are introduced into the mapping process. With respect to DEM's two different types of accuracy can be addressed; those inherent to the source documentation and those associated with the use of the source documentation.

2.4.1 Digital Elevation Point Model Source Accuracies

Digital Elevation Point Model source accuracies are, for the purpose of this analysis, separated into horizontal, vertical, and miscellaneous accuracies. Horizontal accuracy is primarily dependent upon the scale of the source document. Vertical accuracy, according to the USGS, is scale independent, and is process dependent. Specifically, the vertical accuracy is directly dependent upon the process of vertical interpretation used. Finally, the miscellaneous accuracies are dependent upon Federal organizational procedures as they relate to the source document.

Horizontal accuracies for all Federal DEPM's are defined by the national map accuracy standards which state that:

For maps of publication scales of 1:20000 or smaller, not more than 10 percent of the points tested shall be in error by more than 0.020 inches. These limits of accuracy shall apply in all cases to positions of well defined points only (NCIC).

The USGS DEM's are distributed at a scale of 1:24000 and 1:250000 which by definition means they have a horizontal accuracy of +- 40 feet and +- 416.66 feet respectively. It should be noted that the USGS test limits apply only to well defined points and do not include contour

lines which is, of course, the primary use of the DEPM.

Vertical Accuracy for the all Federal DEPM is based on how the maps are compiled and is determined differently for the 7.5 minute (1:24000) and 1 degree (1:250000) map product.

For the 7.5 minute DEM the following vertical accuracy applies:

... is that no point will have a absolute error over 50 meters when compared to the true height from mean sea level (msl) or that an array of points not to encompass more that 49 contiguous elevations (an effective 7 by 7 array) wherein the relative integrity is not in error by more than 21 meters (USGS, 1987).

If the source data for the DEPM is from the National High Altitude Program (NHAP) then the Root Mean Square Error (RMSE, see appendices) of 7 meters or less is considered reasonable.

In effect the USGS is stating that for a 7.5 series DEM the vertical accuracy for any given point will not have an absolute error of greater than 50 meters or a relative error of not more than +- 21 meters or RMSE of 7 meters the latter error calculations depending upon the source documentation.

For the 1 degree DEPM the following vertical accuracy applies:

...and an absolute vertical accuracy (feature to mean sea level (MSL)) of +- 30 meters, linear error at 90 percent probability (USGS, 1987).

From other quotation regarding the vertical accuracy of the 1:25000 DEPM:

...A RMSE of one-third of the contour interval is the maximum permitted. There are no errors greater than one contour interval in magnitude (USGS, 1987).

In conversations with the USGS these two statements regarding the one degree DEM can, depending on geographic location, be contradictory. It is suggested that the first quotation be used for the vertical accuracy standard as the contour interval stated in the second quotation represents the SOURCE documentation and NOT that found on a 1:250000 map

which leads to confusion.

Miscellaneous source accuracies are those which are a function of the operational procedures of the entity collecting the data, in this case the USGS or DMA. Because the USGS samples the 7.5 minute DEM at intervals of 30 meters and the 1 degree DEM at 3 arc-seconds the minimal feature which can be defined must be larger than 60 meters and 6 arc-seconds respectively, based upon spatial sampling theory (Nyquist frequency). Additionally the USGS has recently published a list of DEPM point models and stratified them as those which have a RMSE between 0 to 7 meters and those 8 to 15 meters (RMSE). It is interesting to note that for Massachusetts the map accuracies range from 1 to 15. Generally, this published figure simply indicates that for an area of low relief the RMSE will be less than for one with high relief.

2.4.2 Digital Elevation Point Model Application Accuracies

The purpose of analyzing the application accuracies of the digital elevation point model is to determine if significant error is introduced into the model through processing manipulation. In order to conduct this analysis the Digital Geography Laboratory (DGL) at Salem State College, Salem MA (SSC) developed contour maps using 7.5 minute 1:24000 DEPM from the USGS for the north central area of the CONCORD quadrangle. The difference between the two contour maps were; a) the number of points used to develop the contours and b) the method by which they were developed. As plotted, the maps showed no significant error with respect to distance measurements based upon stratified random distance measurements using manual digitization. Indeed, the measurements indicated an error of .04 inches which can be totally attributed to the digitizer operator. These results would indicate that the spatial integrity of the DEM employed stays constant even though two different methods and number of points were used. Of note, however, is the number of points selected did have an effect on the contour definitions. Specifically, the greater number of points selected resulted in more contours and more highly defined contour lines.

2.4.3 Digital Elevation Line Model Source Accuracies

Digital Elevation Line Models source accuracies can be stratified into horizontal, vertical, and miscellaneous.

The horizontal accuracies are the same as defined for Digital Elevation Point Models. The vertical accuracies differ from the Digital Elevation Point Models as they match the national map accuracy standards which are

as follows:

Vertical accuracy, as applied to contour maps on all publication scales, shall be such that not more than 10 percent of the elevations tested shall be in error more than one-half the contour interval (RMSE and not to exceed 7 meters) and no error to exceed one contour interval (RMSE) (NCIC).

This standard would indicate that if the contour interval were 10m then 90 percent of the points tested would have vertical error of less than $\pm 5m$ and that 10 percent may vary more than the $\pm 5m$.

With respect to miscellaneous source accuracies issues, none could be found.

Recent studies (Carter, 1988) bring into question the stated USGS accuracy standard. Currently the USGS assumes no error is introduced in the digitization process from which the DLG is made. Studies have indicated that there is always error introduced in the digitization process. However, until further research is accomplished the user of the USGS DLG must assume the stated accuracy of the source document is valid.

2.5 RAMIFICATIONS OF DEM ACCURACIES ON CARTOMETRIC ANALYSIS

Given the aforementioned accuracies of the DEM currently employed by the USGS and the Defense Mapping Agencies (DMA) it is logical to try and ascertain their effect upon cartometric analysis. The following text uses examples to define the possible range of cartometric values which theoretically could be obtained using DEM products. The probability of attaining these outer limit values is unknown as the DEMs are not based on random samples and little research has been conducted on the requisite spatial statistical analysis required to resolve these questions. However, given the methods by which the DEM's have been developed there is a reasonable degree of probable error within any cartometric measurement. The following discussion of cartometric analysis assumes a Digital Elevation Point Model of 1:24000 using the stated USGS source accuracies, reasonable spatial data integrity, and does not address processing or algorithmic errors.

2.5.1 Accuracies of Distance Measurements

Given a straight line measurement between any two points on a map and a horizontal positional accuracy of ± 40 ft then the actual measurement

could have maximum variation of 80 ft. Thus a distant measurement of 300 feet could, based on source documentation error, range from 220 feet to 380 feet. Use of more sophisticated distance measurement techniques such as the Pythagorean theorem which are based on geometric assumptions could be invalidated if the source accuracies significantly contaminate the geometric configurations (ie. forcing a right triangle to an obtuse triangle).

2.5.2 Accuracies of Area Measurements

The effect of horizontal (linear) accuracies on area calculations magnifies error in some form of power function based upon the spatial integrity of the DEM and the geometric shape under analysis. This error magnification can be demonstrated through the area calculation for a square. Given a square parcel of land 200 feet on each side the land area contained within that parcel is equal to 40,000 square feet. However given the stated source accuracies, the actual area contained in the square parcel could possibly range from 14,400 square feet to 78,400 square feet.

2.5.3 Accuracies Of Volumetric Measurements

The calculations of volumetric measurements from DEM's need to consider both the stated horizontal and vertical accuracies of the source documentation. Again taking a elementary scenario with respect to spatial integrity and geometric shape the range of possible values for a volumetric measures can be calculated. Given the same parcel of land is section 2.5.2 and calculating the volume given a constant depth of 21 meters the possible solutions range from 660,983.607 cubic feet to 7,197,377.048 cubic feet.

2.5.4 Accuracies of DEM Derivatives (Slope, Aspect, Convexity, and Concavity)

The effect of DEM source documentation accuracies for derivative products is moderated by the algorithms used, spatial integrity, and processing precision of the computing system. Thus trying to calculate the final accuracies of DEM derivative products is a monumental task not commonly employed except for the most precise GIS analysis. However, one can gain insight into the effect of source documentation accuracies on gradient calculations commonly used to produce slope maps. The gradient is defined as the maximum rate change of altitude between two locations. Given a ground distance between two points of 1000 ft and a measured altitude range of 60 ft the possible gradient solutions span from 3.43 percent to 9.0 percent.

The ranges of possible answers for various cartometric solutions expands as the DEM map scales become smaller. Thus a DEM at a 1:250000 scale would produce a significantly wider range of possible solutions. As stated previously, the probability of incurring significant error is unknown as those statistical measurements are under investigation by a small number of researchers.

2.6 DEM RELIABILITY AND VALIDITY

The reliability of the DEM products under review can be addressed, as is most scientific investigations, based upon the ability to replicate results within certain limits of accuracy. Given that the DEM's under investigation are source verified and that manipulation of the DEM's is accomplished using digital technology then the DEM derivative materials can be considered to be reliable. The caveat on this statement of DEM reliability is that any number of end users following the same procedures should all attain the exact same end product. Given the technology employed by ARISTA the final judgement of product reliability is determined by the end users ability to understand and document their procedures so that valid replication producing high reliability can occur.

Validity of the DEM's can only be judged against their intended use. Knowledge of DEM accuracies allow ARISTA scientists to determine the valid uses of the DEM products. For example, if a GIS project required identification of features smaller than 40 meters (measured along the primary axis) then use of DEM which are created with a sampling interval of 30 meters would be invalid. Inversely, should an analysis be able to accept specified measurements with ± 7 meter (RMSE) accuracy then use of some DEMs are valid. Hence, as with most scientific investigations, determination of validity is driven by the intended application of the results. Generally product validity, unlike accuracy, is binary for any given application. Here again, however, the judgement of validity is based upon the user ability to understand data accuracy (in this case DEM data) and its implications when employed in scene simulations.

2.7 OPERATIONAL DEM ISSUES, POSSIBLE SOLUTIONS, AND RECOMMENDATIONS

From an operational perspective three issues arise with respect to use of DEM's in the ARISTA project; banding in DEPM, edge matching of topographic quadrangles represented by different DEM type (DEPM versus DLG), and expanding the applicability of existing DEPMs by repopulating their altitude matrix with more precise data.

2.7.1 Banding of Digital Elevation Point Models

As documented in previous sections Digital Elevation Point Models can possess significant banding problems. The effect of this banding problem is to shift the point elevation data by some linear distance in the direction of the scanning head used to capture the digital data from source documentation. This problem is rather common to digital image processing, especially the early LANDSAT systems which rely on an oscillating mirror to project reflected light onto sensor banks. Obviously, this banding problem causes properly encoded elevation data to be encrypted with the wrong spatial location and if not corrected can corrupt the spatial integrity of part if not the whole DEM. Fortunately there are several methods available which can be employed to remove the banding error. If one views the DEPM as a raster image (albeit a gross one) then image processing rectification techniques can be employed. One frequently used approach is to determine the degree of lateral shift creating the banding error and then develop an algorithm to shift the picture elements (pixels) in the opposite direction by the same degree of lateral shift. This researcher contacted various offices in the USGS to try and obtain a value for the lateral shift but was unsuccessful in acquiring a meaningful answer (Although the USGS readily admitted that it does sell heavily banded DEM's!). My recommendation would be to run a low band pass filter and then evaluate the DEM matrix as to both the elimination of banding and how the filter effected the general integrity of the DEM. Should the banding prove too subtle and the low band pass filter violate the integrity of the DEM then executing an analysis of variance on the DEM matrix should allow for identification of the shifted pixels. While the USGS does not know if it has software available to the general public which would remove the banding there are commercially vended image processing programs which contain geometric rectification algorithms. Additionally, given that USGS DEM's are widely distributed, it would seem likely that someone in the user community has already developed software to remove the banding problem.

2.7.2 Edge Matching of Different DEM Types

Another operational issue is how to accomplish an edge match of digital quadrangles using different types of DEM's. Because ARISTA may need to use both the DEPM and the Digital Elevation Line Model (DLG) for different areal coverage a solution to this issue must be found. It is known from the maps developed at the DGL that the two models differ significantly with respect to contour placement. However, this difference may be significantly reduced by employing various contouring and smoothing algorithms. At this point in time it is difficult to

suggest a method for edge matching as analysis of DEPM contour development requires extensive future research.

2.7.3 Expanding The Applicability Of The DEM

As previously stated most GIS employs the DEPM and DLG either of which can be obtained from the Federal Government and both having advantages and disadvantages. Many GIS also possesses the triangular irregular network (TIN) algorithm which allows for the development of sophisticated Digital Elevation Point Models. The major benefit of the TIN procedure are as follows:

- allows selection of specific stratified point data in information rich areas (with respect to elevation, areas of high relief) yielding greater surface reality with improved accuracy.
- Reduces data redundancy by not overloading points in areas of low relief.
- sampling intensity can be manipulated to match the terrain variation thus data redundancy is reduced or eliminated.
- points resulting from the specific stratified point process are surface specific and represent points along major geomorphic breaks (ridges, stream channels, etc., etc.). This feature keeps the spatial geometry intact and maximizes the contour algorithms ability to show real terrain features rather than arbitrarily generated from usual altitude matrix.
- Absolute precision limits are eliminated which allows the user to define gradient and aspect ratios (the components of slope) yielding more accurate portrayal of areas of low and high slope values.

The only disadvantage to employing the TIN is in areas of abruptly changing topography the algorithms usually generate spurious triangles.

Given the importance DEM data in scene simulations it would seem appropriate to develop a strategy by which the full potential of the TIN algorithms. The effective use of TINing is accomplished through the proper selection of Stratified Specific Points (SSP).

The criteria for SSP is to select those locations which have greater

significance to DEPM development than any other set of points. By combining a high band pass filter with the SSP procedure a level of significance can be assigned to each point in the DEPM matrix. The significance level is established by quantitatively evaluating each point value in relation to its neighbors. Once all the points have been assigned a significance a histogram can be developed showing number of points on the y axis and level of significance on the x axis. The user can then decide on the number of desired points for the TIN procedure (usually the maximum allowed by the software) and have the computer collect that number by cascading from the most significant to the least significant locations until the maximum number is reached. Once the SSP analysis is performed then a TIN could be executed and the DEM data stored in this format reducing data redundancy and total number of points necessary to create the final contoured map.

Should the need arise to produce DEM with a higher spatial net TINing can be of great utility. By properly engaging the selecting SSPs one can obtain zones where data capture would greatly enhance the DEM. For example, should a higher spatial altitude net be required for a specific analysis, engaging the proper SSP function could identify areas from which new altitude could be sampled. By using the SSP technique in this manner the collection of data is made more efficient as those areas which will maximize the use of the data in the TIN procedure are automatically identified. The number of samples to be collected in those zones would be dependent upon the sampling resolution required for the analysis. While this approach may seem tedious it does demonstrate a method by which existing DEPM can be augmented in an efficient manner should the need arise.

2.8 DEVELOPMENT OF THE HANSCOM DEM WITH TOPOLOGIC CORRECTION

The development of the DEM for the Hanscom area was accomplished through manual digitization and first order topologic corrections. Specifically the USGS topologic quadrangles of Maynard, Lexington, and Concord were digitized employing an ALTEK board digitizer with .05 inch resolution and 90C controller. The concept of the digitization process was to collect contour and bench mark locations with associate elevation data which would be interpolated into a raster grid. Point data was collected for 8325 locations along contour lines and significant elevations. This point file was then interpolated into a 512 by 512 grid system employing the UNIRAS mapping program. The method used to develop the raster was a bivariate double linear interpolation.

2.8.1 Bivariate Double Linear Interpolation (BDLI)

The purpose of the BDLI is to produce the value of a bivariate function at a point (x_0, y_0) when the function is known at the points belonging to a finite set S .

Let (a_i, b_i) for $i=1,2,3,4$, be the point which, among all points (a, b) in S such that $(a-x_0, b-y_0)$ belongs to the i 'th quadrant, is closest to the (x_0, y_0) and let c_i denote the function value at (a_i, b_i) .

Let (x_1, y_1) denote the intersection point between the line $y=y_0$ and the line connecting (a_4, b_4) and (a_1, b_1) .

A is a temporary function value z_1 given by:

$$z_1 = c_4 + (y_1 - y_0) * (c_1 - c_4) / (y_1 - y_4)$$

This temporary function is associated with (x_1, y_1) and the z_1 is obtained by linear interpolation.

Another temporary function z_2 is associated with the intersection point (x_2, y_2) between the line $x=x_0$ and the line connecting (a_1, b_1) and (a_2, b_2) , a value z_3 is associated with the intersection point (x_3, y_3) between the line $y=y_0$ and the line connecting (a_2, b_2) and (a_3, b_3) and the value of z_4 is associated with the intersection point (x_4, y_4) between the line $x=x_0$ and the line connecting (a_3, b_3) and (a_4, b_4) .

The function value z_0 at the point (x_0, y_0) is estimated as:

$$z_0 = 0.5 * (z_x + z_y)$$

where z_x and z_y are given by:

$$z_x = z_3 + (x_0 - x_3) * (z_1 - z_3) / (x_1 - x_3)$$

$$z_y = z_4 + (y_0 - y_4) * (z_2 - z_4) / (y_2 - y_4) \quad (\text{UNIRAS, 1988}).$$

This interpolation is conducted for each of the 262,144 grid points of the 512 by 512 raster.

2.9 TOPOLOGIC CORRECTION

Given the parent data source for the DEM was a USGS topographic quadrangle with its inherent accuracy issues a method to topologically correct and enhance the positional accuracy of the interpolated data was implemented.

The use of Global Positioning Systems (GPS) was employed within the map area to generate higher resolution control points (± 5 meter resolution). Specifically receivers were located at random point locations throughout the map area and spatial coordinates acquired. These data were then differentially corrected to achieve a ± 5 meter accuracy. A six point Affine transformations was employed using these high resolution control points to geometrically rectify the digitized data before interpolation and rasterization.

The Affine transformation are three distinct transforms performing translation, rotation, and scaling adjustments in Euclidean space. The translation function regenerates a new coordinate origin, the rotation function regenerates the coordinate axes system to match the new coordinate origin, and the scale function regenerates the new axes scale to meet those of the new coordinate origin. The algebraic expression of the Affine transform is:

$$\begin{aligned}x' &= S_x(\cos\theta(x-x_0) - \sin\theta(y-y_0)) \\y' &= S_y(\sin\theta(x-x_0) + \cos\theta(y-y_0))\end{aligned}$$

By applying the six point Affine transformation the original digitized point data is brought into greater topologic precision alignment with those control points located by the GPS. This topologic integrity is maintained through the interpolation and rasterization process. Two maps, a two dimension view and three dimension view, of the resulting Hanscom AFB DEM are found in the appendix.

2.10 RECOMMENDATIONS

The following recommendations are offered as a possible guideline to help improve the efficiency and expand the applicability of DEM's for EOTDA operations. The recommendations relate to data structures and type of DEM to use from an applied perspective. Recommendations on when to employ a DEM can only be made by the individual based upon the required analysis specification and the DEM accuracy levels. To this end discussion of USGS DEM accuracies and sensitivity analysis in section 2.4 should lend some insight to proper use of DEM data. Additionally, recommendations on USGS DEM analysis application are presented.

2.10.1. General Recommendations For DEM Applications

The first recommendation is to use only one form for DEM for analysis purposes. It is suggested that the Digital Elevation Point Model (altitude matrix) be used as opposed to the Digital Elevation Line Model

(DLG) for the following reasons.

- The DEPM has known stated associated accuracies which have been generally accepted in the scientific community while the DLG stated accuracies are under some question and investigation.
- The DEPM requires less storage space and lends itself to easier numerical manipulation with respect to topographic derivative products. The DLG requires more mass storage, must be reduced to some form of a DEPM before topographic derivatives can be developed, and creates a higher order generation product with respect to interpolation procedures allowing for possible introduction of processing error.
- While the DLG develops a surface that very closely resembles the quadrangle from which it was developed, for analysis purposes, the DEPM can provide the same digital information with less computational overhead.

It may be within the realm of the ARISTA procurement budget to stratify the DEM acquisition based upon use. For derivative development the DEPM is recommended for reasons previously stated. For display purposes, that is using the DEM as a backdrop on which to project thematic data, then the DLG is the model of choice. From a economic perspective the DEPM, in my professional opinion, offers more utility and applicability per unit cost.

The second recommendation would be to store the DEPM as TIN data structures as the SSP procedure reduces the DEPM to the least number of significant points necessary to develop viable topographic derivatives. The elimination of unnecessary points reduces both the amount of mass storage and seek time to locate either interpolated or fixed points within the model.

Given sufficient accuracies the following list suggests possible uses of DEM's with the EOTDA.

o Hydrology

- Flood Plain Identification and Delineation
- Storm Water Flow Analysis
- Contaminant Flow Analysis
- Waste Water Treatment Plant Setting

- Surface Flow Analysis
- Meteorology
 - Boundary Layer Contaminant Flow Analysis
 - Urban Wind Stream Analysis
- Wetlands
 - Wetland Identification and Delineation
 - Wetland Linkage Flow Analysis
 - Wetland Management Practices
- Hazardous Waste
 - Hazardous Waste Facility Setting

2.10.2 Recommendations On DEM Analytic Applicability

From an applied analytic perspective the current Federal DEM's have limited value. Given their stated accuracies approximations of distance are possible employing large scale DEM's (1:24000). However little credence can be given to area calculations or cartometric calculations utilizing DEM altitude data (slope, aspect, concavity, convexity, etc., etc.,) unless they are topologically corrected or enhanced.

2.11 DEVELOPMENT OF DIGITAL FEATURE DATA

After much review of the Digital Feature Analysis Data (DFAD) information it was determined that such data was at a resolution not suited for the current needs of the ARISTA project. There were two main concerns regarding DFAD data which are as follows:

- DFAD data is currently being reissued on CD-ROM with concomitant restructuring of the file format. The new file format does not adhere to the recently adopted Spatial Data File Transfer Standards and may not function correctly in commercially available GIS software without further extensive file rectification.
- The DFAD information is not available on a world wide basis and is comprised of varying spatial resolutions.

In order to achieve both a stable file format and requisite spatial resolution for DFD LANDSAT 5 digital imagery was employed.

2.11.1 The LANDSAT Platform

The LANDSAT program, initiated in 1972 under the name Earth Resources Technology Satellite (ERTS), was renamed LANDSAT in 1975. There are currently six platforms in the history of the program known respectively as LANDSAT 1 through LANDSAT 6 (LANDSAT 1 through 3 are now inactive, 4 is partially active, 5 is totally functional, and 6 is waiting for launch). Administratively, the LANDSAT system was originally operated by the National Aeronautic and Space Administration (NASA) was turned over to the National Oceanic and Atmospheric Administration (NOAA) and is now a quasi public-private enterprise under the ownership of the Earth Observation Satellite Company (EOSAT). The LANDSAT series is a passive remote sensing system employing a Multi Spectral Scanner (MSS) and the Thematic Mapper (TM) which are an electrical sensor suite that monitor reflected radiation in the seven spectral bands. Throughout past twenty years extensive research has been conducted on data processing techniques relative to the extraction of vegetation and land use information from the LANDSAT digital image.

2.11.2 Digital Image Processing To Acquire Digital Feature Data

The primary concept behind using the LANDSAT data is that every Earth target has a unique spectral signature which if known can be identified by computer analysis. The data collected by the TM on the LANDSAT 5 platform numerically encodes the intensity of reflected light in seven spectral bands from the Earth's surface in a raster sweep with each square or picture element (pixel) having dimension of thirty by thirty meters. Thus every pixel of a LANDSAT scene has a seven digit sequence of numbers representing the spectral signature of the Earth target.

The principle of digital image processing is to link the spectral signatures to their respective earth targets so that the computer can be programmed to identify the target. This process of linking the spectral signatures to the earth target is known as training the classifier and requires extensive "ground verification" or "ground truthing". Once an area has been ground verified the satellite scene can be processed yielding a map based on the spectral signatures in a relatively short period of time.

For the purpose of this study a TM scene acquired from the LANDSAT 5 platform was purchased from EOSAT centered on the Civil Airport Runway adjacent to the AFB with coordinates of W071D 17M 25S LON; N042D 28M 06S LAT. LANDSAT 5 has an orbital altitude of 705 Km with a circular sun-

synchronous orbit. Repeat orbital coverage occurs on a 16 day cycle at the same local time. The sensor array from the TM payload yield 7 bands with the following characteristics (from Jensen, 1986).

Band 1: 0.45-0.52 um (blue) Allows penetration of water bodies and wetted perimeters of lakes and coastlines.

Band 2: 0.52-0.60 um (green) Sensitive to the reflectance of healthy vegetation.

Band 3: 0.63-0.60 um (red) Provides the best vegetation discrimination capability and has significant use for soil and geologic boundary delineations.

Band 4: 0.76-0.90 um (reflective infrared) Sensitive to vegetative biomass and is useful for crop identification and soil-crop and land-water contrasts.

Band 5: 1.55-1.75 um (mid-infrared) Can be used to discriminate between clouds, snow, and ice and is useful for determining crop drought and turgidity.

Band 6: 2.08-2.35 um (mid-infrared) Discriminates geologic rock formations.

Band 7: 10.4-12.5 um (thermal-infrared) Measures amount of infrared radiant flux from surfaces. Useful for mapping geothermal activity, soil moisture, and vegetation stress analysis.

The scene dimensions were fifteen by fifteen kilometers with thirty meter pixel accuracy. This scene configuration represents approximately 11,111,111 pixels of data each comprised of a seven digit spectral signature. The information to be obtained from this LANDSAT scene was vegetation and land use information. Secondary ground verification was achieved through the Commonwealth Of Massachusetts MAPDOWN series which classifies vegetation/landuse types on USGS topographic maps. Using a standard matrix discrimination over 150 sites were established to match spectral signature with MAPDOWN information. Further, 52 of these sites were visited with position verified employing Global Positions Systems (GPS) with an accuracy of +/- 15 meters.

Actually processing of the digital image was engaged using the ground verification data and employing a maximum likelihood classification method. The maximum likelihood classification procedure is based upon a multidimensional probability function to determine which pixel belongs to which ground verification class. The statistical derivation of maximum likelihood classification is as follows:

- Assuming there are n number of classes let $p(x|w_i)$ represent the probability density function of vector X (X is derived from a pattern in class i).
- $p(w_i)$ prior probability of class i or the probability of observing a pattern from class i .

The decision rule of the maximum likelihood is $X = w_i$

if

$$p(x|w_i)p(w_i) > p(x|w_j)p(w_j) \\ \text{for all } j = 1, 2, \dots, n.$$

Thus a computer employing the maximum likelihood decision rule computes the product $p(X|w_i)p(w_i)$ for each class and assigns the classification value to the class having the greatest product (Swain, 1987).

After processing the TM Hanscom image thirty eight distinct classes were derived with a 92 percent confidence limit and resulted in a remarkably resolute image. However, due to ASTER model requirements these classifications were aggregated to twelve classes and then re-aggregated to match model requirement for TV, Laser, and IR sensors (see appendix for classification table and digital image).

2.12 RECOMMENDATIONS - DIGITAL IMAGE PROCESSING

Given the high confidence rating of the maximum likelihood classification and the requirements for highly aggregated classifications it is recommended that a cluster unsupervised classification procedure be exploited. An unsupervised approach will speed processing time without significant degradation of results. The unsupervised classification operates on the development of natural clusters of the spectral properties of pixels. The computer is allowed to collect the class means and covariance and the analyst assigns, after the fact, identifiers to the

spectral clusters. In many cases some of the natural clusters which are developed have little meaning as they represent agglomerations of various earth targets (Jensen, 1986). However, engaging an unsupervised classification of the same TM data set used in the previous section still provided more classifications than necessary for the ARISTA program. The reason for such high definition information from the unsupervised classification is that program requirements only need primary land use classifications which, given the urban nature of the Hanscom area, are easily derived from cluster technology. However, it should be noted, the success of the unsupervised classification depends on the ability of the analyst to assign correct identification to the clusters. This means the analyst must be familiar with the study area or have extensive ground verification data to complete the analysis. Also if the area under investigation does not possess a naturally high spectral stratification (ie. an area comprises of various forms of woodlands) then an unsupervised classification would be impossible to implement and necessitate a supervised approach.

3 INTEGRATION OF SPATIAL DATA INTO ARISTA PROGRAM ARCHITECTURE

Given the development of the DEM using GPS adjusted digitizing and Digital Feature Data from LANDSAT TM imagery the final step was to integrate the data into a GIS spatial database.

3.1 Logical Data Structure

The logical data structure of the geographic information database was originally developed under an RDL summer RIP grant (see appendix). Further rectification of the initial logical data flow was achieved using the SSC DGL relational database capabilities. The logical data structure is based upon an object oriented relational data architecture. The primary assumption for the data structure is that GIS analyses require multiple input maps features. As such, each map feature may exist in one moment of space and time and is given the name of feature instance. A feature instance is equivalent to the subject or the main thesis of the map and can be spatially subdivided into facets. Each facet, in turn, can be subdivided in various spatial strata. The various spatial strata are comprised of a number of spatial objects. Given the requirements of ARISTA, it is recommended that three spatial object be employed for each spatial strata; source, model, and accuracy. Each of the spatial objects have related informational attributes and associated sub attributes. Non spatial information about each spatial strata is contained in an item table. Each item is comprised of feature objects which can encompass any number of attributes and sub attributes. The many to many join between the

strata is essential as it enables the user to obtain spatial information about non spatial items or inversely, non-spatial information about spatial strata.

3.2 PHYSICAL SPATIAL DATA BASE IMPLEMENTATION

The physical implementation of the spatial database and associated GIS functions were accomplished using the SYBASE relational database system. Mr. Tim Hyatt of Phillips Laboratory - U.S. Geophysics Directorate has programmed the SYBASE on a UNIX platform (NEXT station) and initiated implementation of the logical data structure. The SYBASE system now acts as a functional GIS as relational queries using structured query language (SQL) can be implemented using spatial coordinates as the "key words". For example one can now ask by latitude and longitude for DEM and DFD information. The SYBASE quickly allows the end user to find geographic information about a particular point in space. Further SYBASE graphic routines allow the for the maps to be shown on a split screen of the geographic area under query thus allowing for both textual and graphic answers to the spatial query.

4 SUMMARY

The use of digital geographic data in the form of DEM's and DFD's provide necessary information to the ARISTA program. The preceding text has investigated two methods of providing geographic information and has detailed the requisite need for determining the scale of resolution required of the spatial data. As was shown in section 2, DEM can at one scale be used simply for orientation purposes but at a higher scale of resolution can be used to derive critical derivative data. Obviously, one must use care in selecting or developing a DEM with adequate resolution to meet mission standards. With respect to DFDs it is apparent that many mission requirements will allow for unsupervised classification of relatively high resolution digital imagery to achieve necessary information needs. However, the success of the unsupervised classification procedure is highly dependent on the analysts knowledge of the target area and the spectral diversity of the target itself. If the area under investigation possesses a low spectral diversity and/or the analyst does not have a priori knowledge of the area then a more time consuming supervised classification may be warranted. From an operational perspective one must be concerned with the availability and utility of the both DEM and DFD data. If digital geographic information is to play an operational role in tactical scene simulation then clearly more emphasis is need on global acquisition of that data at a resolution which enable viable spatial analysis. Inherently the use of digital geographic data requires the development and management of large spatial databases through

geographic information systems. Information from these databases is normally queried and cross referenced by spatial coordinate. A functional GIS can be implemented employing common relational database technologies. However, the operational use of GIS through relational technologies will require extreme amounts of mass data storage with elaborate partitioning schemes to maintain data integrity and access speed.

5 FUTURE RESEARCH

As with most research endeavors this project has raised as many questions as it has answered. DEM future research should investigate the use of triangular irregular networks (TIN's) as a method of reducing mass storage requirements and improving model resolution. Also, research on the use of GPS to provide geodetic information for spatial transforms as a method to enhance both the vertical and horizontal position accuracy should be encouraged. DFD future research should include field verification of the necessary spatial and thematic resolution requisite for tactical models. Data from such an analysis may allow for coarser DFD data to be employed in the modeling domain. Lastly, much research is needed on the physical requirements to establish a GIS on a relational database platform in a operational mode. This research is imperative as the volume of digital geographic data requisite for modeling demands will be overwhelming if not properly managed and maintained in an operational GIS.

BIBLIOGRAPHY & REFERENCES

- Brabb, E.E., 1987, Analyzing and portraying geologic and cartographic information for land use planning, emergency response, and decision making in San Mateo County, California. Proceedings GIS '87, San Francisco, 1987, pp. 362-374.
- Burrough, P.A., 1986, Principles of Geographical Information Systems for Land Resource Assessment. (Oxford: Clarendon Press).
- Carter, J.R., 1988, Digital Representations Of Topographic Surfaces: An Overview. Proceedings ACSM-ASPRS Annual Convention - Technical Papers, St. Louis, pp. 54-60.
- Chen, Z.T., 1984. Quad-tree spatial spectrum: its generation and application, Proceedings of the International Symposium on Spatial Data Handling, Zurich, August 1984, pp. 218-237.
- Chen, Z.T. and Guevara, J.A., 1987, Systematic selection of very important points (VIP) from digital terrain models for constructing triangular irregular networks. Proceedings AUTO-CARTO 8, Baltimore, March 1988, pp. 50-56.
- Clark, K.C. 1990. Analytical And Computer Cartography. (New Jersey: Prentice-Hall).
- Elassal, A.A. and Caruso, V.M., 1985, Digital Elevation Models. Geological Survey Circular 895-B. USGS Digital Cartographic Data Standards.
- ESRI, 1987, TIN User's Manual. (Redlands, CA: ESRI)
- Evans, I. S., 1972, General geomorphometry, derivatives of altitude, and descriptive statistics. In Spatial Analysis in Geomorphology, Chorley, R.J., (ed.)
- Jensen, J.R., 1986. Digital Image Processing. (New Jersey: Prentice-Hall).
- MacEacheren, A., and Davidson, J.V., 1987, Sampling and isometric mapping of continuous geographic surfaces. The American Cartographer 14 (4), 299-320.
- National Cartographic Information Center (NCIC), no date, Map Accuracy Statement on USGS Survey Maps. (Reston, VA: NCIC)
- Peucker, T.K., Fowler, R.J., Little, J.J., and Mark, D.M., 1978, The Triangulated Irregular Network. Proceedings of the DTM Symposium, St. Louis, May 9-11, pp. 516-540.
- Pike, R.J., Thelin, G.P., and Acevedo, W., 1987, A topographic base for GIS from automated TINs and image-processed DEMs. Proceedings GIS '87, San Francisco.
- Rinehart, Robert E. and Coleman, E. J., 1988, Digital Elevation Models produce from digital line graphs. Technical Papers 1988 ACSM-ASPRS Annual Convention, St. Louis, pp. 291-299.
- Swain, P.H. 1978. Remote Sensing The Quantitative Approach. (New York: McGraw-Hill)
- Uniras, 1988. AGL/INTERPOLATION Manual. (Soborg: UNIRAS)
- USGS, 1987, US GeoData Digital Elevation Models Data User Guide (Reston, VA: USGS)

Weibel, R. and DeLotto, J.S., 1988, Automated terrain classification for GIS modeling, Proceedings GIS/LIS '88, San Antonio, pp. 618-627.

APPENDICES

The RMSE is given by:

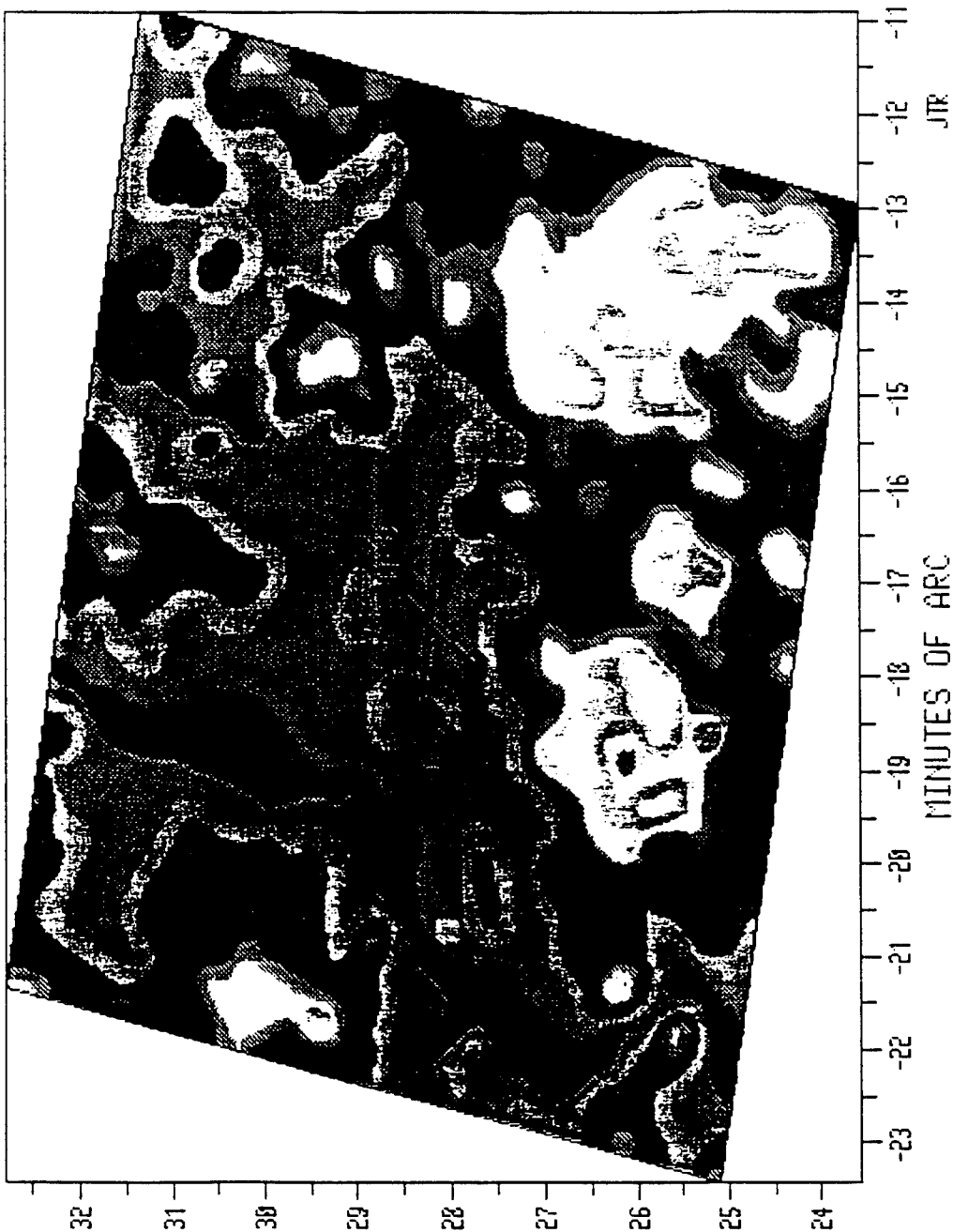
where:

n = number of test points
 I_i = interpolated DEM elevation of test point i
 T_i = true (most probable) elevation of test point i

Source: Rinehart and Coleman, 1988.

HANSCOM STUDY AREA 2D CONTOUR MAP

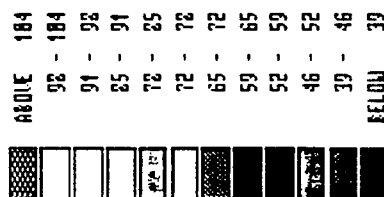
42 32 46 N
71 10 51 W



N ↑

ELEVATION

Ft



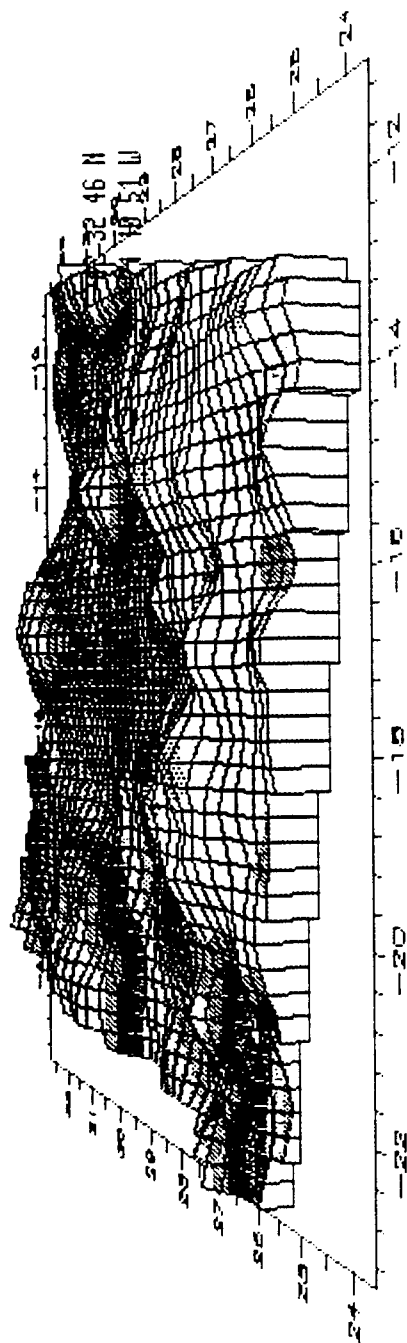
42 23 33 N
71 23 25 W

3D CONTOUR MAP

N
★

ELEVATION

Pt.



ABOVE 88	88 - 83	83 - 77	77 - 72	72 - 66	66 - 61	61 - 55	55 - 50	50 - 44	44 - 39	39 - 33	BELOW 33
----------	---------	---------	---------	---------	---------	---------	---------	---------	---------	---------	----------

42 23 33 N
71 23 25 W

TM HANSCOM AFB CLASSIFICATION

Thematic Class	TV and Laser Digital Class	IR Digital Class
1 Hardwoods/Deciduous	1 through 11	5
2 Softwoods/Conifers	12 through 18	7
3 Mixed Woods	None Listed	18
4 Tall Grass-Live	23	2
5 Mowed Grass-Live	25	3
6 Sand	56	28
7 Soils	62 through 84	20
8 Concrete	116 through 122	24 through 25
9 Asphalt	123	23 through 26
10 Water	159	29
11 Residential	None Listed	None
12 Industry/Urban	None Listed	None



LANDSAT 5 TM Scene HANSCOM AFB and Surrounding Area

GIS LOGICAL DATA STRUCTURE

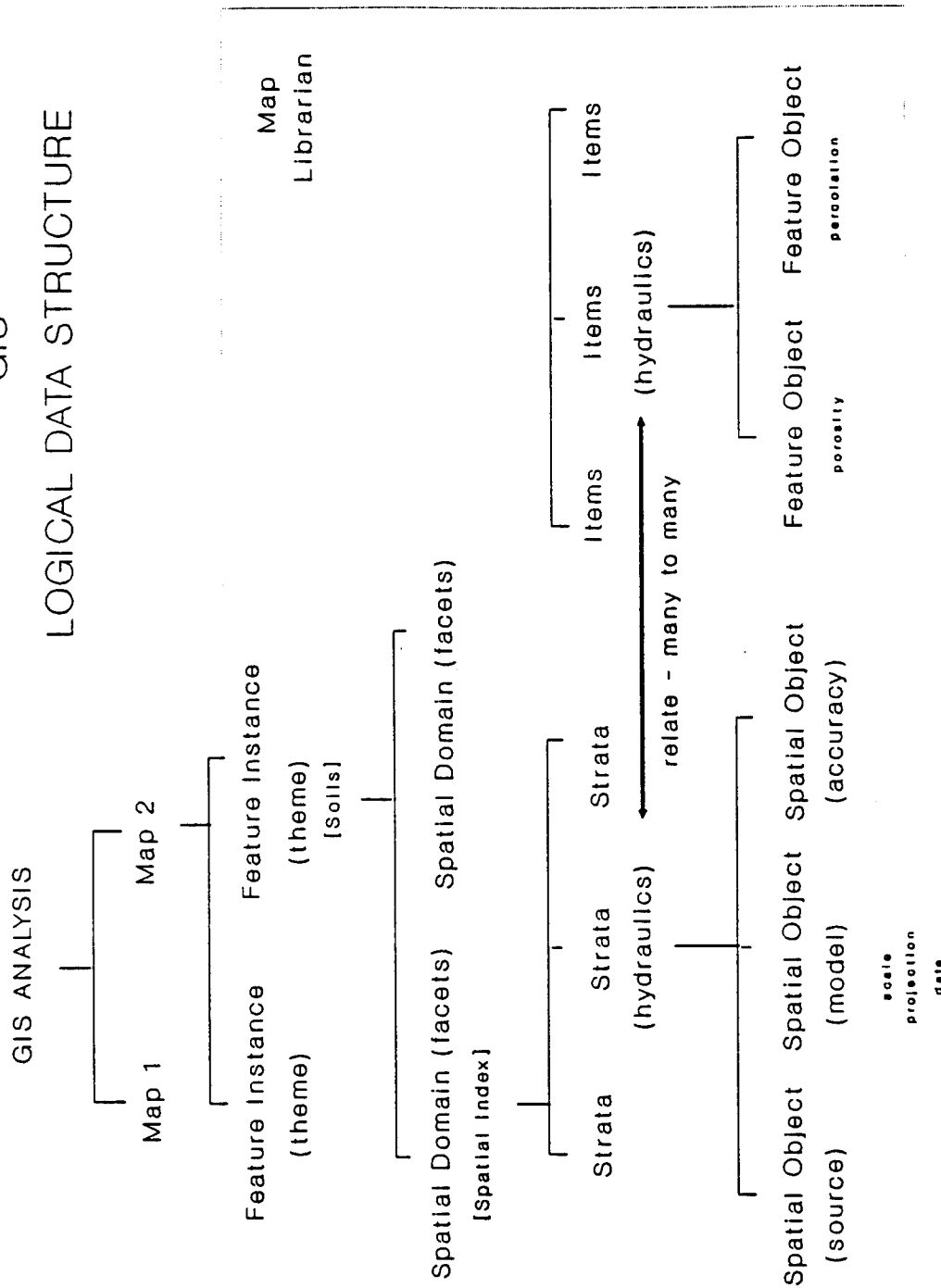


Figure 1

MODELING OF LIQUID JET ATOMIZATION PROCESSES

Dr. Stephen D. Heister
Assistant Professor
School of Aeronautics and Astronautics

Purdue University
1282 Grissom Hall
West Lafayette, IN 47907-1282

Final Report for:
Research Initiation Program (Grant 92-05)
Phillips Laboratory

Sponsored by:
Air Force Office of Scientific Research
Bolling Air Force Base, Washington, D.C.

and

Purdue University

December 1992

Modeling of Liquid Jet Atomization Processes

Dr. Stephen D. Heister
Assistant Professor
School of Aeronautics and Astronautics
Purdue University

Abstract

This report summarizes the developments leading to a model capable of describing the time-dependent evolution of a liquid jet injected into a chamber containing a stagnant gas. The numerical technique employed centers on the use of Boundary Element Methods (BEMs) as a means to determine the velocities of nodes on the surface of the jet. To properly validate all elements of the model, a two-dimensional (rather than axisymmetric) formulation was first developed. This formulation has permitted a validation of the treatment of the free surface. In addition, the main "solver" in the axisymmetric formulation has been developed. In the near future, this solver will be integrated with the existing free surface tracking routine to complete the axisymmetric jet model.

Modeling of Liquid Jet Atomization Processes

Dr. Stephen D. Heister

Introduction/Background

During the summer of 1991, the author participated in the AFOSR Summer Faculty Program at Phillips Laboratory, Edwards AFB, California. As a result of interactions with lab personnel during this program, a proposal for new analytic methods of modeling jet atomization processes was developed. This proposal, entitled: "Modeling of Liquid Jet Atomization Processes" was subsequently funded through an AFOSR Minigrant 92-05. The resulting efforts on this grant are summarized in this report.

Since the beginning of the Minigrant, funding has also been obtained through an AFOSR single-investigator grant entitled: "Modeling of Liquid Jet Atomization Processes". In this contract (AFOSR Award No. F49620-92-J-0390), a more advanced model will be created to investigate the effects of viscosity on this complex process. In addition, the author recently completed instruction in a graduate course entitled: *Stability of Free Surfaces, AAE 690P*, in which nine graduate students were trained in the analytic methods required for modeling of this type.

As a consequence of these developments, a multistep approach has been formulated in order to create computer codes capable of predicting free surface behavior for both inviscid and viscous jets. The heart of these models centers on the use of Boundary Element Methods (BEMs), which have been proven¹⁻⁴ to be attractive for problems of this nature. To insure the validity of the codes, it was necessary to formulate the problem for a 2-D situation, then extend models to the axisymmetric case. For this reason, the following approach has been employed:

1. Create a 2-D BEM Solver for Laplace's Equation
2. Validate 2-D Solver using Known Analytic Solutions
3. Create Free Surface Module
4. Integrate Free Surface Module with 2-D BEM and Validate using Nonlinear Standing Wave Solution⁵
5. Create Axisymmetric BEM Solver for Laplace's Equation
6. Validate Axisymmetric Solver for Flow over Sphere
7. Integrate Free Surface Module with Axisymmetric BEM and Validate using Oscillating Droplet Solution⁶
8. Apply Validated Inviscid Model to Liquid Jet
9. Include Viscous Effects in Axisymmetric BEM Solver
10. Validate Viscous Model using Oscillating Viscous Droplet Solution⁷
11. Apply Validated Viscous Model to Liquid Jet

To date, we have completed the first six tasks in the above list and we expect to complete the inviscid liquid jet model early in 1993. In the remainder of this report, we will describe results in accomplishing tasks 1-5 and will discuss prospects for future developments.

Two-Dimensional BEM Development

As discussed in the previous section, we felt it was prudent to begin our research with a 2-D formulation rather than the axisymmetric formulation required for the liquid jet. The rationale for this approach include the fact that the 2-D formulation has been much better documented in previous research and it more readily permits direct comparison with analytic results. Since the free surface module can be applied to any formulation, we felt it was wise to validate this portion of the code for a 2-D result prior to applying it toward the liquid jet model. Proper code validation is critical for problems of this type since we are investigating a flowfield which is unstable, i.e. instabilities generated by the numerical model cannot be tolerated.

The inviscid flow of an incompressible fluid can be expressed in terms of a velocity potential, ϕ , which is defined:

$$\nabla \cdot \phi = \vec{v} \quad (1)$$

where ∇ is a gradient operator and \vec{v} is the local velocity vector. Under this assumption, the equation governing the behavior of the velocity potential is Laplace's equation:

$$\nabla^2 \phi = 0 \quad (2)$$

which holds for either steady or unsteady flows.

Following Liggett and Liu⁴, the BEM formulation of Eq. 2 becomes:

$$\alpha \phi(\vec{r}_i) + \int_{\Gamma} [\phi \frac{\partial G}{\partial n} - q G] d\Gamma = 0 \quad (3)$$

where $\phi(\vec{r}_i)$ is the value of the potential at a point \vec{r}_i , Γ denotes the boundary of the domain, and G is the Green's function corresponding to the governing equation. Since Eq. 3 involves an integration only around the boundary, we need not discretize the entire domain. It is presumed that either ϕ or $q = \partial\phi/\partial n$ is specified at each "node" on the boundary. Here n is the direction normal to the boundary so that q represents the velocity normal to the boundary.

Finally, the quantity α in Eq. 3 results from singularities introduced as the integration passes over the boundary point, \vec{r}_i . For the 2-D formulation, α represents the angle between successive nodes on the boundary. For example, for nodes lying on the same line, $\alpha = \pi$; for a node placed at a corner of a box, $\alpha = \pi/2$, etc.

The geometry for the integration process is shown in Fig. 1. For the 2-D Laplacian, the applicable Green's function is given by:

$$G = \ln|\vec{r} - \vec{r}_i| \quad (4)$$

Physically, the Green's function represents the contribution of a source (at location \vec{r}) of strength 2π as sensed at the "base point", \vec{r}_i . In addition, the quantity $\partial G/\partial n$ represents the contribution of a doublet at location \vec{r} as sensed at the base point. By properly weighting all these source and doublet strengths, we can solve Laplace's equation for an arbitrary 2-D domain as shown in Fig. 1.

By substituting for the Green's function in Eq. 3, we could presumably perform the desired integration provided that we assume a behavior for ϕ and q over the length of an element. Following Liggett and Liu⁴, we shall assume that both ϕ and q vary linearly over the length of the element. For example, we could write the value of the potential lying on an element bounded by nodes j and $j+1$ as:

$$\phi = \phi_j \frac{\Gamma_{j+1} - \Gamma}{\Gamma_{j+1} - \Gamma_j} + \phi_{j+1} \frac{\Gamma - \Gamma_j}{\Gamma_{j+1} - \Gamma_j} \quad (5)$$

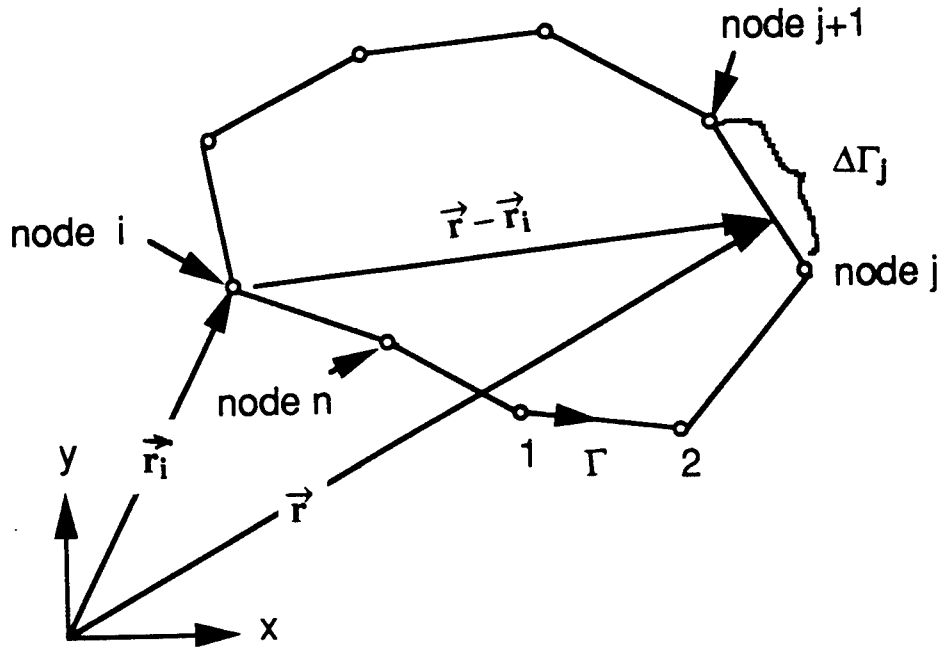


Figure 1: Geometry and Nomenclature for 2-D BEM

with a similar expression for q . Since the nodal values are assumed to be constant, the integration in Eq. 3 can now be performed using results of Eqs. 4 and 5. Note that the integrations are simply a function of the specific geometry of the nodal locations on the boundary. The resulting solutions of the various integrals appearing in Eq. 3 will not be presented here in the interest of brevity. Interested readers should see Liggett and Liu⁴ for a summary of the fairly lengthy results.

Assuming that we have obtained values for all the integrals around the domain, the following matrix structure is formed:

$$[\phi]([D] + [I][\alpha]) = -[S][q] \quad (6)$$

where $[D]$ and $[S]$ are $n \times n$ matrices containing results of doublet and source term integrations respectively, and $[I]$ is the identity matrix. The quantity $[\alpha]$ is a column vector of the angle intercepted by each of the nodes and the vectors $[\phi]$ and $[q]$ contain given boundary information and unknowns for the problem. At any node, either ϕ or q must be specified for a well posed problem.

Regardless of which quantity is given, the matrices can be pivoted into the standard linear algebra form $[A][X] = [B]$ where $[A]$ and $[B]$ matrices contain known values and $[X]$ would contain all unknown q and ϕ values. This set of equations is solved using a standard Gaussian elimination package with partial pivoting⁸.

Validation of 2-D BEM

To validate this portion of the model, a problem with a known analytic solution was treated. One can show that the function:

$$\phi = x^4 - 6x^2y^2 + y^4 \quad (7)$$

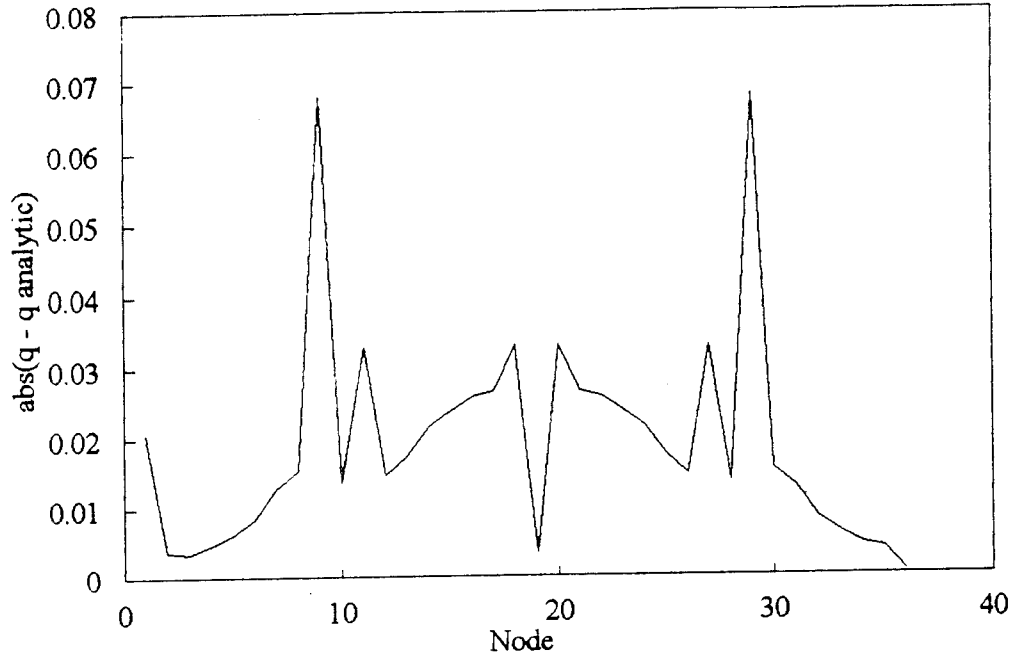


Figure 2: Comparison of Analytic and BEM Velocities Around the Periphery of a Unit Square

satisfies Laplace's equation. We specified a Dirichlet problem (with values of ϕ given at all boundary points) on a unit square for the validation. In this case, the code will return velocities normal to the surface (q) at all nodes. Special treatment is required at the corners since the unit normal vector is multivalued at these points. Since the sides of our unit square are aligned in either the x or y directions, we can compare q values from the code with $\partial\phi/\partial x$ or $\partial\phi/\partial y$ from the analytic result given above.

Figure 2 highlights the error in surface normal velocity in comparing analytic and numerical results for a case with 36 nodes evenly spaced around the periphery of the box. Errors in Fig. 2 amount to less than 1% of the maximum velocity present in the domain. Peaks in the error occur at the corners of the box where the variable α changes from π to $\pi/2$. This type of behavior is inherent to BEMs (as well as other numerical approaches).

Grid function convergence tests were also performed by determining the amount of error reduction resulting from successive refinements of the mesh. Results of these tests confirmed second order accuracy for all nodes except those lying at the corners. Corner nodes converged to the exact solution at a slightly lower rate of 1.4. (Note that second order accuracy implies that doubling the number of nodes will reduce errors by a factor of four).

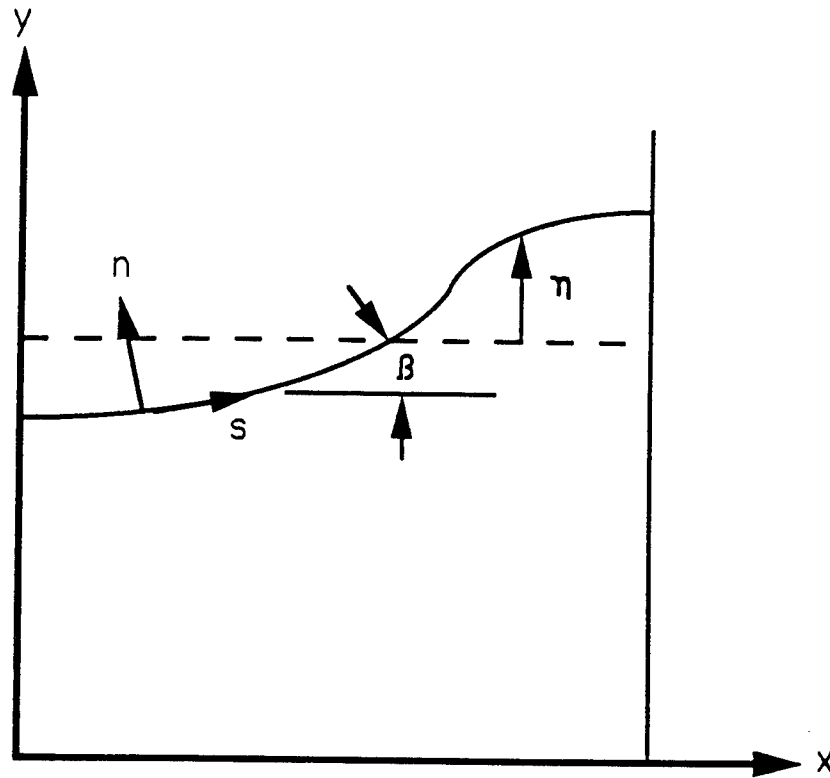


Figure 3: Variables Defining Location and Motion of a Free Surface

Free Surface Module

Having validated the "Laplace Solver" using the BEM methodology, we employ the method first developed by Longuet-Higgins and Cokelet⁹ to effectively track the free surface. To formulate this method, consider a free surface whose deflection from an equilibrium state is measured by a distance η as depicted in Fig. 3. The kinematic condition governing the motion of the surface states that points which are originally on the surface will remain there for all time.

If we permit surface nodes to move with the local surface velocity at any instant, this condition implies:

$$\frac{D\eta}{dt} = \frac{\partial\phi}{\partial y} \quad (8)$$

$$\frac{Dx}{dt} = \frac{\partial\phi}{\partial x} \quad (9)$$

where the notation $D()/dt$ implies a material or Lagrangian derivative.

Recognizing that our BEM solver will return velocities normal to the surface, we employ the velocity transformations:

$$\frac{\partial\phi}{\partial y} = q\cos(\beta) + \frac{\partial\phi}{\partial s}\sin(\beta) \quad (10)$$

$$\frac{\partial\phi}{\partial x} = -q\sin(\beta) + \frac{\partial\phi}{\partial s}\cos(\beta) \quad (11)$$

where β is the local wave slope and $\partial\phi/\partial s$ is the velocity tangential to the local surface as noted in Fig. 3. For given surface shape with known ϕ values, these functions were determined using a cubic spline curvefit of the surface. More specifically, existing spline curvefit subroutines were used from the IMSL¹⁰ library.

Equations 8-11 could be solved provided that the value of the potential is known along the surface. We obtain a means of updating ϕ by considering the unsteady Bernoulli relation. This relation states that pressure changes across the surface must be consistent with surface tension forces, static head, dynamic pressures and any external forces applied to the system. For our problem, the dimensionless representation of this equation is:

$$\frac{\partial\phi}{\partial t} = -\eta - \frac{1}{2}(\nabla\phi)^2 - \frac{\kappa}{We} \quad (12)$$

where κ represents the local surface curvature:

$$\kappa = -\frac{\frac{\partial^2\eta}{\partial x^2}}{(1 + (\partial\eta/\partial x)^2)^{3/2}} \quad (13)$$

and We is a type of Weber number:

$$We = \frac{\rho L^2 g}{\sigma} \quad (14)$$

Here ρ is fluid density, L is a characteristic distance, g is the acceleration due to gravity and σ is the fluid surface tension.

Now, Eq. 12 gives changes in ϕ with time at a fixed x, y location. If we wish to find out how ϕ changes with time for points traveling along the wave, we must transform the time derivative from Eulerian to Lagrangian representation:

$$\frac{D()}{dt} = \frac{\partial()}{\partial t} + \vec{v}_s \cdot \nabla() \quad (15)$$

where $\vec{v}_s = \nabla\phi$ is the surface velocity. Using this result, the change in ϕ for points on the surface can be described:

$$\frac{D\phi}{dt} = -\eta + \frac{1}{2}(\nabla\phi)^2 - \frac{\kappa}{We} \quad (16)$$

Equations 8,9, and 16 provide a means to update surface location and boundary values of the potential with time. Numerous authors have pointed out the strong nonlinearity in these equations since new surface values of the potential depend on new surface shape, but surface shape in turn depends on ϕ . It is this nonlinearity which poses a major challenge to those interested in free surface flows.

In order to integrate Eqs. 8,9, and 16, we employ the Adams- Bashforth-Moulton⁸ (ABM) predictor/corrector method. Consider the equation:

$$\frac{\partial z}{\partial t} = f(x, y, t) \quad (17)$$

Applying the ABM time integration to this equation gives:

$$z_p = z_0 + \frac{\Delta t}{24}(55f_0 - 59f_{-1} + 37f_{-2} - 9f_{-3}) \quad (18)$$

$$z_c = z_0 + \frac{\Delta t}{24}(9f_p + 19f_0 - 5f_{-1} + f_{-2}) \quad (19)$$

where Δt is the time step, z_p and z_c represent predicted and corrected values at the new time level, and z_0 represents the value at the previous time level. The notation f_{-2} indicates the value of the function from

two time steps previous to the present calculation, while the value f_p is the predicted function using z_p and other predicted information.

The ABM scheme is formally fourth-order accurate which implies that errors are proportional to $(\Delta t)^4$. Since the scheme requires four time levels of information, we must use a different method in starting the code. We selected Huen's method⁸, which can be written:

$$z_p = z_0 + \Delta t f_0 \quad (20)$$

$$z_c = z_0 + \frac{\Delta t}{2}(f_0 + f_p) \quad (21)$$

While this scheme is only second-order accurate, it performs quite adequately as a means of starting the calculations. In our problems, it is not terribly crucial to have high accuracy at the very start of the calculation since surface velocities are typically quite small at this time.

2-D Model Integration and Validation

The free surface module discussed in the previous section was integrated with the 2-D BEM Laplace solver to create a model capable of describing the time-dependent evolution of a free surface. The overall procedure followed in the code is described below:

1. Read program inputs and generate initial grid
2. Initialize free surface conditions
3. Begin time stepping ($t = t + \Delta t$)
4. Predict new ϕ , x , and η values on surface using Huen's method or ABM predictor steps
5. Call BEM solver to get surface velocities for predicted shape
6. Correct ϕ , x , and η values on surface using Huen's method or ABM corrector steps
7. Call BEM solver for corrected surface shape
8. Store all necessary information and return to Step 3

To validate the performance of the code, a test case was developed to reproduce a solution for a nonlinear standing wave in a 2-D channel. A series expansion solution of this flow was obtained initially by Penny and Price⁵. The wave is assumed to be confined to a box of length and height π as illustrated in Fig. 4. The solution on this domain is actually for a half-wave, i.e. results are symmetric about the y axis in Fig. 4.

The walls of the channel and the free surface were discretized into a series of elements. The initial surface shape was obtained from the solution of Penny and Price. A typical initial grid assuming 15 nodes on each side of the domain is shown in Fig. 4. On the three sides of the domain with solid walls, the condition $q = \partial\phi/\partial n = 0$ was employed, while on the free surface, the conditions in Eqs. 8, 9, and 16 were utilized. Surface tension forces were neglected in this problem; this assumption amounts to setting $We = \infty$ in Eq. 16.

Results from the calculation are depicted in Figs. 5-8. Figure 5 provides a comparison of the code with the analytic results for the motion of free surface points at the left and right ends of the channel. Datapoints in this figure correspond to the analytic series solution of Penny and Price⁵. A time step of 0.0125 was

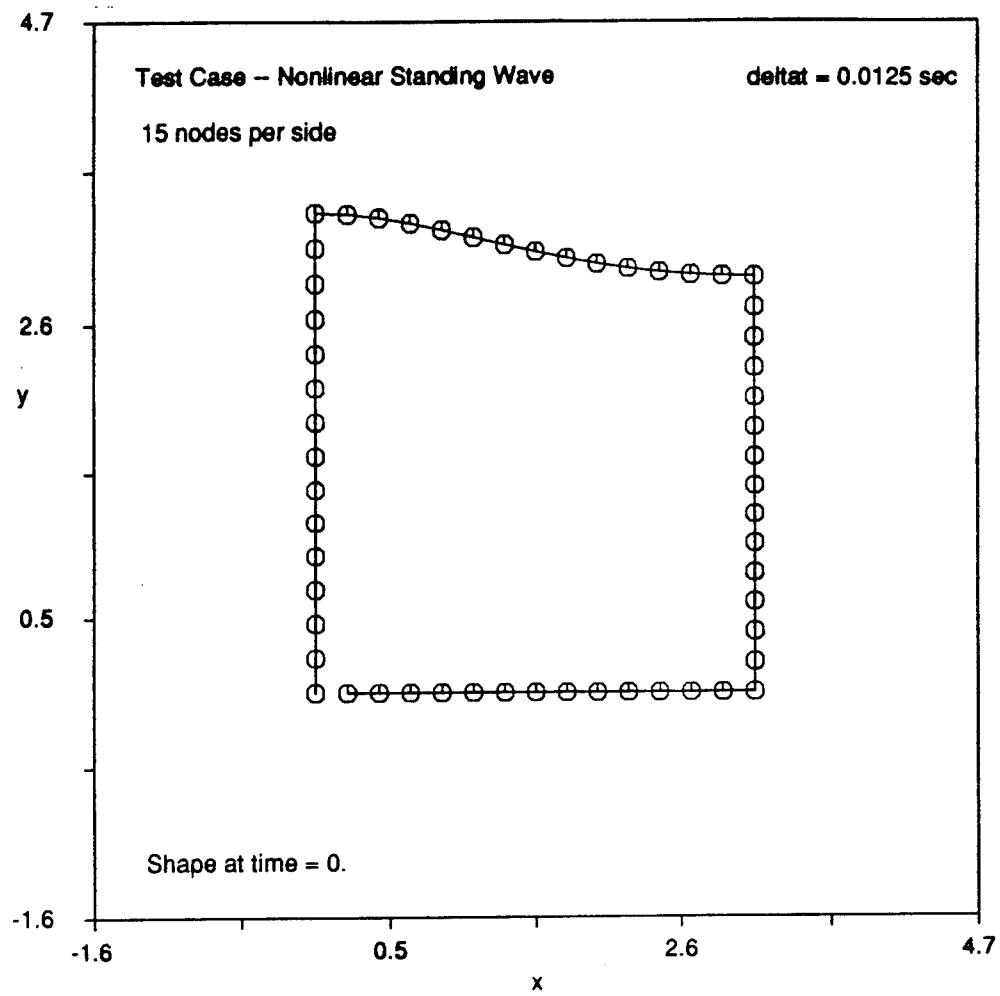


Figure 4: Initial Grid For Standing Wave Problem

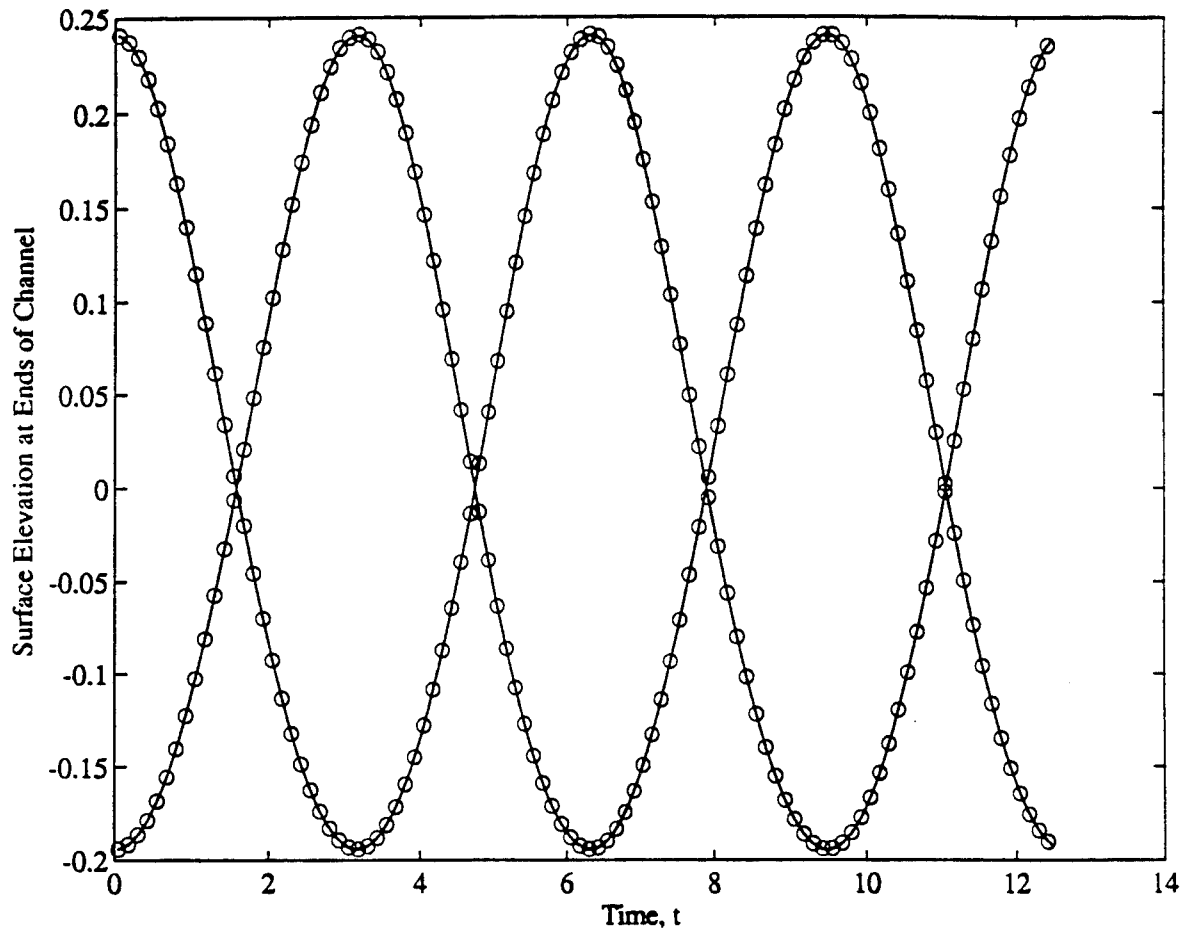


Figure 5: Comparison of Surface Motion with Analytic Solution

utilized in this calculation. As is evidenced in the figure, excellent agreement is obtained over the entire time domain.

Figure 6 depicts the evolution of the entire surface with time on a 3-D plot. The periodic nature of the solution is evident here as various points oscillate about an equilibrium position. Figures 7 and 8 demonstrate that the code is conserving mass to a very high accuracy. In Fig. 7, the net massflow across the surface, defined as:

$$Net\ Massflow = \int q \cdot ds \quad (22)$$

is shown to be very small for the entire time domain. This result confirms the accuracy of the BEM calculation since the net massflow across the surface must be zero for a valid solution to Laplace's equation.

In Fig. 8, the error in mean surface height is plotted as a function of time. Since we have no sources or sinks in this problem, the mean surface height:

$$\bar{y} = \frac{1}{\pi} \int_0^{\pi} y dx \quad (23)$$

should be equal to π at all times to compensate for the fact that the mass of fluid in the channel is constant. Figure 8 demonstrates that the model predicts the correct mean surface height to within 0.006%. For this reason, we are confident that numerical errors introducing spurious massflows are very small.

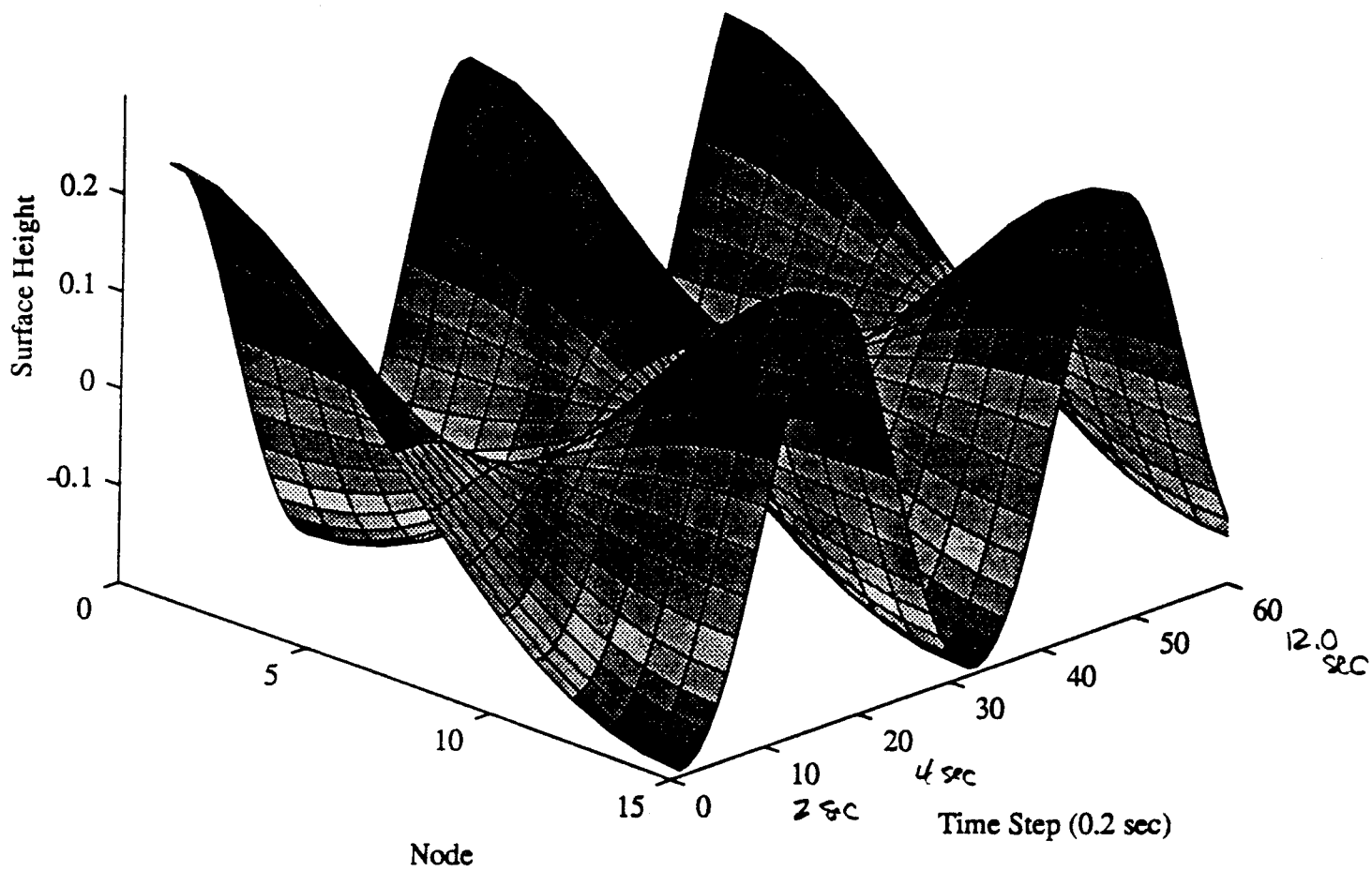


Figure 6: Time Evolution of Nonlinear Standing Wave

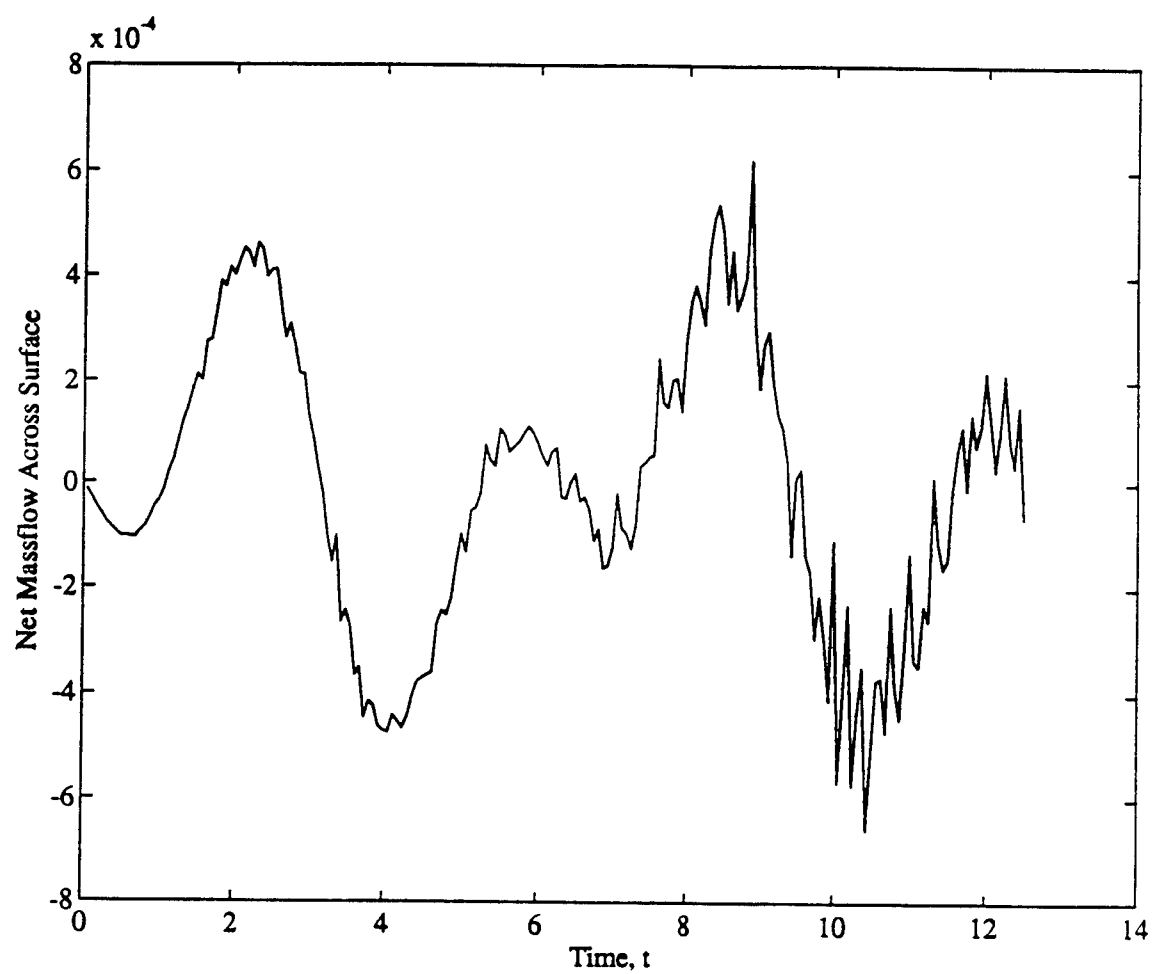


Figure 7: Calculations Confirm Essentially Zero Net Massflow Across the Free Surface

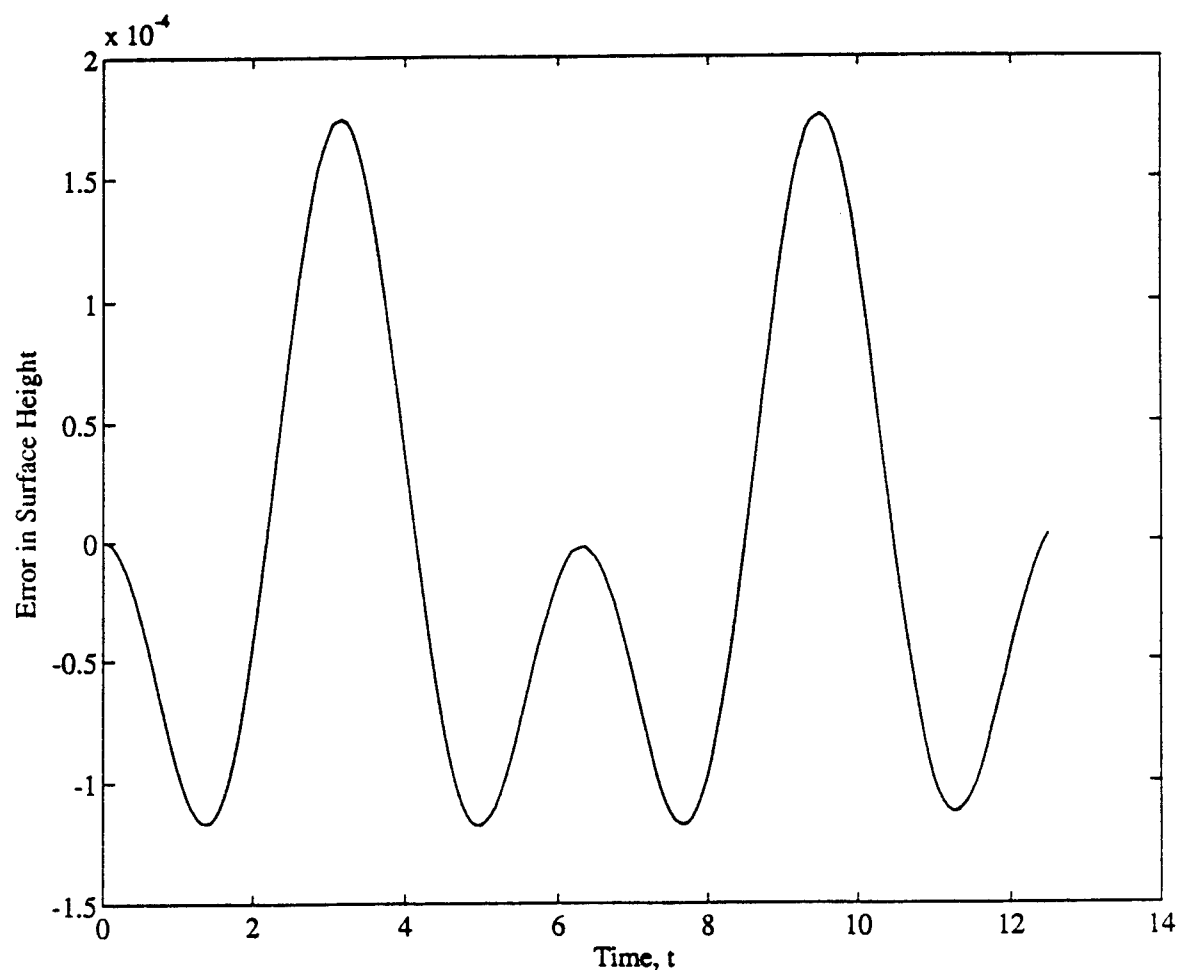


Figure 8: Calculations Confirm Essentially Zero Mass Gain or Loss

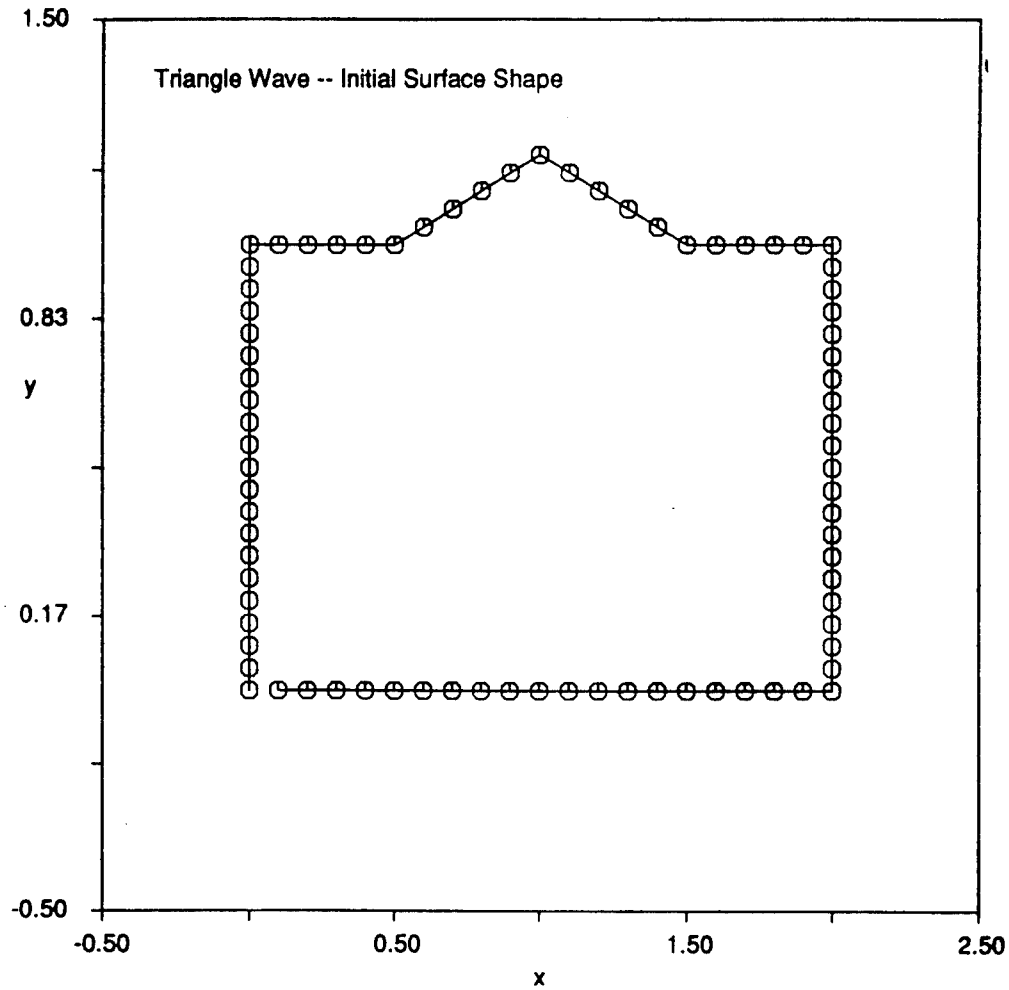


Figure 9: Initial Grid/Surface Geometry for Triangular Wave Calculation

Students in the *Stability of Free Surfaces* course were required to reproduce the results presented above with their own computer codes. In addition, the students performed many other 2-D calculations with their validated models. One such calculation, performed for a triangular wave, is shown in Figs. 9 and 10. Figure 9 depicts the initial grid and surface geometry, while Fig. 10 shows the nonlinear evolution of this surface as a function of time.

Development of Axisymmetric BEM Code

Having validated the 2-D formulation, we next set out to develop an axisymmetric code capable of describing the behavior of a liquid jet. In this case, the Green's function applicable to the solution of the axisymmetric form of Laplace's equation is much more involved than the 2-D result. If we let r and z denote radial and axial coordinates and denote the base point with subscript "i" as before, we can write:

$$G = \frac{4rE_1(p)}{\sqrt{a}} \quad (24)$$

where

$$a = (r + r_i)^2 + (z - z_i)^2 \quad (25)$$

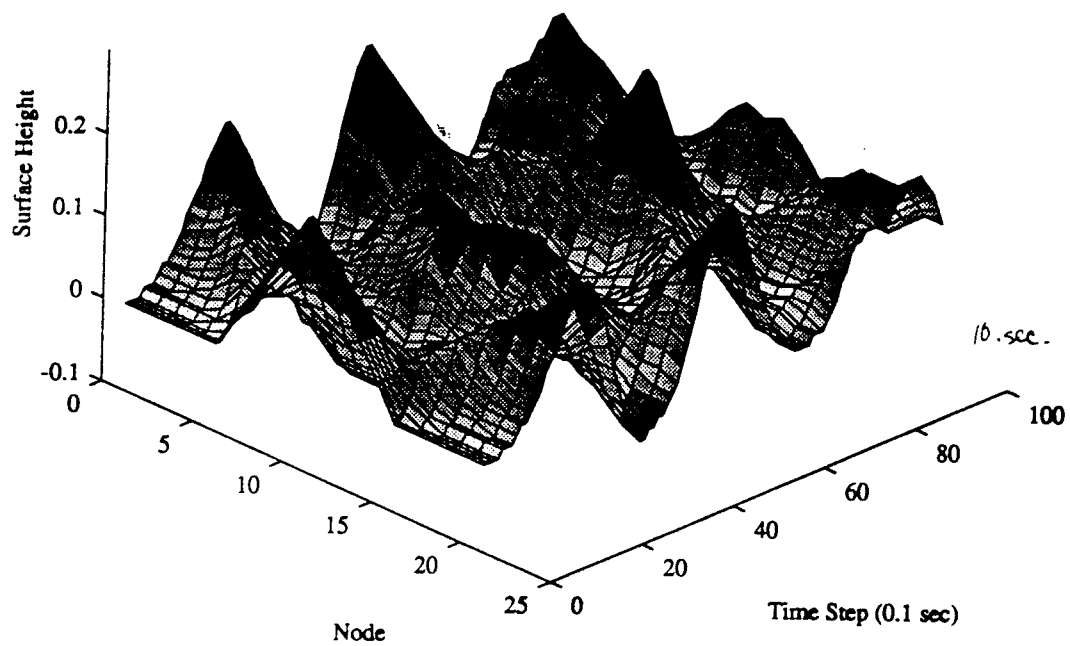


Figure 10: Predicted Surface Evolution for Triangular Wave

and

$$p = \frac{(r - r_i)^2 + (z - z_i)^2}{a} \quad (26)$$

Here, E_1 is the elliptic integral of the first kind. To promote efficiency in calculation of the quantity, a curvefit from Abramowitz and Stegun¹² is employed:

$$E_1(p) = \sum_{i=0}^{i=4} a_i p^i + b_i \ln(p) p^i \quad (27)$$

where the quantities a_i and b_i are constants.

Using these definitions, the applicable form of Eq. 3 becomes:

$$\alpha \phi_i + \int_{\Gamma} [\phi D_{kern} - q S_{kern}] d\Gamma = 0 \quad (28)$$

where S_{kern} is the kernel for the source integrals:

$$S_{kern} = \frac{4rE_1}{\sqrt{a}} \quad (29)$$

and D_{kern} is the kernel for the doublet terms:

$$D_{kern} = \frac{-1}{2\sqrt{a}} [n_r E_1 + \frac{E_2}{c} (dn_r + 2rn_z(z - z_i))] \quad (30)$$

In this expression, the quantities n_r and n_z are components of the unit normal vector, E_2 is an elliptic integral of the second kind, and the quantities c and d are defined:

$$c = (r - r_i)^2 + (z - z_i)^2 \quad (31)$$

$$d = (r - r_i)^2 - (z - z_i)^2 \quad (32)$$

The elliptic integral E_2 is curvefit using an expression similar to Eq. 27 using results from Abramowitz and Stegun. The quantity α in Eq. 28 is defined as in the 2-D problem.

As in the 2-D formulation, we employ linear elements to describe the behavior of ϕ and q along a given element. The resulting integrals are too complicated to be solved analytically since they involve elliptic integrals within the kernel functions. For this reason, we must evaluate integrals numerically in the axisymmetric formulation. Following Liggett and Liu⁴, we employ Gaussian quadrature to insure high accuracy in evaluating integrals. Using this approach, we approximate an integral as:

$$\int_a^b f(x) dx \approx \frac{b-a}{2} \sum_{i=1}^{i=n_g} w_i f(z_i) \quad (33)$$

where w_i values are the weighting functions for the quadrature, and z_i values are the Gauss points determined from:

$$z_i = \frac{b-a}{2} \psi_i + \frac{b+a}{2} \quad (34)$$

Here ψ_i are known as the abscissas of the method. Values of w_i and ψ_i are tabulated in Abramowitz and Stegun for a number of Gauss points n_g between 2 and 24. In practice, we use four Gauss points which implies four function evaluations to approximate a given integral. Many BEM studies^{4,3} have shown that this is sufficiently accurate to approximate integrals in this formulation.

As in the case of the 2-D formulation, the resulting set of integrals fill in elements of $[D]$ and $[S]$ matrices which can then be pivoted and solved by Gaussian elimination. Finally, we note that a special treatment is required to approximate integrals involving segments neighboring the base point¹².

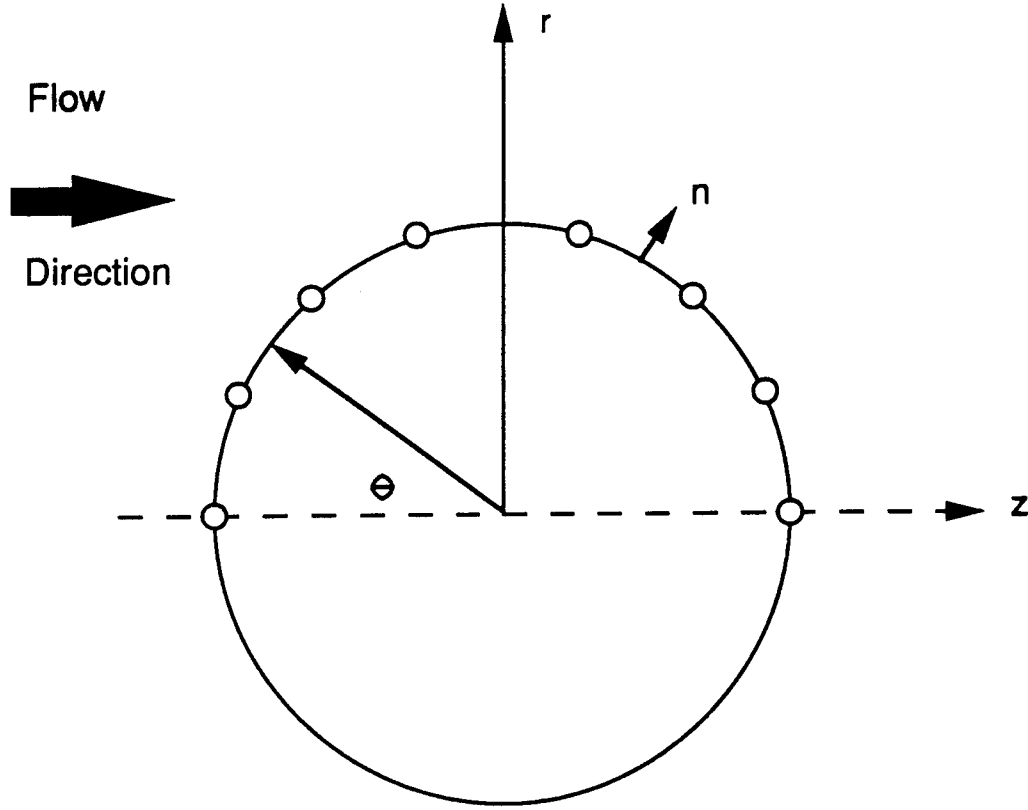


Figure 11: Geometry for Calculation of Flow over Sphere

Validation of Axisymmetric BEM Laplace Solver

To validate the axisymmetric BEM code, we generated a solution for the flow over a sphere. This flowfield has an analytic solution which is provided in most texts which discuss potential flows. To formulate the problem, consider the discretization of the surface as shown in Fig. 11.

Since the contributions from the sources and doublets placed on the surface vanish as we move far from the body, we must pose the problem as a perturbation to the mean flow ($\phi_m = U_\infty z$). If we regard ϕ and q as perturbation quantities, then the analytic results¹³ for a sphere of unit radius are:

$$\phi_a = \frac{\cos(\theta)}{2} \quad (35)$$

$$q_a = -\cos(\theta) \quad (36)$$

where θ is defined in Fig. 11.

We can effectively check the behavior of the code for a Dirichlet problem by imposing Eq. 35 on the boundary of the sphere and a Neumann problem by imposing Eq. 36. The surface of the sphere is discretized into nodes at equal angular spacing. No nodes are required along the axis of symmetry since the Green's function vanishes at this location giving no net contribution to boundary integrals.

Results of calculations are presented in Figs. 12 and 13 for a case with 29 nodes along the boundary. In Fig. 12, the Dirichlet problem was specified so errors in velocities between the code and the analytic result

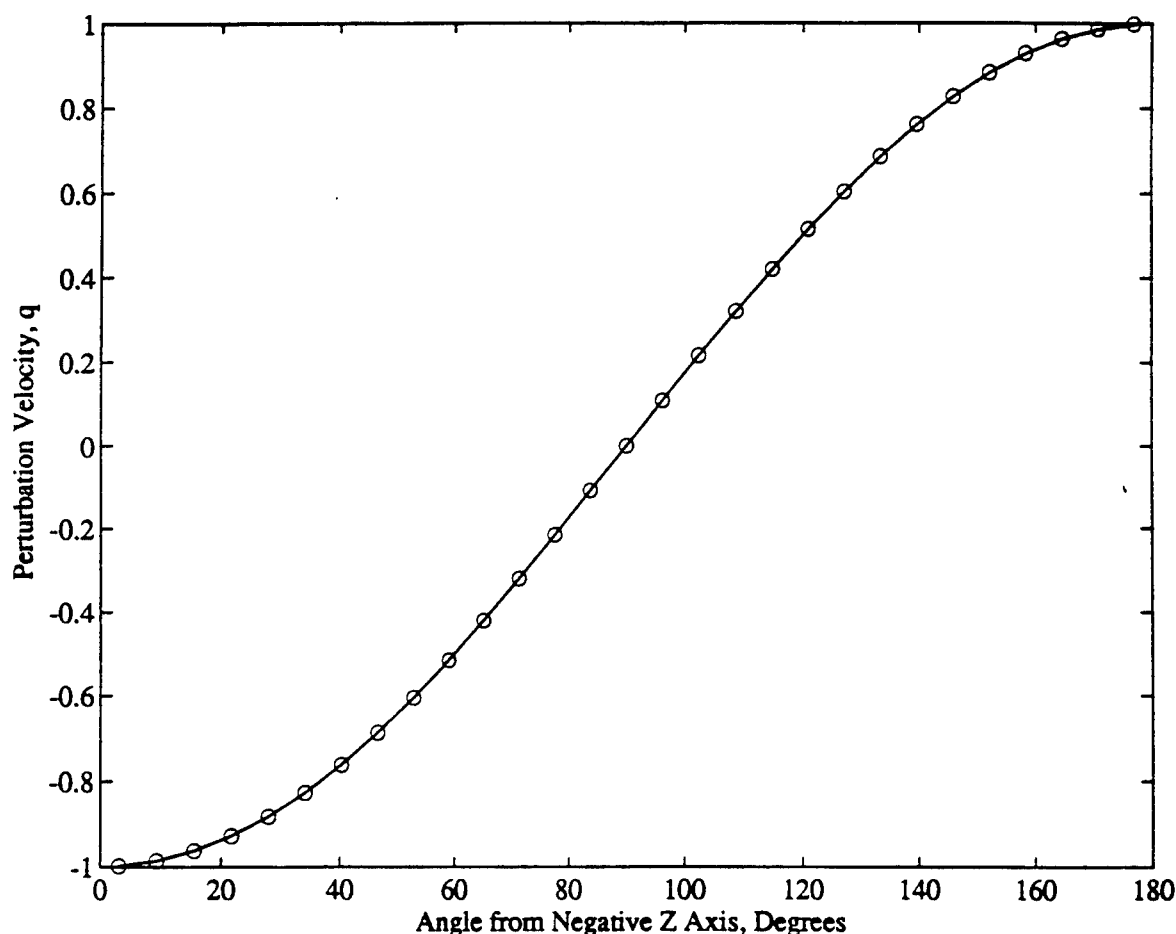


Figure 12: Comparison of Perturbation Velocities with Analytic Results

are depicted here. In Fig. 13, errors in potential are shown for a specified boundary velocity. Both results indicate very small errors (less than 0.1%) for a domain using only a modest number of points.

Future Plans

In the near future, we anticipate completion of the inviscid model for an axisymmetric formulation. We intend to use this code to model liquid jets with arbitrary time-dependent injection conditions. A parallel effort will also be undertaken to include the effects of viscosity on the behavior of the jet. This is not a trivial extension of existing models, so a great deal of development work lies ahead in this area.

We are excited about the prospects of building a family of BEM codes capable of treating a wide variety of free surface problems. While student interest is high, the current funding limitations have restricted us to a single graduate student in this area. We are hoping to enhance this effort by proposing additional modeling tasks and have recently submitted a proposal through the Augmentation Awards for Science and Engineering Research Training (AASERT) program and the AFOSR for two additional students in this area. Should this proposal be funded, we could investigate many other interesting aspects of jet injection problems using boundary element methods.

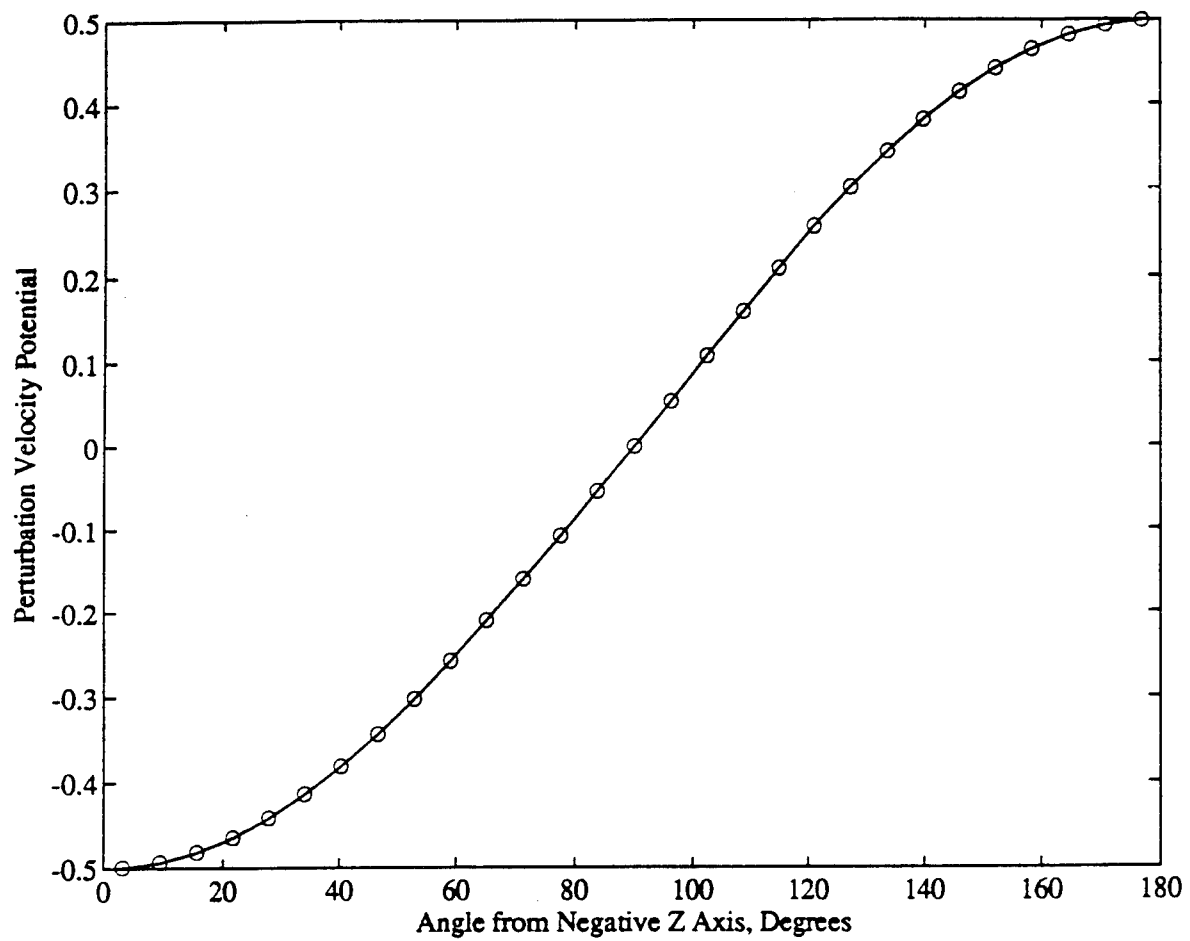


Figure 13: Comparison of Perturbation Potential with Analytic Results

References

1. Dold, J. W., and Peregrine, D. H., "Steep unsteady water waves, an efficient computational scheme," *Proc. 19th Coastal Engineering Conf.*, Vol. 1, Houston, ASCE, pp. 955-967, 1984.
2. Medina, D. E., Liggett, J. A., Birchwood, R. A., and Torrance, K. F., "A Consistent Boundary Element Method for Free Surface Hydrodynamic Calculations," *International Journal for Numerical Methods in Fluids*, Vol. 12, pp. 835-857, 1991.
3. Gipson, G. S., Boundary Element Fundamentals, Topics in Engineering Volume 2 (C. A. Brebbia and J. J. Conner (ed.)), Computational Mechanics Publications, 1987.
4. Liggett, J. A., and P. L.-F. Liu, The Boundary Integral Equation Method for Porous Media Flow, Allen and Unwin, London, 1983.
5. Penney, W. G., and Price, A. T., "Finite Periodic Stationary Gravity Waves in a Perfect Liquid", *Phil. Trans. R. Soc. Lond., Ser. A*, V244, pp 254-282, 1952.
6. Lamb, H., Hydrodynamics, 6th Ed., Dover Publications, 1982.
7. Lundgren, T. S., and Mansour, N. N., "Oscillations of Drops in Zero Gravity with Weak Viscous Effects", *Journal of Fluid Mechanics*, V194, pp 479-510, 1988.
8. Numerical Recipes in Fortran, 2nd Edition, Cambridge University Press, 1992.
9. Longuet-Higgins, M. S., and Cokelet, E. D., "The deformation of steep surface waves on water. I. A numerical method of computation," *Proc. R. Soc. Lond. A*, **350**, pp. 1-26, 1976.
10. IMSL Math Library User's Manual, Version 1.0, 1987.
11. Abramowitz, M., and Stegun, I. A. (ed), Handbook of Mathematical Functions, 9th Edition, Dover Publications, 1970.
12. Lennon, G. P., Liu, P. L-F., and Liggett, J. A., "Boundary integral equation solution to axisymmetric potential flows, 1, Basic formulation," *Water Resources Res.*, **15** (5), pp. 1102-1106, 1979a.
13. Currie, I. G., Fundamentals Mechanics of Fluids, McGraw Hill Publishing, 1974.

**SCANNING TUNNELING MICROSCOPY (STM) AND
ATOMIC FORCE MICROSCOPY (AFM)**

AND

**SYNCHROTRON RADIATION WORK FOR
THE DEVELOPMENT OF A NEW DETECTOR**

R. W. Hoffman

Ambrose Swasey Professor Emeritus of Physics

**Case Western Reserve University
Cleveland, OH 44106-7079**

**Final Report for:
Research Initiation Program
Phillips Laboratory**

**Sponsored by:
Air Force Office of Summer Research
Bolling Air Force Base, Washington, D.C.**

December 1992

INTERIM REPORT

1) STM/AFM

This research was divided roughly equally in terms of scanning tunneling, microscopy, (STM) and atomic force microscopy, (AFM) and synchrotron radiation work for the development of a new detector. We describe our progress for the two projects in that order.

Based on the preliminary work carried out while at Edwards Air Force Base during the summer of 1990, and based in part on the mechanical property measurements made at CWRU, we have proposed that the thin film mechanics of diamond like carbon films is highly dependent on the stress and the development of cracks in the film. Some cracks were observable optically, and it was decided to investigate the structure using an STM. Tunneling microscopy (STM) was chosen not because it is necessarily the best technique, but that it was available and promising with the new apparatus then available at EAFB. The continuation of work initiated in this way formed the basis for the present effort. Fortunately for this problem, atomic resolution is not required as the cracks are expected to range in width up to about 1 micron.

The progress on this portion of the work has been "spotty". Initial commitments for the update of an existing STM were withdrawn on the CWRU campus, and as a result, that portion was not finished. In September, 1992 it became obvious that there was a possibility of getting a combined research quality STM/AFM instrument and electronics from Park Instrument Corporation with the major

instrumental funding coming from NSF as part of the diamond and diamond like films project. This funding although following a successful May, 1992 review, still has not reached the CWRU campus. In October, 1992 Professor J.A. Mann, chairman of the department of Chemical Engineering and Professor R.W. Hoffman, in Physics made a trip to Purdue University to see the new Park instrument in operation. It's purchase was recommended after the visit. The addition of the AFM would allow the examination of surfaces routinely. Several insulating DLC films were taken with us which showed a well resolved structure. With the samples chosen and the areas examined, no cracks were observed.

In order to provide hard copy from the electronic information, the purchase of a Mitsubishi hard copier was approved. The initial discussions called for immediate delivery upon receipt of the PO with both sufficient time and emphasis to allow the completion of the RDL effort on schedule.

Unfortunately the NSF equipment funding was further delayed thus not received; hence the PO could not be issued on time and this state is still being resolved by re-examining the entire bidding process with updated information.

Both Professors Hoffman and Mann are committed to finishing the project and we expect completion approximately three months after the delivery of the instrument. The samples must be redone, but AFM will now be available.

2) SYNCHROTRON RADIATION EXPERIMENTS

A. X-RAY FOCUSING SPECTROGRAPH AT BEAMLINE X-11A

1. Introduction

Development and testing of a mica crystal x-ray focussing spectrograph continued during a trip to Brookhaven's Nation Synchrotron Light Source from 30 January to 4 February 1993. The testing was done on beamline X-11A at energies around the florescence edge of iron. The objectives of the trip were twofold. First we wanted to determine the alignability of the mica crystal. Secondly we wanted to test the apparatus in an actual EXAFS experiment. Figures 1 and 2 show the geometry of the prototype system used.

2. Alignment Study

Figure 1 shows the setup for the crystal alignment study. The x-ray beam was directed at the mica crystal, incident at the Bragg angle, and photographic film was placed in the path of the diffracted beam. In order to determine the angular tolerance of the Bragg condition, the crystal was rotated through the Bragg rotation. It was determined that the alignment tolerance is about plus or minus 20 minutes of an arc.

3. EXAFS Data

Figure 2 shows the setup for collecting EXAFS data. The photographic film was replaced by an ionization chamber and the x-ray energy was ramped from 6883eV in order to scan across the iron florescence energy (7112eV). Figure 3 shows data collected to check the alignment of the crystal and detector. The x-rays were

incident directly on the mica. The Bragg angle was set at 20.24 deg. which corresponds to an energy of 7183eV. Clearly there is a prominent peak at about 7183eV. The background signal is an iron florescence signal, probably from a stainless steel screw used to hold the mica in place. Because of space and time limitations, we were not able to completely eliminate this background. We were not able to eliminate the line of sight between the screw and the detector face.

Figures 4 and 5 are EXAFS data collected from an Fe foil. The foil was placed in the beam path before the mica crystal. Again there is a peak at 7183eV, as one would expect. This time the background is primarily from the sample itself. We were unable to eliminate the line of sight. The smaller peak in figure 5 is probably due to another Bragg diffraction event.

4. Future Work

Further attempts to perfect this device are in order.

On this trial, we also collected over 130 other unrelated scans. For the spectrograph, we demonstrated that radiation from a fluorescing sample can be diffracted into an ionization chamber. Alignment is tedious at the present time, but with assistance from a laser it may be easier. In order to eliminate background problems, the line of sight problem must be eliminated. This is best done by collimating the ionization detector face.

B. X-RAY FOCUSING SPECTROGRAPH AT BEAMLINE X-19A

1. Introduction

Testing of the mica crystal x-ray focussing spectrograph progressed during a trip to BNL's NSLS from 18 February to 23 February 1993. The beamline used was X-19A and the energies under study were the fluorescence edges of Ti and Cl. The objective was to see if the mica spectrograph would function in proper capacity in the soft x-ray region of the Cl fluorescence edge. The mica crystal spectrograph has the most potential in this energy regime, since good filters for low energy x-rays are lacking.

2. Setup

The experimental geometry was similar to that of the X-11A run. However, the Cl. edge work required that the entire apparatus be enclosed in a He flushed plexiglass box. The box was necessary because the absorption length of Cl fluorescence edge x-rays in air is much shorter than our prototype setup. By enclosing the spectrograph in a He environment, we were able to use the apparatus without noticing a significant attenuation of the x-ray beam. The box was equipped with the necessary feedthroughs to operate an ionization chamber as the main detector for Bragg scattered operators to change setup parameters without opening the lid. Typical He flush times were about 15 minutes.

3. Data Collection

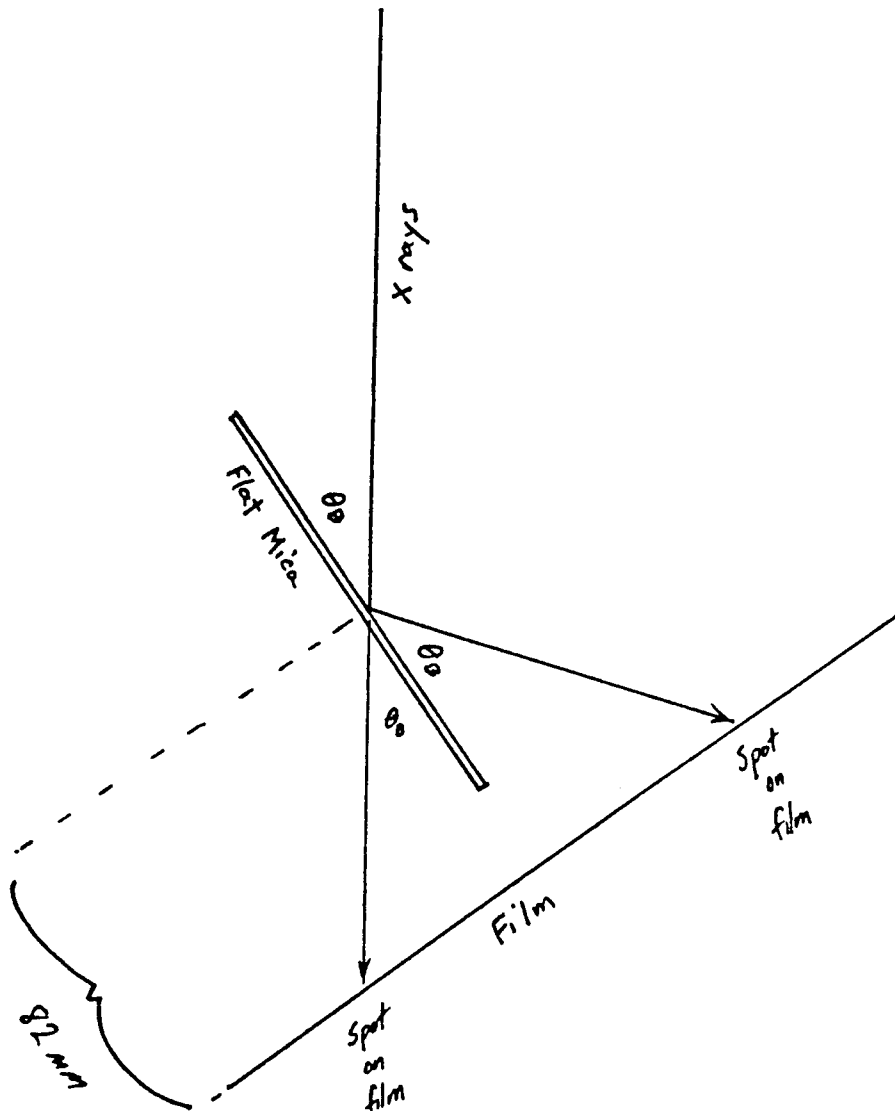
Figure 6 shows a typical energy scan at the Cl edge. The data shows that once a Bragg condition is met, a significant signal is detected by the ionization chamber. The background is quite low, as one would expect. The incident x-rays were not quite striking the mica at the Bragg angle for Cl fluorescence radiation, as seen in the energy shift of the Bragg peak. The second peak (at slightly lower energy) is not understood at this time.

Figure 7 shows data collected over a broad energy range. the diffraction peaks are clearly seen, as is an EXAFS spectrum. This spectrum is the fluorescence spectrum from potassium in the mica crystal.

4. Future Work

The next step in developing the mica spectrograph for use with low energy x-rays is to reduce the overall size of the apparatus. This must be done in order to make the device useful with existing fluorescence detector rigs. Also the geometry must be adjusted in order to Bragg diffract fluorescence radiation from the incident beam side of the sample. This eliminates any sample thickness problems. Sensitivity issues (Ion chamber vs electron yield) must also be explored. We expect these to be solved by the next X-11 Beam time in June.

FIGURE 1



MICA CRYSTAL ALIGNMENT GEOMETRY

FIGURE 2

DETECTOR/MICA CRYSTAL ALIGNMENT GEOMETRY

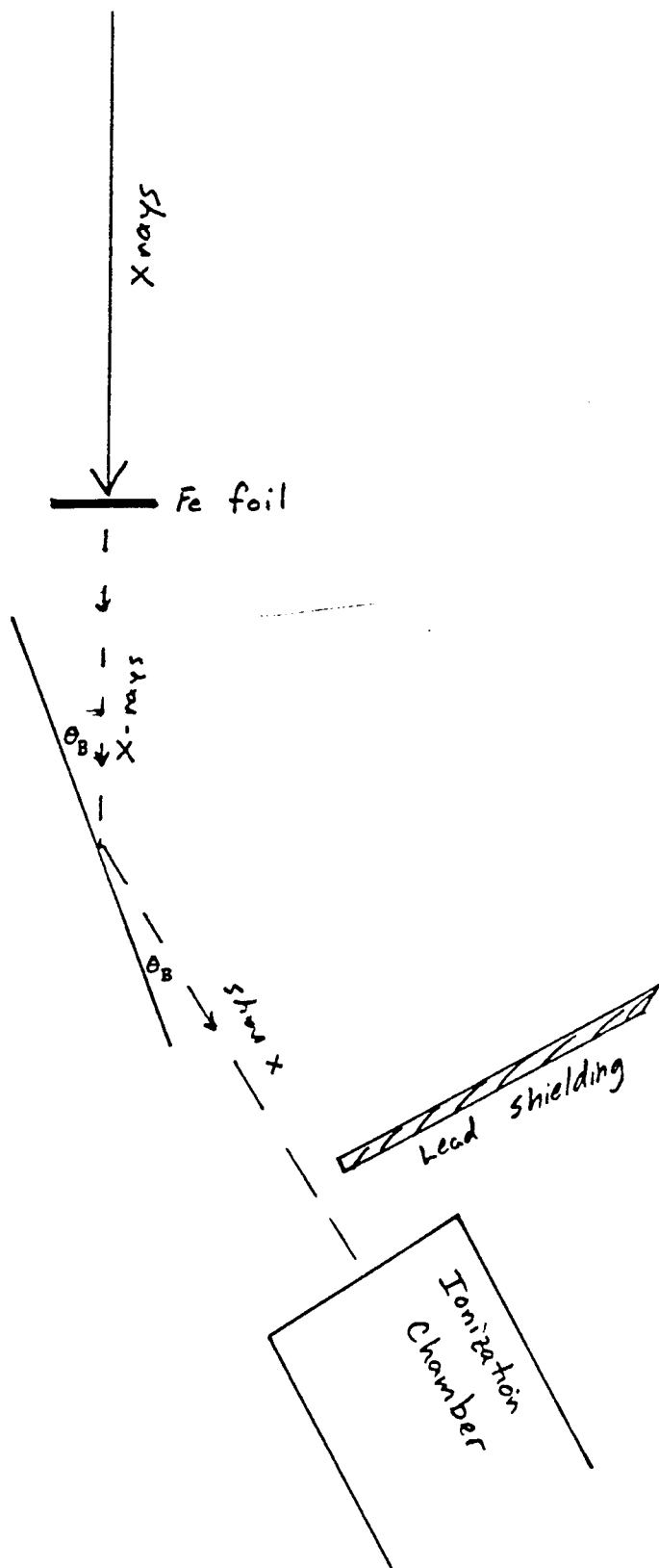


FIGURE 3

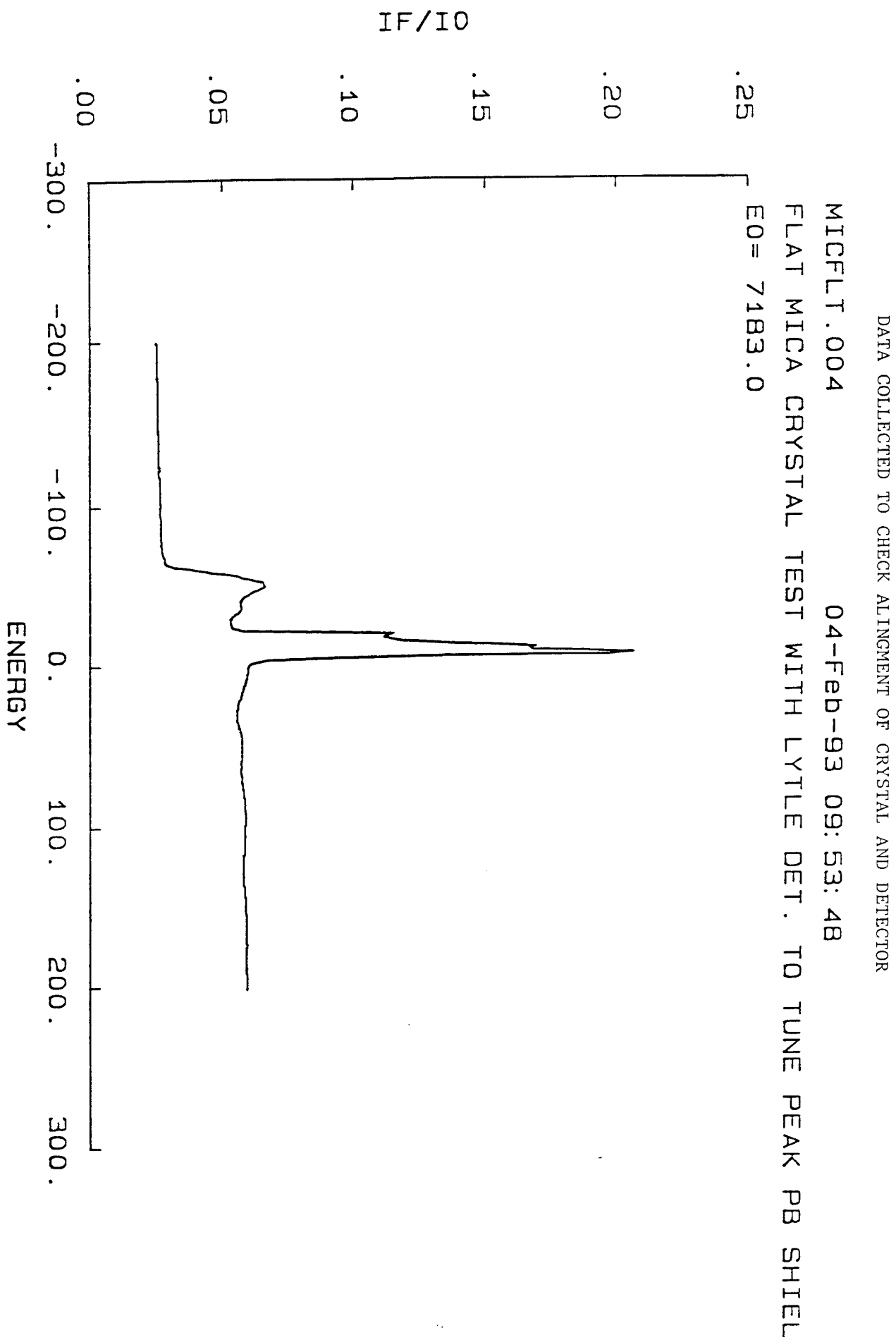


FIGURE 4

EXAFS DATA COLLECTED FROM AN Fe FOIL USING THE MICA CRYSTAL

FEMIC.002

04-Feb-93 10:52:45

FE FOIL WITH FLAT MICA DISPERSION TEST

E0 = 7112.0

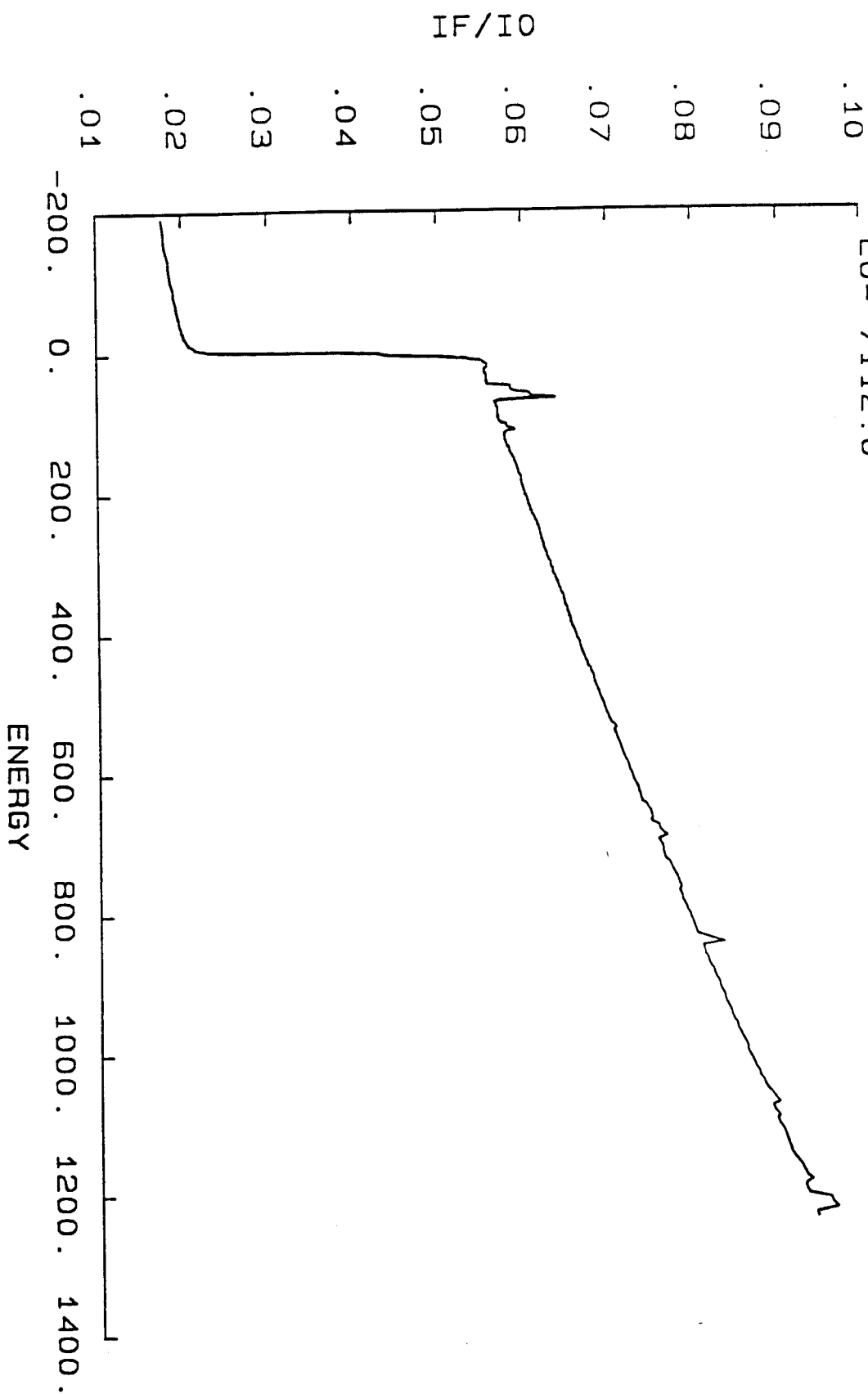


FIGURE 5

BLOWUP OF FIGURE 4 ABOUT THE DIFFRACTION PEAKS

FEMIC.002

04-Feb-93 10:52:45

FE FOIL WITH FLAT MICA DISPERSION TEST

EO = 7112.0

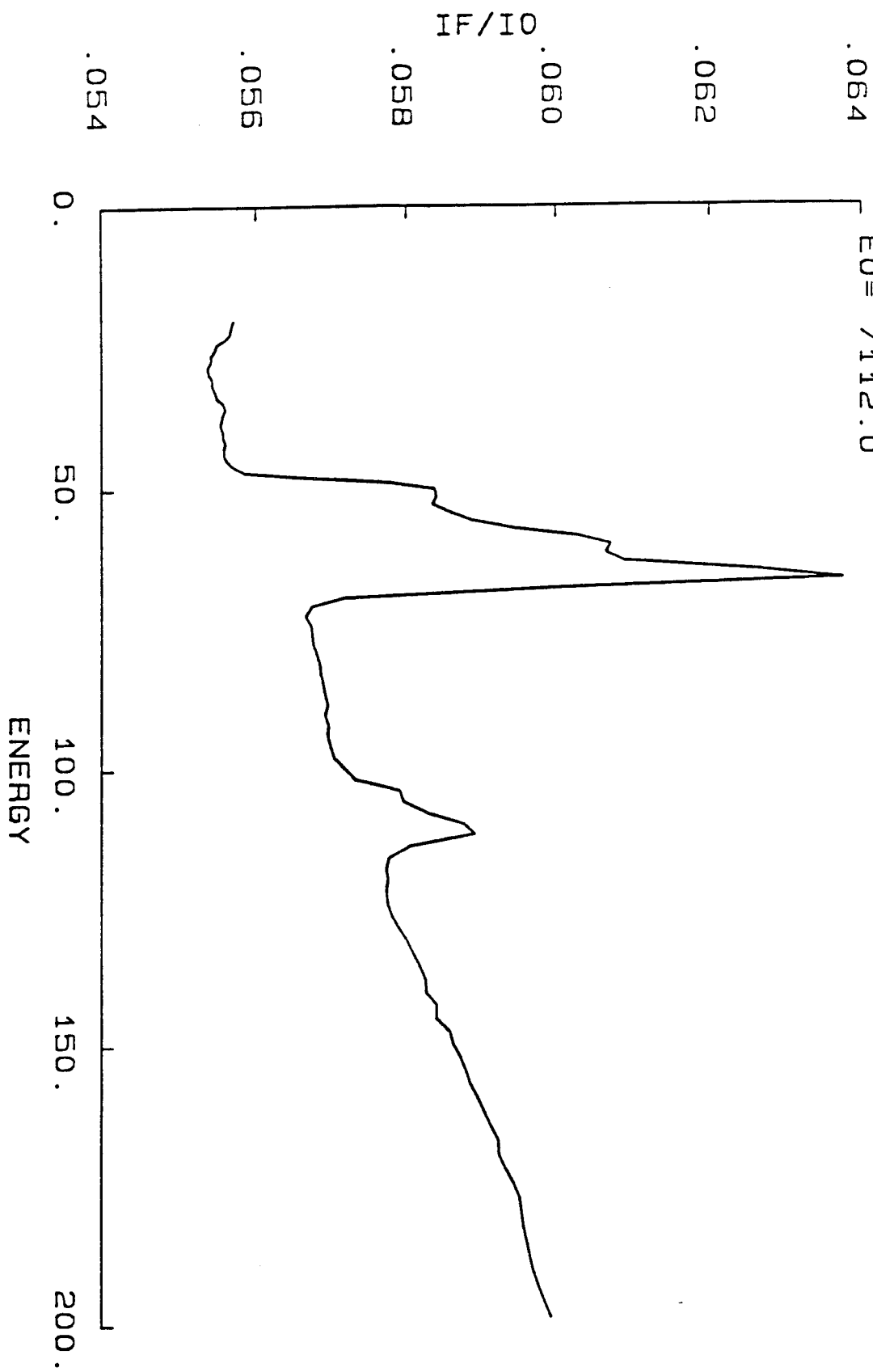


FIGURE 6

DIFFRACTION PEAK FROM THE MICA AT THE Cl K ALPHA 1 ENERGY

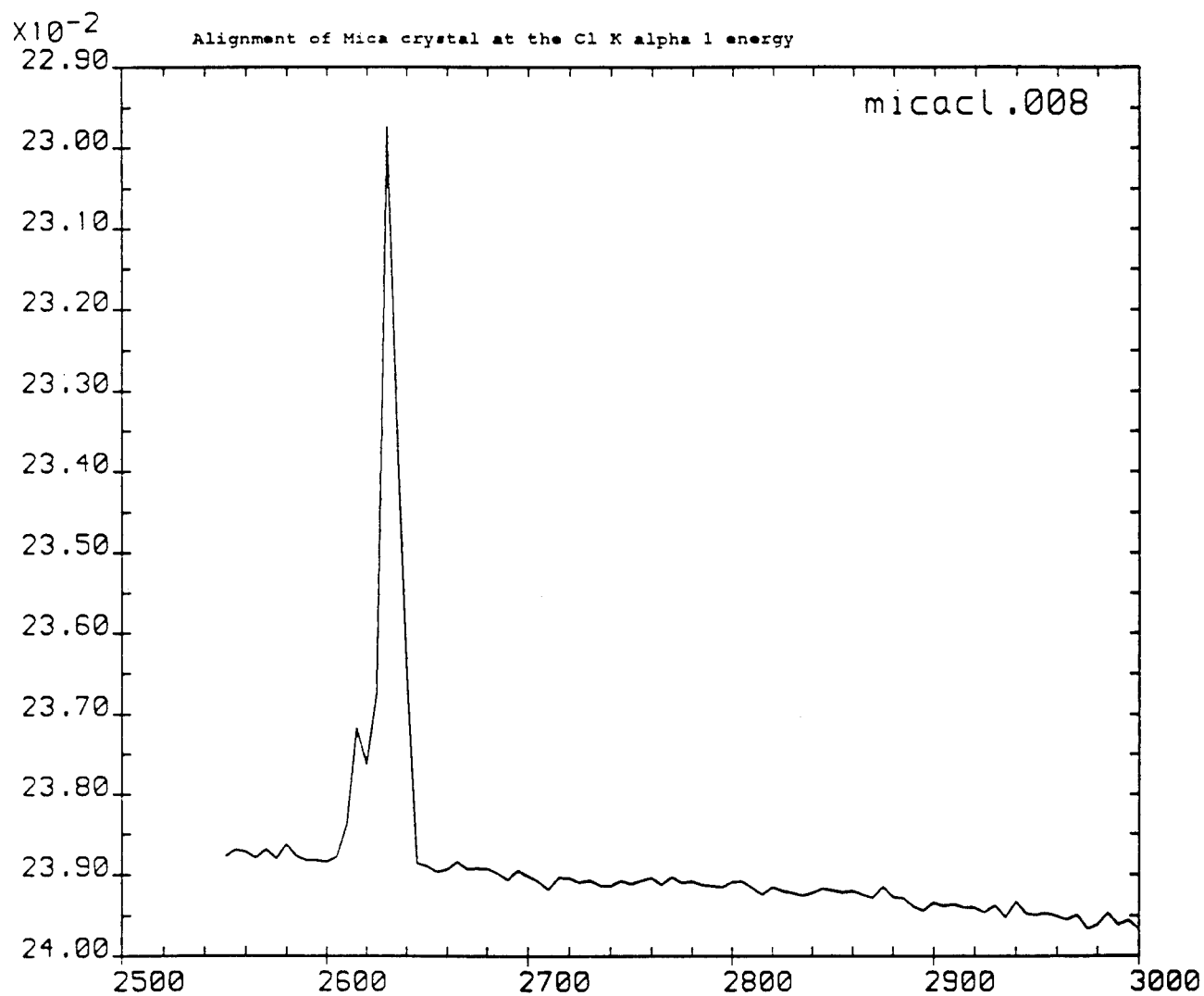
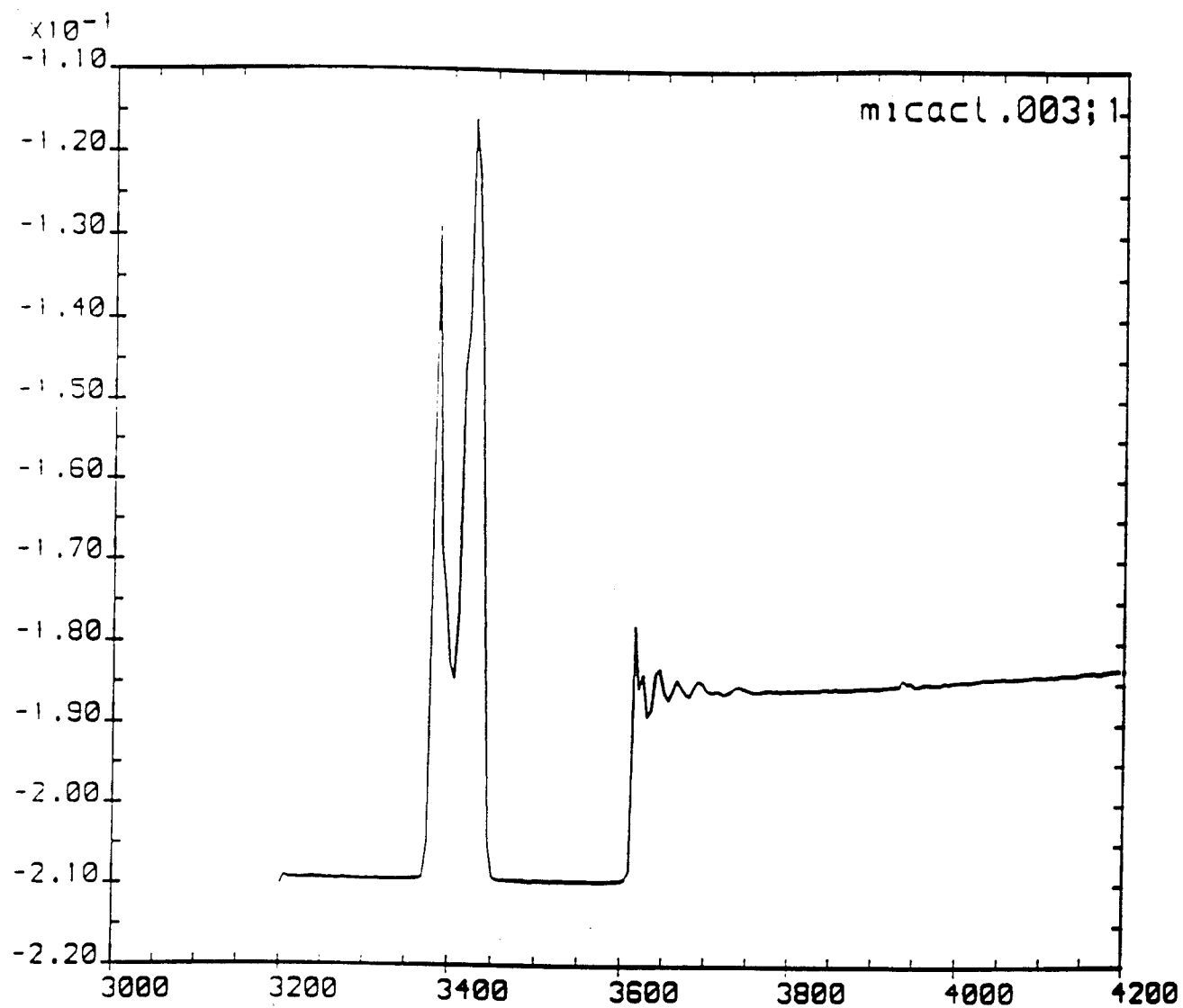


FIGURE 7

DIFFRACTION PEAKS NEAR THE C1 EDGE AND POTASSIUM EXAFS FROM THE MICA



MODEL REDUCTION AND CONTROL OF ASTREX

Ashok Iyer, Associate Professor
and
Kathryn Watkins, Graduate Assistant

Department of Electrical & Computer Engineering
University of Nevada, Las Vegas
Las Vegas, NV 89154

Final Report for:
Research Initiation Program
Phillips Laboratory

Sponsored by:
Air Force Office of Scientific Research
Bolling Air Force Base, Washington, D.C.
and
University of Nevada, Las Vegas

December 1992

MODEL REDUCTION AND CONTROL OF ASTREX

Ashok Iyer, Associate Professor

Kathryn Watkins, Graduate Assistant

Department of Electrical & Computer Engineering

University of Nevada, Las Vegas

Las Vegas, NV 89154

Abstract

The Advanced Space Structures Technology Research Experiments (ASTREX) is a precision structure situated at the Phillips Laboratory, Edwards Air Force Base, CA. The structure is a test bed to develop, test and validate control strategies for large-angle, three axis slewing maneuvers and vibration suppression. The ASTREX facility consists of the test article (with primary, secondary and tertiary substructures along with mirrors. Model Reduction using Schur decomposition and balanced truncation and control strategies using state estimation and regulator design and optimization using LQG to reduce vibrations were implemented. The controller was evaluated using the full order ASTREX model.

1 Introduction

The Advanced Space Structures Technology Research Experiments (ASTREX) is a precision structure situated at the Phillips Laboratory, Edwards Air Force Base, CA. The structure is a test bed to develop, test and validate control strategies for large-angle, three axis slewing maneuvers and vibration suppression [2] [3]. The facility is funded by Air Force and is supported by on-site staff. Number of investigators from universities and industries have been involved in the research pertaining to the control-structure interaction.

ASTREX Hardware Description

The ASTREX facility [2] [3] [7] consists of a pedestal with an air bearing system on which the test article is placed. The pedestal consists of pneumatic components, electronics, power supplies and computer at its base and an air bearing with a cable follower and electronics at the other end. The front, side, top views and the Models axes system are shown in Figures 1 to 3. The desired specification of the air bearing system are:

- Load capacity 14,500 lbs.
- $\pm 20^\circ$ Pitch and Roll, $\pm 180^\circ$ Yaw
- Measure attitude to within 1 arc second at rates up to $10^\circ/\text{sec}$ and accelerations up to $10^\circ/\text{sec}/\text{sec}$.
- Cable follower to bring supply lines from "Ground" to test article: Crossover frequency at least 5 Hz.

The mirror mass simulator consists of a support truss with the primary mirror, secondary mirror and a tertiary mirror. The state space model is obtained from the finite element model of the test article and the pedestal. The ASTREX hardware is summarized below:

ASTREX Hardware Summary

Facility: 40ft by 40ft by 40ft, laboratory Overhead crane, temperature control

Air Bearing: Spherical(3-Axis) Air Bearing, 19 inch ball, cable follower: Two gimbal - 3 axis mechanical arrangement, Rigid Body attitude sensing - 1 arc sec accuracy.

Computer: Real time Control and Data Acquisition Computer, 32 Inputs, 32 Outputs, 1000 Hz + Sampling rate, 10-15 MFLOP Parallel Processor based system.

Structure: 3 Mirror Beam Expander, 1/3 - 1/2 Dynamically scaled structure, Modular Graphite Epoxy construction

Sensors/Actuators: Throttleable Cold Gas Thrusters, up to 200 lb force. The accelerometers locations are given in Figure 4.

- Proof Mass Actuators
- Reaction Wheels
- Provision for Control Moment Gyroscopes
- Accelerometers
- Optical Line of Sight Sensor

Section 2 contains analytical development of the control system matrices from dynamical model generated by the NASTRAN program. Section 3 discusses the model reduction schemes. Section 4 contains a simple controller design and simulation results and Section 5 the conclusions.

2 Analytical Development

For a detailed description of the model development please see [1]. A physical structure is often represented by its dynamical model defined by an equation

$$M\ddot{x} + E\dot{x} + Kx = f \quad (1)$$

where M , E , and K are mass, viscous damping, and stiffness matrices, respectively. x is a vector representing generalized deflections (degrees of freedom) of grid points or nodes. An overdot indicates time derivative. The vector f includes forces and moments applied to the structure. The equation can be written in a state-space form as given by

$$\begin{Bmatrix} \dot{x} \\ \ddot{x} \end{Bmatrix} = \begin{bmatrix} 0 & I \\ -M^{-1}K & -M^{-1}E \end{bmatrix} \begin{Bmatrix} x \\ \dot{x} \end{Bmatrix} + \begin{Bmatrix} 0 \\ M^{-1}f \end{Bmatrix} \quad (2)$$

such that

$$\dot{X} = AX + F \quad (3)$$

where $X = \begin{Bmatrix} x \\ \dot{x} \end{Bmatrix}$, $A = \begin{bmatrix} 0 & I \\ -M^{-1}K & -M^{-1}E \end{bmatrix}$ and $F = \begin{Bmatrix} 0 \\ M^{-1}f \end{Bmatrix}$.

A transformation from physical degrees of freedom (n) to a modal state (m modes) can be made by defining $x = \Phi\eta$; the modal state vector η ($m \times 1$) includes modal amplitudes, and the column of modal matrix Φ ($n \times m$) defines the mode shape for a particular mode. The modal matrix Φ is normalized with respect to the mass matrix M such that $\Phi^T M \Phi = I$ and $\Phi^T K \Phi = \Lambda$; I is an identity matrix, and Λ is a diagonal eigenvalue matrix. Using the transformation, and multiplying by Φ^T , eq.(1) is given by

$$\Phi^T M \Phi \ddot{\eta} + \Phi^T E \Phi \dot{\eta} + \Phi^T K \Phi \eta = \Phi^T f$$

which from normalization, and assuming a proportional damping, reduces to

$$\ddot{\eta} + [2\zeta_{diag}\omega]\dot{\eta} + \Lambda\eta = \Phi^T f \quad (4)$$

In the diagonal modal damping matrix $[2\zeta_{diag}\omega]$, ζ_{diag} is a diagonal modal damping factor matrix, and ω is the square-root matrix of Λ representing natural frequencies of the structure. The equation (4) can be written in a state space form as follows.

$$\begin{bmatrix} \dot{\eta} \\ \ddot{\eta} \end{bmatrix} = \begin{bmatrix} 0 & I \\ -\Lambda & -(2\zeta_{diag}\omega) \end{bmatrix} \begin{bmatrix} \eta \\ \dot{\eta} \end{bmatrix} + \begin{bmatrix} 0 \\ \Phi^T f \end{bmatrix} \quad (5)$$

In the compact notation.

$$\dot{X}_\eta = A_\eta X_\eta + F_\eta \quad (6)$$

where $X_\eta = \begin{bmatrix} \eta \\ \dot{\eta} \end{bmatrix}$, $A_\eta = \begin{bmatrix} 0 & I \\ -\Lambda & -\zeta_{\mathbf{mat}} \end{bmatrix}$, and $F_\eta = \begin{bmatrix} 0 \\ \Phi^T f \end{bmatrix}$. The damping matrix is written as $\zeta_{\mathbf{mat}} = [2\zeta_{diag}\omega]$. Due to the fullness of the modal matrix Φ , a force on the structure, theoretically, affects all modal states.

The participation of a force or a moment, applied in certain direction on the structure, in the modal state form can be explained as follows. Let the generalized displacement vector be written as $x = \{U, V, W, \psi, \theta, \phi\}^T$, where U, V, W are the displacement vectors along local x, y, z coordinates, and ψ, θ, ϕ are the slope vectors about the coordinates, respectively; each vector has dimension equal to number of nodes ($\text{numnodes} \times 1$). The modal matrix Φ corresponds to this particular arrangement of the generalized displacement vector x .

If a force is applied at location j in the local z direction, the force vector f is given by

$$f = \begin{bmatrix} 0 \\ 0 \\ \vdots \\ 0 \\ f_{w_j} \\ \vdots \\ 0 \\ 0 \end{bmatrix} \quad (7)$$

The number of zeros in the top of eq. (7) equal to $2 \cdot \text{numnodes} + j - 1$, and in the bottom equal to $6 \cdot \text{numnodes} - \{2 \cdot \text{numnodes} + j\}$. This can also be written as a unit vector with all zeros except at the location of z direction at node j , multiplied by the magnitude f_{w_j} . Symbolically, it is written as $f_{w_j} = S_{uv_{w_j}} |f_{w_j}|$. This representation helps in relating F_η to applied force directly.

$$F_\eta = \begin{bmatrix} 0 \\ \Phi^T S_{uv_{w_j}} \end{bmatrix} f_{w_j}$$

Thus only the $\{w_j\}$ displacement contribution of the modal matrix Φ is effective. For multiple force and moment inputs at different location or in different direction, a summation is carried out with appropriate placement unit vector:

$$F_\eta = \begin{bmatrix} 0 \\ \Phi^T \sum_j \sum_d [S_{uv_{d_j}} \cdot f_{d_j}] \end{bmatrix}$$

where d signifies the degree of freedom at node j . Effectively, a unit column- vector matrix is created leading

to equation,

$$F_\eta = \begin{bmatrix} 0 \\ \Phi^T S_{uvmat_{d_j}} \end{bmatrix} u = B_\eta u \quad (8)$$

in which u is the actual control input vector (non-zero terms in f of eq. (1)), $uvmat$ indicates that a matrix having unit vectors as columns is generated, and B_η is the control input matrix in the modal form. The force vector

$$F = \begin{bmatrix} 0 & 0 \\ 0 & M^{-1}\Phi^{-T} \end{bmatrix} F_\eta = \begin{bmatrix} 0 & 0 \\ 0 & \Phi \end{bmatrix} B_\eta u = B u \quad (9)$$

where B is the influence matrix which could also be formulated from equation (2).

The output equation is given by $y = ax + b\dot{x} + c\ddot{x}$. The a , b , and c matrices provide the combination of displacement, velocity, and acceleration output from the sensors. The equation can be written as

$$y = \begin{bmatrix} a & b \end{bmatrix} \begin{bmatrix} x \\ \dot{x} \end{bmatrix} + \begin{bmatrix} 0 & c \end{bmatrix} \begin{bmatrix} \dot{x} \\ \ddot{x} \end{bmatrix}$$

$$y = \begin{bmatrix} a & b \end{bmatrix} X + \begin{bmatrix} 0 & c \end{bmatrix} [AX + F]$$

Using the transformation relation

$$A \begin{bmatrix} \Phi & 0 \\ 0 & \Phi \end{bmatrix} = \begin{bmatrix} \Phi & 0 \\ 0 & \Phi \end{bmatrix} A_\eta$$

and substituting for X , the output equation can be written in the modal form as

$$y = \begin{bmatrix} (a\Phi - \Phi\Lambda) & (b\Phi - c\Phi\zeta_{\mathbf{mat}}) \end{bmatrix} \begin{bmatrix} \eta \\ \dot{\eta} \end{bmatrix} + \begin{bmatrix} 0 & c \end{bmatrix} F$$

$$y = \begin{bmatrix} (a\Phi - \Phi\Lambda) & (b\Phi - c\Phi\zeta_{\mathbf{mat}}) \end{bmatrix} \begin{bmatrix} \eta \\ \dot{\eta} \end{bmatrix} + \begin{bmatrix} 0 \\ c\Phi \end{bmatrix} B_{\eta} u$$

$$y = C_{\eta} X_{\eta} + D_{\eta} u \quad (10)$$

This equation is used to obtain response of the system.

The resulting state space model

$$\begin{aligned} \dot{x} &= A_{\eta} X + B_{\eta} u \\ y &= C_{\eta} x + D_{\eta} u \end{aligned} \quad (11)$$

where $A_{\eta} \in R^{50 \times 50}$, $B_{\eta} \in R^{50 \times 8}$, $C_{\eta} \in R^{9 \times 50}$ and $D_{\eta} \in R^{9 \times 8}$.

3 Model Reduction

A Schur method for balanced Model Reduction was used [9]. This reduction method overcomes the ill conditioning problems encountered in reduction procedures of most non-minimal models. The Moore reduced model [6] can be directly computed without balancing via projections defined in terms of arbitrary bases for the left and right eigenspaces associated with the “large” eigenvalues of the product PQ of the reachability and controllability grammians.

A brief discussion of the model reduction theory is presented here. Further details can be obtained from [9]. The general procedure of calculating a k^{th} order reduced model \hat{S} is given below.

Procedure

Input Data A, B, C, D, k

Step 1 Compute the matrices $V_{R,BIG}, V_{L,BIG} \in R^{n \times k}$ whose columns are bases for the respective right and left eigenspaces of PQ associated with the “big” eigenvalues $\sigma_1^2, \dots, \sigma_k^2$.

Step 2 Let

$$E_{BIG} := V_{L,BIG}^T V_{R,BIG}$$

and compute its singular value decomposition

$$U_{E,BIG} \Sigma_{E,BIG} V_{E,BIG}^T = E_{BIG}$$

Step 3 Let

$$S_{L,BIG} := V_{L,BIG} U_{E,BIG} \Sigma_{E,BIG}^{\frac{1}{2}} \in R^{n \times k}$$

$$S_{R,BIG} := V_{R,BIG} V_{E,BIG} \Sigma_{E,BIG}^{\frac{1}{2}} \in R^{n \times k}$$

and compute the state space realization of \hat{S}

$$\begin{bmatrix} \hat{A} & \hat{B} \\ \hat{C} & \hat{D} \end{bmatrix} := \begin{bmatrix} S_{L,BIG} A S_{R,BIG} & S_{L,BIG}^T B \\ C S_{R,BIG} & D \end{bmatrix}$$

End of Procedure

Schur Method The numerical robustness of the procedure outlined in the previous section depends precisely how the bases $V_{R,BIG}$ and $V_{L,BIG}$ in Step 1 are computed and the properties of these bases. The first k columns of the matrices T_{BAL}^{-1} and T_{BAL}^T would be one choice for $V_{R,BIG}$ and $V_{L,BIG}$, respectively. However as mentioned before, the computation of the balanced transform T_{BAL} may be numerically ill-conditioned.

To address the problem the following procedure based on the Schur decomposition of PQ computing orthonormal bases V_R, V_L is proposed. As is well known, the use of orthonormal transformations tends to promote numerical stability in algorithms. This procedure described in detail in [], is outlined below.

Procedure

Step 1 Solve for P and Q via the Lyapunov equations

$$PA^T + AP + BB^T = 0$$

$$A^T Q + Q A + C^T C = 0$$

Step 2 Compute the orthogonal real matrix V such that $VPQV^T$ is upper right triangular, i.e. put PQ in real Schur form.

Step 3 Using orthogonal Givens rotations (e.g. [6]) compute orthogonal real transformations V_A and V_D which order the Schur forms in the ascending and descending order respectively:

$$V_A^T P Q V_A = \begin{bmatrix} \lambda_{A_n} & * & * & \cdots & * \\ 0 & \lambda_{A_{n-1}} & * & \cdots & * \\ \vdots & \cdots & \cdots & \cdots & \cdots \\ 0 & \cdots & \cdots & 0 & \lambda_{A_1} \end{bmatrix}$$

$$V_D^T P Q V_D = \begin{bmatrix} \lambda_{D_n} & * & * & \cdots & * \\ 0 & \lambda_{D_{n-1}} & * & \cdots & * \\ \vdots & \cdots & \cdots & \cdots & \cdots \\ 0 & \cdots & \cdots & 0 & \lambda_{D_1} \end{bmatrix}$$

such that

$$\begin{aligned} & \{\lambda_{A_i} \mid i = 1, \dots, k\} \\ = & \{\lambda_{D_i} \mid i = 1, \dots, k\} \\ = & \{\sigma_i^2 \mid i = 1, \dots, k\} \end{aligned}$$

$$\begin{aligned} & \{\lambda_{A_i} \mid i = k+1, \dots, n\} \\ = & \{\lambda_{D_i} \mid i = k+1, \dots, n\} \\ = & \{\sigma_i^2 \mid i = k+1, \dots, n\} \end{aligned}$$

Step 4 Partition V_A and V_D as

$$V_A = \left[\begin{array}{c|c} \overbrace{V_{R,SMALL}}^{n-k} & \overbrace{V_{L,BIG}}^k \end{array} \right]$$

$$V_A = \left[\begin{array}{c|c} \overbrace{V_{R,BIG}}^k & \overbrace{V_{L,SMALL}}^{n-k} \end{array} \right]$$

End of Procedure

4 ASTREX Controller Design and Simulation

The Schur model reduction described in the earlier section was used. Actuator dynamics were not modeled as the actuator dynamics were very fast compared to the system dynamics. The 50th order system was reduced to an 8th order system. Using this reduced 8th order system, a Kalman Filter for state reconstruction was constructed. The 8th order system described by

$$\begin{aligned} \dot{x}_r &= A_r x_r + B_r u + Gw \\ y &= C_r x + D_r u + v \end{aligned} \tag{12}$$

where $A_r \in R^{8 \times 8}$, $B_r \in R^{8 \times 8}$, $C_r \in R^{9 \times 8}$ and $D_r \in R^{9 \times 8}$. Here w is the input disturbance and G is the input disturbance matrix. v is the measurement noise. The noise intensity matrices are defined as

$$\begin{aligned} E(Gw(t)w'(\tau)G') &= Q_{xx}\delta(t-\tau) \\ E(v(t)v'(\tau)) &= Q_{yy}\delta(t-\tau) \\ E(Gw(t)v'(\tau)) &= Q_{xy}\delta(t-\tau) \end{aligned}$$

where E is the expectation operator and δ is the Dirac delta function. w and v were assumed to be white noise with zero mean. input and output disturbances were assumed to be uncorelated, and hence the matrix Q_{xy} was taken to be the null matrix. For the simulation Q_{xx} and Q_{yy} were taken as identity matrices.

A linear optimal regulator was then designed under the assumption of full state feedback (obtained via the Kalman Filter). The quadratic cost function was of the form

$$J(x, u) = \int_0^{\infty} (x_r' R_{xx} x_r + u' R_{uu} u) dt$$

The design weighting matrices R_{xx} and R_{uu} were taken as identity matrices.

Using the the estimated states and the optimal regulator a Linear Quadratic Compensator was designed. This compensator designed for the reduced order system was then used to simulate the full order system. Simulation for regulation using initial conditions $x_i(0) = \frac{1}{w_i}$ results for the outputs for the secondary displacements in the x , y and z directions are shown in Figure 5 through Figure 13 are open loop step responses with the Proof Mass Actuators excited. Figure 14 through Figure 22 are closed loop step responses with the Proof Mass Actuators excited.

5 Conclusion

A Schur method for balanced Model Reduction was used. This reduction method overcomes the ill conditioning problems encountered in reduction procedures of most non-minimal models. Using the reduced order model, a Kalman filter to estimate the states and a linear optimal regulator was designed. Using the the estimated states and the optimal regulator a Linear Quadratic Compensator was designed. This compensator designed for the reduced order system was then used to simulate the full order system. Simulation for regulation using initial conditions

This study is an initial attempt to control the ASTREX structure. Only the flexible modes were considered. The model needs to be improved to include the rigid modes also. Non-linear coupling may also be a major factor if large angle maneuvers are to be considered. Future work will include models that have the rigid modes. Optimal controllers will be designed along the lines described in [4] [11] [12] and [10] will be designed and implemented.

6 Acknowledgment

The author wishes to express his sincere thanks to Dr. Alok Das and Mr. Kevin Slimak for the opportunity which they provided and their support during the course of this research. It is also pleasure to thank Mr. Joel Berg, Dr. Nandu Abhyankar and Mr. Monty Smith for many useful discussions.

References

- [1] Abhyankar, N. S. and Berg, J. L., "ASTREX Model Information: Supplement to astabed.mat file", *AFAL, Philips Lab Report*, August 1991.
- [2] Alok Das, "Large Angle Maneuver Experiments in Ground-Based Laboratories", *AIAA Progress Report in Astronautics and Aeronautics: Mechanics and Control of Large Flexible Structures*, Editor: John Junkins, Vol. 129, pp491-506, 1990.
- [3] Alok Das, Berg, J. L., Norris, G. A., Cossey, D. F., Strange, J. T. and Schlaegel, W. T., "ASTREX- A Unique Test Bed for CSI Research", *Proceedings of the 29th. IEEE Conference on Decision and Control*, Honolulu, Hawaii, pp 2018-2023, 1990.
- [4] Glover, K. and Doyle, J., "State-space formulae for all stabilizing controllers that satisfy an H_∞ -norm bound and relations to risk sensitivity", *System and Control Letters*, 11, pp 167-162, 1988.
- [5] Hu, A., Skelton, R. E., Norris, G. A. and Cossey, D. F., "Selection of Sensors and Actuators with Applications to the ASTREX Facility", *4th NASA/DOD CSI Conference*, Orlando, FL, Nov. 1990.
- [6] Moore, B. C., "Principal component analysis in linear systems: controllability, observeability, and model reduction," *IEEE Transactions on Automatic Control*, AC-26, pp 17-31, 1981.
- [7] Ramakrishnan, J., Byun, K. W., and Skelton, R., "ASTREX Controller Design: OVC and OCC Approach", *4th NASA/DOD CSI Conference*, Orlando, FL, Nov. 1990.
- [8] Rao, V., Ngo, K., Berg, J. L. and Das A., "Derivation of Reduced Order Models for Large Flexible Structures", *AIAA Guidance, Navigation and Control Conference*, New Orleans, LA, 1991.
- [9] Safonov, M. G. and Chiang, R. Y., "A Schur Method for Balanced Model Reduction", *IEEE Conference on Decision and Control, Tampa, Florida*, pp 1036-1040, 1989.
- [10] Sparks, A. G., Yeh, H. H., Banda, S. S., "Mixed H_2 and H_∞ Optimal Robust Control Design", *Optimal Control, Applications and Methods*, Vol. 11, pp 307-325, 1990.
- [11] Vidyasagar, M. and Kimura, H., "Robust Controllers for Uncertain Linear Multivariable Systems", *Automatica*, Vol 22, No. 1, pp 85-94, 1986.

- [12] Zhou, K. and Khargonekar, P., "An algebraic Ricatti equation approach to H_∞ optimization", *System and Control Letters*, 11, pp 85-91, 1988.

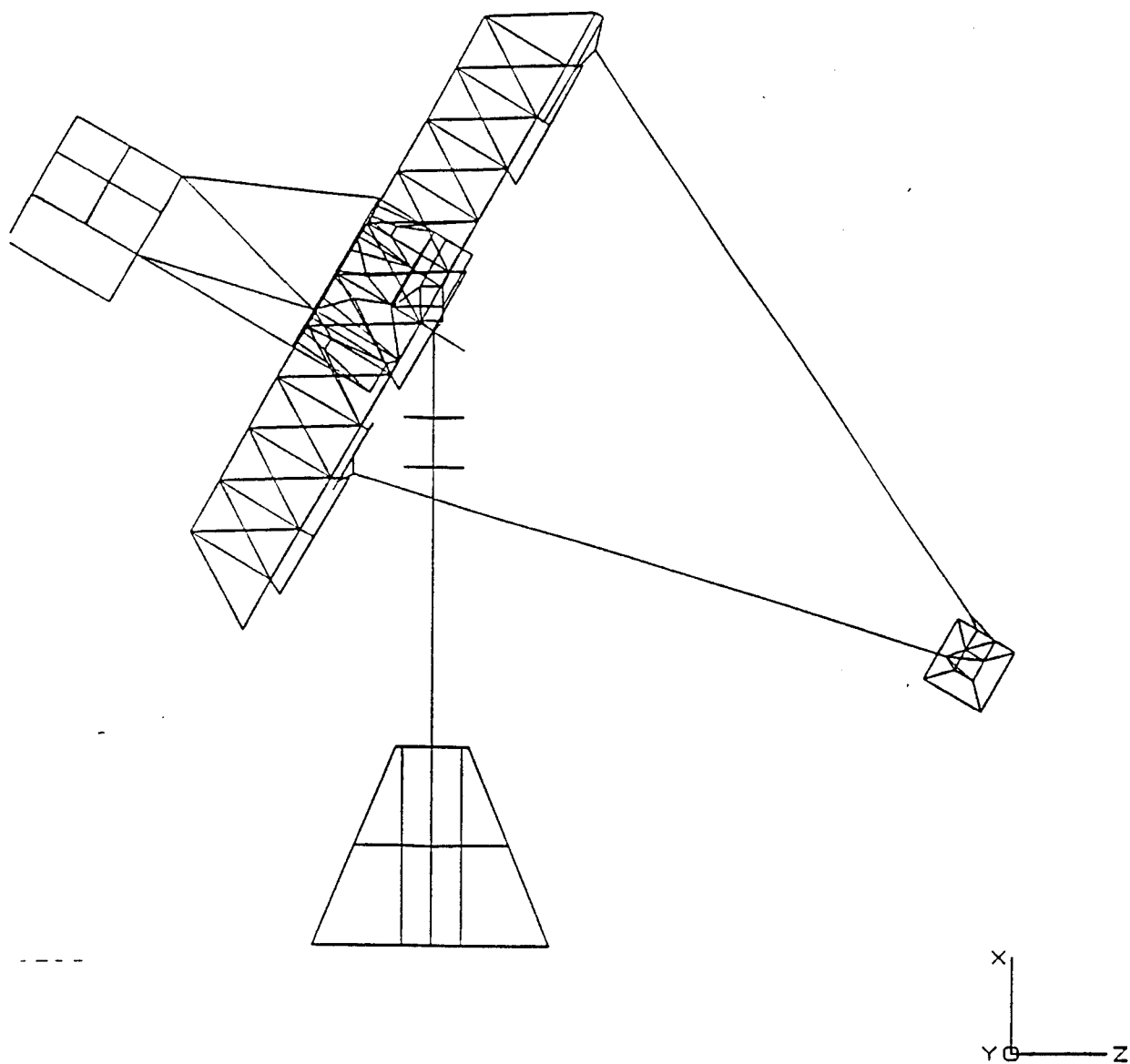


Figure 1: ASTREX Structures Side View

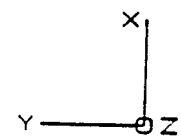
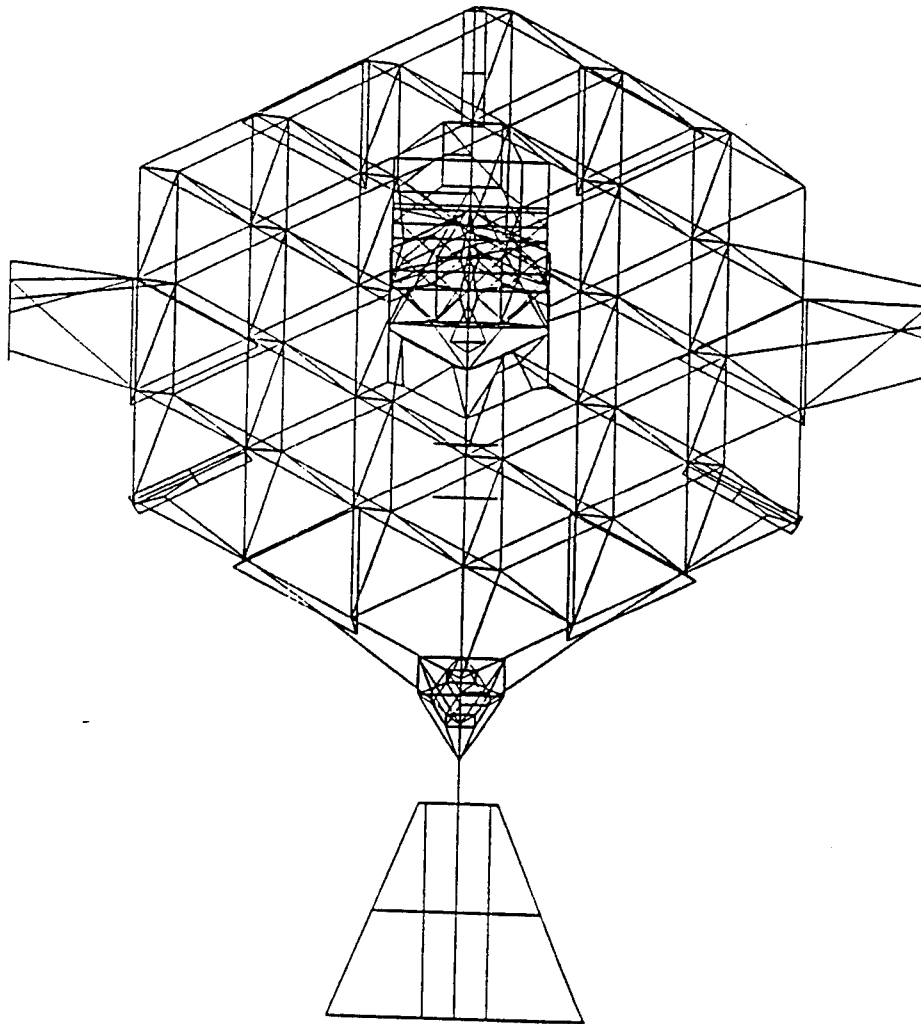


Figure 2: ASTREX Structures Front View

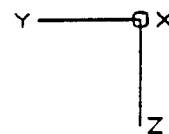
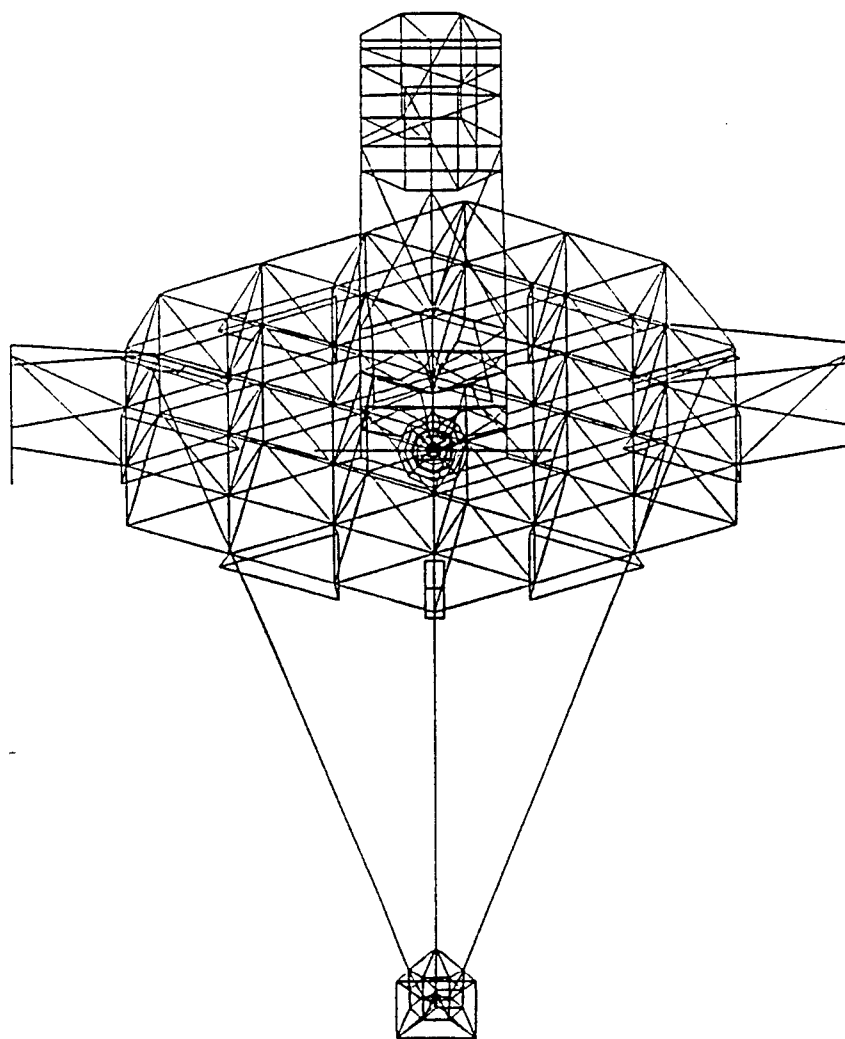


Figure 3: ASTREX Structures Top View

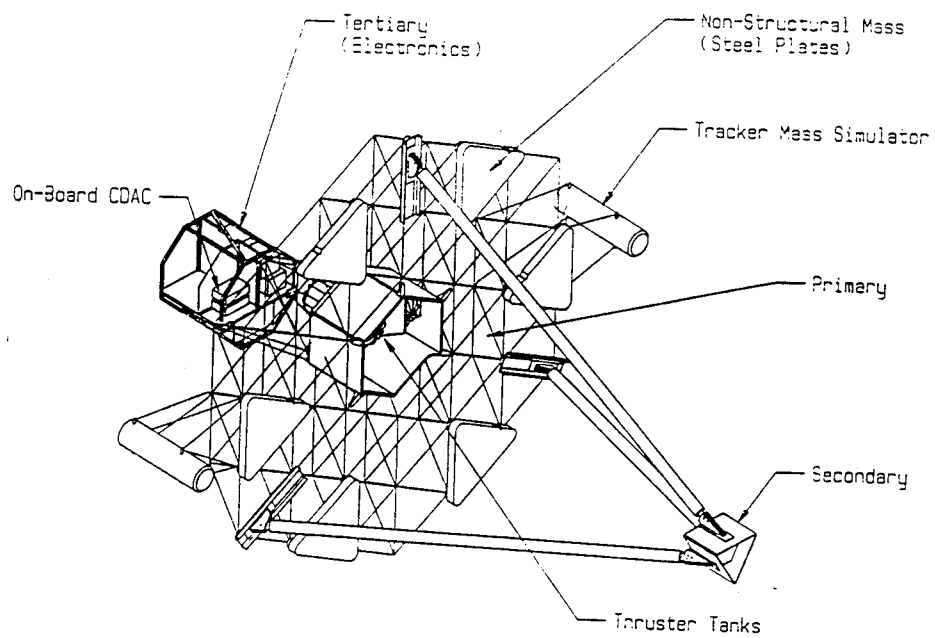


Figure 4: ASTREX Accelerometers Locations

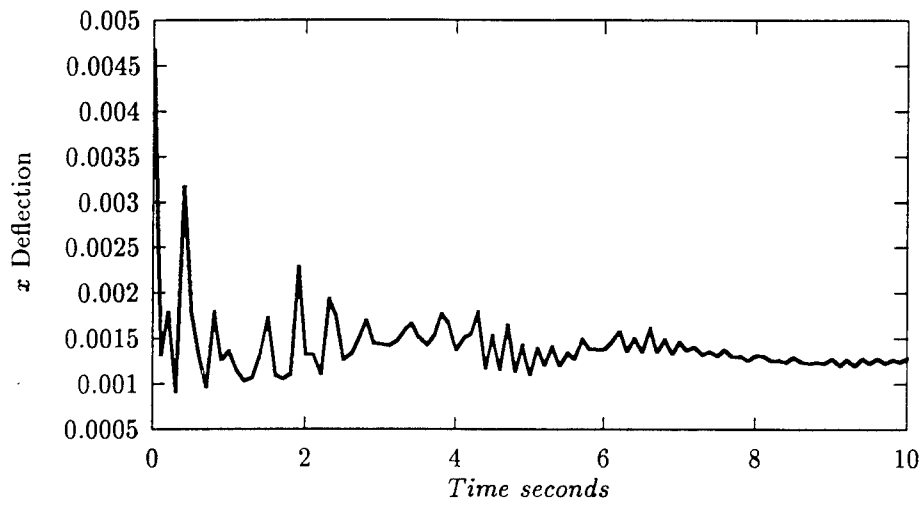


Figure 5: Open Loop: Secondary Deflection in x

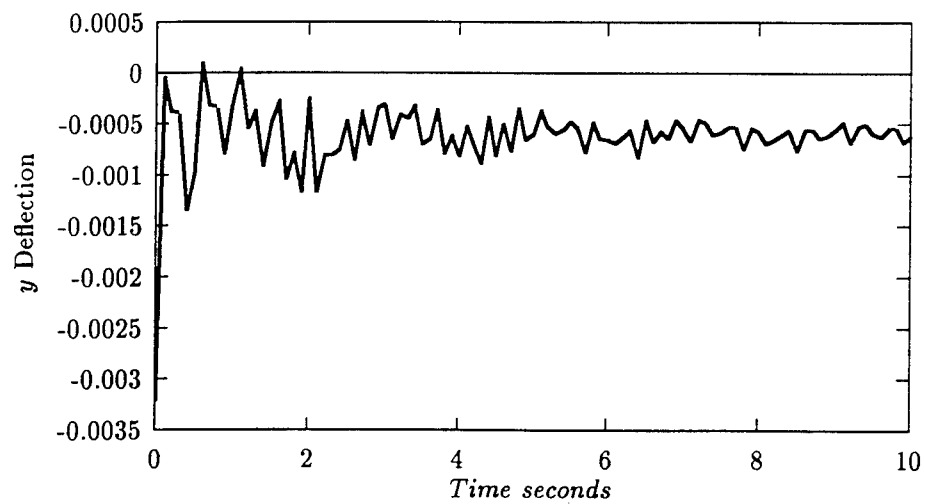


Figure 6: Open Loop: Secondary Deflection in y

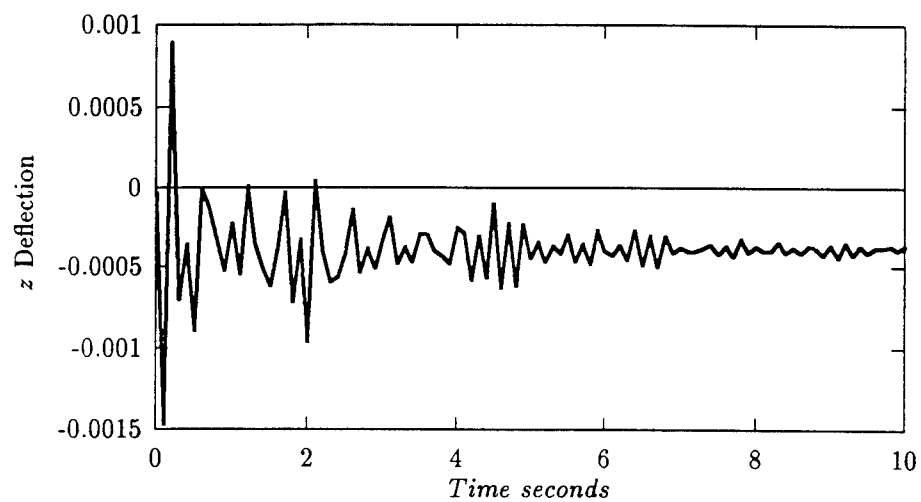


Figure 7: Open Loop: Secondary Deflection in z

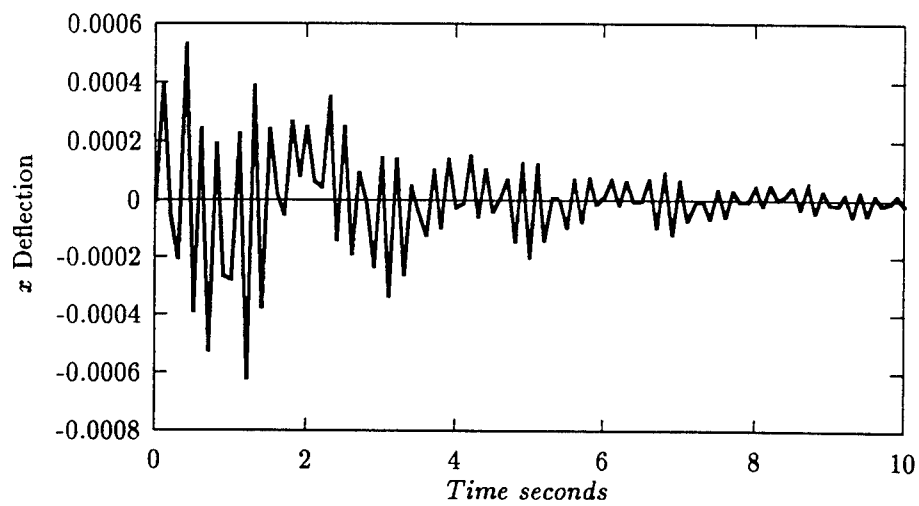


Figure 8: Open Loop: Secondary Deflection in x

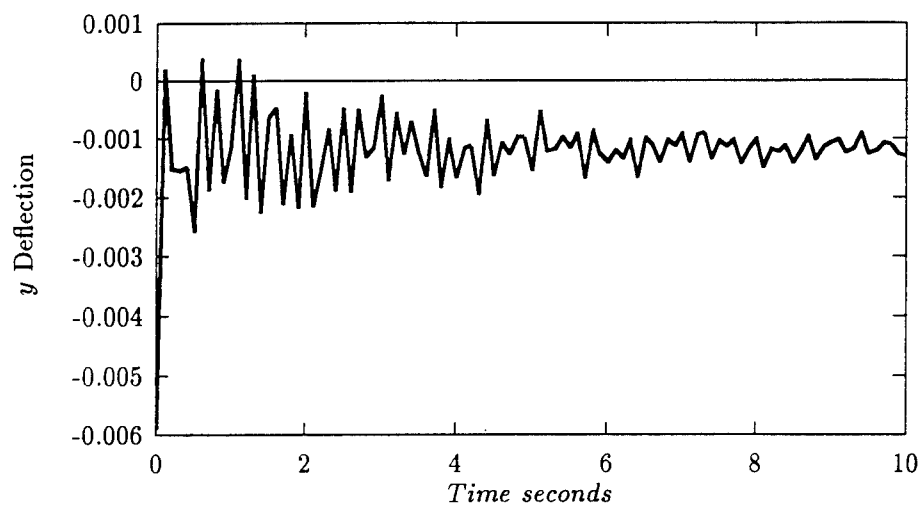


Figure 9: Open Loop: Secondary Deflection in y

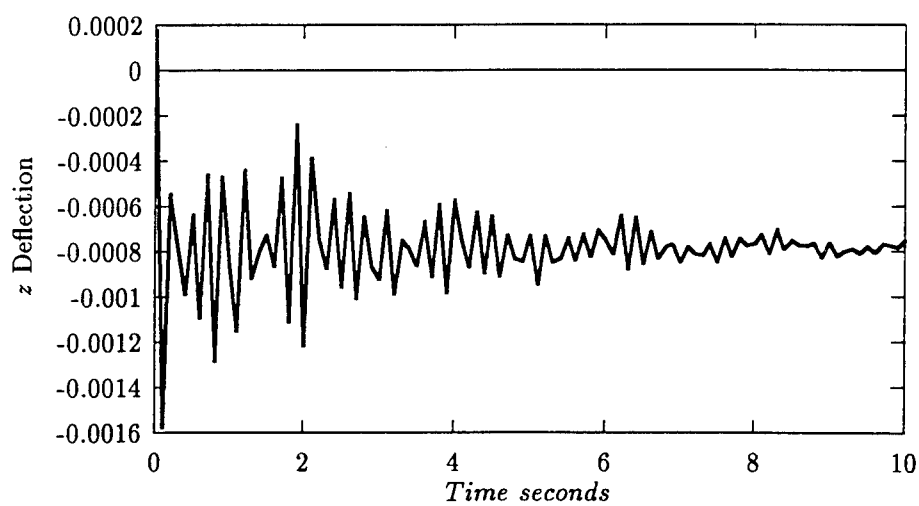


Figure 10: Open Loop: Secondary Deflection in z

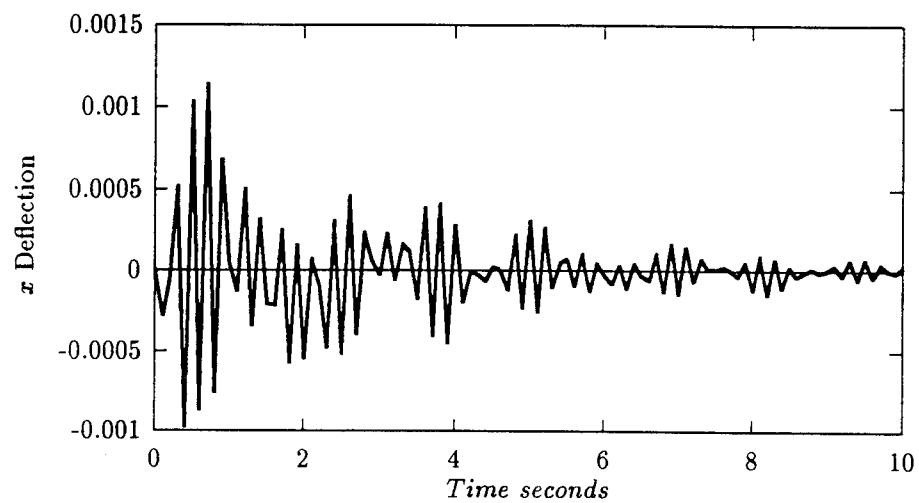


Figure 11: Open Loop: Secondary Deflection in x

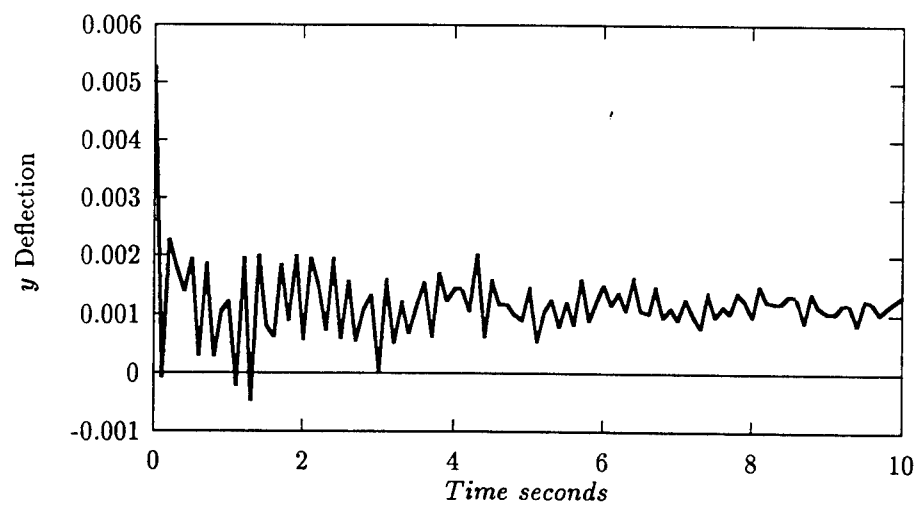


Figure 12: Open Loop: Secondary Deflection in y

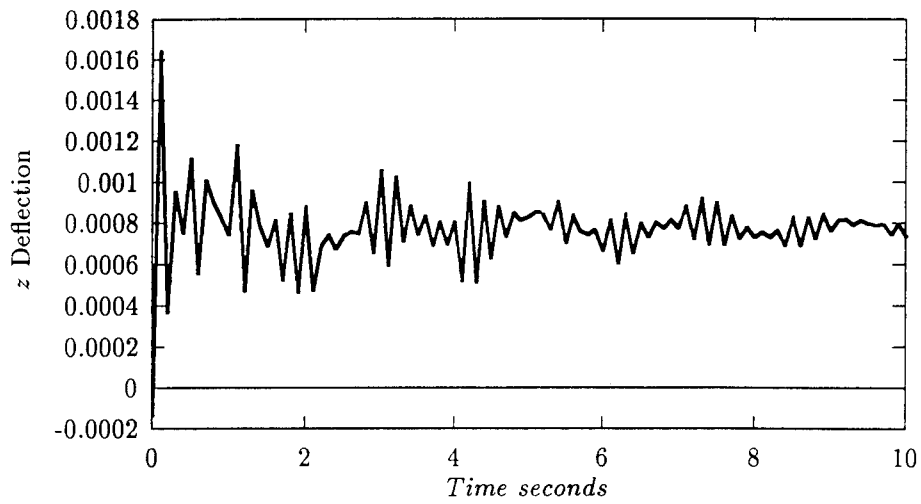


Figure 13: Open Loop: Secondary Deflection in z

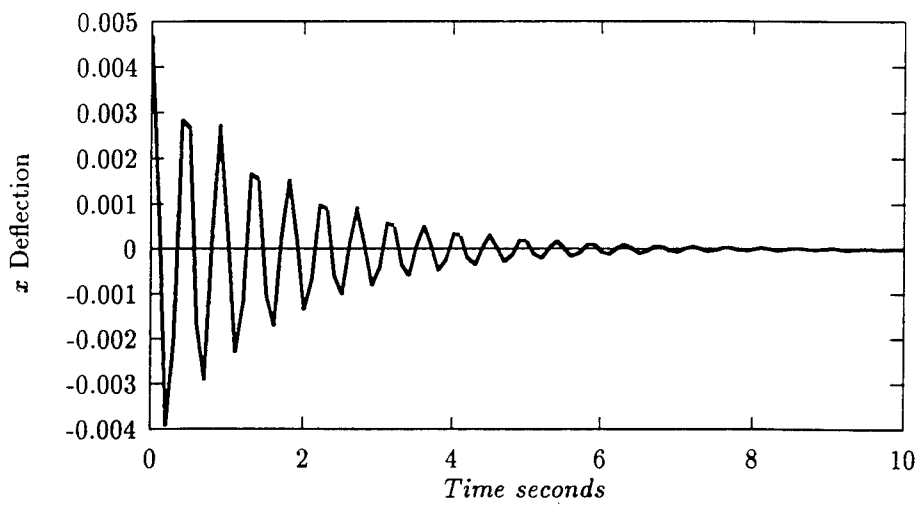


Figure 14: Closed Loop: Secondary Deflection in x

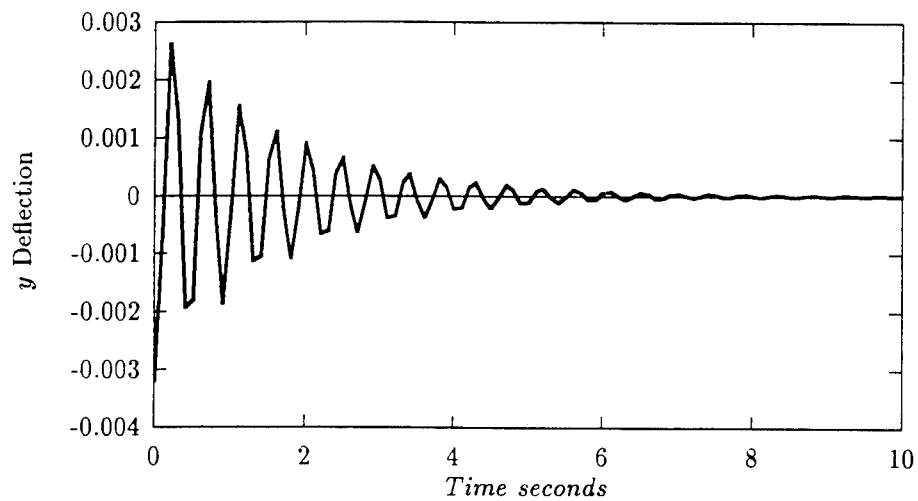


Figure 16: Closed Loop: Secondary Deflection in y

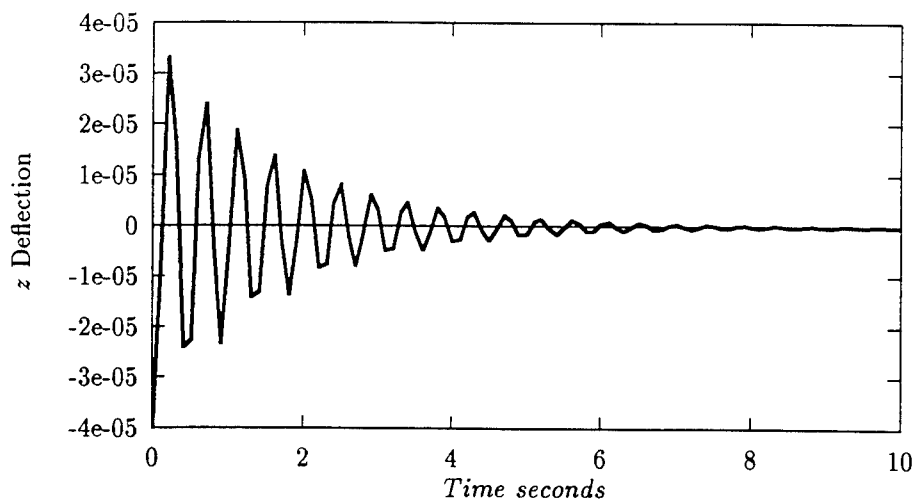


Figure 17: Closed Loop: Secondary Deflection in z

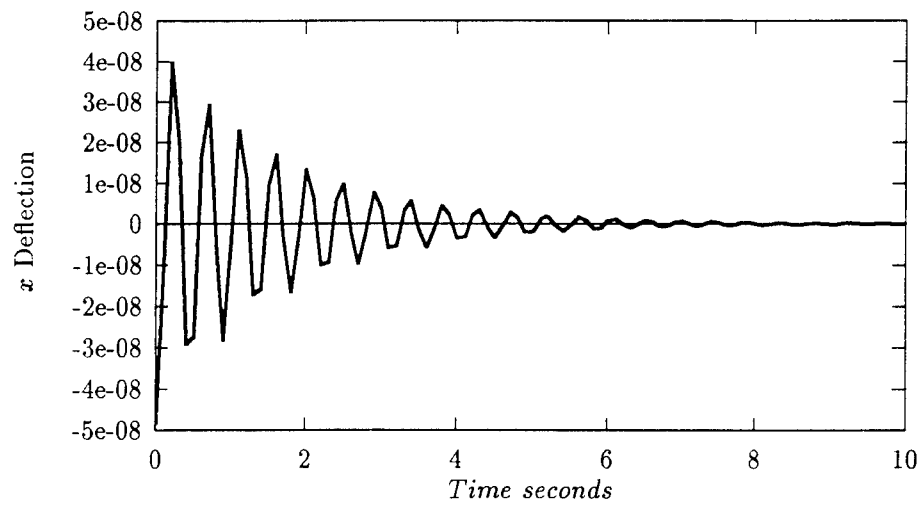


Figure 18: Closed Loop: Secondary Deflection in x

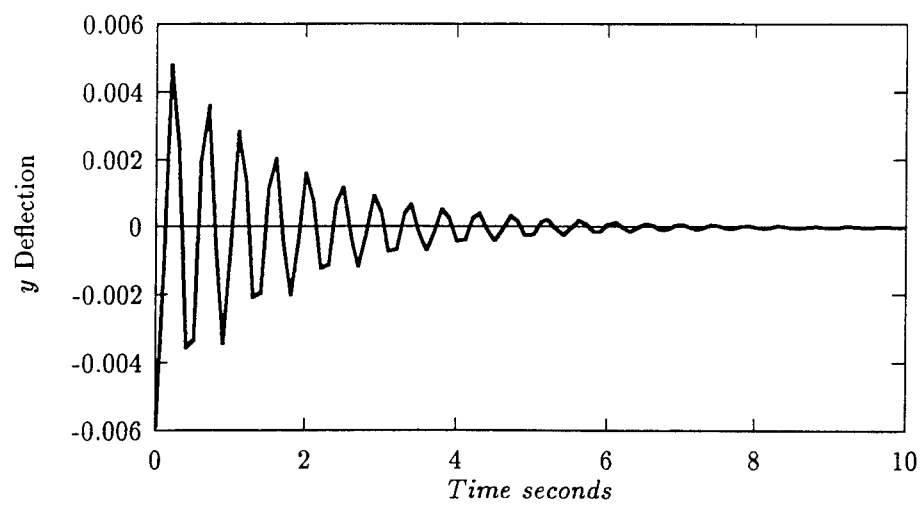


Figure 19: Closed Loop: Secondary Deflection in y

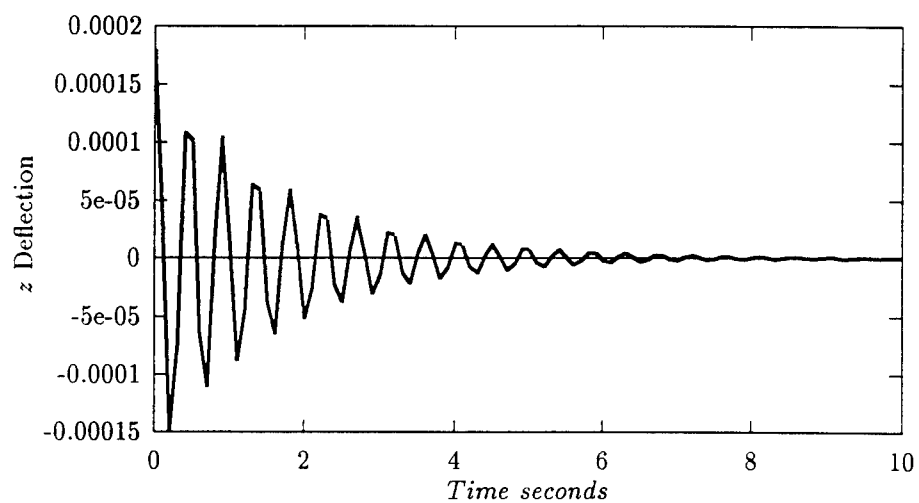


Figure 20: Closed Loop: Secondary Deflection in z

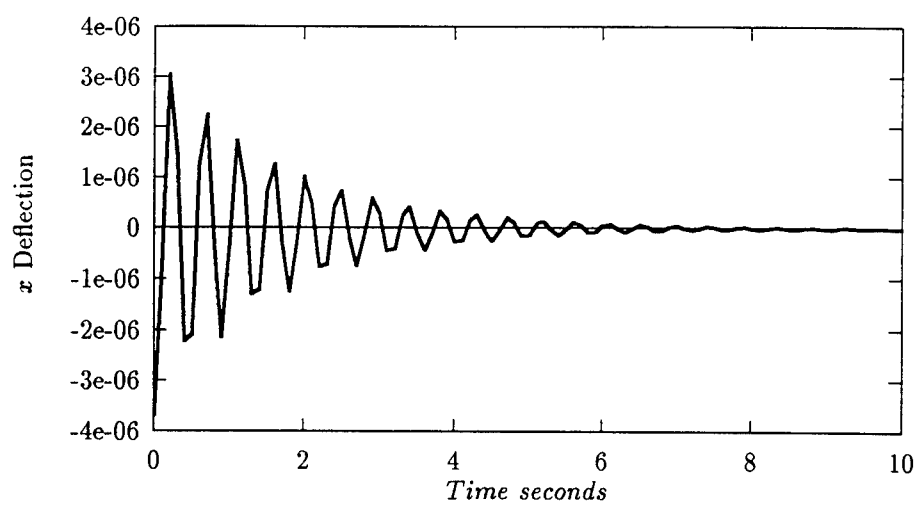


Figure 21: Closed Loop: Secondary Deflection in x

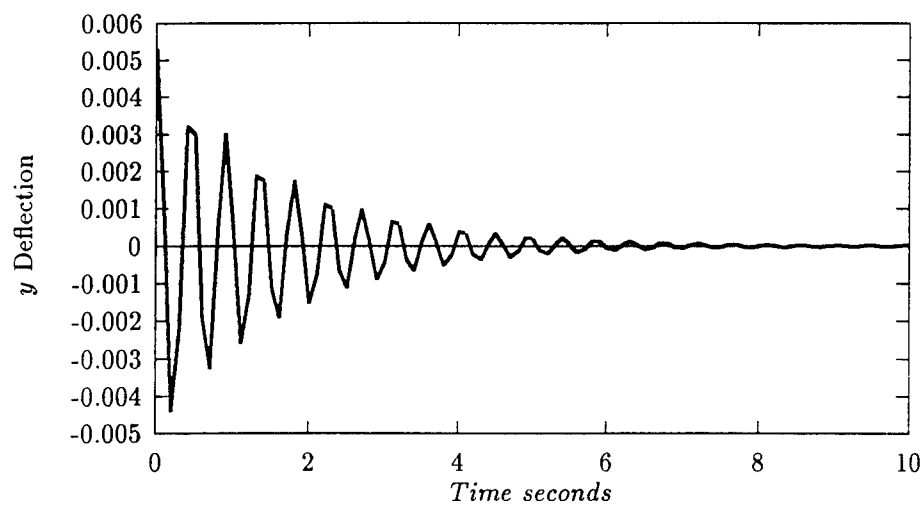


Figure 23: Closed Loop: Secondary Deflection in y

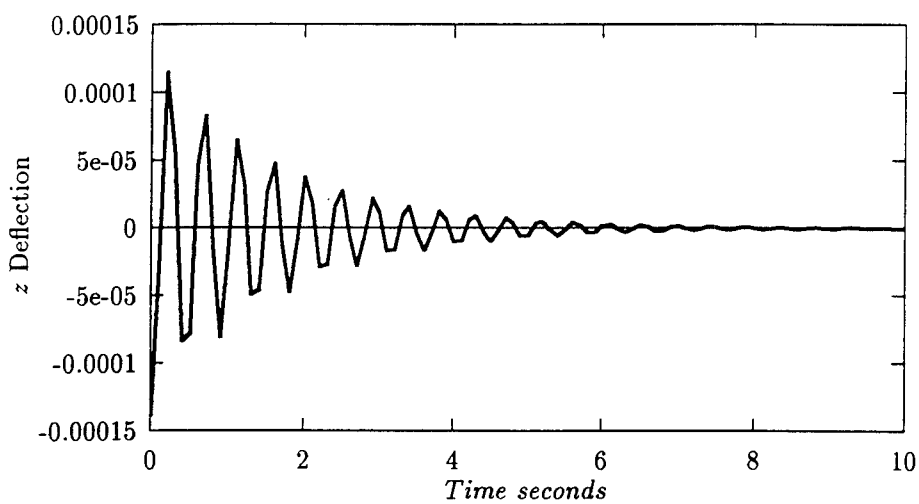


Figure 24: Closed Loop: Secondary Deflection in z

**Theoretical Study Concerning Instabilities Excited in the Ionosphere by the
Obliquely Transmitting Powerful Radio Waves**

(Final Report for AFOSR Research Initiation Program Subcontract 92-59 from the R & D
Laboratory)

S.P. Kuo, Principal Investigator

Joe Huang

Weber Research Institute and Department of Electrical Engineering
Polytechnic University, Route 110, Farmingdale, NY 11735

December 1992

Summary

Using the theory of characteristics, a ray tracing code has been developed for both o-mode and x-mode electromagnetic waves in a magnetized plasma to determine the locations of the caustics and any other locations where the rays converge locally. Near the caustics, the electric field swells (i.e. the electric field profile is an Airy function), and near those locations where the field converges locally, the electric field can also be much higher than that calculated by the $1/r$ rule for the far field radiation from the ground. It is then expected that parametric instability may occur at these locations during the oblique heating ionospheric modification experiments. For the present work, a linear density profile of the ionosphere is assumed. Our numerical results clearly identify the locations of the caustics. It is shown, as expected, that the caustics location for the x-mode is lower than that calculated from the unmagnetized plasma case, while the caustics location for the o-mode is higher. It is also found that for the case of o-mode heater wave with initial propagation angle less than 10° , rays converge locally near the locations where the o-mode waves suddenly change direction and bend the ray paths upward. This feature of locally convergent rays is pertinent to the o-mode heater waves only for the present simple model. Hyperbolic or even more complicated density profile may be used in the future for more realistic modelling of the ionosphere.

Parametric excitation of lower hybrid decay mode together with upper hybrid sideband by an obliquely incident HF pump is then studied. The conditions for the instability, including the frequency range, the elevation angle and the threshold field intensity of the pump are determined. The results show that the instability criteria can be satisfied only when the elevation angle is large enough (e.g. $> 75^\circ$).

The filamentation instability of the obliquely propagating heaters is also analyzed for both o-mode and x-mode polarizations. A general dispersion relation is derived including the effects of

magnetic field and collisions, and the nonlinear effects of ponderomotive force, thermal focusing force and the beating currents. Threshold fields and growth rates are evaluated quantitatively. It is shown that the threshold field of x-mode pump is quite high exceeding 1 V/m. On the other hand, the threshold field of the o-mode pump decreases from several hundred millivolts to a few millivolts for scale lengths of the irregularities ranging from tens of meters to a few kilometers. Moreover, the growth time is found to be relatively insensitive to the scale length and is of the order of a few seconds. Thus, it is likely to have broad scale density irregularities generated by an obliquely transmitting o-mode heater in the caustic region.

I. Introduction

Heating and modification of the ionosphere by high power radio waves transmitted from various ground heating facilities have been actively pursued during the past 30 years. A large number of unexpected phenomena have been observed in addition to the originally anticipated electron temperature and density change. These phenomena including wideband attenuation of the ionosonde signal¹, artificially induced Spread-F¹, large and small-scale irregularities, generation of geometric pulsation^{2,3}, enhancement of fluxes of suprathermal electrons⁴, stimulated electromagnetic emission⁵, plasma line overshoot^{6,7} and the expansion of its originating altitude interval⁸, height difference between the natural line and HFPLs⁹, and asymmetric plasma lines having anomalously upshifted frequencies¹⁰, etc. Most of these phenomena are believed to be attributed to the plasma turbulence excited by the HF heater via parametric instabilities directly or indirectly¹¹⁻¹⁷. In other words, parametric instabilities plays a primary role in the HF heating of the ionosphere^{18,19}, they provide effective channels to convert EM wave energy into electrostatic plasma waves of high and low frequencies which are trapped inside the plasma and cause much more significant perturbation to the plasma than the perturbation caused directly by the original EM heater.

So far these phenomena have been observed while the heater waves are transmitted vertically and polarized at o-mode. It is consistent with the theoretical analyses which show that the frequency and wavevector matching condition as well as the threshold condition of various parametric instabilities can be satisfied near the reflection height of the vertically incident o-mode heater. By contrast, it was thought that the matching conditions for similar parametric instabilities could not be satisfied in the oblique ionospheric heating processes.

The ionospheric heating by obliquely incident heaters has also been investigated experimentally during the past²⁰⁻²³, however, so far there is no report about the observation of any

drastic effect. On the other hand, oblique heating has the advantage of potentially enlarging the modification region of the ionosphere. Moreover, high power radar and communication systems, in general, operate at oblique incidence. In this aspect, it is still of great interest in examining the potential effects of an obliquely incident heater²⁴ which, even though, was believed not being able to produce the same effects as a vertically incident one. Especially, it is noted that near the reflection height, the obliquely transmitted o-mode heater still has a finite wave number. Thus, the wave field of the o-mode pump does not orientate to align with the geomagnetic field and exists a perpendicular wave field component even in the region near the reflection height. This wave field component which does not exist in the vertical incidence case could potentially become a driving force to excite hybrid plasma modes via parametric instabilities²⁵ and result with distinctively different modification effects to the ionosphere.

In this work, the conditions for the excitation of parametric instability of hybrid waves and density irregularities via filamentation instability of the HF heater are examined for the oblique ionospheric heating. These include the frequency range, the elevation angle, and the threshold field intensity of the pump. The threshold field is expected to be a function of the wave frequency, the elevation angle, the magnetic dip angle, the wavenumber of the decay mode, and the collision and plasma frequency. Following these conditions, one can selectively modify the ionospheric region with the obliquely transmitted heater, or estimate the perturbations caused by the feedback of the ionosphere to some radar and communication systems.

Since the obliquely transmitted heater has a larger angular spread (i.e. smaller antenna gain) and a longer propagation path to its reflection height. The field intensity near the reflection height is believed to be much smaller than that of the vertical incidence case which is also enhanced by the swelling effect. On the other hand, the obliquely propagating spreading rays may focus themselves after the reflection height in a so called "caustic region" slightly below their reflection height. In the caustic region the field intensity may be enhanced to exceed the instability

thresholds. Therefore, the first research topic presented in the following will be ray tracing analysis to demonstrate the caustic phenomenon and to determine the caustic region. It will be the region for experimentalists to look for the instability signature.

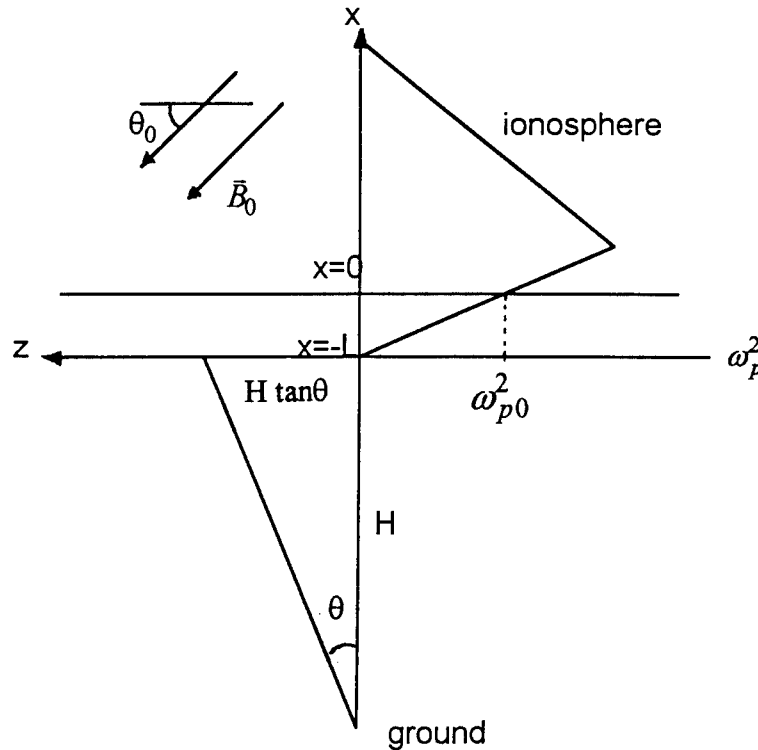
II. Ray Tracing of Obliquely Propagating HF Heater in the Ionosphere

Using the theory of characteristics, a ray tracing code is developed for both o-mode and x-mode electromagnetic waves in a magnetized plasma for determining the locations of the caustics and any other locations where the waves focus locally.

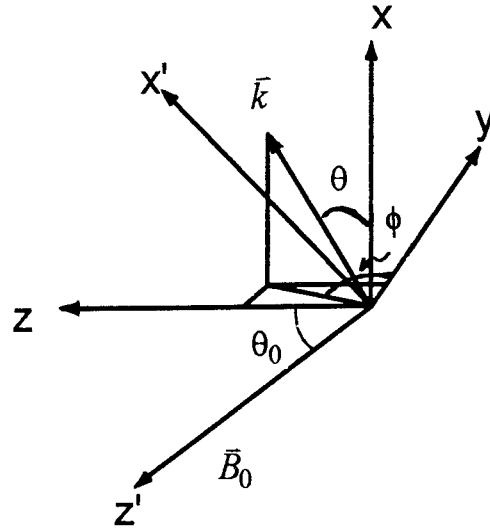
A. Configuration and Model

1. A linear density profile for the bottom side of the ionosphere is modeled

We consider a horizontally stratified ionosphere having a scale length L . Thus, the background electron density is represented by $n_0(x) = n_0(1 + x / L)$, where x is the vertical coordinate and $n_0 = n_0(0)$ is the electron density at a reference plane located at the height $H+L$ from the ground. Below the height H , a free space is assumed and, thus, the ray trajectory from the source (heater) location to $x = -L$ plane is a straight line. Shown in the Figure is a schematic of the model, where $\omega_p^2 = \omega_{p0}^2(1 + x / L)$, θ_0 is the geomagnetic field dip angle and $\theta_i = \pi / 2 - \theta$ is the incident elevation angle of the HF heater wave.



2. Coordinate system



For the coordinate system chosen above, the following relationships can be identified:

$$k'_x = k_x \cos \theta_0 + k_z \sin \theta_0$$

$$k'_z = -k_x \sin \theta_0 + k_z \cos \theta_0$$

and

$$k'^2_{\perp} = k'^2_x + k'^2_y = k^2 [(\cos \theta \cos \theta_0 + \sin \theta \sin \theta_0 \sin \phi)^2 + \sin^2 \theta \cos^2 \phi]$$

$$k'^2_z = k^2 (-\cos \theta \sin \theta_0 + \sin \theta \cos \theta_0 \sin \phi)^2$$

B. Ray Trajectory

For a wave with dispersion relation $\omega = \omega(\vec{k}, \vec{r}, t)$ in an weakly inhomogeneous plasma, the rate equations of the ray trajectory are found from the theory of characteristics to be:

$$\frac{d}{dt} \vec{r} = \nabla_{\vec{k}} \omega(\vec{k}, \vec{r}, t)$$

and

$$\frac{d}{dt} \vec{k} = -\nabla \omega(\vec{k}, \vec{r}, t)$$

In an unmagnetized plasma, the dispersion relation for an electromagnetic wave is known to be $\omega^2 = \omega_p^2 + k^2 c^2$. The ray trajectory equations for the assumed linear density profile is:

$$\frac{d}{dt} \vec{r} = \frac{\vec{k} c}{\omega}$$

$$\frac{d}{dt} k_x = -\frac{\omega_{p0}^2}{2\omega L}$$

$$\frac{d}{dt} k_y = 0$$

$$\frac{d}{dt} k_z = 0$$

Hence, the ray trajectory can be determined analytically²⁶ to be.

$$x - x_0 = -(Lc / \omega_{p0}^2)(k_x^2 - k_{x0}^2)$$

$$y - y_0 = (k_{y0} c / \omega) t$$

$$z - z_0 = (k_{z0} c / \omega) t$$

where (x_0, y_0, z_0) and (k_{x0}, k_{y0}, k_{z0}) are the initial position and the initial wave vector of the ray, and x and k_x are also related through the dispersion relation $\omega^2 = \omega_{p0}^2(1 + x/L) + (k_{x0}^2 + k_{y0}^2 + k_{z0}^2)c^2$.

When the geomagnetic field is included, the ray trajectory equations are complicated and two differently polarized waves should be considered separately.

C. O-mode heater wave

1. Dispersion relation

$$\omega^3 + \Omega_e \omega^2 - (\omega_p^2 + k^2 c^2) \omega - \Omega_e (k_{\perp}^2 \omega_p^2 / k^2 + k^2 c^2) = 0$$

2. Ray trajectory equations

$$\frac{d}{dt} x = 2c^2 [(\omega + \Omega_e) k_x - \frac{1}{2} \Omega_e (\frac{\omega_p^2}{k^4 c^2}) a_1] / f$$

$$\frac{d}{dt} y = 2c^2 [(\omega + \Omega_e) k_y + \frac{1}{2} \Omega_e (\frac{\omega_p^2}{k^4 c^2}) k_y a_2] / f$$

$$\frac{d}{dt} z = 2c^2 [(\omega + \Omega_e) k_z - \frac{1}{2} \Omega_e (\frac{\omega_p^2}{k^4 c^2}) a_3] / f$$

$$\frac{d}{dt} k_x = -(\frac{\omega_{p0}^2}{L}) [(\omega + \Omega_e) - \frac{\Omega_e^2}{2k^2} a_2] / f$$

$$\frac{d}{dt} k_y = 0 = \frac{d}{dt} k_z$$

where

$$f = 3\omega^2 + 2\omega\Omega_e - (\omega_p^2 + k^2 c^2)$$

and

$$a_1 = k_x k_y^2 (1 - \cos 2\theta_o) - 2k_x k_z^2 \cos 2\theta_o + k_z (k_x^2 - k_y^2 - k_z^2) \sin 2\theta_o$$

$$a_2 = k_x^2 (1 - \cos 2\theta_o) + k_z^2 (1 + \cos 2\theta_o) - 2k_x k_z \sin 2\theta_o$$

$$a_3 = k_z k_y^2 (1 + \cos 2\theta_o) + 2k_z k_x^2 \cos 2\theta_o - k_x (k_x^2 + k_y^2 - k_z^2) \sin 2\theta_o$$

D. X-mode heater wave

1. Dispersion relation

$$\omega^5 - \Omega_e \omega^4 - (2\omega_p^2 + \Omega_e^2 + k^2 c^2) \omega^3 + \Omega_e [(1 + k_\perp'^2 / k^2) \omega_p^2 + \Omega_e^2 + k^2 c^2] \omega^2 + [(\omega_p^2 + \Omega_e^2)(k^2 c^2 + k_z'^2 \omega_p^2 / k^2) + k_\perp'^2 \omega_p^4 / k^2] \omega - \Omega_e [k^2 c^2 (\omega_p^2 + \Omega_e^2) + k_\perp'^2 \omega_p^4 / k^2] = 0$$

2. Ray trajectory equations

$$\frac{d}{dt} x = 2c^2 [(\omega - \Omega_e)(\omega^2 - \omega_p^2 - \Omega_e^2) k_x + \frac{1}{2} \Omega_e (\frac{\omega_p^2}{k^4 c^2})(\omega^2 - \omega \Omega_e - \omega_p^2) a_1] / g$$

$$\frac{d}{dt} y = 2c^2 [(\omega - \Omega_e)(\omega^2 - \omega_p^2 - \Omega_e^2) k_y - \frac{1}{2} \Omega_e (\frac{\omega_p^2}{k^4 c^2})(\omega^2 - \omega \Omega_e - \omega_p^2) k_y a_2] / g$$

$$\frac{d}{dt} z = 2c^2 [(\omega - \Omega_e)(\omega^2 - \omega_p^2 - \Omega_e^2) k_z + \frac{1}{2} \Omega_e (\frac{\omega_p^2}{k^4 c^2})(\omega^2 - \omega \Omega_e - \omega_p^2) a_3] / g$$

$$\frac{d}{dt} k_x = -(\frac{\omega_{p0}^2}{L}) [(\omega - \Omega_e)(2\omega^2 - 2\omega_p^2 - k^2 c^2) + \frac{1}{2k^2} \Omega_e (\omega^2 - \omega \Omega_e - 2\omega_p^2) a_2] / g$$

$$\frac{d}{dt} k_y = 0 = \frac{d}{dt} k_z$$

where

$$g = 5\omega^4 - 4\Omega_e \omega^3 - 3(2\omega_p^2 + \Omega_e^2 + k^2 c^2) \omega^2 + 2\Omega_e (2\omega_p^2 + \Omega_e^2 + k^2 c^2) \omega + \omega_p^4 + k^2 c^2 (\omega_p^2 + \Omega_e^2) - \omega_p^2 \Omega_e (\omega - \frac{1}{2} \Omega_e) a_2 / k^2$$

and a_1, a_2 and a_3 are defined the same as those given in the previous subsection C.

E. Numerical results

The calculated results for the ray equations are plotted using the following parameters:

$$\begin{aligned}\theta_0 &= 45^\circ \\ L &= 50 \text{ km} \\ H &= 250 \text{ km} \\ \omega_{p0} &= 3.5 \Omega_e (1 + x/L)^{1/2} \\ \omega_0 &= 5.5 \Omega_e \\ \Omega_e &= 1.1 \times 10^6 \text{ } 2\pi\end{aligned}$$

In Figures 1 and 2 the ray trajectories of the o-mode and x-mode heater waves propagating in the meridian plane (i.e. $\phi = \pi/2$) for initial propagation angle spread from 10° to 45° with respect to the vertical axis are shown. As a reference, the ray trajectories for the unmagnetized plasma case are also plotted and shown in Figure 3. Moreover, the case that the o-mode heater wave having an initial propagation angle spread from 1° to 10° is also examined. The result is plotted in Figure 4 which indicates the existence of locally convergent rays in addition to caustics for the o-mode heating case.

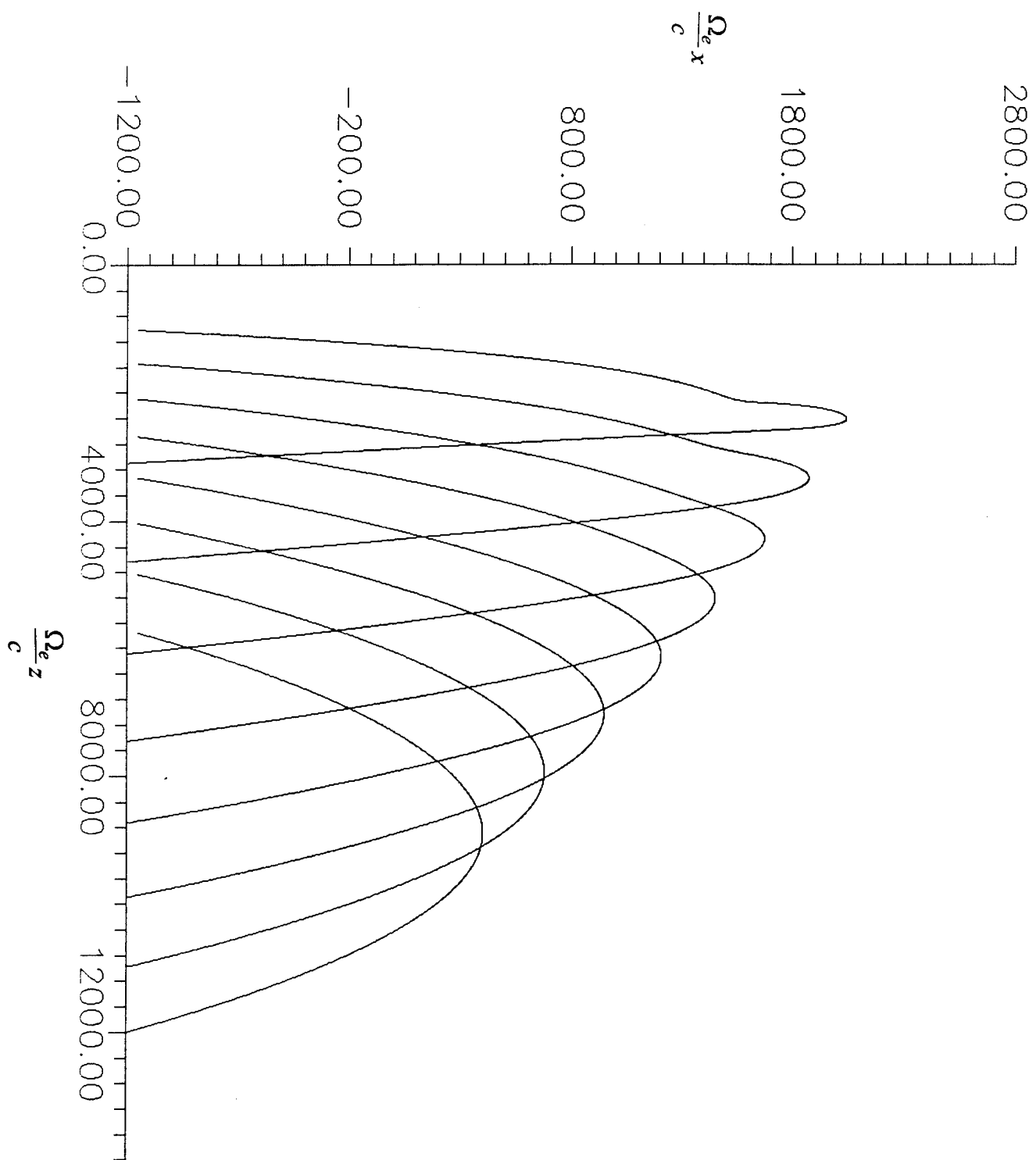


Figure 1

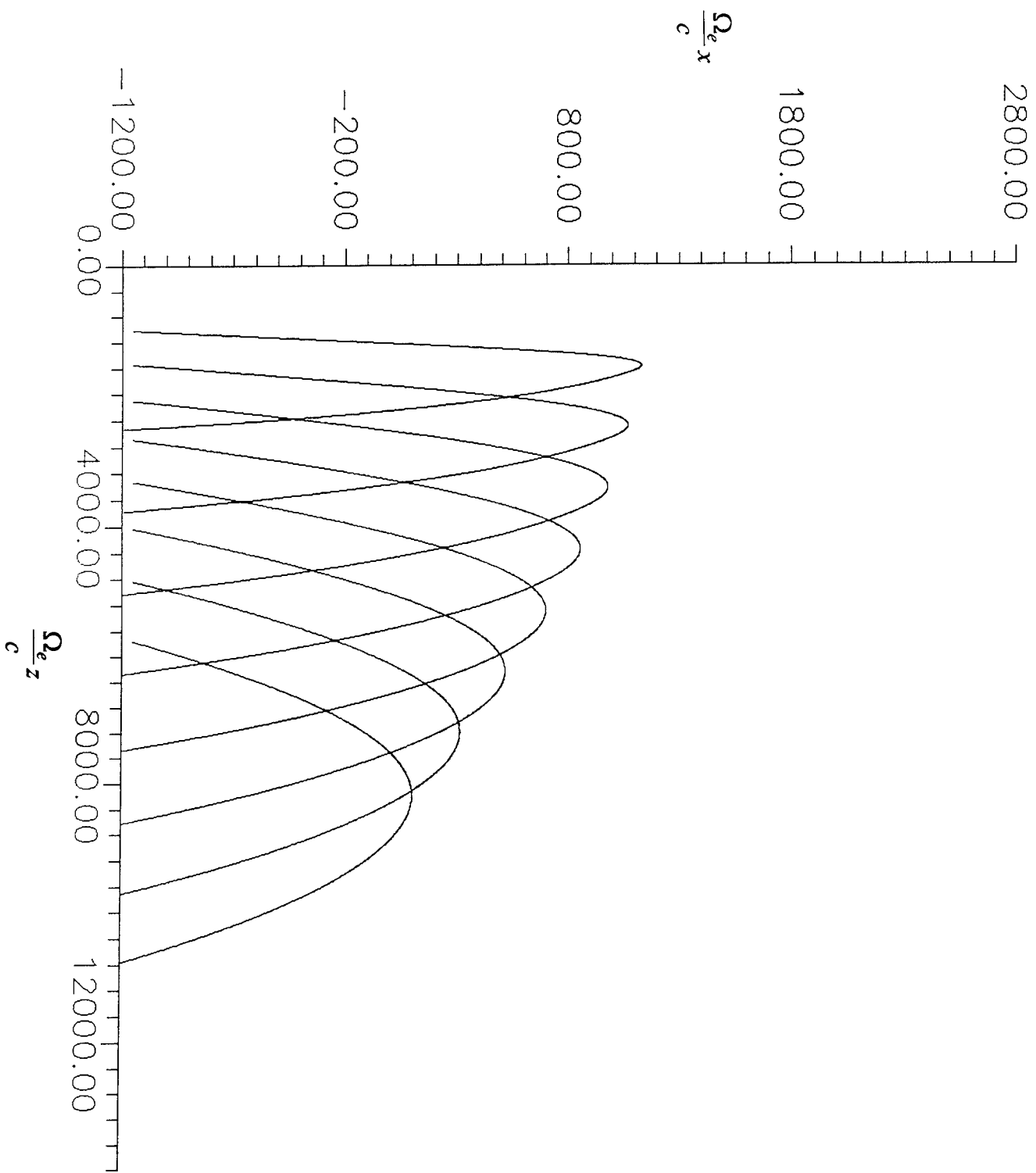


Figure 2

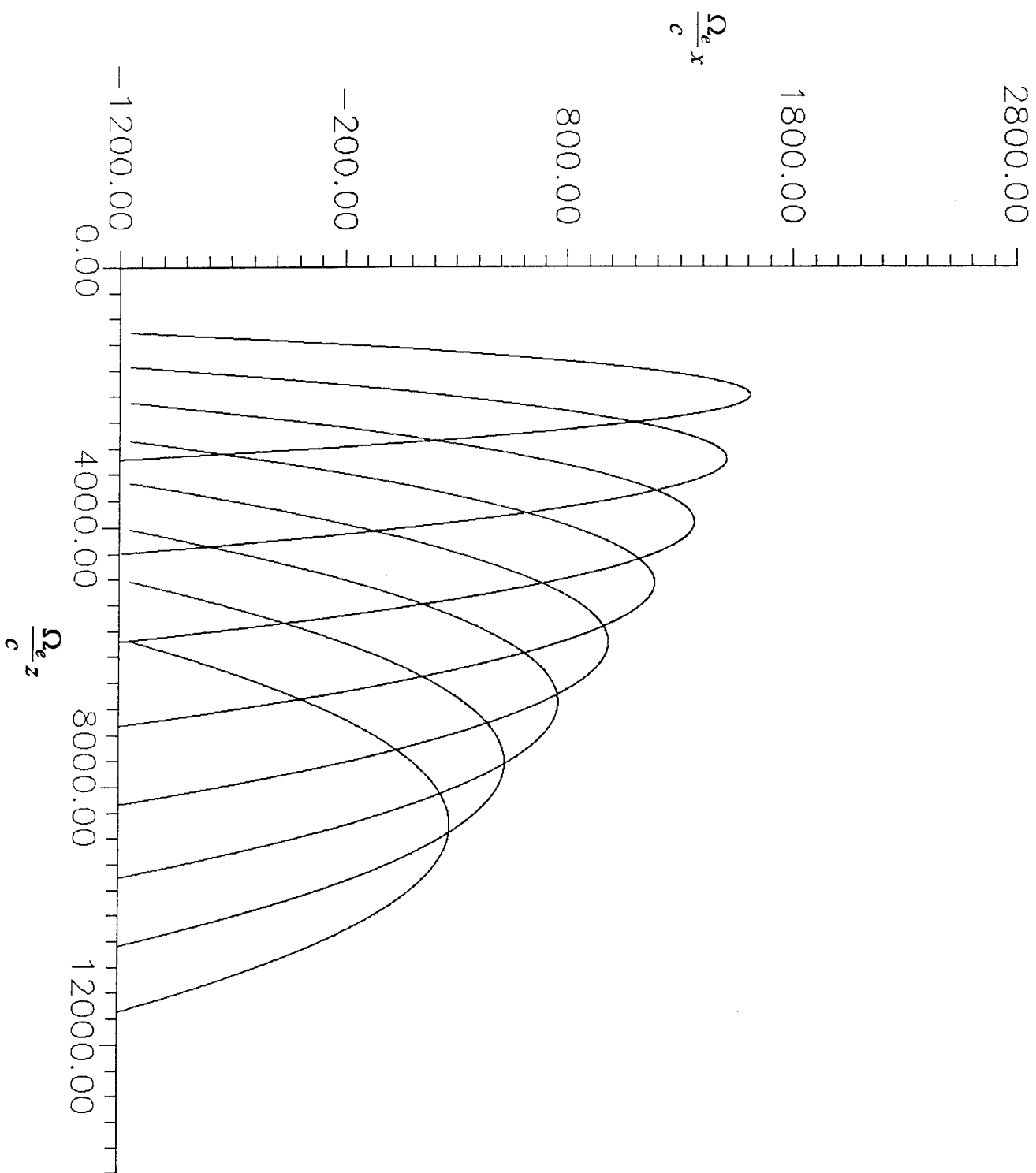


Figure 3

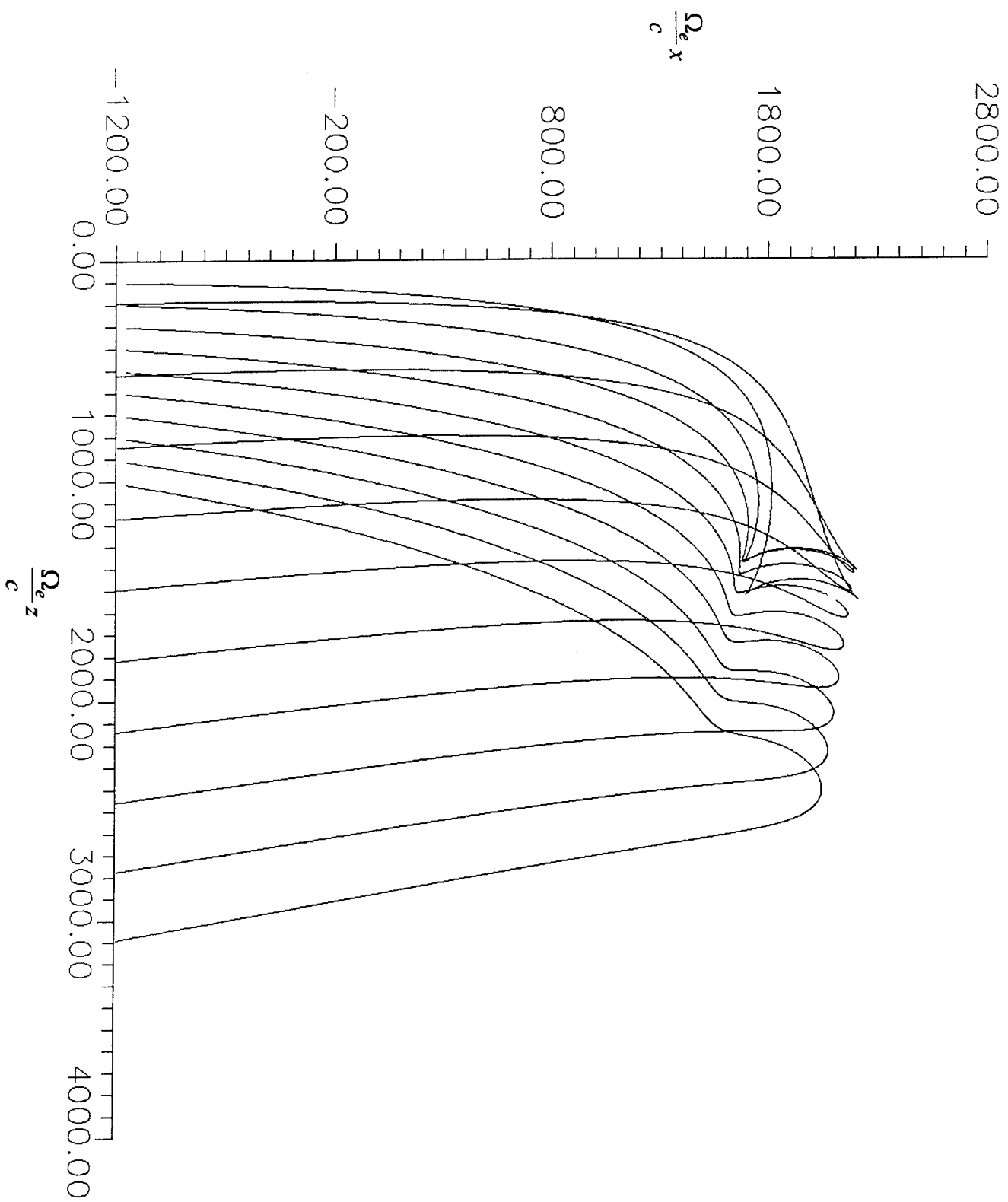


Figure 4

III. Parametric Excitation of Lower Hybrid Decay Mode together with Upper Hybrid Sideband by an Obliquely Transmitted HF Heater

Different from the vertically transmitting case, the wavenumber of the obliquely incident heater always has a finite component in the horizontal direction. Thus, the wave field of the o-mode (vertical polarization) heater does not orientate toward the direction of geomagnetic field and exists a perpendicular wave field component near the reflection height. Choosing the coordinate system as shown in Figure 5 which is different from that used for ray tracing analysis, the wave vector \mathbf{k}_0 of the heater near the reflection height can be expressed to be

$$\mathbf{k}_0 = (\mathbf{x} \sin\theta_0 - \mathbf{z} \cos\theta_0) k_0 \cos\theta_i \quad (1)$$

where θ_0 and θ_i are the magnetic dip angle and the incident elevation angle of the heater respectively; $k_0 = \omega_0/c = (\omega_p^2 + \omega_0^2 \cos^2\theta_i)^{1/2} / c$ is the wave number of the heater on the ground; ω_p is the plasma frequency at the reflection height of the heater.

Since $\omega_0 \gg \omega_p \gg \Omega_e$, heater can be considered still being a transverse wave near the reflection height. Its wave field is then given by

$$\mathbf{E}_p = [-(\mathbf{x} \cos\theta_0 + \mathbf{z} \sin\theta_0)E_0 + \mathbf{y} E_{0y}] \exp[i(\mathbf{k}_0 \cdot \mathbf{r} - \omega_0 t)] + \text{c.c.} \quad (2)$$

where the horizontally polarized wave field component ($\mathbf{y} E_{0y}$) is included for generality.

We now study parametric instability excited by a pump (heater) featured with (1) and (2) in a region slightly below the reflection height of the pump (e.g. in the caustic region). The process under consideration is the decay of the pump wave (\mathbf{k}_0, ω_0) into upper hybrid wave (\mathbf{k}, ω) and

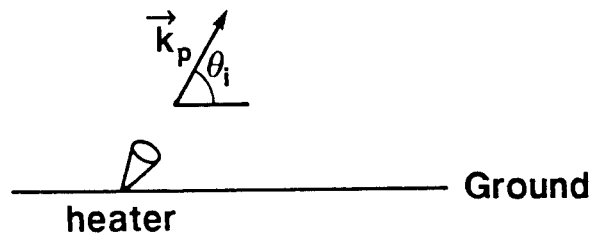
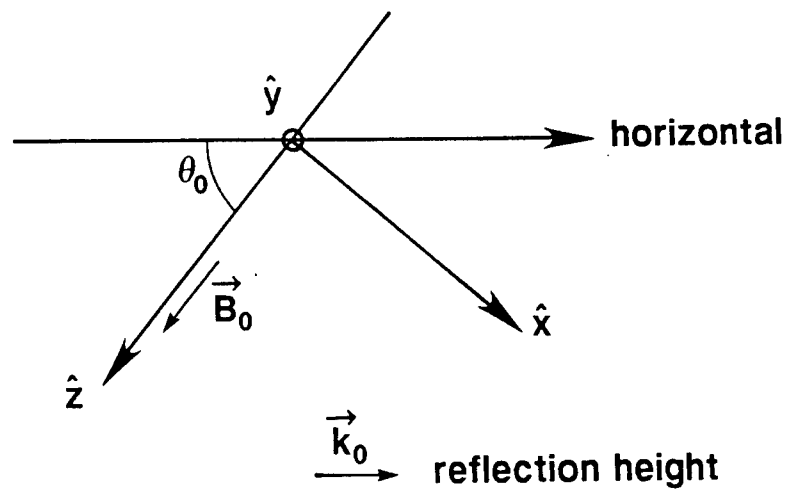


Fig. 5 Coordinate system and the orientation of the wavevector of the heater wave on the ground and at the reflection height.

lower hybrid wave (\mathbf{k}_3, ω_3) pair through the nonlinearity of the plasma²⁷. It is represented by the following wavevector and frequency matching relations

$$\begin{aligned}\mathbf{k}_0 &= \mathbf{k} + \mathbf{k}_3 \\ \omega_0 &= \omega + \omega_3^*\end{aligned}\tag{3}$$

In the following analysis, $\mathbf{k} = x\mathbf{k}_x$ is assumed to simplify the analysis. However the extension of the analysis to the more general case that $\mathbf{k} = x\mathbf{k}_x + y\mathbf{k}_y$ is straightforward.

A. Upper hybrid wave excited by an EM pump coupling with a lower hybrid wave

The coupled mode equation for the potential function ϕ of the upper hybrid sideband (\mathbf{k}, ω) in terms of the obliquely incident pump (\mathbf{k}_0, ω_0) and lower hybrid decay wave (\mathbf{k}_3, ω_3) is derived from the electron continuity equation and momentum equation as

$$\begin{aligned}& \left(\frac{\partial}{\partial t} + \nu_e\right) \left[\frac{\partial^2}{\partial t^2} + \nu_e \frac{\partial}{\partial t} \omega_p^2 - \nu_{te}^2 \nabla_{\perp}^2 \right] \nabla_{\perp}^2 \phi + \Omega_e^2 \frac{\partial}{\partial t} \nabla_{\perp}^2 \phi \\ &= \omega_p^2 \left[\left(\frac{\partial}{\partial t} + \nu_e\right) \nabla_{\perp} \cdot \mathbf{E}_p (\delta \mathbf{n}_{e3}^* / n_0) - \Omega_e \nabla_{\perp} \cdot (\mathbf{E}_p \times \hat{\mathbf{z}}) (\delta \mathbf{n}_{e3}^* / n_0) \right]\end{aligned}\tag{4}$$

where ν_e is the electron collision frequency; $\nu_{te} = (3T_e/m_e)^{1/2}$ is the electron thermal speed; ω_p and Ω_e are the electron plasma and cyclotron frequency respectively; $\delta \mathbf{n}_{e3}$ is the electron density perturbation associated with the lower hybrid decay wave..

We assume that the perturbations take the form $\phi = \phi \exp[i(\mathbf{k}x - \omega t)] + \text{c.c.}$ and $\delta \mathbf{n}_{e3} = \delta \mathbf{n}_{e3} \exp[i(\mathbf{k}_3 \cdot \mathbf{r} - \omega_3 t)] + \text{c.c.}$

Substituting them into (4) and using the matching relation (3) to cancel out the common exponential phase factor, the coupled mode equation (4) is then reduced to

$$\tilde{\phi} = -(\omega_p^2/k)(\delta n_{e3})^* [(\omega + i\nu_e)E_0 \cos \theta_0 + i\Omega_e E_{0y}] / [i\omega\Gamma + \nu_e(\omega^2 + \Omega_e^2)] \quad (5)$$

!

where $\Gamma = \omega_k^2 + \Omega_e^2 + n_e^2 - \omega^2$ and $\omega_k^2 = \omega_p^2 + k^2 v_{te}^2$.

Eq.(5) gives the potential perturbation of the upper hybrid sideband as a function of the pump field and the density fluctuation of the lower hybrid decay mode.

B. Coupled Mode Equation for the Lower Hybrid Decay Mode

The governing equations describing the lower hybrid wave include the continuity equations and momentum equations of electrons and ions, and the Poisson Equation:

$$\delta n_{e3}/n_0 = \mathbf{k}_3 \cdot \delta \mathbf{v}_{e3} / \omega_3 + \mathbf{k}_3 \cdot (\delta n_e^* / n_0) \mathbf{v}_{pe} / \omega_3 \quad (6)$$

$$\delta n_{i3}/n_0 = \mathbf{k}_3 \cdot \delta \mathbf{v}_{i3} / \omega_3 \quad (7)$$

$$\omega_3 \delta \mathbf{v}_{e3} + i\Omega_e \delta \mathbf{v}_{e3} \times \mathbf{z} = -i\mathbf{A} + \mathbf{k}_3 D_e \quad (8)$$

$$\omega_{3i} \delta \mathbf{v}_{i3} - i\Omega_i \delta \mathbf{v}_{e3} \times \mathbf{z} = \mathbf{k}_3 D_i \quad (9)$$

and

$$k_3^2 \phi_3 = 4\pi e (\delta n_e - \delta n_{e3}) \quad (10)$$

where dn_e is the electron density perturbation associated with the upper hybrid sideband; v_{pe} is the electron velocity introduced by the pump field; $A = \langle v_e \cdot \nabla v_e \rangle$ and $\langle \rangle$ stands for average over the period of the pump; $D_{i,e} = \pm e\phi_3 / m_{i,e} + v_{ti,e}^2 \delta n_{e,i3} / n_0$; $\omega_{3e} = \omega_3 + i\nu_e$, and $\omega_{3i} = \omega_3 + i\nu_{in}$.

Using (8) and (9) to determine δv_{e3} and δv_{e3} explicitly and substituting the results into (6) and (7), yield

$$\begin{aligned} \delta n_{e3}/n_0 \cong & (\omega_{3e}/\omega_3)(k_{3x}^2/\Omega_e^2 - k_{3z}^2/\omega_{3e}^2)(e\phi_3/m_e) + \{ (k_3 \cdot v_{pe}/\omega_3)(\delta n_e^*/n_0) + \\ & (k_{3x}^2/\Omega_e^2)[iA_x + (\Omega_e/\omega_3)A_y - i(k_{3z}/k_{3x})(\Omega_e^2/\omega_3^2 A_z)] \} \end{aligned} \quad (11)$$

and

$$\delta n_{e3}/n_0 \cong k_3^2 (e\phi_3 / m_i \cdot \omega_3^2) \quad (12)$$

Substitute (11) and (12) into (10), the coupled mode equation for the lower hybrid decay mode is derived to be

$$\begin{aligned} [\omega_3^2 + i(2 - 1/\xi)\nu_e\omega_3 - \omega_{Lk3}^2]\phi_3 = & -[4\pi n_0 e\omega_3/k_3^2(1 + \omega_p^2/\Omega_e^2)] \\ & \{ (k_3 \cdot v_{pe})(\delta n_e^*/n_0) + (k_{3x}/\Omega_e^2)[i\omega_3 A_x + \Omega_e A_y] - ik_{3z} A_z/\omega_3 \} \end{aligned} \quad (13)$$

where $\xi = 1 + (m_i/m_e)(k_{3z}^2/k_3^2)$, $\omega_{Lk3}^2 = \omega_{LH}^2 \xi$, and $\omega_{LH}^2 = \omega_{pi}^2 / (1 + \omega_p^2/\Omega_e^2)$.

The RHS of (13) shows that the decay mode is produced by the net effect of the nonlinear beating current and the radiation pressure force introduced by the coupling of the pump to the sideband through the nonlinearity of the plasma.

Using the electron momentum equation to determine the linear velocity responses to the high frequency wave field, thus, A can be expressed explicitly in terms of the product of the pump and sideband wave field. Similarly, δn_e can be expressed explicitly in terms of the sideband wave field via the Poisson equation. Substituting these explicit expression for A and δn_e into (3), results to

$$[\omega_3^2 + i(2-1/\xi)v_e\omega_3 - \omega_{Lk3}^2]\tilde{\phi}_3 = -i(e/m_e)[\omega_{Lk3}^2 k_{3x} k \omega^* \omega_0 / k_3^2 (1 + \omega_p^2 / \Omega_e^2) \Omega_e^2 (\omega_0^2 - \omega_3^2)] \\ \{ [k_{3x} + (\Omega_e^2 / \omega_0 \omega_3) k_{0x}] E_0 \cos \theta_0 + i(\Omega_e / \omega_0) (k_{3x} + k_{0x} \omega_0 / \omega_3) E_{0y} - \\ (k_{3z} / k_{3x}) (\Omega_e^2 / \omega_3^2 \omega_0^2) (\omega_0^2 - \Omega_e^2) (k_{3x} + k \omega_3 / \omega^*) E_0 \sin \theta_0 \} \hat{\phi}^* \quad (14)$$

Eqs. (5) and (14) form a complete coupled set of equations describing the parametric instability process considered in the present work.

C. Dispersion Relation

Substituting (5) into (14) and with the aid of (11), a dispersion relation for the proposed instability process is derived to be

$$[\omega_3^2 + i(2-1/\xi)v_e\omega_3 - \omega_{Lk3}^2] [-i\omega^* \Gamma^* + v_e(\omega^{*2} + \Omega_e^2)] \xi \\ = i(e/m)^2 [\omega_{Lk3}^2 \omega^* \omega_0 k_{3x}^3 / k_3^2 (\omega_0^2 - \Omega_e^2) \Omega_e^2] \{ [k_{3x} + (\Omega_e^2 / \omega_0 \omega_3) k_{0x}] E_0 \cos \theta_0 \\ + i(\Omega_e / \omega_0) (k_{3x} + k_{0x} \omega_0 / \omega_3) E_{0y} - (k_{3z} / k_{3x}) (\Omega_e^2 / \omega_3^2) (1 - \Omega_e^2 / \omega_0^2) (k_{0x} + k \omega_3 / \omega^*) E_0 \sin \theta_0 \} \\ [(\omega^* - i\nu_e) E_0 \sin \theta_0 - i\Omega_e E_{0y}^*] \quad (15)$$

where the higher order terms proportional to $|E_p|^4$ arising from the second term on the RHS of (11) are neglected.

This is the general expression of the dispersion relation for parametric excitation of lower hybrid decay mode together with an upper hybrid sideband by an EM pump of elliptical polarization.

In order to minimize the instability threshold field, it is preferred that the excited waves are the natural modes of the medium, i.e. satisfying the dispersion relation. Thus, we set $\omega = \omega_{UH} + i\gamma$ and $\omega_3 = \omega_{LK3} + i\gamma$ in (15), where $\omega_{UH} = (\omega_k^2 + \Omega_e^2 + v_e^2)^{1/2}$ is the upper hybrid resonance frequency and γ is the growth rate of the instability, an equation for the growth rate γ is obtained to be

$$\begin{aligned} & [\gamma + (1 - 1/2\xi)v_e][\gamma + v_e(1 + \Omega_e^2/\omega_{UH}^2)/2] \\ &= \frac{1}{4}(e/m)^2[\omega_0 k_{3x}^3 \omega_{LK3}/k_3^3(\omega_0^2 - \Omega_e^2)\xi\Omega_e^2]\{[k_{3x} + (\Omega_e^2/\omega_0 \omega_{LK3})k_{0x}]E_0 \cos\theta_0 \\ &+ i(\Omega_e/\omega_0)(k_{3x} + k_{0x}\omega_0/\omega_{LK3})E_{0y} - (k_{3z}/k_{3x})(\Omega_e^2/\omega_{LK3}^2)(1 - \Omega_e^2/\omega_0^2) \\ &(k_{0x} + k\omega_{LK3}/\omega_{UH})E_0 \sin\theta_0\}[E_0^* \cos\theta_0 - i(\Omega_e/\omega_{UH})E_{0y}^*] \end{aligned} \quad (16)$$

This equation is analyzed in the following for two cases of independently polarized pumps:

1. Horizontal polarization, i.e. $E_p = \hat{y}E_{0y}$

Eq.(16) is then reduced to

$$(\gamma + v_e)(\gamma + v_e/2) \cong \frac{1}{4}(e/m)^2(k_{3x}^2 k_{0x}/k_3^2 \omega_0^2 \xi) |E_{0y}|^2 \quad (17)$$

where $\Omega_e^2 \ll \omega_{UH}^2 < \omega_0^2$ and $k_{0x}\omega_0/k_{3x}\omega_{LK3} \gg 1$ are assumed.

Setting $\gamma=0$ in (17), the threshold field of the instability is determined to be

$$|eE_{th}/m\omega_0| = (2\xi/k_{3x}k_{0x})^{1/2} v_e(k_3/k_{3x}) \quad (18)$$

In terms of the threshold field, the growth rate γ of the instability is given by

$$\gamma = (v_e/2) \{ [2(E_{0y}/E_{th})^2 + 1/4]^{1/2} - 3/2 \} \quad (19)$$

2. Vertical polarization, i.e., $\mathbf{E}_p = -(\hat{x} \cos\theta_0 + \hat{z} \sin\theta_0)E_0$

One can reduce (16) to

$$(\gamma + v_e)(\gamma + v_e/2) \approx \frac{1}{4} (e/m)^2 (k_{3x}^2 k_{0x} / k_3^2 \omega_0^2 \xi) E_0^2 \cos^2\theta_0 [1 - k_{3z}\omega_0/k_{3x}\omega_{Lk3}] (\sin\theta_0/\cos\theta_0) \quad (20)$$

The threshold field and the growth rate are derived in a similar way to be

$$|eE_{th}/m\omega_0| = \sqrt{2\xi} [v_e k_3/k_{3x} (k_{3x} k_{0x})^{1/2}] / \cos\theta_0 [1 - (k_{3z}\omega_0/k_{3x}\omega_{Lk3}) \tan\theta_0] \quad (21)$$

and

$$\gamma = (v_e/2) \{ [2(E_0/E_{th})^2 + 1/4]^{1/2} - 3/2 \} \quad (22)$$

So far, the threshold conditions of the instability for two cases of independently polarized pumps have been derived. However, the instability process also requires that the frequency and wavevector matching conditions be satisfied. They impose additional instability criterions for obliquely incident pumps.

D. Additional Criteria for the Instability

In order to satisfy the matching conditions (3), the pump's frequency ω_0 and the incident angle θ_i can not be chosen arbitrarily, Their applicable regions are determined in the following.

Using the relations $\omega + \omega_3^* = \omega_{UH} + \omega_{Lk3}$, and $\omega_{UH}^2 = \omega_k^2 + \Omega_e^2 + v_e^2$, $\omega_{Lk3}^2 = \omega_{LH}^2 \xi$, and $\omega_0^2 = k_0^2 c^2 = \omega_p^2 + k_0^2 c^2 \cos^2 \theta_i$, (3) leads to

$$\cos^2 \theta_i = (\Omega_e^2 + v_e^2 + 2\omega_0 \omega_{Lk3}) / \omega_0^2 (1 + \Omega_e^2 \cos^2 \theta_0 / k_3^2 c^2)$$

Thus, $\theta_i \geq \pi/2 - \sin^{-1}[(\Omega_e^2 + v_e^2 + 2\omega_0 \omega_{3m})^{1/2} / \omega_0]$ is required, where ω_{3m} is the maximum possible value of ω_{Lk3} , and $|k_{3x}c| \gg \Omega_e \cos \theta_0$ is assumed.

Let ω_{pf} be the F-peak plasma frequency, hence, the plasma frequency at the reflection height of the incident wave, $\omega_p^2 = k_0^2 c^2 \sin^2 \theta_i$, has to be less than ω_{pf}^2 , thus,

$$\sin^2 \theta_i \leq \omega_{pf}^2 / \omega_0^2, \text{ or } \theta_i \leq \sin^{-1}(\omega_{pf} / \omega_0).$$

One then has

$$\pi/2 - \sin^{-1}[(\Omega_e^2 + v_e^2 + 2\omega_0 \omega_{3m})^{1/2} / \omega_0] \leq \sin^{-1}(\omega_{pf} / \omega_0)$$

It leads to the condition

$$\omega_0 \leq \omega_{3m} + (\omega_{3m}^2 + \omega_{Um}^2)^{1/2}$$

Where $\omega_{Um} = (\omega_{pf}^2 + \Omega_e^2 + v_e^2)^{1/2}$ is the maximum upper hybrid resonance frequency.

In summary, it is shown that the frequency ω_0 and the elevation angle θ_i of the heater must satisfy these conditions

$$\begin{aligned}\omega_0 &\leq \omega_{3m} + (\omega_{3m}^2 + \omega_{Um}^2)^{1/2} \\ \theta_i &\geq \pi/2 - \sin^{-1}[(\Omega_e^2 + \nu_e^2 + 2\omega_0\omega_{3m})^{1/2}/\omega_0]\end{aligned}\tag{23}$$

So that the necessary frequency and wavevector matching conditions for the parametric coupling process considered in the present work, i.e. pump decays into a lower hybrid decay mode together with an upper hybrid sideband, can be satisfied.

Considering a case that the heater is operated at a frequency $\omega_0/2\pi = 6$ MHz, and an incident angle $\theta_i = 75^\circ$. In order to satisfy (23), it requires that $\omega_{3m}/2\pi \cong 110$ KHz and $\xi \cong 2.40$, i.e. $k_{3z}/k_{3x} \sim 0.09$. These are reasonable values for the lower hybrid wave in the ionosphere. Using the parameters $\nu_e = 130 \text{ sec}^{-1}$, $k_0 = 2\pi/50 \text{ m}^{-1}$, and $\theta_0 = 60^\circ$, the threshold field of the instability excited by horizontally polarized heater is calculated from (18) to be

$$E_{th} \sim 10(k_0/k_3)^{1/2} \text{ (V/m)} \sim 0.7 \text{ V/m, for } k_0/k_3 \sim 5 \times 10^{-3}\tag{24}$$

For vertically polarized heater the threshold field obtained from (21) is given by

$$E_{th} \sim 20(k_0/k_3)^{1/2} \text{ (V/m)} \sim 1.4 \text{ V/m, for } k_0/k_3 \sim 5 \times 10^{-3}\tag{25}$$

IV. Electromagnetic Filamentation Instability Leading to the Generation of Large-Scale Field-Aligned Density Irregularities

A. Coupling Equations

We investigate the filamentation of the obliquely incident HF heater having frequency ω_0 and wave vector \bar{k}_0 in the caustic region. The same coordinate system as Figure 5 is using the following analysis. The process under consideration is the scattering of the HF heater wave into sidebands (propagating oblique to the heaters propagation direction) by the simultaneously excited purely growing density irregularities. Therefore, the expression for the total wave electric field is written as

$$\bar{E} = \sum_{j=0}^2 \bar{e}_j(t) e^{i(\bar{k}_j \cdot \bar{r} - \omega_j t)} + c.c. \quad (1)$$

where $\bar{k}_{1,2} = \bar{k}_0 \pm \bar{k}$, $\bar{e}_0(t) = \bar{e}_0$ and $\bar{e}_{1,2}(t)$ are the electric field amplitudes of the incident (unperturbed pump) and scattered sideband waves, and \bar{k} is the wave vector of the excited purely growing density perturbation and is assumed to be perpendicular to \bar{k}_0 .

We next express the total electron density as

$$n = n_0 + [n_1 e^{i\bar{k} \cdot \bar{r}} + \sum_{j=0}^2 \delta n_j e^{i(\bar{k}_j \cdot \bar{r} - \omega_j t)} + c.c.] \quad (2)$$

and the total electron velocity as

$$\bar{v}_e = \delta \bar{v}_e e^{i\bar{k} \cdot \bar{r}} + \sum_{j=0}^2 \bar{v}_j e^{i(\bar{k}_j \cdot \bar{r} - \omega_j t)} + c.c. \quad (3)$$

where $n_1(t)$ and $\delta \bar{v}_e(t)$ are the electron density and velocity perturbations associated with the excited non-oscillatory purely growing mode, whereas $\delta n_j(t)$ and $\bar{v}_j(t)$ are the electron density and velocity perturbations induced by the pump field ($j = 0$) and the excited high frequency sidebands ($j = 1, 2$). In a magnetized plasma, the incoming waves may not be pure transverse waves, but in general hybrid waves, hence δn_j may be non-zero and can be determined by the Poisson Equation as

$$\delta n_j = -i \bar{k}_j \cdot \bar{e}_j / 4 \pi e \quad (4)$$

However, when the heater frequency much higher than the electron cyclotron frequency, the electrostatic components of the high frequency waves become negligibly small.

We now proceed to derive the coupling equations for the sidebands. The wave equation for each wave yields

$$(\nabla^2 - \nabla \nabla \cdot) \bar{E} - \frac{1}{c^2} \frac{\partial^2}{\partial t^2} \bar{E} = \frac{4\pi}{c^2} \frac{\partial}{\partial t} \bar{J} \quad (5)$$

where the electron current density \bar{J} is obtained by collecting those components of the product of Eqns. (2) and (3) which contribute to the pump and sidebands. If only small amplitude sidebands are considered, the effect of pump depletion can be neglected in the first order approximation. It is also reasonable to neglect $\delta n_j \delta \bar{v}_e$ coupling terms. This is because in general $|\delta n_j| \ll |n_1|$ and $|\delta \bar{v}_e| \ll |\bar{v}_j|$. Therefore, we have

$$\bar{J} = -en_0 \sum_{j=0}^2 \bar{v}_j e^{i(\bar{k}_j \cdot \bar{r} - \omega_j t)} - e(n_1 e^{i\bar{k} \cdot \bar{r}} + c.c.) \bar{v}_0 e^{i(\bar{k}_0 \cdot \bar{r} - \omega_0 t)} + c.c. \quad (6)$$

where the current induced by coupling to the low frequency mode is given by the second term on the right hand side.

Equations for the first order quantities (i.e. sideband waves) are thus obtained as

$$\chi_j \cdot \bar{\epsilon}_j = \frac{\omega_p^2}{\omega_0^2 - \Omega^2} [\bar{\epsilon}_{0\perp} + \hat{z} (1 - \frac{\Omega^2}{\omega_0^2}) \epsilon_{0z} + i \frac{\Omega}{\omega_0} \hat{z} \times \bar{\epsilon}_0] (n_1 \delta_{j,1} + n_1^* \delta_{j,2}) / n_0 \quad (7)$$

where

$$\begin{aligned} \chi_j &= (1 - \frac{\omega_p^2}{\omega_0^2 - \Omega^2}) \frac{1}{\omega_0^2} + \frac{\Omega^2}{\omega_0^2} \frac{\omega_p^2}{\omega_0^2 - \Omega^2} \hat{z} \hat{z} - i \frac{\Omega}{\omega_0} \frac{\omega_p^2}{\omega_0^2 - \Omega^2} \hat{z} \times 1 - \frac{k_j^2 c^2}{\omega_0^2} (1 - \frac{\bar{k}_j \bar{k}_j}{k_j^2}) \\ &= (1 - \frac{k_j^2 c^2}{\omega_0^2}) \frac{1}{\omega_0^2} + \frac{c^2}{\omega_0^2} \bar{k}_j \bar{k}_j + i \frac{4\pi}{\omega_0} \sigma \end{aligned} \quad (8)$$

$\sigma = i \frac{\omega_p^2}{4\pi} \frac{\omega}{\omega^2 - \Omega^2} [1 - \frac{\Omega^2}{\omega^2} \hat{z} \hat{z} + i \frac{\Omega}{\omega} \hat{z} \times 1]$, $\omega = \omega_0 + i\nu_e$, ν_e is the electron-ion collision frequency, and $\sigma_0 = \sigma(\omega = \omega_0)$; $\delta_{1,j}$ is the Kramer's Delta function, $\omega_p = (4\pi n_0 e^2 / m)^{1/2}$ and $\Omega = eB_0 / mc$ are the electron plasma and electron cyclotron frequency respectively,

the relations $\bar{v}_0 = -\frac{1}{n_0 e} \sigma_0 \cdot \bar{e}_0$ and $\bar{v}_j = -\frac{1}{n_0 e} \sigma \cdot \bar{e}_j$ for $j = 1, 2$ is used $|\bar{k}_j| \ll k_{de}$ (electron Debye wave number) is assumed.

Equation (7) can be inverted to obtain

$$\bar{e}_j = -i \frac{4\pi}{\omega_0} \chi_j^{-1} \cdot \sigma \cdot \bar{e}_0 (n_1 \delta_{j,1} + n_1^* \delta_{j,2}) / n_0 \quad (9)$$

which determines the polarization and amplitude of the excited sideband waves arising through the coupling between the pump field and the purely growing density perturbations.

The coupling equation for the purely growing mode can be obtained from the continuity equations of electrons and ions

$$\gamma n_1 + i n_0 \bar{k} \cdot \delta \bar{v}_i = 0 = \gamma n_1 + i n_0 \bar{k} \cdot \delta \bar{v}_e + \bar{k} \cdot \bar{D} \quad (10)$$

where quasi-neutrality is assumed, γ is the linear growth rate, and

$$\bar{D} = (\delta n_1 \bar{v}_0^* + \delta n_2^* \bar{v}_0 + \delta n_0^* \bar{v}_1 + \delta n_0 \bar{v}_2^*) \quad (11)$$

The momentum equations for electrons and ions can be written

$$\gamma \delta \bar{v}_e + \bar{A} = -i \bar{k} (n_1 T_e + n_0 \delta T_e) / n_0 m + i \bar{k} e \delta \phi / m - \Omega \delta \bar{v}_e \times \hat{z} - v_e (\delta \bar{v}_e - \delta \bar{v}_i) \quad (12)$$

and

$$\gamma \delta \bar{v}_i = -i \bar{k} n_1 T_i / n_0 M - i \bar{k} e \delta \phi / M + \Omega_i \delta \bar{v}_i \times \hat{z} + (m / M) v_e (\delta \bar{v}_e - \delta \bar{v}_i) - v_n \delta \bar{v}_i \quad (13)$$

where

$$\bar{A} = i \bar{k} (\bar{v}_0^* \cdot \bar{v}_1 + \bar{v}_0 \cdot \bar{v}_2^*) - \bar{A}_1 \quad (14)$$

and

$$\bar{A}_1 = \frac{\Omega}{\omega_0} \{ k_z (\bar{v}_0^* \times \bar{v}_1 + \bar{v}_0 \times \bar{v}_2^*) + \hat{z} \times (\bar{v}_0^* \bar{v}_1 + \bar{v}_0 \bar{v}_2^*) \cdot \bar{k} + \hat{z} \times (\bar{v}_0^* \bar{v}_1 + \bar{v}_1 \bar{v}_0^* + \bar{v}_0 \bar{v}_2^* + \bar{v}_2^* \bar{v}_0) \cdot \bar{k}_0 \} \quad (15)$$

and $\delta \phi$ is the electrostatic potential perturbation associated with the purely growing mode. m and M are the masses of electron and ions respectively. v_e and v_n are the electron-ion and ion-neutral collision frequency respectively and $\Omega_i = e B_0 / M c$ is the ion cyclotron frequency.

The equation for the electrons is

$$\frac{3}{2}n_0\gamma\delta T_e + in_0T_e\bar{k} \cdot \delta\bar{v}_e = -(k_z^2K_{//} + k_\perp^2K_\perp)\delta T_e - 3n_0(m/M)v_e\delta T_e + 2v_en_0m(\bar{v}_0^* \cdot \bar{v}_1 + \bar{v}_0 \cdot \bar{v}_2) \quad (16)$$

where $K_{//} = \frac{3}{2}(n_0T_e/mv_e)$ and $K_\perp = \frac{3}{2}v_en_0T_e/m(\Omega^2 + v_e^2)$ are the parallel and the cross field thermal diffusion coefficients respectively.

We first combine Eqns. (12) and (13) to obtain a one fluid equation for the zero frequency mode

$$\bar{v}_n\delta\bar{v}_i = -[(m/M)\bar{A} + i\bar{k}(c_s^2n_1/n_0 + \delta T_e/M)] + \Omega_i(\delta\bar{v}_i - \delta\bar{v}_e) \times \hat{z} \quad (17)$$

where $\bar{v}_n = \gamma + v_n$, $c_s^2 = (T_e + T_i)/M$ and $(m/M)|\delta\bar{v}_e| \ll |\delta\bar{v}_i|$ is assumed.

To simplify the analysis without losing the generality, we choose a coordinate system such that \bar{k} is on the y-z plane, i.e. $\bar{k} = k_y\hat{y} + k_z\hat{z}$. Then Eq. (17) reduces to

$$\delta v_{ix} = -[(m/M)A_x - \Omega_i(\delta\bar{v}_i - \delta\bar{v}_e)_y]/\bar{v}_n \quad (18)$$

$$\delta v_{iy} = -[(m/M)A_y + ik_y(c_s^2n_1/n_0 + \delta T_e/M) + \Omega_i(\delta\bar{v}_i - \delta\bar{v}_e)_x]/\bar{v}_n \quad (19)$$

$$\delta v_{iz} = -[(m/M)A_z + ik_z(c_s^2n_1/n_0 + \delta T_e/M)]/\bar{v}_n \quad (20)$$

and the x-component of Eq. (12) is simplified to

$$(\delta\bar{v}_e - \delta\bar{v}_i)_x \cong -(A_x + \Omega\delta v_{ey})\bar{v}_e \quad (21)$$

where $\bar{v}_e = \gamma + v_e$.

Substituting Eq. (21) into Eq. (19), yields

$$\delta v_{ey} = -(\bar{v}_e/\Omega\Omega_i)[\bar{v}_n\delta v_{iy} + (m/M)A_y + ik_y(c_s^2n_1/n_0 + \delta T_e/M)] - (m/M)A_x/\Omega_i \quad (22)$$

We next take the x-component of the curl of Eq. (12), and the result is

$$k_y(\delta\bar{v}_i - \delta\bar{v}_e)_z - k_z(\delta\bar{v}_i - \delta\bar{v}_e)_y \cong [k_z\Omega\delta v_{ex} - (k_zA_y - k_yA_z)]/\bar{v}_e \quad (23)$$

Eqs. (1) and (23) can be combined, with the aid of Eqs. (18), (21), and (22) to give

$$K \delta v_{iy} = [k_y \bar{k} \cdot \bar{D} / n_0 - k^2 A_x / \Omega + k_z (k_z A_y - k_y A_z) / \bar{v}_e] - (\bar{v}_e / \Omega \Omega_i) [k_y^2 + (1 + \Omega \Omega_i / \bar{v}_e \bar{v}_n + \Omega^2 / \bar{v}_e^2) k_z^2] [(m / M) A_y + i k_y (c_s^2 n_1 / n_0 + \delta T_e / M)] \quad (24)$$

where

$$K = (1 + \bar{v}_e \bar{v}_n / \Omega \Omega_i) [k_y^2 + (1 + \Omega \Omega_i / \bar{v}_e \bar{v}_n) k_z^2] + (M / m) k_z^2 (\bar{v}_n / \bar{v}_e) \\ \bar{\gamma} = \gamma + 2(m / M) v_e + v_e v_i^2 [k_y^2 / (\Omega^2 + v_e^2) + k_z^2 / v_e^2]$$

$\delta T_e / M = \frac{2}{3} (m / M) (v_i^2 / \bar{\gamma}) [(\gamma + i \bar{k} \cdot \bar{D}) / n_0 + 2 v_e (\bar{v}_0^* \cdot \bar{v}_1 + \bar{v}_0 \cdot \bar{v}_2^*) / v_i^2]$ is given by Eq. (16), and $v_i^2 = T_e / m$.

We now substitute Eqs. (20) and (24) into the continuity Equation (10) for ions. The coupling equation for the purely growing destiny perturbation is obtained as

$$P n_1 = -n_0 Q (\bar{v}_0^* \cdot \bar{v}_1 + \bar{v}_0 \cdot \bar{v}_2^*) - i R \bar{k} \cdot \bar{D}_0 - i n_0 (m / M) (\bar{\gamma} / \bar{v}_n) \{ (1 + \Omega \Omega_i / \bar{v}_n \bar{v}_e) [k_y^2 + (1 + \Omega \Omega_i / \bar{v}_e \bar{v}_n) k_z^2] + k^2 \Omega^2 / \bar{v}_e^2 \} k_z A_{1z} + [k_y^2 + (1 + \Omega \Omega_i / \bar{v}_e \bar{v}_n) k_z^2] k_y A_{1y} + \Omega k^2 k_y A_{1x} / \bar{v}_e \} \quad (25)$$

where

$$P = \{ \gamma \bar{\gamma} + (k_z^2 v_s^2 / \bar{v}_n) [2 \gamma / 3 + \eta \bar{\gamma}] \} \{ (1 + \Omega \Omega_i / \bar{v}_e \bar{v}_n) [k_y^2 + (1 + \Omega \Omega_i / \bar{v}_e \bar{v}_n) k_z^2] + k_z^2 \Omega^2 / \bar{v}_e^2 \} + (k_y^2 v_s^2 / \bar{v}_n) [2 \gamma / 3 + \eta \bar{\gamma}] [k_y^2 + (1 + \Omega \Omega_i / \bar{v}_e \bar{v}_n + \Omega^2 / \bar{v}_e^2) k_z^2] \quad (26)$$

$$Q = (m / M) [(4 v_e / 3 + \bar{\gamma}) / \bar{v}_n] \{ k_y^2 [k_y^2 + (1 + \Omega \Omega_i / \bar{v}_e \bar{v}_n + \Omega^2 / \bar{v}_e^2) k_z^2] + k_z^2 \{ (1 + \Omega \Omega_i / \bar{v}_e \bar{v}_n) [k_y^2 + (1 + \Omega \Omega_i / \bar{v}_e \bar{v}_n) k_z^2] + k_z^2 \Omega^2 / \bar{v}_e^2 \} \} \quad (27)$$

$$R = k_y^2 \Omega \Omega_i / \bar{v}_e \bar{v}_n + \frac{2}{3} (v_s^2 / \bar{v}_n) \{ k_y^2 [k_y^2 + (1 + \Omega \Omega_i / \bar{v}_e \bar{v}_n + \Omega^2 / \bar{v}_e^2) k_z^2] + k_z^2 \{ (1 + \Omega \Omega_i / \bar{v}_e \bar{v}_n) [k_y^2 + (1 + \Omega \Omega_i / \bar{v}_e \bar{v}_n) k_z^2] + k_z^2 \Omega^2 / \bar{v}_e^2 \} \} \quad (28)$$

$v_s^2 = T_e / M$ and $\eta = 1 + T_i / T_e$.

Equation (9) gives the sideband fields as produced by the pump and the low frequency density perturbation. Equation (25) give the low frequency density perturbation as a function of the high frequency pump and sidebands.

B. Dispersion Relation:

The dispersion relation is obtained by combining Eqs. (9) and (25), the result is

$$P = i(4\pi/n_0^2 e^2 \omega_0 \bar{\epsilon}_0^* \cdot [QH - RG - i(\bar{\gamma}\Omega_i / \omega_0 \bar{v}_n)(\{(1 + \Omega\Omega_i / \bar{v}_e \bar{v}_n)[k_y^2 + (1 + \Omega\Omega_i / \bar{v}_e \bar{v}_n)k_z^2] + k^2\Omega^2 / \bar{v}_e^2\}k_z^2 M_z - [k_y^2 + (1 + \Omega\Omega_i / \bar{v}_e \bar{v}_n)k_z^2]k_y (k_z M_y + L_x) + (\Omega / v_e)k^2 k_y (k_z M_x - L_y)])] \cdot \bar{\epsilon}_0 \quad (29)$$

$$\text{where } H = \sigma_0^{*+} \cdot \alpha_1 - \alpha_2^{*+} \cdot \sigma_0 \quad (30)$$

$$\text{with } \alpha_1 = \sigma \cdot \chi_1^{-1} \cdot \sigma_0 \quad \text{and} \quad \alpha_1 = \sigma \cdot \chi_1^{-1} \cdot \sigma_0$$

$$G = [(\sigma_0^{*+} \cdot \bar{k}\bar{k}_1 \cdot \sigma^{-1} - \bar{k}_0\bar{k}) \cdot \alpha_1 + \alpha_2^{*+} \cdot (\sigma_0^+ \cdot \bar{k}\bar{k}_2 \cdot \sigma^{*-1} - \bar{k}_0\bar{k})^+] \quad (31)$$

$$M_\beta = \sigma_0^{*+} \times \hat{\beta} \cdot \alpha_1 - \alpha_2^{*+} \cdot \hat{\beta} \times \sigma_0 \quad \text{with } \beta = x, y, z \quad (32)$$

$$L_\beta = \sigma_0^{*+} \cdot (\hat{\beta}\bar{k}_1 + \bar{k}_0\hat{\beta}) \cdot \alpha_1 - \alpha_2^{*+} \cdot (\bar{k}_2\hat{\beta} + \hat{\beta}\bar{k}_0) \cdot \sigma_0 \quad \text{with } \beta = x, y \quad (33)$$

and "+" represents the adjoint of the operator.

Equation (29) is a general expression of the dispersion relation for filamentation instability in a magnetized plasma. It is quite complicated because all the non-linearities, namely, the ponderomotive force, differential ohmic heating and beating currents, and the anisotropic effect of magnetic field, have been included. This dispersion relation can however be simplified in the practical application for oblique heating as considered in the following.

C. Analysis

The dispersion relation [Eq. (29)] will be examined for two cases: normal incidence of (1) ordinarily and (2) extraordinarily polarized pump waves thus the region of consideration is slightly below the reflection layer.

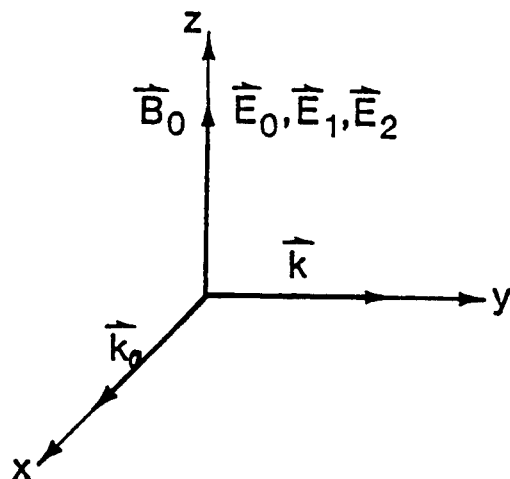


Figure 6. The relative orientation of the various vector quantities for ordinary pump case

(1). Ordinarily Polarized Pump Field:

For the ordinary pump $\bar{k}_0 = k_0 \hat{x}$ and $\bar{\varepsilon}_0 = \varepsilon_0 \hat{z}$. In this case the pump field and the excited sideband field are polarized in the same direction as seen by Eq. (9) and show in Figure 6. Hence, $\bar{k} = k \hat{y}$ and Eq. (29) become

$$\begin{aligned} \gamma^4 + \gamma^3 [v_n + v_e(1 + k^2 v_t^2 / \Omega^2)] + \gamma^2 [\Omega \Omega_i + v_n v_e + (2/3 + \eta) k^2 v_s^2 + v_e(v_e + v_n) \\ (2m/M + k^2 v_t^2 / \Omega^2) - 2f(\omega_{pi} e \varepsilon_0 / m \omega_0 c)^2] + \gamma v_e [(\Omega \Omega_i + v_n v_e + k^2 v_s^2) \\ (2m/M + k^2 v_t^2 / \Omega^2) + (2/3 + \eta) k^2 v_s^2 - 2f(7/3 + k^2 v_t^2 / \Omega^2)(\omega_{pi} e \varepsilon_0 / m \omega_0 c)^2] \\ - 2f v_e^2 (4/3 + k^2 v_t^2 / \Omega^2)(\omega_{pi} e \varepsilon_0 / m \omega_0 c)^2 (\varepsilon_0^2 - \varepsilon_{th}^2) = 0 \end{aligned} \quad (34)$$

where

$$\varepsilon_{th}^2 = (3\eta/8) (mc\omega_0 / e\omega_p)^2 k^2 v_t^2 (2m/M + k^2 v_t^2 / \Omega^2) / (1 + 3k^2 v_t^2 / 4\Omega^2) f \quad (35)$$

$$f = (1 + v_e^2 \omega_p^2 / \omega_0^2 k^2 c^2) / (1 + v_e^2 \omega_p^4 / \omega_0^2 k^4 c^4)$$

and $\Omega^2 \gg v_e^2$ is assumed.

Equation (35) is examined for two wavelength regions. In the long wavelength region, $k^2 v_t^2 / \Omega^2 \ll 1$, the instability is dominated by the thermal effect. The threshold field approximately reduces to

$$\varepsilon_{th} \sim (3m/2M + 3k^2 v_t^2 / 4\Omega^2)^{1/2} \varepsilon_{th}^{(0)} / f^{1/2} \quad (36)$$

and the growth rate is given by

$$\gamma \sim (4M/3m) v_e \gamma_0''^2 / [2\Omega \Omega_i + (5/3 + \eta) k^2 v_t^2]$$

$$\text{for } \gamma_0'' < (2m/M)^{1/2} [2 + (5/3 + \eta) k^2 v_t^2 / \Omega \Omega_i] \Omega_i$$

$$\sim (2M/\dot{m})^{1/2} (7 v_e \gamma_0'' / 6\Omega) \left[(M/2m)^{1/2} (\gamma_0'' / \Omega) + (24/49 + \gamma_0''^2 / 2\Omega \Omega_i)^{1/2} \right]$$

$$\text{for } [2 + (5/3 + \eta) k^2 v_t^2 / \Omega \Omega_i]^{1/2} \Omega_i < \gamma_0'' < (M/m)^{1/2} \Omega_i$$

$$\sim \gamma_0'' \quad \text{for } \gamma_0'' > (M/m)^{1/2} \Omega_i \quad (37)$$

where

$$\gamma_0''^2 = \gamma_0^2 + k^2 c_s^2 \left[1 - 3 \left(m / 2M + k^2 v_i^2 / 4\Omega^2 \right) / f \right]$$

and $v_e v_n \ll \Omega \Omega_i$ is assumed. In the short wavelength region, $k^2 v_i^2 / \Omega^2 \gg 1$, the ponderomotive force effect becomes dominant and $\varepsilon_{th} \sim \varepsilon_{th}^{(0)} = k c_s c \omega_0 m / \sqrt{2} e \omega_{pi}$, the threshold field in the collisionless and unmagnetized case. The growth rate is calculated as follows

$$\begin{aligned} \gamma &\sim v_e \gamma_0^2 / k^2 c_s^2 \quad \text{for } \gamma_0 < (2m/M)^{1/2} k^2 v_i^2 / \Omega \\ &\sim \left(\gamma_0^2 + v_e^2 k^2 v_i^2 / \Omega^2 \right)^{1/2} \quad \text{for } \gamma_0 > \sqrt{2} k v_s \end{aligned} \quad (38)$$

(2) Extraordinarily Polarized Pump Field:

Let $\vec{k}_0 = k_0 \hat{x}$, $\vec{\varepsilon}_0 = \hat{x} \varepsilon_{0x} + \hat{y} \varepsilon_{0y}$ and $\vec{k} = k \hat{z}$, Equation (29) thus become

$$\begin{aligned} &\gamma^3 + \gamma^2 \left[v_n + 2(m/M) v_e + k^2 v_i^2 / v_e \right] + \gamma(m/M) \left[2 v_n v_e + (M v_n / m v_e + 2/3 + \eta) \right. \\ &\left. k^2 v_i^2 - \alpha T f_1 \varepsilon_0^2 \right] - (4m/3M) \alpha f_1 v_e \left[S + 3(2m/M + k^2 v_i^2 / v_e^2) T / 4 \right] (\varepsilon_0^2 - \varepsilon_{th}^2) = 0 \end{aligned} \quad (39)$$

where

$$\varepsilon_{th}^2 = (3\eta/4) k^2 v_i^2 (2m/M + k^2 v_i^2 / v_e^2) / \alpha \left[S + 3(2m/M + k^2 v_i^2 / v_e^2) T / 4 \right] f_1 \quad (40)$$

$$\alpha = \left[e \omega_p \omega_0 / m c (\omega_0^2 - \Omega^2) \right]^2 / \left\{ \left[\omega_0^2 - \omega_u^2 - (\omega_0^2 - \Omega^2) (\ell k_0^2 + k^2) c^2 / 2 \omega_0^2 \right] \left[1 + \Omega^2 \omega_p^4 / \omega_0^2 (\omega_0^2 - \omega_u^2)^2 \right] \right\} \quad (41)$$

$$\begin{aligned}
S = & \left[\omega_0^2 - \omega_p^2 - (k^2 + k_0^2 / 2) c^2 \right] \left\{ \left(1 + \Omega^2 / \omega_0^2 \right) \left[1 + \Omega^2 \omega_p^4 / \omega_0^2 (\omega_0^2 - \omega_u^2)^2 \right] + 4 \Omega^2 \omega_p^2 / \omega_0^2 (\omega_0^2 - \omega_u^2) \right\} \\
& + (k_0^2 c^2 / 2 \omega_0^2) (\omega_0^2 - \Omega^2) \left[1 - \Omega^2 \omega_p^4 / \omega_0^2 (\omega_0^2 - \omega_u^2)^2 \right] + 2 (\Omega^2 / \omega_0^2) \left[\omega_0^2 - (k^2 + k_0^2 / 2) c^2 \right] \\
& \left[1 + \Omega^2 \omega_p^4 / \omega_0^2 (\omega_0^2 - \omega_u^2)^2 + (1 + \Omega^2 / \omega_0^2) \omega_p^2 / (\omega_0^2 - \omega_u^2) \right] \quad (42)
\end{aligned}$$

$$\begin{aligned}
T = & (1 - \Omega^2 / \omega_0^2) \left\{ \left[\omega_0^2 - \omega_p^2 - (k^2 + k_0^2 / 2) c^2 \right] \left[1 + 2 \Omega^2 \omega_p^2 (\omega_0^2 + \omega_p^2 / 2 - \omega_u^2) / \right. \right. \\
& \left. \left. \omega_0^2 (\omega_0^2 - \omega_u^2)^2 \right] + (k_0^2 c^2 / 2 \omega_0^2) (\omega_0^2 - \Omega^2) \left[1 - \Omega^2 \omega_p^4 / \omega_0^2 (\omega_0^2 - \omega_u^2)^2 \right] + \right. \\
& \left. (\Omega^2 / \omega_0^2) \left[\omega_0^2 - (k^2 + k_0^2 / 2) c^2 \right] \left[1 + 2 \omega_p^2 (\omega_0^2 - \omega_u^2 + \Omega^2 \omega_p^2 / 2 \omega_0^2) / (\omega_0^2 - \omega_u^2)^2 \right] \right\} \quad (43)
\end{aligned}$$

$$\begin{aligned}
f_1 = & \left[1 + v_e^2 \omega_p^2 (\omega_0^2 + \Omega^2) (\omega_0^2 - \omega_u^2 + 2 \Omega^2) / k^2 c^2 (\omega_0^2 - \Omega^2)^2 (\omega_0^2 - \omega_u^2) \right] / \left[1 + v_e^2 \omega_0^2 \omega_p^4 \right. \\
& \left. (\omega_0^2 - \omega_u^2 + 2 \Omega^2)^2 / k^4 c^4 (\omega_0^2 - \Omega^2)^2 (\omega_0^2 - \omega_u^2)^2 \right] \\
\ell = & \left[k^2 c^2 + \omega_p^2 \Omega^2 / (\omega_0^2 - \Omega^2) \right] / (\omega_0^2 - k^2 c^2 - \omega_p^2)
\end{aligned}$$

$\omega_u^2 = \omega_p^2 + \Omega^2$, and the relation $\varepsilon_{0x} = -i \left[\Omega \omega_p^2 / \omega_0 (\omega_0^2 - \omega_u^2) \right] \varepsilon_{0y}$ for extraordinary pump is used.

Equation (39) is similar to the result of unmagnetized case, except for a few modifications in the coefficients of the equation by the presence of the magnetic field. This is because the direction of \vec{k} is along the magnetic field and the (slow) particle motion is along \vec{B}_0 . Near the cutoff of extraordinary mode, $k_0 \rightarrow 0$,

$\omega_0 \rightarrow \Omega / 2 + (\omega_p^2 + \Omega^2 / 4)^{1/2}$ and $\varepsilon_{0x} = -i \varepsilon_{0y}$, Equations (41)-(43) reduce to

$$S \sim 4 \Omega \omega_0 (1 + \Omega / \omega_0)^2 \left[1 - k^2 c^2 (1 + \Omega / \omega_0) / 2 \Omega \omega_0 \right], \quad T \sim (1 - \Omega / \omega_0) S, \quad \text{and}$$

$$\alpha \sim \left[e \omega_0 / m c (\omega_0^2 - \Omega^2) \right]^2 (\omega_0 / 2 \Omega) / \left[1 - k^2 c^2 (1 + \Omega / \omega_0) / 2 \Omega \omega_0 \right]. \quad \text{Hence,}$$

$\alpha S \sim 2[e\omega_0 / mc(\omega_0 - \Omega)]^2$ and $\alpha T \sim 2(e / mc)^2 / (1 - \Omega / \omega_0)$. In the long wavelength region, $k^2 v_t^2 \ll v_e^2$, the threshold field is obtained as

$$\varepsilon_{th} \sim (1 - \Omega / \omega_0) (\omega_p / \omega_0) [3m / 2M + 3k^2 v_t^2 / 4 v_e^2]^{1/2} \varepsilon_{th}^{(0)} / f_1^{1/2} \quad (44)$$

and the growth rate is given by

$$\begin{aligned} \gamma &\sim (4M / 3m) v_e (\omega_0 / \omega_p)^2 \gamma_1^2 / (1 - \Omega / \omega_0)^2 [2 v_e v_n + k^2 v_t^2 (M v_n / m v_e + 2 / 3 + \eta)] \\ &\text{for } \gamma_1 < (1 - \Omega / \omega_0) (\omega_p / \omega_0) (\sqrt{3}m / 2M) [2 v_n v_e + k^2 v_t^2 \\ &\quad (M v_n / m v_e + 2 / 3 + \eta)] / [v_n v_e + 2m v_e^2 / M + k^2 v_t^2]^{1/2} \\ &\sim [4 v_e \omega_0^2 \gamma_1^2 / 3 \omega_p^2 (1 - \Omega / \omega_0) 2]^{1/3} \\ &\quad \text{for } (2m / M + k^2 v_t^2 / v_e^2)^{3/2} \sqrt{2} v_e \ll \omega_0 \gamma_1 / \omega_p (1 - \Omega / \omega_0) \ll \sqrt{2} v_e \\ &\sim \omega_0 \gamma_1 / \omega_p (1 - \Omega / \omega_0)^{1/2} \text{ for } \gamma_1 \gg \sqrt{2} v_e \omega_p (1 - \Omega / \omega_0)^{1/2} / \omega_0 \end{aligned} \quad (45)$$

where

$$\gamma_1^2 = \gamma_0^2 + k^2 c_s^2 \left[1 - 3(1 - \Omega / \omega_0)^2 (\omega_p / \omega_0)^2 (m / 2M + k^2 v_t^2 / 4 v_e^2) / f_1 \right].$$

In the short wavelength region, $k^2 v_t^2 \gg v_e^2$, the threshold field becomes

$$\varepsilon_{th} \sim (1 - \Omega / \omega_0)^{1/2} (\omega_p / \omega_0) \varepsilon_{th}^{(0)} \quad (46)$$

and the growth rate is obtained to be

$$\begin{aligned} \gamma &\sim (M / m) (\omega_0 / \omega_p)^2 \gamma_2^2 / (1 - \Omega / \omega_0) v_e (M v_n / m v_e + 2 / 3 + \eta) \\ &\text{for } \gamma_2 < (\sqrt{2}m / M) (\omega_p / \omega_0) (1 - \Omega / \omega_0)^{1/2} v_e (M v_n / m v_e + 2 / 3 + \eta)^{1/2} \end{aligned} \quad (47)$$

$$\sim \omega_0 \gamma_2 / \omega_p (1 - \Omega / \omega_0)^{1/2} \text{ for } \gamma_2 \gg \sqrt{2} (m / M) \omega_p (1 - \Omega / \omega_0)^{1/2} v_e / \omega_0$$

where

$$\gamma_2^2 = \gamma_0^2 + k^2 c_s^2 \left[1 - (1 - \Omega / \omega_0) (\omega_p / \omega_0)^2 \right]$$

For quantitative analysis, the following ionospheric parameters for the F region heating experiments are used: $m/M(O^+) \sim 3.4 \times 10^{-5}$, $\nu_e \sim 130$ Hz, $T_i \approx T_e$, $\Omega/2\pi \sim 1.1$ MHz, $\nu_t \sim 1.3 \times 10^5$ (m/sec), $\omega_0/2\pi \sim 6$ Mhz, $\theta_i = 60^\circ$, and $\nu_n \sim 0.5$ Hz. One can first evaluate $\varepsilon_{th}^{(0)} = 1.6 \times 10^3 / \lambda$ (V/m), where λ is in meters. Since the heating pump fields used in the experiments are believed to be less than 1V/m, this threshold could only be exceeded with wavelengths larger than a few kilometers, which puts us outside the range of applicability of the short wavelength threshold formula. In the long wavelength region, the threshold field of the ordinary mode pump is given by Eq. (36), which can be expressed explicitly as

$$\varepsilon_{th} \sim (11.5 / \lambda) \left(1 + (14.4 / \gamma)^2 \right)^{1/2} \left[1 + (\lambda / 3.1 \times 10^4)^4 \right]^{1/2} / \left[1 + (\lambda / 1.67 \times 10^7)^2 \right]^{1/2}.$$

It shows that, the threshold field decreases from several hundred milivolts to a few millivolts for wavelengths ranging from tens of meters to a few kilometers.

For the extraordinarily pump case, we consider only instability in the kilometer range where $k^2 \nu_t^2 \ll \nu_e^2$ is satisfied. The threshold field is then obtained from Eq. (44) as

$$\varepsilon_{th}^e \sim (8.1 / \lambda) \left[1 + (7.7 \times 10^5 / \lambda)^2 \right]^{1/2} \left[1 + (\lambda / 2.6 \times 10^4)^4 \right]^{1/2} / \left[1 + (\lambda / 1.4 \times 10^7)^2 \right]^{1/2}.$$

For $\lambda = 2.5 \times 10^3$ m, $\varepsilon_{th}^e \cong 1$ V/m, which is quite high. Thus it is expected to observe density irregularities only when the heater is transmitting a mode wave. In this case, the growth time is relatively insensitive to the wavelength and is found to be of the order of a few seconds. It suggests that the excited density irregularities have a broad scale lengths ranging from tens of meters to a few kilometers.

Acknowledgements

Part of this work was performed at the Geophysics Directorate of the U.S. Air Force's Phillips Laboratory (PL/GP), Hanscome AFB, Massachusetts. The author would like to thank PL for its hospitality. He also wishes to acknowledge the frequent and useful discussions with Dr. Paul Kossey, Mr. John Heakscher and Mr. John Rasmussen of the PL/GP, and professor M.C.Lee of the Massachusetts Institute of Technology.

This work was supported by the AFOSR reseach Initiation program subcontract 92-59 from the Research and Development Laboratory, Culver City, CA.

References

1. Special Issues, "ionospheric Modification by High Power Transmitters." J. Geophys. Res., 75, Nov. 1970, and Radio Science, 9 (11), Nov. 1974.
2. Stubbe, P., H. Kopka , "Generations of PC5 Pulsations by Polar Electrojet Modulations: First Experomental Evidence," J. Geophys. Res., 86, 1606 , 1981.
3. Stubbe, P., H. Kopka and R.L. Dowden, "Generation of ELF and VLF Waves by Polar Electrojet Modulation: Experimental Results," J. Geophys. Res., 86, 9073, 1981.
4. Carlson, H.C., V.B. Wickwar and G. Mantas, "Observations of Fluxes of Suprathermal Electrons Accelerated by HF Excited Instabilities," JATP, 44, 1089,1982.
5. Thide, E. et al., "Observations of Stimulated Electromagnetic Emmissions in Ionospheric Heating Experiments," Radio Science, 18, 851,1983.
6. Showen, R.L. and R.A. Behnke, "The Effect of HF-Induced Plasma Instabilities on Ionospheric Electron Temperatures," J.Geophys. Res. 82, 1839, 1977.
7. Showen, R.L. and D.M. Kim, "Time Variations of HF-Induced Plasma Waves," J. Geophys. Res. 83, 623, 1978.
8. Djuth, F.T. , M.P. Sulzer and J.H.Elder High Resolution Observations of HF-Induced Plasama Waves in the Ionosphere," Geophys. Res. Lett., 17, 1893, 1990.

9. Muldrew, D.B., and R.L. Showen, "Height of the HF-Enhanced Plasma Line in Arecibo, J. Geophys. Res. 82, 4783, 1977.
10. Isham, B., W. Kofman, T. Hagfors, J. Nordlang, B. Thide, C. LaHoz and P.Stubbe, "New Phenomena Observed by EISCAT During an RF Ionospheric Modification Experiment," Radio Science, 25, 251, 1990
11. Kuo, S.P., B.R. Cheo and M.C. Lee, "The Role of Parametric Decay Instabilities in Generating Ionospheric Irregularities," Geophys. Res., 88 (A1), 417, 1983.
12. Kuo, S.P. and G. Schmidt, "Filementation Instability in Magneto Plasma," Phys. Fluids, 26, 2529, 1983.
13. Kuo, S.P. and M.C. Lee, "Earth Magnetic Field Fluctuations Produced by Filementation Instabilities of Electromagnetic Heater Waves," Geophys. Res. Lett., 10,979,1983.
- 14 Kuo, S.P., M.C. Lee and F.T. Djuth, "A New Interpretation of Plasma-Line Overshoot Phenomena," Geophys. Res. Lett., 14, 961, 1987.
- 15 Kuo, S.P., and F.T. Djuth, "A Thermal Instability For the Spread_F Echoes from HF-Heated Ionosphere," Geophys. Res. Lett., 15, 1345, 1988.
16. Kuo, S.P., and M.C. Lee, "Intensity Modulation of HF Heater-Induced Plasma Lines," J. Geophys. Res. 85, 2063, 1990.
17. Kuo, S. P., A.Y. Ho, and M.C. Lee, "Temporal Evaluation of HF-Enhanced Plasma LinesEchoes," Geophys. Res. Lett. 17, 2209, 1990.

18. Perkins, F.W., C. Oberman and E.J. Valeo, "Parametric Instabilities and Ionospheric Modification," J. Geophys. Res. 79, 1678, 1974.
19. Fejer, J.A., "Ionosphere Modification and Plasma Instabilities," Rev. Geophys. Space Phys., 17, 135, 1979.
20. Bochkarev, G.S., et al., "Effect of Artificial Perturbations of the Ionosphere on the Propagation of Short-Wave Signals," Radiofizika, 20, 158, 1979.
21. Bochkarev, G.S., et al., "Interaction of Decametric Radio Waves on Frequencies Close to the MUF of F2 During Oblique Propagation," Geomagnet. Aeron., 19, 557, 1979.
22. Bochkarev, G.S., et al., "Nonlinear Interaction of Decametric Radio Waves at Close Frequencies in Oblique Propagation," J. Atmos. Terr. Phys., 44, 1137, 1982.
23. Bochkarev, G.S., et al., "Simulation of the Action of a Strong Obliquely Incident Waves," Geophys. Res. Lett., 12, 761, 1985.
25. Kuo, S.P. and B.R. Cheo, "Parametric Excitation of Coupled Plasma Waves," Phys. Fluids, 21, 1753, 1978.
26. Kuo, S.P., M.C. Lee and S.C. Kuo, "A Theoretical Model of Artificial Spread F Echoes", Radio Sci., 20, 546, 1985.
27. Kuo, S.P., "Criteria for Excitation of Parametric Instability in the Ionosphere by Obliquely Incident High frequency (HF) Heater", Phys. Fluids B, 4, 1012, 1992.

**STUDIES OF BROAD-BAND OPTICAL ABSORBERS
FOR SOLAR-POWERED ROCKET SYSTEMS**

**Peter W. Langhoff
Professor
Department of Chemistry**

**Indiana University
Bloomington, IN 47405**

**Interim Report for:
Research Initiation Program
Phillips Laboratory, Edwards AFB**

**Sponsored by:
Air Force Office of Scientific Research
Bolling AFB, Washington, DC
and
Indiana University**

December 1992

STUDIES OF BROAD-BAND OPTICAL ABSORBERS FOR SOLAR-POWERED ROCKET SYSTEMS

Peter W. Langhoff
Department of Chemistry
Indiana University
Bloomington, IN 47405

Abstract

Calculations are reported of atomic Li and molecular Li₂ transmission spectra under conditions appropriate to the Larson Plasma Spectroscopy Cell employing known spectroscopic constants and gas kinetic parameters identified below. Voigt line-shapes are adopted for the atomic Li cross section, dominated by the (unresolved) resonance doublet 2s → 2p transition, and for the Li₂ X → A, B bands in ro-vibronic resolution. The calculated transmission spectra obtained with sensible parameter estimates are in generally good agreement with measured values in the particular cases considered. Accordingly, the analysis and code system devised should provide a basis for quantitative interpretation of the full set of measured data.

Studies of Broad-Band Optical Absorbers for Solar-Powered Rocket Propulsion Systems

Peter W. Langhoff
Department of Chemistry
Indiana University
Bloomington, IN 47405

1. Introduction

Studies are reported in support of the AF Solar Rocket Propulsion Program (SRPP) [1], and of related programs pertaining more generally to aspects of radiant power conversion devices. The principle objective of the SRPP is the design, construction and operation of a high kW to low MW propulsion system employing concentrated solar radiation for the production of high-temperature, high-pressure gas propellant in the absence of chemical fuel combustion [2].

Strategies under investigation for achieving high specific impulse from concentrated radiation have centered on use of H_2 propellant gas and (i) black-body metal (Re) surface absorbers with appropriate heat-exchanger configurations [3] or (ii) trace amounts of solar absorbers seeded in the propellant gas in a suitable windowed configuration [4]. Fluid absorption systems (ii) studied to date include halogens [5] and alkali metals in H_2 or inert buffer gas flows [4]. Optical absorbance characteristics, and hence local heating, in the flow stream in such high-temperature, high-pressure situations are sensitive functions of propellant gas temperature and density conditions, which conditions are conversely strong functions of local heating. Accordingly, this circumstance generally necessitates adoption of a self-consistent approach to the absorbance and propellant flow-field combination to obtain a satisfactory device design, for which purpose precise values of state-to-state absorbance cross sections are required.

In furtherance of these requirements, attention is focused in the present study on theoretical modelling and computational interpretation of recently performed optical absorbance measurements in Li/Li₂ vapor seeded in H_2 and inert gas mixtures employing a high-temperature spectroscopy cell [4]. The calculations employing detailed Li/Li₂ state-to-state absorbance cross sections are found to account satisfactorily for the measured transmission spectra in all cases considered, suggesting the theoretical quantitative spectroscopy approach can be adopted with confidence for design studies of solar energy conversion and related power devices employing alkali metal and other absorbers over a broad range of physical conditions.

2. High-Temperature Spectroscopy Cell

The Larson spectroscopy cell is design for the study of metal vapors at temperatures up to 3,000°K and 100 atmospheres pressure [4]. The flow apparatus operates under well-characterized conditions of thermal equilibrium, and is fitted with optical ports for emission and absorbance spectroscopy measurements. An optical multi-channel analyzer

has been employed in obtaining a first set of transmission spectra in the wavelength interval of 440 to 740 nanometers (nm) at a resolution of ≈ 0.5 nm over the measured spectral interval. Approximately twenty data sets have been taken at 1 atmosphere pressure and cell temperatures up to 1,800°K employing varying concentrations of Li(v) seeded into He/Ar/H₂ entrainment gas flows.

In Figure 1 are show typical data taken at $\approx 1,600^\circ\text{K}$ employing He/Ar entrainment gas and a Li(v) concentration of $\approx 10^{17} \text{ cm}^{-3}$. A number of aspects of Figure 1 are noteworthy. The saturated broad absorption feature at ≈ 670 nm is the Li 2s \rightarrow 2p resonance absorption line [6], the bands centered at 490 and 680 nm are the molecular Li₂ X \rightarrow B and A transitions, respectively [7], and the absorption feature at ≈ 580 nm is due to the 3s \rightarrow 3p resonance line of impurity Na(v). These features and the quantitative nature of the spectrum are interpreted on basis of the state-to-state theoretical model and computations described immediately below.

3. Theory and Computations of Li/Li₂ Absorbance Spectra

The calculated transmission function for atomic Li and molecular Li₂ absorption is written in the familiar form [8]

$$T_{\Delta x}(h\nu) \equiv I_{\Delta x}(h\nu)/I_0(h\nu) \\ = \exp\{-\sigma_{Li}(h\nu)(N_{Li}/V)\Delta x - \sigma_{Li_2}(h\nu)(N_{Li_2}/V)\Delta x\},$$

where the column densities $(N_{Li}/V)\Delta x$ and $(N_{Li_2}/V)\Delta x$ are measured in cm^{-2} , and the cross sections $\sigma_{Li}(h\nu)$ and $\sigma_{Li_2}(h\nu)$, measured in cm^2 , are given by sums over products of unity normalized Voigt lineshape functions, transition-strengths, thermal-population factors for the individual lines considered, and a numerical conversion factor between cross section (cm^2) and oscillator strength density (eV^{-1}) [9]. Illustrative calculations are reported here in the case of a cell temperature of $\approx 1,600^\circ\text{K}$, a total pressure of 1 atmosphere, a total He/Ar buffer gas number density of $\approx 5.0 \times 10^{18} \text{ cm}^{-3}$, and a Li(v) seeding mole fraction of ≈ 0.15 .

In Figure 2 is shown a transmission function in vibrational resolution in the absence of lineshapes, constructed employing vibrational energies and Franck-Condon factors only for the X \rightarrow A and B band systems [10,11]. These calculated results are qualitative, and indicate the extent to which the known bands coincide with strong features in the experimental data of Figure 1.

In Figure 3 is shown the rotational structure of an individual X \rightarrow A band ($v'' = 0 \rightarrow v' = 3$), constructed in the presence of instrument broadening employing a Lorentzian pressure width of $\approx 1 \text{ cm}^{-1}$ [12,13], a Doppler width of $\approx 0.1 \text{ cm}^{-1}$ [8], and a Gaussian instrument width of $\approx 0.5 \text{ nm} \approx 15 \text{ cm}^{-1}$.

In Figure 4 is shown a calculated transmission spectrum employing values of parameters appropriate to the measured data of Figure 1. Evidently, the calculations are in good

accord with the measured transmission spectrum. The numerical values of all parameters are consistent with the temperature/pressure conditions in the observation zone, with the estimated temperature ($T \approx 1,300$ °K) in the Li evaporator in this case, with Li atom resonance pressure broadening data [12,13], and with values of the Li/Li₂ concentration ratio based on partition function estimates.

4. Concluding Remarks

The calculations reported here are designed to provide support for and clarify the nature of measured Li/Li₂ transmission spectra obtained from the Larson spectroscopy cell employing an optical multi-channel analyser. Comparison of the experimental data of Figure 1 with the calculations of Figure 4 indicates the extent to which theoretically-based quantitative spectroscopic calculations employing appropriate parameter values for the Li/Li₂ system are in accord with the measured data.

5. References

- [1] K.K. Laug, "The Solar Propulsion Concept is alive and Well at the Astronautics Laboratory," JANNAP Propulsion Meeting, Cleveland, OH, May 1989.
- [2] C.W. Larson, "Specifications for Solar-Powered Rocket Engine," Department of the Air Force Solicitation F04611-90-R-001, AF Flight Test Center, Edwards AFB, CA, April 1990.
- [3] J.M. Shoji, "Solar Rocket Component Study," AFRPL Final Report TR-84-257, Rockwell International, Rocketdyne Divison, Canoga Park, CA, February 1985
- [4] C.W. Larson, "The Spectroscopy of Hydrogen/Metal-Vapor Mixtures at High Temperatures and Pressures," AL-TR-88-080, August 1990.
- [5] E.J. Bair, D. Antolovic, and P.W. Langhoff, "Radiation Augmented Fluid Technology, WPAFB Final Report WRDC-TR-89-2036, Wright Patterson AFB, OH 45433, June 1989.
- [6] C.E. Moore, "Atomic Energy Levels," National Bureau of Standards Circular 467, Vol. 1, 1949.
- [7] K.P. Huber and G. Herzberg, *Molecular Spectra and Molecular Structure: IV. Constants of Diatomic Molecules*, (Van Nostrand Reinhold, New York, 1979), pp. 374-5.
- [8] A.C.G. Mitchell and M.W. Zemansky, *Resonance Radiation and Excited Atoms*, (Cambridge Press, Cambridge, 1971), chaps. 3-4.
- [9] J.I. Steinfeld, *Molecules and Radiation*, 2nd Ed., (MIT Press, Cambridge, MA, 1986), pp. 31-6, 295-6.
- [10] P.Kusch and M.M. Hessel, J. Chem. Phys. **67**, 586 (1977).
- [11] M.M. Hessel and C.R. Vidal, J. Chem. Phys. **70**, 4439 (1979).
- [12] N. Allard and J. Kielkopf, Rev. Mod. Phys. **54**, 1103 (1982).
- [13] K. Niemax and G. Pichler, J. Phys. **B8**, 179 (1975).

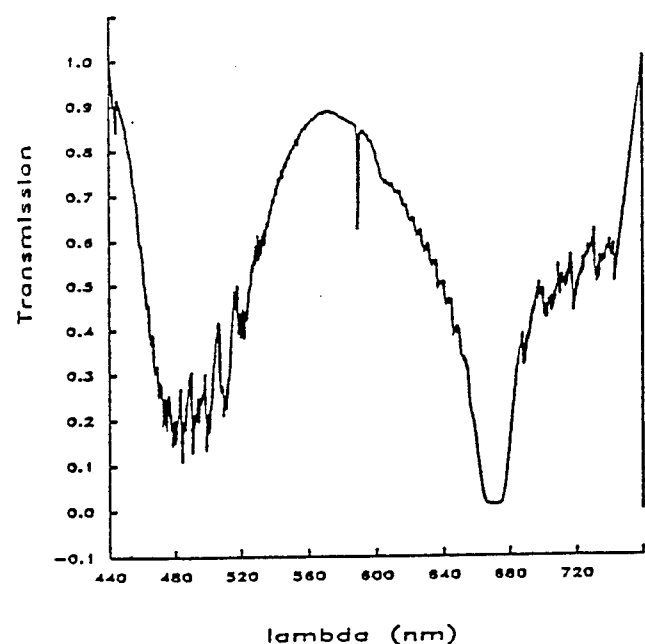


Figure 1. Experimentally determined Li/Li₂ transmission spectrum taken at an instrument resolution of $\Delta\lambda \approx 0.5$ nm and $T \approx 1,600^\circ\text{K}$ in the presence of He/Ar buffer gas. Additional description of the experimental circumstances is provided elsewhere [4].

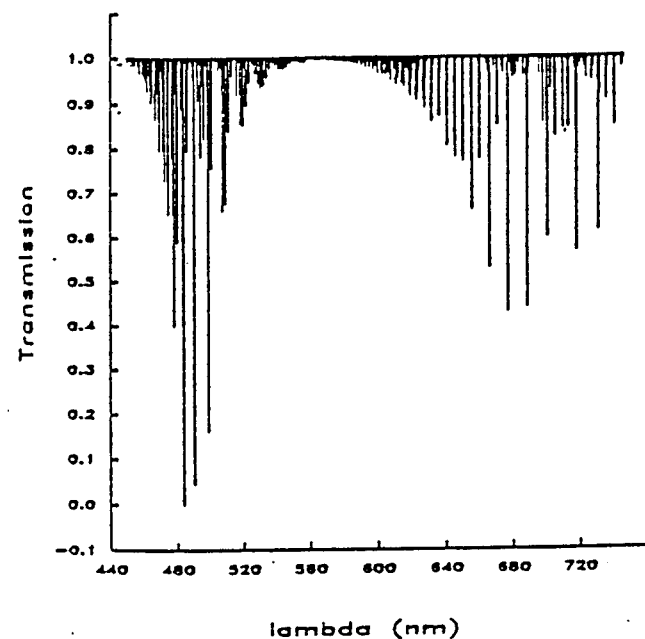


Figure 2. Calculated qualitative transmission spectra for Li₂ X \rightarrow A, B bands constructed employing vibrational energies and Franck-Condon factors [10,11] in the absence of lineshape functions.

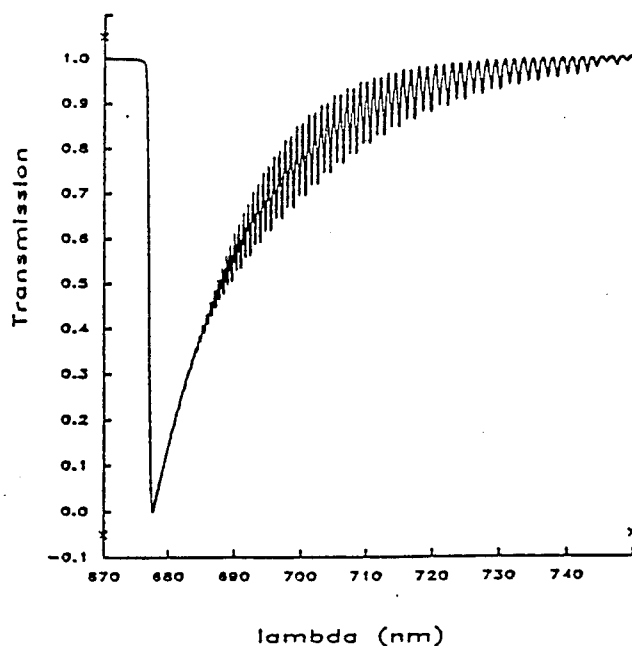


Figure 3. Calculated rotational structure in the X \rightarrow A ($v=0 \rightarrow v'=3$) band of Li₂ obtained employing Voigt lineshapes, a Lorentzian width of ≈ 1 cm⁻¹, and a Gaussian width of ≈ 0.6 nm, corresponding to instrumental resolution.

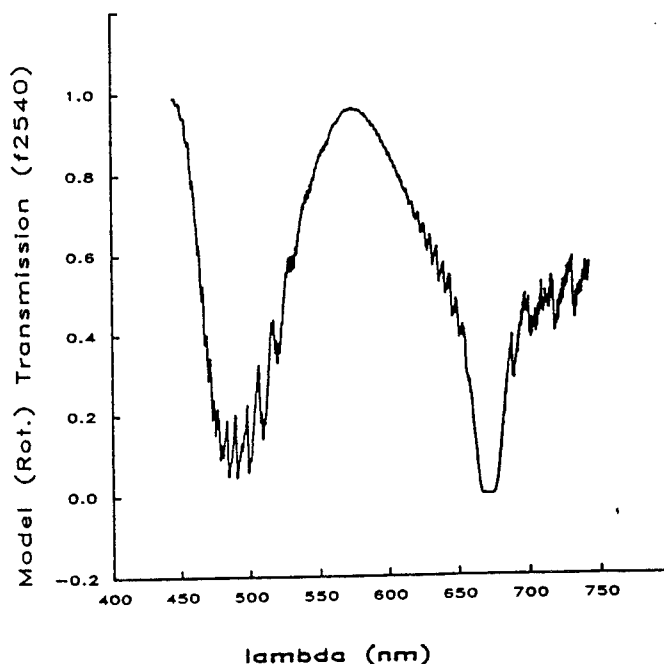


Figure 4. Calculated Li/Li₂ transmission spectrum obtained employing the development described in the text under conditions corresponding to the measured data of Figure 1.

RADIATIVE ENERGY TRANSFER IN WAVE OPTICS

Arvind S. Marathay
Professor
Optical Sciences Center

University of Arizona
Tucson, AZ 85721

Final Report for:
Research Initiation Program
Phillips Laboratory
Hanscom AFB

Sponsored by:
Air Force Office of Scientific Research
Bolling Air Force Base, Washington, D.C.

December 1992

RADIATIVE ENERGY TRANSFER IN WAVE OPTICS

Arvind S. Marathay
Professor
Optical Sciences Center
University of Arizona

Abstract

The conventional equation of radiative transfer is formulated in the frame work of ray optics. It is applicable to scalar waves. Since light is an electromagnetic wave, the ray optic and scalar description is incomplete.

The research reported here formulates the energy transfer problem in the language of wave optics. Starting from Maxwell equations, a radiative energy transfer equation is derived. It shows explicitly the wave optics contributions and includes the source terms generated by induced dielectric polarization. The usual parabolic approximation is not applicable. Without such an approximation the equation so obtained is an exact statement of radiative energy transfer. In the ray-optical limit, it shows a term that depends on the divergence of the flow vector. This term is new. It has not been studied in the context of radiative transfer.

Starting from Maxwell equations progress on obtaining the equations governing the propagation of correlation functions is also reported. This will provide the basis for studying the effects of light in any state of polarization and properly account for coherence effects in applications where radiative transfer of energy is important.

RADIATIVE ENERGY TRANSFER IN WAVE OPTICS

Arvind S. Marathay
Optical Sciences Center
University of Arizona
Tucson, AZ 85721

(1) INTRODUCTION

In the 1992 Research Initiation Program several attempts were made to obtain an equation of radiative transfer of energy in wave optics. Maxwell equations are taken as a starting point and the energy transfer is studied. This is a very desirable approach, since the results of the present research can be treated as the basis for future studies. In this way conditions under which the traditional equation is applicable may be established.

The concepts of traditional radiometry and the traditional equation of radiative transfer are all in the framework of ray or geometrical optics. It is applicable to scalar waves in the geometrical optical limit. It can treat noncoherent and/or unpolarized radiation. But the clear conditions of its applicability, where wave optic contributions may or may not be important are not known. The traditional equation is indiscriminately used in all studies, since a more complete theory is not available.

Traditional radiative transfer theory attempts to propagate specific intensity. It is counter to the strict wave theoretic point of view. In wave theory it is the wave amplitude or field correlation functions¹ that propagate. Wave aspects are lost in any attempt to limit the description to specific intensity. It is clear that there is a need for a more complete approach to the study of radiative energy transfer.

Also the concept of specific intensity (termed radiance in the radiometric literature) is based on the concepts of ray optics. Wave theoretic counterpart requires the introduction of amplitude correlation functions. The space of coordinates and angle is used

to define a quantity called radiance in the wave theory which is the closest analog to specific intensity mentioned above.

(2) EQUATION OF RADIATIVE TRANSFER

With this background information, the work began with an attempt to obtain an equation to describe energy transfer in wave optics. Maxwell equations contain the dielectric polarization, \vec{P} , magnetization, \vec{M} , charge density, ρ , and current density, \vec{j} . It was assumed that the medium is free of charges and currents and is nonmagnetic. The radiation induced dipole moment was used as a model source term. The medium was taken to be a vacuum containing isolated particles or clusters of particles interacting with radiation. Along with the work done during the summer, the above approach was completed and an equation for radiative transfer of energy was obtained in the parabolic approximation. The summer report is written as a self contained document, (its contents are not reproduced here). The result obtained there is reproduced here for further discussion,

$$\begin{aligned}
 & \frac{\partial}{\partial \zeta} (w_s |\nabla S|) + \nabla_T \cdot (w_s \nabla S) \\
 & + \frac{i}{4k_0} (\epsilon_0 \mathcal{E}_s \cdot \nabla_T^2 \mathcal{E}_s^* - c.c.) + \frac{i}{4k_0} (\mu_0 \mathcal{H}_s \cdot \nabla_T^2 \mathcal{H}_s^* - c.c.) \\
 & = -\frac{1}{4} [\mathcal{E}_s^* \cdot \nabla (\mathcal{P}_s \cdot \nabla S) + c.c.] + \frac{1}{4} \sqrt{\frac{\mu_0}{\epsilon_0}} [\mathcal{H}_s^* \cdot (\nabla \times \mathcal{P}_s) + c.c.] \\
 & + \frac{i}{4k_0} [\mathcal{E}_s^* \cdot \nabla (\nabla \cdot \mathcal{P}_s) - c.c.]
 \end{aligned} \tag{1}$$

This equation contains two types of terms. There are terms that are independent of $k_0 = 2\pi/\lambda_0$, that is the ones that do not contain the wavelength and hence constitute the ray-optic contributions. There are others that contain the wavelength and they form the wave-optic contributions. Thus the coefficient of

$1/k_0$ on the right-hand side is the wave-optics contribution of the interaction energy.

The ray-optic contributions are,

$$\begin{aligned} & \frac{\partial}{\partial \zeta} (w_s |\nabla S|) + \nabla_{\mathbf{r}} \cdot (w_s \nabla S) \\ &= -\frac{1}{4} [\mathcal{E}_s^* \cdot \nabla (\mathcal{P}_s \cdot \nabla S) + c.c.] + \frac{1}{4} \sqrt{\frac{\mu_0}{\epsilon_0}} [\mathcal{H}_s^* \cdot (\nabla \times \mathcal{P}_s) + c.c.] \end{aligned} \quad (2)$$

This is the equation that wave optics offers in the ray-optic limit. The first term on the left side, the longitudinal derivative of a quantity proportional to the total energy density, is like the one that appears in the traditional equation of transfer. However the second term, containing the transverse divergence (which belongs there in the ray-optic limit), is missing from the traditional equation. It is the transverse divergence of the flow vector, $w_s \nabla S$, whose direction is parallel to the light rays. Hence it is important to evaluate the contribution of this term in future studies. The right-hand side contains the source terms. No explicit loss mechanism was introduced. These may be included in later investigations through the imaginary part of the dielectric constant.

The traditional equation works with the specific intensity and not the energy density as it appears in the above equation. This paradox can be resolved only after the program of research related to the wave amplitude correlations is completed. At that point the space and angle coordinates can be brought together for constructing a generalized function akin to the specific intensity of traditional equation of transfer.

As discussed in the summer report the radiative transfer equation (1) was derived by using the parabolic approximation, wherein the second partial derivative on ζ is neglected. It is important to note however, that in the context of wide angle wave-

optics contributions, the $\partial^2 / (\partial \zeta^2)$ term is just as important as the terms containing the transverse Laplacian (∇_T^2) appearing on the left-hand side of Eq.(1). Thus to study wave-optics contributions the parabolic approximation should not be made. Instead of (∇_T^2) the Laplacian (∇^2) appears in Eq.(1),

$$\begin{aligned}
& \frac{\partial}{\partial \zeta} (w_s |\nabla S|) + \nabla \cdot (w_s \nabla S) \\
& + \frac{i}{4k_0} (\epsilon_0 \mathcal{E}_s \cdot \nabla_T^2 \mathcal{E}_s^* - c.c.) + \frac{i}{4k_0} (\mu_0 \mathcal{H}_s \cdot \nabla_T^2 \mathcal{H}_s^* - c.c.) \\
& = -\frac{1}{4} [\mathcal{E}_s^* \cdot \nabla (\mathcal{P}_s \cdot \nabla S) + c.c.] + \frac{1}{4} \sqrt{\frac{\mu_0}{\epsilon_0}} [\mathcal{H}_s^* \cdot (\nabla \times \mathcal{P}_s) + c.c.] \\
& + \frac{i}{4k_0} [\mathcal{E}_s^* \cdot \nabla (\nabla \cdot \mathcal{P}_s) - c.c.]
\end{aligned} \tag{3}$$

which is now an exact statement of energy transfer, since no approximations were made in deriving it.

(3) PROPAGATION OF CORRELATION FUNCTIONS

In dealing with the electromagnetic field, several auto-correlation functions and the cross-correlation functions of the field quantities are required. Furthermore each function has to be defined with components of the fields. Since Maxwell field equations are coupled, an equation derived for a single correlation function contains contributions from other correlation functions. An attempt is made to derive the equation of transfer by first obtaining the propagation equation for each correlation function.

The Maxwell equations in tensor form are,

$$\begin{aligned}
\epsilon_{ijk} \partial_j \mathcal{E}_k &= i\omega \mu_0 \mathcal{H}_i, & \epsilon_0 \partial_i \mathcal{E}_i &= -\partial_i \mathcal{P}_i \\
\epsilon_{ijk} \partial_j \mathcal{H}_k &= -i\omega \epsilon_0 \mathcal{E}_i - i\omega \mathcal{P}_i, & \mu_0 \partial_i \mathcal{H}_i &= 0
\end{aligned} \tag{4}$$

where the indexes $i, j, k=1, 2, 3$ and summation over repeated index is understood. For the correlation functions use the notation,

$\overline{A_k^{(1)} B_l^{(2)}}$, where A and B stand for the fields \mathcal{E} , \mathcal{H} , or \mathcal{P} , and the overline denotes ensemble average. The superscripts (1) and (2) indicate space points x_1, y_1, z_1 and x_2, y_2, z_2 respectively which appear as the arguments of the field quantities. The operators will also carry superscripts to indicate the variables they operate on, for example, $\partial_j^1 \overline{\mathcal{E}_k^{(1)} \mathcal{E}_l^{(2)}}$, here the first partial derivative with respect to the jth variable, is on the kth component of the electric field whose arguments are labelled with subscript 1. The field, whose arguments are labelled with subscript 2, is not operated on by, ∂_j^1 . The procedure is involved and long but it will yield a basic equation that governs the propagation of the Maxwell field correlations. With the help of this equation, the specific intensity and the law for radiative energy transfer can be obtained in the frame work of wave optics.

The basic layout of Maxwell equation is maintained in the following equations where correlation functions are introduced,

$$\begin{aligned} \epsilon_{ijk} \partial_j^{(1)} \overline{\mathcal{E}_k^{(1)} \mathcal{E}_l^{(2)}} &= i\omega \mu_0 \overline{\mathcal{H}_i^{(1)} \mathcal{E}_l^{(2)}}, & \epsilon_0 \partial_i^{(1)} \overline{\mathcal{E}_i^{(1)} \mathcal{E}_l^{(2)}} &= -\partial_i^{(1)} \overline{\mathcal{P}_i^{(1)} \mathcal{E}_l^{(2)}} \\ \epsilon_{ijk} \partial_j^{(1)} \overline{\mathcal{H}_k^{(1)} \mathcal{E}_l^{(2)}} &= -i\omega \epsilon_0 \overline{\mathcal{E}_i^{(1)} \mathcal{E}_l^{(2)}} - i\omega \overline{\mathcal{P}_i^{(1)} \mathcal{E}_l^{(2)}}, & \mu_0 \partial_i^{(1)} \overline{\mathcal{H}_i^{(1)} \mathcal{E}_l^{(2)}} &= 0 \end{aligned} \quad (5)$$

where the indexes $i, j, k, l = 1, 2, 3$ and summation over repeated index is assumed. A similar equation is obtained by multiplying from the right by the magnetic field at space point labelled (2),

$$\begin{aligned} \epsilon_{ijk} \partial_j^{(1)} \overline{\mathcal{E}_k^{(1)} \mathcal{H}_l^{(2)}} &= i\omega \mu_0 \overline{\mathcal{H}_i^{(1)} \mathcal{H}_l^{(2)}}, & \epsilon_0 \partial_i^{(1)} \overline{\mathcal{E}_i^{(1)} \mathcal{H}_l^{(2)}} &= -\partial_i^{(1)} \overline{\mathcal{P}_i^{(1)} \mathcal{H}_l^{(2)}} \\ \epsilon_{ijk} \partial_j^{(1)} \overline{\mathcal{H}_k^{(1)} \mathcal{H}_l^{(2)}} &= -i\omega \epsilon_0 \overline{\mathcal{E}_i^{(1)} \mathcal{H}_l^{(2)}} - i\omega \overline{\mathcal{P}_i^{(1)} \mathcal{H}_l^{(2)}}, & \mu_0 \partial_i^{(1)} \overline{\mathcal{H}_i^{(1)} \mathcal{H}_l^{(2)}} &= 0 \end{aligned} \quad (6)$$

where the indexes $i, j, k, l = 1, 2, 3$ and summation over repeated index is assumed as before.

By use of the standard tensor identities, Eqs.(5 and 6) may be combined to obtain the following two relationships involving electric field correlations and magnetic field correlations:

$$\partial_j^{(1)} \partial_j^{(1)} \overline{\mathcal{E}_i^{(1)} \mathcal{E}_i^{(2)}} + k_0^2 \overline{\mathcal{E}_i^{(1)} \mathcal{E}_i^{(2)}} = -\frac{1}{\epsilon_0} [\partial_i^{(1)} \partial_k^{(1)} \overline{\mathcal{P}_k^{(1)} \mathcal{E}_i^{(2)}} + k_0^2 \overline{\mathcal{P}_i^{(1)} \mathcal{E}_i^{(2)}}] \quad (7)$$

$$\partial_j^{(1)} \partial_j^{(1)} \overline{\mathcal{H}_i^{(1)} \mathcal{H}_i^{(2)}} + k_0^2 \overline{\mathcal{H}_i^{(1)} \mathcal{H}_i^{(2)}} = \frac{ik_0}{\sqrt{\epsilon_0 \mu_0}} \epsilon_{ijk} \partial_j^{(1)} \overline{\mathcal{P}_k^{(1)} \mathcal{H}_i^{(2)}} \quad (8)$$

These two equations are similar to the ones obtained in the context of the vector form as given in the summer report, with the exception of the field variables with superscripts (2) which appear in the correlation functions.

At this point assume that all the auto-correlation and cross-correlation functions have the form,

$$\overline{A_i^{(1)} B_i^{(2)}} = (AB)_{sit}^{(12)} \exp[ik_0 S^{(12)}] \quad (9)$$

where A and B stand for one of the fields $\mathcal{E}_i^{(1)}$, $\mathcal{H}_i^{(1)}$, or $\mathcal{P}_i^{(1)}$. The double symbol in parenthesis is used to designate the factor multiplying the exponential function. This factor can be complex in general. The exponent contains $k_0 = (2\pi)/\lambda_0$, and all correlations are assumed to have the same function $S^{(12)}$, akin to the eikonal function used for a single field variable in the last section. Both the double-symbol variable and $S^{(12)}$ are functions of the coordinates x,y,z. This assumed form of the correlations helps transform Eqs.(7 and 8) into the form,

$$K_{it} + \frac{i}{k_0} L_{it} + \frac{1}{k_0^2} M_{it} = 0 \quad (10)$$

The functions K, L, and M for the respective equations are listed below.

Thus for Eq.(7) get,

$$K_{it} = [-\partial_j^{(1)} S^{(1,2)} \cdot \partial_j^{(1)} S^{(1,2)} \cdot (\mathcal{E}\mathcal{E})_{sit}^{(1,2)} + (\mathcal{E}\mathcal{E})_{sit}^{(1,2)}] \\ + \frac{1}{\epsilon_0} [-\partial_k^{(1)} S^{(1,2)} \cdot \partial_i^{(1)} S^{(1,2)} \cdot (\mathcal{P}\mathcal{E})_{skt}^{(1,2)} + (\mathcal{P}\mathcal{E})_{sit}^{(1,2)}] \quad (11)$$

$$L_{it} = [\partial_j^{(1)} \partial_j^{(1)} S^{(1,2)} \cdot (\mathcal{E}\mathcal{E})_{sit}^{(1,2)} + 2\partial_j^{(1)} S^{(1,2)} \cdot \partial_j^{(1)} (\mathcal{E}\mathcal{E})_{sit}^{(1,2)}] \\ + \frac{1}{\epsilon_0} [\partial_i^{(1)} \partial_k^{(1)} S^{(1,2)} \cdot (\mathcal{P}\mathcal{E})_{skt}^{(1,2)} + \partial_i^{(1)} S^{(1,2)} \cdot \partial_k^{(1)} (\mathcal{P}\mathcal{E})_{skt}^{(1,2)} + \partial_k^{(1)} S^{(1,2)} \cdot \partial_i^{(1)} (\mathcal{P}\mathcal{E})_{skt}^{(1,2)}] \\ M_{it} = [\partial_j^{(1)} \partial_j^{(1)} (\mathcal{E}\mathcal{E})_{sit}^{(1,2)}] + \frac{1}{\epsilon_0} [\partial_i^{(1)} \partial_k^{(1)} (\mathcal{P}\mathcal{E})_{skt}^{(1,2)}] \quad (12)$$

In a like manner Eq.(8) gives,

$$K'_{it} = [-\partial_j^{(1)} S^{(1,2)} \cdot \partial_j^{(1)} S^{(1,2)} \cdot (\mathcal{H}\mathcal{H})_{sit}^{(1,2)} + (\mathcal{H}\mathcal{H})_{sit}^{(1,2)}] \\ + \frac{1}{\sqrt{\epsilon_0 \mu_0}} [\epsilon_{ijk} \partial_j^{(1)} S^{(1,2)} \cdot (\mathcal{P}\mathcal{H})_{skt}^{(1,2)}] \quad (13)$$

$$L'_{it} = [\partial_j^{(1)} \partial_j^{(1)} S^{(1,2)} \cdot (\mathcal{H}\mathcal{H})_{sit}^{(1,2)} + 2\partial_j^{(1)} S^{(1,2)} \cdot \partial_j^{(1)} (\mathcal{H}\mathcal{H})_{sit}^{(1,2)}] \\ - \frac{1}{\sqrt{\epsilon_0 \mu_0}} \epsilon_{ijk} \partial_j^{(1)} (\mathcal{P}\mathcal{H})_{skt}^{(1,2)} \quad (14)$$

$$M'_{it} = \partial_j^{(1)} \partial_j^{(1)} (\mathcal{H}\mathcal{H})_{sit}^{(1,2)}$$

A prime is used on these symbols to distinguish them from the ones used for Eq.(7).

The ray optical limit of these equations results in,

$$[\partial_j^{(1)} S^{(1,2)} \cdot \partial_j^{(1)} S^{(1,2)} - 1] (\mathcal{E}\mathcal{E})_{sit}^{(1,2)} \\ = -\frac{1}{\epsilon_0} [\partial_i^{(1)} S^{(1,2)} \cdot \partial_k^{(1)} S^{(1,2)} \cdot (\mathcal{P}\mathcal{E})_{skt}^{(1,2)} - (\mathcal{P}\mathcal{E})_{sit}^{(1,2)}] \quad (15)$$

$$\begin{aligned}
& [\partial_j^{(1)} S^{(1,2)} \cdot \partial_j^{(1)} S^{(1,2)} - 1] (\mathcal{H})_{sit}^{(1,2)} \\
& = \frac{1}{\sqrt{\epsilon_0 \mu_0}} [\epsilon_{ijk} \partial_j^{(1)} S^{(1,2)} \cdot (\mathcal{P}\mathcal{H})_{skt}^{(1,2)}]
\end{aligned} \tag{16}$$

These two conditions are analogous to those found with the field variables as reported fully in the Summer Report.

If these conditions are fulfilled, Eqs. (11 to 14) are reduced to the form, $M_{it} + ik_0 L_{it} = 0$. The resulting equations yield equations similar to the transport equations.

This work although much involved is aimed at obtaining the set of equations governing the propagation of field correlations. The correlations will contain fields at different space points and different polarization. A propagation equation for the correlation function of the scalar field is reported in the literature, see McCoy and Beran ². Such an equation for the electromagnetic field has not been attempted in the literature. This work is in line with the discussion regarding correlation functions in section (1) of this report. The governing equations will form the basis with which to obtain the radiative-transfer equation of spectral radiance (specific intensity) of the vector field as indicated in section (2) of this report. The work is still in progress and the relevant equations will be reported in a journal article.

(4) OUTLOOK

The work with the electromagnetic correlation functions should be extended to include the traditional³ emission coefficient j_v , the absorption coefficient k , and the source function which is defined as the ratio, $S_v = \frac{j_v}{k}$. These quantities are introduced

phenomenologically. In the wave-theoretic approach it is desirable to introduce these terms from first principles. For this purpose the usual Einstein A and B coefficients are used,

$$k = (N_1 B_{12} - N_2 B_{21}) \frac{h\nu}{4\pi}$$

$$S_v = \frac{N_2 A_{21}}{N_1 B_{12} - N_2 B_{21}}$$

where N_1 and N_2 are the populations of the lower and upper states respectively. The required terms are more appropriately included in the theory by studying the interaction of radiation and matter. But this requires that the electromagnetic field be quantized to properly include the contribution of spontaneous emission. To avoid the procedure of quantization an approach by MacGillivray and Feld⁴ may be used, where spontaneous emission is simulated by a model of a fluctuating dipole. A complete theory to formulate the equation of transfer from first principles is obviously important, since the equation is used widely for different applications.

REFERENCES

1. Marathay, A. S., Elements of Optical Coherence Theory, Wiley, New York, (1982).
2. McCoy, J. J. and M. J. Beran, "Propagation of beamed signals through inhomogeneous media: A diffraction theory," J. Acoust. Soc. Am. **59** 1142-1149, (1976)
3. T. L. Swihart, "Basic physics of stellar atmospheres," section 5, Pachart Pub. House, Tucson, 1971
4. MacGillivray, J. C. and M. S. Feld, "Theory of superradiance in an extended, optically thick medium," Phys. Rev. A **14** #3 1169-1189 (1976)

IMPROVED PASSIVE DAMPING IN COMPOSITE TUBES
USED IN LARGE SPACE STRUCTURES

Dr. Christopher A. Rotz
Associate Professor and Principal Investigator
Department of Manufacturing Engineering and Engineering Technology

Dr. Dennis D. Olcott
Former Graduate Student
Department of Mechanical Engineering

Brigham Young University
435 CTB
Provo, Utah 84602

Final Report for:
Research Initiation Grant Program
Phillips Laboratory

Sponsored by:
Air Force Office of Scientific Research
Edwards Air Force Base, California

JANUARY 1993

IMPROVED PASSIVE DAMPING IN COMPOSITE TUBES USED IN LARGE SPACE STRUCTURES

Dr. Christopher A. Rotz
Associate Professor and Principal Investigator
Department of Manufacturing Engineering and Engineering Technology

Dr. Dennis D. Olcott
Former Graduate Student
Department of Mechanical Engineering

Brigham Young University

Abstract

Stress Coupling Activated Damping (SCAD) is a unique design concept developed at Brigham Young University to combine the high stiffness and low weight of composite materials with significant passive damping. It uses the stress coupling effect of anisotropic materials, like fiber reinforced composites, to increase the damping effectiveness of embedded viscoelastic layers beyond what is possible with the previous technology. This new approach is able to damp both in-plane and out-of-plane modes of vibration. A theoretical model has been developed for axially-loaded thin wall tubes and flat membranes, and used to conduct non-dimensional parametric studies. Several damped tubes were constructed and tested to validate the model. The predicted and measured natural frequencies and loss factors were in close agreement. One application for these tubes is the one-third scale model of a space-based laser structure currently being studied in the Phillips Laboratory's ASTREX facility. Damped tubes were fabricated to replace the composite tubes supporting ASTREX's tertiary mirror. The new tubes match the originals in both stiffness and weight, but should have loss factors of 10.8% at the 17 Hz vibration mode in ASTREX. This loss factor is over 10 times higher than that of the original tubes.

IMPROVED PASSIVE DAMPING IN COMPOSITE TUBES USED IN LARGE SPACE STRUCTURES

Dr. Christopher A. Rotz, Principal Investigator
Dr. Dennis D. Olcott

1. INTRODUCTION

The vibrational behavior of a structure is an important consideration in many design applications. Problems associated with uncontrolled vibrations include fatigue damage of the structures themselves; pilot and passenger discomfort in aerospace vehicles; damage to sensitive electronic equipment; and camera and antenna misalignment causing blurred photographs and radar images in aircraft and satellites. Studying methods for controlling such vibrations is one of the primary tasks of the Phillips Laboratory's ASTREX (Advanced Space Structure Technology Research Experiment) facility at Edwards Air Force Base, California.

Several methods are commonly used to reduce the effects of unwanted vibrations including stiffening the structure, adding rubber or viscoelastic materials to absorb vibrations (passive damping), and using electronic sensors and actuators to control vibrations (active damping).

One of the most common passive damping technologies is called Constrained Layer Damping (CLD) (1, 2). In its most common form CLD is achieved by bonding a thin layer of aluminum sheet to an existing structure with a viscoelastic adhesive. When out-of-plane deformations occur during vibration, differential in-plane displacements between the original structure and the aluminum sheet induce shear strains in the viscoelastic material. Through hysteresis losses, vibration energy is converted to thermal energy which is dissipated to the environment. The chief limitations of CLD are that it adds weight, it can only be applied to the surface of a structure, and it is only effective for *out-of-plane* vibrations. CLD is most commonly used as a fix for problems on an existing structure, not as part of its original design.

Viscoelastic layers can also be embedded within a composite structure during lay-up (or other manufacturing process) and cocured (3). Unfortunately, the practical application of cocured damping layers has been limited by the negative effects they have on structural stiffness. For example, in the case of a plate in bending, the greatest damping is obtained when the viscoelastic layer is placed at the mid plane along the neutral axis. But this also dramatically reduces the plate's bending stiffness, because useful viscoelastic materials are generally very flexible. In addition, the embedded layer would still only be effective for out-of-plane vibrations.

1.1 BYU's Damping Concept: Stress Coupling Activated Damping

A unique design concept which significantly increases the damping in composite structures without large reductions in stiffness or increases in weight has recently been developed at Brigham Young University (4). This patent-applied-for technology is called Stress Coupling Activated Damping (SCAD). SCAD uses the stress coupling effect of nonisotropic materials, like fiber reinforced composites, to increase the damping in embedded viscoelastic layers, far beyond what is possible with the previous technology.

Fig. 1.1 shows a simple SCAD part consisting of one layer of damping material embedded between two layers of fiber reinforced composite materials. Throughout this report, the layers will be called damping and stiffness layers, respectively. The fiber orientation angle in the top layer (indicated by the zig-zag lines) is varied several times along the length. The fibers in the bottom layer are oriented in the opposite directions. Since all the fibers are "off-axis", an axial load will cause the upper and lower layers to move transversely in opposite directions, thus shearing the damping layer. In addition, vibration modes which induce in-plane shear strains will cause differential axial displacements, again shearing the viscoelastic layer and increasing the damping.

It is important to understand that with Stress Coupling Activated Damping, the structure will be damped regardless of whether it experiences in-plane or out-of-plane vibrations. No matter what kind of motion is imposed, the damping layer will be sheared. Contrast this with the present technology (e.g., CLD) in which shear strains in a damping layer are only produced when the part undergoes out-of-plane motion. Consequently, there is no control of in-plane vibrations. SCAD will actually damp out-of-plane motions more effectively than will CLD because of the additional shearing produced by the stress-coupling effect.

When the part shown in Fig. 1.1 is loaded axially, the resulting transverse motions, and thus the shear strains, are greatest in the locations where the fiber orientation angle changes. If the fiber angle in each layer did not change along the length (i.e., each layer were composed of only one segment) most of the shearing (and hence damping) would occur near the ends of the part. If the ends were clamped in fixtures that did not permit relative motion between the top and bottom layers, the damping would be eliminated. Therefore, if the orientation angle is varied several times along the length, as shown, areas of high shear will be produced all along the part, not just at the ends. This increases the amount of damping overall and permits the use of simple end fixtures.

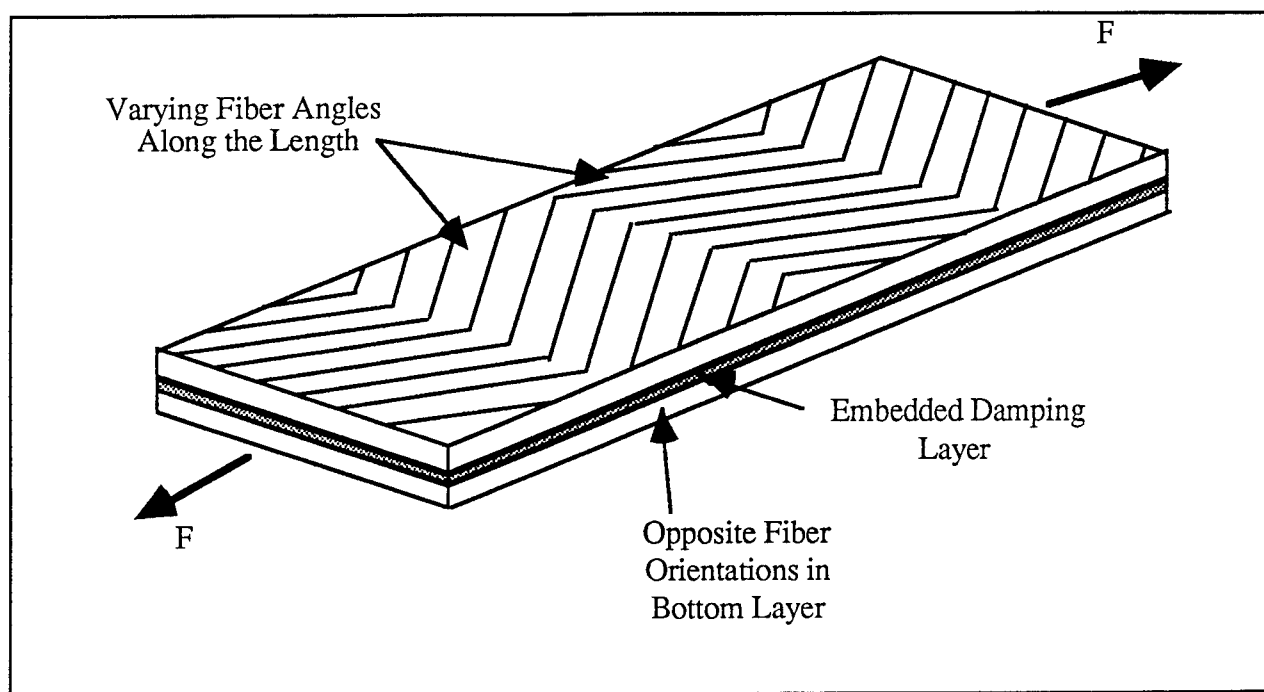


Figure 1.1. New concept for optimizing the damping and stiffness of composite structures: Stress Coupling Activated Damping. The lines on the upper surface indicate the orientation of the fibers in the top layer. The fibers in the bottom layer are oriented in the opposite directions. When loaded in tension, as shown, the off-axis fibers produce transverse motions which intensely shear the embedded damping layer.

It should be emphasized that with SCAD the axial stiffness of the bar is largely unaffected because the load path passes through the stiffness layers only. The axial stiffness is almost entirely controlled by the properties of the composite layers.

1.2 Goals of the Project

It was proposed that a research project be carried out to determine the feasibility of applying the SCAD technology to the type of thin wall composite tubes being considered for large space structures. The proposed tasks included the following:

1. Complete the development of the existing SCAD theory (4), as applied to thin wall tubes. Model the effects of the overlap joints between adjacent segments.
2. Non-dimensionalize the theory so design calculations will be simplified. Report the results in charts and figures suitable for design calculations.
3. Experimentally verify the theory and modeling methods by dynamically testing damped tubes in axial vibration.
4. Determine the effects of the design changes on static axial stiffness.

5. Experimentally measure the behavior of the tubes in bending vibration.
6. Construct several passively damped tubes for the ASTREX research structure. Specifically, design and build new support members for the tertiary mirror. Phillips Laboratory will provide all necessary end fittings.
7. Deliver a final report summarizing all work completed, new findings, conclusions, and suggested future research to the Phillips Laboratory.

This report will describe the development of a theoretical model for applying SCAD to axially loaded thin wall tubes, the experimental work done to verify the theory, and finally, the design and testing of the damped tertiary mirror support members for ASTREX.

2. ANALYTICAL MODELING

2.1 Damped Membranes

A model will first be developed for damped flat membranes. Membranes are defined here as a combination of stiffness and damping layers which together have in-plane stiffness only. The properties of the membrane as a whole may vary in only one direction (along the x-axis). As will be shown later, the model of a damped flat membrane can then be used to predict the behavior of damped thin wall tubes where the effects of curvature are negligible.

2.1.1 Notation, Coordinate Axes, and Sign Conventions

In general, a damped laminate may consist of N stiffness layers and $N-1$ damping layers. Fig. 2.1, shows one damping and two stiffness layers extracted from such a structure. Each layer is parallel to the xy -plane with its properties varying in the x -direction only. Stiffness layers are numbered 1 to N , from bottom to top. Damping layers are numbered 1 to $N-1$, with each having the same number as the stiffness layer directly below it. Thus, damping layer j in Fig. 2.1 has stiffness layer j directly underneath and stiffness layer $j+1$ directly above. Fiber orientation in layer j is designated by the angle ϕ_j . Note that each ϕ_j is a function of x . Either a superscript or a subscript d will be used to denote all stresses, strains, displacements, and material properties within a damping layer. Coordinate variables (x,y,z) will not be so denoted. Displacements in the x , y , and z directions are u , v , and w , respectively.

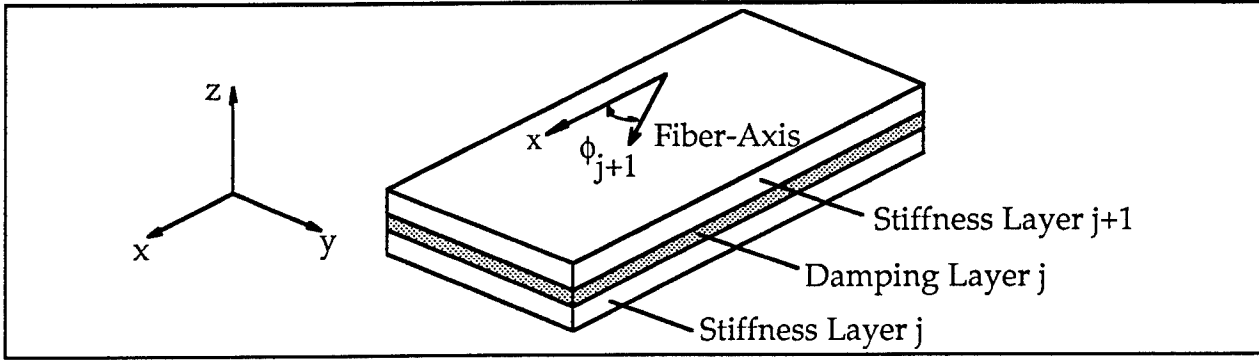


Figure 2.1 Coordinate axes and sign conventions used in the analysis. Properties may vary from layer to layer. Within a layer, properties may vary in the x-direction only.

2.1.2 Assumptions

The assumptions made in the analysis of the stiffness and damping layers are:

General

1. The only external loads acting on the laminate are an axial (x-direction) load and an in-plane shear load.
2. There is no slip at the interface between a stiffness layer and a damping layer.
3. Displacements are not functions of y, therefore: $\frac{\partial u}{\partial y} = 0$ and $\frac{\partial v}{\partial y} = 0$.

Damping Layers

4. Each damping layer is isotropic and has a complex shear modulus G_{dj}^* . Since these moduli are much lower than those of the stiffness layers, the normal stresses in the damping layers are assumed negligible; only τ_{xz}^d and τ_{yz}^d are important.

Stiffness Layers

5. The orthotropic composite material properties in each stiffness layer may be determined from traditional laminate theory.
6. Each stiffness layer is assumed to be thin enough that all in-plane stresses and displacements do not vary through its thickness. The only important stresses in each stiffness layer are σ_{xx} , and τ_{xy} . (σ_{yy} is assumed to be zero.)

2.1.3 Damping Layers

From the above assumptions, the shear stresses in damping layer j are:

$$\tau_{xzj}^d = G_{dj}^* \gamma_{xzj}^d = G_{dj}^* \frac{\partial u_j^d}{\partial z} \quad \text{and} \quad \tau_{yzj}^d = G_{dj}^* \gamma_{yzj}^d = G_{dj}^* \frac{\partial v_j^d}{\partial z} \quad (2.1)$$

Stress equilibrium requires that shear stresses be functions of x only. In light of Equation 2.1, this can only be true if

$$u_j^d(x, z) = f_1(x)z + f_2(x) \quad \text{and} \quad v_j^d(x, z) = f_3(x)z + f_4(x) \quad (2.2)$$

where f_1, f_2, f_3 , and f_4 are functions of x . Since there is no slip at the interfaces between the damping and stiffness layers,

$$u_j(x) = u_j^d(x, 0) \quad u_{j+1}(x) = u_j^d(x, t_{dj}) \quad v_j(x) = v_j^d(x, 0) \quad \text{and} \quad v_{j+1}(x) = v_j^d(x, t_{dj}) \quad (2.3)$$

where t_{dj} is the thickness of damping layer j . Equations 2.1, 2.2, and 2.3 can then be combined to express the shear stresses in the damping layer entirely in terms of the displacements of the adjacent stiffness layers:

$$\tau_{xzj}^d = G_{dj}^* \left[\frac{u_{j+1} - u_j}{t_{dj}} \right] \quad \text{and} \quad \tau_{yzj}^d = G_{dj}^* \left[\frac{v_{j+1} - v_j}{t_{dj}} \right] \quad (2.4)$$

2.1.4 Stiffness Layers

Since the only non-zero stresses in the stiffness layers are σ_{xx} and τ_{xy} , the general orthotropic stress-strain relationships can be written:

$$\begin{bmatrix} \sigma_{xx} \\ \tau_{xy} \end{bmatrix}_j = \begin{bmatrix} K_{11} & K_{16} \\ K_{16} & K_{66} \end{bmatrix}_j \begin{bmatrix} \epsilon_{xx} \\ \gamma_{xy} \end{bmatrix}_j \quad (2.5)$$

The terms K_{11j} , K_{16j} , and K_{66j} are functions of E_{11j}^* (the complex modulus along the fiber axis), E_{22j}^* (the complex modulus transverse to the fiber axis), E_{12j}^* (the complex shear modulus), ν_{12j}^* (the complex Poisson's ratio), and ϕ_j . These relationships may be found in any reference on composite laminate analysis.

Consider the differential stiffness layer element shown in Fig. 2.2. The stresses within the element are σ_{xx} and τ_{xy} . The adjacent damping layers exert shear stresses $\tau_{xz\text{lower}}$ and $\tau_{yz\text{lower}}$ on the bottom surface and $\tau_{xz\text{upper}}$ and $\tau_{yz\text{upper}}$ on the top surface. Equilibrium of forces in the x -direction implies that

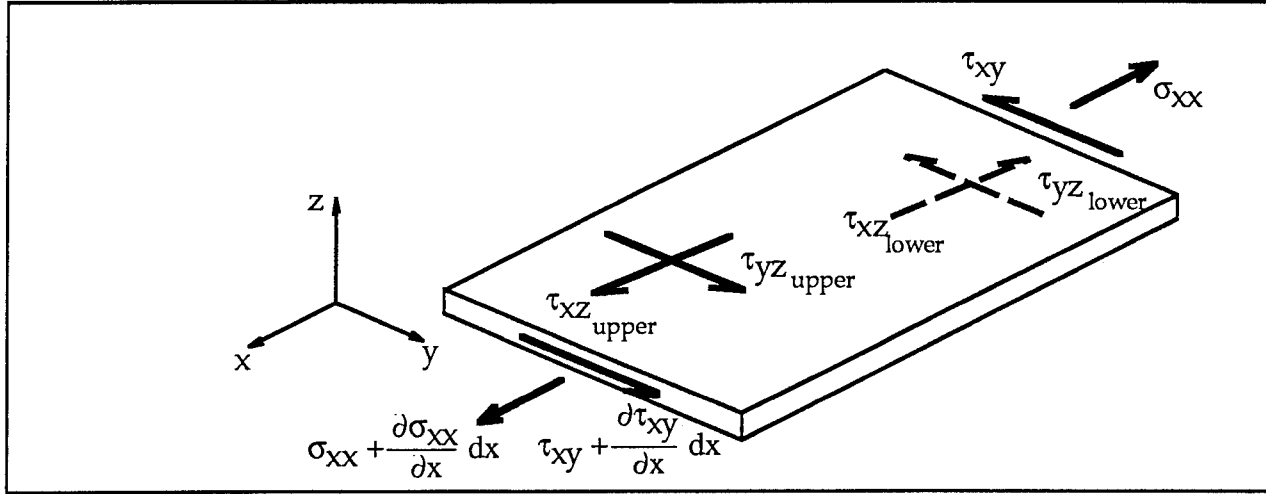


Figure 2.2. Stress equilibrium diagram for a single stiffness layer element of length dx and thickness t_s . Only the stress components affecting equilibrium in the x - and y -directions have been included; the others have been left off for clarity.

$$\frac{\partial \sigma_{xx}}{\partial x} t_s + (\tau_{xz_{upper}} - \tau_{xz_{lower}}) = 0 \quad (2.6)$$

where t_s is the thickness of the stiffness layer.

Note that the shear stresses acting on the surface of stiffness layer j must be equal in magnitude and opposite in direction to the shear stress at the contacting surfaces of the neighboring damping layers. Thus,

$$\begin{aligned} (\tau_{xz_{upper}})_j &= (\tau_{xz}^d)_{j+1} & (\tau_{yz_{upper}})_j &= (\tau_{yz}^d)_{j+1} \\ (\tau_{xz_{lower}})_j &= (\tau_{xz}^d)_{j-1} & (\tau_{yz_{lower}})_j &= (\tau_{yz}^d)_{j-1} \end{aligned} \quad (2.7)$$

Equation 2.6, can be simplified to an equation involving displacements only, using the normal strain-displacement relations from elasticity theory and Equations 2.4, 2.5, and 2.7:

$$K_{11j}^* \frac{\partial^2 u_j}{\partial x^2} + K_{16j}^* \frac{\partial^2 v_j}{\partial x^2} + G_{dj}^* \left[\frac{u_{j+1} - u_j}{t_{sj} t_{dj}} \right] - G_{dj-1}^* \left[\frac{u_j - u_{j-1}}{t_{sj} t_{dj-1}} \right] = 0 \quad (2.8)$$

By a similar process, equilibrium in the y-direction leads to the result

$$K_{16j}^* \frac{\partial^2 u_j}{\partial x^2} + K_{66j}^* \frac{\partial^2 v_j}{\partial x^2} + G_{dj}^* \left[\frac{v_{j+1} - v_j}{t_{sj} t_{dj}} \right] - G_{dj-1}^* \left[\frac{v_j - v_{j-1}}{t_{sj} t_{dj-1}} \right] = 0 \quad (2.9)$$

2.1.5 Multiple Stiffness Layers with Uniform Damping Layers

If all the damping layers have the same thickness, t_d , and complex shear modulus, G_d^* , Equations 2.8 and 2.9 may be simplified and written in matrix form:

$$\begin{bmatrix} K_{11j}^* & K_{16j}^* \\ K_{16j}^* & K_{66j}^* \end{bmatrix} \frac{\partial^2}{\partial x^2} \begin{bmatrix} u_j \\ v_j \end{bmatrix} + D_j^* \begin{bmatrix} 1 & 0 & -2 & 0 & 1 & 0 \\ 0 & 1 & 0 & -2 & 0 & 1 \end{bmatrix} \begin{bmatrix} u_{j-1} \\ v_{j-1} \\ u_j \\ v_j \\ u_{j+1} \\ v_{j+1} \end{bmatrix} = 0 \quad j=1,2,\dots,N \quad (2.10)$$

where
$$D_j^* = \frac{G_d^*}{t_{sj} t_d} \quad (2.11)$$

Note that when $j = 1$, the displacements u_{j-1} and v_{j-1} should be eliminated from Equation 2.10. Similarly, when $j = N$, the displacements u_{j+1} and v_{j+1} should be eliminated.

2.1.6 Non-dimensionalization For Components With Stiffness Layers Having Identical Material Properties and Thicknesses

The problem will now be simplified to the case where all the stiffness layers have the same thickness, t_s , and the same principal complex engineering constants (E_{11}^* , E_{22}^* , E_{12}^* , and ν_{12}^*). Equation 2.10 can then be non-dimensionalized:

$$\begin{bmatrix} \hat{K}_{11j}^* & \hat{K}_{16j}^* \\ \hat{K}_{16j}^* & \hat{K}_{66j}^* \end{bmatrix} \frac{\partial^2}{\partial \hat{x}^2} \begin{bmatrix} \hat{u}_j \\ \hat{v}_j \end{bmatrix} + D_0^* \begin{bmatrix} 1 & 0 & -2 & 0 & 1 & 0 \\ 0 & 1 & 0 & -2 & 0 & 1 \end{bmatrix} \begin{bmatrix} \hat{u}_{j-1} \\ \hat{v}_{j-1} \\ \hat{u}_j \\ \hat{v}_j \\ \hat{u}_{j+1} \\ \hat{v}_{j+1} \end{bmatrix} = 0 \quad j=1,2,\dots,N \quad (2.12)$$

$$\text{where } \hat{K}_{pqj}^* = \frac{K_{pqj}^*}{E_{11}^*} \quad \hat{u}_j = \frac{u_j}{L} \quad \hat{v}_j = \frac{v_j}{L} \quad \hat{x} = \frac{x}{L} \quad D_0^* = \frac{G_d^*}{E_{11}^*} \left(\frac{L}{t_s} \right) \left(\frac{L}{t_d} \right) \quad (2.13)$$

The choice of the length, L , will be discussed in Section 2.1.9. Note that

$$\hat{K}_{pqj} = \hat{K}_{pqj}(\hat{E}_{22}^*, \hat{E}_{12}^*, v_{12}^*, t_s, \phi_j(\hat{x})) \quad \text{where} \quad \hat{E}_{22}^* = \frac{E_{22}^*}{E_{11}^*} \quad \text{and} \quad \hat{E}_{12}^* = \frac{E_{12}^*}{E_{11}^*} \quad (2.14)$$

Equations 2.12-2.14 can be assembled into a matrix equation with $2N$ complex unknowns:

$$\left[\hat{K}^* \right] \frac{\partial^2}{\partial \hat{x}^2} \{ \hat{u} \} + \left[D^* \right] \{ \hat{u} \} = 0 \quad \text{where} \quad \{ \hat{u} \} = \begin{Bmatrix} \hat{u}_1 \\ \hat{v}_1 \\ \dots \\ \dots \\ \hat{u}_N \\ \hat{v}_N \end{Bmatrix} \quad (2.15)$$

(The elements of the matrices $[\hat{K}^*]$ and $[D^*]$ will not be listed here since they can be easily obtained when Equation 2.15 is formed.)

2.1.7 Components With Constant Fiber-Angle Sections

It will now be assumed that the membrane is composed of sections in which the fiber angles, $\phi_j(\hat{x})$, are constant, i.e., $\phi_j(\hat{x}) = \phi_{0j}$. Then within each segment, Equation 2.15 is an eigenvalue problem whose solution is

$$\begin{aligned} \{ \hat{u} \} &= \sum_{n=1}^N \{ \hat{u}_0 \}_n \left[\hat{c}_{+n}^* e^{\lambda_n \hat{x}} + \hat{c}_{-n}^* e^{-\lambda_n \hat{x}} \right] & \text{for } \lambda_n^2 \neq 0 \\ &\quad \text{or} & \\ &\left[\hat{c}_{+n}^* + \hat{c}_{-n}^* \hat{x} \right] & \text{for } \lambda_n^2 = 0 \end{aligned} \quad (2.16)$$

where λ_n^2 and $\{ \hat{u}_0 \}_n$, are the n^{th} eigenvalues and eigenvectors, respectively, and \hat{c}_{+n}^* and \hat{c}_{-n}^* are complex constants. (Note that for the case, $\lambda_n^2 = 0$, the terms in the square brackets on the right side of the equation must be replaced by the second expression indicated above.) The constants in Equation 2.16 are found by applying the appropriate boundary conditions for each section.

If a membrane is composed of P sections, there will be P sets of Equations 2.15 and 2.16. As will be discussed later, under certain circumstances it is possible to model an entire component composed of many sections with one analysis element of only 3 sections, substantially reducing the complexity of the necessary calculations.

2.1.8 Boundary Conditions

The corresponding displacements in each layer of adjoining sections must be equal. The corresponding resultant shear and axial loads in each layer of adjoining sections must be equal and opposite. The resultant axial and shear loads on opposite ends of the entire component must be equal and opposite and balance with any applied external loads. Rigidly clamping a single stiffness layer at one end of the component and allowing all of the other layers to displace freely results in no loss of generality.

2.1.9 Flat Membrane Laminates With 2 Stiffness Layers

The analysis will now be restricted to in-plane-loaded membranes with two stiffness layers, similar to the one shown in Fig. 1.1. The membrane is constructed of several segments of length L (see the sketch in the lower right of Fig. 2.3). The fiber orientation angles in adjacent segments are equal and opposite in sign ($+\phi_0$ and $-\phi_0$), with the angles in the bottom layer also equal and opposite to those in the top. To strengthen the joints between segments, the plies which make them up are overlapped by a distance, L_{overlap} .

Such a component can be accurately modeled by analyzing the three-section element shown in Fig. 2.3. Note that the analysis element extends between the midpoints of two adjacent segments. Thus it has a total length equal to the segment length, L . The two end sections of the element have the same length, L_{sub} , where

$$L_{\text{sub}} = \frac{L - L_{\text{overlap}}}{2} \quad (2.17)$$

The dimensionless overlap, \hat{L}_{overlap} , is

$$\hat{L}_{\text{overlap}} = \frac{L_{\text{overlap}}}{L} \quad (2.18)$$

The stiffness layers in the overlap section are modeled as having the properties of a balanced laminate with an equal number of $+\phi_0$ and $-\phi_0$ plies. (Note, the segment length L is used to non-dimensionalize the terms in Equation 2.13. Thus, the effects of varying different combinations of

length, thickness, and material properties may be evaluated simply by varying D_O^* , and the other dimensionless parameters appropriately.)

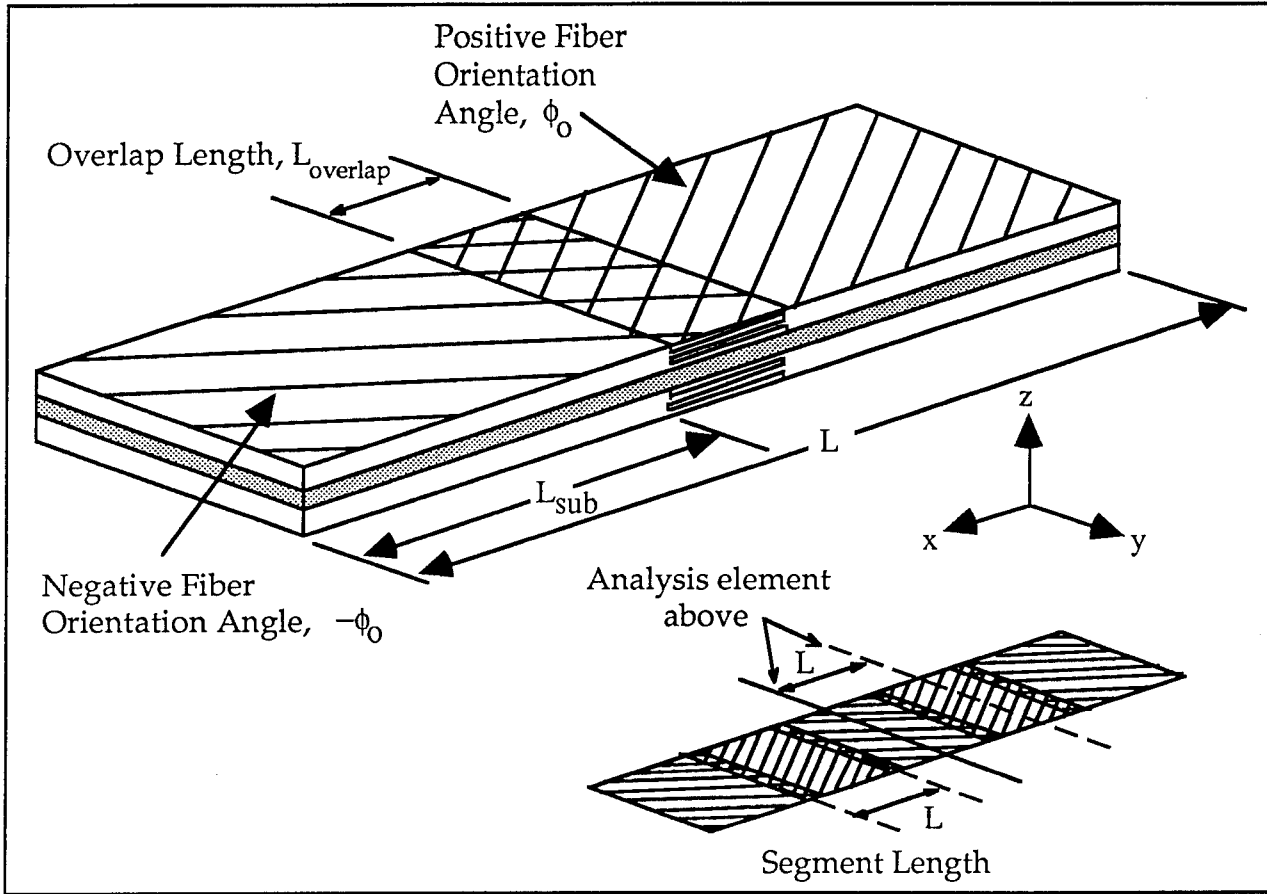


Figure 2.3. Analysis element for a two stiffness layer, damped membrane with an overlap joint. The effective moduli of the element are the same as those for a multiple segment membrane.

For axial or shear loads (or combinations of the two), the two stiffness layers will displace equally at the endpoints of the analysis element. Therefore, at one end, all of the displacements can be set equal to zero, while at the other end, the necessary four boundary conditions are:

1. The two axial displacements, \hat{u}_1 and \hat{u}_2 , are both equal to \hat{U} .
2. The sum of the resultant axial loads is equal to F_x , the externally applied axial load. It is convenient to work in terms of stress, so the average dimensionless axial stress, $\hat{\sigma}_a$, is defined:

$$\hat{\sigma}_a = \frac{F_x}{2t_s b E_{11}^*} \quad (2.19)$$

where b is the width of the membrane.

3. The two shear displacements, $\hat{\phi}_1$ and $\hat{\phi}_2$, are both equal to \hat{V} .
4. The sum of the resultant shear loads is equal to F_{xy} , the externally applied shear load. In all the cases studied in this work, $F_{xy} = 0$.

Once Equation 2.16 is solved for the complex displacements, $\{\hat{u}\}$, an effective dimensionless axial modulus, \hat{E}_x^* , and damping loss factor, η_x , can be calculated for the analysis element:

$$\hat{E}_x^* = \hat{E}_x' + i\hat{E}_x'' = \hat{\sigma}_a \frac{\hat{L}}{\hat{U}} \quad \eta_x = \frac{\hat{E}_x''}{\hat{E}_x'} \quad (2.20)$$

where $i = \sqrt{-1}$. The entire membrane would have these same effective properties.

2.2 Extension To Thin Wall Tubes

For the foregoing analysis to be applicable to tubes the laminate thickness must be much less than the tube diameter. Then the effects of curvature are small and the tube may be analyzed as a flat membrane with the x -axis corresponding to the axis of the tube (5).

2.3 Computer Program: DAMSEG

A computer program was written to conduct parametric studies on the damped membrane described in Sections 2.1.8-9. Inputs to the program included ϕ_0 , D_0^* , η_d , \hat{E}_{22}^* , \hat{E}_{12}^* , and v_{12}^* .

The eigenvalues and eigenvectors for these relatively simple damped components can be determined explicitly. The eigenvalues are:

$$\lambda_1^2 = 0 \quad \lambda_2^2 = 0 \quad \lambda_3^2 = \frac{2D_0^* \hat{K}_{11}^*}{\hat{K}_{11}^* \hat{K}_{66}^* - \hat{K}_{16}^{*2}} \quad \lambda_4^2 = \frac{2D_0^* \hat{K}_{66}^*}{\hat{K}_{11}^* \hat{K}_{66}^* - \hat{K}_{16}^{*2}} \quad (2.21)$$

The corresponding eigenvectors are:

$$\{\hat{u}_0\}_1 = \begin{Bmatrix} 0 \\ 1 \\ 0 \\ 1 \end{Bmatrix} \quad \{\hat{u}_0\}_2 = \begin{Bmatrix} 1 \\ 0 \\ 1 \\ 0 \end{Bmatrix} \quad \{\hat{u}_0\}_3 = \begin{Bmatrix} \hat{K}_{16}^* \\ -\hat{K}_{11}^* \\ \hat{K}_{16}^* \\ \hat{K}_{11}^* \end{Bmatrix} \quad \{\hat{u}_0\}_4 = \begin{Bmatrix} \hat{K}_{66}^* \\ -\hat{K}_{16}^* \\ -\hat{K}_{66}^* \\ -\hat{K}_{16}^* \end{Bmatrix} \quad (2.22)$$

The boundary conditions are developed in matrix form and satisfied using the IMSL FORTRAN library functions DLFTCG and DLFICG to solve for all the complex displacements. Finally, the effective modulus and loss factor are determined as discussed in Section 2.1.9.

3. ANALYTICAL RESULTS

Parametric studies to determine the effect of both the ϕ_0 and D_0^* on the axial stiffness and damping of flat membranes and thin wall tubes were conducted using the program DAMSEG. The material properties used in the parametric studies were:

$$\begin{aligned} \hat{E}'_{22} = 0.05 \quad \hat{E}''_{22} = 0.0005 \quad \hat{E}'_{12} = 0.05 \quad \hat{E}''_{12} = 0.0005 \\ \nu'_{12} = 0.28 \quad \nu''_{12} = 0 \end{aligned} \quad (3.1)$$

These relationships are fairly typical for most carbon fiber/epoxy composites available today.

Except where noted, the loss factor for the damping layer was set at

$$\eta_d = 1 \quad (3.2)$$

from which it follows that

$$D'_0 \approx D''_0 \quad (3.3)$$

The externally applied axial stress was set at

$$\hat{\sigma}_a = 1 \quad (3.4)$$

3.1 Displacements And Stresses In A Damped Component

DAMSEG was used to determine the axial (\hat{u}_1 and \hat{u}_2) and transverse (\hat{v}_1 and \hat{v}_2) displacements for an axially-loaded element. The results are shown in Figs. 3.1 to 3.3. Values used in the calculations were: $D'_0 = 0.27$, $\hat{L}_{\text{overlap}} = 0.125$, and $\phi_0 = 26^\circ$. (As will be shown in Section 3.2, these values result in the highest loss factor).

The real parts of the axial and tangential displacements are plotted as functions of \hat{x} in Figs. 3.1 and 3.2, respectively. Fig. 3.1 shows that the axial displacements are equal ($\hat{u}_1 = \hat{u}_2$). From this result and Equation 2.4, it follows that $\tau_{xz}^d = 0$.

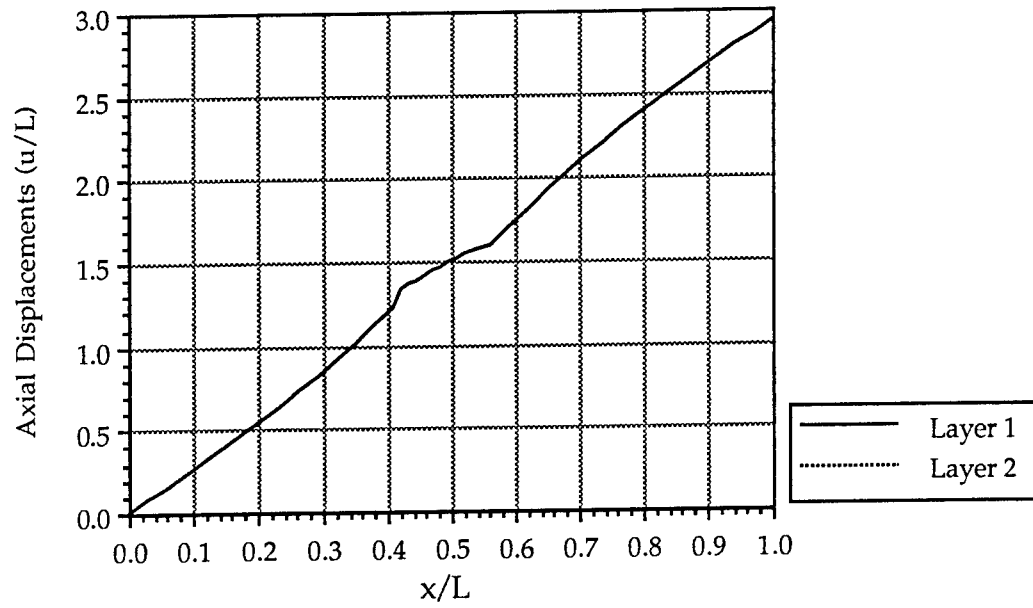


Figure 3.1. Real parts of the axial displacements for an axially-loaded element, with $N = 2$, $D'_O = 0.27$, $\phi_O = 26^\circ$, $\hat{L}_{\text{overlap}} = 0.125$, and $\hat{\sigma}_a = 1$.

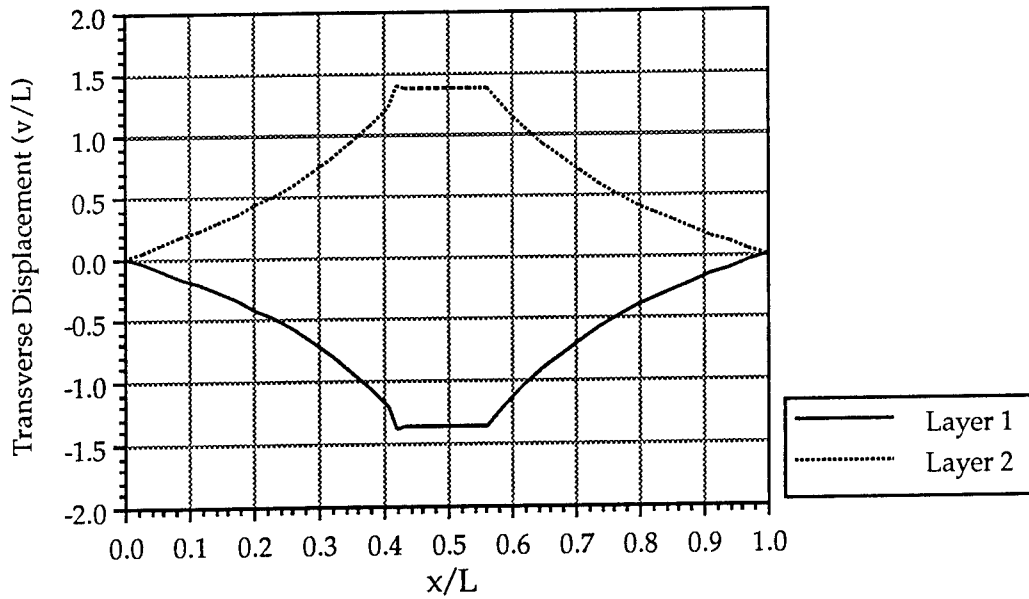


Figure 3.2. Real parts of the transverse displacements for an axially-loaded element, with $N = 2$, $D'_O = 0.27$, $\phi_O = 26^\circ$, $\hat{L}_{\text{overlap}} = 0.125$, and $\hat{\sigma}_a = 1$.

Fig. 3.2 shows that the real part of the transverse displacements are equal and opposite, and confirms that the stress coupling effect does cause additional shearing of the damping layer. This point is emphasized in Fig. 3.3, where the real part of the differential transverse displacement ($\hat{v}_1 - \hat{v}_2$) is plotted as a function of \hat{x} . Since this differential displacement is proportional to τ_{yz}^d (see Equation 2.4) it can be seen that the shear stress reaches its maximum value at the edges of the overlap region (at $\hat{x} = 0.44$ and 0.56 in this case) and remains constant within the overlap. Had the overlap been smaller, the shear stress would have increased to a higher value before leveling off. However, for larger overlaps the shear stress does not remain constant, but instead decreases from its value at the edges to a local minimum at $\hat{x} = 0.5$ (this will be discussed further in Section 3.4).

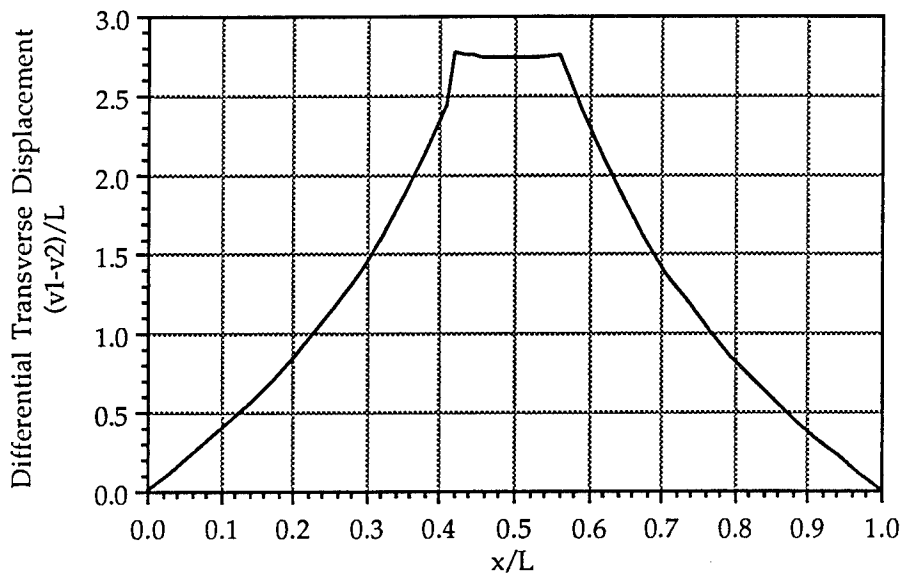


Figure 3.3. Real part of the differential transverse displacement for an axially-loaded element, with $N = 2$, $D'_0 = 0.27$, $\phi_0 = 26^\circ$, $\hat{L}_{\text{overlap}} = 0.125$, and $\hat{\sigma}_a = 1$.

Fig. 3.3 also shows that the differential displacement is zero at $\hat{x} = 0$ and 1 . These points correspond to the midpoints of adjacent segments in a multi-segment component (see Fig. 2.3). Thus almost none of the stress coupled damping comes from the midpoints of the segments. Nearly all of it comes from the joint (overlap) regions.

3.2 Parametric Study Of Axial Loading

When designing a part, it is important to know how the choice of materials and geometry will affect both its loss factor and stiffness. If the modulus of the damping material is too high

(large D'_O), the relative displacement between the stiffness layers would be so small that damping would be eliminated. On the other hand, low modulus damping materials (small D'_O), would produce large relative displacements but the stresses in the damping layer would be so small that little energy would be absorbed. Since these same factors will also influence the part stiffness, there should be an optimum value of D'_O which gives the best combination of high damping and stiffness. Similarly, since fiber orientation angles of 0° or 90° induce no stress coupling, an optimum angle between 0° and 90° should produce the highest loss factors. An analytical study was carried out to find these relationships for axially -loaded thin wall tubes and flat membranes. The results are summarized in Figs. 3.4-3.7.

Fig. 3.4 shows the loss factor, η_x , as a function of ϕ_O and D'_O . As expected, the loss factor is low when ϕ_O is near zero or 90° , and for large and intermediate values of D'_O . The highest loss factor of the four cases examined occurs at about $\phi_O = 26^\circ$ and $D'_O = 1.0$.

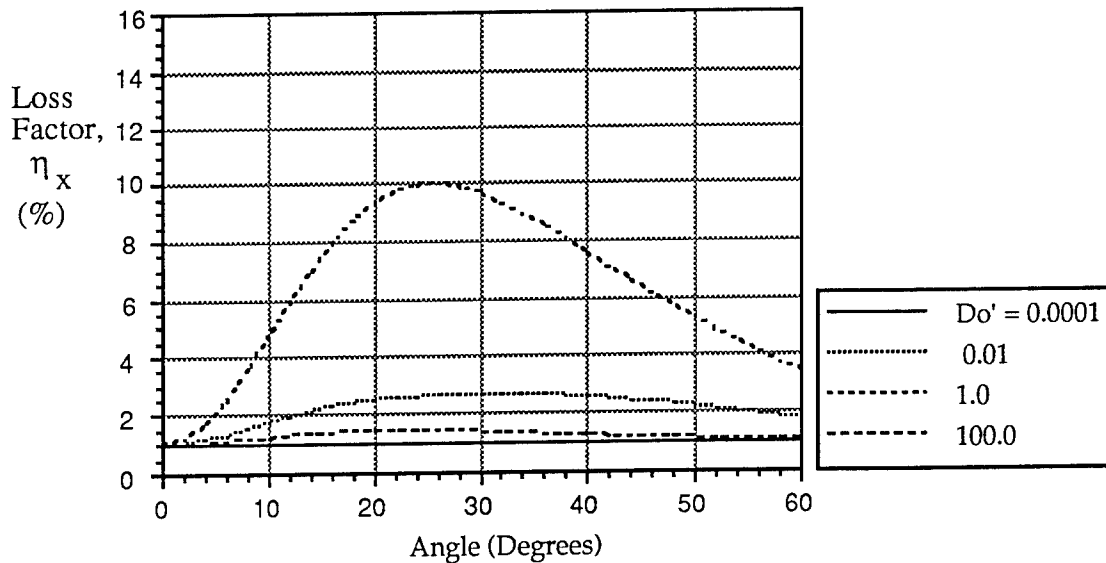


Figure 3.4. Loss factor, η_x , for axially-loaded thin wall tubes and flat membranes as a function of fiber angle, ϕ_O , for a wide range of values of D'_O . $N=2$, and $\hat{L}_{\text{overlap}} = 0.125$.

Fig. 3.5 is a plot of \hat{E}_x (the effective axial modulus) as a function of ϕ_O and D'_O . A large value of D'_O gives a high modulus, as expected. In the limit, the value approaches that of a balanced laminate with $+\phi_O$ and $-\phi_O$ plies. As D'_O is decreased the modulus drops, eventually reaching a value equivalent to that of a single laminae with $+\phi_O$ plies only. When $D'_O = 1$, the modulus lies between these two extremes. The modulus also decreases as ϕ_O increases from 0° .

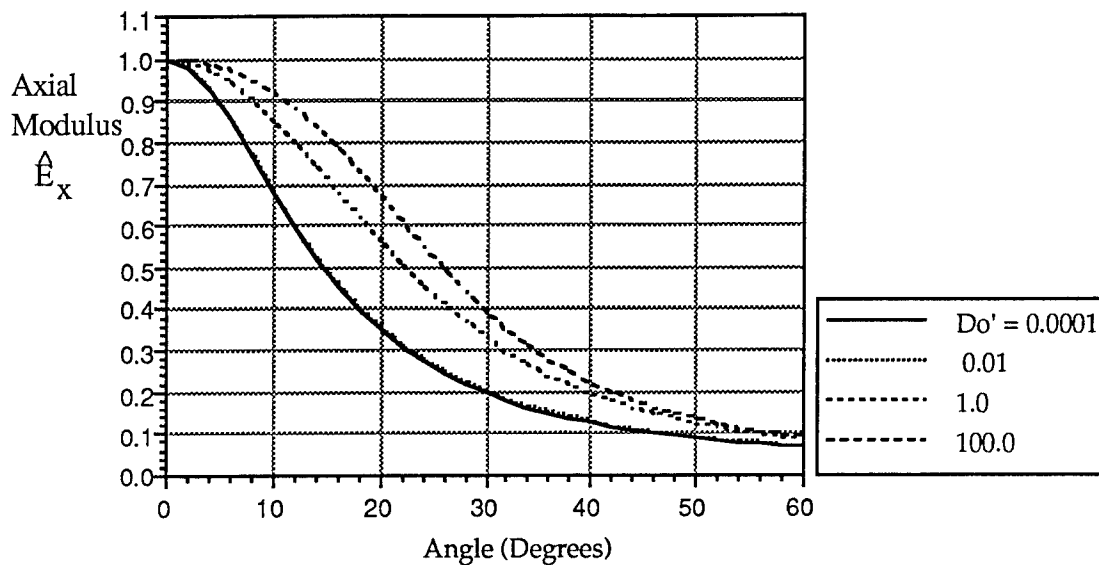


Figure 3.5. The effective axial modulus, \hat{E}_x , for thin wall tubes and flat membranes, as a function of fiber angle, ϕ_0 , for a wide range of values of D_o' . $\hat{L}_{\text{overlap}} = 0.125$, and $N=2$.

Figs. 3.6 and 3.7 give greater detail of the behavior of η_x and \hat{E}_x for values of D_o' near 1. Note that the loss factor does not change very much for values of D_o' between 0.25 and 0.30. The highest loss factor ($\eta_x \approx 14\%$) is achieved for $D_o' = 0.27$ and $\phi_0 = 26^\circ$. For this case, the axial modulus $\hat{E}_x = 0.34$. The same laminate with no damping layer would have a modulus $\hat{E}_x = 0.50$. Thus the damped tube has a stiffness 32% lower and a damping level 14 times higher than the comparable undamped tube.

Remember, however, that composites are very tailorable, so many combinations of stiffness and damping can be selected. For example, when ϕ_0 is 15° , the damping increases by a factor of 10 and the stiffness decreases by only 20%, when compared to the undamped case.

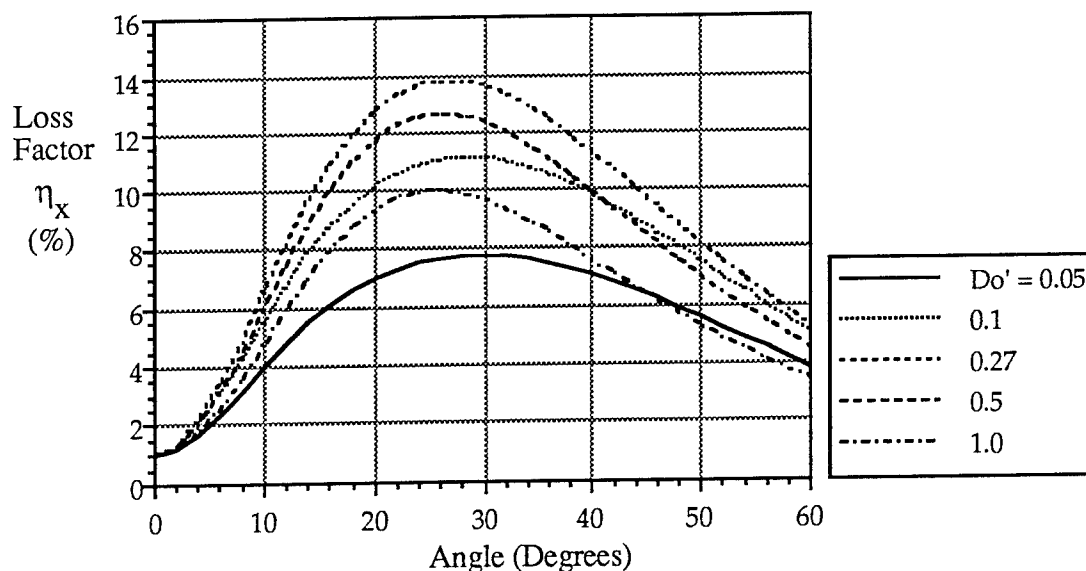


Figure 3.6. Loss factor, η_x , for axially-loaded thin wall tubes and flat membranes as a function of fiber angle, ϕ_0 , for values of D_o' between 0.05 and 1. $N=2$, and $\hat{L}_{\text{overlap}} = 0.125$.

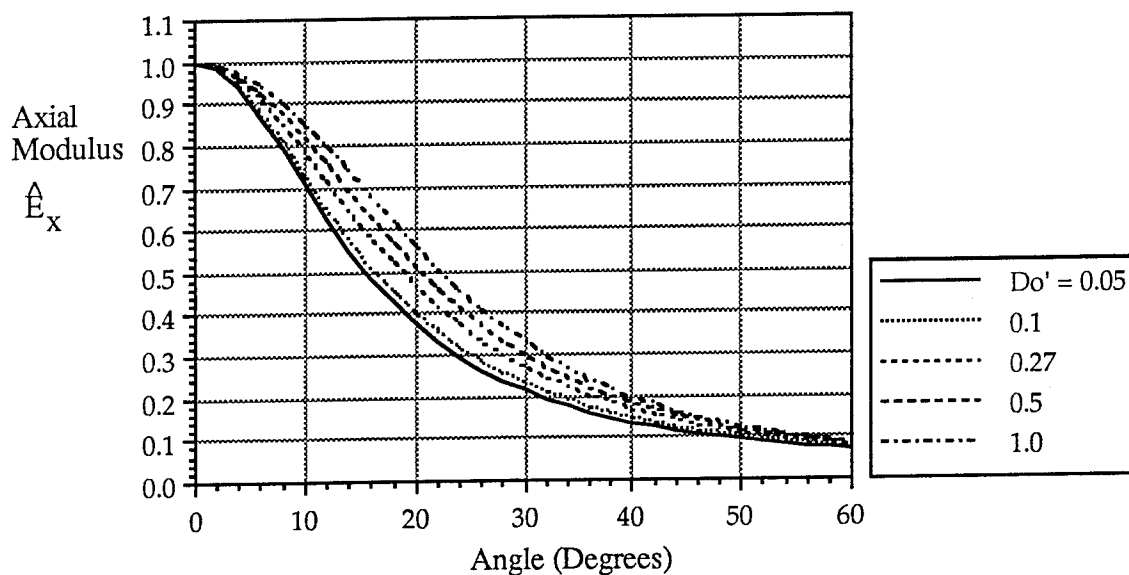


Figure 3.7. The effective axial modulus, \hat{E}_x , for thin wall tubes and flat membranes, as a function of fiber angle, ϕ_0 , for values of D_o' between 0.05 and 1. $\hat{L}_{\text{overlap}} = 0.125$, and $N=2$.

3.3 Effect Of Overlap Length On Loss Factor And Strength

Fig. 3.8 shows the effects of different overlap lengths on the transverse displacements of a stiffness layer in a damped element. The displacements are plotted as functions of \hat{x} for several different overlap lengths. The calculations were done with $N = 2$, $\phi_0 = 25^\circ$ and $D_0' = 0.27$. The results show that as the \hat{L}_{overlap} is increased it decreases the magnitude of the maximum displacements, but increases the size of the region in which the displacements are large. As long as the overlap is not too large, these tendencies should compensate for each other.

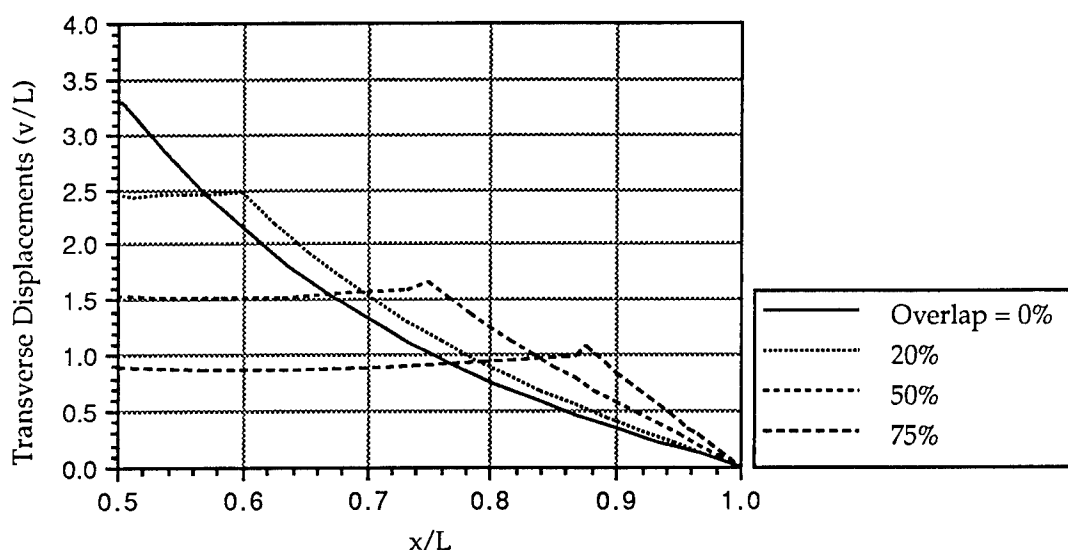


Figure 3.8. Effect of overlap length on transverse displacements under axial loading. $N=2$, $D_0' = 0.27$, $\phi_0 = 26^\circ$, and $\hat{\sigma}_a = 1$.

This expectation is verified in Fig. 3.9, where the loss factor, η_x , is plotted as a function of overlap length. Note that for overlaps of 0.1 or smaller, the effect on the loss factor is negligible. For overlaps between 0.1 and 0.2 the effect is still small. Above 0.2, the decreasing size of the shear coupled region begins to dominate the situation and the loss factor decreases rapidly.

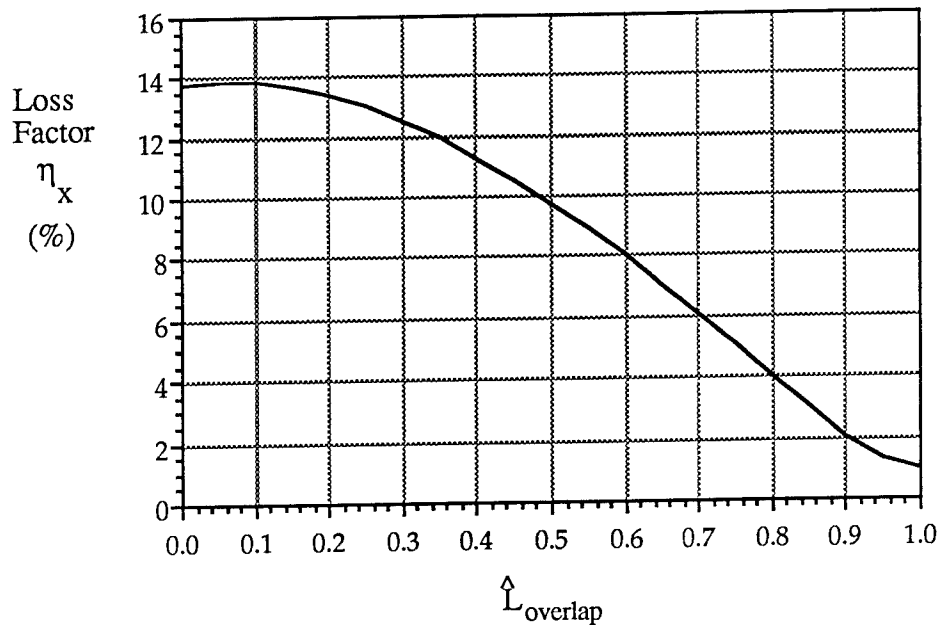


Figure 3.9. Effect of overlap length on loss factor for axial loading. $N = 2$, $D'_O = 0.27$ and $\phi_O = 26^\circ$.

The current method for making segmented tubes requires overlap joints between the segments. Fig. 3.10 is a diagram of such a joint in one layer of the stiffness material. The joint will have less strength in tension than the rest of the layer because of the discontinuities in the plies at locations A and B. For components in which an appropriately designed segment length, L , is large enough, an overlap of 0.2 is not required for strength or ease of manufacturing. (When the overlap is too small, it is difficult to accurately layup the plies.) In these cases, the step-lap joint shown in Fig. 3.11 can be used to increase the joint strength while retaining high loss factors.

If prepreg with a "zig-zag" geometry of continuous fibers can be produced (i.e., the fibers are continuous through the locations where the angle changes), the discontinuities in Fig. 3.10 would be eliminated and the joint strength would be increased. In actual practice the corners of the "zig-zag" would be rounded since the fibers cannot be bent at a sharp angle. This would create a joint region with reduced stress coupling, just as with the current method. However, there should be little, if any, loss of damping performance as long as the size of the region is less than about 20% of the segment length.

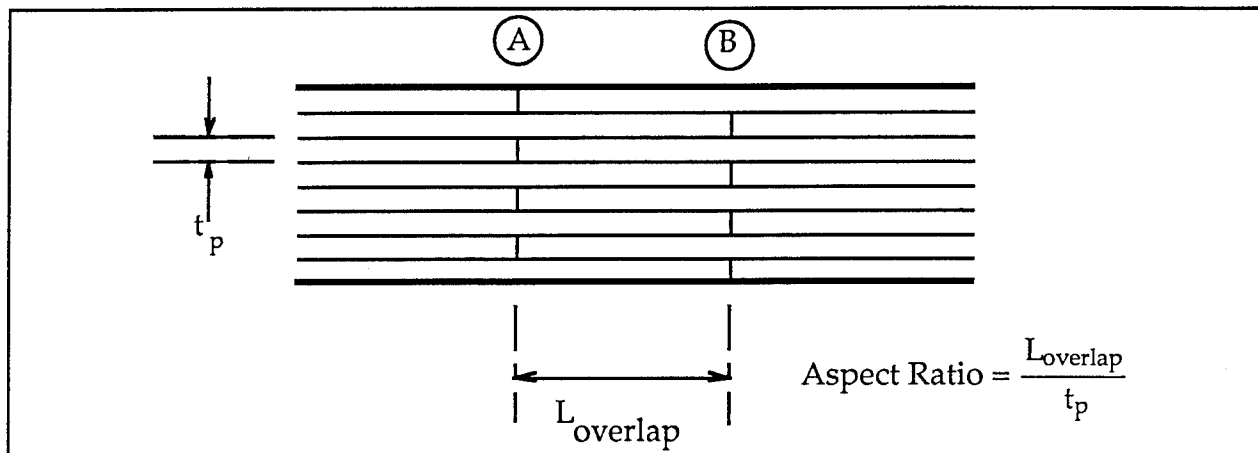


Figure 3.10. An alternating overlap joint creates a short overlap region.

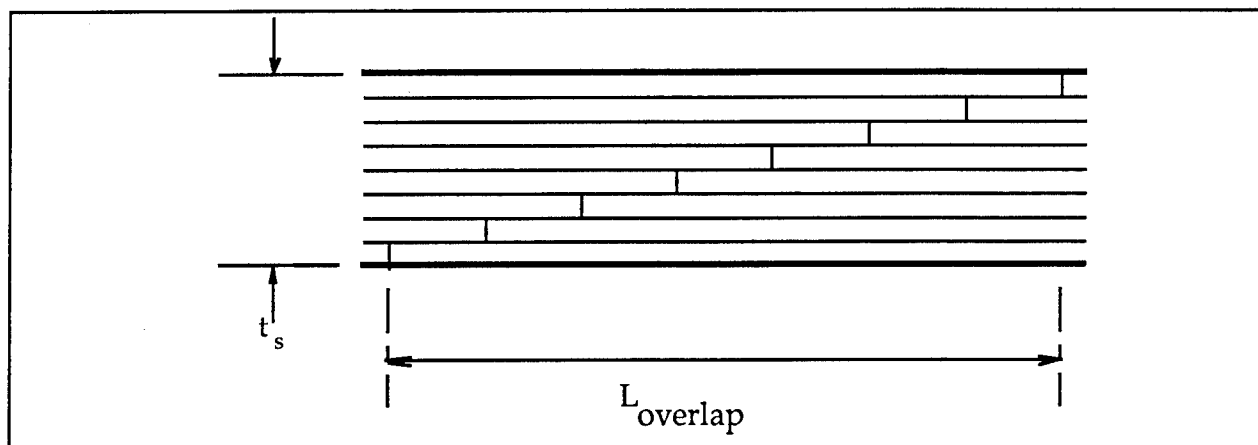


Figure 3.11. Step-lap joint. This joint design is much longer than the one shown in Fig. 3.10, but should be significantly stronger.

3.4 Effect Of Damping Material Loss Factor On Component Loss Factor

All of the previous results were calculated for a damping material with a loss factor of 100% ($\eta_d = 1$). Unfortunately, such materials which also meet strength and processing requirements are not always available for the service temperatures and vibration frequencies desired. Fig. 3.12 shows the effect of damping material loss factor on the component loss factor. In the figure, η_x is plotted as a function of ϕ_0 for different values of η_d .

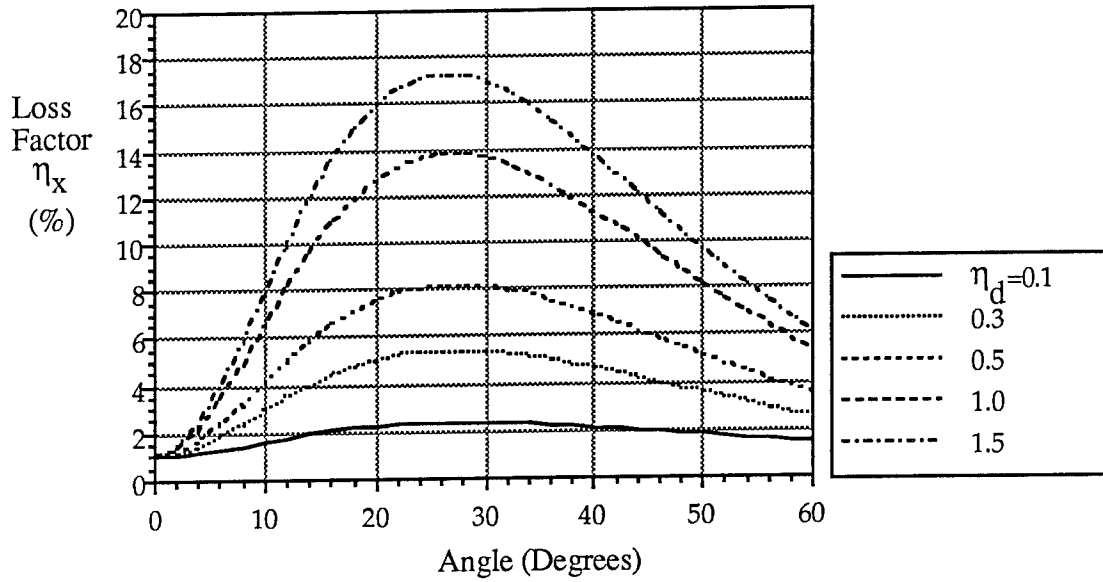


Figure 3.12. Loss factor, η_x , for axially-loaded thin wall tubes and flat membranes, as a function of ϕ_0 , for different damping material loss factors, η_d . $N = 2$, $D'_0 = 0.27$, and $\hat{L}_{\text{overlap}} = 0.125$.

The results show that the loss factor of the component is directly related to the loss factor of the damping material. However, since some damping comes from the stiffness layer, the relationship between the two is not linear. The Loss Factor Ratio is defined:

$$\text{Loss Factor Ratio} = \frac{\eta_x}{\eta_x \text{ when } \eta_d = 1} \quad (3.5)$$

This ratio is plotted in Fig. 3.13 as a function of fiber angle for different values of η_d . Note that decreasing the damping material loss factor by 50%, reduces the component loss factor by only 40%.

Since the effect of η_d on stiffness is negligible, no plot is given.

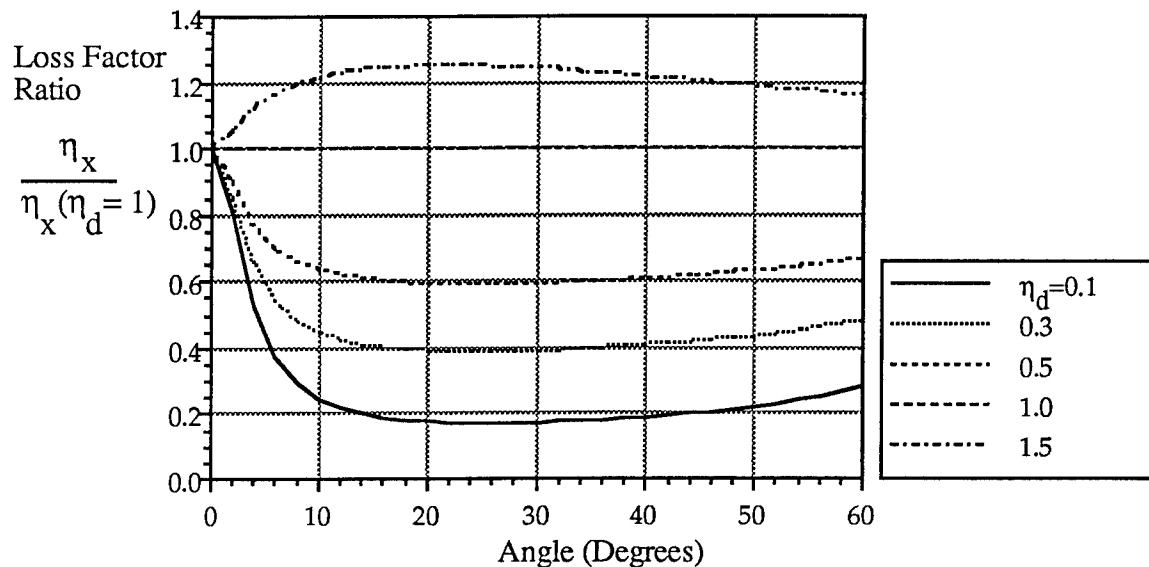


Figure 3.13. Effect of damping material loss factor on the loss factor of axially-loaded thin wall tubes and flat membranes. The loss factor ratio is the component loss factor, η_x , divided by its value when $\eta_d = 1$. $N = 2$, $D'_O = 0.27$, and $\hat{L}_{\text{overlap}} = 0.125$.

4. EXPERIMENTAL WORK

The SCAD damping concept can be applied to a wide range of designs, with the best results obtained in parts subjected to high axial or in-plane shear loading. Tubes in truss structures, such as ASTREX, are subjected to the desired high axial loads as well as bending type loads during vibration.

4.1 Damped Tubes For Testing

Nine tubes with different geometric configurations, with and without damping layers, were fabricated and tested.

4.1.1 Manufacturing Damped Tubes

The tubes were manufactured at Brigham Young University in the Snell Building Composites Lab. The process consisted of 5 steps:

1. First, segmented stiffness layer prepreg was hand laid up from small rectangular pieces of prepreg, as shown in Fig. 4.1. The pieces were put down like shingles on a roof, each being offset both axially (to form the segment overlap) and transversely from the one below

it. The transverse offset was put in so that when the prepreg was rolled into a tube, the two edges would come together in a strong overlap joint along the tube axis. Overlap lengths of 6.5 mm (0.25 in) were used, creating an effective joint aspect ratio, $L_{\text{overlap}}/\text{ply thickness}$ (see Fig. 3.10), of 45. An aspect ratio of 50 is commonly specified for composite repair joints. This is considered sufficient to transmit as much load to the fibers as they can withstand through shear stress in the matrix resin. It was also found that 6.5 mm was the smallest overlap length that could be consistently formed by hand layup.

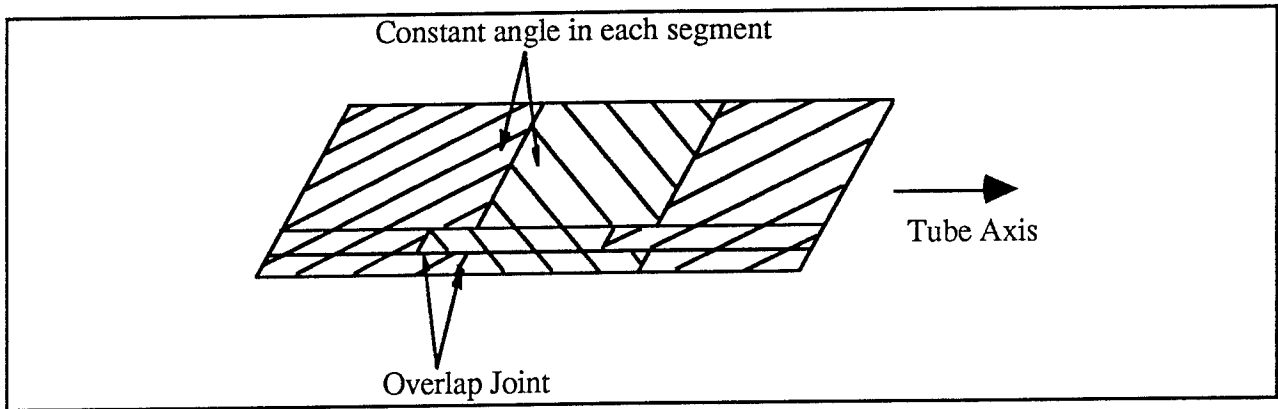


Figure 4.1. Prepreg for the segmented stiffness layers was made by laying up precut rectangular pieces of unidirectional tape.

2. The laminates were then rolled onto a metal mandrel using two heated and padded plates to consolidate the plies as the tube is rolled (see Fig. 4.2).
3. The damping material, in the form of flat sheets, was simply rolled around the mandrel during the proper stage in the manufacturing process.
4. After rolling all of the necessary material onto the mandrel, cellophane or nylon tape was wound around the prepreg under high tension. This tape shrinks at high temperatures consolidating the prepreg and holding the material in place during cure.
5. The tubes were suspended vertically in an oven and cured for 4 hours at 178°C (350°F).

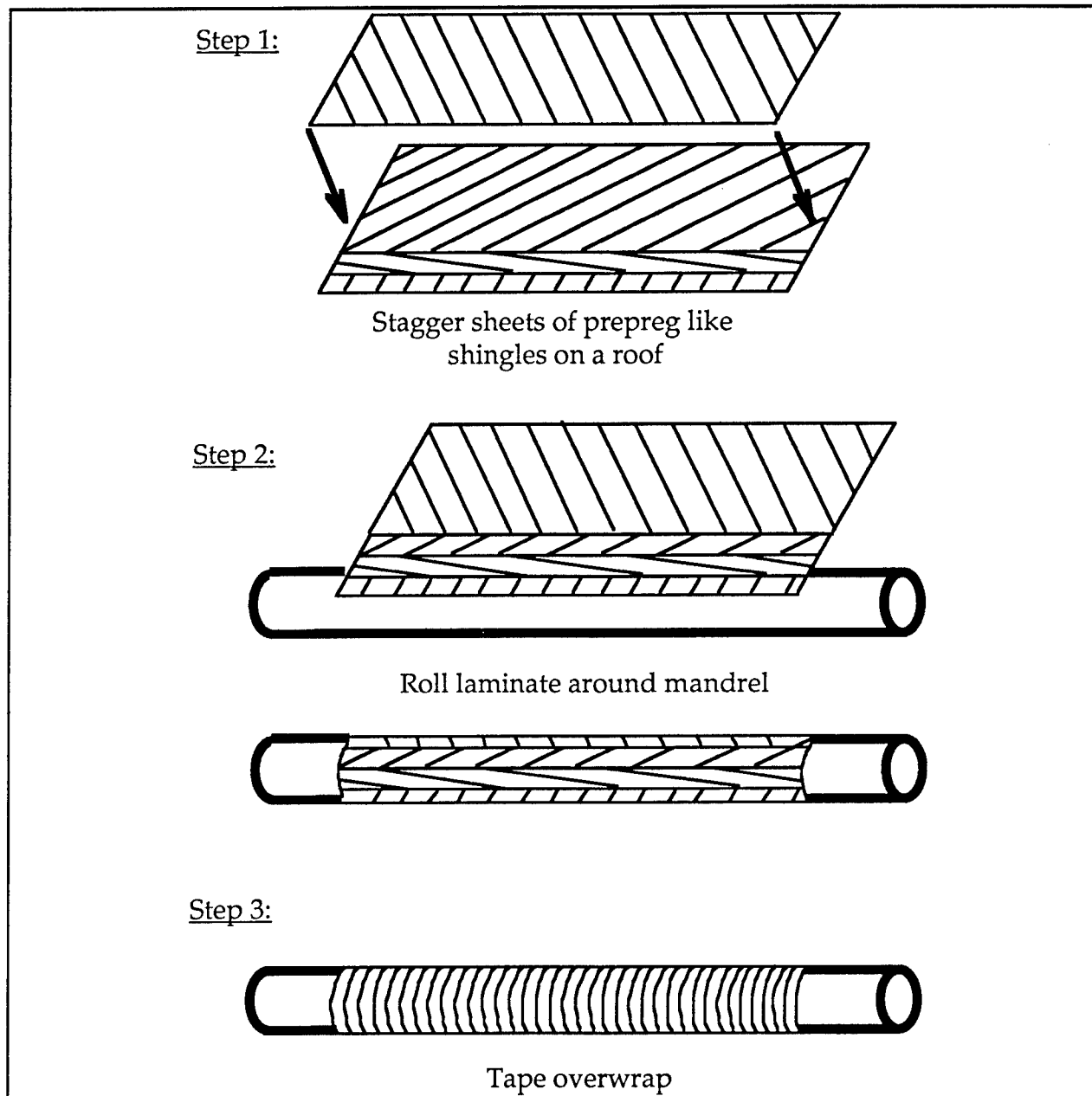


Figure 4.2. Tube manufacturing method.

4.1.2 Tube Specifications

Nine tubes were fabricated. All were laid up 560 mm (22 in) long and cut to 510 mm (20 in) after curing. The inner tube diameter was 26.7 mm (1.05 in). Five plies of Hercules IM7/8551-7A graphite/epoxy prepreg tape were used in both stiffness layers, giving a total layer thickness of 0.699 mm (0.0275 in). Three-level studies on segment length and fiber orientation angle and two-level studies on damping material type and thickness were carried out.

4.1.3 Tube Test Setup and Procedure

The tubes were all tested in axial vibration at Brigham Young University. Equipment used included: a structural dynamics analyzer (Hewlett-Packard HP5423A); an accelerometer (PCB Piezotronics, Inc. Model 309A); a force hammer (PCB Model 086B01); and two power/signal conditioners (PCB Model 480D06).

The tubes were suspended at each end by soft rubber bands to approximate free-free boundary conditions. Axial motion of the tube was monitored by attaching the accelerometer to one end, as shown in Fig. 4.3. The tube was then struck at the same end, at a point diametrically opposite the accelerometer, with the force hammer. The force and acceleration signals were fed into the structural analyzer which calculated the transfer function. A zoom window 6.4 kHz wide was used around the primary natural frequency. The tube was struck ten times and the data averaged by the analyzer. The fundamental vibration frequency and 3 dB bandwidth were recorded for each test, and each tube was tested three times. The loss factor was calculated by

$$\eta_x = \frac{B}{f_{\text{res}}} \quad (4.1)$$

where B is the 3 dB bandwidth, and f_{res} is the resonance frequency.

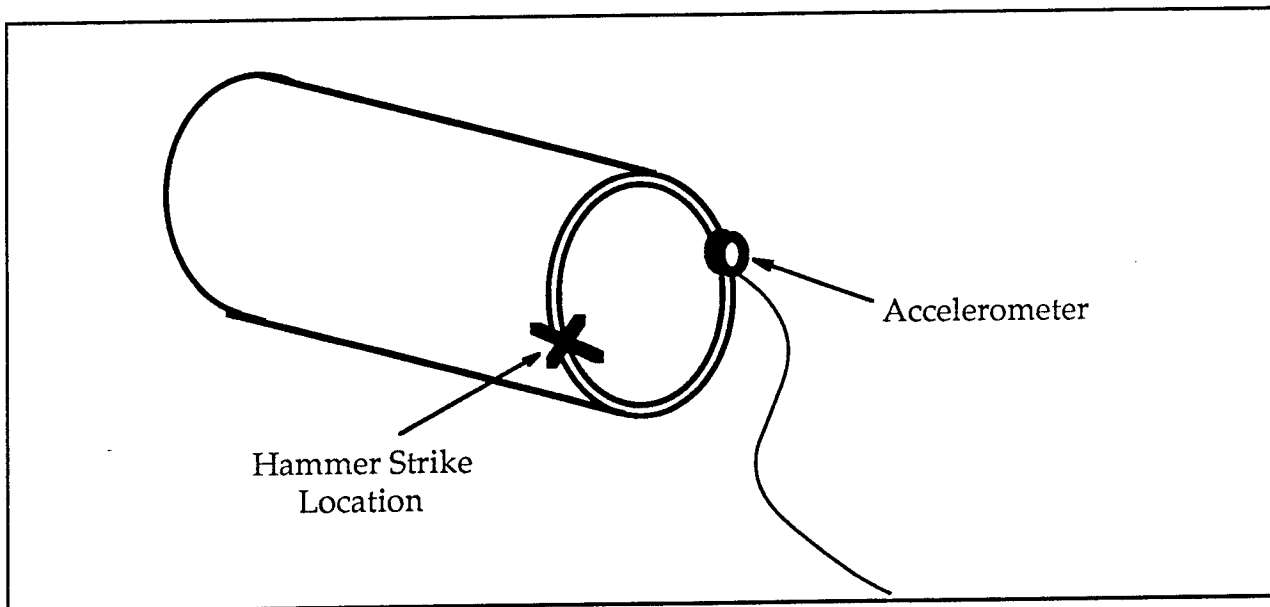


Figure 4.3. Detail of the accelerometer hammer strike locations for testing the damped tubes.

4.1.4 Axial Vibration Test Results

The results for all nine tubes in axial vibration are contained in Table 4.1.

Table 4.1.
Thin Wall Tubes in Axial Vibration: Experimental and Analytical Results.

Shown below are the measured and predicted natural frequencies, ω_n , and loss factors, η , for tubes in axial vibration. The tubes were all 510 mm (20 in) long, had an inner diameter of 26.7 mm (1.05 in), and had two stiffness layers (5 plies each of Hercules' IM7/8551-7A carbon fiber/epoxy prepreg) and one damping layer. (The measured loss factors in bending were about 20-30%.)

Specimen Configuration						Measured Values		Predicted Values	
Label	Damping Material	Damping Layer Thickness (mm)	Fiber Angle (°)	Segment Length (mm)	D_0	ω_n (Hz)	η (%)	ω_n (Hz)	η (%)
a	ISD-112	0.25	25	64	0.39	5840	6.69	5720	6.80
b	ISD-112	0.25	10	64	0.39	8390	2.30	8040	3.03
c	ISD-112	0.25	40	64	0.39	3650	6.86	3940	6.92
d	ISD-112	0.25	25	38	0.14	5690	8.54	5400	7.08
e	ISD-112	0.25	25	89	0.76	5820	5.87	5920	5.89
f	ISD-112	0.12	25	64	0.78	5830	5.97	5970	5.77
g	AF-32	0.25	25	64	24.1	5820	5.49	6470	3.06
h	None	n. a.	25	None	n. a.	6750	2.36	6560	2.02
i	None	n. a.	0	None	n. a.	8780	1.07	8780	1.00

The computer program DAMSEG was used to calculate the material properties which were then used to estimate the natural vibration frequency:

$$f = \frac{1}{2L_{\text{total}}} \sqrt{\frac{E}{\rho}} \quad (4.2)$$

where $E \approx E_x'$, and the density, ρ , of the composite was approximately 1605 kg/m³ (0.058 lbm/in³).

Two problems involving material properties were encountered: the first with the composite material used to make the damped tube specimens and the second with the material properties for the AF-32 adhesive film.

Hercules specified that E_{11} for IM7/8551-7A was 166 GPa (24 Mpsi). This modulus leads to predicted frequencies far higher than were measured, even for the 0° tube with no damping material. Calculations for a 0° tube do not depend on the validity of orthotropic plate theory or the damped component analysis developed in Section 2 and should be reliable. In addition, a 0° flat specimen was loaded axially in an Instron tensile test machine and the modulus calculated using total specimen deflection (rather than strain gage data which would have been more accurate). This indicated that the true modulus of the Hercules graphite/epoxy was approximately 117 GPa (17 Mpsi) and this value was used in calculating all of the predicted frequencies. The transverse and shear moduli used in the calculations were those supplied by Hercules, since no accurate way to determine them was available and since the theory is relatively insensitive to these values.

The material properties used in predicting the loss factors and natural frequencies found in Table 4.1 are given in Table 4.2. The composite material loss factor was determined by testing a 0° tube with no damping layers. The measured loss factor of 1% is identical to that measured for an ICI Fiberite 6048 carbon fiber/epoxy tube in an earlier work (5). Other tests have shown that the loss factors in carbon fiber/epoxy composites can be as low as 0.25% in the fiber direction, and 2.5-5% in the transverse direction and for in-plane shear. Since exact data were not available for this material, a loss factor of 4.0% was assumed.

Table 4.2. Material Properties used in Analytical Modeling.

Material		Modulus		Loss Factor (%)
IM7/8551-7A	E_{11}	117 GPa	(17 Mpsi)	1
	E_{22}	6.9 GPa	(1 Mpsi)	4
	E_{12}	6.9 GPa	(1 Mpsi)	4
AF-32	G	124 MPa	(18 kpsi)	66
ISD-112	(800 Hz) G	3.50 MPa	(508 psi)	35
	(5 kHz) G	2.00 MPa	(290 psi)	35

Reported Young's moduli and loss factors for AF-32 film adhesive differed by two orders of magnitude. The most reliable data for Young's modulus and loss factor were recommended by another researcher (7) and were found in a graph he did not know the origin of. Isotropic material properties and a Poisson ratio of 0.3 were assumed, resulting in a shear modulus of 124 MPa (18 kpsi) with a loss factor of 66%.

New material data for ISD-112 were recently supplied to the authors by 3M (3M Scotchdamp), Table 4.2. Although several other sources specify different material properties for ISD-112, all reported data are within the same order of magnitude. Previous tubes constructed at

BYU (5) showed excellent correlation with the new 3M material properties. These previous tubes had been cured at 250°F for two hours.

ISD-112 is designed to withstand temperatures up to 300°F, but the IM7/8551-7A cure process required four hours at 350°F. Examinations after curing showed possible severe degradation of the ISD-112 material. The loss factor used in the calculations was therefore obtained from tube specimen a and was equal to 35%. This partially explains why the following measured and calculated loss factors are so close, but considering the visible degradation in damping layers cured at 350°F, the 3M supplied data was no longer accurate. Also, the trends in the data were as important as the actual magnitudes.

Fig. 4.4 shows the measured and predicted natural frequencies of tubes a, b, and c. The predicted decrease in axial vibration frequency with increasing ϕ_0 agreed well with the measured data.

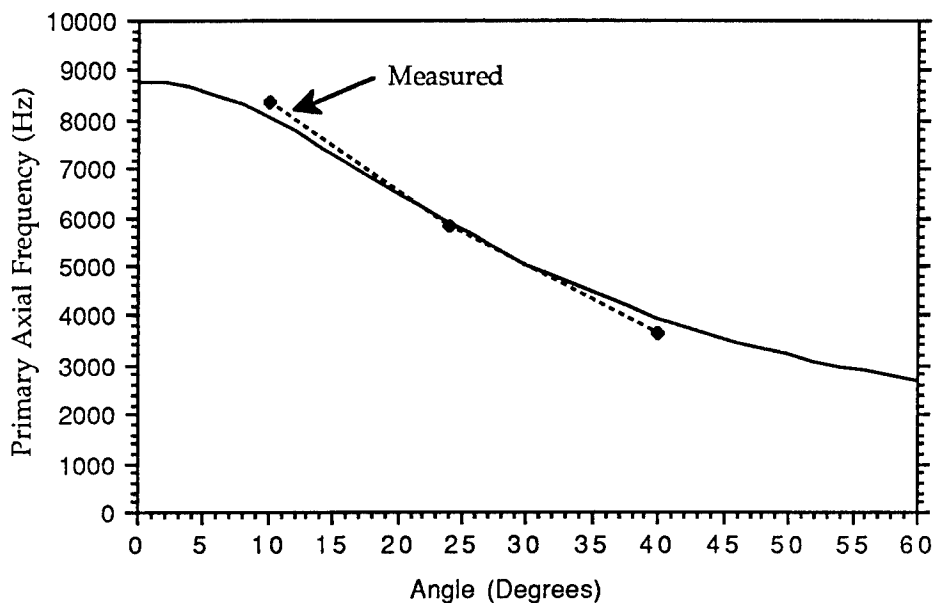


Figure 4.4. Measured and predicted axial vibration frequency in damped tubes as a function of fiber angle.

Fig. 4.5 shows that the predicted and measured loss factors for different fiber orientation angles also matched well.

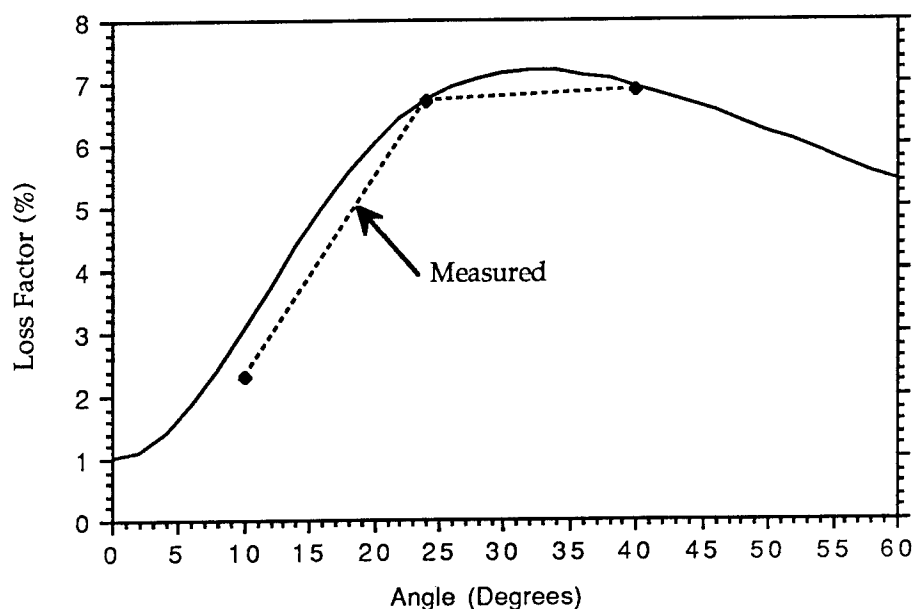


Figure 4.5. Measured and predicted loss factors in damped tubes as a function of fiber angle.

Fig. 4.6 shows that the measured change in axial vibration frequency for different segment lengths was minimal, as predicted by the analytical model. However, as Fig. 4.7 shows, the effect of segment length on the loss factor was predicted to be significant for the three specimens a, d, and e, as they had D_0 values on either sides of the optimum. As the segment length decreases with L_{overlap} held constant, the measured loss factor should go through a maximum and then decrease. These predicted trends are indicated in Fig. 4.7. However, the measured loss factors indicate that short segment lengths do not decrease the loss factor as much as predicted.

The effects of damping material and damping layer thickness are shown in Figs. 4.8 and 4.9. The measured and predicted stiffnesses do not differ significantly. However, the measured loss factor for the one of the tubes (tube g) was significantly higher than predicted (see Fig. 4.9). This, however, was not surprising considering the wide spread of reported AF-32 data mentioned earlier.

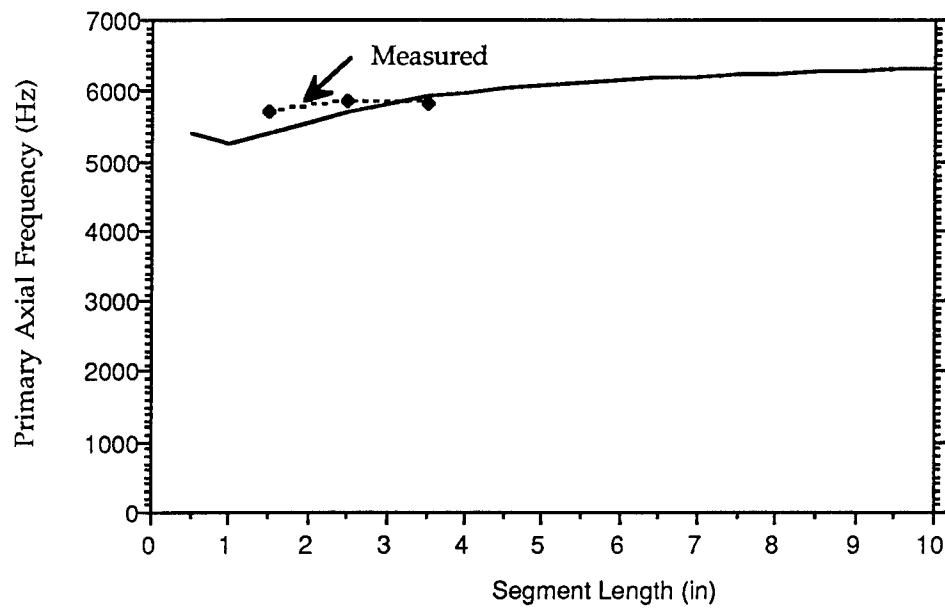


Figure 4.6. Measured and predicted axial vibration frequency in damped tubes as a function of segment length. $L_{\text{overlap}} = 6.5 \text{ mm (0.25 in)}$.

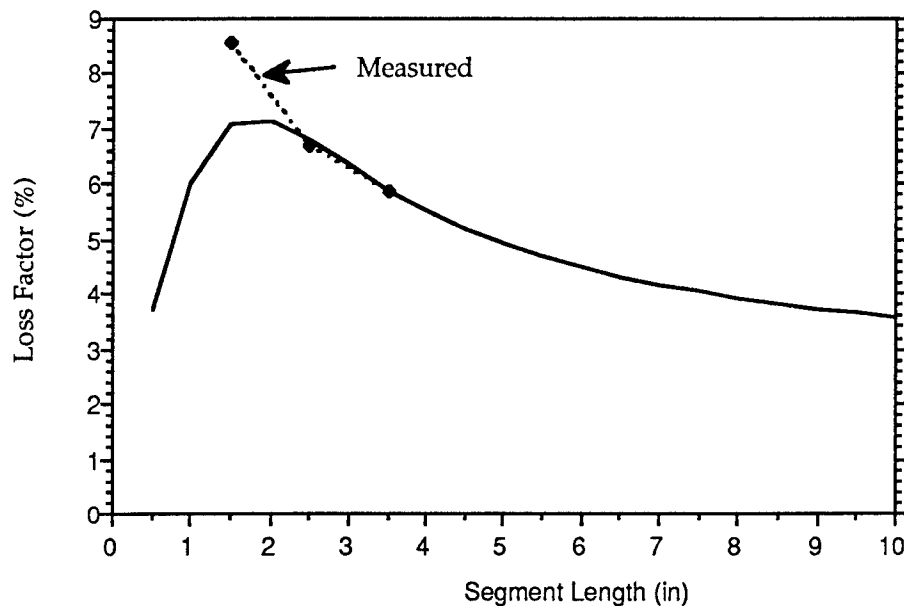


Figure 4.7. Measured and predicted loss factors in damped tubes as a function of segment length.

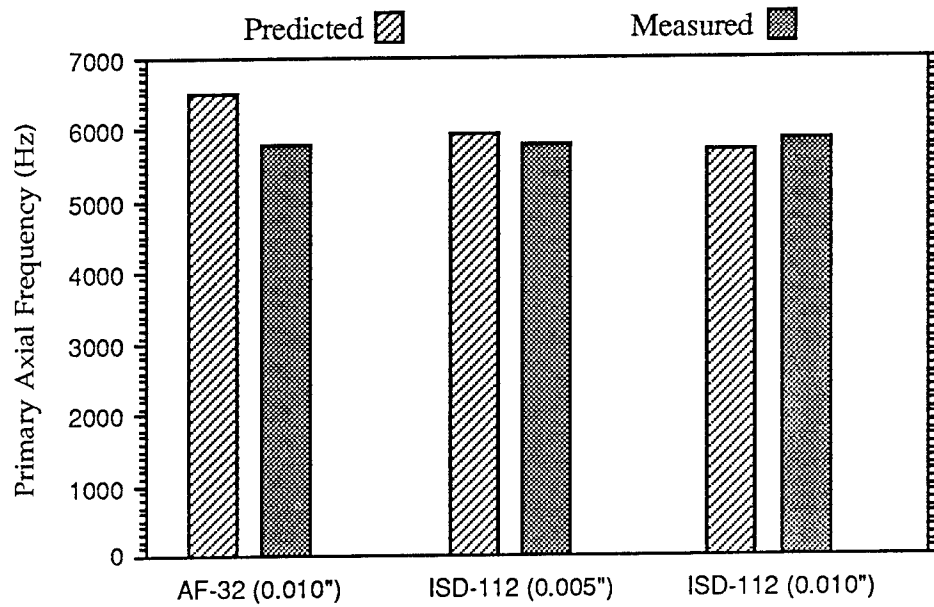


Figure 4.8. Measured and predicted natural frequencies in damped tubes with different damping materials and damping layer thicknesses.

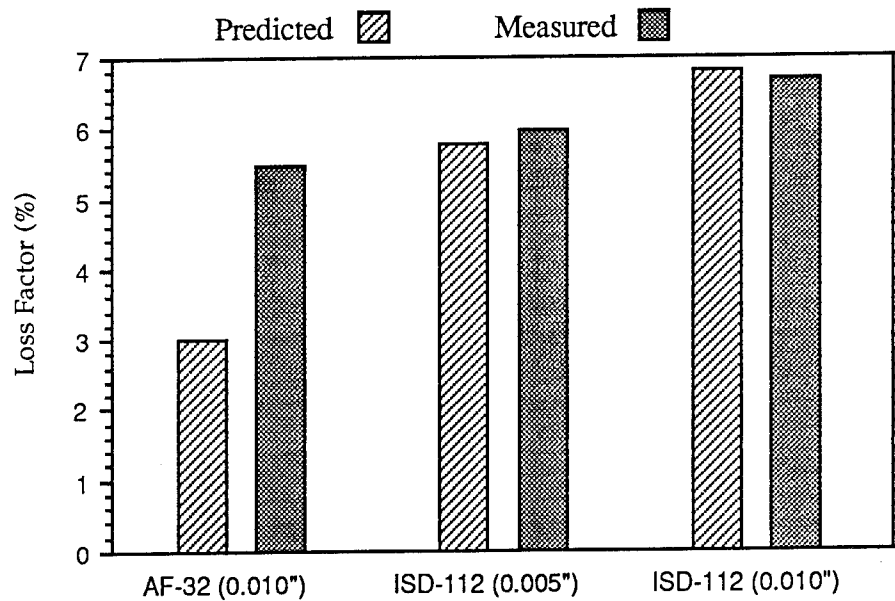


Figure 4.9. Measured and predicted loss factors in damped tubes with different damping materials and damping layer thicknesses.

4.2 ASTREX TUBES

The U.S. Air Force's Advanced Structural Research Experiment (ASTREX) is a 1/3 scale spaced based laser structure. ASTREX is used to correlate large space structure analysis methods with actual test data, to predict and correct vibration problems on future space platforms.

The ASTREX structure supports three separate mirrors. Six cylindrical truss members, each approximately 1.5 m (5 ft) long, 76 mm (3.0 in) in outer diameter, with 3.2 mm (0.125 in) wall thicknesses, support one of these, called the tertiary mirror. The truss members currently used are made of filament-wound carbon fiber reinforced epoxy with wind angles of $\pm 15^\circ$, $\pm 38^\circ$, and 90° .

Six damped struts were constructed to replace the present filament-wound members. The design objectives were to match the originals' axial stiffness and weight and to increase the inherent damping loss factor as much as possible in the region of 17 Hz. 17 Hz corresponds to one of the first three vibration modes where a large percentage of the vibration energy is in the form of axial deformations in the tertiary mirror support members (6).

The six tubes had fiber angles of 24° , with ten plies of ICI Fiberite HYE 6049W graphite/epoxy in each stiffness layer, and a single 0.25 mm (0.01 in) layer of 3M ISD-112 for the damping layer. The inner diameter was 70 mm (2.75 in), and the length 1800 mm (6 ft). This gives a D'_0 of approximately 0.15 at 17 Hz and 1.13 at 1.7 kHz. This was designed to give very good damping properties at the 17 Hz frequency encountered within the ASTREX structure, yet still maintain reasonable properties at the room temperature, free-free boundary test condition of 1.7 kHz.

The tubes were manufactured using the methods described in Section 4.1.1 except that curing was done for 2 hours at 121°C (250°F). The 121°C (250°F) cure ICI Fiberite prepreg was used to minimize degradation of the 3M damping material. Thus, the 3M-supplied material data were used in the subsequent analysis.

The tubes were tested as described in Section 4.1.3. The experimental and analytical results are summarized in Table 4.3. The measured damping loss factor for the axial vibration mode was 6.3% at 1.7 kHz. The associated vibration frequency was used to determine an effective axial modulus of 67 GPa (9.6 Mpsi). These results correlate well with the predictions; the measured loss factor is actually higher than predicted. The properties of the tube at 17 Hz are predicted to be $E_X = 53$ GPa (7.7 Mpsi) and $\eta_X = 10.8\%$. This will have to be verified by

mounting the tubes in the ASTREX structure and conducting vibration tests. Six tubes will be delivered to the Phillips Laboratory for their evaluation.

These results show that large space structures can be fabricated with weight and stiffness properties equivalent to the conventional components, but with damping properties 10 times higher than previously attainable.

Table 4.3.
ASTREX Tubes in Axial Vibration: Experimental and Analytical Results.

Shown below are the measured and predicted natural frequencies, ω_n , and loss factors, η , for ASTREX cylindrical truss members in axial vibration. Each member was approximately 1500 mm (5 ft) long with an outer diameter of 76 mm (3 in).

Test Condition	Measured Values		Predicted Values		
	ω_n	η (%)	ω_n (Hz)	η (%)	D_o
Within ASTREX	-	-	17	10.8	0.15
Free-free	1740	6.3	1790	5.1	1.13

A modal analysis of the free-free ASTREX tubes in bending vibration was conducted using the same accelerometer, impulse hammer, and spectrum analyzer mentioned earlier. The bending modes were so highly damped it was difficult to isolate them. The damping loss factors were 20-30% between 200 and 1000 Hz compared to $\leq 3\%$ for the undamped tubes.

5. SUMMARY OF THE SCAD TUBE DESIGN PROCESS

The following is a step by step procedure for designing damped composite tubes using the SCAD technology. Similar procedures would be used for flat membranes.

1. Determine the part's overall geometry (e.g., diameter and length) and desired performance values (stiffness, damping loss factor, and/or weight). Note, however, that only two performance values may be specified. The third may then be maximized (or minimized) by suitably selecting other design features like the stiffness and damping materials, layer thicknesses, and segment length. A common problem might be to maximize the damping for tube having a specified length, diameter, stiffness and weight.
2. Determine the cross-sectional area of the part from the specified part weight and the density of the composite material selected for the stiffness layers. To begin with, assume

the weight of the damping layer is negligible. Then determine the thickness of the two stiffness layers.

3. Using the stiffness and cross-sectional area, determine the required effective axial modulus, E_X . Next calculate \hat{E}_X .

(Note, the curves obtained in Section 3 are only valid for the material property ratios specified, which only approximate most carbon fiber/epoxy systems.)

4. Use Figs. 3.6 and 3.7 to select a combination of D'_O and ϕ_O that will give the desired part stiffness and greatest possible damping loss factor.

5. Using values for the shear modulus and loss factor of the selected damping material at the appropriate frequency and temperature, determine the ratio of the square of the segment length, L^2 , to damping material thickness, t_d :

$$\frac{L^2}{t_d} = \frac{E'_{11} t_s D'_O}{G'_d}$$

6. Select an available damping material thickness, t_d , that will give a section length L that can be easily manufactured.

7. Correct predicted loss factor from Fig. 3.6 for the actual damping material loss factor using Fig. 3.13.

8. Repeat the above steps as needed for other choices of stiffness and/or damping materials.

6. CONCLUSIONS

Stress Coupling Activated Damping is a valid design concept, applicable to a wide range of engineering problems. Analytical models for both flat membranes and thin wall tubes were derived and non-dimensionalized. The models were incorporated into a simple computer code, DAMSEG, and used for parametric studies.

DAMSEG was used to quantify the effects of D'_O and fiber orientation angle on stiffness and damping. If the overlap joints were kept to less than 20% of the segment length they had little effect on the overall loss factor.

Several damped tubes were fabricated and dynamically tested to verify the damping concept and analytical models. The analytical models proved to be very accurate at predicting both stiffness and loss factor.

Information learned from the specimen testing was applied to the design and fabrication of tubes for the ASTREX structure. The new tubes match the originals in both stiffness and weight, but should have loss factors of 10.8% at the 17 Hz vibration mode in ASTREX. This loss factor is over 10 times higher than that of the original tubes. In addition, the measured loss factors for bending vibration modes between 200 and 1000 Hz were 20-30%, compared to $\leq 3\%$ for the original tubes.

Future work should include the fabrication of a complete truss structure incorporating SCAD tubes. In addition this technology should be applied to other structural members including plates and isogrid panels.

7. REFERENCES

1. E. M. Kerwin, "Damping of Flexural Waves by a Constrained Viscoelastic Layer", Journal of the Acoustical Society of America, Vol. 31, No. 7, 1959, pp. 952-962.
2. D. J. Mead and S. Markus, "The Forced Vibration of a Three-Layer, Damped Sandwich Beam with Arbitrary Boundary Conditions", Journal of Sound and Vibration, Vol. 10, No. 2, 1969, pp. 163-175.
3. C. A. Rotz and D. J. Barrett, "Cocured Damping Layers in Composite Structures", Proceedings, 23rd International SAMPE Technical Conference, Vol. 23, Oct 1991, pp. 352-363.
4. D. D. Olcott, C. A. Rotz, and D. J. Barrett, "Improved Damping in Composite Tubes Through Stress Coupling and Co-cured Damping Layers," Proceedings, 23rd International SAMPE Technical Conference, Vol. 23, Oct 1991, pp. 373-387.
5. D.D. Olcott, Improved Damping in Composite Structures Through Stress Coupling, Co-cured Damping Layers, and Segmented Stiffness Layers, Ph.D. Dissertation, Brigham Young University, Provo, Utah (1992).
6. Personal communication with personnel at Phillips Laboratory, Edwards AFB, California.
7. R. A. Ely, LTV Aircraft Products Group, personal communication (1991).

CHEMICAL AND STRUCTURAL EFFECTS CAUSED BY HYPERVELOCITY IMPACTS TO
POLYSULFONE GRAPHITE REINFORCED COMPOSITE AND ITS RESIN

JON H. SHIVELY
PROFESSOR
CIVIL AND INDUSTRIAL ENGINEERING AND APPLIED MECHANICS DEPARTMENT

CALIFORNIA STATE UNIVERSITY-NORTHRIDGE
SCHOOL OF ENGINEERING AND COMPUTER SCIENCE
18111 NORDHOFF STREET
NORTHRIDGE CA 91330

Final Report for:
Research Initiation Program
Phillips Laboratory, Kirtland AFB

Sponsored by:
Air Force Office of Scientific Research
and
California State University-Northridge
December 7, 1992

CHEMICAL AND STRUCTURAL EFFECTS CAUSED BY HYPERVELOCITY IMPACTS TO
POLYSULFONE GRAPHITE REINFORCED COMPOSITE AND ITS RESIN

JON H. SHIVELY
PROFESSOR
CIVIL AND INDUSTRIAL ENGINEERING AND APPLIED MECHANICS
DEPARTMENT
SCHOOL OF ENGINEERING AND COMPUTER SCIENCE

Abstract

The chemical changes and structural damage to spacecraft materials were studied as the result of collisions by simulated space debris particles traveling at velocities in the range of 4 to 8 km/s . A method was developed to study the chemistry of ejecta from hypervelocity collisions in spacecraft materials using a laser-launched flyer plate. The plate collision produces a vapor plume in the ejecta of the target material. The vapor plume is then analyzed with a time-of- flight mass spectrometer. The resultant damage from the collision was also characterized using optical and scanning electron microscopy.

Table of Contents

	Heading	Page
1.0	Introduction	4
2.0	Experimental	5
3.0	Results and Discussion	6
4.0	Conclusions and Recommendations	7
	References	10
	List of Figures	11

1. Introduction

The effects of hypervelocity collisions on the structural integrity of materials has been the subject of numerous studies (Ref 1-5). The phenomena of damage while well documented, is not well understood. Much of what happens inside a material after a hypervelocity collision apparently occurs after the initial compressive shock wave has passed through the material and has reflected back as a rarefaction wave. Reflections occur when the density suddenly changes as at the back surface and/or at internal discontinuities in the material such as precipitates or fibers.

This study has two major objectives. One objective is to determine the feasibility of measuring the chemistry of the ejecta from hypervelocity collisions. The material selected for the chemistry study is a polysulfone resin which was used to construct a fiber reinforced composite for the Long Duration Exposure Facility (LDEF). The choice of polysulfone composite stems from the exposure of this material on LDEF which spent 5 1/2 years in space in Low Earth Orbit (LEO) before being retrieved by the Space Shuttle. The simulation of LEO and its space environment is of special interest to the Phillips Laboratory, especially the effects of hypervelocity collisions from space debris and micro meteorites. Hypervelocity collisions with space debris and micro meteorites is one aspect of the space environment which causes dramatic changes in the materials. Post-examination of LDEF specimens at Phillips has revealed craters caused by hypervelocity collisions. Also, through careful characterization of undamaged surfaces, Phillips found deposits on surfaces indicating that chemical changes had occurred while in orbit. These deposits on aluminum contained sulfur which had somehow migrated from some other location on LDEF. One possibility is that the sulfur came from chemical changes in the ejecta from hypervelocity collisions in the polysulfone composite coupon which happened to be next to the aluminum coupon with the sulfur bearing deposits. It is well known that hypervelocity collisions produce adiabatic heating in the area immediately under the colliding particle. This heating is sufficient to produce decomposition and vaporization of the polymer chain in the composite resin. Thereby, sulfur may have been released to migrate and condense on the aluminum.

The other objective is to determine the nature of damage caused by hypervelocity collisions in composite materials. While considerable work has been performed on the damage to composites at low velocities, less than 100 m/s, little data is available from collisions at hypervelocities. The usual way to produce damage at hypervelocities involves the use of air guns and rail guns to produce particles traveling at hypervelocities in air. For this reason it has never been possible to look at damage caused by small particles. The nature of the damage observed in composites and resins needs to be studied systematically. This study will help refine future work.

The report below describes the results of two related studies performed to meet the objectives as outlined above. The effort was rewarded with meeting both objectives. It is noteworthy that the measurement of the chemical species ejected from a hypervelocity collision has never been achieved before, and therefore represents a significant technological breakthrough. However, the collisions by

hypervelocity particles is not the whole story as far as chemical changes and structural damage in LEO. is concerned. Obviously, these effects are also affected by ultraviolet light, charged-particle irradiation, and atomic oxygen erosion.

2.0 Experimental

The method of producing hypervelocity collisions was developed at Los Alamos National Laboratory (LANL). (See Ref 6). It involves launching a thin plate of aluminum, 5 microns thick, from an aluminum coated piece of quartz. The thin aluminum plate is produced by deposition from a plasma on the backside of the aluminum coating. The plasma in turn causes an extremely high pressure at the interface between the aluminum coating and the quartz. The coating bulges outward from the quartz and a disc 600 microns in diameter eventually breaks off and flies outward at hypervelocities. In this experiment, the plasma is produced by bombarding the aluminum-quartz interface with a pulsed beam from a YAG laser focused on a 600 micron diameter region for 8 nanoseconds.

The laser-launched flyer-plate has several advantages over the conventional methods of producing hypervelocity particles. One advantage is that the laser method is compact and the coated quartz disc fits conveniently into the chamber of the time-of-flight mass spectrometer. Secondly, it produces very little extraneous chemical debris as compared to the electric gun or the use of explosives to accelerate a flyer plate. Also, the use of a laser to produce a hypervelocity flyer-plate enables it to be accurately aimed at the collision location on the target. The laser can be directed externally to the vacuum chamber used to simulate space through a window in the space environment chamber. Finally, the polysulfone target can be oriented relative to the flyer to maximize the ejecta plume entering the ionization chamber of the TOF mass spectrometer.

The velocities of the launched discs are measured using the VISAR System which is a interferometric technique (Ref 7). The fringes from the interferometer are compared to the photograph of the flyer plate taken with a streak camera (Ref 7). The conversion of laser energy into aluminum kinetic energy of the aluminum flyer plate is linear as can be seen in Figure 1. The slope, however, depends upon the thickness and density of the flyer material and the laser pulse conditions. A calibration curve must be established for each flyer plate. When the conditions are held constant, the relation between input energy and kinetic energy is quite reproducible. Thus the use of the pulsed-laser is a convenient and reliable way to study damage in materials from hypervelocity shock. Of course, other materials besides aluminum can be launched. However, the size and density of aluminum most closely represents that of the average particle of space debris. (Ref 8).

Figure 2 shows the configuration used to study the chemical species produced by hypervelocity collisions of simulated particles of space debris. The flyer plate strikes the polysulfone target at an angle of 45° relative to the direction of flight. This arrangement provides a favorable orientation for the vapor ejecta to escape and to enter the mouth of the TOF mass spectrometer. The quartz launch plate and the

polysulfone target are shown in Figure 3 after five collisions.

The TOF mass spectrometer is capable of evaluating a complete mass spectra from mass one to 200 in 12 milliseconds. A hypervelocity collision rapidly and adiabatically heats the polysulfone and ejects the resultant chemical species in the form of a vapor outwardly and circumferentially around the collision zone. The ejected chemical species generated by the impact travel from the polysulfone target to the throat of the mass spectrometer where the vapor from the ejecta are ionized and accelerated to the mass spectrometer detector. The species are scanned as a function of time to produce a mass spectra. Chemical species arriving later than 12 ms will be detected in the next spectral scan. This has the advantage that the first chemical species that form after collision can be differentiated from those which form at later stages; the TOF spectrometer will display different spectra at different times. (Ref 9)

Polysulfone was selected because it is the resin used to make coupons of a graphite reinforced composite which spent several months in low-earth orbit in LDEF. Before examining the chemical results of collisions on the composite materials, a series of scoping studies were conceived in which the polysulfone resin was used as a target material. Experimentally, the laser-launched flyer-plates were aimed at the target of polysulfone in a vacuum chamber and were located next to the entrance to the throat of a Time-of Flight (TOF) mass spectrometer which is located at LANL.

In order to study the damage mechanism, some preliminary collisions were made in air apart from the TOF mass spectrometer. In these experiments, the laser-launched aluminum was fired at both polysulfone resin target and a composite target. The collisions were carried out in a range of velocities from 3 to 7 kilometers per second. The impacted samples were then examined using optical and scanning electron microscopy at Phillips Laboratory. The samples were first examined and photographed using the Nikon optical system at 50 and 100X. After optical studies, the specimens were sputter coated with a thin conductive layer of gold-palladium alloy for viewing in the scanning microscope. The coating prevents excessive charging during the bombardment with the electron beam of the microscope. The samples were also examined using the energy dispersive analysis of X-rays produced by the electron beam excitation of the atoms (EDAX).

A sample of 6061 Aluminum was obtained from LLNL for study. The results of a collision of a plastic flyer traveling at 10 km/s is quite dramatic. In this test a crater 2 inches wide by 3 inches long by 1/4 inch deep was generated by a 5 mil Kapton projectile. This test involved the use of an electric gun developed and operated by LLNL. The sample also experienced considerable internal damage.

4.0 Results and Discussion

The effort to measure chemical species produced by hypervelocity collisions of aluminum with polysulfone resin were successful. The spectrum produced is shown in Figure 4. and is averaged over several scans to provide better statistical results. No change in the spectrum were observed once the species were detected which would have affected the averaging. As can be seen, the spectrum covers masses 1 through 100. The relevant species are identified on the chart. The mer of polysulfone for

reference is also shown. Sulfur, which is one species easily removed from the polysulfone mer, shows up at 32 amu on the spectrum. It could have been overshadowed by the oxygen molecule which also has the same mass, 32 amu. However, the amount of oxygen present should be quite small in the vacuum chamber and the oxygen that is present is already combined with the aluminum flyer plate. Therefore, the peak at 32 amu is an indication of sulfur and is therefore positive verification that the polysulfone de-polymerized.

Other species were present which undoubtedly came from the de-polymerization of the polysulfone. For example, the aromatic species are present, C_6H_x . Also monomers of carbon-hydrogen species, such as C_2H_2 , came from the breakup of the mer of polysulfone. In short, the spectrum seen is the direct result of the collision of a hypervelocity particle with the resin. This is the first time shock induced chemical changes from simulated space debris have been observed.

The damage caused by hypervelocity collisions is also striking. In the case of the resin without fibers, the results are quite similar to that observed in the collision of other homogeneous materials in that the collision produces a crater on the surface. The size of the crater matches the size of the aluminum particle launched from the quartz. The depth and extent of crater are quite similar to that observed in shock studies on plastics. As can be seen, debris from the collision coats the neighboring surface with small sub-particles of aluminum from the flyer plate. The crater in the resin exhibits evidence of melting and a crack forms around the edge of the crater due to shrinkage after melting. See Figures 5 to 7. There is nothing unusual about the collisions that has not been observed in shock studies on other materials, except that the scale of these tests is small leaving the surrounding material in a relatively undisturbed state.

The shock damage in the composite materials is quite different. The craters from the collision are presented in Figure 8 to 9. As can be seen, in all cases except the very highest velocity, little evidence of melting of the resin is evident. This suggests that the energy associated with the compression is not totally absorbed by the resin but that it is partly dissipated by the underlying fibers. Moreover, considerable fracture damage is evident to both the matrix and the fibers as a result of the collisions. The matrix is observed to spall off the surface and the fibers underneath are uncovered. The fibers around the edges of the craters are also severely fractured. Thus, damage in a composite material after hypervelocity collision is fundamentally different than in the resin itself.

In contrast, the damage in the 6061 Aluminum plate struck by the flyer plate from the electric gun at LLNL produces considerable internal damage. Most prominent in the observation is the presence of micro voids at the interfaces between precipitates and the aluminum matrix. These formed predominately at grain boundaries in the aluminum because these are favored sites for the formation of precipitates in 6061. In some cases the precipitates themselves were fractured.

5.0 Conclusions and Recommendations

A series of experiments on shock damage in spacecraft materials were performed. The

experiments are intended to simulate hypervelocity collisions encountered in low earth orbit which produce chemical changes and shock damage in the spacecraft materials. The hypervelocity collisions were achieved by propelling a 5 micron thick flyer-plate of aluminum at a polysulfone composite. The flyer-plate is launched by focusing a pulsed laser beam at the interface between a thin coating of aluminum and a quartz substrate.

The scoping tests clearly demonstrated that the laser-launched shock processes in the resin system match those observed for other homogeneous materials in other shock experiments. The collision process vaporizes the resin and causes it to de-polymerize as would be expected from the pressures and temperature present during the early stages of the collision. This represents the first time that ejected vapors from hypervelocity collisions were trapped and analyzed by a mass spectrometer.

Scoping studies were also conducted to determine shock damage to both the polysulfone composite and to the resin alone from hypervelocity collision in the range of 3 to 8 km/s. These studies were conducted in air at a separate facility at LANL but used the same laser-launch techniques as described above. The impact craters were examined under optical and scanning electron microscopes. The collision craters in the resin matrix were typical of those shown in conventional shock experiments. However, the hypervelocity collisions on the polysulfone composite were remarkably different than on the resin itself. Little evidence of melting was observed on the composites for comparable impact velocities. The composite appeared to shatter upon impact and the light coating of resin on the surface spalled off. Underneath the front surface the graphite fibers fractured in tension. The fracture process extends deep into the composite compared to the depth of surface craters in observed in the pure resin.

It is recommended that further studies be initiated using the laser-launched flyer plates to cause damage in composites. Internal examination in the region of the collision needs to be performed to determine the depth of the fiber fractures. Specimens should be examined for evidence of delamination between layers which is observed when composites experience low-velocity impacts. Other resins and fibers need to be studied. The matrix and fibers used in these composites are brittle. More ductile fibers may resist breakage during collision. The use of thermoplastic resins could partly reduce the brittleness in the matrix. Finally, particulated metal matrix composite materials such as SiC or graphite particles in an aluminum matrix would be of interest for shock studies.

The interface between matrix and fiber was obviously a weak point in the response to shock waves caused by hypervelocity collisions. (The resin separated from the fibers). In the case of 6061 aluminum, micro-voids and micro-cracks form at the interface between the inter-metallic precipitates in the grain boundaries of the aluminum matrix. Thus damage may be a result of the mismatch in acoustic impedance, $Z = \rho C$, between the matrix and the strengthening agent, (inter-metallic precipitates, particulates or fibers). Depending on the impedance difference between the matrix and the strengthening agent, a shock wave which encounters a precipitate in an alloy, a particulate, or a fiber in a composite material will be reflected as either a compression wave or as a rarefaction wave. In the case where the

matrix has a higher acoustic impedance than the precipitate, the particulate, or fiber, a rarefaction wave is reflected at the interface. This leads to spalling. On the other hand, if the matrix has a lower density than the strengthening agent, a rarefaction wave would be produced in the particulates, particulates or the fibers. Rarefaction means that very large tensile stresses are developed. If the tensile stresses are high enough, the strengthening agent will crack. While these preliminary experiments have not enabled these details to be completely determined, the metallographic and fractographic results are consistent with the wave propagation mechanisms. Thus, an acoustic mismatch may explain the fracturing observed at the surface of the composite. The matrix has a density of 1.24 and the carbon fibers a density of 1.77. Since the fiber has a higher density, the reflected shock wave at the matrix fiber interface would be a compressive wave and the transmitted shock wave a rarefaction (tensile) wave. The compression wave from the collision is very large at the collision velocities used in this experiment. The associated rarefaction wave would produce comparable tensile stresses which would be sufficiently high to cause the fibers to fracture. The multiple reflections will disperse the shock wave but leave in their wake a severely damaged composite with broken fibers. While the above mechanisms are speculative, the laser-launched flyer plate could be used very effectively to study the interface between the resin and the fibers more systematically. Other interfaces such as the aluminum-SiC could also be studied in an effort to evaluate the shock mechanisms. There is a need to confirm these mechanisms with additional experimental work.

References

1. J. Dein, R. Tokheim, D. Curran, H. Chau, R. Weingart, and R. Lee, "Aluminum Damage Simulation in High-Velocity Impact", in Shock Wave in Condensed Matter, 1983, J.R. Asay, R.A.Graham, and G.K. Straub, eds, Elsevier, BV, 1984.pp 171.
2. A.M. Rajendran, M.A.Dietenberger, and D.J. Grove, "A Void Growth-Based Failure Model to Describe Spallation", J. Appl. Phys. **65**, 15 Feb 1989, p1521
3. T.D. Riney and E.J. Halda, "Effectiveness of Meteoroid Bumpers Composed of Two Layers of Distinct Materials", AIAA Journal, **6**, No. 2, Feb 1968, p338
4. G.R. Fowles, "Shock Wave Compression of Hardened and Annealed 2024 Aluminum", J. Appl. Phys. **32**, No 8, Aug 1961, p 1475.
5. D.R. Curran, D.A. Shockley, and L. Seaman, J. Appl. Phys., **44**, 4025, (1973)
6. D. L. Paisley, R.H. Warnes, and R.A. Kopp, "Laser-Driven Flat Plate Impacts to 100 GPa with Sub-nanosecond Pulse Duration and Resolution for Material Property Studies", in Shock Compression of Condensed Matter 1991, S.C. Schmidt, R.D.Dick, J.W. Forbes, and D.G. Tasker, eds, Elsevier Science BV, 1992, p 825
7. L.M. Barker and R.E. Hollenbach, "Shock-Wave Studies of PMMA, Fused Silica, and Sapphire", J. Appl. Phys., **41**, No. 10, Sep 1970, p4208
8. N.L. Johnson and D.S. McKnight, Artificial Space Debris, Orbit, p25 ff
9. N.C. Blais, H.A. Fry, and N.R. Greiner, "Apparatus for the Mass Spectrographic Analysis of Detonation Products Quenched by Adiabatic Expansion," Review of Sci Instr, TBP

List of Figures

	Figure Title	Page
Figure 1	Laser Impulse Energy Versus Flyer Plate Velocity Squared (Kinetic Energy)	13
Figure 2	Experimental Arrangement Used to Study Chemical Reactions from Hypervelocity Particle Collisions	14
Figure 3	The Laser Flyer-Plate Target in the Chamber of the TOF Mass Spectrometer	15
Figure 4	The Spectra Produced From Hypervelocity Collision of Aluminum with Polysulfone	16
Figure 5	Top View of the Crater in Polysulfone Photographed Optically After Collision at 6 km/s	17
Figure 6	Scanning Electron Microscope Top View of Crater Formed in Polysulfone After Collision at 6 km/s	18
Figure 7	Scanning Electron Microscope Tilt Angle View of Crater in Polysulfone After Collision at 6 km/s	19
Figure 8	Scanning Electron Microscope Top View of Crater Formed on Polysulfone Composite After Collision at 5 Km/s	20
Figure 9	Scanning Electron Microscope Tilt Angle View of the Crater Formed on Polysulfone Composite After Collision at 6 km/s	21
Figure 10	Photomicrograph of Damage Produced in 6061 Aluminum After Collision at 10 km/s	22

FIGURES

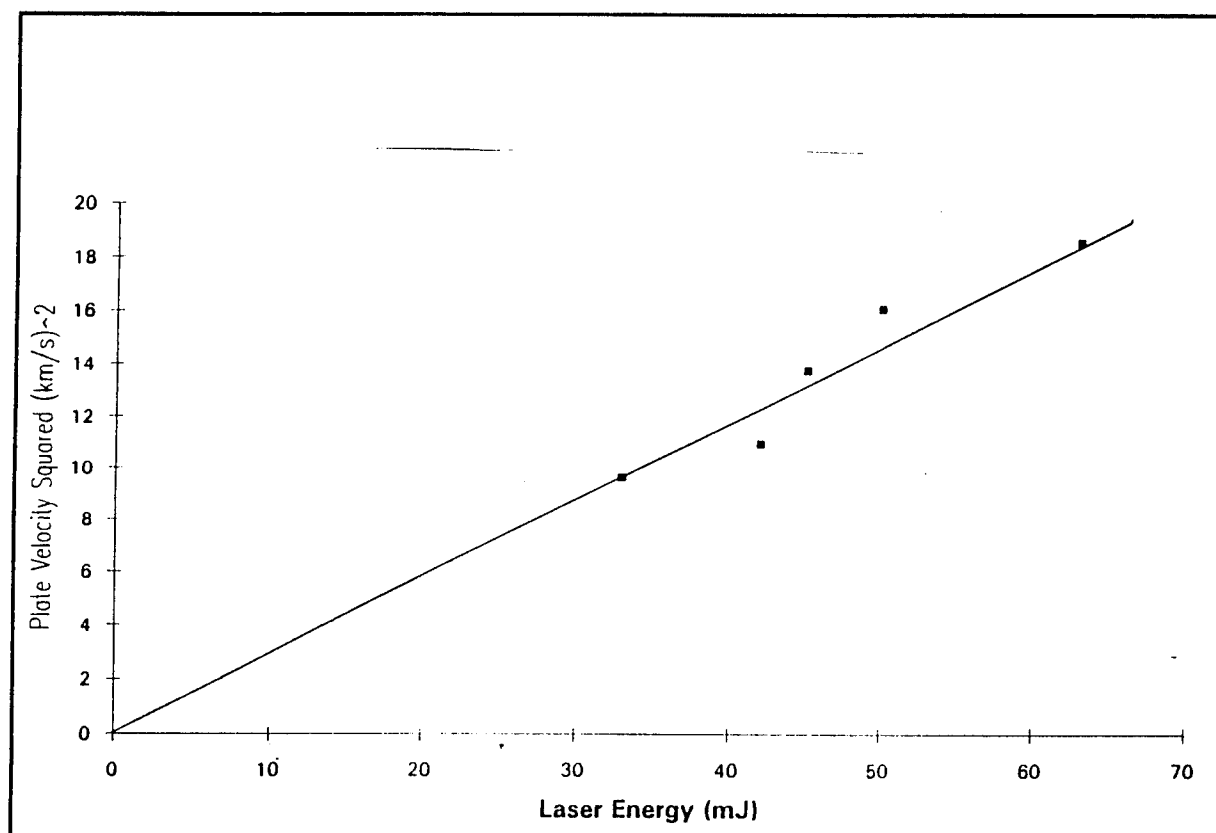


Figure 1 Laser Impulse Energy Versus Flyer Plate
Velocity Squared (Kinetic Energy)

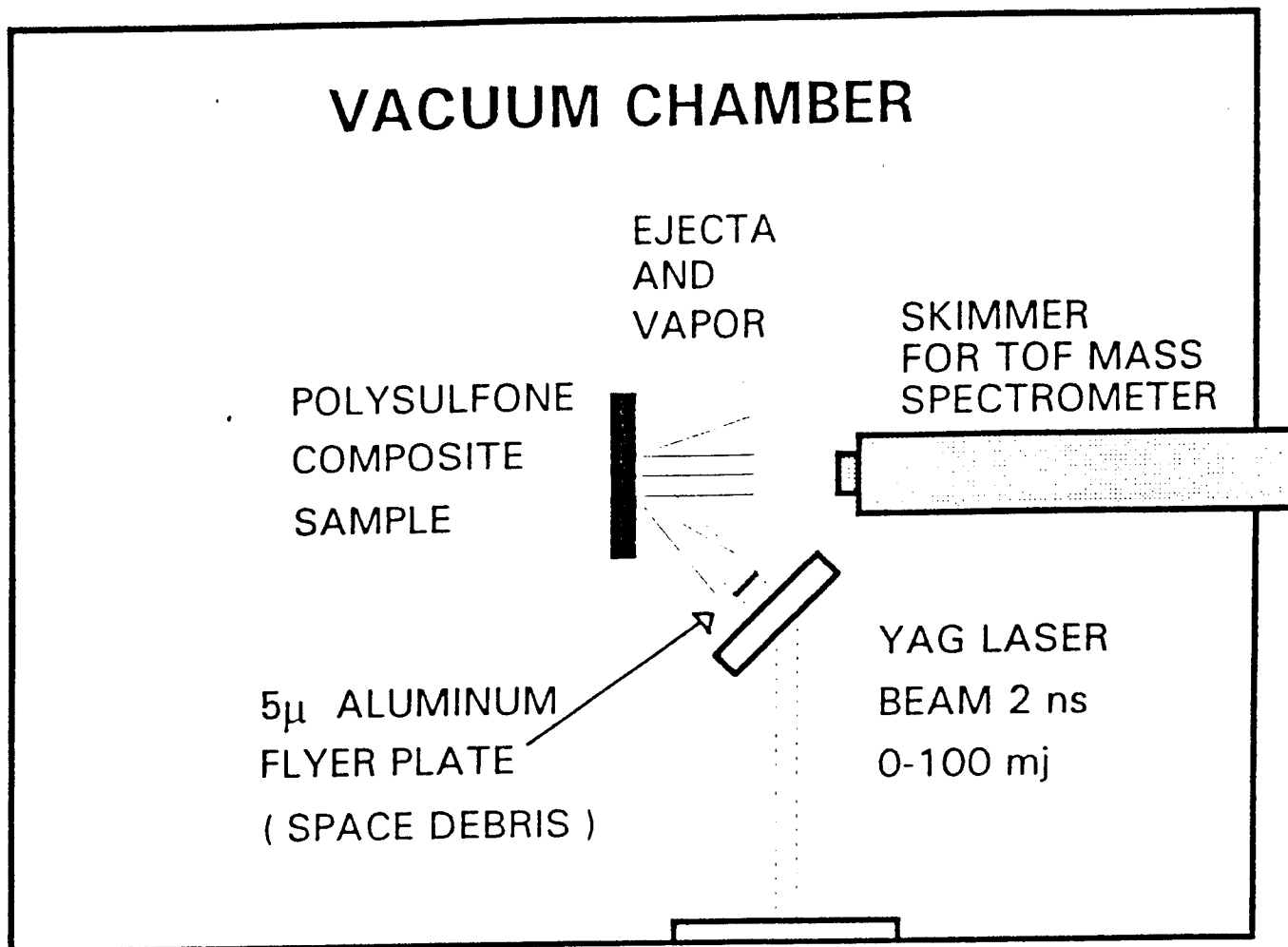


Figure 2 Experimental Arrangement Used to Study
Chemical Reactions from Hypervelocity Particle
Collisions

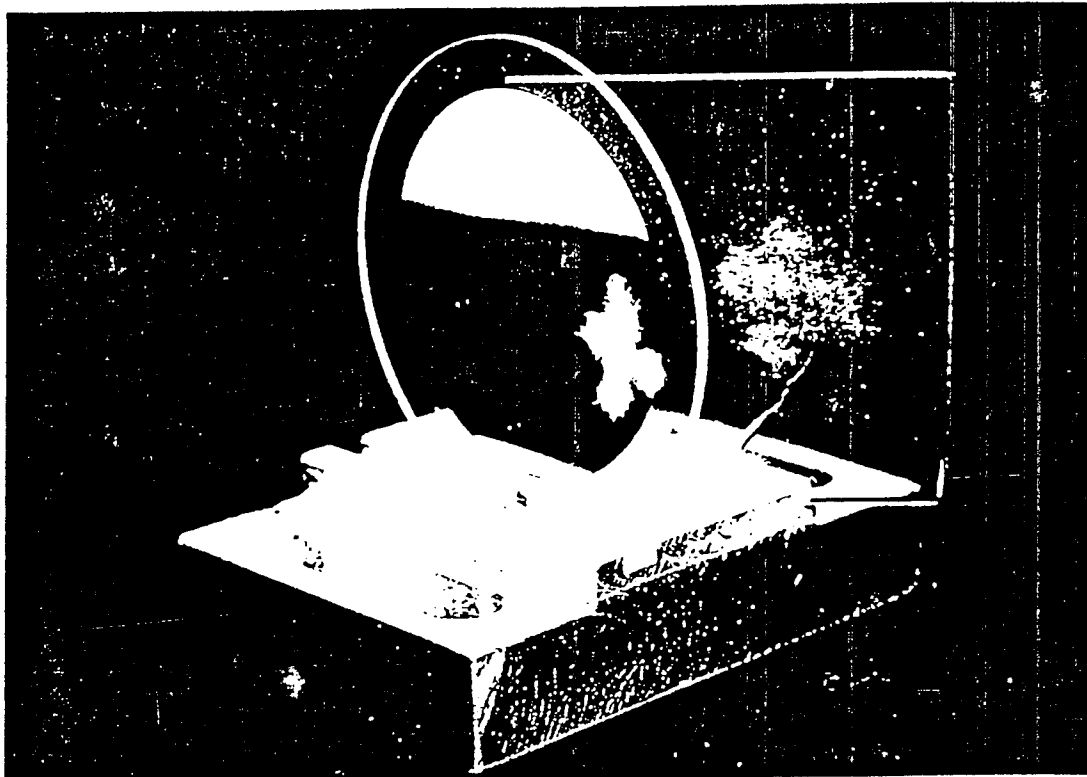


Figure 3 The Laser Flyer-Plate Target in the
Chamber of the TOF Mass Spectrometer

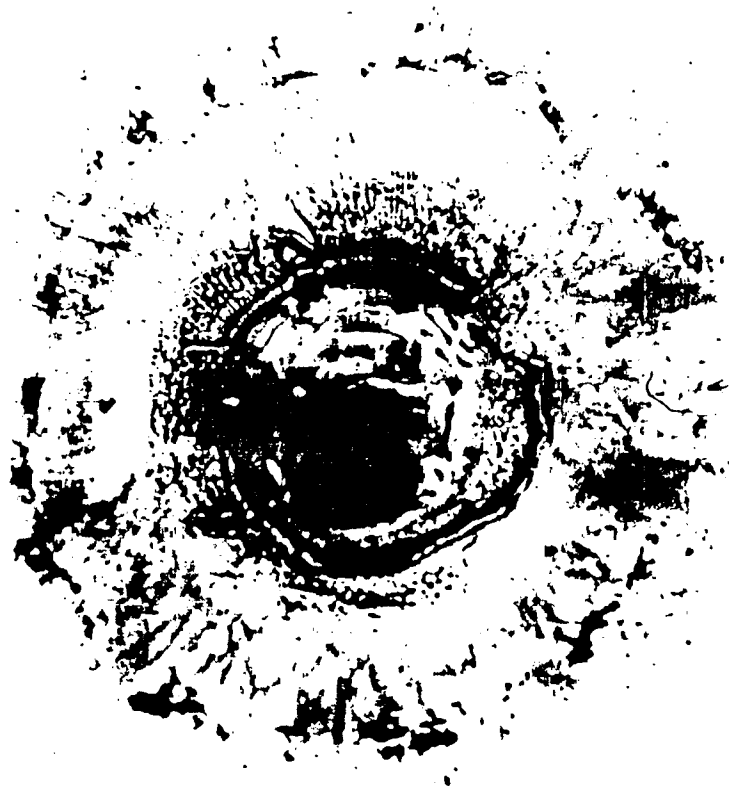


Figure 5 Top View of the Crater in Polysulfone
 Photographed Optically After Collision
 at 6 km/s

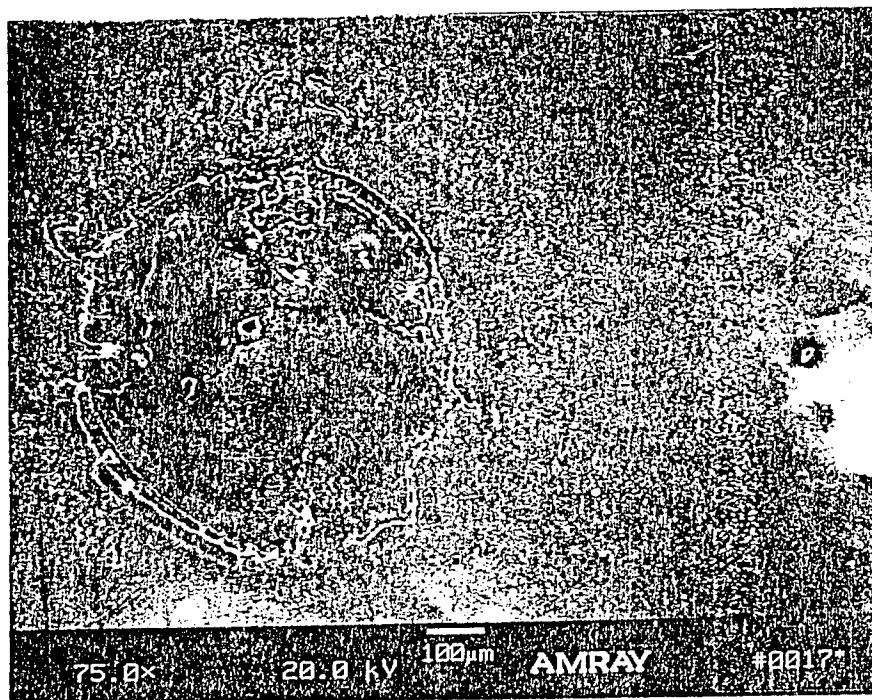


Figure 6 Scanning Electron Microscope Top View of
Crater Formed in Polysulfone After
Collision at 6 km/s

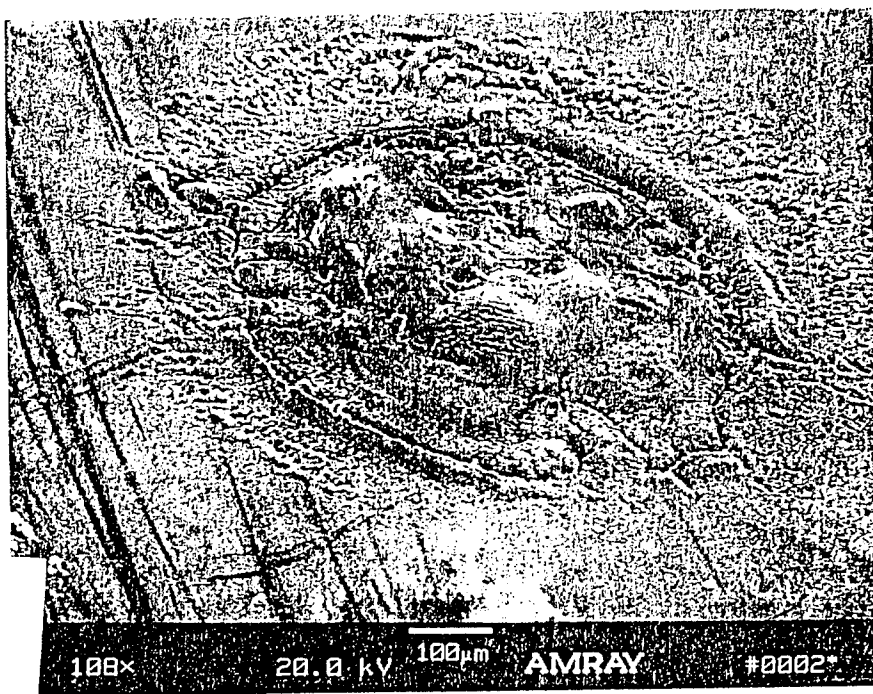


Figure 7 Scanning Electron Microscope Tilt Angle
View of Crater in Polysulfone After
Collision at 6 km/s

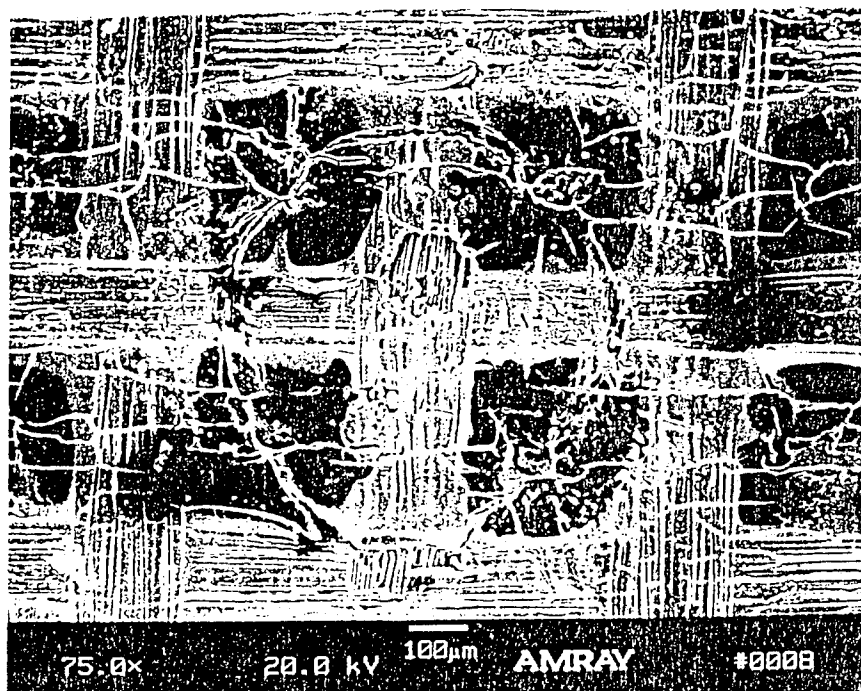


Figure 8 Scanning Electron Microscope Top View of
Crater Formed on Polysulfone Composite
After Collision at 5 Km/s

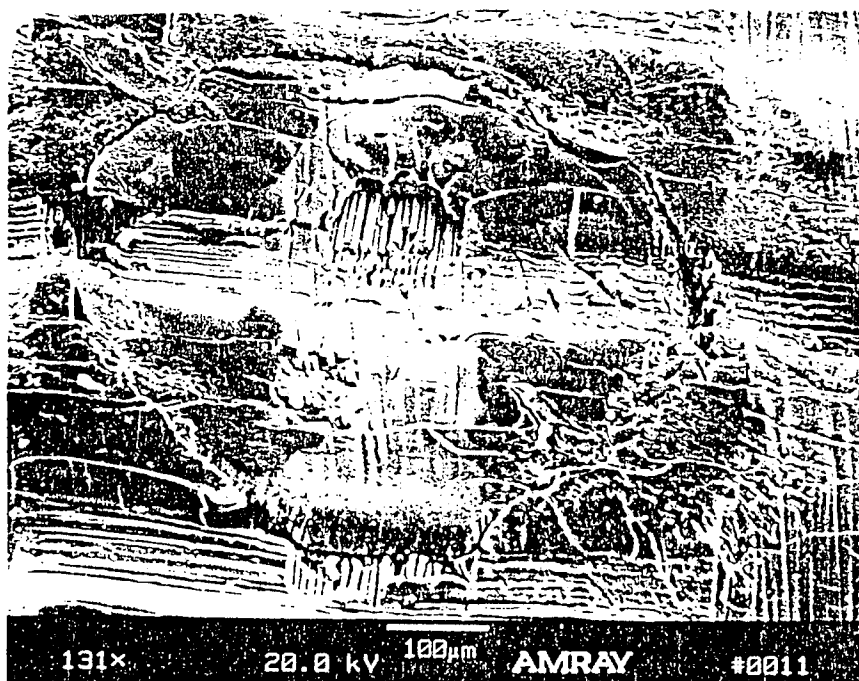


Figure 9 Scanning Electron Microscope Tilt Angle
View of the Crater Formed on Polysulfone
Composite After Collision at 6 km/s

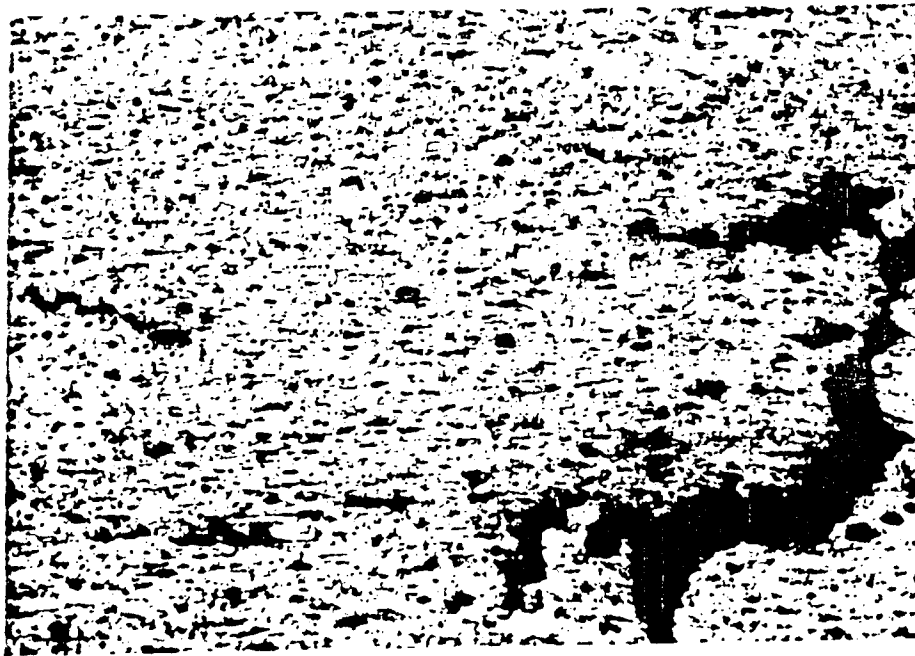


Figure 10 Photomicrograph of Damage Produced in
6061 Aluminum After Collision at 10 km/s

END POINT TRAJECTORY CONTROL OF ELASTIC MULTI-BODY SYSTEM

Sahjendra N. Singh, Professor

and

Shailaja Chenumalla, Graduate Assistant

Department of Electrical & Computer Engineering

University of Nevada, Las Vegas

Las Vegas, NV 89154

Final Report for:

Research Initiation Program

Phillips Laboratory

Sponsored by:

Air Force Office of Scientific Research

Bolling Air Force Base, Washington, D.C.

and

University of Nevada, Las Vegas

December 1992

END POINT TRAJECTORY CONTROL AND OF ELASTIC MULTI-BODY SYSTEM

Sahjendra N. Singh, Professor

Shailaja Chenumalla, Graduate Assistant

Department of Electrical & Computer Engineering

University of Nevada, Las Vegas

Las Vegas, NV 89154

Abstract

We treat the question of control and stabilization of the elastic multibody system developed in the Phillips Laboratory, Edwards Air Force Base, California. This system consists of two elastic links actuated by electric motors at the joints and rotate on a smooth horizontal granite table. An air bearing is used, which allows the whole system to float on the air so that the friction forces do not exist between the support plate and the granite table. The controlled output is judiciously chosen such that the zero dynamics are stable or almost stable. For the control of the end point, two kinds of parameterizations of end effector position are considered. A variable structure control (VSC) law is derived for the end point trajectory control for each chosen output. Stability of zero dynamics associated with end point control is examined. Although, the VSC law accomplishes precise end point tracking, elastic modes are excited during the maneuver of the arm. A Linear stabilizer is designed for the final capture of the terminal state. Simulation results are presented to show that the trajectory tracking and vibration damping are accomplished in the closed loop system in spite of the payload uncertainty.

1 INTRODUCTION

In the Phillips Laboratory, Edwards Air Force Base, CA, a multibody system has been set up for the study of dynamics and control-structure interaction. This project is called the Planar Articulating Controls Experiment (PACE). The system has two elastic links and two revolute joints. The arm rotates in the horizontal plane on a smooth granite table. When the arm is maneuvered, both the links undergo elastic deformation. Recently some theoretical and experimental studies related to end point control have been done [1-11]. In these papers, inverse control systems and variable structure systems have been designed.

This research is related to end point trajectory control of the multibody system. For the trajectory control, a control law based on variable structure system (VSS) theory [11-12] is derived. It turns out that the zero dynamics correspondingly to the end point control in the closed-loop system is unstable. Instability of the zero dynamics is avoided by choosing the coordinates of a point in the neighborhood of the tip position of controlled output variables. Such a choice of controlled outputs is not unique. We have made two parameterizations of the controlled output in this study. Each parameterization of the output leads to a different control law for the trajectory control.

The VSC law is a discontinuous function of the state variables. Using the VSC law, tip trajectory is accurately tracked. However, this excites the elastic modes of the links. Based on a linearized system about the terminal equilibrium point, a stabilizer is designed using pole assignment technique. Simulation results are presented to show that in the closed-loop system, precise trajectory tracking and vibration damping are accomplished in spite of the payload uncertainty.

In this study it is assumed that all the state variables are available for the feedback. For the synthesis of the control law in the laboratory, some of these variables can be measured by sensors and the remaining variables must be estimated using an observer. Furthermore, study related to control spillover is not treated here.

2 MATHEMATICAL MODEL AND PROBLEM STATEMENT

The robotic arm is shown in the Fig.1. OXY is an inertial frame with origin at joint 1, OX_1Y_1 is a reference frame with X_1 along link 1, and OX_2Y_2 is a reference frame with origin at joint 2 with X_2 axis along link 2. OX_1 and O_2X_2 are tangent to the links. $OO_{N1}O_{N2}$ represents the position of the arm for the case of rigid links. θ_1 and θ_2 are the joint angles. OO_2O_{E2} represents the position of the deformed arm.

By the assumed mode method, the elastic deflection is represented as linear combination of admissible functions $\phi_{1j}(l_1)$, $\phi_{2j}(l_2)$ multiplied by time-dependent generalized coordinates $q_{ij}(t)$. In this study ϕ_{ij} are the mode shapes of a clamped-free beam. Let $\delta_1(l_1, t)$ and $\delta_2(l_2, t)$ denote the elastic deflections of the links at a distance l_1 from O along OX_1 and at a distance l_2 from O_2 along O_2X_2 . These elastic deformations can be expressed as

$$\begin{aligned}\delta_1(l_1, t) &= \sum_{i=1}^n \phi_{1i}(l_1) q_{1i}(t) \\ \delta_2(l_2, t) &= \sum_{i=1}^n \phi_{2i}(l_2) q_{2i}(t)\end{aligned}\tag{1}$$

where n denotes the number of significant modes. Here it is assumed that the links do not undergo longitudinal and torsional deformations and the contribution of higher modes is negligible.

The equations of motion of the arm can be obtained by Lagrangian method. These are given by

$$\frac{d}{dt} \left(\frac{\partial T}{\partial \dot{z}_i} \right) - \frac{\partial T}{\partial z_i} + \frac{\partial P}{\partial z_i} = B_1 u\tag{2}$$

where

$$z = (\theta^T, q^T), \quad \theta = (\theta_1, \theta_2)^T, \quad q = (q_{11}, \dots, q_{1n}, q_{21}, \dots, q_{2n})^T,$$

T is the kinetic energy of the arm,

P is the potential energy of the arm,

$u = (u_1, u_2)^T$, is the vector of joint torques,

$$B_1 = [I_{2 \times 2}, O_{2 \times 2n}]^T$$

Here, T denotes transposition and I and O denote the identity and null matrices of indicated dimensions. The potential energy P is a function of q and is independent of θ since the arm rotates in the horizontal plane. The kinetic energy is a quadratic function of generalized velocities and thus $T = (\dot{z}^T M(z) \dot{z})/2$, where $M(z)$ is the positive definite symmetric inertia matrix. Using the expression of T in (2), gives

$$M(z)\ddot{z} + h_o(z, \dot{z}) + \partial P(z)/\partial z = B_1 u\tag{3}$$

where

$$h_o(z, \dot{z}) = \dot{M}(z)\dot{z} - (1/2)(\partial z^T M(z)\dot{z}/\partial z)$$

$$M(z) = \begin{bmatrix} M_{11}(z) & M_{12}(z) \\ M_{21}(z) & M_{22}(z) \end{bmatrix}$$

where M_{11} is a 2×2 submatrix.

Defining $x = (z^T, \dot{z}^T)^T$, one obtains a state variable representation of (3) given by

$$\dot{x} = f(x) + B(x)u \quad (4)$$

where

$$\begin{aligned} n_0 &= 2(n+1), \\ f(x) &= \begin{bmatrix} \dot{z} \\ M^{-1}(z)(-h_o(z, \dot{z}) - \partial P(z)/\partial z) \end{bmatrix} \triangleq \begin{bmatrix} \dot{z} \\ h(z, \dot{z}) \end{bmatrix} \\ B(x) &= \begin{bmatrix} O_{2 \times n_0}, & (M^{-1}(z)B_1)^T \end{bmatrix}^T \end{aligned}$$

To this end a judicious choice of the controlled variables is made for the design of the control system. Assuming small elastic deflections, the angular positions of the links are given by

$$\rho_i = \tan^{-1} \left[\frac{\sin(\theta_i + \frac{\delta_i(L_i, t)}{L_i})}{\cos(\theta_i + \frac{\delta_i(L_i, t)}{L_i})} \right], i = 1, 2 \quad (5)$$

$$\rho_e = \tan^{-1} \left[\frac{L_1 \sin(\theta_1 + \frac{\delta_1(L_1, t)}{L_1}) + L_2 \sin(\theta_1 + \theta_2 + \frac{\delta_2(L_2, t)}{L_2})}{L_1 \cos(\theta_1 + \frac{\delta_1(L_1, t)}{L_1}) + L_2 \cos(\theta_1 + \theta_2 + \frac{\delta_2(L_2, t)}{L_2})} \right]$$

Thus, for $i = 1, 2$, one has from (5) that

$$\rho_i = \theta_i + \frac{\delta_i(L_i, t)}{L} \quad (6)$$

where $L_i (i = 1, 2)$ denote the lengths of the links.

Although, one can consider ρ_e given in (5) for the controller design, certain simplification results for the arm under consideration for which $L_1 = L_2$. Using $L_1 = L_2 = L$ in (5) and simplifying, gives

$$\rho_e = \theta_1 + \frac{\theta_2}{2} + \frac{1}{2} \left(\frac{\delta_1(L, t) + \delta_2(L, t)}{L} \right) \quad (7)$$

According to (6) and (7), ρ_i and ρ_e denote the angular position of the end points of the links and one can choose these as output variables for control system design. However, it will be seen later that such a choice leads to unstable zero dynamics. In order to avoid instability of the zero dynamics, we shall choose angular positions of points close to the end points of the links as output variables. These are given by either of the two sets of output equations

$$y = \begin{bmatrix} \rho_1 \\ \rho_2 \end{bmatrix} = \begin{bmatrix} \theta_1 + \alpha_1 \frac{\delta_1(L_1, t)}{L_1} \\ \theta_2 + \alpha_2 \frac{\delta_2(L_2, t)}{L_2} \end{bmatrix} \quad (OV_1) \quad (8)$$

$$y = \begin{bmatrix} \rho_1 \\ \rho_e \end{bmatrix} = \begin{bmatrix} \theta_1 + \alpha_1 \frac{\delta_1(L_1, t)}{L_1} \\ \theta_1 + \frac{\theta_2}{2} + \frac{1}{2} \left(\frac{\alpha_1 \delta_1(L, t) + \alpha_2 \delta_2(L, t)}{L} \right) \end{bmatrix} \quad (OV_2) \quad (9)$$

We have chosen OV_1 and OV_2 as two forms of parameterized output variables where the parameter $\alpha_i \in [0, 1]$. For $\alpha_i = 1, i = 1, 2$, one obtains the angular positions of the tip of the links and $\alpha_i = 0$ corresponds to the angular position of the links if the arm is rigid. For $\alpha_i \in [0, 1)$, outputs are the angular positions of points close to the end points of the links. The choice of the outputs in (8) and (9) leads to different control laws.

Let $y_r(t) = [y_{r1}(t), y_{r2}(t)]^T$ be a given reference trajectory. We are interested in designing control system such that in the closed-loop system $y(t)$ tracks $y_r(t)$ and elastic vibration is suppressed.

3 VARIABLE STRUCTURE SYSTEM

In this section, based on the variable structure system, control laws are derived. The system (4) together with the outputs OV_1 or OV_2 can be written as

$$\dot{x} = f(x) + B(x)u \quad (10)$$

$$y = Cx = [C_1 \quad O]x$$

where for the choice of y according to (8), one has

$$C_1 = \begin{bmatrix} 1 & 0 & \alpha_1 \frac{\phi_{11}(L_1)}{L_1} & \dots & \alpha_1 \frac{\phi_{1n}(L_1)}{L_1} & 0 & \dots & 0 \\ 0 & 1 & 0 & \dots & 0 & \alpha_2 \frac{\phi_{21}(L_2)}{L_2} & \dots & \alpha_2 \frac{\phi_{2n}(L_2)}{L_2} \end{bmatrix} \quad (11)$$

$$\triangleq R\theta + Hq, \quad R = I,$$

and for the output given by (9), the C_1 matrix is

$$C_1 = \begin{bmatrix} 1 & 0 & \alpha_1 \frac{\phi_{11}(L_1)}{L_1} & \dots & \alpha_1 \frac{\phi_{1n}(L_1)}{L_1} & 0 & \dots & 0 \\ 1 & 0.5 & \alpha_1 \frac{\phi_{11}(L)}{2L} & \dots & \alpha_1 \frac{\phi_{1n}(L)}{2L} & \alpha_2 \frac{\phi_{21}(L)}{2L} & \dots & \alpha_2 \frac{\phi_{2n}(L)}{2L} \end{bmatrix} \quad (12)$$

$$\triangleq R\theta + Hq$$

Here, matrices R, and H are defined in (11) and (12). We note that the matrix H is a function of α_i . The matrices R and H have different forms and depend on the choice of output variables.

Differentiating y and using (10) gives

$$\dot{y} = C_1 \dot{z} \quad (13)$$

$$\ddot{y} = C_1 h(z, \dot{z}) + C_1 M^{-1}(z) B_1 u$$

We shall be interested in a region of state space $\Omega \subset R^{2n_0}$ in which $B^*(z) \triangleq C_1 M^{-1}(z) B_1$ is nonsingular. Thus the tracking order of the system (10) is 2 and the system (10) and (13) is invertible.

Now we proceed to derive the variable structure system. The VSC law is a discontinuous function of state variables. For the design of the variable structure system (VSS), we choose a switching surface in the state space for the control function to have discontinuity, and the control law is chosen such that the trajectories of the system beginning from any initial condition are attracted towards this surface.

The switching surface $S = (S_1, S_2)^T$ is chosen of the form

$$S(\tilde{y}, \dot{\tilde{y}}) = \dot{\tilde{y}} + 2\zeta_e \omega_{ne} \tilde{y} + \omega_{ne}^2 w, \quad (14)$$

where $\tilde{y} = (\tilde{y}_1, \tilde{y}_2)^T$,

$$\dot{w} = \tilde{y}, w \in \mathbb{R}^2 \quad (15)$$

We note that when the trajectory is confined to the surface $S = 0$ during the sliding phase, one has

$$\ddot{\tilde{y}} + 2\zeta_e \omega_{ne} \dot{\tilde{y}} + \omega_{ne}^2 \tilde{y} = 0 \quad (16)$$

and $\tilde{y}(t) \rightarrow 0$, as $t \rightarrow \infty$, for $\zeta_e > 0, \omega_{ne} > 0$.

Now we can choose the control law such that the trajectories are attracted towards $S = 0$ when $S(\tilde{y}(0), \dot{\tilde{y}}(0)) \neq 0$. Differentiating (14) and using (13) and (15) gives

$$\dot{S} = C_1 h(z, \dot{z}) + B^*(z)u - \ddot{y}_r + 2\zeta_e \omega_{ne} \dot{\tilde{y}} + \omega_{ne}^2 \tilde{y} \quad (17)$$

$$\triangleq a(z, \dot{z}) + B^*(z)u$$

where $a(z, \dot{z}) = C_1 h(z, \dot{z}) - \ddot{y}_r + 2\zeta_e \omega_{ne} \dot{\tilde{y}} + \omega_{ne}^2 \tilde{y}$

To this end, it is assumed that

$$a(z, \dot{z}) = a_n(z, \dot{z}) + \Delta a(z, \dot{z}) \quad (18)$$

$$B^*(z) = B_n^*(z) + \Delta B^*(z)$$

where a_n, B_n^* are the nominal values of a and B^* and $\Delta a, \Delta B^*$ denote uncertain portions of a and B^* , respectively.

Assumption 1: There exists functions γ_i such that

$$\|\Delta B^*(z) B_n^{*-1}(z)\| \leq \gamma_1(x) < \gamma_0 < 1 \quad (19)$$

$$\|\Delta a(x) - \Delta B^*(z) B_n^{*-1}(z) a_n(x)\| \leq \gamma_2(x, t)$$

We choose control law u such that $\dot{S} < 0$ if $S \neq 0$ and the trajectory reaches the surface $S = 0$ in a finite time. In view of (17), we select u of the form

$$u = B_n^{*-1}(z)[-a_n(x) - k \operatorname{sgn}(S) + v] \quad (20)$$

where $v = (v_1, v_2)^T$ is the stabilization signal to be determined later and

$$\operatorname{sgn}(S_i) = \begin{cases} 1, & S_i > 0 \\ 0, & S_i = 0 \\ -1, & S_i < 0 \end{cases}$$

Substituting (20) in (17), gives

$$\dot{S} = \Delta a(x) + \Delta B^*(z)u - k \operatorname{sgn}(S) + v \quad (21)$$

where

$$\operatorname{sgn}(S_i) = \begin{cases} 1, & S_i > 0 \\ 0, & S_i = 0 \\ -1, & S_i < 0 \end{cases}$$

For $v = 0$, and when there is no uncertainty in the system (i.e $\Delta a = 0, \Delta B^* = 0$), (21) gives

$$\dot{S} = -k \operatorname{sgn}(S) + v \quad (22)$$

In view of (22) with $v = 0$, $\dot{S} < 0$, if $S \neq 0$.

By selecting a proper value of k , one can also show using Lyapunov theory that the surface $S = 0$ is reached even in the presence of model uncertainty when $v = 0$. Consider a Lyapunov function

$$v(s) = |S_1| + |S_2| \quad (23)$$

Let us choose the gain k such that

$$k \geq (1 - \gamma_1(x))^{-1}(\delta + \gamma_2(x, t)) \quad (24)$$

where $\delta > 0$. Then it follows that in the closed loop system with $v = 0$, one has

$$\dot{v}(t) \leq -\delta \quad (25)$$

for all $S \neq 0$ and $t \in [0, \infty)$. Since $v(0) > 0, S \neq 0$, it follows that indeed the trajectory reaches

the surface $S = 0$ in spite of the uncertainty in the system model provided, the Assumption 1 holds.

The VSC law (20) is a discontinuous function of x . However, discontinuity in control input causes chattering behavior, which is undesirable. It is well known that chattering can be avoided by using a smooth approximation of the discontinuous control input. Here, for obtaining a continuous control law, we use the *sat* function instead of the *sgn* function. Thus in the control law (20) $\text{sgn}(S_i)$ is replaced by $\text{sat}(S_i)$ where

$$\text{sat}(S_i) = \begin{cases} 1, & S_i > \epsilon_1 \\ S_i/\epsilon_1, & |S_i| \leq \epsilon_1 \\ -1, & S_i < -\epsilon_1 \end{cases} \quad (26)$$

where $\epsilon_1 > 0$

Remark 1: When the system model is exactly known, in the closed-loop system including the VSC law, (22) holds in the reaching phase and (16) holds in the sliding phase. However when there is uncertainty in the system (16) holds after a finite time. In view of (15), it follows that in the closed-loop system, the responses are asymptotically linearized and the tracking error response satisfies a linear differential equation even though the system is nonlinear.

Remark 2: For the system (10), it is easy to obtain an inverse control law of the form

$$u = B^{*-1}(z)[-C_1 h(z, \dot{z}) - k_d \dot{\tilde{y}} - k_p \tilde{y} - k_i w + \ddot{y}_r + v] \quad (27)$$

Substituting (27) in (13) gives

$$(s^3 + k_d s^2 + k_p s + k_i) \tilde{y}(s) = v(s) \quad (28)$$

where s denotes the Laplace variable.

Thus \tilde{y}_i satisfies a linear response and is independently controlled by v_i . One chooses the gains k_d , k_p , k_i to obtain desirable responses. It follows that in the presence of uncertainty, it is not possible to cancel the uncertain functions in (13), and thus (28) is not obtained. For the robotic arm model it has been found by simulation that the inverse controller is relatively sensitive to payload parameters. Therefore, variable structure technique has been chosen for designing the controller in this study.

4 ZERO DYNAMICS STABILITY AND STABILIZATION

Using the inverse control law or the VSC law, one can track given reference trajectories. However, this excites the elastic modes of the arm. Since only the output variables are controlled, the closed-loop system may be internally unstable. In the following section only local stability will be examined.

In order to study the behavior of the internal dynamics, it will be convenient to obtain the system representation in a new state space. Further, we assume that $y_r = y_r^*$, $\dot{y}_r = 0$, $\ddot{y}_r = 0$. Let $x^* = (z^{*T}, 0)^T$, $z^* = (\theta^{*T}, q^{*T})^T$ be the equilibrium state vector. Let $\Delta\theta = \theta - \theta^*$, $\Delta q = q - q^*$, $\Delta y = y - y_r$. In view of (11) and (12), one has

$$\Delta y = R\Delta\theta + H\Delta q \quad (29)$$

We note that for the parameterization (8), $R = I$. Neglecting the second-order terms in $\dot{\theta}$ and

\dot{q} , the linearized q-responses obtained from (3) are governed by

$$M_{21}(z^*)\Delta\ddot{\theta} + M_{22}(z^*)\Delta\ddot{q} + P_{qq}\Delta q = 0 \quad (30)$$

For the stability analysis, we assume that there is no uncertainty in the system. The perturbed Δy dynamics obtained from (14) and (15) are given by

$$\Delta\dot{y} = S - 2\zeta_e\omega_{ne}\Delta y - \omega_{ne}^2\Delta w \quad (31)$$

$$\Delta\dot{w} = \Delta\tilde{y}$$

Using (31) gives

$$\Delta\ddot{y} = \dot{S} - 2\zeta_e\omega_{ne}\Delta\dot{y} - \omega_{ne}^2\Delta y \quad (32)$$

Using the modified continuous control law obtained from (20) with the sat function in (26) one has from (22) that

$$\dot{S} = -\frac{kS}{\epsilon_1} + v \quad (33)$$

when there is no uncertainty in the system.

Define the state vector ξ as

$$\xi = \begin{bmatrix} \Delta y^T & S^T & \Delta q^T & \Delta\dot{q}^T & \Delta w^T \end{bmatrix}^T \quad (34)$$

Then the linearized system is given by

$$\xi = \begin{bmatrix} A_{11} & I & 0 & 0 & A_{15} \\ 0 & A_{22} & 0 & 0 & 0 \\ 0 & 0 & 0 & I & 0 \\ F_1 & F_2 & F_3 & 0 & F_4 \\ I & 0 & 0 & 0 & 0 \end{bmatrix} \xi + \begin{bmatrix} 0 \\ I \\ 0 \\ B_2 \\ 0 \end{bmatrix} v \quad (35)$$

$$\triangleq \tilde{A}\xi + \tilde{B}v$$

where

$$\tilde{M}_{22} = (M_{22}(z^*) - M_{21}(z^*)R^{-1}H), M_{21}^* = M_{21}(z^*),$$

$$b_1 = 2\zeta_e \omega_{ne}^2,$$

$$F_1 = \tilde{M}_{22}^{-1} [M_{21}^* R^{-1} (-b_1^2 + \omega_{ne}^2)]$$

$$F_2 = \tilde{M}_{22}^{-1} M_{21}^* R^{-1} \left(\frac{k}{\epsilon} + b_1 \right)$$

$$F_3 = \tilde{M}_{22}^{-1} (H - P_{qq})$$

$$F_4 = -\tilde{M}_{22}^{-1} M_{21}^* R^{-1} b_1 \omega_{ne}^2$$

$$B_2 = -\tilde{M}_{22}^{-1} M_{21}^* R^{-1}$$

$$A_{11} = \begin{bmatrix} -b_1 & 0 \\ 0 & -b_1 \end{bmatrix}$$

$$A_{15} = \begin{bmatrix} -\omega_{ne}^2 & 0 \\ 0 & -\omega_{ne}^2 \end{bmatrix}$$

$$A_{22} = \begin{bmatrix} -\frac{k}{\epsilon} & 0 \\ 0 & -\frac{k}{\epsilon} \end{bmatrix}$$

The linearized zero dynamics of the system are obtained from (35) by setting

$\Delta y = 0, S = 0, \Delta w = 0$ and $v = 0$. Thus the zero dynamics of the system when $y = y^*_r$, are given by

$$\tilde{M}_{22}\Delta\ddot{q} + P_{qq}\Delta\dot{q} = 0 \quad (36)$$

We note that H is a function of the parameter α_i . The stability of q -responses depends on the stability of the zero dynamics. Numerically, one can solve the characteristic equation of (36) which is

$$\det(\tilde{M}_{22}\lambda^2 + P_{qq}) = 0 \quad (37)$$

to examine the stability of the zero dynamics where \det denotes the determinant of the matrix. It is found that for $\alpha > \alpha^*$, a critical value, the roots of (34) have significantly large positive real parts and q -responses diverge rapidly when $\tilde{y} = 0$

For the design of the stabilizer, α is chosen such that $\alpha \in [0, \alpha^*)$. For the final capture of the terminal state, a stabilization signal of the form

$$v = -\tilde{F}\xi \quad (38)$$

is chosen such that the closed-loop system matrix $\tilde{A}_c = (\tilde{A} - \tilde{B}\tilde{F})$ is Hurwitz. For the computation of \tilde{F} , one can use optimal control theory or pole placement technique. In this study we have chosen the design of the stabilizer using pole assignment technique. In order to obtain desirable responses, a proper selection of closed-loop poles of the matrix \tilde{A}_c is essential. In view of the equations (31) and (33), the set of poles ρ_r associated with Δy , Δw , and S responses have negative real parts.

The set of poles ρ_q associated with zero dynamics (36) are almost on the imaginary axis for $\alpha \in [0, \alpha^*)$. A good choice of pole locations for \tilde{A}_c is

$$\rho_c = \rho_r \cup \tilde{\rho}_q$$

where the set $\tilde{\rho}_q$ is given by

$$\tilde{\rho}_q = \left\{ (\alpha + j\beta) : \alpha < 0, \beta \in \rho_q \right\}$$

That is, in the closed-loop system, the poles associated with the zero dynamics are shifted by α units to the left in the complex plane keeping the imaginary component unchanged.

5 DIGITAL SIMULATION RESULTS

This section explores the results of the digital simulations carried out for each of two parameterizations of the end effector position. The model is highly nonlinear and includes the functions causing rigid and elastic mode interactions. The parameters assume the nominal values that are listed in the Appendix. The value of α is 0.4 for the both the parameterizations. Also, simulation is done for $\alpha = 0.8$ for the case of parameterization denoted by OV_1 . The mode shapes ' ϕ_{ij} ' are selected as clamped-free modes. Assuming that the amplitude of higher modes of the flexible links is very small when compared to the first ones, the case with $n = 2$ in the expression for elastic deflection, i.e (1), is illustrated.

For the derivation of equations of motion using the Lagrangian approach, the expression for the potential energy is obtained that includes the effect of elasticity. With the choice of $n = 2$, one

has the state vector x of dimension 12 where $x = (z^T, \dot{z}^T)^T$ and $z = [\theta_1, \theta_2, q_{11}, q_{12}, q_{21}, q_{22}]^T$. It can be seen that the elements of inertia matrix are functions of θ and q . Also, the following initial conditions are assumed: $y_r(0) = \dot{y}_r(0) = \ddot{y}_r(0) = 0$, $x(0) = 0$ and $w(0) = 0$

A command trajectory $y_r(t)$ was generated to control $y(0) = 0$ to y_r^* . It was assumed that the given tip position corresponds to $y_r^* = (90^\circ, 60^\circ)^T$ for the parameterization denoted by the output variable OV_1 and $y_r^* = (90^\circ, 120^\circ)^T$ for the parameterization denoted by the output variable OV_2 . The terminal value ' $y_r^*(t)$ ' was set to $y_r^* = \theta^* + E q^*$ with $\alpha = 0.4$ for each of the two parameterizations.

Let $\rho_{it} = (\rho_{1t}, \rho_{2t})^T$ (for parameterization OV_1) and $\rho_{et} = (\rho_{1t}, \rho_{et})^T$ (for parameterization OV_2) denote the angular positions of the tip of the two links and $\theta = (\theta_1, \theta_2)^T$ for each of two cases of parameterizations. Defining the vector of tip position as $y_t = (y_{t1}, y_{t2})^T$, we note that

$$y_t = y = \begin{pmatrix} \rho_1 \\ \rho_2 \end{pmatrix}$$

for the choice of $\alpha_1 = \alpha_2 = 1$ for parameterization OV_1 in (8) and

$$y_t = y = \begin{pmatrix} \rho_1 \\ \rho_e \end{pmatrix}$$

for the choice of $\alpha_1 = \alpha_2 = 1$ for parameterization OV_2 in (9).

$\alpha = 0.8$	$0.000 \pm 37.83i$
$\alpha = 0.82$	$0.000 \pm 40.65i$
$\alpha = 0.84$	$0.000 \pm 44.20i$
$\alpha = 0.86$	$0.000 \pm 28.37i$
$\alpha = 0.88$	$21.68 \pm 239.02i$
$\alpha = 0.9$	$101.90 \pm 220.43i$
$\alpha = 0.92$	$164.34 \pm 181.16i$
$\alpha = 0.94$	$230.07 \pm 0.000i$
$\alpha = 0.96$	$102.91 \pm 0.000i$
$\alpha = 0.98$	$7.51 \pm 0.000i$
$\alpha = 1.$	$6.13 \pm 0.000i$

Table 1: Dominant Poles for parameterization OV_1

The command trajectory was generated by a third order filter

$$\ddot{y}_r + P_2 \dot{y}_r + P_1 y_r + P_0 (y_r - y^*) = 0$$

The matrices P_i of the command generator are taken as $P_i = p_i I_{2 \times 2}$, $i=0,1,2$ and are selected such that the poles associated with $y_{ri}(t)$, the i^{th} component of $y_c(t)$, are at $\{-2, -2 \pm i2\}$. The parameters were selected as $k = 100$, $\zeta_e = 0.707$ and $\omega_{ne} = 3.5$ yielding poles associated with \tilde{y}_i , of values $\{-333.33, -2.47 \pm i2.48\}$, where

$$\tilde{y} = (\tilde{y}_1, \tilde{y}_2)^T.$$

These poles are chosen to obtain fast tracking error responses.

To examine the stability of zero dynamics the poles of (34) are computed for different values of α . Table 1 and Table 2 show the most significant unstable roots belonging to the set S_e (the set of eigen values associated with the flexible modes), for different value of α for the parameterization OV_1 and parameterization OV_2 respectively.

It can be seen that as α increases beyond 0.86 the dynamic behavior of the zero dynamics is highly sensitive to the value of α , since the positive real part of the unstable eigenvalue rapidly increases as the value of α approaches 1.

$\alpha = 0.8$	$0.000 \pm 33.68i$
$\alpha = 0.82$	$0.000 \pm 35.54i$
$\alpha = 0.84$	$0.000 \pm 37.75i$
$\alpha = 0.86$	$0.000 \pm 40.43i$
$\alpha = 0.88$	$0.000 \pm 43.77i$
$\alpha = 0.9$	$3.69 \pm 278.34i$
$\alpha = 0.92$	$88.96 \pm 278.04i$
$\alpha = 0.94$	$139.29 \pm 276.50i$
$\alpha = 0.96$	$194.91 \pm 271.69i$
$\alpha = 0.98$	$273.00 \pm 255.57i$
$\alpha = 1.$	$321.62 \pm 0.000i$

Table 2: Dominant Poles for parameterization OV_2

For the chosen feedback gains, the sets S_r and S_e of poles of (34) for $\alpha = 0.4$ are

$$S_r = [-333.33, -333.33, -2.47 \pm 2.48i, -2.47 \pm 2.48i] \quad (39)$$

$$S_e = [\pm 19.67i, \pm 71.73i, \pm 449.73i, \pm 459.96i] \quad OV_1$$

and for the case denoted by OV_1 the sets S_r and S_e are

$$S_r = [-333.33, -333.33, -2.47 \pm 2.48i, -2.47 \pm 2.48i] \quad (40)$$

$$S_e = [\pm 19.32i, \pm 72.85i, \pm 449.60i, \pm 460.92i] \quad OV_2$$

It can be noted that the sets of poles S_r are equal in both cases of parameterizations but the set of poles S_e is different and the poles are approximately same. The feedback matrix 'L' of the stabilizer was chosen such that the set of eigenvalues of the matrix ' S_{cl} ' is

$$S_{cl} = S_r \cup S_e \quad (41)$$

where $S_c = \{-2.5 + Im(\lambda), \lambda \in S_e\}$. Notice that in the closed-loop system the set of eigenvalues of S_r is retained, and the elements of S_e are simply moved to the left in the complex plane.

In the simulations that follow, y_1 and y_2 denote the chosen outputs ; $e_1 = \tilde{y}_1$ and $e_2 = \tilde{y}_2$ are the trajectory errors ; θ_1 and θ_2 are the joint angles ; u_1 and u_2 denote the control inputs ; D_{1e} and D_{2e} are the tip deflections for the two links ; y_{t1} and y_{t2} give actual end effector positions and $tipe_1 = y_{t1} - y_1$ and $tipe_2 = y_{t2} - y_2$ are errors of angular position of the tip of two links. Even though we denote the outputs for both parameterizations by the same notation, we note that they do not represent the same output. In the following, simulation is done using $\alpha = 0.4$ for which the zero dynamics are almost stable. Simulation is also done for $\alpha = 0.7$ for the parameterization denoted by OV_1 . It should be noted here that the outputs y_1 and y_2 are those that actually correspond to the point on the beam we have chosen to control (a point close to the actual tip). The simulation results show that these outputs follow the tip positions y_{t1} and y_{t2} accurately, as the tip errors are of extremely small magnitudes, thus validating our choice. The simulation results are also shown for off payload for both cases of parameterizations.

5.1 SIMULATION RESULT FOR THE CASE DENOTED BY THE OUTPUT VARIABLE OV_1

5.1.1 Trajectory tracking : Control without stabilization

In this case, simulation was carried out for nominal payload and the stabilizer loop was left open. Digital simulations were performed using (4), (15) and (20) with the stabilizer loop left open. The value of the constant factor ' α ' is chosen to be 0.4. The trajectory errors were found to be equal to zero as predicted, and efficient tracking of the chosen outputs (y_1 and y_2) and joint angles (θ_1 and θ_2) is evident from Fig.3(a) and Fig.3(b). The absence of the stabilizer leads to persistent

elastic mode oscillations of the tips of the two links (Fig.3(c)). The θ response (Fig.3(b)) depicts oscillations of extremely small magnitudes.

5.1.2 Trajectory tracking : Control with Stabilization

Nominal payload

The closed-loop system defined by (4), (15), (20) and (38) was digitally simulated (with $\alpha = 0.4$) and the switching logic closes the stabilizer loop when the trajectory enters the neighborhood of the terminal value (in about 3 seconds). It can be observed from Fig.4(b) that though the tracking error was zero prior to switching of the stabilizer, the error tends to increase and after the instant of switching but dies down to zero in about 5 seconds. The stabilizer dampens out the elastic mode oscillations (Fig.4(e)) and forces the control inputs to a constant value as illustrated in Fig.4(d). The system quickly settles down to its steady state values. It can also be noted that the chosen outputs y_1 and y_2 (Fig.4(a)) very closely follow the actual end effector outputs y_{t1} and y_{t2} (Fig.4(f)).

Simulation was also done for $\alpha = 0.7$, for nominal case (Fig.5). The trajectory error is extremely small in this case as compared to the case with $\alpha = 0.4$ (Fig.4(b) and Fig.5(b)). Also the elastic mode oscillations are of smaller frequency than that of the former case (Fig.4(e) and Fig.5(e)). The maximum control input is smaller in this case (Fig.4(d) and Fig.5(d)). But the time taken for them to settle down to a steady state value is the same.

Higher payload uncertainty

Simulations were carried for a higher payload uncertainty of 125% ($\alpha = 0.4$). The controller used here is the one that was designed with nominal parameters and the initial conditions were assumed to be zero. It can be observed that the stabilizer takes more or less the same time to dampen the

oscillations as it takes in case of nominal payload (Fig.6(e) and (Fig.4(e)). But the trajectory error in this case is not zero before the stabilizer was switched on, as it is in the case of nominal load.(Fig.6(b) and Fig.4(b)). After it is switched on it dies down to zero in about 5 seconds Moreover, the chosen outputs y_1 and y_2 (Fig.6(a)) very closely follow the actual end effector outputs y_{t1} and y_{t2} (Fig.6(f)).

Lower payload uncertainty

Simulation results for a lower payload uncertainty of 25% ($\alpha = 0.4$) are presented in this section. When compared to the higher payload uncertainty case, it can be noted that though the time taken by the system to attain steady state conditions is more or less the same, the frequency of the oscillations in the lower payload case is much higher (Fig.7(e) and Fig.6(e)), which is also a physical reality. Moreover, the values of the control input are lower than the higher payload case (Fig.7(d) and Fig.6(d)) and so is the elastic deflections (Fig.7(e) and Fig.6(e)) and the tip deflection(Fig.7(f) and Fig.6(f)). Also, the chosen outputs y_1 and y_2 (Fig.7(a)) very closely follow the actual end effector outputs y_{t1} and y_{t2} (Fig.7(f)).

5.2 SIMULATION RESULT FOR THE CASE DENOTED BY THE OUTPUT VARIABLE OV_2

5.2.1 Trajectory tracking : Control without stabilization

In this case, simulation was carried out for nominal payload and the stabilizer loop was left open with $\alpha = 0.4$ for the parameterization OV_2 . Digital simulations were performed using (4), (15) and (20) with the stabilizer loop left open. The trajectory errors were found to be equal to zero and efficient tracking is evident from Fig.8(a) and Fig.8(b) for Fig.3.2(b). The absence of the stabilizer

leads to persistent elastic mode oscillations of the tips of the two links (Fig.8(c)). The θ response (Fig.8(b)) depict oscillations of extremely small magnitudes.

5.2.2 Trajectory tracking : Control with Stabilization

Nominal payload

The closed-loop system defined was simulated (with $\alpha = 0.4$) and the the stabilizer loop is closed when the trajectory enters the neighborhood of the terminal value (in about 3 seconds). It can be observed from Fig.9(b) that though the tracking error was zero prior to switching of the stabilizer, the error tends to increase and after the instant of switching but dies down to zero in about 5 seconds. The stabilizer dampens out the elastic mode oscillations (Fig.9(e)) and forces the control inputs to a constant value as illustrated in Fig.9(d). The elastic deflection and the control input are found to oscillate with small frequency before settling down to a constant value (Fig.9(d) and Fig.9(e)). Also the θ response depicts oscillation if extremely small magnitudes at the instant of switching the stabilizer (Fig.9(c)). The system quickly settles down to its steady state values. It can also be noted that the chosen outputs y_1 and y_2 (Fig.9(a)) very closely follow the actual end effector outputs y_{t1} and y_{t2} (Fig.9(f)).

Higher payload uncertainty

Simulations were carried for a higher payload uncertainty of 150% ($\alpha = 0.4$). The controller used here is the one that was designed with nominal parameters and the initial conditions were assumed to be zero. In comparison with the case with the parameterization OV_1 this parameterization is found to tolerate more overload. But the tracking error is more in this case (Fig.10(a) and Fig.6(a)). It can be observed that the stabilizer takes a more or less the same time to dampen the oscillations as it does for the case of nominal payload (Fig.10(e) and Fig.9(e)). It settles down to its steady

state values in about 5 seconds. It can also be noted that the control torque required in this case is larger than that required for the nominal case (Fig.10(d) and Fig.9(e)) and so is the case with the total elastic mode deflection (Fig.10(c) and Fig.9(c)) The tracking error is not zero before the stabilizer is switched on in this case, as it is in the nominal payload case. Moreover, the chosen outputs y_1 and y_2 (Fig.10(a)) very closely follow the actual end effector outputs y_{t1} and y_{t2} (Fig.10(f)).

Lower payload uncertainty

Simulation results for a lower payload uncertainty of 50% ($\alpha = 0.4$) are presented in this section. When compared to the case with parameterization OV_1 this parameterization is found to tolerate more lower payload uncertainty, but then the trajectory error is slightly more in this case which is logical (Fig.11(b) and Fig.7(b)). When compared to the higher payload uncertainty case, it can be noted that though the time taken by the system to attain steady state conditions is more or less the same, the frequency of the oscillations in the lower payload case is much higher (Fig.11(e) and Fig.10(e)), which is also a physical reality. Moreover, the values of the control input are lower than the higher payload case (Fig.11(d) and Fig.10(d)) and so is the elastic deflections (Fig.11(e) and Fig.10(e)). Also, the chosen outputs y_1 and y_2 (Fig.11(a)) very closely follow the actual end effector outputs y_{t1} and y_{t2} (Fig.11(f)).

6 CONCLUSIONS

The control and stabilization of the multibody system developed in the Phillips Laboratory was considered. Two Parameterizations of the controlled output variables were considered. Stability of the zero dynamics was examined. Based on the variable structure system theory control laws were derived for the control of the selected output variables. Control system includes error integral term. A smooth approximation of the discontinuous law was used for the elimination of control chattering. A linear stabilizer was designed for the final capture of the terminal state and vibration suppression. It was shown that control of a point close to the tip position gave stable zero dynamics. The complete closed-loop system was simulated on the digital computer. Extensive simulations were performed to verify the performance of the system. These results show that in the closed-loop system, large maneuvers of the arm and vibration suppression are accomplished by the combined action of the *VSC* law and the stabilizer.

ACKNOWLEDGMENTS

Authors would like to thank Dr.Alok Das (PL/Edwards AFB) for his constant support to pursue this research. It is also our pleasure to thank Mr.Monty Smith (PL/Edwards AFB) for the valuable discussions related to the multibody laboratory experiment.

REFERENCES

1. Luca, A. De., Lucibello P., and Ulivi, G. "Inversion techniques for trajectory control of flexible robot arms," *J.Robotic Systems*, Vol.6, no.4, pp- 25-344 (1989).
2. Luca, A. De., and Siciliano, B., "Trajectory control of a nonlinear one-link flexible arm," *Int. J. of Control*, Vol.50, no.5, pp. 1699-1715 (1989).
3. Lucibello, P., "Nonlinear regulation with Internal stability of a two-link flexible robotic arm," *Proc. IEEE Conf. on Decision and Control, Tampa, FL*, pp.1645-1650 (1989).
4. Madhavan, S. K., and Singh, S. N., "Inverse Trajectory control and Zero dynamic sensitivity of an elastic manipulator," *International Journal of Robotics and Automation*, vol. 6, no. 4, pp. 179-192 (1991).
5. Wang, D., and Vidyasagar, M., "Transfer functions for a single flexible link," *IEEE International Conference on Robotics and Automation, Scottsdale, Arizona*, pp. 1042-1047, May 1989.
6. Canon Jr., R. H., and Schmitz, E., "Initial experiments on the end-point control of a one link flexible experimental manipulator," *Journal of Robotic Systems.*, vol. 3, pp. 62-75 (1984).
7. Nemir, D., C., Koivo, A. J., and Kashyap, R.,L., "Pseudolinks and the self-tuning control of a nonrigid link mechanism," *IEEE Transactions on Systems, Man and Cybernetics*, vol. 18, pp. 40-48 (1988).
8. Bayo, E., "A Finite-element approach to control the end-point motion of a single-link flexible robot," *J. of Robotic Systems*, Vol.4, pp. 63-75 (1987).

9. Bayo, E., Movaghar, R., and Medus, M., "Inverse Dynamics of Single- Link Flexible Robot. Analytical and Experimental Results," *IEEE International Conference on Robotics and Automation* Vol.3, No. 3, 1988, pp. 150-157.
10. Bayo, E., Papadopoulos, P., Stubbe, J., and Serna, M., "Inverse Dynamics and Kinematics of Multi-Link Elastic Robots. An Iterative Frequency Domain Approach," *Journal Of Robotic Systems.*, vol. 8, No. 6, 1989, pp 49-62,
11. Madhavan, S. K., and Singh, S. N., "Variable Structure Trajectory Control of an Elastic Robotic Arm," *Journal Of Robotic Systems.*, 1993
12. Slotine, J.- J. E., and W. Li, *Applied Nonlinear Control*, Prentice Hall,1991

APPENDIX

Listed below are the parameter values for the two-link elastic robotic arm for which the digital simulations were carried out :

Mass of each Link = $.58 \text{ kg}$

Stiffness of each link = 466.9 Nm^2

Length of each link = 1.0 m

Joint mass at Joint 2 = $.0012 \text{ kg}$

Nominal payload = $.325 \text{ kg}$

Inertia of payload = 5.241 kgm^2

Inertia of mass at Joint 1 = 0.00217 kgm^2

Inertia of mass at Joint 2 = 0.01934 kgm^2

CAPTIONS FOR FIGURES

Fig.1 Model of the Robotic arm denoted by OV_1

Fig.2 Model of the Robotic arm denoted by OV_1

Fig.3 The case denoted by OV_1 : Trajectory tracking : Control without stabilization

- (a) Actual outputs y_1 and y_2
- (b) Joint angles θ_1 and θ_2
- (c) Elastic deflections D_{1e} and D_{2e}
- (d) Tip deflections $tipe_1$ and $tipe_2$

Fig.4 The case denoted by OV_1 : Trajectory tracking : Control with stabilization;nominal payload

- (a) Actual outputs y_1 and y_2
- (b) Trajectory errors e_1 and e_2
- (c) Joint angles θ_1 and θ_2
- (d) Control Torques u_1 and u_2
- (e) Elastic deflections D_{1e} and D_{2e}
- (f) Tip angular positions y_{t1} and y_{t2}
- (g) Tip deflections $tipe_1$ and $tipe_2$

Fig.5 The case denoted by OV_1 : Trajectory tracking : Control with stabilization with $\alpha = 0.7$:
nominal payload

- (a) Actual outputs y_1 and y_2
- (b) Trajectory errors e_1 and e_2
- (c) Joint angles θ_1 and θ_2
- (d) Control Torques u_1 and u_2

- (e) Elastic deflections D_{1e} and D_{2e}
- (f) Tip angular positions y_{t1} and y_{t2}
- (g) Tip deflections $tipe_1$ and $tipe_2$

Fig.6 The case denoted by OV_1 : Trajectory tracking : Control with stabilization;Higher payload

- (a) Actual outputs y_1 and y_2
- (b) Trajectory errors e_1 and e_2
- (c) Joint angles θ_1 and θ_2
- (d) Control Torques u_1 and u_2
- (e) Elastic deflections D_{1e} and D_{2e}
- (f) Tip angular positions y_{t1} and y_{t2}
- (g) Tip deflections $tipe_1$ and $tipe_2$

Fig.7 The case denoted by OV_1 : Trajectory tracking : Control with stabilization;Lower payload

- (a) Actual outputs y_1 and y_2
- (b) Trajectory errors e_1 and e_2
- (c) Joint angles θ_1 and θ_2
- (d) Control Torques u_1 and u_2
- (e) Elastic deflections D_{1e} and D_{2e}
- (f) Tip angular positions y_{t1} and y_{t2}
- (g) Tip deflections $tipe_1$ and $tipe_2$

Fig.8 The case denoted by OV_2 : Trajectory tracking : Control without stabilization

- (a) Actual outputs y_1 and y_2
- (b) Joint angles θ_1 and θ_2

(c) Elastic deflections D_{1e} and D_{2e}

Fig.9 The case denoted by OV_2 : Trajectory tracking : Control with stabilization;nominal payload

(a) Actual outputs y_1 and y_2

(b) Trajectory errors e_1 and e_2

(c) Joint angles θ_1 and θ_2

(d) Control Torques u_1 and u_2

(e) Elastic deflections D_{1e} and D_{2e}

(f) Tip angular positions y_{t1} and y_{t2}

Fig.10 The case denoted by OV_2 : Trajectory tracking : Control with stabilization;Higher payload

(a) Actual outputs y_1 and y_2

(b) Trajectory errors e_1 and e_2

(c) Joint angles θ_1 and θ_2

(d) Control Torques u_1 and u_2

(e) Elastic deflections D_{1e} and D_{2e}

(f) Tip angular positions y_{t1} and y_{t2}

Fig.11 The case denoted by OV_2 : Trajectory tracking : Control with stabilization;Lower payload

(a) Actual outputs y_1 and y_2

(b) Trajectory errors e_1 and e_2

(c) Joint angles θ_1 and θ_2

(d) Control Torques u_1 and u_2

(e) Elastic deflections D_{1e} and D_{2e}

(f) Tip angular positions y_{t1} and y_{t2}

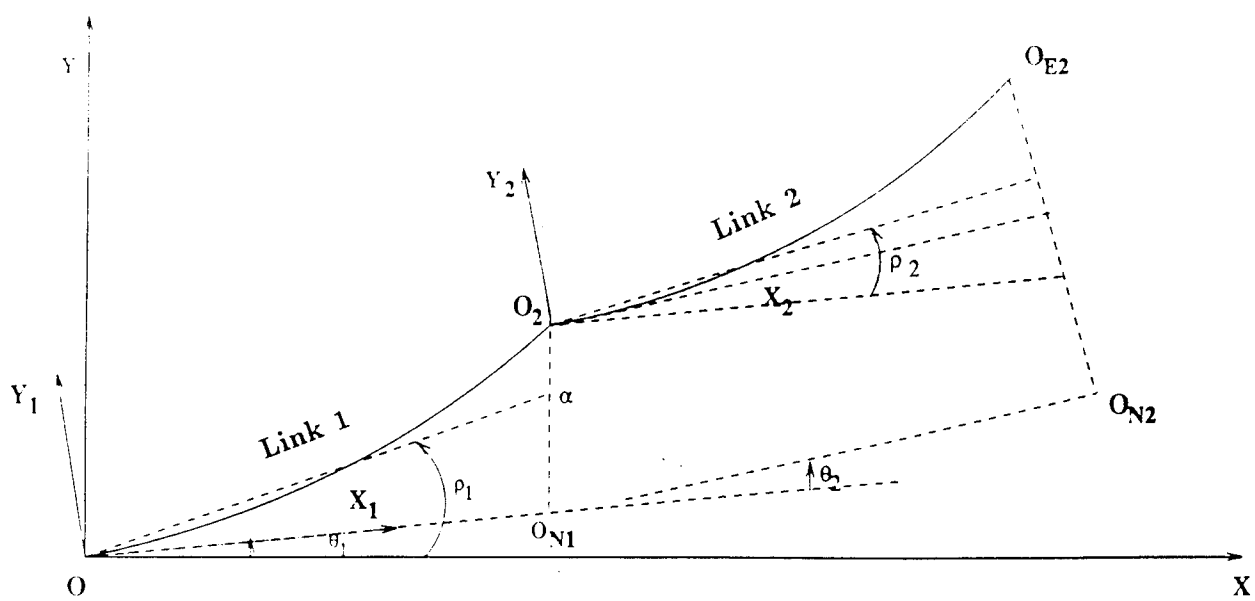


Figure 1

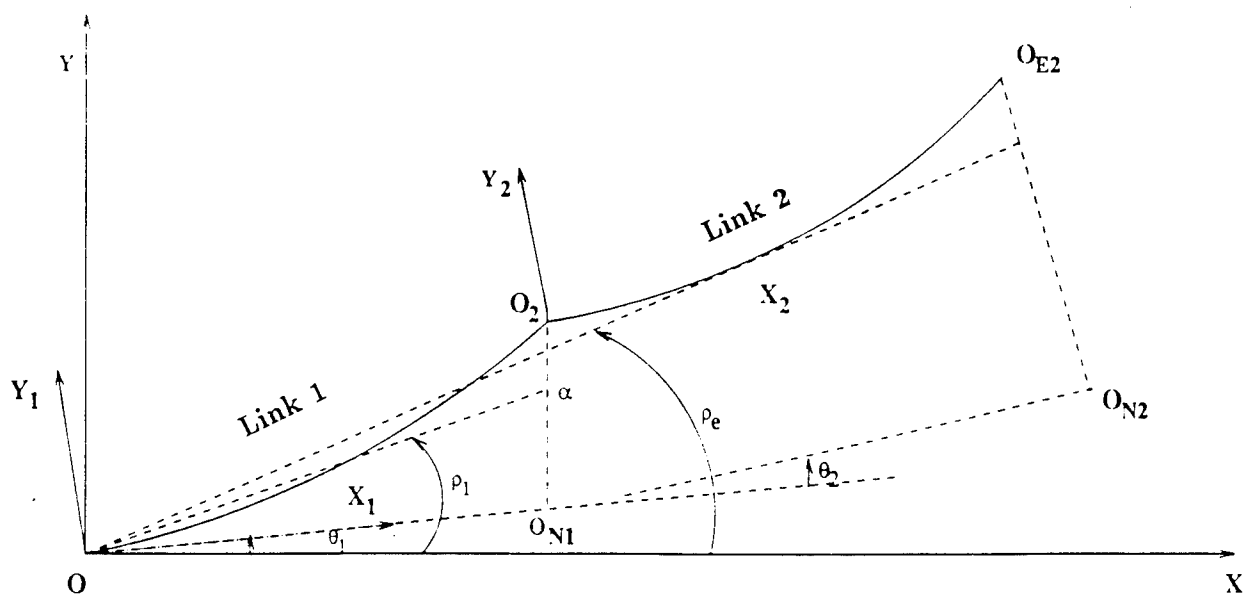


Figure 2

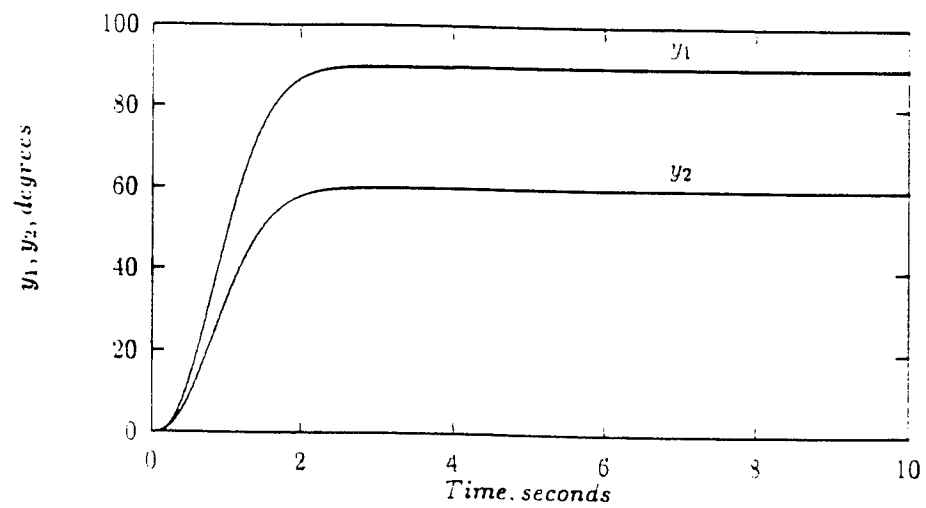


Fig.3(a)

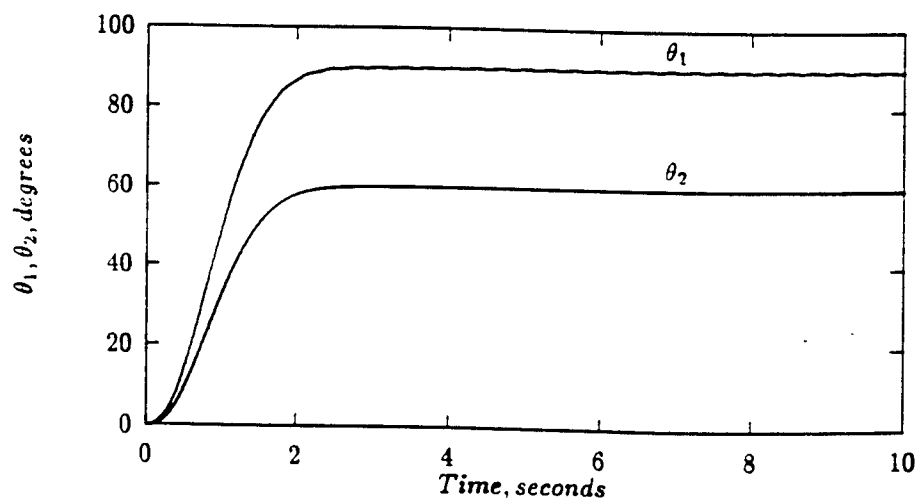


Fig.3(b)

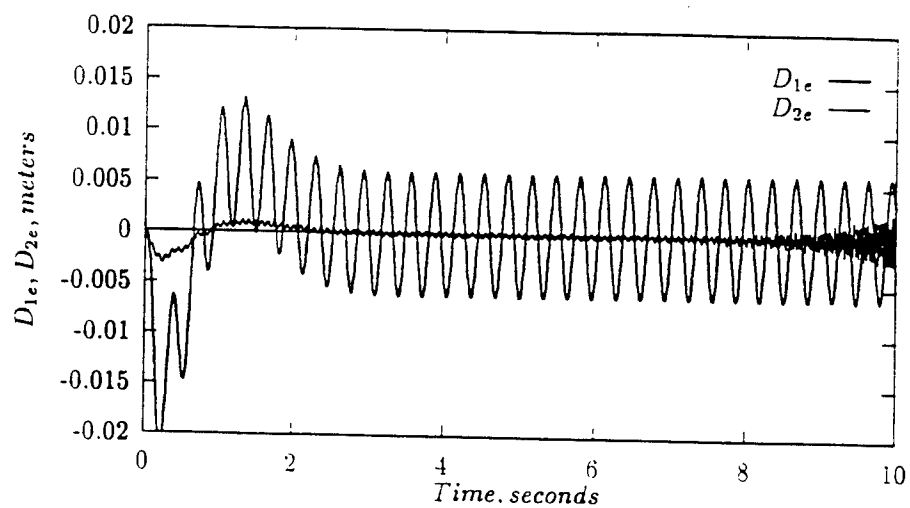


Fig.3(c)

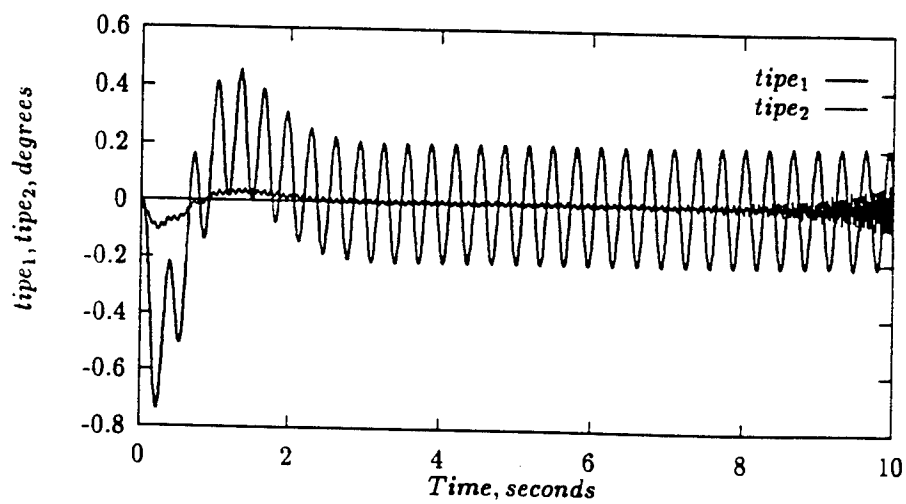


Fig.3(d)

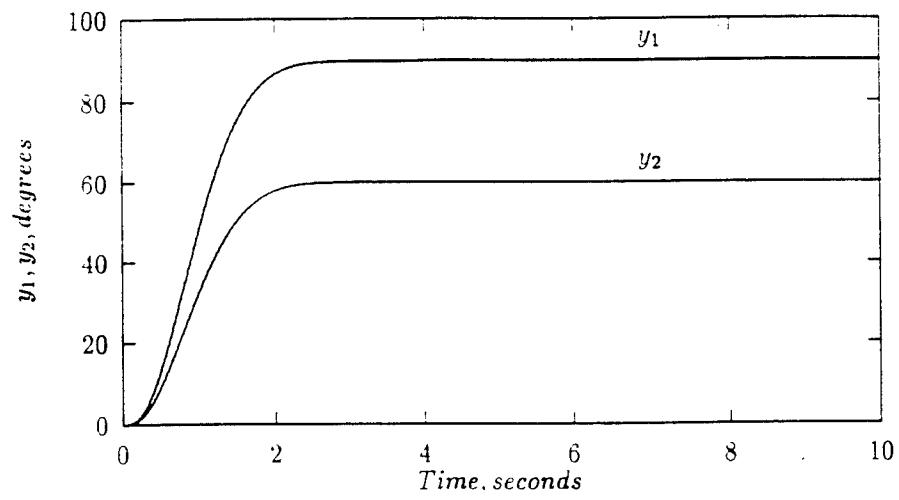


Fig.4(a)

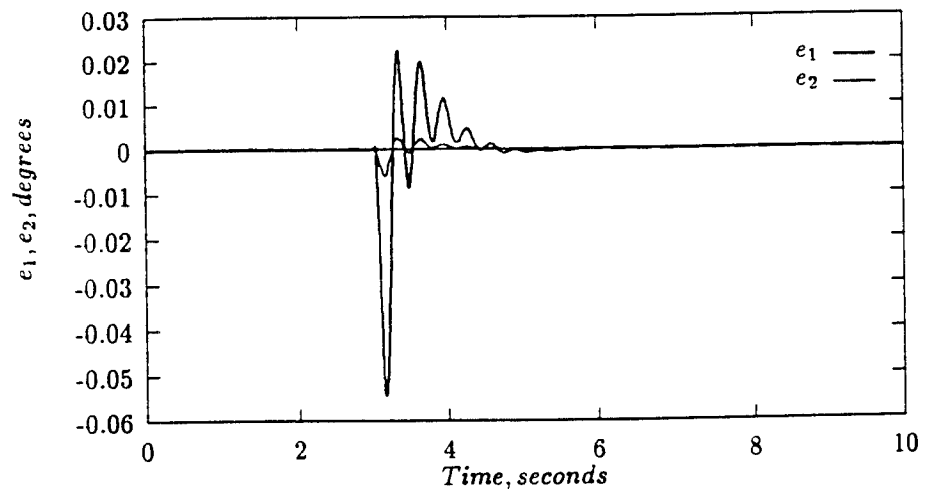


Fig.4(b)

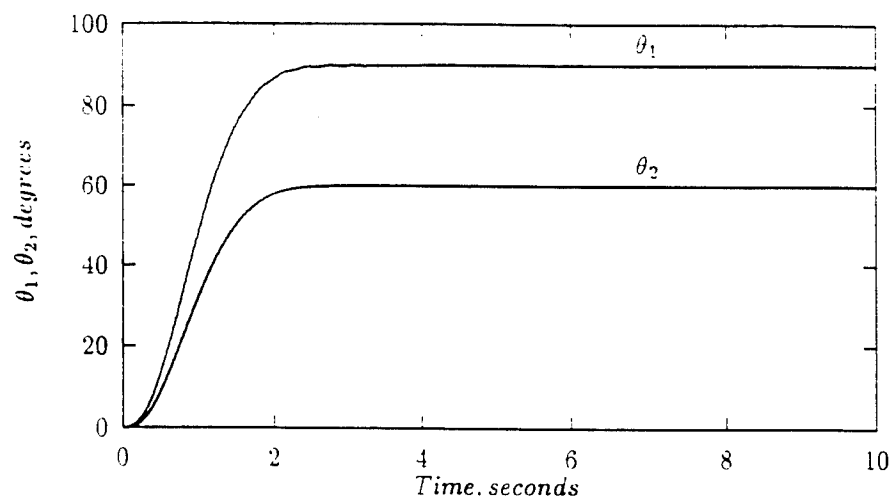


Fig.4(c)

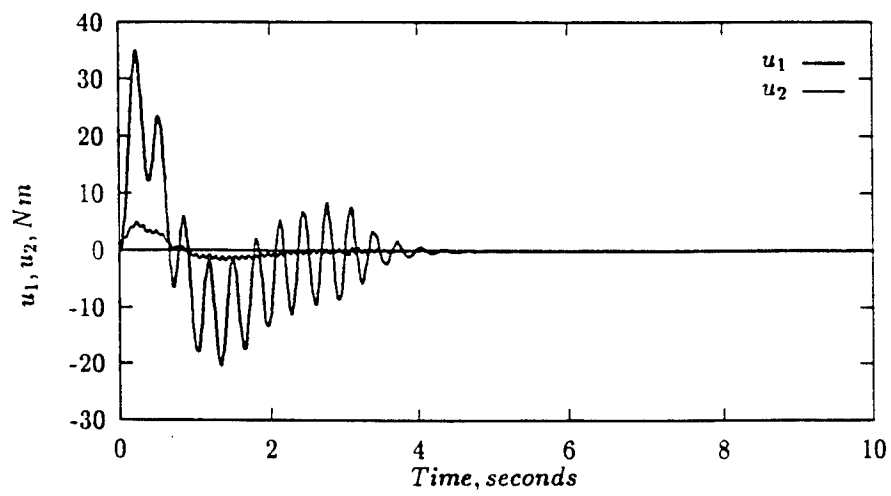


Fig.4(d)

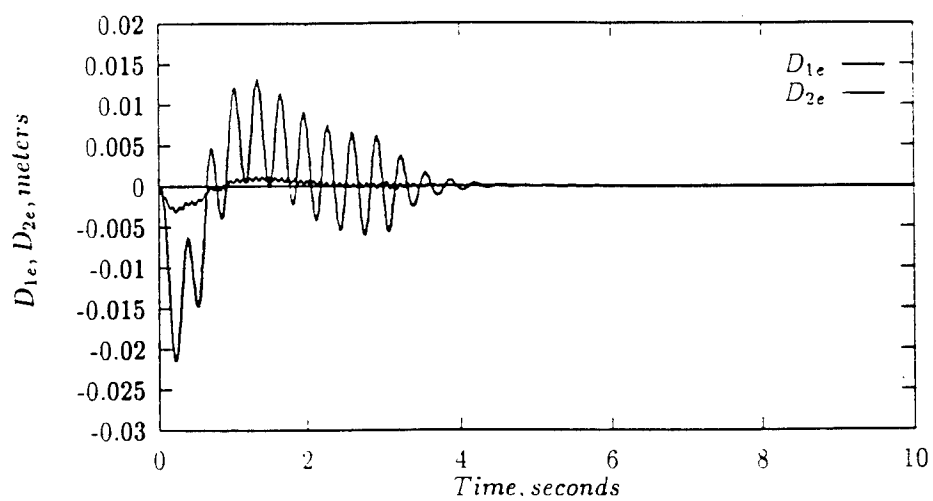


Fig.4(e)

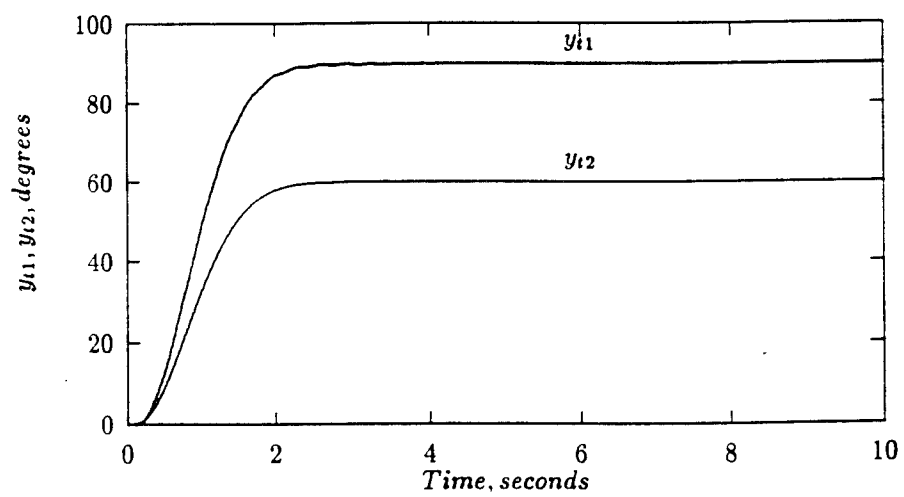


Fig.4(f)

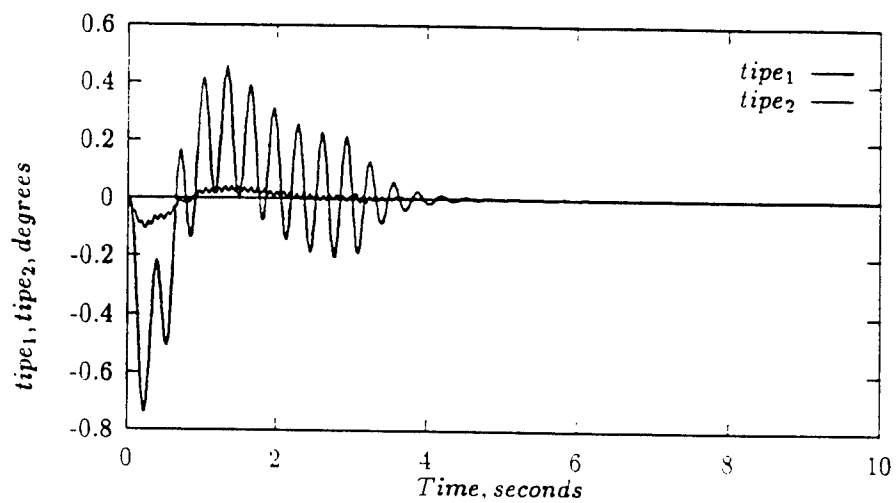


Fig.4(g)

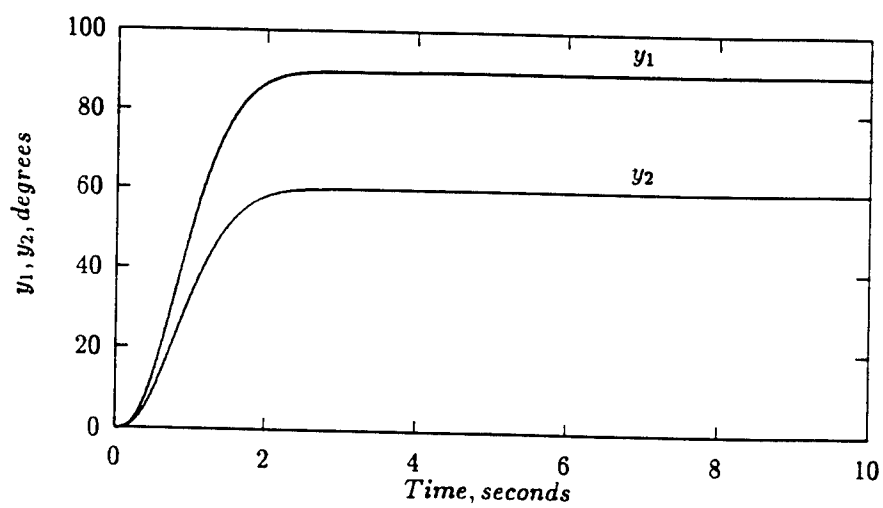


Fig.5(a)

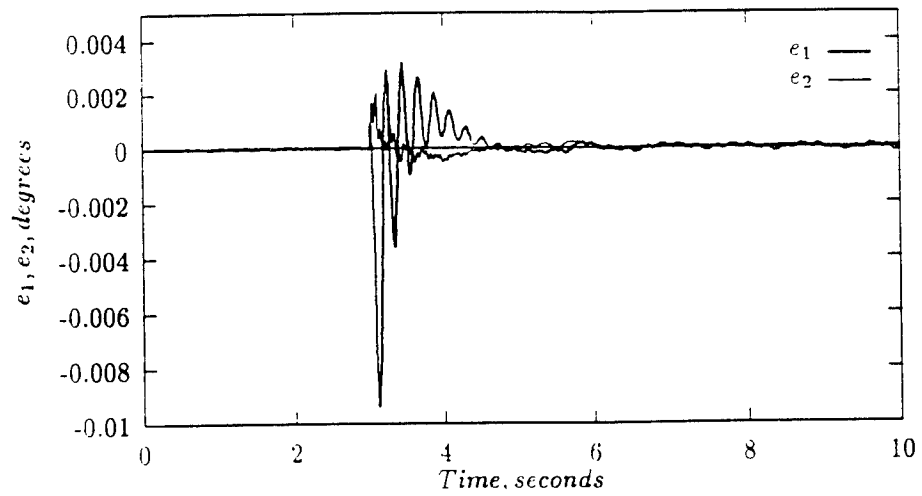


Fig.5(b)

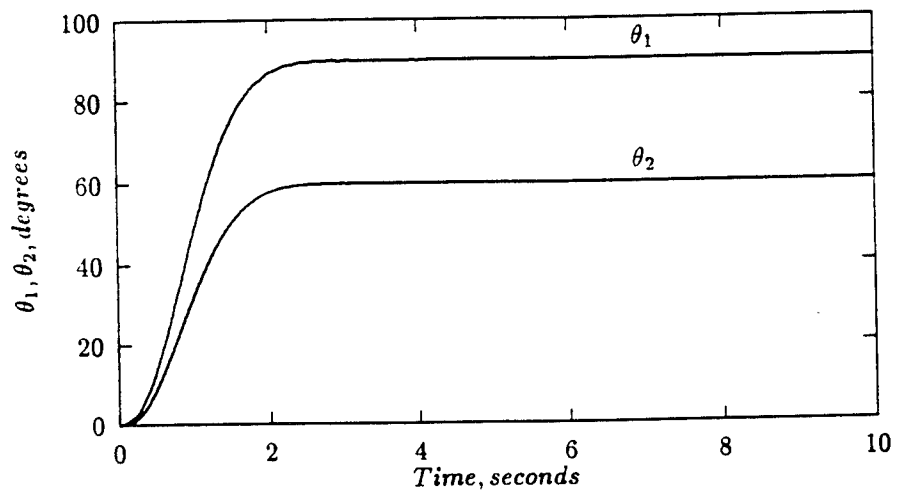


Fig.5(c)

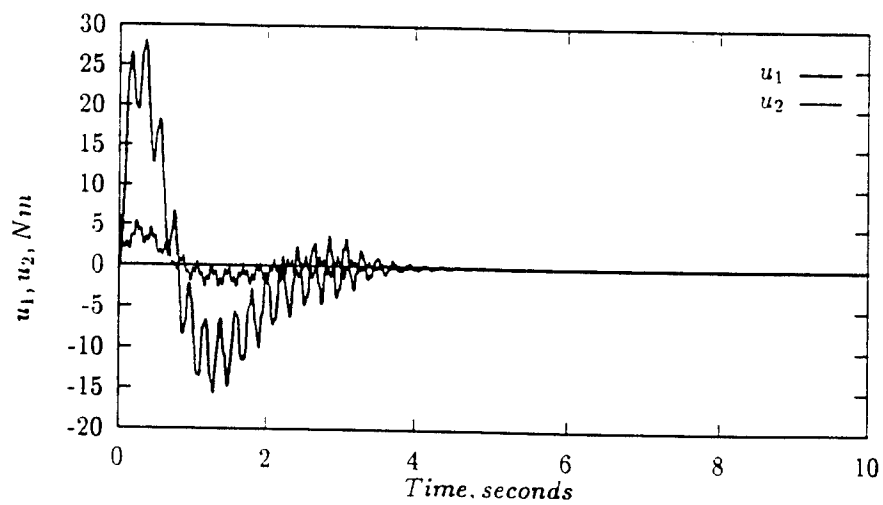


Fig.5(d)

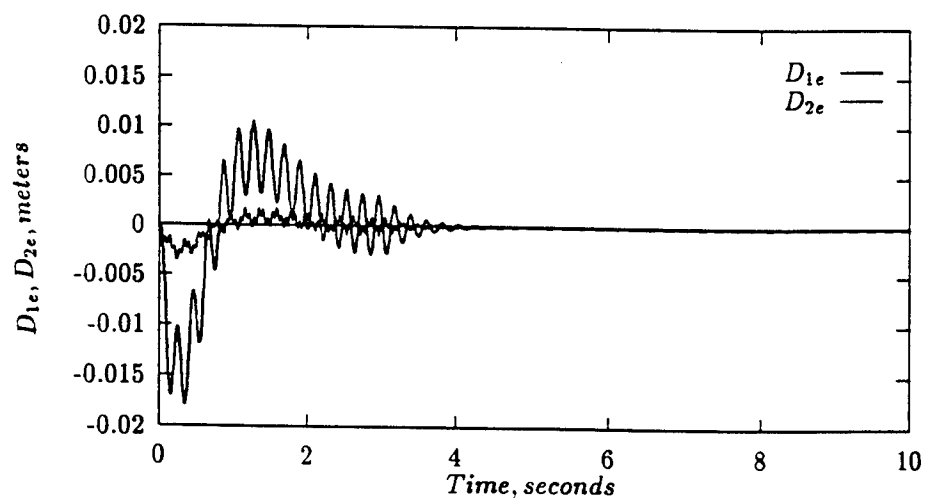


Fig.5(e)

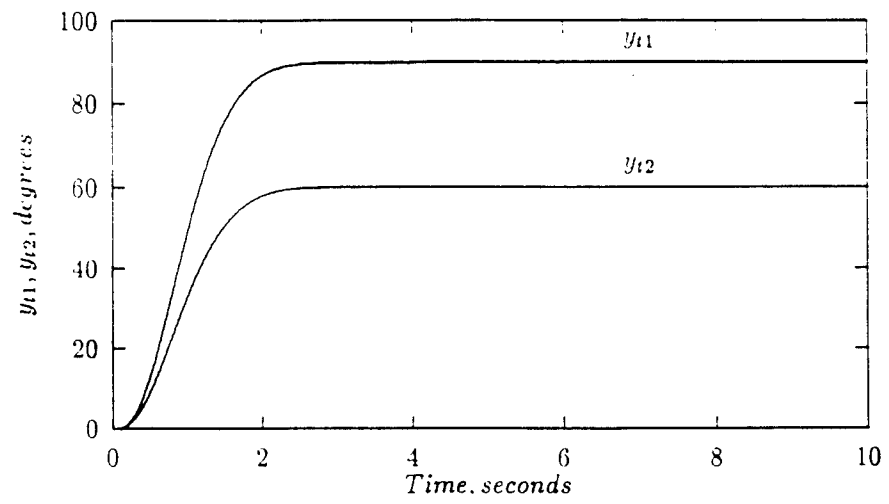


Fig.5(f)

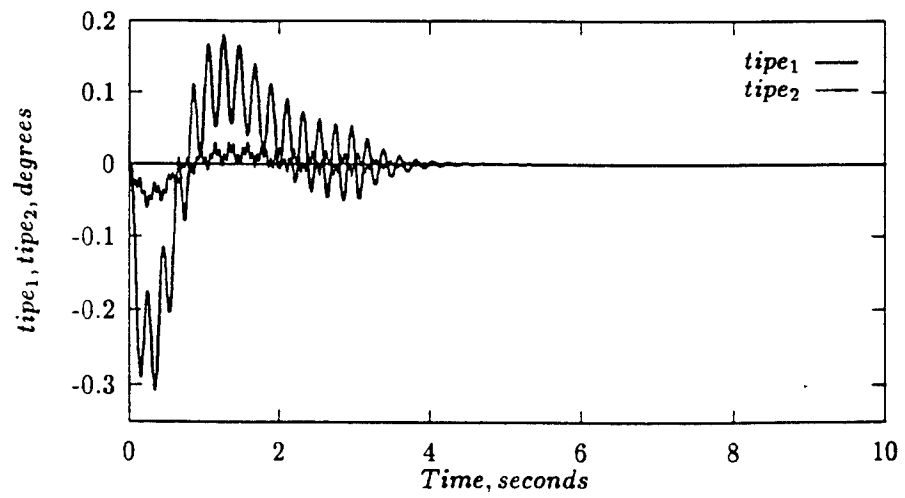


Fig.5(g)

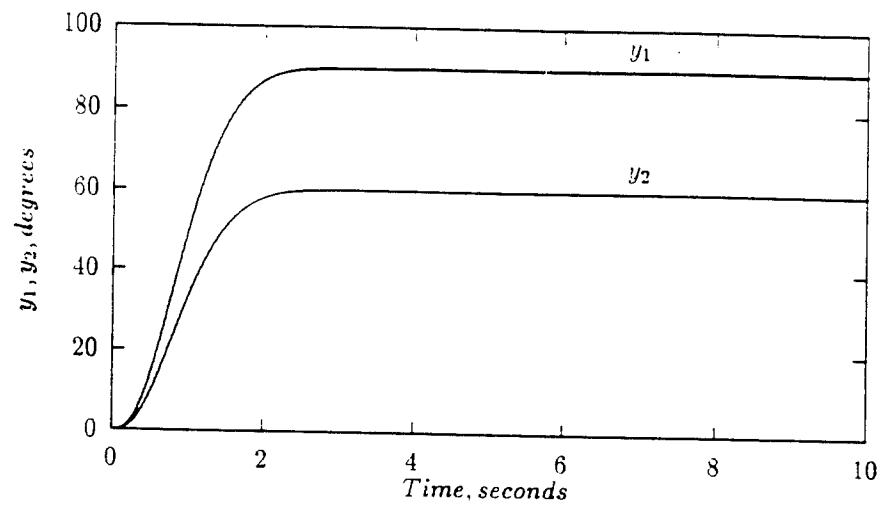


Fig. 6(a)

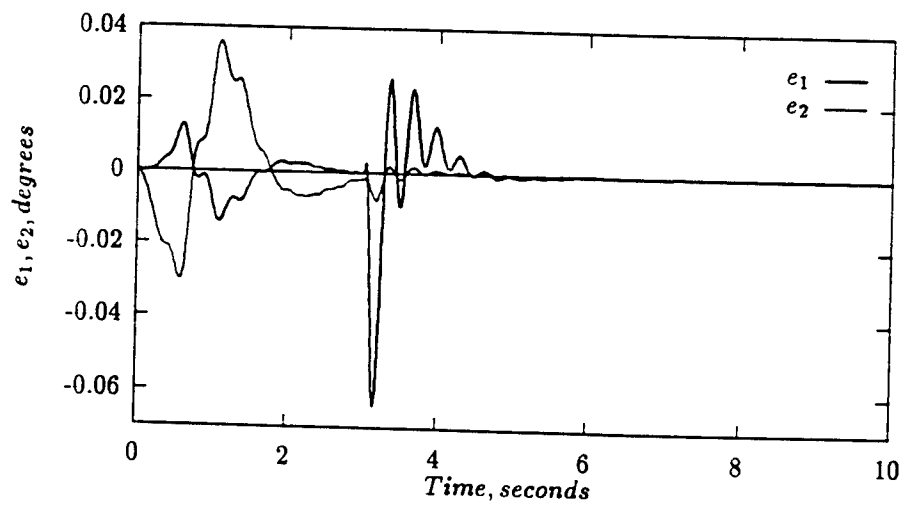


Fig. 6(b)

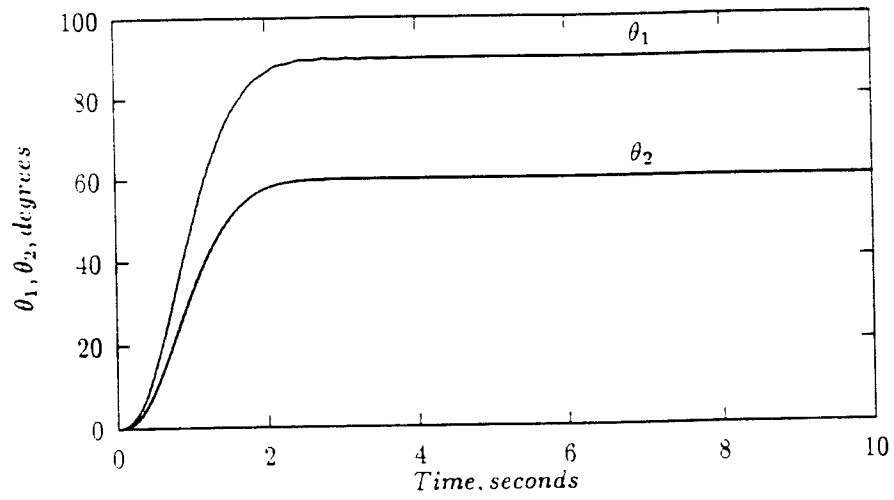


Fig.6(c)

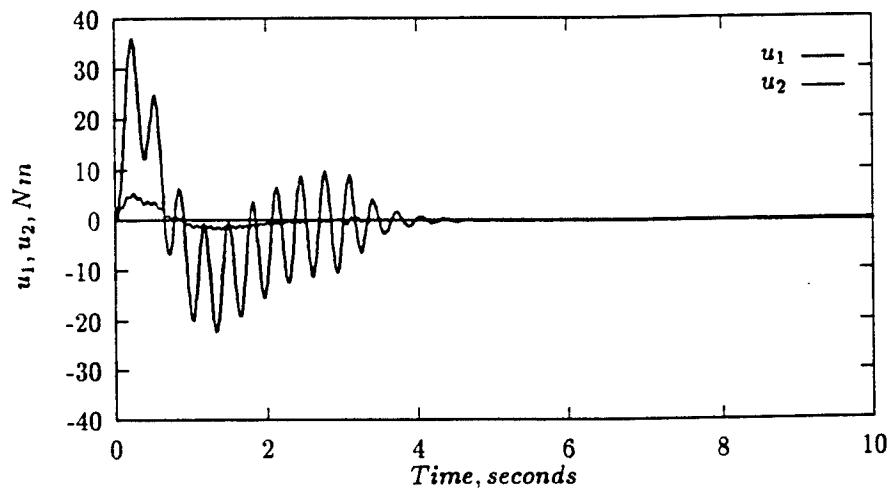


Fig.6(d)

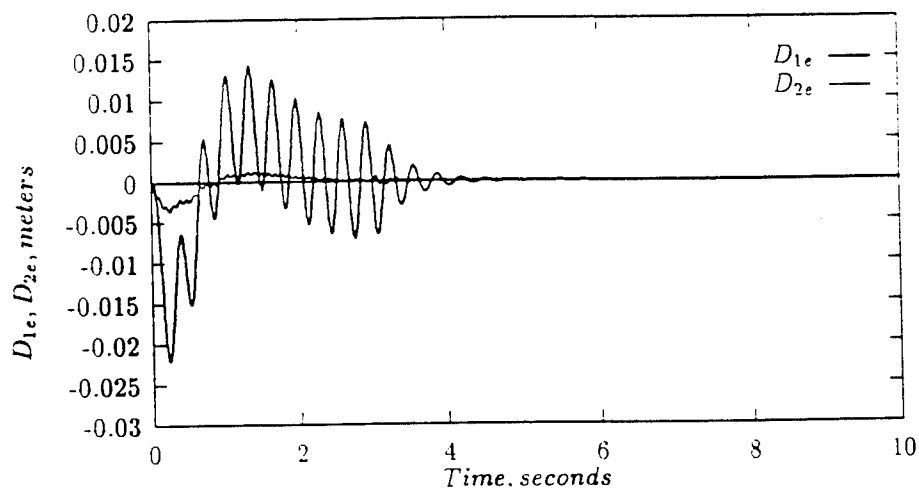


Fig.6(e)

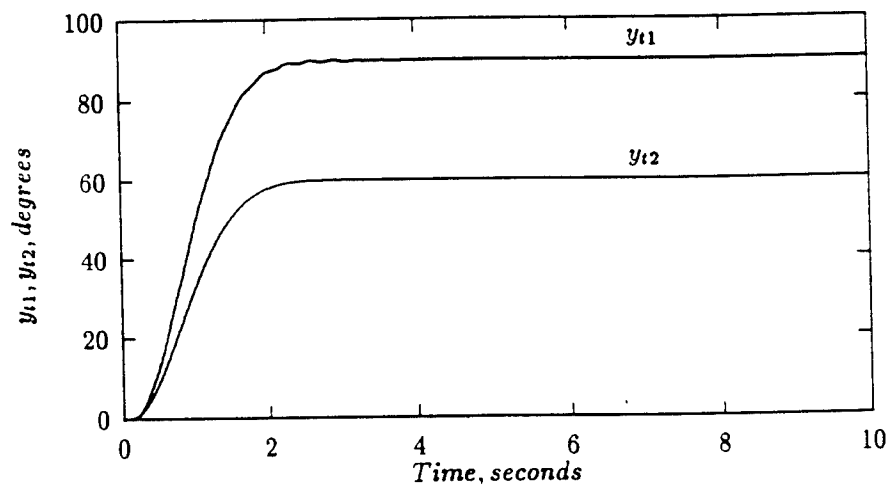


Fig.6(f)

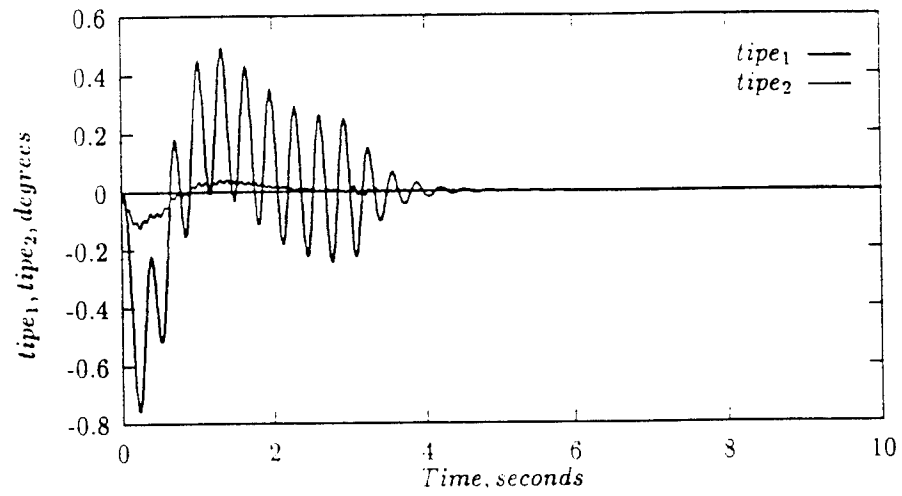


Fig.6(g)

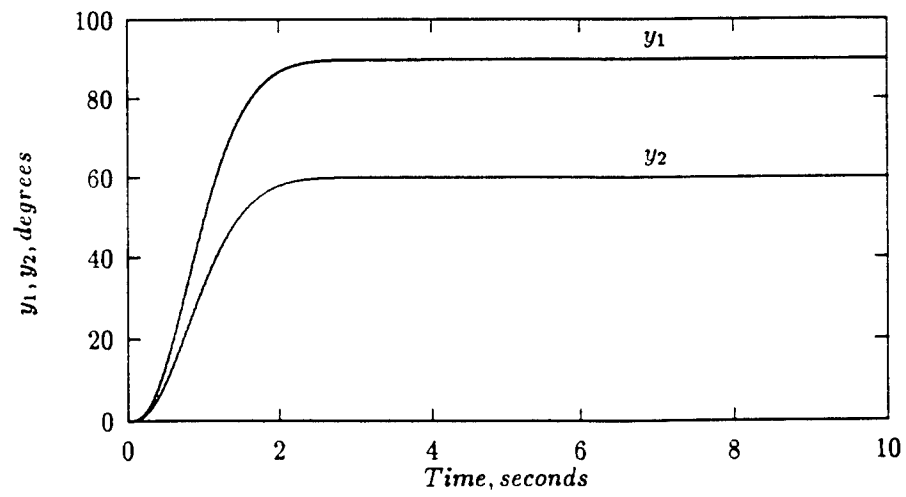


Fig.7(a)

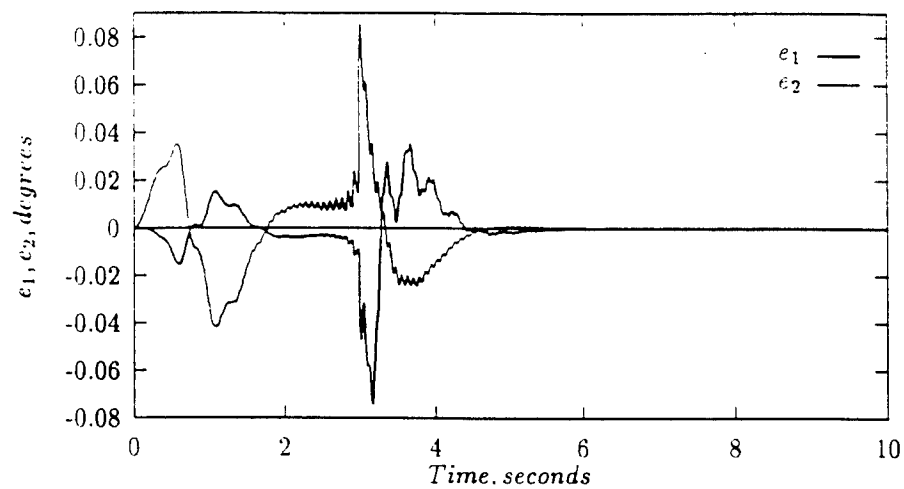


Fig.7(b)

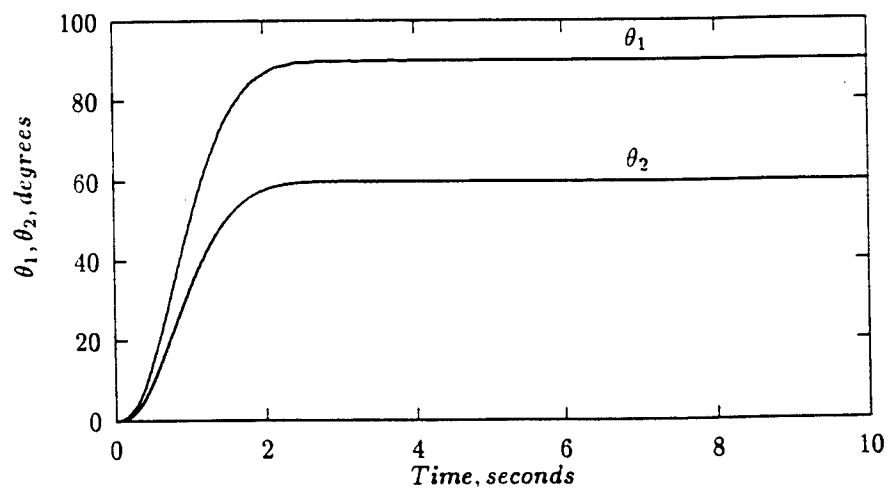


Fig.7(c)

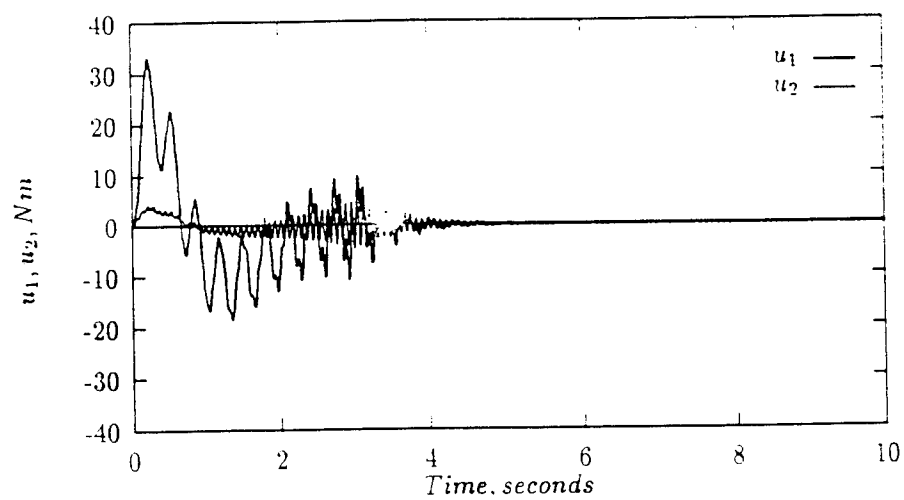


Fig.7(d)

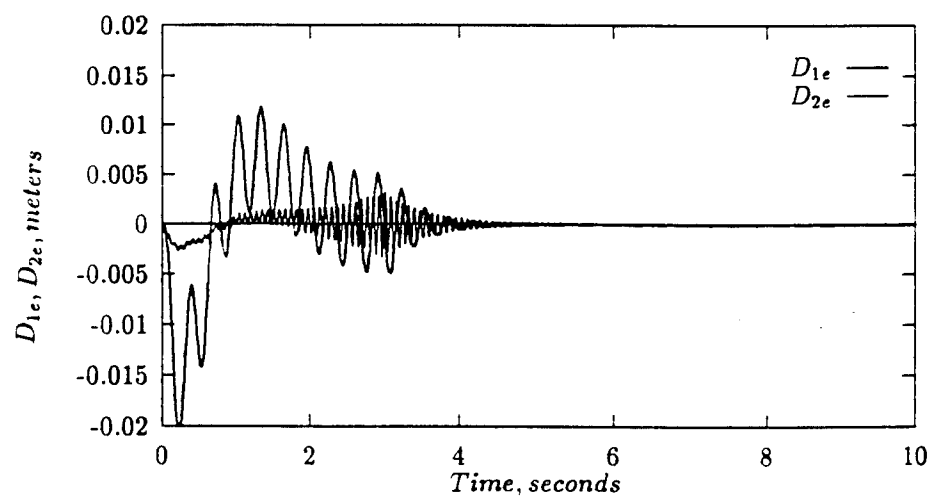


Fig.7(e)

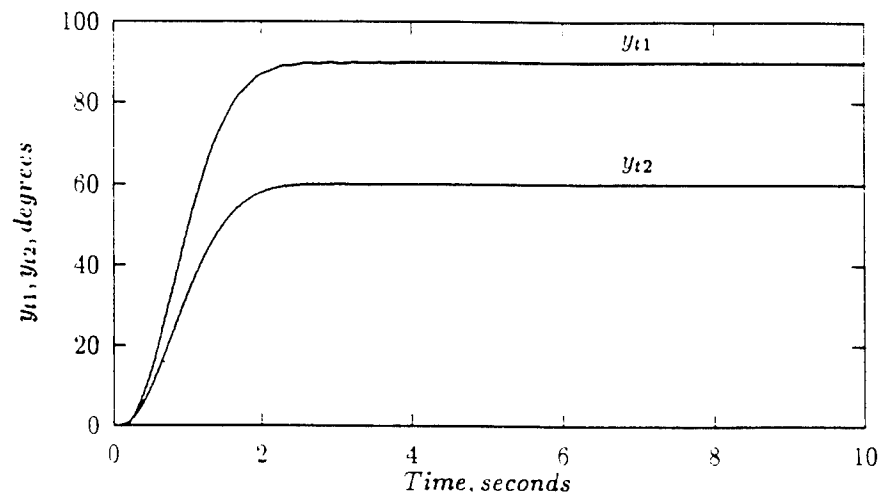


Fig.7(f)

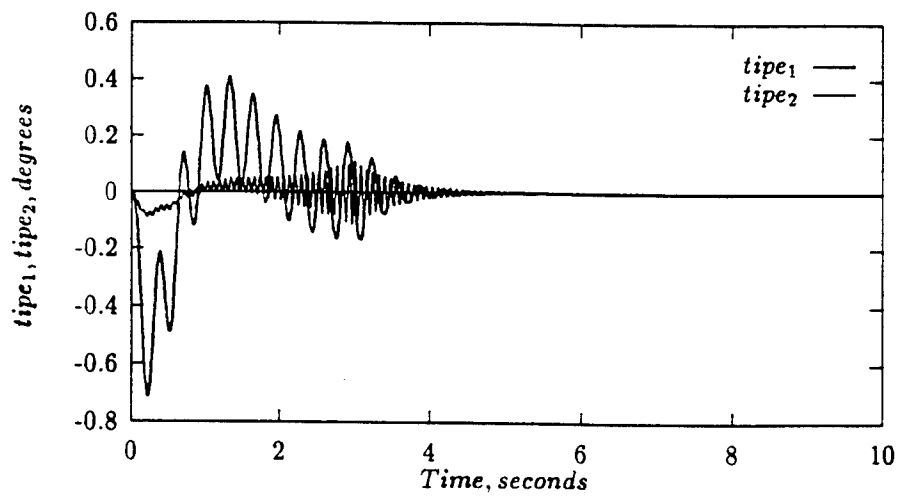


Fig.7(g)

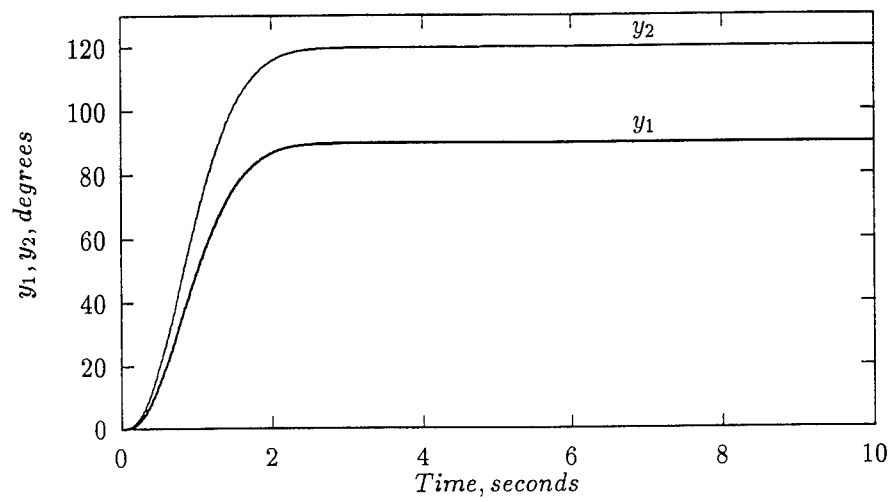


Fig.8(a)

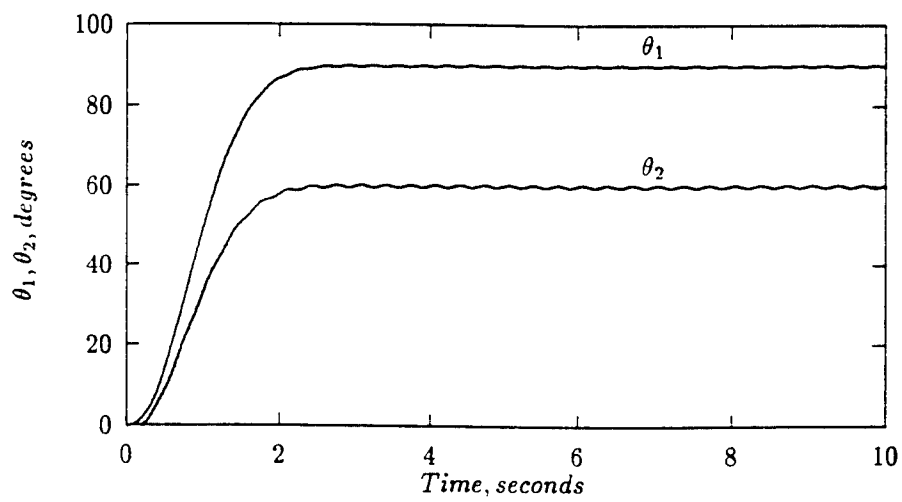


Fig.8(b)

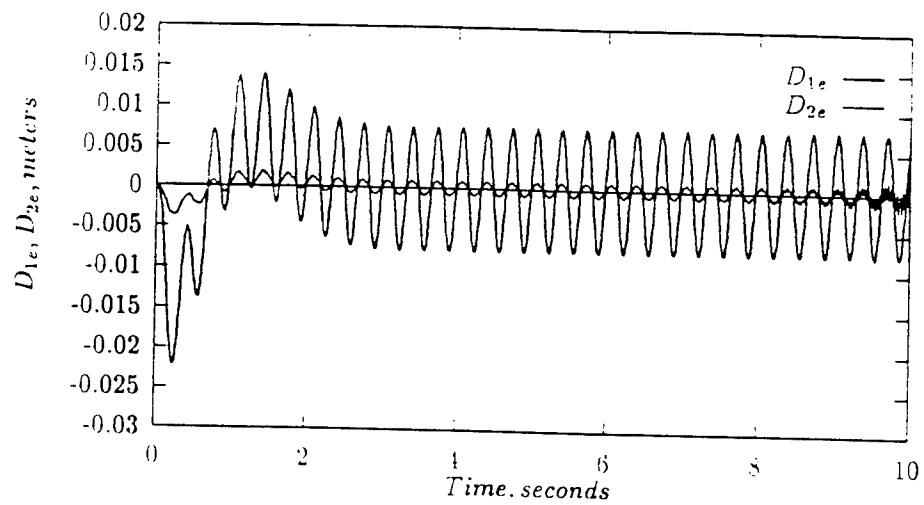


Fig.8(c)

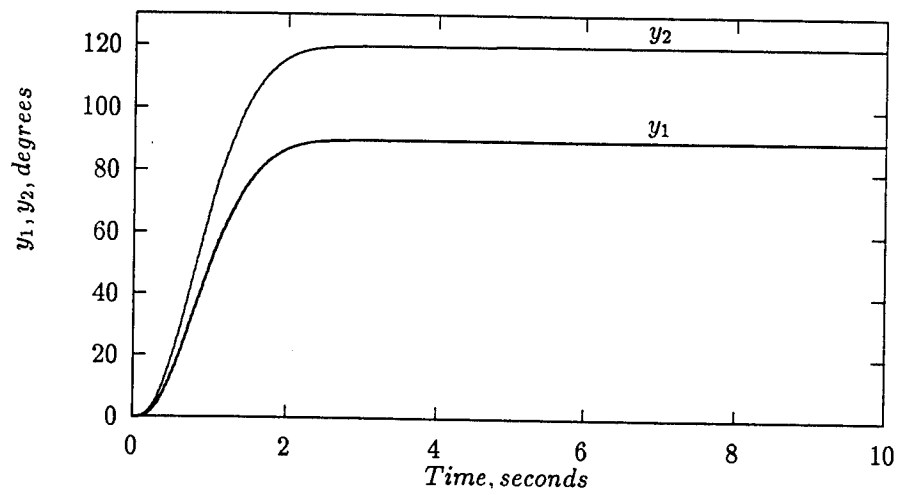


Fig.9(a)

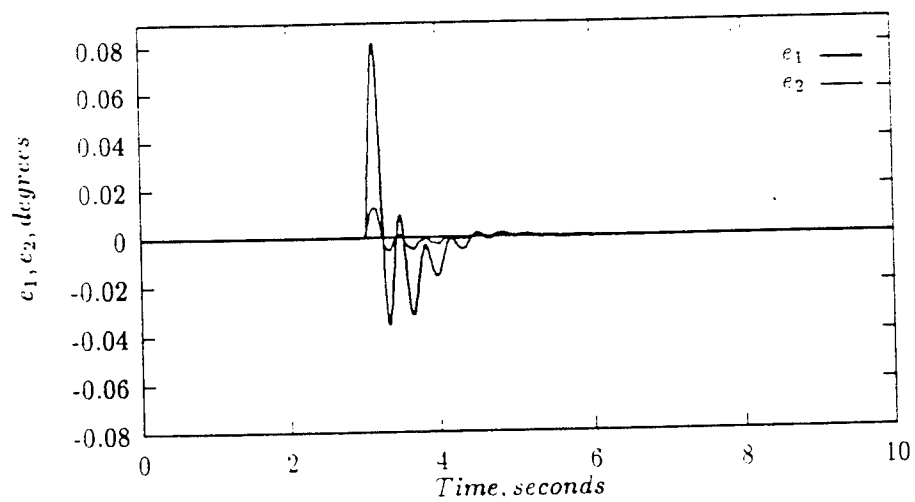


Fig.9(b)

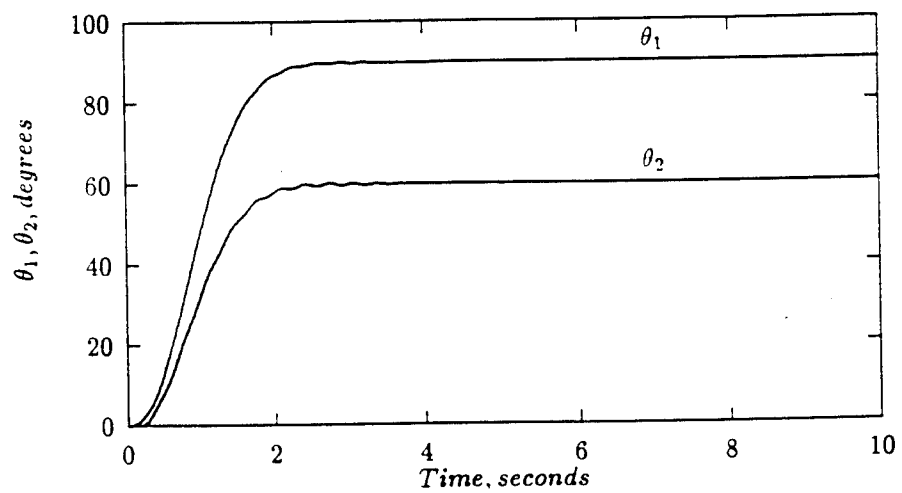


Fig.9(c)

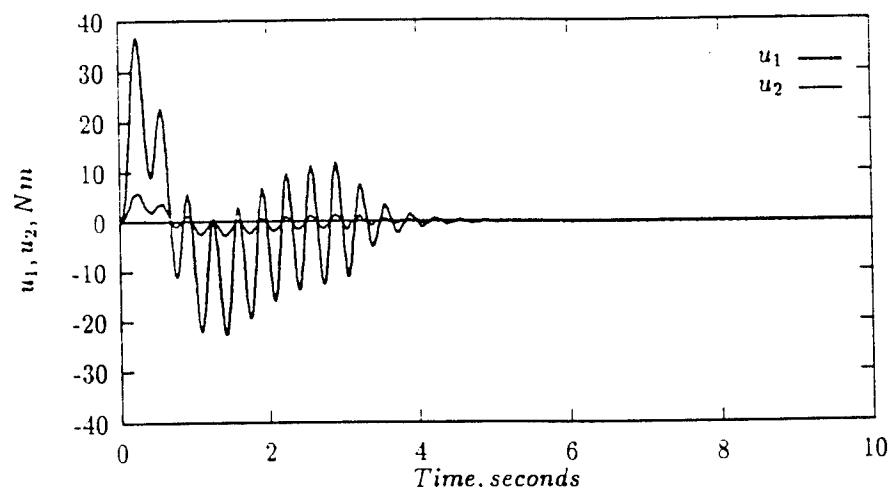


Fig.9(d)

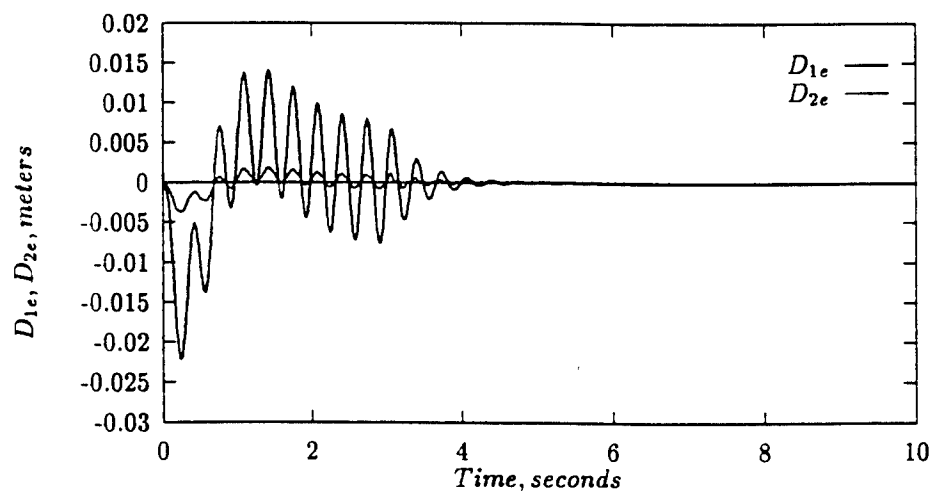


Fig.9(e)

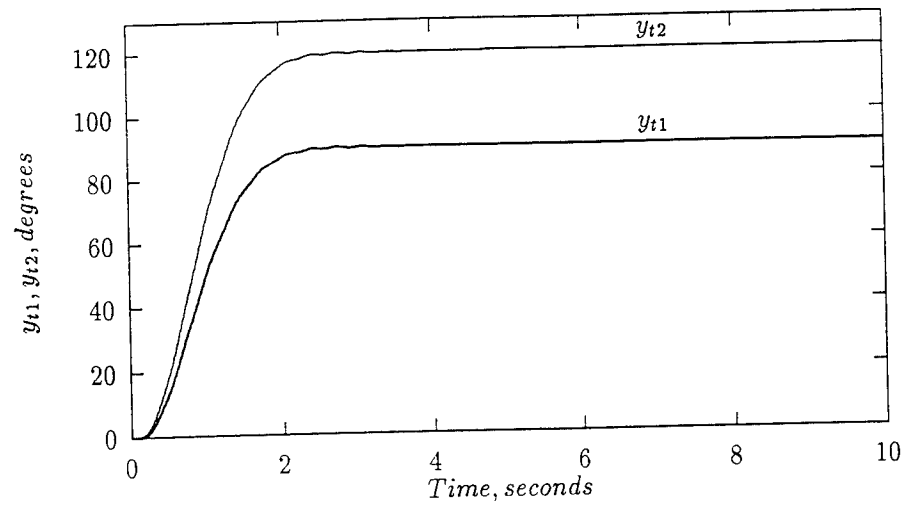


Fig.9(f)

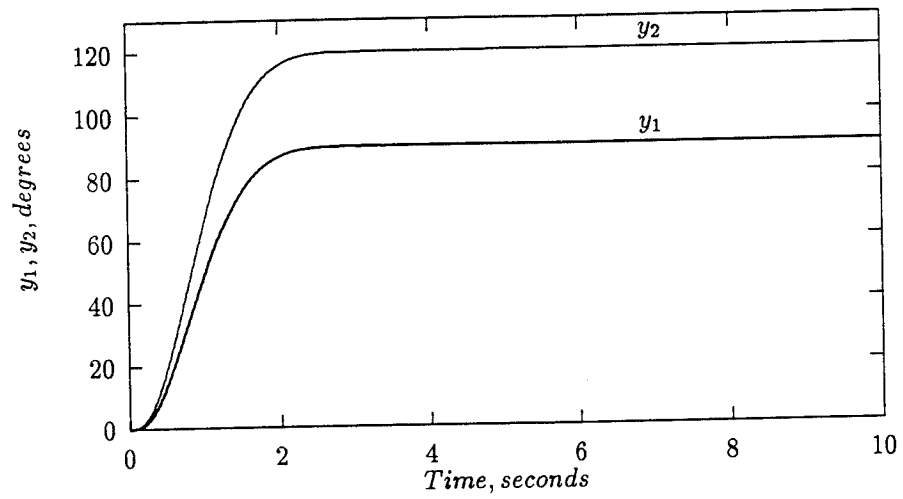


Fig.10(a)

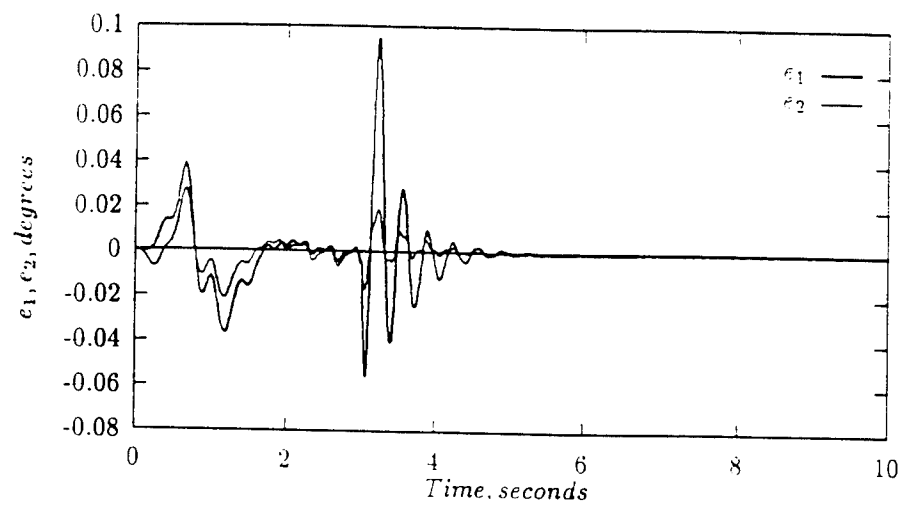


Fig.10(b)

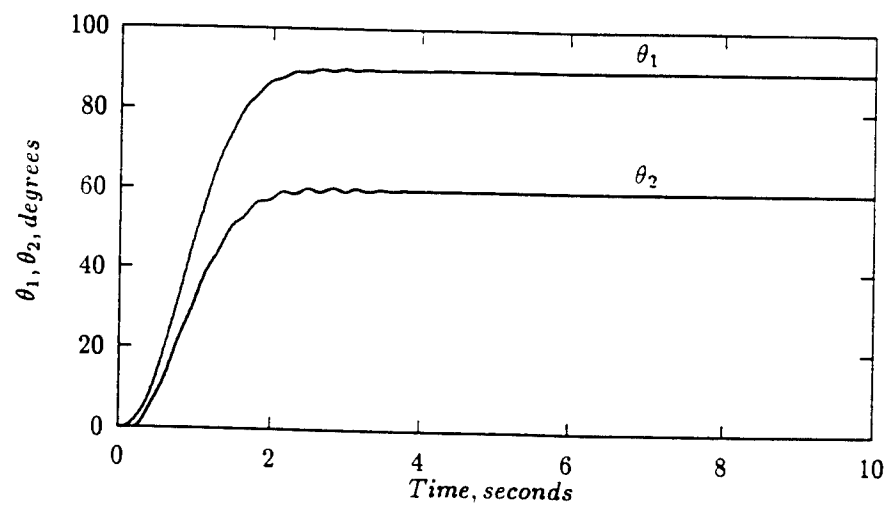


Fig.10(c)

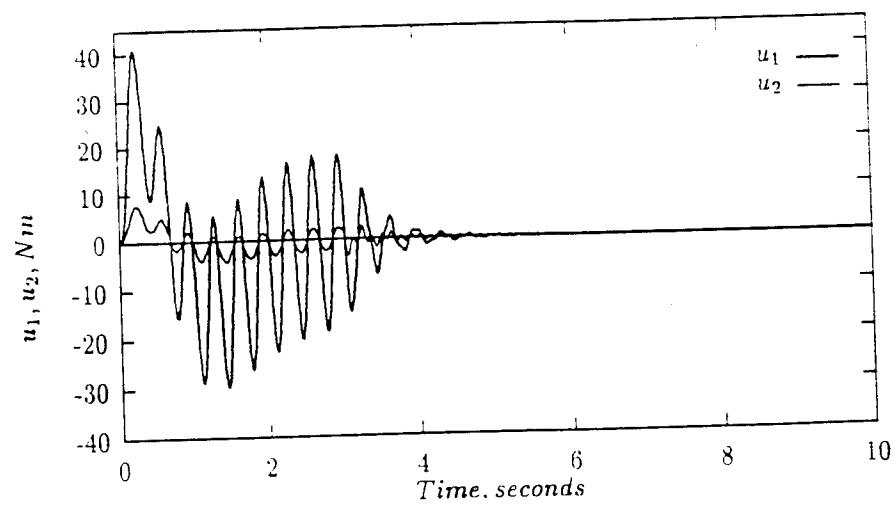


Fig.10(d)

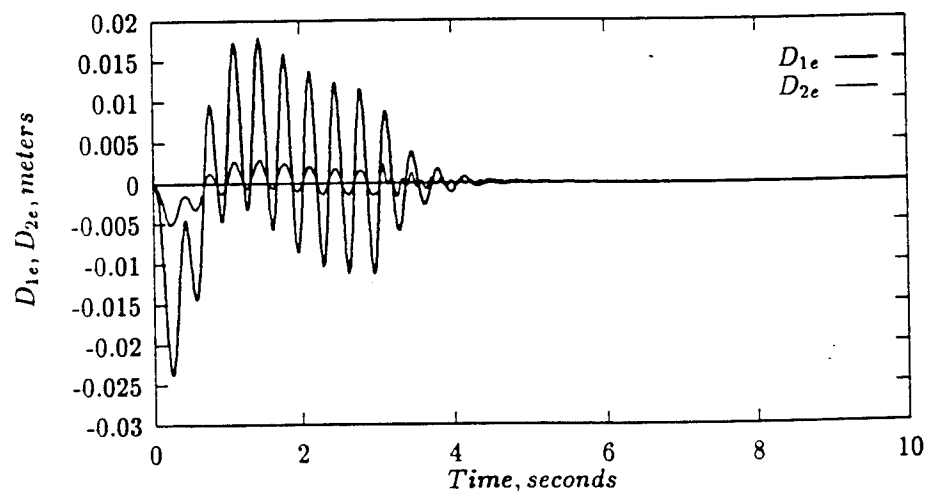


Fig.10(e)

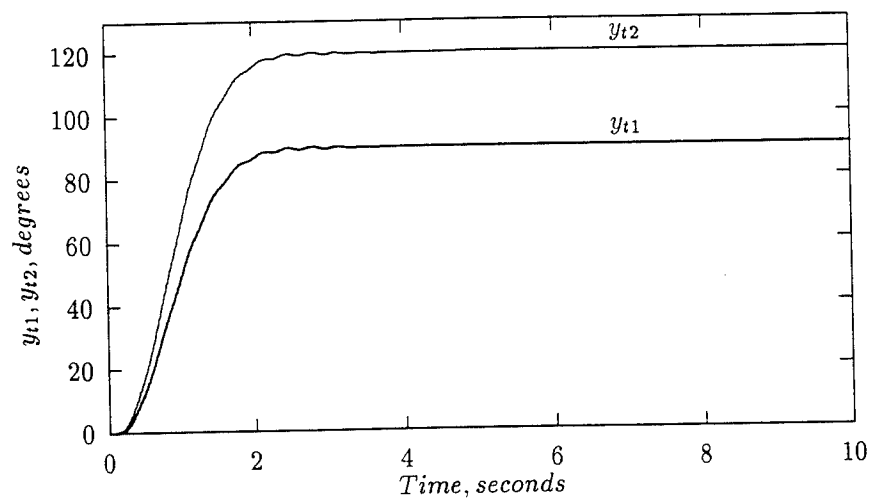


Fig.10(f)

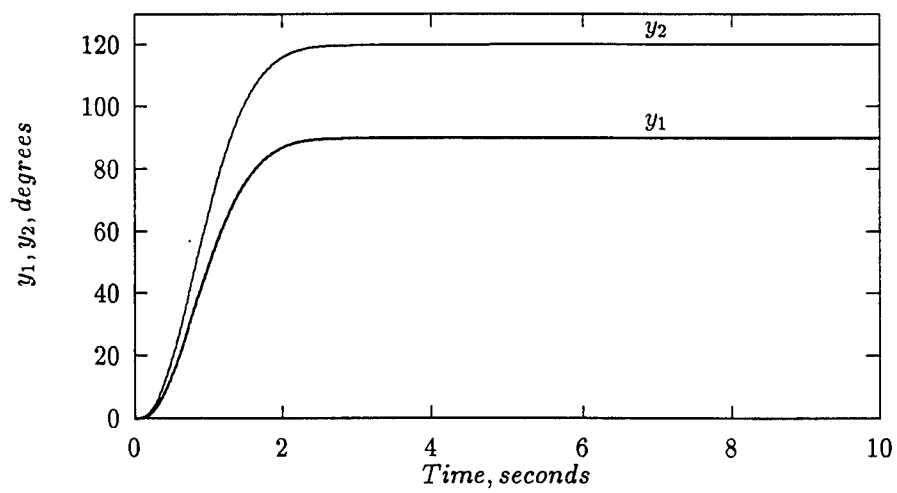


Fig.11(a)

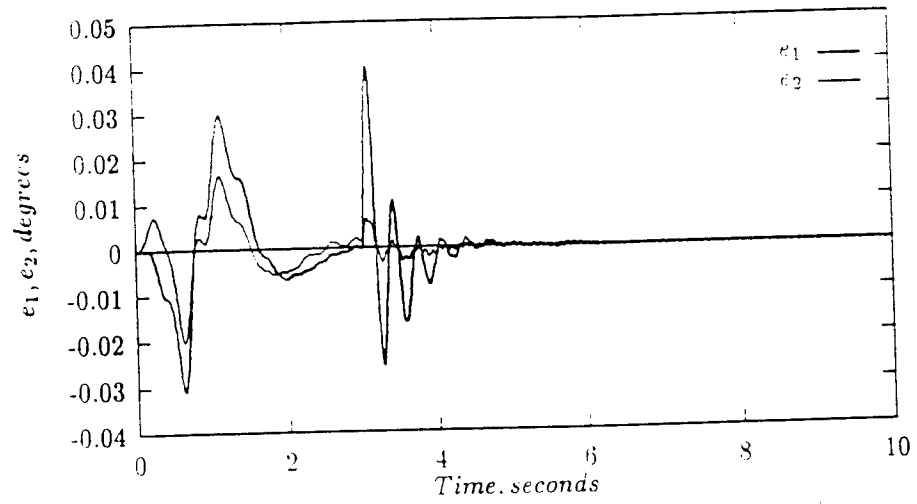


Fig.11(b)

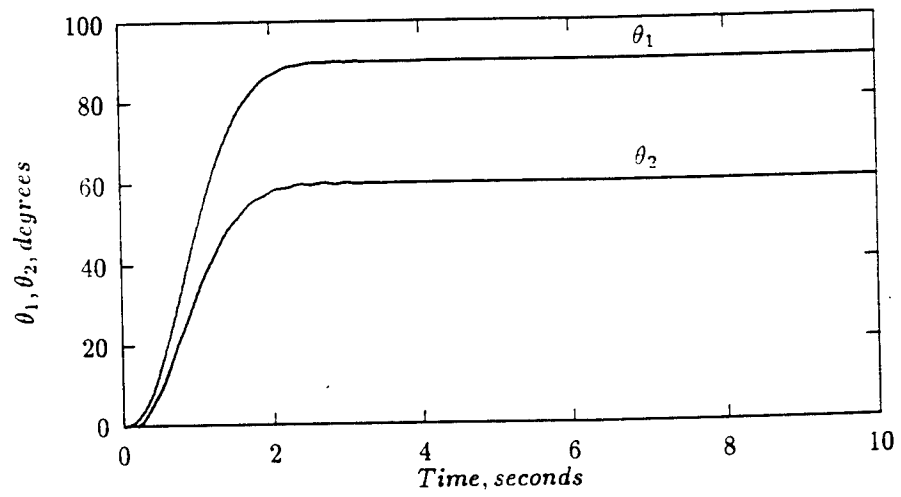


Fig.11(c)

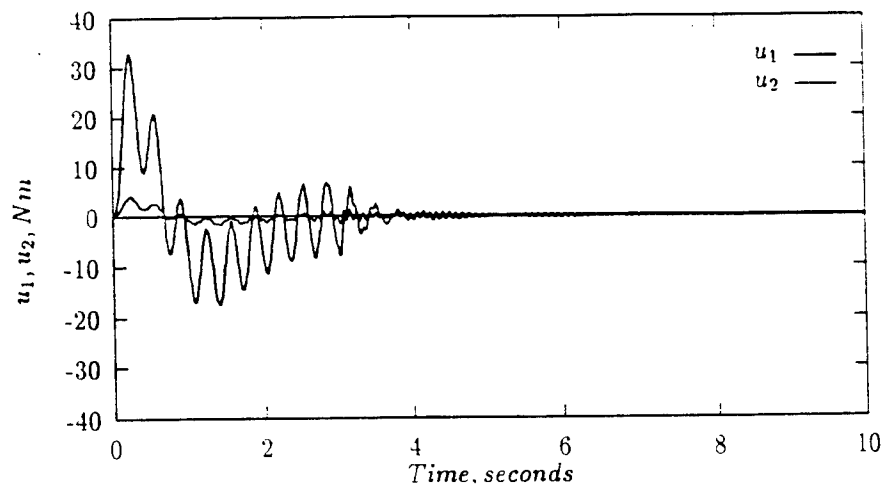


Fig.11(d)

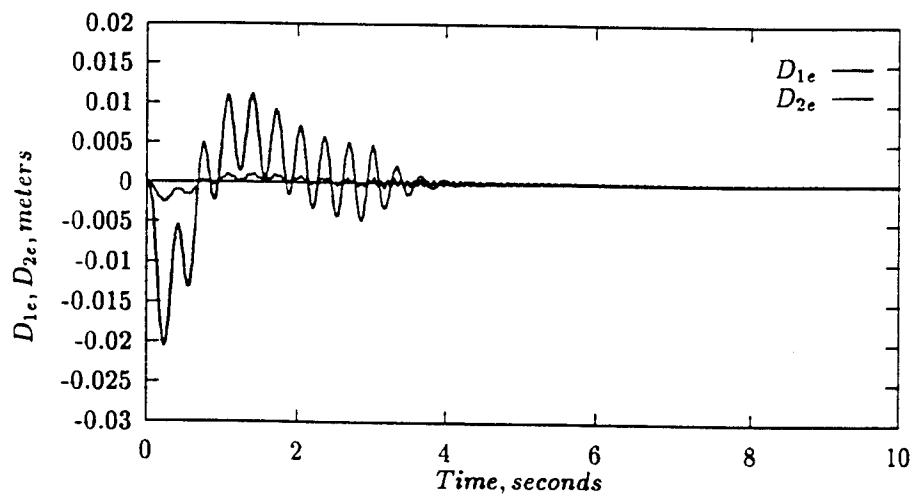


Fig.11(e)

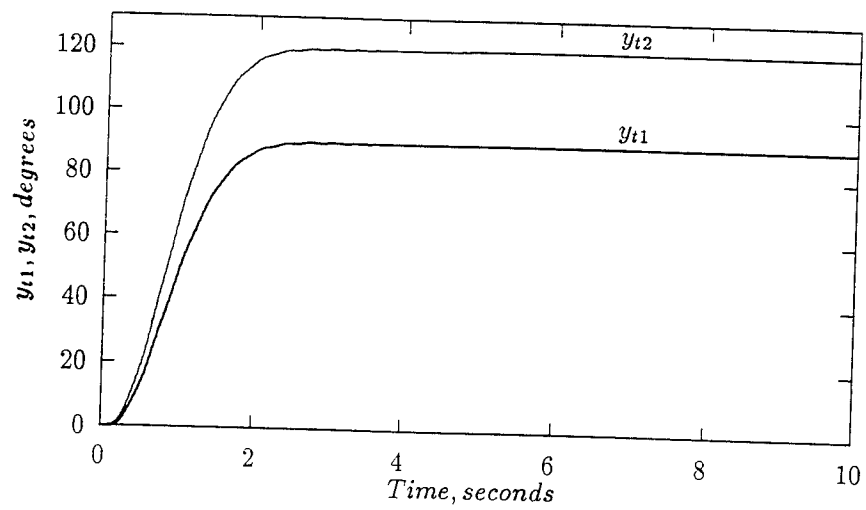


Fig.11(f)

NUCLEAR AND PLASMA PHYSICS
WITH ANTIPROTONS

Gerald A. Smith
Professor
Department of Physics

Pennsylvania State University
303 Osmond Laboratory
University Park, PA 16802

Interim Report for:
Research Initiation Program
Phillips Laboratory, Kirtland AFB, NM

Sponsored by:
Air Force Office of Scientific Research
Bolling Air Force Base, Washington, D.C.

and

Pennsylvania State University

December 1992

NUCLEAR AND PLASMA PHYSICS
WITH ANTIPROTONS

Gerald A. Smith
Professor
Department of Physics
Pennsylvania State University

ABSTRACT

Energy density considerations require the use of nuclear energy for rapid interplanetary travel. We describe an inertial confinement fusion propulsion system which has as a novel feature antiproton injection to assist in target ignition. We show that large thrust and I_{sp} can be achieved using proposed driver technologies and currently available quantities of antiprotons. An approved proof-of-principle test of the concept planned for the SHIVA Star facility at the Phillips Laboratory, Kirtland AFB is described.

NUCLEAR AND PLASMA PHYSICS WITH ANTIPROTONS

Gerald A. Smith

INTRODUCTION

The greatest challenge to space exploration at this time is to travel to the planets and return in the shortest possible time. Theoretical energy densities of candidate nuclear propulsion systems are compared with chemical systems in Table I. The two processes with the greatest specific energy density are fusion and antimatter annihilation. Studies have shown that efficiencies for capturing the considerable energy carried away by the relativistic products of antimatter annihilation are very low.¹ Therefore, in our opinion antiproton annihilation alone does not offer a solution to these challenges, at least within the constraints of projected antiproton production for the foreseeable future (~ 1-10 nanograms per year). The purpose of this paper is to show that when antimatter annihilation and fusion are combined into one system, a viable candidate propulsion system for planetary exploration emerges.

TABLE I

Theoretical energy densities of candidate
propulsion systems.

SYSTEM	$\epsilon_{TH}[\text{J/Kg}]$	$\Delta E/mc^2$
Chemical		
$\text{H}_2 + \text{O}_2$	1.3×10^7	1.4×10^{-10}
Metastable Helium	4.8×10^8	5.4×10^{-9}
Fission		
U(235)	8.2×10^{13}	9.1×10^{-4}
Fusion		
DD	7.9×10^{13}	8.8×10^{-4}
DT	3.4×10^{14}	3.8×10^{-3}
Antimatter Annihilation		
p+p	9.0×10^{16}	1.0

SPACE APPLICATIONS OF FUSION ENERGY

The desirability of nuclear, and especially fusion, propulsion for exploration of Mars is well-documented.² A laser driven, inertially confined fusion spacecraft called VISTA with a specific power of 20 kW/kg, I_{sp} of 17,000 sec and power of 20 GW illustrates such a system.³ We have developed an alternative concept utilizing antiproton catalyzed fusion based on the Ion Compressed Antimatter Nuclear (ICAN) system under development in this Laboratory.

In order to determine the potential benefits of the ICAN propulsion system, we have conducted a mission analysis. Preliminary calculations were made using the MULIMP2 code,⁴ which assumes impulsive velocity changes. Four impulses were used, one for each departure or arrival in the vicinity of a planet. A candidate manned exploration mission from Earth to Mars was selected for detailed examination. It is a sprint mission with a 130 day round trip time and a 30 day stay time in Mars orbit. Figure 1 shows the total mission velocity increment (Δv) needed for this mission with launch dates from the beginning of 2010 until the start of 2015. Assuming ICAN will deliver a specific impulse in the 10,000 sec regime, launch windows last for about four months for low initial mass in low Earth orbit (IMLEO).

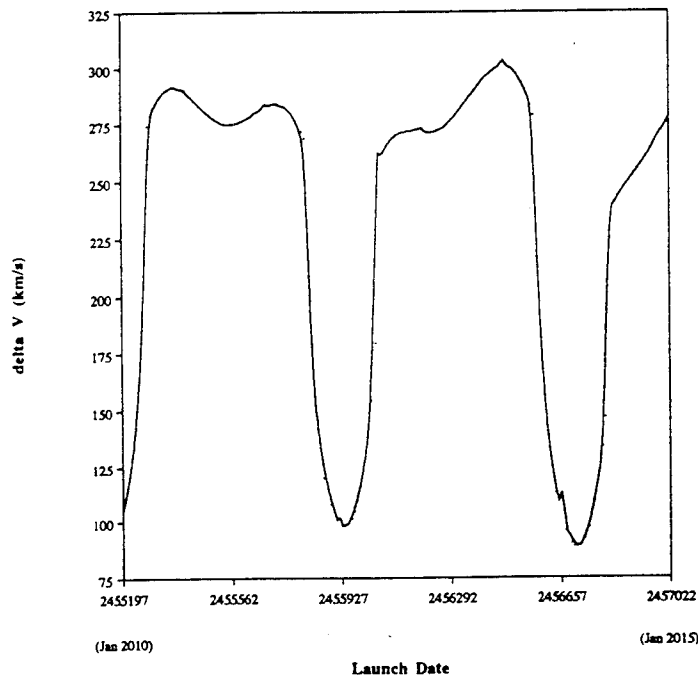


Fig. 1. Total Mission Δv vs. Launch Date.

The relationship between mission Δv and propulsion system specific impulse (I_{sp}) is important for mission planning and budgeting. This is shown in the simplified form of the rocket equation for a single stage vehicle, $MR = \exp(\Delta v / I_{sp} g_0)$, where MR (mass ratio) is the ratio of the fully fueled spacecraft mass to the unfueled spacecraft mass, and g_0 is the average acceleration due to gravity at the Earth's surface. Small gravitational losses near planetary bodies are ignored.

Typical Δv values during a launch window are approximately 100 km/sec. With projected I_{sp} of about 10,000 sec, this gives a mass ratio of approximately 2.8. By comparison, a nuclear thermal particle bed rocket is expected to yield an I_{sp} of around 1,000.⁵ This would mean a mass ratio of about 27,000 for our fast Mars mission! Clearly the fast interplanetary trip times needed for exploration, colonization, and utilization of the Solar System cannot be supported by solid nuclear thermal concepts. Extremely high energy missions being conceived for the 21st century demand propulsion capability far beyond that being designed today. A view of the complete Mars mission is provided in Fig. 2.

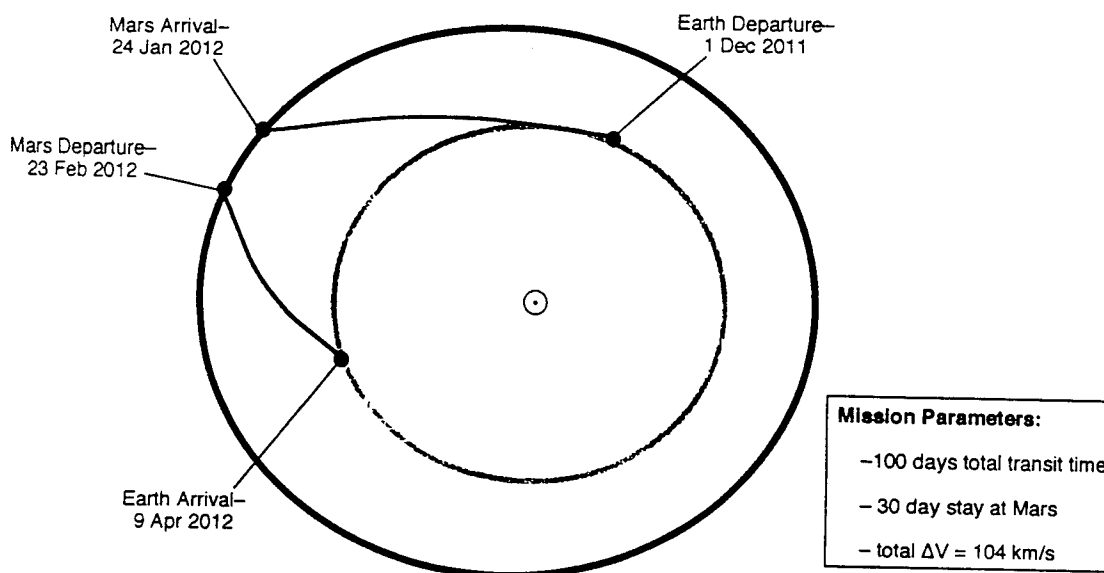


Fig. 2. ICAN Mission Plot for 1 Dec 2011 Launch.

ANTIPROTON-INDUCED FISSION

In a recent series of experiments at the Low Energy Antiproton Ring (LEAR) at CERN, Geneva, Switzerland our group and others observed for the first time antiproton-induced fission in a natural uranium target.⁶⁻⁹ Based on the number of neutrons measured, as well as the direct observation of neutrons in coincidence with heavy charged fission fragments,⁹ it was concluded that fission occurs nearly 100% of the time. On average, 16.3 neutrons are produced per antiproton. The neutron momentum spectrum and fitted yields and temperatures are shown in Fig. 3 and Table II respectively. As will be discussed later, such a reaction appears to be ideally suited to igniting an inertially confined (ICF) microfission/fusion reaction in a miniature target, utilizing antiprotons which can be trapped and stored for space applications.

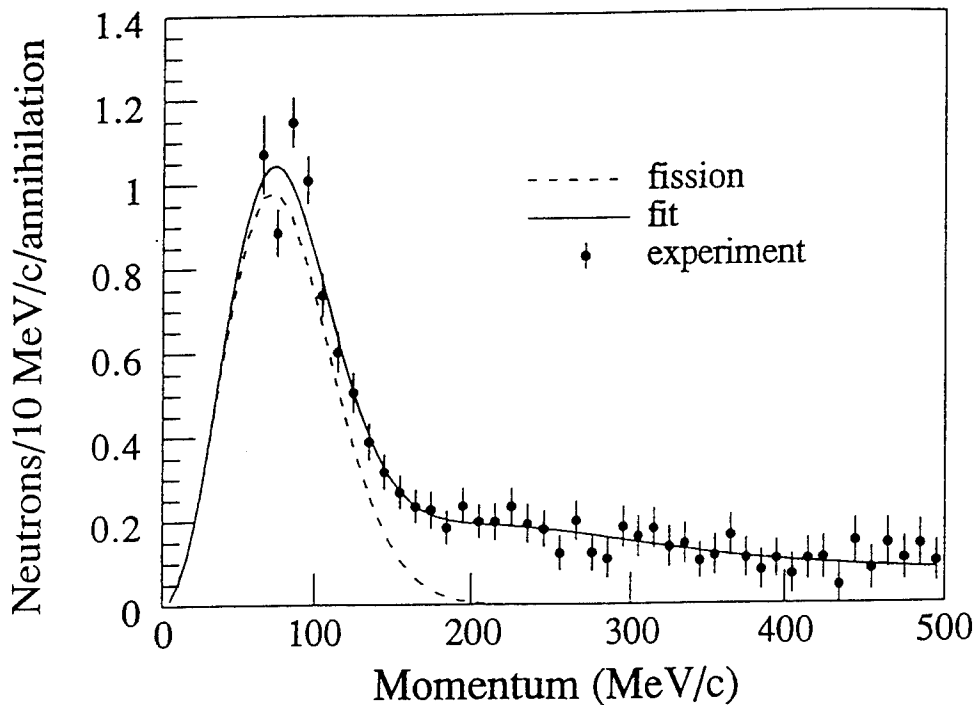


Fig. 3. Neutron momentum spectrum from stopped antiproton annihilation in uranium.

STORAGE OF ANTIPROTONS

Recent advances in storing antiprotons in Penning traps at LEAR for long periods of time have been spectacular.¹⁰ It now appears possible to store as

TABLE II

Fitted neutron yields per annihilation (a) and temperature (T). The three processes involved are: (D) direct neutrons ejected by collisions with annihilation pions; (EV) evaporation neutrons from the heated nucleus; and (F) neutrons emitted from fission fragments. The quantity E_F is the average energy per amu carried by the fission fragments.

a_D (no./ann)	4.49 ± 0.75
T_D (MeV)	99.6 ± 11.1
a_{EV} (no./ann)	3.40 ± 0.35
T_{EV} (MeV)	18.9 ± 2.0
a_F (no./ann)	8.42 ± 0.25
T_F (MeV)	2.18 ± 0.20
E_F (MeV/nuc)	0.74 ± 0.12
Total No. Neutrons	16.3 ± 0.9

many as 10^8 antiprotons in a trap for many months. Tests planned for this summer at LEAR by a Los Alamos group should confirm this prediction. With expected improved efficiencies for decelerating antiprotons down to trap energies and enlargement of the trap itself, up to 10^{12} trapped antiprotons could be realized in a few years. Such expectations are still far from the theoretical limit, which is expressed in terms of a density of 10^{12} per cm^3 . Therefore, we can assume that one could carry into space in the foreseeable future of order one thousand traps, each carrying 10^{12} antiprotons, for a total of one-two nanograms of antiprotons. This number is $\sim 10\%$ of the anticipated production capability at Fermilab after completion of the Main Injector in 1997, and as discussed below, capable of catalyzing a rapid ICAN roundtrip mission to Mars.

SELECTION OF APPROPRIATE DRIVER

All ICF systems require compression to boost the rates for nuclear reactions. Because of their potential compactness and low mass, as well as their ability to deliver intense pulses of beam with characteristics nicely matched to the needs of driving fission/fusion targets, we consider charged light ion accelerators as contenders for space applications. Specifically, we have considered the 32 MeV Li^+ system called PBFA-II presently under development at the Sandia National Laboratory.¹¹

Energy deposition is provided by electronic excitation of the target pusher, assumed to be gold. Energy densities have been evaluated at the Bragg peak near the end of the particle's range, using the TRIM85 code.¹² Efforts have been made to include realistic beam parameters, corresponding to a total beam energy on target of 1.5 MJ.

Table III illustrates the beam and energy deposition characteristics of the 32 MeV Li⁺ ion driver. These calculations point to a gold pusher of ~ 80 μm thickness which is capable of totally absorbing the energy of the intense, pulsed beam. We note that this energy density corresponds to an instantaneous pressure of 260 Gbar.

TABLE III

Beam and Energy Deposition Characteristics at the Bragg Peak for 32 MeV Li⁺.

<u>Size</u>	<u>Energy Spread</u>	<u>Intensity</u>	<u>Pulse length</u>	<u>dE/dx (ev/μm)</u>	<u>dE/dV (J/cm^3)</u>	<u>dP/dV (W/cm^3)</u>
$\pm 500 \mu\text{m}$	$\pm 2.5 \text{ MeV}$	2.9×10^{17}	10 ns	0.8×10^6	26×10^9	2.6×10^{18}

THE MICRO-FISSION/FUSION CONCEPT

In order to burn up small amounts of material in an ICF device, it is necessary to find methods of speeding up the nuclear reactions, so that most of the fuel is consumed before the material ablates. In this application, we use antiprotons to initiate a large number of early fission reactions, which bypasses the time-consuming early stages of the reaction chain. A short burst (10 ns, 10^7 – 10^9) of antiprotons is injected into a compressed uranium/DT target, typically of one gram mass, initiating a fission/fusion burn in the target. Under optimum conditions, 10's of GJ's of energy are released in the form of kinetic plasma and radiant energy.¹³ The reader is referred to a paper in this session presented by B.R. Wienke of Los Alamos National Laboratory for more discussion.¹⁴

Careful consideration must be given to matching pressure and compression work requirements with driver capabilities, such as those projected for light ion drivers (PBFAII). In addition, the challenge, as discussed below, of converting this energy into thrust and I_{sp} for space applications must be met and solved.

THRUST AND SPECIFIC IMPULSE OF ICAN

Based on our earlier discussion, we assume the pellet burn provides 5 GJ of energy, 90% of which is radiant and 10% kinetic plasma energy. Because of the large radiant component, we admix a 0.125% molar concentration of lead with the hydrogen propellant. Table IV illustrates the conversion of radiant energy to kinetic energy for 50 g of propellant. One sees that an efficiency of approximately 30% of total pellet energy is possible, providing an I_{sp} of 13,000 sec and a thrust of 30 kN. The jet energy quoted assumes 45% conversion in a magnetic nozzle. Figure 4 shows the result of varying the propellant mass up to 100 grams with the same lead admixture for a 5 Hz system. The large apparent dynamic ranges of I_{sp} and thrust will be used in further refinements to mission profiles discussed earlier.

TABLE IV

Expected Propulsion Parameters of ICAN Target.

Total Expellant Mass	- 50 grams
Lead Molar Fraction	- 0.125%
Pellet Energy Absorbed	- 29.6%
Jet Energy	- 0.412 GJ
Specific Impulse	- 13,000 sec
Average Thrust	- 30,000 N

ICAN SYSTEMS STUDY

The ion compressed antimatter nuclear (ICAN) concept described in this paper has been compared with solid-core nuclear thermal rockets (NTR), which is currently considered the most likely near-term advanced propulsion option for a piloted Mars mission. The ICAN system assumes a 100 MT round trip payload, while the NTR mission assumes 120 MT outbound and 40 MT inbound payloads.¹⁵ As can be seen in Fig. 5, the ICAN system would outperform a solid-core nuclear thermal rocket, achieving round trip times less than one-third that of nuclear thermal rockets. For reference, also shown is a baseline chemical rocket system.¹⁶ Since piloted missions require much shorter trip times to minimize the hazard due to cosmic radiation, ICAN would therefore seem to be a much better choice for a piloted Mars mission.

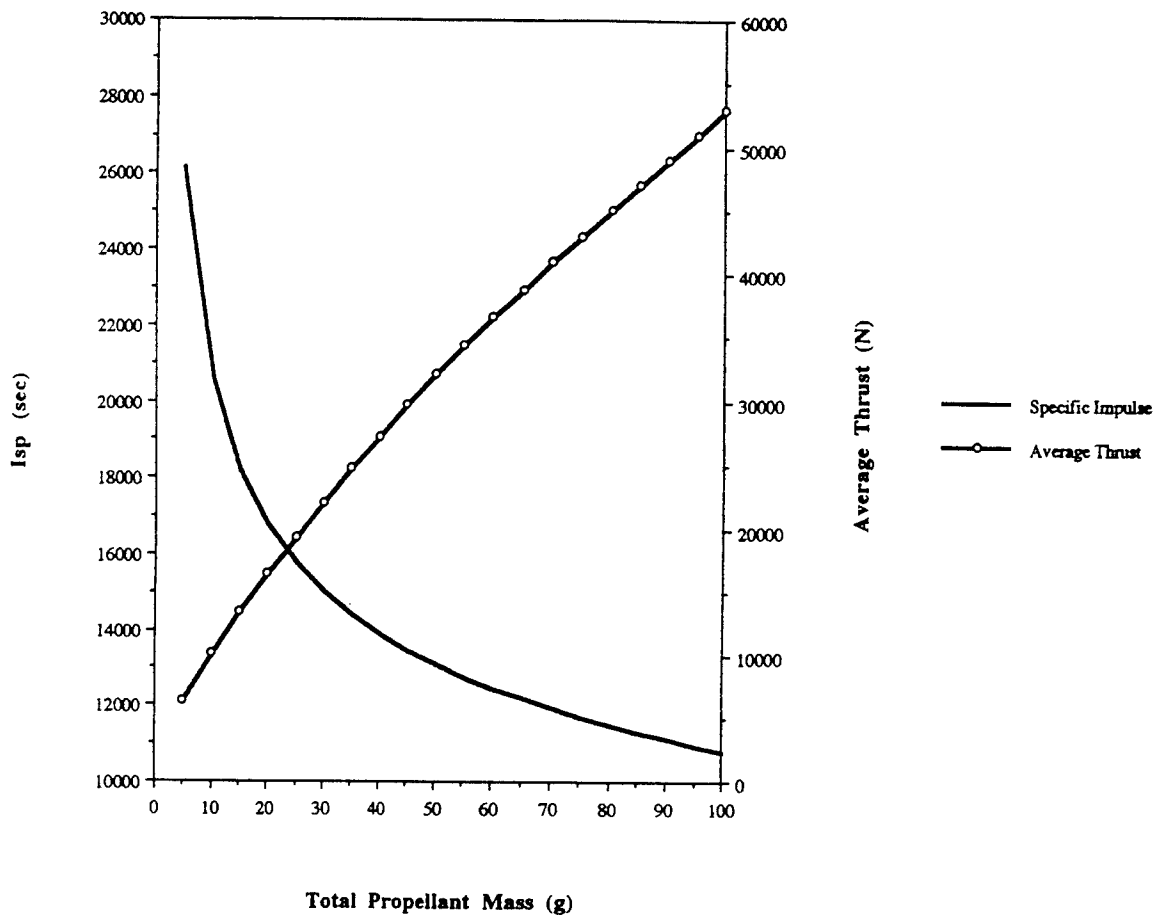


Fig. 4. Specific Impulse and Thrust vs. ICAN Expellant Mass.

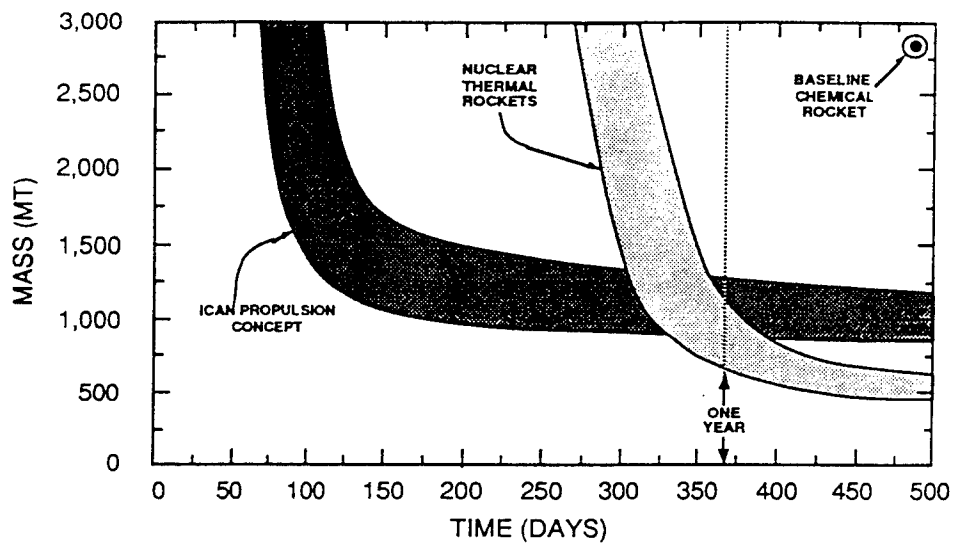


Fig. 5. Total initial mass vs. round trip time for a piloted mission to Mars.

We have also compared ICAN with VISTA, shown in Fig. 6.¹⁷ The quantity W_c/E_d is the ratio of compression work to driver energy, expected to be in the range 10 to 30%. We see that ICAN provides rapid round trip times to Mars with roughly twice the weight as VISTA. This additional weight can be used to advantage, as the driver infrastructure provides synergistic shielding from cosmic rays and solar flares. For such an ICAN mission, power delivery would be required for approximately 50 days. As a rate of 5 Hz @ 10^8 antiprotons per shot, this requires approximately 3 nanograms of antiprotons, within predicted production capabilities by the turn of the century.

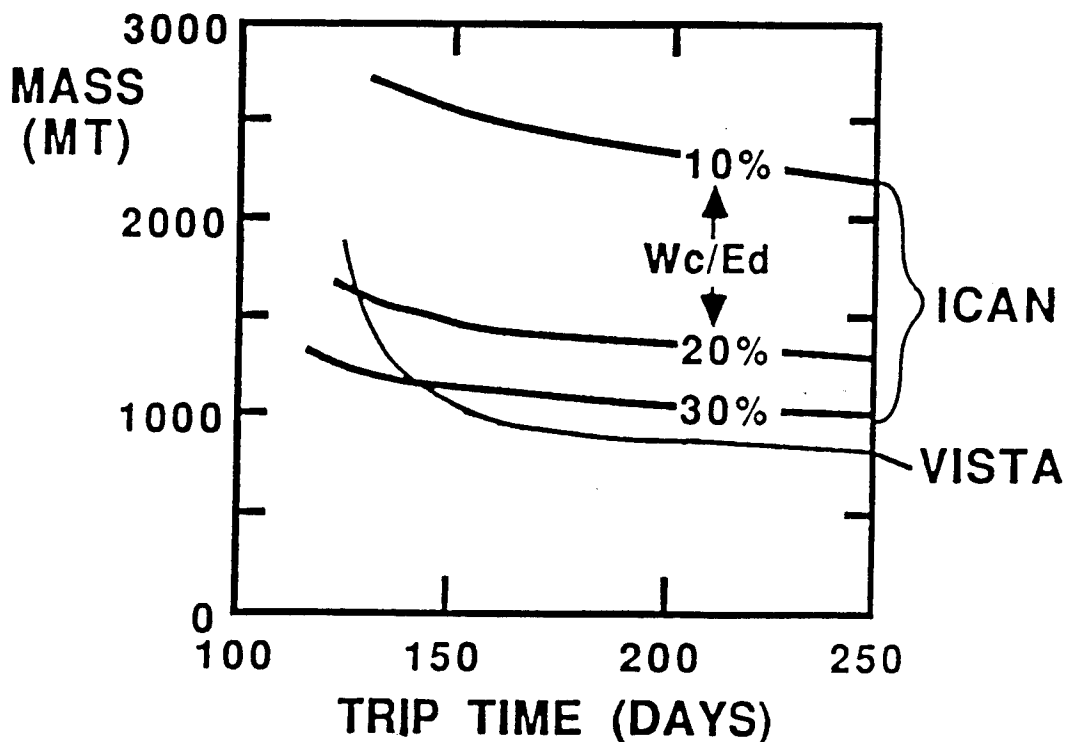


Fig. 6. Comparison of ICAN and VISTA systems for a piloted round trip to Mars.

ANTIPROTON EXPERIMENTS AT SHIVA STAR

In previous sections we describe conditions under which a complete burn of a fission/fusion microtarget can be achieved. The requirements on numbers of antiprotons are within present delivery capabilities of antiproton sources. However, further developments with light ion beams are required.

In the meanwhile, it is important to find conditions under which the concept of antiproton-boosted microfission can be tested. This can be done

under relaxed conditions of compression work and pressure (typically 200–1000 KJ and 10–40 Mbar respectively), provided the target mass is in the tens of gram range. Calculations show that, with one-thousand antiprotons injected into such a target in a short burst, significant subcritical neutron multiplication (20–40%) can be expected (Fig. 7). We assume a U(235) target, 250KJ compression work, a neutron detector with 5% net efficiency, and a 10 ns pulse of only 10^3 antiprotons. The test would be considered a success if neutron multiplication relative to uncompressed targets in the mass range 10–30 grams (1000–1200 versus 900–950 counts) was observed, and scaled in proportion to the number of antiprotons.

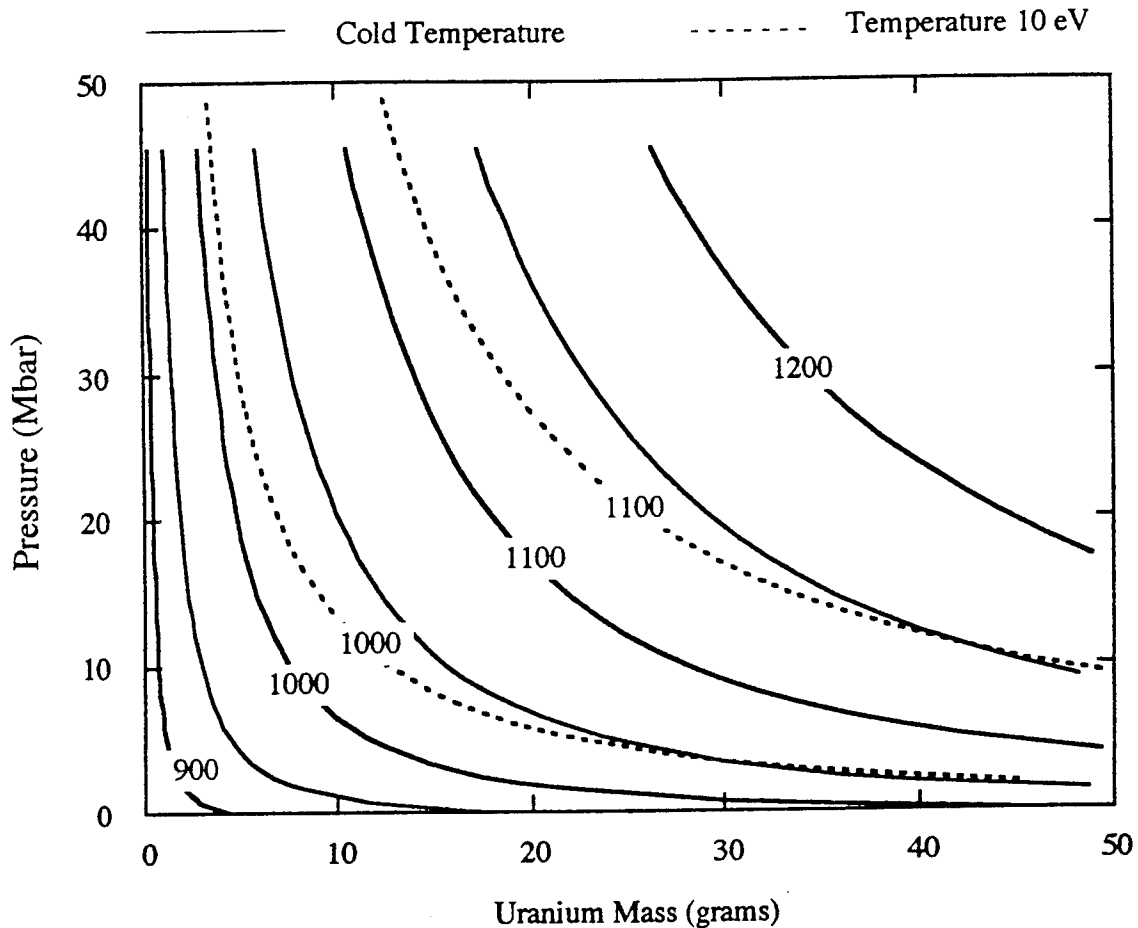


Fig. 7. Dependence of neutron yield on pressure in subcritical experiments. The lines indicate isoneutron yields at target temperatures of 0 eV and 10 eV.

SHIVA Star is a solid liner imploder¹⁸ operated at the Phillips Laboratory, Kirtland AFB, Albuquerque, NM. Energy is provided from a 9.45MJ capacitor bank, which is inductively discharged through an anode-cathode structure. The resultant multi-megamp current which flows down the liner (Fig. 8) forces it to collapse inwardly. For the antiproton-boostered microfission application, the liner will be used to compress a working fluid, such as hydrogen, with a large speed of sound to avoid shock formation. This produces a pressure field around the target which is positioned at the center of the liner, leading to a fast (several hundred ns) uniform pressure up to ~ 40 Mbar on the spherical target.

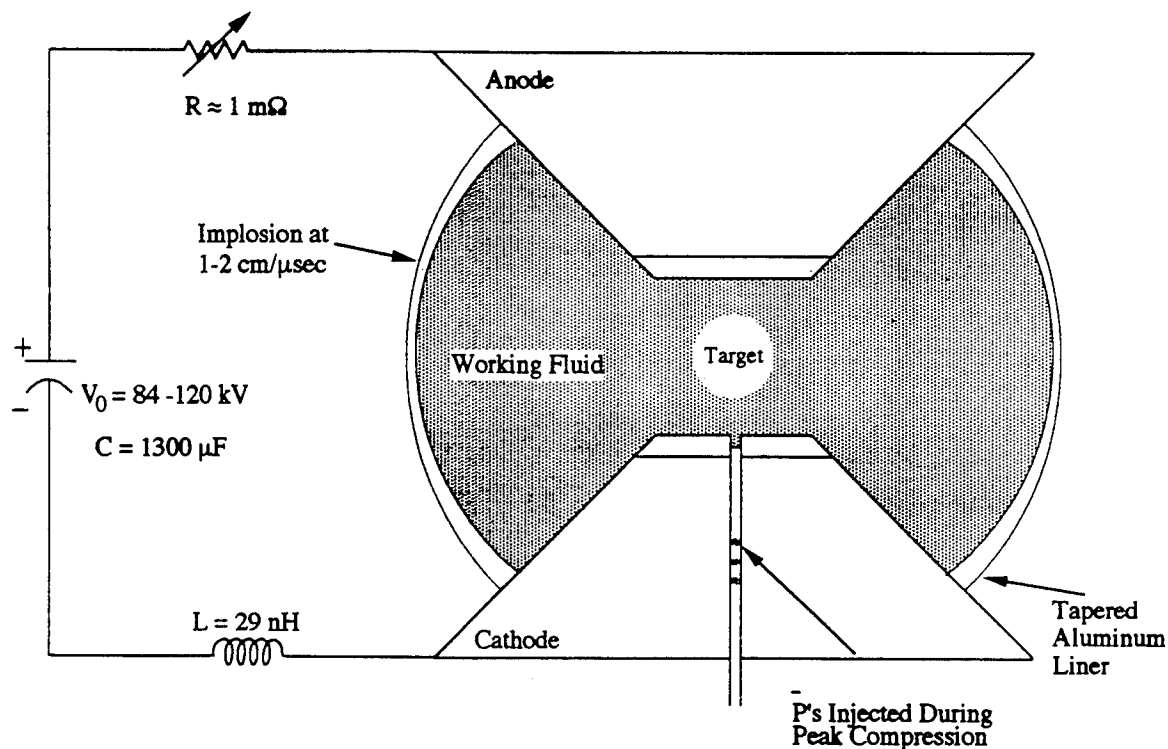


Fig. 8. Technique of compression used in subcritical experiments at SHIVA Star.

The apparatus consists of a portable Penning trap, a radiofrequency quadrupole for accelerating and focusing proton(antiprotons) released from the trap onto the target, and the target arrangement situated inside SHIVA Star (Fig. 9). Particles are injected along the symmetry axis of the anode-cathode system to avoid transverse magnetic fields.

\bar{p} μ fission at Shiva Star

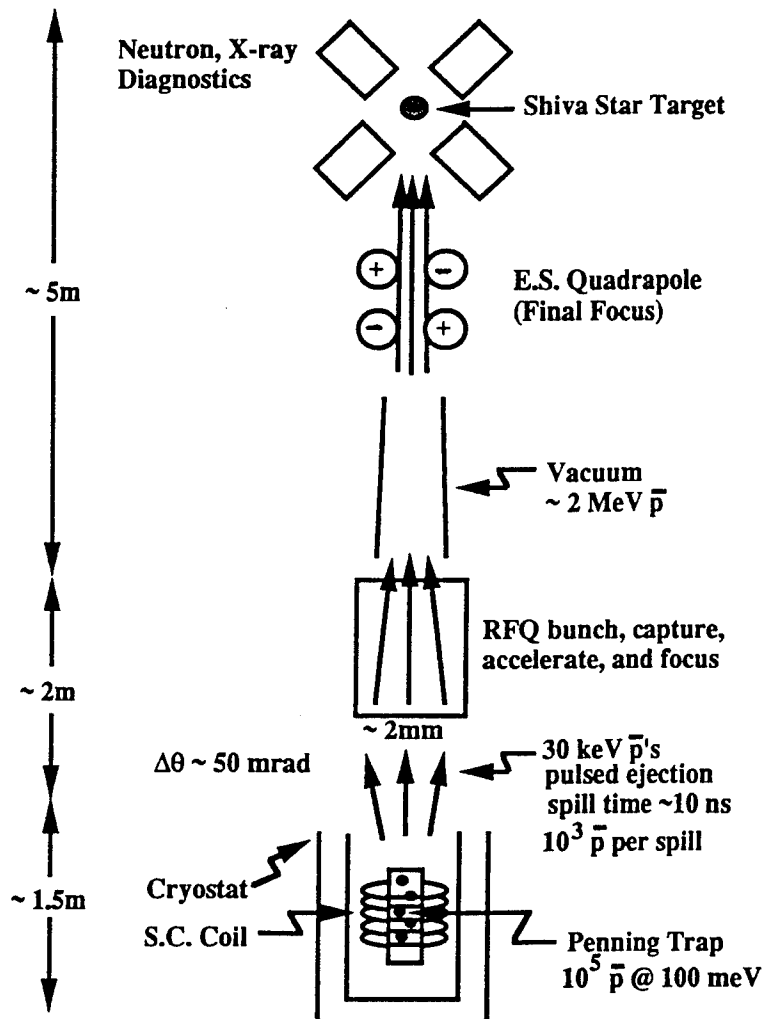


Fig. 9. Schematic of subcritical experiments at SHIVA Star.

A diamond window (1 mm radius, 0.6 mm thick) prevents the hydrogen plasma from escaping the target chamber during compression. Properties of the plasma were evaluated using the 2D MHD program CALE¹⁹ with the following starting parameters: density = 1.0×10^{19} atoms/cm³, temperature = 1 eV, mass = 0.1 mg and peak liner current = 14 Mamps. It is found that the window breaks at a pressure of 200 kbar and time of 360 ns before peak compression. This permits a small amount of the plasma to stream up the beam pipe a distance of

approximately 8 cm before encountering the antiprotons. Antiprotons have been swum through the plasma to the target using energy loss codes developed in this Laboratory.²⁰ The beam pipe is flared 45 deg. from the window to minimize energy loss in the beam pipe. The results are shown in Fig. 10 for 3 MeV antiprotons. At this energy, the antiprotons successfully reach the target and annihilate on its surface. More studies are currently underway to find conditions to reduce the antiproton energy even further.

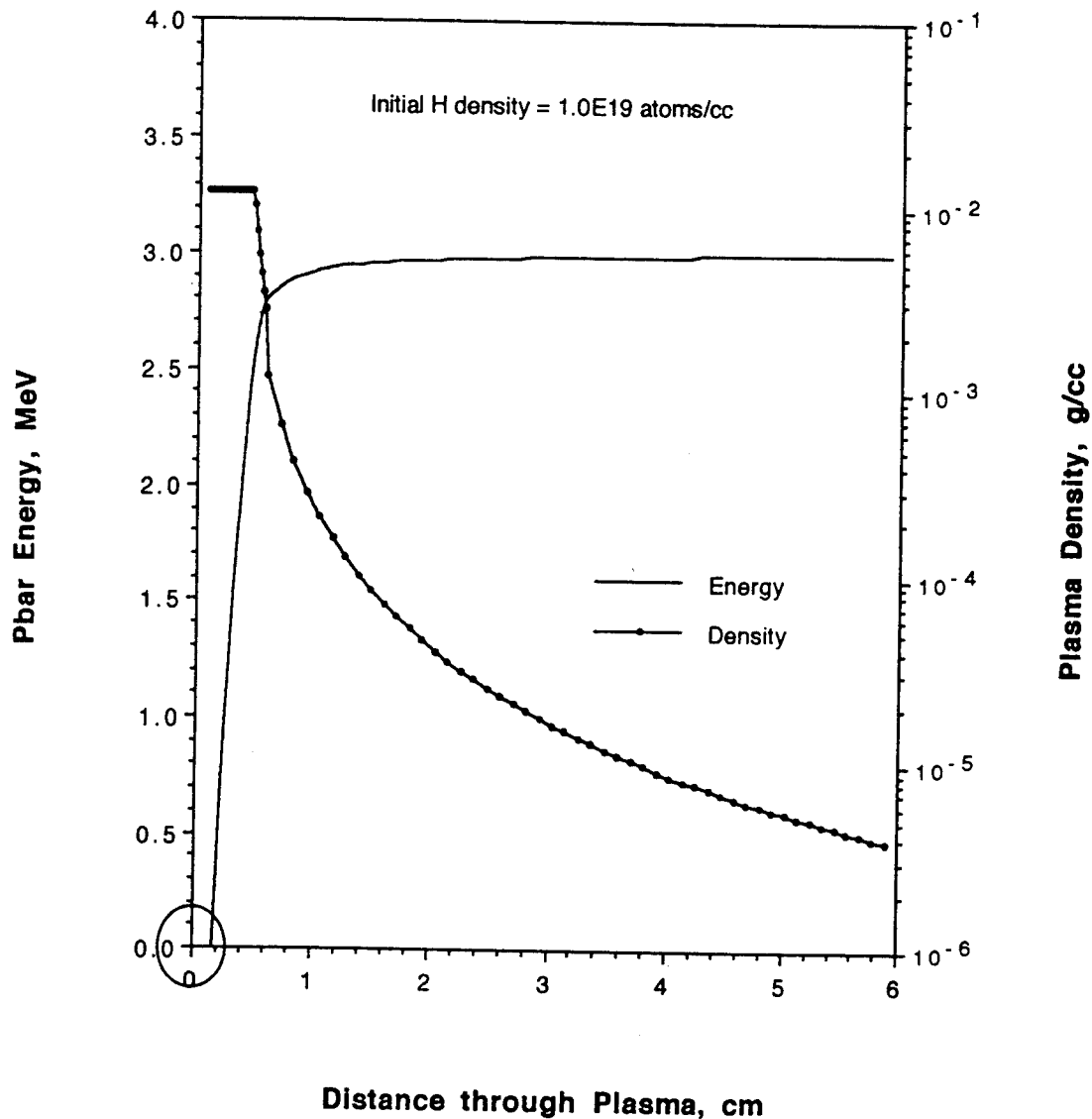


Fig. 10. Plasma density and antiproton energy at injection versus distance from target.

The experiment will be staged. First, implosion tests will be made on an inert gold target to test the working fluid concept. Then, the trap will be filled with deuterons, which will be injected into the gold target, yielding a signal from stripped neutrons which tests the injection concept and neutron detector. Finally, the trap will be filled with roughly 100 million antiprotons and transported to SHIVA Star. This will provide many shots of 1000-100,000 antiprotons each for subsequent injections into a uranium (235) target under compression.

The program of experiments described above has been approved by AFOSR, starting in FY93. It will be carried out in close collaboration with the staff of the High Energy Plasma Branch, Phillips Laboratory, Kirtland AFB.

CONCLUSIONS

The ICF target discussed in this paper can be completely burned using compression provided by beams of 32 MeV lithium ions. The process is speeded up within the limits of confinement time by a burst of 10^7 - 10^9 antiprotons. This unique application of antiprotons as a catalyst permits the complete burn of the target before it ablates. Technologies for creating compression within the target with light ion beams and trapping and storing of antiprotons are well advanced and should be available for space applications in the foreseeable future. The target can readily provide multi-CW jet power for the duration of a round trip, piloted mission to Mars. Tests during 1993-7 using SHIVA Star are designed to confirm the concept and engineering principles.

REFERENCES

1. J.L. CALLAS, "The Application of Monte Carlo Modeling to Matter-Antimatter Annihilation Propulsion Concepts," Jet Propulsion Laboratory, Pasadena, CA, JPL D-6830, October 1, 1989.
2. J. REECE ROTH, Fusion Technol., 15, 1375 (1989).
3. C.D. ORTH et al., "The Vista Spacecraft - Advantages of ICF for Interplanetary Fusion Propulsion Applications," paper presented at the IEEE 12th Symposium on Fusion Engineering, Monterey, Ca, Oct. 12-16, 1987.

4. A.L. FRIEDLANDER, "Multi-Impulse Trajectory and Mass Optimization Program (MULIMP)," Report No. SAI 1-120-383-T4, Science Applications, Inc., 5005 Newport Drive, Suite 305, Rolling Meadows, IL 6008, April 18, 1975.
5. Aviation Week and Space Technology, January 20, 1992, p. 20.
6. A. ANGELOPOULOS et al., Phys. Lett. B, 205, 590 (1988).
7. T.A. ARMSTRONG et al., Z. Phys. A, 331, 519 (1988).
8. J.P. BOCQUET et al., Physics at LEAR With Low Energy Antiprotons, Proc. of the 4th LEAR Workshop, Villars-sur-Ollon, Switzerland, September 6-13, 1987, p. 793, C. AMSLER et al., Eds., Harwood Academic Publishers, Switzerland (1988).
9. B. CHEN et al., Phys. Rev. C, 45, 2332 (1992).
10. G. GABRIELSE et al., Phys. Rev. Lett., 63, 1360 (1989); Phys. Rev. Lett., 65, 1317 (1990).
11. J.P. VANDEVENDER et al., Laser and Particle Beams, 3, 93 (1985); Laser and Particle Beams, 5 (3), 439 (1987); Proceedings of the 1987 IEEE Particle Accelerator Conference, Vol. 3, p. 1975, IEEE, New York (1987).
12. J.F. ZIEGLER, J.P. BIRSACK and U. LITTMARK, The Stopping and Range of Ions in Solids, Pergamon Press, New York (1986).
13. R.A. LEWIS et al., Nucl. Sci. Eng., 109, 411 (1991); Fusion Technol., 20, 1046 (1991).
14. B.R. WIENKE, paper presented at the Nuclear Technologies for Space Exploration Meeting, Jackson, WY, Aug. 16-19, 1992.
15. T. NUGENT, "A Performance Evaluation of the Ion Compressed Antiproton Catalyzed Nuclear (ICAN) Propulsion System," Jet Propulsion Laboratory Internal Document D-8572 (1991).
16. R.H. FRISBEE et al., JPL Internal Document D-8023, October, 1990.
17. R.H. FRISBEE, "Mission Studies," paper presented at the NASA OAST Third Annual Advanced Propulsion Workshop, Jet Propulsion Laboratory, Pasadena, CA, Jan. 30-31, 1992.
18. J.H. DEGNAN et al., IEEE Trans. on Plasma Sci., PS-15, No.6, 760 (1987); Megagauss Technology and Pulsed Power Applications, p. 699, C.M. FOWLER et al., Eds., Plenum Publishing Corp., New York (1987).
19. Courtesy Dr. Robert Tipton, Lawrence Livermore National Laboratory, Livermore, CA 94550.
20. R.A. LEWIS et al., Phys. Rev. A, 44, 392 (1991).

SPECTROSCOPIC PARAMETERS OF OXYGEN FOR ATMOSPHERIC MODELING

R. H. Tipping
Professor
Department of Physics and Astronomy

University of Alabama
Tuscaloosa, AL 35487-0324

Final Report for:
Research Initiation Program
Phillips Laboratory

Sponsored by:
Air Force Office of Scientific Research
Bolling Air Force Base, Washington, D. C.

January 1993

SPECTROSCOPIC PARAMETERS OF OXYGEN FOR ATMOSPHERIC MODELING

R. H. Tipping
Professor
Department of Physics and Astronomy
University of Alabama

Abstract

Improved spectroscopic parameters were calculated for the oxygen molecule that will be eventually incorporated into the HITRAN database. These include the following revisions and/or improvements: a programming error that resulted in the intensity of a single line (an $^{16}\text{O}^{18}\text{O}$ transition at 7.8 cm^{-1}) being too strong by a factor of four was corrected; improved fundamental and molecular constants were incorporated for the calculation of the magnetic dipole transitions, and a refined treatment of the intensities shows that differences as much as 20 % can result for some SQ and SR transitions in the pure rotational band; more accurate quadrupole moment matrix elements have been introduced, resulting in improved intensities of these transitions; more recent experimental data for the molecular constants and dipole transition strength have led to refinements in the $a^1\Delta_g \leftarrow x^3\Sigma_g^+$ and $b^1\Sigma_g^+ \leftarrow x^3\Sigma_g^+$ bands. Several additional extensions to the existing database are discussed briefly.

SPECTROSCOPIC PARAMETERS OF OXYGEN FOR ATMOSPHERIC MODELING

R. H. Tipping

INTRODUCTION

The oxygen molecule is unique among the more abundant species found in the Earth's atmosphere in that it has two unpaired electrons. Because of this, the ground electronic state is a triplet ($X^3\Sigma_g^+$) and the molecule has an electronic magnetic dipole moment. The electron spin also leads to a splitting of the vibration-rotational levels due to spin-spin and spin-rotation interactions.¹ However, within the Born-Oppenheimer approximation, none of the isotopic species ($^{16}\text{O}_2$, $^{16}\text{O}^{18}\text{O}$, $^{16}\text{O}^{17}\text{O}$, etc.) has a dipole moment and therefore, there are no allowed dipole transitions. Because of the interaction during a binary collision, however, a transient dipole moment is created and dipole transitions do occur. The importance of this mechanism in the Earth's atmosphere will be discussed briefly in the final section of this report. All the species have quadrupole moments, and as a consequence, the far infrared spectrum consists of quadrupole and magnetic dipole transitions. In addition to these vibration-rotational transitions, there are important electronic bands due to transitions to low-lying electronic levels; in particular, the $a^1\Delta_g \leftarrow X^3\Sigma_g^+$ and $b^1\Sigma_g^+ \leftarrow X^3\Sigma_g^+$ bands.

The current edition of HITRAN² contains data for the different types of transitions mentioned above. In the next section, we will discuss revisions and/or improvements that have

been incorporated into a computer program that calculates the requisite data. In the final section, we discuss briefly some additional transitions and extensions of the oxygen database that can be made to enhance its usefulness for atmospheric scientists. Finally, we present the conclusions from the present study.

IMPROVEMENTS IN THE OXYGEN DATABASE

In the present section, we discuss the improvements made in the computer program and in the data contained in the program as input for the calculation of the magnetic dipole transitions, of the electric quadrupole transitions, and of the two electronic bands. Eventually, the data generated by this program will be used to supplant that currently in the HITRAN database.

A. Magnetic Dipole Transitions

The first improvement made was to update the fundamental constants (e.g., c , h , N_A , N_L , μ_B , etc.); these were obtained from the work of Cohen and Taylor.³ Similarly, improved reduced masses and isotopic abundances were taken from the data compiled in Ref. (4). More recent and accurate molecular parameters were adopted for the $v = 0$ level⁵ and $v = 1$ level⁶ of the $^{16}\text{O}_2$ isotope, and for the $v = 0$ levels of the $^{16}\text{O}^{17}\text{O}$ isotope⁷ and $^{16}\text{O}^{18}\text{O}$ isotope,⁸ respectively. These modifications will slightly improve the frequencies of the transitions.

It was noted that the strengths on the present edition of HITRAN for some SQ and SR rotational lines differed significantly from the values listed in the JPL catalogue.⁹ After some work, it was ascertained that these differences arise from deviations

of the rotational magnetic moment from the free electron value. These corrections to the strengths can be as large as 20 % for some transitions and the more accurate values incorporating these corrections will be implemented in the next HITRAN edition. Also, a minor programming error that resulted in the intensity of a single line (an $^{16}\text{O}^{18}\text{O}$ transition at 7.8 cm^{-1}) being too strong by a factor of four was corrected.

Because of the weakness of the magnetic dipole transitions, very little experimental has been reported for the halfwidths or for their variation with temperature. Consequently, we have not modified substantially the values for the halfwidths that are in the present compilation, although we have adopted for the temperature coefficient the value 0.83; this is an average value for a few measured transitions that was obtained by Chance et al.¹⁰

B. Quadrupole Transitions

Because of the absence of an electric dipole moment, the lowest non-vanishing electric moment is the quadrupole. Like the magnetic dipole transitions discussed above, the strengths of these transitions are also weak, but have been observed both in the laboratory¹¹ and in atmospheric spectra.¹² Using the same refined molecular data mentioned above, improved energy levels for the ground state and for the transition frequencies have been calculated. The largest improvement is for the strengths and transition moments of the pure rotational transitions resulting from the use a more accurate value of the quadrupole moment (0.34×10^{-26} versus an older value of 0.82×10^{-26} esu cm^2).¹³

C. Electronic Transitions

There are two electronic transitions currently in the HITRAN database: the $a^1\Delta_g \leftarrow x^3\Sigma_g^+$ and the $b^1\Sigma_g^+ \leftarrow x^3\Sigma_g^+$ bands. For the $v' = 0$ level of the $a^1\Delta_g$ state of $^{16}\text{O}_2$, we have adopted the improved molecular constants of Hillig et al.¹⁴ determined from the pure rotational spectrum; the constants for the other levels were not modified. Further, we have used the recently reported absolute band strength of Lin et al.¹⁵ [$A(0,0) = 1.3 \times 10^{-4} \text{ s}^{-1}$ versus the older value¹⁶ of $2.68 \times 10^{-4} \text{ s}^{-1}$], together with the same relative values of $A(1,0)$ and $A(0,1)$. As a result of this change, the intensities of all transitions in the band are reduced by approximately a factor of 2. No new data on halfwidths or their temperature dependence have been reported, so these parameters remain unchanged.

For the $b^1\Sigma_g^+ \leftarrow x^3\Sigma_g^+$ transitions in $^{16}\text{O}_2$, new intensities for self- and a few air-broadened halfwidths for the A-band ($v' = 0 \leftarrow v = 0$),¹⁷ and intensities and self-broadened halfwidths for the γ -band ($v' = 2 \leftarrow v = 0$),¹⁸ have been reported and incorporated into the compilation. The other parameters remain unchanged. We note in passing that it would be desirable to have similar data for the other less abundant isotopes as well as more extensive measurements of air-broadened halfwidths and their temperature dependence.

DISCUSSION, CONCLUSIONS, AND RECOMMENDATIONS

As discussed above, there have been major changes in the strengths of some of the magnetic dipole transitions, all the

quadrupole transitions, and for many of the electronic transitions. For the most part, only slight refinements in the frequencies resulted by incorporating more recent and accurate molecular constants. There are only minor changes in the halfwidths and their dependence on temperature.

There are other transitions which could eventually be included in the HITRAN compilation or in a separate compilation. These include: 1. The Schumann-Runge and Herzberg bands in the visible region; 2. The fundamental band of the magnetic dipole transitions in the ground electronic state;¹⁹ 3. The quadrupole branches of the A-band (i.e., the $v' = 0 \leftarrow v = 0$ rotational lines in the $b^1\Sigma_g^+ \leftarrow x^3\Sigma_g^+$ electronic transition;²⁰ 4. The $b^1\Sigma_g^+ \leftarrow a^1\Delta_g$ electronic transitions;²¹ and 5. The fine-structure atomic oxygen transitions in the 161 and 226 cm^{-1} spectral regions.²²

In addition to the transitions discussed above that can be incorporated into the current format of the HITRAN database, there are two other effects involving molecular oxygen that are important for atmospheric calculations. These are: interference due to overlapping of spectral lines, and collision-induced absorption. The effects of interference in the millimeter spectrum of O_2 are well known, and along with Zeeman effects, affect the propagation and absorption of radiation.²³ The collision-induced fundamental band of O_2 plays a significant role in transmission through the upper atmosphere²⁴ and is included approximately in the LOWTRAN computer codes.²⁵ A more accurate theoretical treatment including the absorption induced by other

species (e.g., N_2 , H_2O , etc.) and an improved temperature dependence would be useful for modeling the upper atmosphere. We note that similar effects in N_2 are even more important, especially in the spectral region beyond the band head of the $4.3\ \mu$ band of CO_2 .

In conclusion, although improvements (mainly in the strengths of the transitions) have been made, there is still a dearth of data for the oxygen molecule. Given the important role that this molecule plays in the Earth's atmosphere, it would be worthwhile not only to carry out further laboratory studies, but also to reconcile some of the discrepant data that exists in the literature. In particular, it would be useful to corroborate the strength of the $a^1\Delta_g \leftarrow x^3\Sigma_g^+$ transitions, whose values differ by a factor of two.

ACKNOWLEDGMENT

The author would like to acknowledge many useful conversations with Dr. L. S. Rothman of the Phillips Laboratory, and the Air Force Office of Scientific Research for their financial support.

REFERENCES

1. W. Steinbach and W. Gordy, Phys. Rev. **8**, 1753 (1973).
2. L. S. Rothman, R. R. Gamache, R. H. Tipping, C. P. Rinsland, M. A. H. Smith, D. C. Benner, V. M. Devi, J.-M. Flaud, C. Camy-Peyret, A. Perrin, A. Goldman, S. T. Massie, and L. R. Brown, J. Quant. Spec. Rad. Transfer, **48**, 469 (1992).
3. E. R. Cohen and B. N. Taylor, Phys. Today, Aug., (1990).
4. P. De Bievre, M. Gallet, N. E. Holden, and I. L. Barnes, J. Phys. Chem. Ref. Data **13**, 809 (1984).
5. L. R. Zink and M. Mizushima, J. Mol. Spectrosc. **125**, 154 (1987).
6. M. Mizushima, K. M. Evenson, J. A. Mucha, D. A. Jennings, and J. M. Brown, J. Mol. Spectrosc. **100**, 303 (1983).
7. M. Mizushima, L. R. Zink, and K. M. Evenson, J. Mol. Spectrosc. **107**, 395 (1987).
8. M. Mizushima and S. Yamamoto, J. Mol. Spectrosc. **148**, 447 (1991).
9. R. L. Poynter and H. M. Pickett, Appl. Optics **22**, 2235 (1985).
10. K. V. Chance, W. A. Traub, K. W. Jucks, and D. G. Johnson, Int. J. of Infrared and Millimeter Waves **12**, 581 (1991).
11. J. Reid, R. L. Sinclair, A. M. Robinson, and A. R. W. Mc Kellar, Phys. Rev. **A24**, 1944 (1981).
12. A. Goldman, J. Reid, and L. S. Rothman, Geophys. Res. Letts. **8**, 77 (1981); L. S. Rothman and A. Goldman, Appl. Optics **20**, 2182 (1981).
13. E. R. Cohen and G. Birnbaum, J. Chem. Phys. **66**, 2443 (1977).

14. K. W. Hillig, C. C. W. Chiu, W. G. Read, and E. A. Cohen, J. Mol. Spectrosc. **109**, 205 (1985).
15. L.-B. Lin, Y.-P. Lee, and J. F. Ogilvie, J. Quant. Spec. Rad. Transfer, **39**, 375 (1988).
16. R. M. Badger, A. C. Wright, and R. F. Whitlock, J. Chem. Phys. **43**, 4345 (1965).
17. K. J. Ritter and T. D. Wilkerson, J. Mol. Spectrosc. **121**, 1 (1987).
18. M. A. Melieres, M. Chenevier, and F. Stoeckel, J. Quant. Spec. Rad. Transfer, **33**, 337 (1985).
19. M. Dhang-Nhu, R. Zander, A. Goldman, and C. P. Rinsland, J. Mol. Spectrosc. **144**, 366 (1990).
20. J. W. Brault, J. Mol. Spectrosc. **80**, 384 (1980).
21. E. H. Fink, H. Kruse, K. D. Setzer, D. A. Ramsay, and M. Vervloet, Acta Phys. Hung. **67**, 67 (1990).
22. T. G. Kyle in *Atmospheric Transmission, Emission and Scattering*, Pergamon Press, New York, 1991.
23. P. W. Rosenkranz, J. Quant. Spec. Rad. Transfer, **39**, 287 (1988).
24. C. P. Rinsland, R. Zander, J. S. Namkung, C. B. Farmer, and R. H. Norton, J. Geophys. Res. **94**, 16303 (1989).
25. F. X. Kneizys et al. AFGL-TR-88-0177, Hanscom AFB, MA.

EXPERIMENTAL INVESTIGATION OF HOMOGENEOUS AND HETEROGENEOUS
NUCLEATION/CONDENSATION PROCESSES AND PRODUCTS IN COIL.

Philip D. Whitefield
Research Associate Professor
Department of Chemistry
Cloud and Aerosol Sciences Laboratory,
University of Missouri - Rolla. (UMR/CASL).
Norwood Hall G11
Rolla, MO 65401

Final Report for:
Research Initiation Program
Phillips Laboratory

Sponsored by:
Air Force Office of Scientific Research
Bolling Air Force Base, Washington, D.C.

October 1992

EXPERIMENTAL INVESTIGATION OF HOMOGENEOUS AND HETEROGENEOUS
NUCLEATION/CONDENSATION PROCESSES AND PRODUCTS IN COIL.

Philip D. Whitefield
Research Associate Professor
Department of Chemistry
Cloud and Aerosol Sciences Laboratory,
University of Missouri - Rolla.

Abstract

This paper describes the preliminary results of an ongoing study to characterize the nature and sources of sub-micron aerosols in the Phillips Laboratory small scale supersonic COIL device and other COIL devices. Aerosols from both sub- and supersonic flow regimes were sampled and characterized using the University of Missouri-Rolla, Mobile Aerosol Sampling System (MASS). Under all operating conditions where the oxygen generator discs were rotating, significant concentrations of aerosols were detected. Typically these aerosols had peak dry diameters of <0.05 microns and nascent wet diameters of <0.08 microns. Their total number density increased with increasing rotating disc velocity and with the addition of chlorine. A maximum number density of $<3000/\text{cc}$ was observed at maximum chlorine flow rates when the initial generator mixture had been heavily depleted (i.e. neutralized with chlorine). Experiments to observe homogeneous nucleation of aerosols in simulated supersonic laser gas flows were unsuccessful. The critical supersaturation spectra for a KOH, KCl, I_2 have been measured and compared to theoretical calculations. Scanning Electron Microscopic analysis has been performed on particulates extracted from both sub- and supersonic flow regions using impaction on stainless steel substrates. The particulate samples were almost exclusively made up of potassium and chlorine in a 1:1 ratio.

EXPERIMENTAL INVESTIGATION OF HOMOGENEOUS AND HETEROGENEOUS
NUCLEATION/CONDENSATION PROCESSES AND PRODUCTS IN COIL.

Philip D. Whitefield

INTRODUCTION.

This report describes how the UMR Mobile Aerosol Sampling System is being used in conjunction with a small scale COIL and a supersonic nozzle flow system, to verify the existence of sub-micron aerosols in COILs, to characterize these species, and to assist in the validation of models addressing the role of such species in COIL performance.

The presence, nature and properties of aerosols in the reactive flow of COIL devices are not well characterized. Excellent beam quality results and the short residence times associated with supersonic flow conditions permit an estimate of less than 0.1 microns for an upper bound on the typical diameter to be expected for such species. Recent anomalous device performance data have been rationalized through models invoking sub-micron aerosols[1]. However, no direct experimental evidence for the creation and or existence of such species exists.

Recent COIL data obtained during the operation of several independent COIL devices demonstrate anomalous pressure increases (typically 38%) in the laser cavity, during a given run[1 - 3]. These pressure increases are estimated to cause on the order of a factor of two reduction in laser output power. Furthermore, these pressure increases are concomitant with significant increases in water vapor concentration approaching 5 mole% of the total laser gas flow. An analysis, intended to rationalize these data, has been performed [1] and has led to the hypothesis of a condensation shock model. In this model the cavity pressure increase is assumed to result from an instantaneous heat release into the reactive flow creating a shock. This heat is assumed to come from the enthalpy of condensation of water droplets that homogeneously nucleate in the extremely high supersaturations of water vapor that occur in the exit plane of

a COIL supersonic nozzle. The calculated heat release and system residence time lead to the prediction that the proposed condensation shock will produce water droplets less than 0.002 micron in diameter with a total number density on the order of $1.0 \times 10^{13} \text{ cm}^{-3}$. The precedents for, and effects of, water condensation in supersonic nozzles have been studied extensively [4], and this model simulates the actual physical performance data of the laser[1].

Identifying homogeneous nucleation in a laser device such as a COIL is complicated by the production of heterogeneously nucleated aerosols in the two phase (gas/liquid) singlet oxygen generator. A schematic diagram of a small scale COIL device is shown in figure (1). The generators employed in COIL devices typically operate at sub-atmospheric pressures (about 50torr) and rely on a two phase heterogeneous reaction between aqueous basic hydrogen peroxide (BHP) and gaseous chlorine to produce gaseous electronically excited oxygen. The generator products including metal salt aerosols, heterogeneously nucleated water and BHP aerosols are swept through liquid separatorss (in two of the three devices cited) and on to the laser nozzle in helium carrier gas. The efficiency of particulate removal by the cold traps is unknown. Inertial and gravitational considerations assist in the efficient removal of large aerosols i.e. those typically with diameters >10 micron. The motion of smaller aerosols is largely Brownian in nature and their removal in the cold traps is expected to be considerably less efficient since these particles will be expected to follow the laser gas flow streamlines. Iodine is introduced into the reactive flow in its gaseous state, having been pre-vaporized. The presence of sub micron aerosols in the nozzle offer the potential for heterogeneous iodine nucleation and reduced device performance efficiency.

This study if performed in the laser device alone has the added complication of having to distinguish between concomitant homogeneously and heterogeneously nucleated aerosols when the sampling port is in the cavity i.e. supersonic region. To avoid this complication it was decided to simulate the condensation shock phenomena in a supersonic nozzle flow system. This facility was essentially the laser flow system operated with no liquid phase reagents in

the generator stage (see figure (1)). In the simulation experiment flows of water vapor laden carrier gas were introduced to the flow system in the subsonic generator region and expanded through the supersonic nozzle under the typical laser operating conditions where the shock had been observed. If the shock was driven by purely a homogeneous mechanism this event would be observed without the complication of concomitant heterogeneously nucleated aerosols being carried in the flow from the generator.

The size range of droplets predicted [1], in the absence of coagulation, falls close to the limit of detectability of even the state of the art UMR facilities employed in this study. At the aerosol number densities predicted [1], however, coagulation will readily occur. The degree of coagulation will depend on the residence time. The coagulation rate for 0.002micron aerosols collecting 0.002micron aerosols is $0.968\text{E}-8 \text{ cm}^3/\text{s}$. this is the number of scavenging events per collector particle per unit concentration of collectees. For an aerosol concentration of $1.0\text{E}13 \text{ cm}^{-3}$, the rate of scavenging events per collector particle is $0.968\text{E}05 / \text{s}$. The size distribution initially monodisperse at size 0.002 microns will broaden with time. The time constant for depletion of the 0.002 micron size is 10.3 microseconds. The net result of coagulation will be a shift in the peak of the size distribution to center on aerosols of larger diameter. Detection of homogeneously nucleated droplets in the cavity could also be hindered by the possibility of the re-evaporation of the droplets once formed either in the flow system or during sampling. Re-evaporation is not predicted within the laser system where all physical parameters and relative humidity appear to remain constant following the shock[1]. Re-evaporation could represent a serious problem during sampling and dilution of the laser flow stream, where the degree of isothermality required to eliminate the potential for re-evaporation will be demanding. The ammonium hydroxide subsystem of the sampling probe facility was included to address this problem (see experimental section). There are, however factors such as, coagulation, residual aerosol and the possibility that the droplets will form as ice particles, that will help to alleviate the problem of droplet non-detectability.

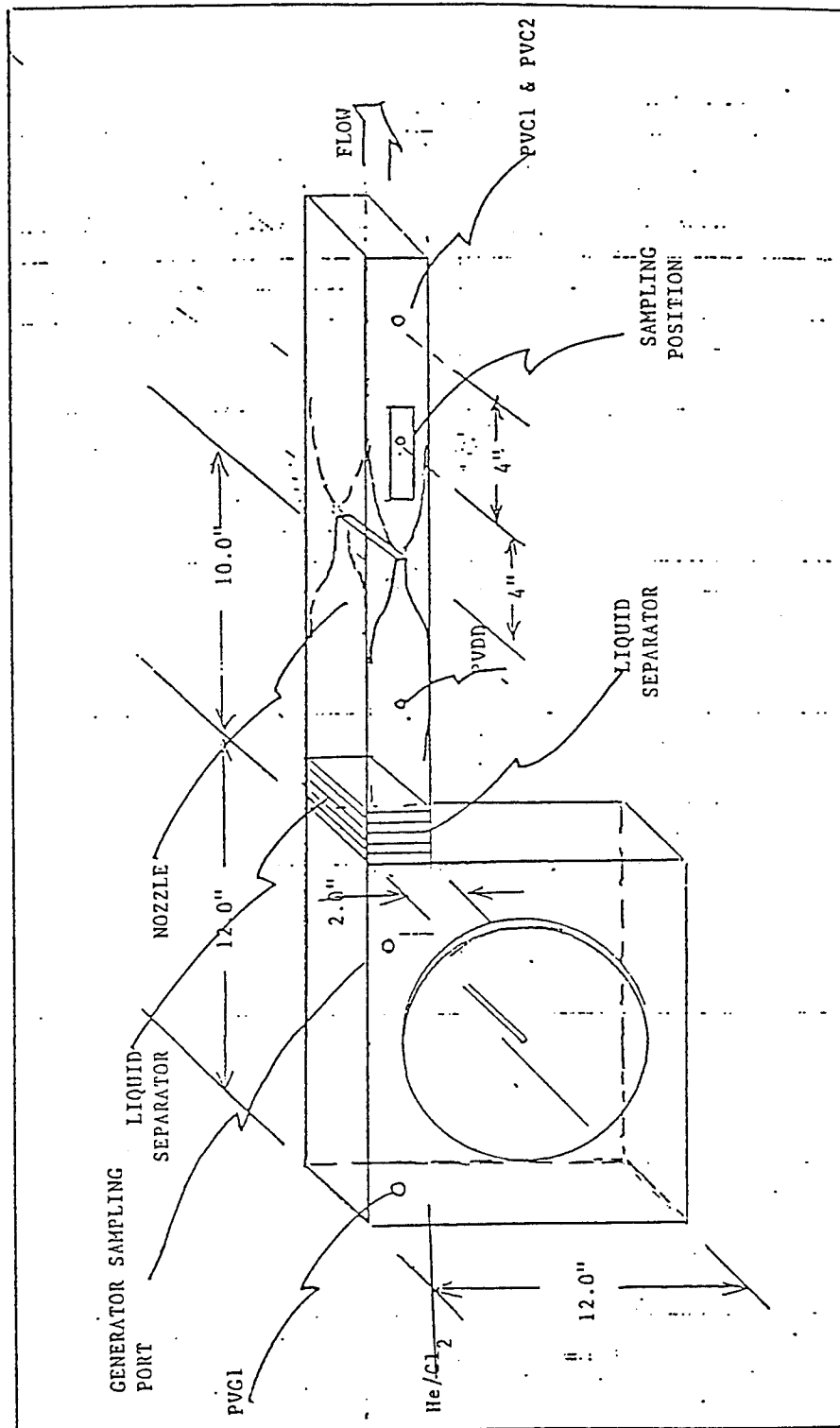


Figure 1. Schematic of "Pee Wee" COIL and Supersonic Flow System

EXPERIMENTAL

The initial experimental activity in this study was associated with designing, constructing and operating a sample probe facility capable of extracting and maintaining the integrity of a multi-phase sample as it is drawn from a sometimes chemically reactive supersonic flow. The physical parameters of the supersonic nozzle simulation device and the laser fall within the ranges: flow velocity Mach 0.2 - Mach 2.0, total pressure 2 - 50 torr, temperature 150 - 350K. The partial pressure of water lies within the range 2 - 5% of the total system pressure. It is important, therefore, in the case of detecting homogeneously nucleated aerosols, to ensure that there is no temperature increase as the sample flow decelerates through the sampling probe and that the ambient water concentration remains the same. These criteria are met by coupling the sample probe to an evacuable chamber in which reactor species can be diluted and pressurized under isothermal and carefully humidified conditions and temporarily held for examination. Figure (2) is a schematic diagram of this facility. The ammonium hydroxide subsystem is used to convert any homogeneously nucleated aerosols to solution aerosols as they are withdrawn from the flow system. This conversion provides a means of establishing the existence of homogeneously generated aerosols in the event that the aerosols should encounter an environment where they could reevaporate. Once converted to solution aerosol a residue that can be detected will persist after reevaporation. The methodology for heterogeneously nucleated aerosol detection is based on the principle that such aerosols will leave a residue (dry particle) upon reevaporation. Such aerosols are dried immediately upon extraction from their source and their dry particle properties are characterized. A knowledge of their hydration properties permits the development of growth models.

During this study no effort was made to design and construct a specialized sampling orifice. Instead, a simple tube (orifice i.d. 0.675") was mounted either in the streamlines of the flow (for large diameter aerosols (>0.01 microns) or perpendicular to the flow through an access port mounted on the side

of the flow system for smaller aerosols (<0.01 microns).

The Mobile Aerosol Sampling System (UMR-MASS), figure (3), and the sampling probe facility described above were employed to characterize aerosols in terms of their total number density, size distribution and/or hydration properties. The experimental sequence of events is as follows. (For a more detailed description of the UMR-MASS methodology see references 5-9)[5-9].

(a) Number Density and Size Distributions -- The particulate stream emanating from the sampling probe and dilution facility is sent through, initially, an alcohol counter to examine the total size range of aerosols sampled and determine the total number density. For a size distribution the aerosol is charged with a bipolar charger and is then sized via its electric mobility. The EAC passes only particles contained in a narrow size range (range width is typically 10% of mean size). A specific particle size is set by the EAC voltage. This voltage and hence the selected particle size is variable. The resulting monodisperse particle stream is then passed through the alcohol counter where it is exposed to a fixed supersaturation of alcohol of sufficient magnitude to condense alcohol on the particle, thus forming aerosols large enough to be detected by the optical particle counter, OPC, sub system of the counter. The enlarged aerosols are passed through the OPC where individual aerosols are counted and the aerosol concentration is determined.

(b) Hydration Properties -- For particulate hydration property measurements, specifically the critical supersaturation spectrum (i.e. the minimum supersaturation of water that will cause condensation of water onto a particle to produce a continuously growing droplet presented as a function of particle diameter) is measured. The particulate stream is first passed through an EAC to select a specific size element of the sample distribution. The resulting monodisperse element is then passed through a saturation chamber holding water vapor at 100% relative humidity. As the aerosols pass through the chamber they deliquesce and increase in diameter. This growth is monitored by passing the droplets, after they exit the saturator, through a second EAC, the

output of which can be monitored by the alcohol counter. Should a particulate prove difficult to hydrate (i.e. require significant supersaturations of water a continuous flow diffusion chamber (CFD) is employed.

The setup and operation of the laser device and supersonic nozzle facility is not described in this report. Detailed descriptions of this activity can be found elsewhere [10-12].

Figure 2. Schematic of the Sample Conditioning system.

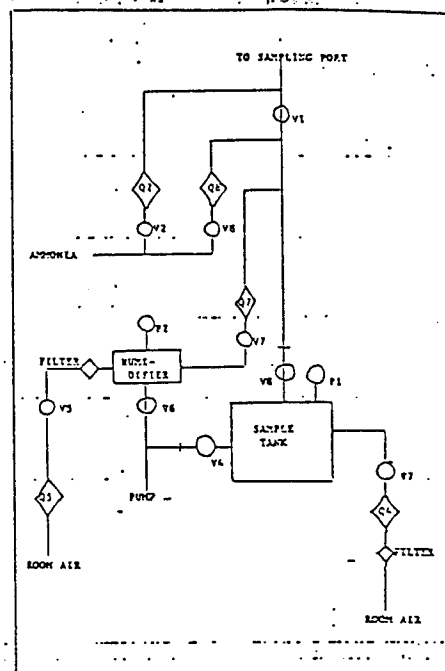
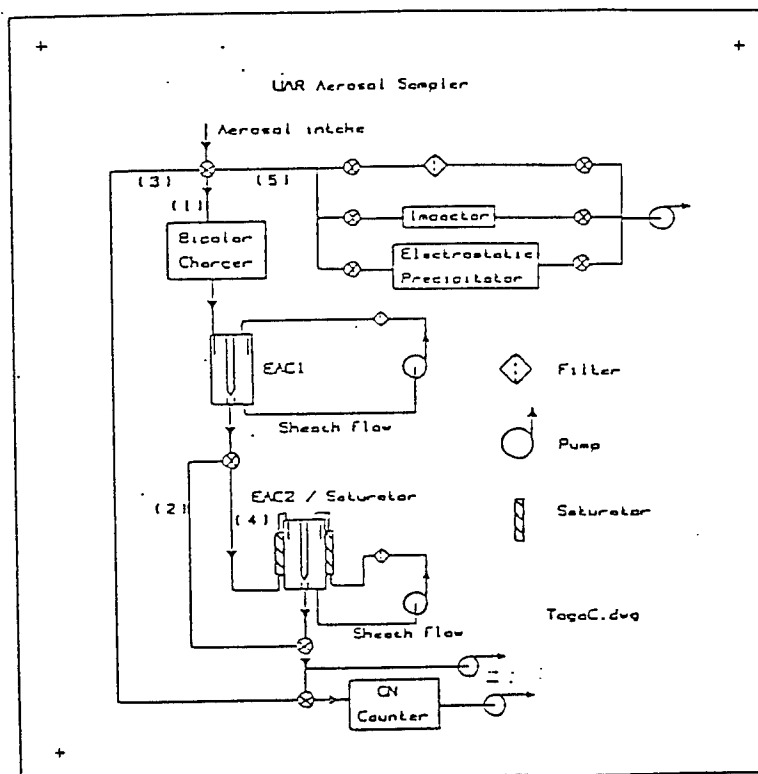


Figure 3. Schematic of UMR-MASS
(Mobile Aerosol Sampling System)



RESULTS

Aerosol size distribution data determined with the use of an inversion application [13], show the mean dry diameter of aerosols generated in the oxygen-singlet-delta generator to be approximately $0.03\ \mu\text{m}$, see Table 1. Typical size distributions for the generator and cavity and data gleaned from such a distribution can be seen in Figures 4 and 5, respectively. Based on the average dry aerosol diameter of $0.03\ \mu\text{m}$ and a 7.0M BHP molarity a nascent wet aerosol diameter was calculated to be $0.047\ \mu\text{m}$. Determination of the aerosol particle densities required the adoption of a unit of measure normalizing the results with pressure so that comparisons could be drawn with respect to varying pressure in different sections of the device. The normal particle concentration unit, usually expressed in number of particles per cubic centimeter, was thus modified by dividing the particle concentration by the environmental pressure from which the sample was drawn. This yielded a unit in concentration per torr, allowing comparison of samples without regard for pressure differences. In this manner, the concentration of aerosol particles in a given sample can be determined by finding the product of its new unit of concentration per torr and environmental pressure. Generator aerosol samples typically yielded aerosol densities around 300 particles/cc/torr with excellent reproducibility, see Figure 6. The generator aerosol density does not appear to be related to generator liquid temperature. Cavity aerosol concentrations are typically an order of magnitude lower than the generator aerosol concentrations, ranging from 20 to 90 particles/cc/torr, see Figure 6. Interestingly, although temperature does not appear to play a major role in the variation of the cavity aerosol concentrations, these concentrations seem to increase as the BHP solution is exhausted, see Figure 7.

Further characterization of the aerosol involved determining the critical supersaturation spectra of potential solutes. Theoretical critical supersaturation curves for KOH, KCl, NaCl, and Iodine were generated using the Kohler Equations [14]. Experimental data for each of the salts were in excellent

agreement with the theoretical calculated spectra; KCl and NaCl experimental data fell directly on their predicted curves, and KOH was within 10% (instrumental error) of its theoretical curve, see Figures 8 and 9. The theoretical critical supersaturation spectra for Iodine differed from its experimental data, possibly due to approximations in the theoretical model. Nevertheless, both theoretical and experimental spectra for Iodine reside in higher supersaturation regimes than those of the ionic salts as would be expected for substances with low solubilities in water.

SEM analysis was performed at UMR/CASL on stainless steel substrates impacted with particulates from both the sub- and supersonic regions of the laser device. Before elemental analysis was performed on the particulate impacted substrates they were examined with an optical microscope to ensure that sample volumes on the order of 1 cubic micron were present. Without this degree of impaction it would not be possible to separate the elemental analysis of the particulates from that of the substrate. Table 2 is a listing of the impacted substrates and their resulting elemental analyses. The control sample appeared to have no aerosol deposited on it. The other samples, 2-5, had microscopic crystals adhering to the substrates. Potassium and chlorine are present in all cases in near 1:1 ratios, suggesting potassium chloride salt as the primary impactant. Sample #3 appears to have other elements impacted, predominantly silicon, calcium and sodium suggesting contamination of the sample by sand or mineral grit.

TABLE OF AEROSOL SIZE DISTRIBUTION DATA TERMINOLOGY

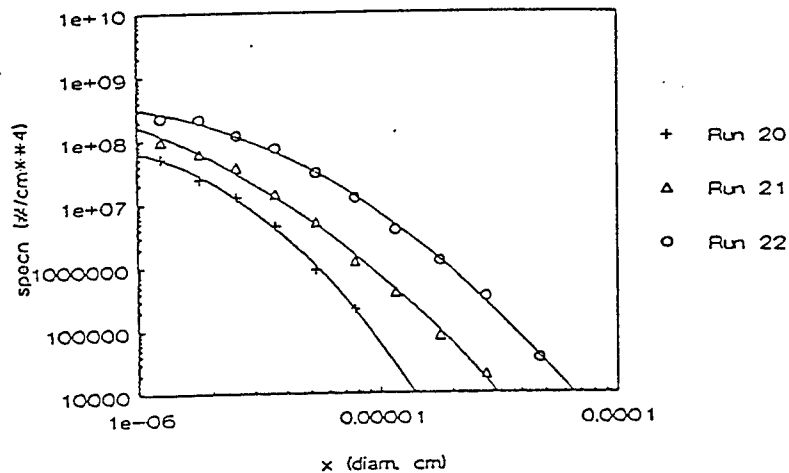
XBAR	Average size (diameter, microns) for this distribution.
XBARA	Diameter corresponding to the aerosol area mean.
XBARV	Diameter corresponding to the aerosol volume mean.
SUMNX	Aerosol's total concentration.
CMASS	Mass of aerosol collected in 60 min at 20 L/min by a cascade impactor which collects particles with diam > 0.2 μ m.
SIZE	Particle diameter for the j-th aerosol family, in μ m.
XN	Concentration of the j-th aerosol size family.
SPECN	Aerosol size differential concentration, dC/dD, per unit diameter interval; $\#/\text{cm}^3$.
SUM4	Conc. of particles with diam D > 0.04 μ m.
SUM5	Conc. of particles with diam D > 0.05 μ m.
STime	Time in seconds that sample was collected.

TABLE OF SELECT AEROSOL SIZE DISTRIBUTION DATA

Sample	Description	XBAR(cm)	#/cc/torr	STime(s)
Run 11	Gen, no chem	0.541e-5	0.6197	35
Run 12	Gen, 0, mix, 5rpm	0.931e-5	0.2117	40
Run 13	Gen, -18, 45rpm	0.892e-5	60.5363	15
Run 14	Gen, -18, chem	0.290e-5	2926.00	20
Run 16	Cav, -18, chem	0.493e-5	108.459	20
Run 18	Gen, -20, chem	0.345e-5	299.697	2
Run 20	Cav, -10, chem	0.244e-5	18.5714	2
Run 21	Cav, -20, chem	0.274e-5	27.9661	4
Run 22	Cav, 0, chem	0.370e-5	89.1176	4
Run 23	Gen, -10, chem-I2	0.333e-5	307.051	3
Run 24	Gen, 0, chem-I2	0.289e-5	294.600	3
Run 26	Cav, -20, chem-I2	0.303e-5	12.9796	4

Table 1

Aerosol Size Distribution Cavity



Aerosol Size Distribution Generator

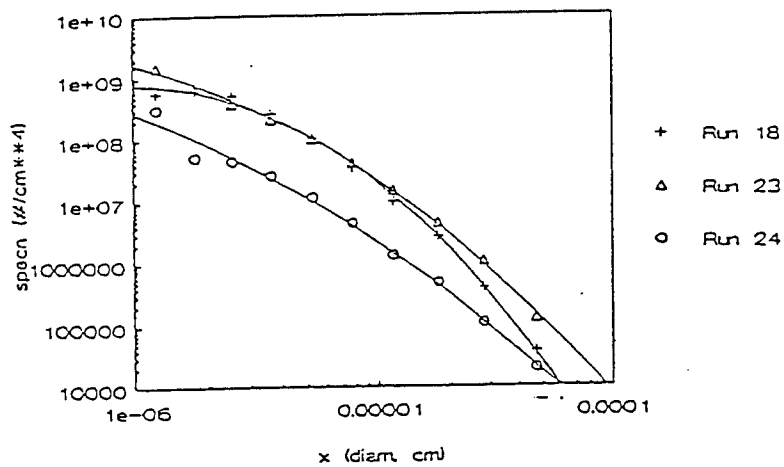
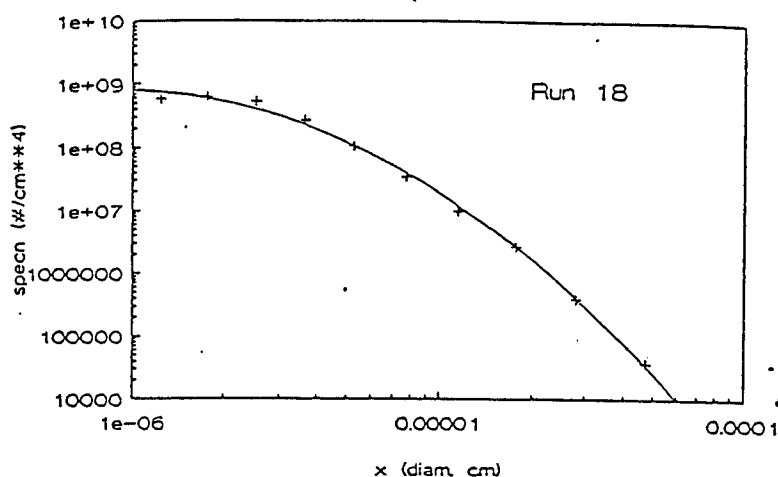


Figure 4

Aerosol Size Distribution Generator

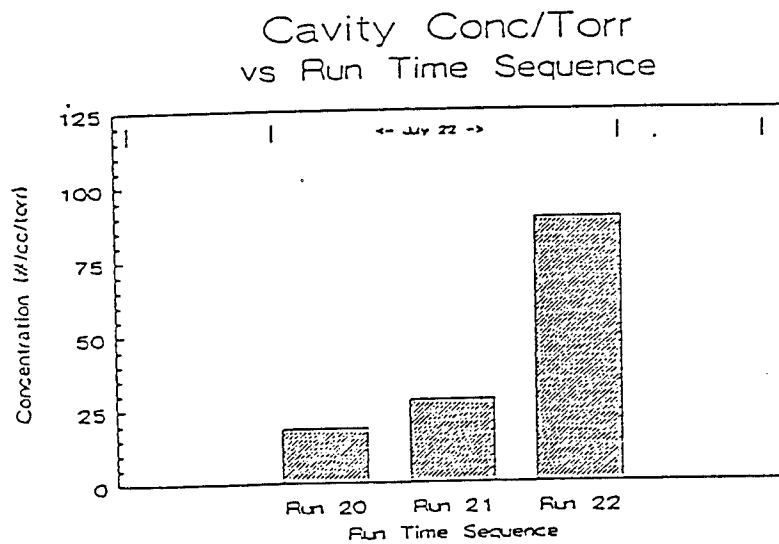
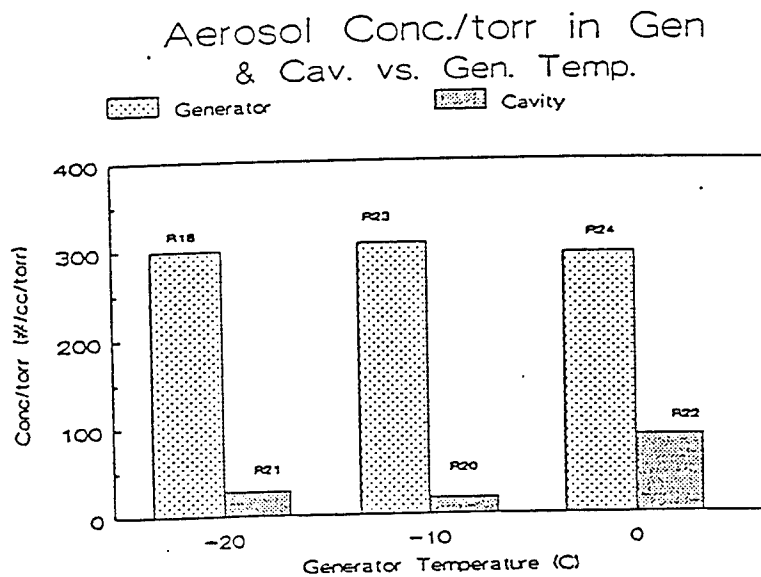


Run 18, decay adjustment (sampling tank):

$\text{XBAR (cm)} = 0.3454\text{D-05}$ $\text{SUMNX (\#/cm**3)} = 1978.$
 $\text{XBARA(WRT AREA, CM)} = 0.4615\text{D-05}$ $\text{XBARV(WRT VOL, CM)} = 0.6392\text{D-05}$
 $\text{CMASS (MICRO-G)} = 0.1292$
 $\text{SUM4 (\#/CM**3, > .4 uM)} = 401.56$
 $\text{SUM5 (\#/CM**3, > .5 uM)} = 401.56$
 $\text{SIGMA} = 0.3060\text{D-05}$
 $\text{CCMASS (TOTAL MASS, MICRO-G)} = 0.3246$

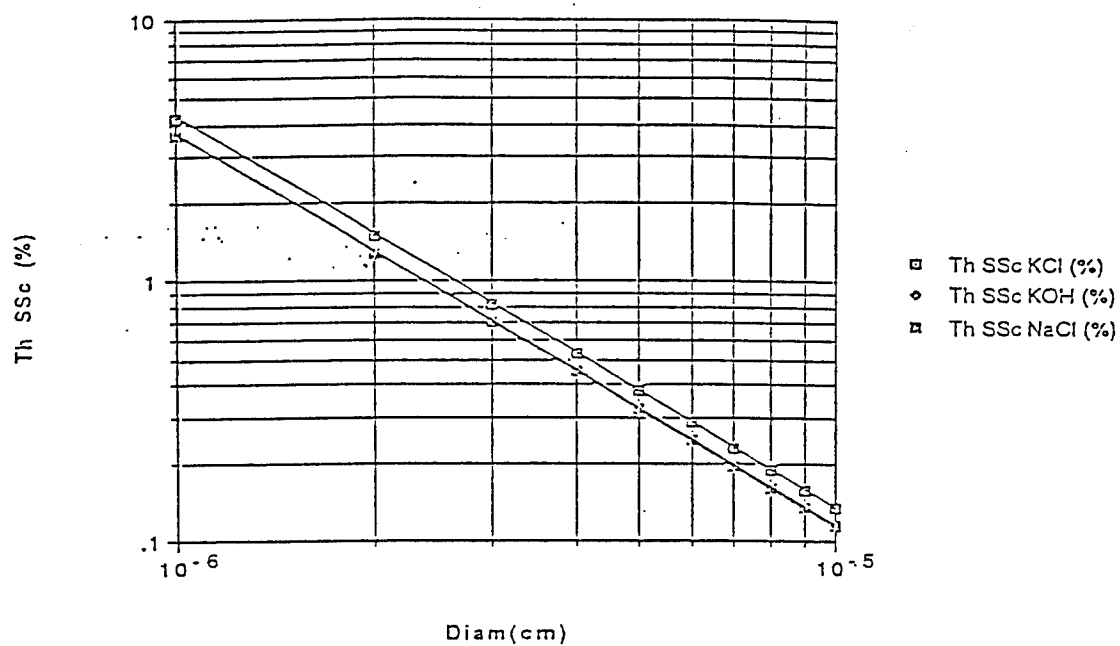
J	POWER	XN (#/CM**3)	SIZE	SPECN	CUMUL
1	1.20	0.310D+03	0.124D-05	0.585D+09	0.216D+10
2	1.20	0.407D+03	0.177D-05	0.630D+09	0.158D+10
3	1.20	0.496D+03	0.254D-05	0.530D+09	0.947D+09
4	2.02	0.363D+03	0.365D-05	0.265D+09	0.417D+09
5	2.64	0.213D+03	0.528D-05	0.104D+09	0.152D+09
6	2.93	0.110D+03	0.774D-05	0.351D+08	0.481D+08
7	3.30	0.494D+02	0.115D-04	0.993D+07	0.131D+08
8	3.74	0.224D+02	0.177D-04	0.270D+07	0.313D+07
9	3.74	0.582D+01	0.282D-04	0.393D+06	0.430D+06
10	3.74	0.711D+00	0.473D-04	0.372D+05	0.372D+05

Figure 5



Figures 6 and 7.

Theoretical SSC of KCl, KOH, and NaCl vs. Diameter of Particle



Theoretical and Experimental SSC of KOH vs. Diameter of Particle

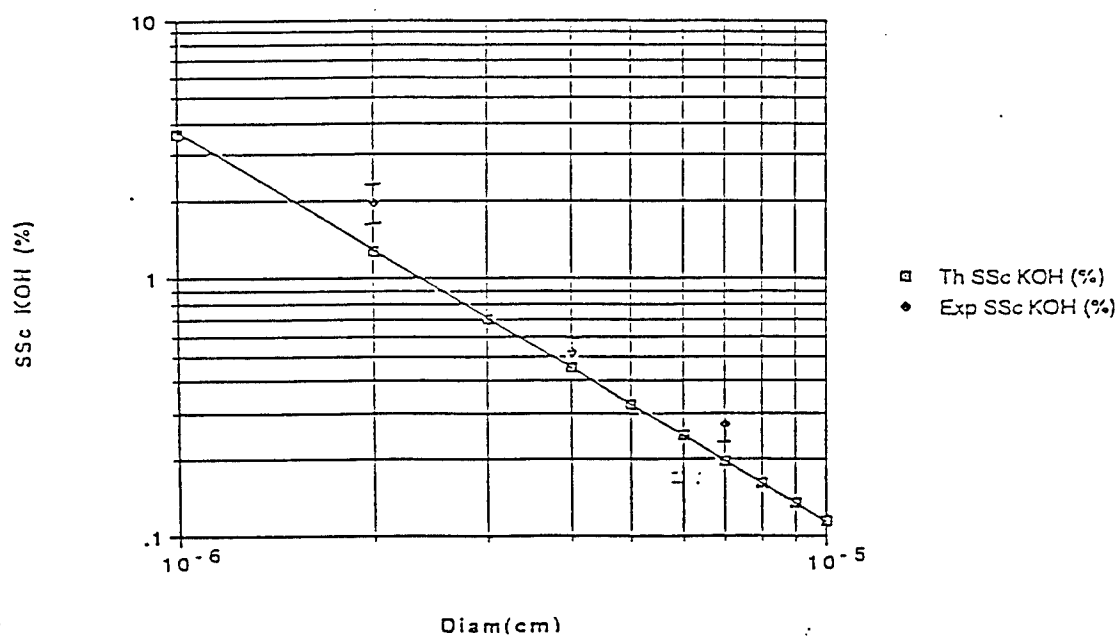
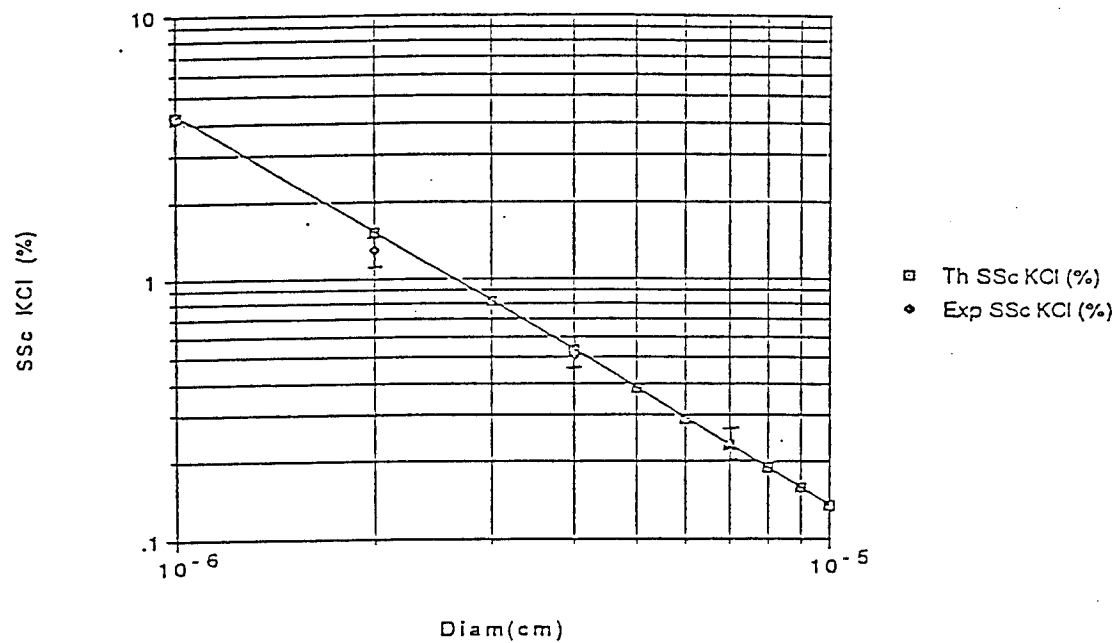


Figure 8.

Theoretical and Experimental SSc of KCl vs. Diameter of Particle



Theoretical and Experimental SSc of NaCl vs. Diameter of Particle

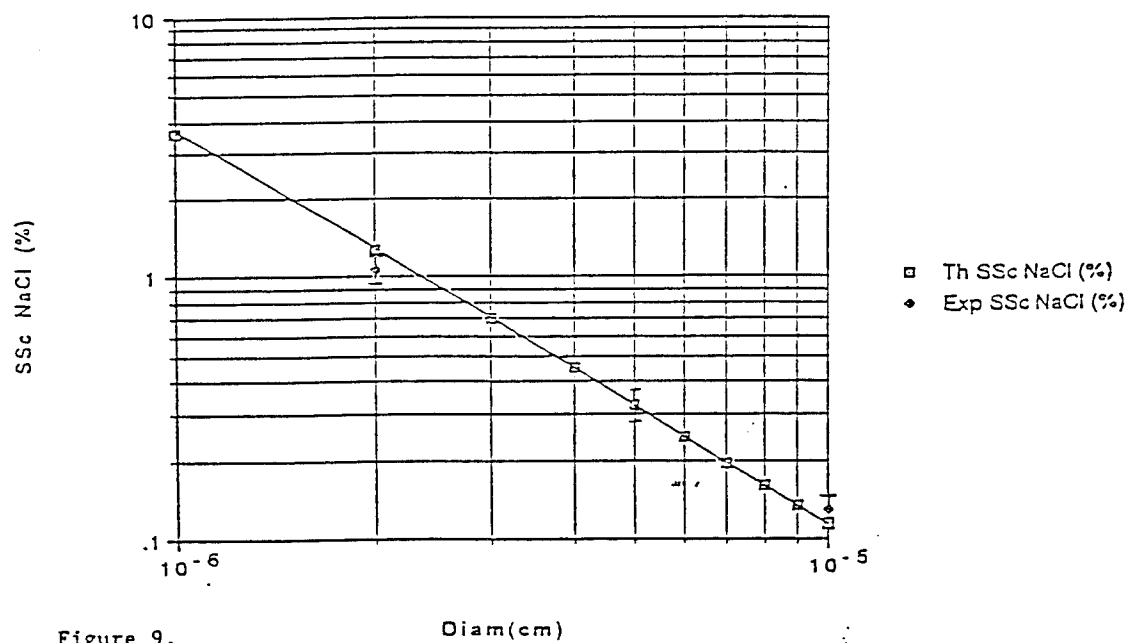


Figure 9.

Table 2. SEM Elemental Analysis Results

SAMPLE	ELEMENT	ATOM %	Wt%
#2	K	51.32	53.77
	Cl	48.68	46.23
#3	Al	7.95	6.72
	Si	26.97	23.73
	S	1.45	1.45
	Cl	4.72	5.24
	K	4.58	5.61
	Ca	33.36	41.89
	Ti	0.00	0.00
	Mg	5.85	4.46
	Na	15.12	10.89
#4	K	49.62	52.07
	Cl	50.38	47.93
#5	K	48.63	51.08
	Cl	51.37	48.92

DISCUSSION

The data acquired with the UMR-MASS was limited by the amount of time the UMR-MASS could be deployed and operated at the Phillips Laboratory based on the funding of this activity through our AFOSR RIP grant. In order to capitalize on this small window of opportunity (10 days) we used this AFOSR sponsored Summer Research Program Faculty Associateship and Graduate Student Associateship to prepare for the arrival of the UMR-MASS, to assist in the data acquisition with the UMR-MASS, to make independent laboratory based measurements (hydration properties) and to interpret the results of this preliminary study.

Homogeneous Nucleation - If the pressure ramp observed; when the three COIL devices were operated with high partial pressures of water vapor; was due to pure homogeneous nucleation down stream of the laser's supersonic nozzle, it should be possible to simulate this event in a supersonic flow system employing the same nozzle, using appropriate mass flows of carrier gas and water vapor. Repeated attempts were made to simulate the pressure ramp in this manner and in all cases no ramp was observed. During the attempts to simulate the pressure ramp cavity gas samples were withdrawn and analyzed with the UMR-MASS for the presence of aerosol. The background aerosol concentration in the supersonic flow system were extremely low < 0.1 particles/cc. and no significant concentrations of aerosol over and above the background count were observed. The logical interpretation of these results are that the pressure increase cannot be a simple gas dynamic effect brought about by homogeneous nucleation.

A re-investigation of the calculations upon which the homogeneous nucleation rational is based is probably warranted at this time. Also, it would be worthwhile to attempt this simulation experiment again but in this case utilizing the Phillips laboratories in-situ water diagnostic to accurately follow the water vapor concentration profile in the supersonic flow facility. A mass spectrometer attached to the flow system would also be a valuable diagnostic to investigate both molecular cluster formation and whether or not charged species emanate from the generator. A justification for such measurements is given later in the discussion.

Heterogeneous Nucleation - This work represents the first experimental data characterizing particulates in the flow stream of a COIL. The typical concentrations measured in this study correlate well with those used in a Mie scattering model to account for non-saturable losses in COILs[15]. As expected the generator is an excellent source of heterogeneously nucleated aerosol. The preliminary data using the UMR-MASS to characterize these aerosols suggests that this is an ideal tool with which to investigate the generation characteristics and fate of these aerosols. These results indicate that heterogeneously nucleated aerosols are mechanically generated during the explosion of gas bubbles on the basic hydrogen peroxide (BHP)/chlorine interface and that certain generator operating parameters such as disc velocity and degree of neutralization of the BHP can strongly influence the aerosol production rate. To understand the role these aerosols play in the performance and efficiency of a COIL device a test plan should be devised and appropriate measurements with the UMR-MASS performed. This data acquisition effort will require the design and construction of extra sample accumulators, and of, an orifice with high sampling efficiency in the supersonic cavity region. Additional sampling ports will also be required before and after the liquid separator plates and cold traps (if applicable) and beyond the cavity region close to the pumps. Data should also be acquired on an independent device such as RADICL. The opportunity for intercomparison of data from two separate devices would be of great value. The impact of these aerosols on iodine dissociation and excitation should also be explored. The hydration property measurements indicate that iodine coated aerosol will have higher critical supersaturations than those of the simple ionic salt aerosols.

These preliminary experiments answer many questions about aerosols in COILs and have led to recommendations for further study particularly in the case of characterizing the role of heterogeneously nucleated aerosols. The pressure ramp and potential condensation shock issue, however, have not been resolved. It is clear from the data on number density, size distribution and hydration properties of heterogeneously nucleated aerosols that these species, as characterized in

these preliminary experiments, alone could not condense enough water within their cavity residence time to release the required amount of heat. There is a possibility, however, that the true number of heterogeneously nucleated aerosols emanating from the generator has been underestimated in the experiments thus far. Should the true number of aerosols exceed the measured number by several orders of magnitude then it would be possible to account for the pressure ramp via an enthalpy of condensation rational. The UMR-MASS, although state of the art in detectability, has a lower limit in aerosol diameter detection of 0.01 microns. This limit is governed by the design of the aerosol counter. A close inspection of the size distribution plots, figures (4) and (5), do not show that the size distribution is single mode or that the peak in the distribution has been clearly met. There is no a priori reason to expect a single mode distribution here. For combustion aerosols from jet engines for example, a single mode distribution is always found[7], but in comparison a typical atmospheric aerosol distribution is far more complex and tends to have a significant number density beyond the limit of detectability of CNC counting systems[14]. The mechanical generation of aerosols via bubble explosions on the liquid/gas interface has been examined previously[15] and may lend credence to the underestimation of aerosol concentrations. The size of the aerosols produced is directly related to the initial bubble diameter. Submicron dry particles in the size ranges of interest in this problem have been detected from sea water foam. Serious thought, therefore, should be given to improving the technique to detect and count smaller diameter aerosols. One other potential mechanism to explain the pressure ramp through condensation on a high concentration of nucleating species ($>10^8/\text{cc}$) is to propose the presence of charged species in the generator effluent. One method for examining this possibility would be to introduce an electric field perpendicular to the flow stream in the subsonic flow region of the duct.

The valuable original research data and inevitable questions arising from this preliminary study open the door to further discussion on the approach for future experiments some of which could be clearly identified as tasks for a 1992 RIP proposal.

CONCLUSIONS

Heterogeneously nucleated aerosols are present in COILs. They are mechanically produced in the generator and their production rate and size are governed by generator operating parameters. The relationship between these parameters and aerosol production should be explored in detail. The limits of detectability of aerosols using the UMR-MASS in its current state of the art configuration may have led to an underestimate of the total concentration of aerosols produced in the generator. As a result of the studies to date, design up grades should be made to the sampling probe system and counting system to customize the UMR-MASS to this COIL investigation.

The inability to simulate the pressure ramp in the supersonic nozzle flow system indicates that the pressure ramp is not a simple gas dynamic effect arising from the enthalpy of condensation associated with a homogeneous nucleation event. The calculations upon which the homogeneous nucleation rational are based should be re-examined.

The principles of operation and performance of the spray generator concepts should be examined to determine whether submicron aerosol formation will occur in these devices and whether it will affect their predicted performance.

ACKNOWLEDGEMENTS

On behalf of my UMR/CASL colleagues I would like to express our appreciation for the financial support and encouragement AFOSR, Phillips Laboratory/(LIDB) and the University of Missouri-Rolla have provided throughout this project. In particular we are indebted to Dr's. Truesdell and Helms at PL/LIDB for their continued close involvement and support.

REFERENCES.

- (1) Private Communication, D. Plummer RDA, 19 July 1991.
- (2) RADICL Data presented at a briefing on the condensation shock phenomena by D. Plummer RDA, March 1992.
- (3) Phillips Laboratory Small Scale COIL data presented by C. Helms, July 1992.
- (4) Fundamentals of Gas Dynamics, Editor H.W. Emmons, Princeton University Press, 1958.
- (5) Alofs, D.J., "Performance of a dual-range cloud nucleus counter", J. Appl. Meteor. 17, 1286-1297 (1978).
- (6) Alofs, D.J., M.B. Trueblood, D.R. White, and V.L. Behr, "Nucleation experiments with monodisperse NaCl aerosols", J. Appl. Meteor. 18, 1106-1117 (1979).
- (7) The influence of jet fuel sulfur impurities on the hydration properties of jet fuel-generated combustion aerosols, P.D.Whitefield,M.Trueblood and D.E. Hagen, presented at the A.A.A.R. 10th annual meeting October 1991.
- (8) Alofs,D.J. and M.B. Trueblood, "UMR Dual Mode CCN Counter (Modes:CFD plus Haze)," J. Rech. Atmos. 15, n' 3-4, 219-223 (1981)
- (9) Hagen, D.E., M.B. Trueblood, and J. Podzimek, "Combustion Aerosol Scavenging", Atmos. Env. 25A, 2581 (1991).
- (10) Benard, D.J., McDermott, W.E., Pchelkin, N.R., and Bousek, R.R., "Efficient Operation of a 100 Watt Transverse Flow Oxygen-Iodine Chemical Laser", Appl. Phys. Letters 34, 40-41, (1979).
- (11) Richardson, R.J., Wiswall, C.E., Carr, P.A.G., Hovis, F.E., and Lilenfeld, H.V., "An Efficient Singlet Oxygen Generator For Chemically Pumped Iodine Lasers", J. Appl. Phys. 52, 4962-4969, (1981).
- (12) Oxygen Iodine Supersonic Technology Program, Part III - Management and Technical Proposal, MDRL/MDAC Report No. D9299-953003, June 1982.

- (13) Hagen, D.E., and D.J. Alofs, "A Linear Inversion Method to Obtain Aerosol Size Distributions from Measurements with a Differential Mobility Analyzer", Aerosol Sci. and Tech. 2, 465-475 (1983).
- (14) Whitefield P.D., D.E. Hagen and M.B. Trueblood, "A field Sampling of Jet Exhaust Aerosols." Particulate Science and Technology, (submitted August 1992)
- (15) H.R. Pruppacher and J.D. Klett Microphysics of Clouds and Precipitation, D.Reidel Publishing Co., Dordrecht, Holland 1978
- (16) RDA Memo 87-A/K-3-02-752 Particulates/Aerosols in Oxygen/iodine Lasers, P.G. Crowell, January 1989.